Australian Government

ansto

Nuclear-based science benefiting all Australians

The Australian Nuclear Science and Technology Organisation (ANSTO)

invites you to join us in Sydney, Australia for

The 20th International Workshop on ECR Ion Sources 25-28 Sept 2012

20th International Workshop

ECRIS 2012

Sydney, Australia 25 - 28 September

on ECR Ion Sources

Workshop topics:

Status of ECRIS performance ~ New developments ~ Plasmas and diagnostics Ion beam extraction and optics ~ Ion production ~ Beam transport ~ Pulsed beams ~ Radioactive beams ~ Charge breeding ~ Applications

Workshop date: 25th – 28th September

Organising committee:

Michael Hotchkis
Lista Choi (secretary)
David Button
Nikolai Lobanov, ANU
Rhiannon Still
Klaus Wilcken
Michael Zettinig

International Scientific Advisory Committee:

J Beijers, KVI, Netherlands
S Bogomolov, JINR, Russia
S Gammino, INFN-LNS, Italy
D Kanjilal, IUAC, India
H Koivisto, University Of Jyväskylä, Finland
T Lamy, LPSC, France
R Leroy, Pantechnik, France
C Lyneis, LBNL, USA
T Nakagawa, RIKEN, Japan
R Vondrasek, ANL, USA
P Spädtke, GSI, Germany
T Thuillier, LPSC, France
H Zhao, Institute Of Modern Physics, China

For further information please see the workshop website:

http://www.ansto.gov.au/ecris2012

Email: ecris2012@ansto.gov.au

Contents

Preface i
Contents . . . iii

Papers 1
TUXO01 – Coupling Microwave Power into ECR Ion Source Plasmas at Frequencies above 20 GHz . . . 1
TUXO02 – An Experimental Study of ECRIS Plasma Stability and Oscillation of Beam Current . . . 5
TUXO03 – Two-frequency Heating Technique for Stable ECR Plasma . . . 10
TUYO01 – Experimental Study of Temperature and Density Evolution During Breakdown in a 2.45 GHz ECR Plasma . . . 13
TUYO02 – Control of the Plasma Transversal Losses, Caused by MHD Instabilities, in Open Mirror Magnetic Trap of the ECRIS: Recent Experiments on SMIS 37 Setup . . . 18
TUYO03 – Secondary-electron-enhanced Plasma as an Alternative to Double/Variable-frequency Heating in ECRIS 22
TUYO04 – Neutral Gas Temperature Measurements of a Radio Frequency Micro-thruster . . . 25
TUZO02 – Detailed Investigation of the 4D Phase-Space of an Ion Beam . . . 30
TUZO03 – New Extraction Design for the JYFL 14 GHz ECRIS . . . 34
TUZO04 – Space Charge Compensation Measurements of Multicharged Ion Beams Extracted from an ECR Ion Source . . . 38
TUPP01 – Quantitative Determination of ^{146}Sm/^{147}Sm Ratios by Accelerator Mass Spectrometry with an ECR Ion Source and Linear Acceleration for ^{146}Sm Half-Life Measurement . . . 43
TUPP03 – Integration of a Third Ion Source for Heavy Ion Radiotherapy at HIT . . . 46
TUPP04 – Design of a Compact ECR Ion Source for Various Ion Production . . . 49
TUPP05 – Charge-breeding at the Texas A&M University Cyclotron Institute . . . 51
TUPP08 – Design Report of the AISHA Ion Source for Hadron Therapy Facilities . . . 54
TUPP10 – Operational Experience with the GTS-LHC Ion Source and Future Developments of the CERN Ion Injector . . . 57
TUPP12 – Design of Web-based Interface to RIKEN 28 GHz Super-conducting ECR Ion Source and the Future Plan . . . 61
TUPP13 – Development of Intense Proton ECR Ion Sources at IMP . . . 64
TUPP14 – Beam Experiments with the Grenoble Test Electron Cyclotron Resonance Ion Source at iThemba LABS 68
TUPP17 – Installation and Operation of a 28 GHz Gyrotron for the RIKEN Superconducting ECR Ion Source . 71
TUPP18 – DECRIS-5 Ion Source for DC-110 Cyclotron Complex Results of the First Tests . . . 74
WEXO02 – Recent Developments and Electron Density Simulations at the ATOMKI 14.5 GHz ECRIS . . . 77
WEXO03 – Numerical Modeling of Ion Production in ECRIS by using the Particle-in-Cell Method . . . 82
WEXO04 – Proton Beams Formation from Dense Plasma of ECR Discharge sustained by 37.5 GHz Gyrotron Radiation . . . 85
WEXO05 – Effect of Source Tuning Parameters on the Plasma Potential of Heavy Ions and its Influence on the Longitudinal Optics of the High Current Injector . . . 90
WEYO01 – The Einzel Lens Longitudinal Chopper . . . 95
WEYO02 – Experimental Results: Charge-state and Current-density Distribution at the Plasma Electrode of an ECR Ion Source . . . 101
WEYO03 – Ion Beam Extraction from Magnetized Plasma . . . 106
WEZO01 – Status of the SEISM Experiment . . . 111
WEZO02 – Design of new 18 GHz ECR for RIKEN RIBF . . . 114
WEZO03 – Recent Results of PHOENIX V2 and New Prospects with PHOENIX V3 . . . 117
WEPP02 – Relationship of Performance and RF Resonance Modes . . . 121
WEPP03 – Plasma Instability in the Afterglow of ECR Discharge Sustained in a Mirror Trap . . . 125
WEPP08 – Emittance Measurements for U Ion Beams Produced from RIKEN 28 GHz SC-ECRIS . . . 130
WEPP13 – Development Update of the LECR4 Ion Source - Dragon at IMP . . . 133
WEPP14 – An Advanced Injection System of Light Ions (AISLI) for Dielectric Wall Accelerator . . . 136
WEPP15 – Metal Ion Beam Production with Improved Evaporation Ovens . . . 140
WEPP16 – Experimental Studies on the ALISES Ion Source at CEA Saclay . . . 143
WEPP17 – A Multi-Sample Changer Coupled to an ECR Source for AMS Experiments . . . 146
THXO01 – Optimization of the New SC Magnetic Structure Design with a Hybrid Magnet . . . 149
THXO02 – Current Developments of the VENUS Ion Source in Research and Operations . . . 153
THXO03 – Recent RIKEN 28 GHz SC-ECRIS Results . . . 159

THYO01 – Operation of an ECRIS Charge State Breeder at TRIUMF 163
THYO02 – LPSC PHOENIX ECR Charge Breeder Beam Optics and Efficiencies 167
THYO03 – Design Status of ECR Ion Sources and LEBT for FRIB 172
THYO04 – Performance of the ANL ECR Charge Breeder with Low Mass Beams 177
FRXA01 – High Intensity Beam Production at CEA/Saclay for the IFMIF Project 182
FRXA02 – All Permanent Magnet ECR Ion Source Development and Operation Status at IMP 185
FRXA03 – Laser Ablation of Actinides into an Electron Cyclotron Resonance Ion Sources for Accelerator Mass Spectroscopy 190
FRYA01 – ECRISs at GANIL Today and Tomorrow 195
FRYA02 – Status of ECR Ion Sources for Carbon-ion Radiotherapy in Japan 200
FRYA03 – ECRIS Related Research and Development Work at JYFL and Some Future Prospects 203

Appendices **209**
List of Authors 209
Institutes List 213

COUPLING MICROWAVE POWER INTO ECR ION SOURCE PLASMAS AT FREQUENCIES ABOVE 20 GHZ

C. Lyneis, J. Benitez, M. Strohmeier, D. Todd, LBNL, Berkeley, CA, 94720, USA

Abstract

Electron Cyclotron Resonance (ECR) ion sources have been built to operate at frequencies from 5 GHz to 28 GHz and typically use a plasma chamber that serves as a multi-mode cavity. For small sources operating at 6 to 14 GHz cavity mode-like behavior has been reported. In these cavities the vacuum mode density is low enough that it may be that the RF power distribution can be understood in terms of excitation of a few modes. The large superconducting ECR ion sources, such as VENUS[1] operating at higher frequencies have a much greater mode density and very strong damping from plasma microwave absorption. In this type of source, how the RF is launched into the plasma chamber will strongly affect the microwave coupling and the chamber walls will be less important.

The VENUS source uses over-sized round waveguide excited in the TE_{01} to couple to the plasma, while most modern fusion devices use quasi-gaussian HE_{11} waves for injection into plasmas. In this paper we will describe the potential advantages of applying this technology to superconducting ECR ion sources as well as designs for doing so with VENUS.

INTRODUCTION

In an ECR ion source the microwave power couples to the electrons through electron cyclotron resonance heating. The electrons are confined by a solenoidal magnetic mirror in the axial direction and by a multipole field, typically a sextupole, in the radial direction. The combined magnetic fields produce a closed surface where electron cyclotron resonance frequency equals the applied microwave frequency. The coupling can be modeled in the case of very low plasma density and single particle models. [2,3] This is generally done by assuming a microwave field distribution that is independent of the plasma density. One approach used is to assume the microwave fields are those of an undamped microwave cavity and to then assume only a single mode is excited. [4] For a cylindrical cavity, the cavity modes can be calculated and the RF electric fields determined. The typical unloaded Q of such a cylindrical cavity with aluminum walls is in the range of 2000 to 4000. On the other hand the damping of the plasma can lower this Q_o significantly and this will decrease the RF stored energy and the resulting RF electric fields.

To date neither experimental measurements nor calculations using the best simulation codes can accurately predict the actual microwave field distribution or even the level of stored energy in a ECR ion source with plasma loading. It is difficult to probe either the plasma density or the RF field strength in an ECR ion source because if a probe is inserted into the chamber the hot electrons in the plasma will destroy it. With two microwave ports on the plasma chamber, both the reflected power on the input port and the transmitted out the second port can be measured. Since the stored microwave energy is proportional to the transmitted power, the relative stored energy versus time can be determined.[5] This was done with VENUS by injecting 18 GHz though the input port and detecting the transmitted power out the 28 GHz port. In Fig. 1 the time dependence of the reflected and transmitted microwave power is shown where the RF power is switched on at t equals 0 with zero plasma density in the chamber. The microwave fill time for the chamber is on the order of 1 μs while the plasma breakdown is on the order of 1 ms. At about 1 ms the plasma density increases rapidly and begins to load the cavity. At this point the transmitted power, which is proportional to the stored energy in the plasma chamber drops almost to zero as the plasma loading depresses it. At about 1.5 ms after some oscillations between the stored RF energy and the plasma density, the microwave fields reach a rough equilibrium. In the initial stage the empty plasma chamber acts as a high Q cavity (with a Q_o of a few thousand) and the high fields can produces a burst of hot electrons and ions in the preglow [6], but as the plasma loading builds up it drastically damps the RF stored energy by about 1/10 in this case. For CW operation, it is this reduced RF field

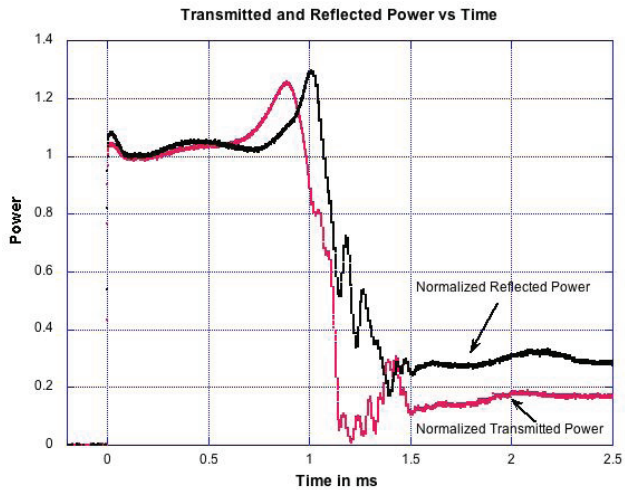

Figure 1: Time dependence of the reflected and transmitted 18 GHz power for the VENUS ECR ion source. At time t=0, the microwave power is switched on. As the plasma reaches maximum density at about 1 ms, the transmitted power decreases rapidly. Both reflected power and transmitted power are normalized to their initial values just after the power is switched on and before the plasma builds up.

ISBN 978-3-95450-123-6

Copyright © 2012 CC-BY-3.0 and by the respective authors

level that continues to heat the electrons. The strong plasma damping means that we cannot view plasma as a small perturbation on the RF fields.

The second difficulty with assuming individually exited cavity modes comes from the fact that as the plasma damps the modes, their bandwidth becomes much wider than the average mode spacing and therefore the RF power can be distributed across many modes simultaneously.[7,8] For a small source such as CAPRICE-14 GHz the average mode spacing is 17.5 MHz [9,10] and once the cavity Q is less than 230, the modes will overlap. For low density plasmas and weak microwave coupling, it is possible to see quasi-single mode behavior in a low frequency, 14 GHz, small volume, .54 l cavity like CAPRICE.[8] For a large superconducting source such as VENUS with an operating frequency of 28 GHz and a volume of 9 l the situation is quite different. Since the mode density scales as inversely with the product of the volume times the square of the microwave frequency, in VENUS the average mode spacing is only 160 kHz, so that hundreds of modes will be simultaneously excited. This means for the large volume, high frequency sources the cavity model with a single or few microwave modes excited is not realistic.[10] For these reasons, we describe below a different approach based on studying the field distribution produced by the antenna as it launches a RF into the cavity and we can look at the field strengths in the first pass absorption.

RF COUPLING IN ECR ION SOURCES AND PLASMA FUSION DEVICES

A number of different approaches including coaxial antennas have been used over the years to couple microwave power into the plasmas of high charge state ECR ion sources. [11,12] In recent years, the most common approach to couple power from a klystron or TWT microwave generator is to use an off-axis rectangular waveguide, extending slightly into the plasma chamber from the injection end. The waveguides are typical just terminated by square cut. The rectangular waveguide is excited with a single TE_{11} waveguide mode, which has its RF electric field transverse to the axial magnetic field of the source. The 18 GHz waveguide system in the VENUS source was initially made this way, but it was modified to use a tapered termination of the waveguide as can be seen in Fig. 2. The tapered cut significantly reduced the reflected power in steady state and may also have increased the local RF field strength on axis at the ECR zone.

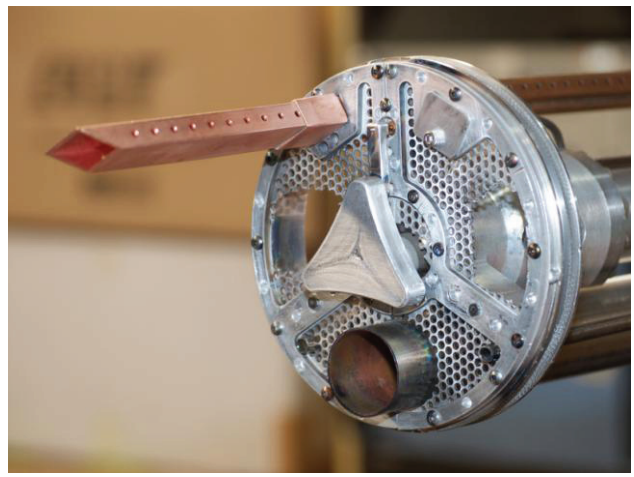

Figure 2: Plasma chamber injection system. Upper left shows the 18 GHz waveguide with a tapered termination. Bottom center is the 28 GHz waveguide injection. The triangular object in the center is the biased disk.

The 28 GHz microwave system for VENUS uses a transmission line that converts the TE_{02} mode produced by the 10 kW CW CPI gyrotron to a TE_{01} round waveguide mode, which is then transported about 4 meters and injected into the VENUS plasma chamber. The TE_{01} microwaves are launched through a simple terminated waveguide into the 9 l plasma chamber, which has a diameter of 144 mm and a length of 500 mm. This approach was chosen because TE_{01} mode has low attenuation. The working assumption was that the chamber walls would serve as a microwave cavity and the power would then couple effectively to the plasma. With this coupling the VENUS source has produced many record beams such as 11 mA of He^{2+}, 3 mA of O^{6+} and 440 μa of $^{238}U^{33+.}$ However, certain aspects of its tuning behavior indicate that the coupling of the 18 GHz power launched from a TE_{11} waveguide is more efficient than the coupling of the 28 GHz power launched from the round TE01 mode. This has prompted us to look into methods to modify and improve the launching of the 28 GHz power into VENUS.

Much of the technology used in the ECR ion source community has come from plasma fusion research including the Geller's first high charge state ECRI ion source, SUPERMAFIOS, which was a converted plasma fusion mirror device.[11] The gyrotrons and RF coupling methods developed for fusion test devices such as tokamaks and stellerators[13-16] offer exciting possibilities for ECRIS applications. In these machines the microwaves are converted for modes such as TE_{01} or TE_{02} into the HE_{11} mode before being launched into the plasma chamber. The HE_{11} mode is a quasi-gaussian polarized mode, which can be launched in a relatively narrow cone into the plasma chamber. This is described by Doane as follows: "The HE_{11} mode in a corrugated waveguide is in many respects ideal for use near plasma devices. Its radiation pattern from an open-ended waveguide has a narrow central beam containing 98% of

Copyright © 2012 CC-BY-3.0 and by the respective authors

ISBN 978-3-95450-123-6

the radiated power. The radiation is linearly polarized with virtually no cross-polarization. Since the field distribution of the HE_{11} mode inside a corrugated waveguide is a close approximation to a gaussian mode, the HE_{11} will couple efficiently to a free space gaussian mode."[14] The power distribution for the HE_{11} mode in a round waveguide is illustrated in the upper left panel of Fig. 3. This mode is linearly polarized as shown in the upper right panel. In contrast to this the power distribution of the TE_{01} mode now utilized in VENUS shows a field distribution with the electric field in a circular direction with zero power on axis as shown in the lower panel of Fig. 3 and the electric field lines are circular. In addition in VENUS the power is launched off-axis and rapidly expands due to the diffraction at the termination of the waveguide. In this case, the first pass absorption is likely to be minimal and the plasma heating relies on multiple reflections at the plasma wall to coupling power into the ECR zone. For right hand wave coupling in an ECR ion source a focused linearly polarized HE_{11} mode directed onto the ECR zone on axis should provide strong heating of the electrons transverse to the local magnetic field.

One of the major differences between the current fusion devices and ECR ion sources is that the fusion devices are circular so that the electrons can be heated in the direction of the toroidal field since there are no end losses, while ECR ion sources are mirror machines and only electrons with large ratio of transverse to longitudinal energy will be reflected by the solenoidal mirrors at injection and extraction. In fusion devices the RF is usually launched at 90 degrees to the toroidal magnetic field and either O-mode (ordinary) with the RF electric field in the same plane as the magnetic field or X-mode (extra-ordinary) with the RF electric field perpendicular to the local magnetic field is used. Due to the differences between the fusion devices and ECR ion source, the advantages of launching a pencil like beam with transverse polarization onto the central area of the ECR zone will need experimental verification.

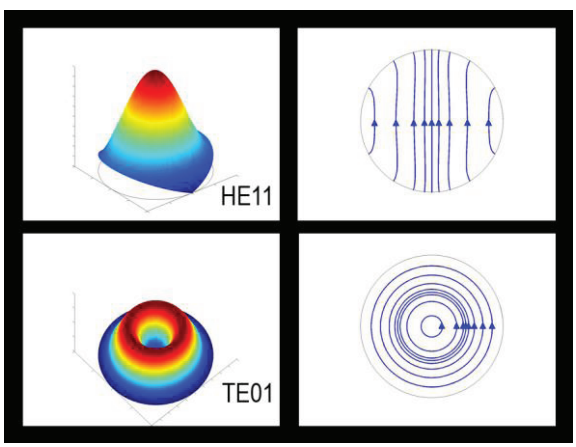

Figure 3: On the top, the power distribution for the Gaussian HE_{11} mode, which is linearly polarized and strongly peaked on axis, and on the bottom is the power distribution for the TE_{01} mode, which has a circular electric field pattern and zero power on axis and a maximum at about .5 times the waveguide radius.

APPLICATION TO VENUS

Various options are being explored to modify the existing 28 GHz transmission line and coupling system for VENUS, which is shown in Fig. 2, so that it can launch the microwaves in a HE_{11} gaussian like pattern to maximize the first pass absorption. Although several methods have been developed to convert TE_{01} into HE_{11}, the challenge is to find the best approach given the physical constraints of the present installation. One approach would be to use a waveguide snake[16] to convert the TE_{01} to TE_{11} and then use a corrugated waveguide to convert to HE_{11}. In principle, this could be installed in the waveguide used to transport the microwaves from the injection flange to the launch point in the plasma chamber. The advantage of this approach is that the existing high voltage break, microwave vacuum window, and set of two 90 degree corrugated bends could all be used since the conversion to HE_{11} would be made down stream of them. A preliminary analysis of this approach shows that a conventional waveguide snake would be too long to fit into the straight waveguide section. Recent developments of more advanced snakes may allow efficient conversion is a shorter length waveguide.[18] A second approach would be to modify the last 90 degree bend so that it has 40 degrees of corrugated waveguide followed by 50 degree of smooth waveguide bend, which will convert the TE_{01} mode to TM_{11}, which can then be converted to HE_{11} in the straight section prior to injection into the plasma chamber. While the smooth waveguide bend with a large radius can convert TE_{01} to TM_{11}, the radius in the existing system is relatively small and this may cause too much growth of the TE_{21}, which has an undesirable field distribution for coupling to the plasma.[14] Another approach might be to convert to HE_{11} in the waveguide section between the gyrotron and the existing HV break and then use quasi-optical mirrors to inject the Gaussian beam directly into the plasma chamber similar to the system on SMIS 37.[19]

Modification the microwave coupling for the 28 GHz power in VENUS to take advantage of the advances made in the plasma fusion community has the potential to significantly improve its performance and these techniques could also be employed on future Fourth Generation ECR ion sources, which are in the conceptual stage. [20]

REFERENCES

[1] D. Leitner , C.M. Lyneis, S.R. Abbott, D. Collins, R.D. Dwinell, M.L. Galloway, M. Leitner, D.S. Todd, Nucl. Instrum. Methods Phys. Res. B 235 486–493 (2005).

ISBN 978-3-95450-123-6

Copyright © 2012 CC-BY-3.0 and by the respective authors

[2] Y. Jongen, Proceedings 6th Int. Workshop on ECR Ion Sources (Berkeley, CA) p 238.
[3] H. Koivisto, Rev. Sci. Instrum. 70, JULY 1999 p 2979.
[4] D. Mascali, L. Neri, S. Gammino, L. Celona, G. Ciavola, N. Gambino, R. Miracoli, and S. Chikin, Rev. Sci. Instrum. 81, 02A334, (2010).
[5] V. Toivanen, O. Tarvainen, C. Lyneis, J. Kauppinen, J. Komppula, and H. Koivisto Rev. Sci. Instrum. 83, 02A306 (2012).
[6] Ivan V. Izotov, Alexander V. Sidorov, Vadim A. Skalyga, Vladimir G. Zorin,Thierry Lamy, Louis Latrasse, and Thomas Thuillier, IEEE Transaction of Plasma Science, Vol. 36 , 1494 (2008).
[7] C. Lyneis, J. Benitez, D. Leaner, J. Noland, M. Strohmeier, H. Kovisto, O. Tarvainen, Proceedings of ECRIS2010, p162.
[8] L. Celona, G. Ciavola, F. Consoli, S. Gammino, F. Maimone, D. Mascali, P. Spädtke, K. Tinschert, R. Lang, J. Mäder, J. Roßbach, S. Barbarino, and R. S. Catalano, , Rev. Sci. Instrum. 79, 023305 (2008).
[9] C.M. Lyneis, Proceedings of the XIII International Conference on Cyclotrons and their Applications, Vancouver, Canada, editors G. Dutto, M.K. Craddock, p 301 (1992).
[10] F. Consoli, L. Celona, G. Ciavola, S. Gammino, F. Maimone, S. Barbarino, R.S. Catalano, D. Mascali, Rev. Sci. Instrum. 79, 02A308.
[11] Geller R, 1996 *Electron Cyclotron Resonance Ion Sources and ECR Plasmas* (Philadelphia: Institute of Physics Publishing) p 211-215.
[12] D. Hitz, High Energy Phys. Nucl. Phys. 31, 123, (2007).
[13] V. Erckmann, H.P. Laqua, H. Maaßberg, N.B. Marushchenko, W. Kasparek and G.A. Müller, *Nucl. Fusion* 43 1313 (2003).
[14] J.L. Doane, Int. J. Electronics, Vol 53, No 6 573 585 (1982).
[15] M. Thumm, W. Kasparek, Fusion Engineering and Design, 26, 291-317.
[16] J.W. Radder, K. M. Likin, F.S.B. Andersen, D.T. Anderson, Int. J. Infrared Milli Waves 29, 360-372, (2008).
[17] M. Thumm, Int. J. Electronics, Vol 57, 1225-1246 (1984).
[18] G. G. Denisov, G. I.Kalynova, and D. I. Sobolev, Radiophysics and Quantum Electronics, Vol. 47, No. 8, (2004).
[19] V Skalyga, V Zorin, I Izotov, S Razin, A Sidorov and A Bohanov, Plasma Sources Sci. Technol. 15 (2006) 727–734.
[20] C. Lyneis, P. Ferracin, S. Caspi, A. Hodgkinson, and G. L. Sabbi Rev. Sci. Instrum. 83, 02A301 (2012).

Copyright © 2012 CC-BY-3.0 and by the respective authors

ISBN 978-3-95450-123-6

AN EXPERIMENTAL STUDY OF ECRIS PLASMA STABILITY AND OSCILLATION OF BEAM CURRENT*

O. Tarvainen#, V. Toivanen, H. Koivisto, J. Komppula, T. Kalvas, University of Jyväskylä, Finland
C. M. Lyneis, M. Strohmeier, LBNL, Berkeley, CA 94720, USA

Abstract

The stability of ion beams extracted from ECR ion sources has been studied with the VENUS ion source at LBNL and the 14 GHz A-ECR at JYFL. Oscillations of the beam current in ~ kHz range are characterized with the Discrete Fourier transform. The effect of the ion source tuning parameters on the frequency and amplitude of the oscillations of various charge states is discussed. It was found that double frequency heating affects the oscillation frequency, the biased disc can be used to mitigate their amplitude, increasing B-minimum results to pronounced instabilities and operating the ion source with significantly higher mirror ratio than suggested by ECRIS scaling laws yields the most stable ion beams. It is argued that the observed beam current fluctuations are correlated with plasma processes.

INTRODUCTION

The stability of the ion beams extracted from ECR ion sources is important for accelerators, especially for high power linacs (e.g. FRIB) due to problems arising from fluctuating beam power and spill, medical applications (e.g. carbon therapy) and industrial applications. The stability of ion beams extracted from an ECRIS is determined by two factors; the long-term stability and rapid oscillations of the beam currents on a millisecond scale. This experimental study focuses on the fast oscillations presumably driven by plasma mechanisms.

EXPERIMENTAL RESULTS

The experiments were performed with the superconducting VENUS ECR ion source (see e.g. [1]) at LBNL and A-ECR type 14 GHz ECRIS at JYFL [2]. The temporal behavior of the beam currents for different charge states of oxygen (O^{2+} thru O^{7+}) was recorded with a resistor directly at the Faraday Cup. The VENUS microwave coupling system has both 18 GHz and 28 GHz waveguide antennas, which are used to inject power into the plasma chamber. The VENUS waveguide system has recently been reconfigured to measure cross coupling of 18 and 28 GHz with diode detectors as described in Ref. [3]. This feature was used for monitoring the 28 GHz power coupled out (transmitted) from the chamber through the 18 GHz waveguide port in order to correlate beam current fluctuations with properties of microwave-plasma coupling. The schematic of the experimental setup for VENUS is presented in Fig. 1. The setup used with the JYFL A-ECR is similar with minor exceptions. The beam stability data analysis procedure and experimental results are described hereafter.

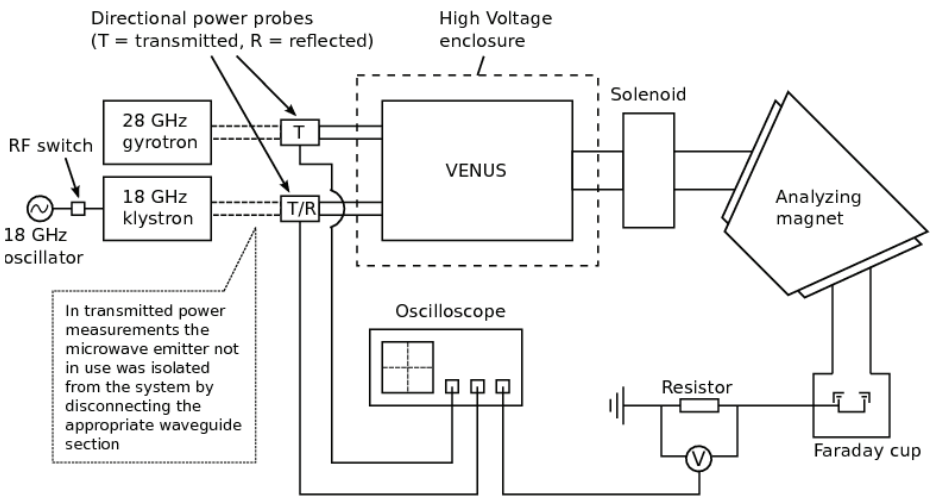

Figure 1: A schematic presentation of the experimental setup used with VENUS.

* This work has been supported by the EU 7th framework programme "Integrating Activities - Transnational Access", project number: 262010 (ENSAR) and by the Academy of Finland under the Finnish Centre of Excellence Programme 2006 - 2011 (Nuclear and Accelerator Based Physics Research at JYFL).
# olli.tarvainen@jyu.fi

Data Analysis

The raw signals recorded from the Faraday cup in time domain were transformed to frequency domain with Discrete Fourier Transform (DFT) for further analysis. With VENUS the results were recorded with an oscilloscope (250 kHz sampling rate) and analyzed offline

ISBN 978-3-95450-123-6

Copyright © 2012 CC-BY-3.0 and by the respective authors

with a Mathematica™ script. A dedicated, LabView-based, measurement and online analysis program [4] was developed for monitoring the beam current stability of the JYFL 14 GHz ECRIS and signals were recorded with a National Instruments data acquisition card. The sampling rate was set to 100 kHz. The given amplitudes correspond to 2σ standard deviation of the time-resolved beam current i.e. rogue points are eliminated by rejecting ~5% of the data points. Frequencies appearing in background, e.g. 50 Hz, and their first harmonics have been eliminated during the analysis. Figure 2 shows a representative example of O^{6+} beam current signal recorded with the JYFL 14 GHz ECRIS together with the corresponding Fourier spectrum. The source was operated with pure oxygen and 650 W of power at 14 GHz resulting to average O^{6+} current of 175 µA and a fluctuation of +8.6 /-12.4 µA i.e. total of 12 % at 860 Hz.

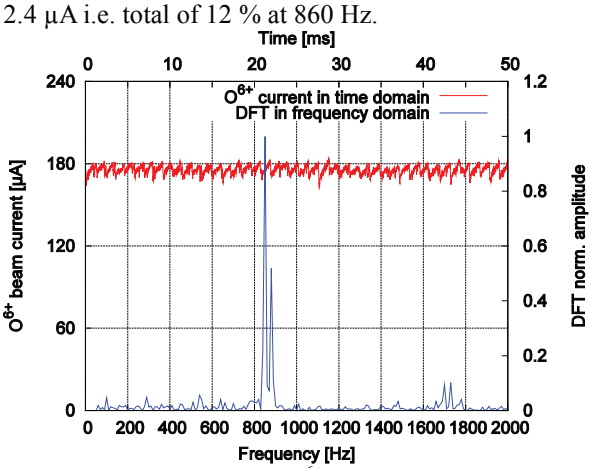

Figure 2: An example of O^{6+} beam current signal and corresponding Fourier spectrum (JYFL A-ECR).

Results

The effect of ion source tuning parameters on the frequency and amplitude of the beam current oscillations has been studied rather extensively and this paper can only summarize the results shortly. Figure 3 illustrates the range of oxygen beam current oscillation (primary) frequencies and amplitudes recorded with the JYFL A-ECR as the source tuning parameters i.e. power, neutral gas feed rate, bias disc voltage and magnetic field were varied. The amplitude of the beam current oscillation varies between 1 - 65 % depending on the tune, the typical value being ~10%. The range of oscillation frequencies is 30 Hz - 1.4 kHz. The corresponding numbers for VENUS are 1 - 25 % and 200 Hz - 6.8 kHz. The lower limit is defined by the duration of the recorded current signal. Beam current monitoring methods applied regularly for the ion source tuning at JYFL fail to detect oscillations at frequencies > 50 Hz due to signal averaging, which highlights the usefulness of the online analysis tool.

It was observed with both VENUS and the JYFL A-ECR that tuning parameters of the ion source affect the characteristics of the beam current oscillations. As an example Fig. 4 shows the amplitude and frequency for O^{6+} beam as a function of power. In the given examples the O^{6+} current increased from 34 µA to 175 µA (A-ECR) and from 190 µA to 980 µA (VENUS) with increasing power. Both, the amplitude and the frequency of the beam current oscillations tend to increase with the power, which has been observed also by Taki et. al. [5].

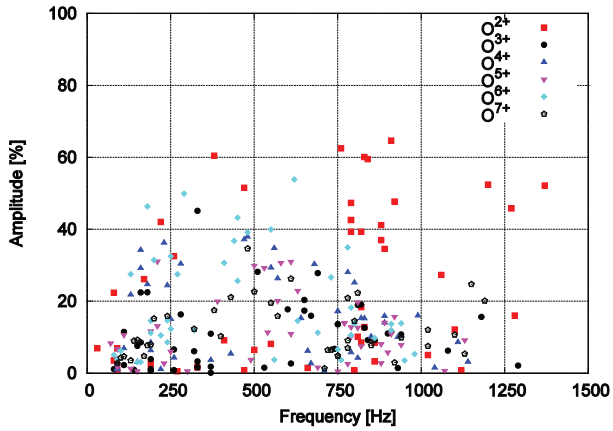

Figure 3: The range of beam current oscillation amplitudes and frequencies (JYFL 14 GHz ECRIS).

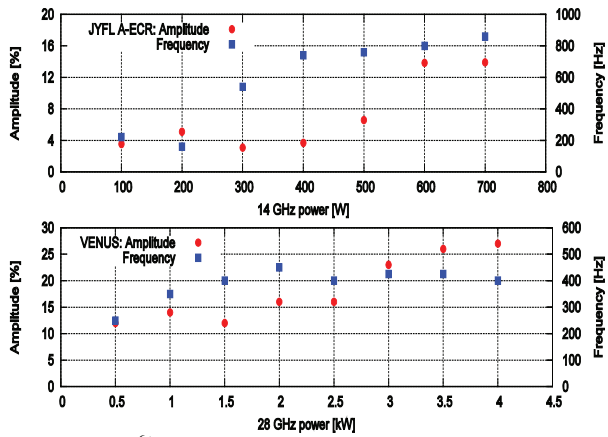

Figure 4: O^{6+} current oscillation as a function of power.

Furthermore, it was observed that (a) the neutral gas pressure had very little effect on the instability characteristics (JYFL A-ECR) although the total extracted current changed by a factor of 2 during the sweep, (b) adjusting the biased disc voltage affects mainly the amplitude of the ripple (VENUS & JYFL A-ECR) offering a tool to mitigate beam current fluctuations and (c) operating the ion sources with a flat magnetic field profile typically yields very unstable beams more than doubling the oscillation amplitude in comparison to magnetic field profiles with steep gradient at the resonance.

The typical charge state dependence of the beam current oscillation amplitude is depicted in Fig. 5. The amplitude of the periodic oscillations is usually observed to increase with the charge state. The ion sources were tuned for O^{6+} in the given example.

Copyright © 2012 CC-BY-3.0 and by the respective authors

ISBN 978-3-95450-123-6

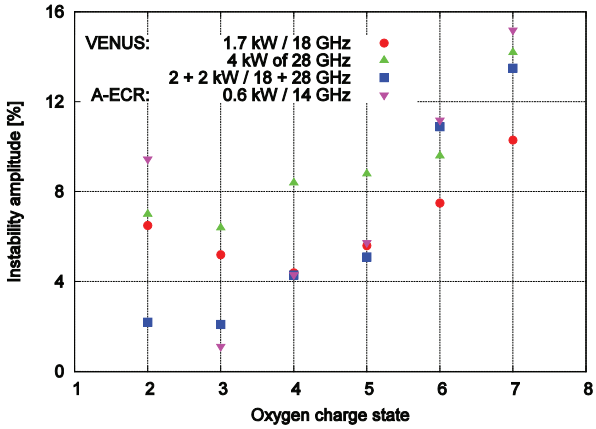

Figure 5: Typical charge state dependence of the beam current oscillation amplitude.

The data in Fig. 5 reveals yet another trend. It was observed that two-frequency heating often improves the stability of the low charge states while the oscillations of high charge states remain virtually unaffected. In the case of oxygen the stability was observed to improve for charge states ≤ 5+ corresponding to M/Q values ≥ 3.2. A representative example of beam current signals of O^{3+} and O^{6+} (measured with VENUS) demonstrating the effect of the secondary frequency is shown in Fig. 6. It is evident that the stabilizing effect is more pronounced for low charge state (O^{3+}).

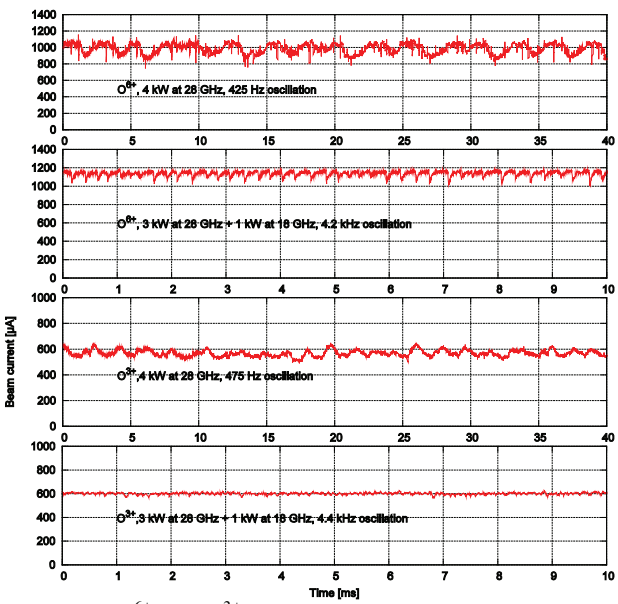

Figure 6: O^{6+} and O^{3+} beam current signals in single and double frequency heating modes of VENUS.

Figure 6 demonstrates that also the oscillation frequency of the beam current increases when double frequency heating is applied making it even more difficult to detect the fluctuation with traditional beam current monitoring methods often filtering and averaging the signals. The increase of the beam current oscillation frequency due to double-frequency heating was observed to be significant in the case of VENUS as further illustrated in Fig. 7. The frequency of the periodic oscillations of O^{6+} beam current increases abruptly from ~ 400 Hz to several kHz with increasing power at secondary frequency (18 GHz) added on top of 3 kW at primary frequency (28 GHz). The average O^{6+} beam current was observed to increase from 920 μA (3 kW of 28 GHz) up to 1170 μA corresponding to 1.5 kW of 18 GHz power + 3 kW of 28 GHz. Similar, although not as pronounced, trend was observed also with the JYFL A-ECR operated with 14 + 11.56 GHz. Increasing the power at 11.56 GHz, added onto 500 W at 14 GHz, from 10 W to 200 W the (primary) frequency of the current oscillation increased from 790 Hz to 1.4 kHz.

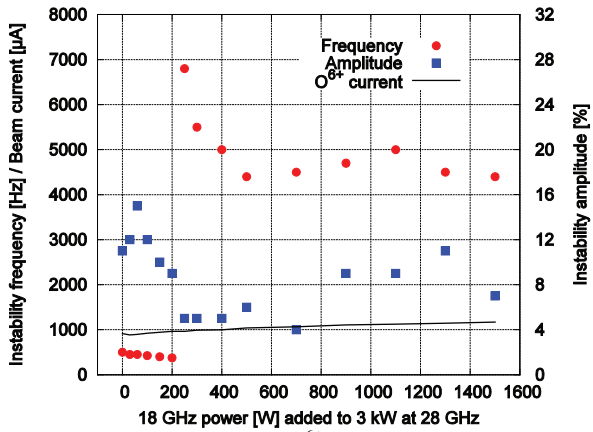

Figure 7: Characteristics of O^{6+} beam current oscillations in double frequency heating mode of VENUS.

For VENUS the most stable setting was found when operating in "high-B mode" i.e. with 18 GHz microwave frequency at field profile optimized for 28 GHz microwave radiation. With the JYFL A-ECR the most stable beams were observed with 11.5 GHz after scaling the injection and extraction mirror ratios to correspond values typical for 14 GHz operation. Table 1 summarizes these observations. The injection, extraction and radial mirror ratios, R, are defined as B_{max}/B_{ECR}.

Table 1: Comparison of Beam Current Oscillation Amplitudes for Different Magnetic Field Profiles

Description	$R_{inj}/R_{ext}/R_{rad}$	O^{6+} amplitude [%]
VENUS 1.7 kW / 18 GHz	3.4 / 2.3 / 2.0	**7.5**
VENUS "high-B" 2 kW / 18 GHz	5.3 / 3.3 / 3.5	**2.2**
JYFL A-ECR 300 W / 14 GHz	4.2 / 2.0 / 2.2	**12.1**
JYFL A-ECR 300 W / 14 GHz	3.7 / 1.7 / 2.2	**3.8**
JYFL A-ECR 300 W / 11.5 GHz	4.3 / 2.0 / 2.7	**3.1**

ISBN 978-3-95450-123-6

Copyright © 2012 CC-BY-3.0 and by the respective authors

DISCUSSION

Changing pattern of beam current oscillations with the ion source settings (at constant total extracted current) suggests that the mechanisms driving the fluctuations are plasma effects. The contributions of the extraction region (plasma meniscus) and beam optics, which are unknown at this time, are a subject of a further study. Evidence of plasma oscillations, synchronized with the beam current fluctuations of VENUS, was observed with dual-port diagnostics studying temporal behaviour of the transmitted and reflected power signals [3]. Figure 8 shows an example of O^{6+} current and transmitted power signal, measured with 4 kW forward power at 28 GHz. The transmitted power and extracted beam current oscillate in phase at 425 Hz suggesting that the plasma properties affecting the microwave coupling and plasma oscillations are linked together. Furthermore, it was observed with 18 GHz that reflected and transmitted powers oscillate in phase i.e. peak of transmitted power corresponds to peak of reflected power. The high frequency ripple of the transmitted power at ~ 40 kHz is due to gyrotron power supply.

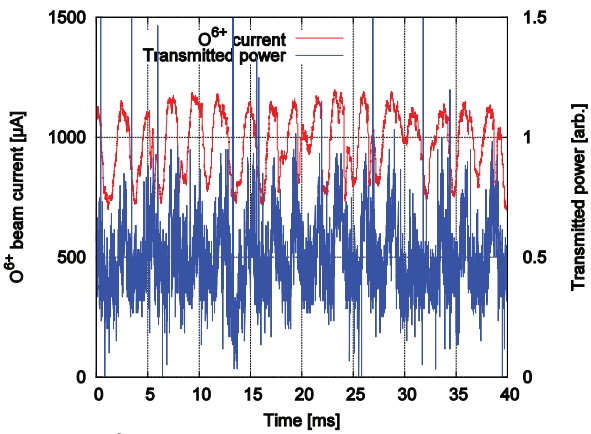

Figure 8: O^{6+} current and 28 GHz transmitted power exhibiting oscillations at 425 Hz. The forward power was observed to fluctuate only at ~ 40 kHz frequency.

Identifying mechanisms causing perturbations of the beam current is challenging. Instabilities are often categorized to (1) kinetic instabilities stemming from the anisotropy of the electron energy distribution function (EEDF) (see e.g. [6,7]) and (2) MHD instabilities driven by the topology of the magnetic field (see e.g. [8-10]). Anisotropic EEDF is prone to kinetic electron cyclotron instabilities. The threshold for the onset of the instability depends on the ratio of the hot electron density to the cold electron density and the difference in their respective temperatures. The existence of kinetic instabilities in ECRIS plasmas has been confirmed by measuring bursts of electrons and bremsstrahlung during the afterglow [11]. MHD-instabilities can lead to observable fluctuation of particle losses e.g. beam current. MHD instabilities are effectively suppressed in minimum-B confinement structures in which the magnetic field increases in radial direction i.e. $\partial B/\partial r \geq 0$ corresponding to concave curvature of the field lines. The superposition of solenoid and sextupole field does not fully satisfy the given condition. The configuration is prone to MHD instabilities in the spatial region where the radial increase of the sextupole field does not overcome the radial decrease of the solenoid field i.e. plasma confined by the field lines intercepting the surface defined by the "minimum-B ring". This region is depicted in Fig. 9 in which the cross section where $\partial B/\partial r$-value is negative has been plotted for the JYFL A-ECR at the plane exactly between the solenoids. Also the ECR-surface is depicted in the figure in order to show that the cross-sectional area where MHD-stability condition is not fulfilled is about 4.5 % of the area defined by the resonance zone. In 3D the minimum-B surface defines nearly ellipsoidal volume prone to MHD-instabilities. It is emphasized that the value of $\partial B/\partial r$ is small enough for diamagnetic effect to shift the minimum-B depending on the spatial distribution of electrons and their energy.

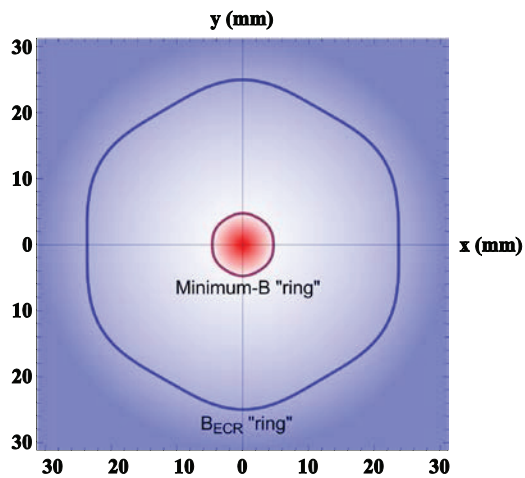

Figure 9: Magnetic field curvature (JYFL A - ECR) at the plane between the solenoids. Red indicates $\partial B/\partial r < 0$, blue $\partial B/\partial r \geq 0$. The minimum -B "ring" and ECR- surface are shown with solid lines.

The magnetic field topology alone does not guarantee the appearance of MHD instabilities. The condition for magnetohydrodynamically "quiet" plasma can be written as *particle pressure* << *magnetic pressure* i.e. $n_e kT_e << B^2/2\mu_0$ where the left hand side corresponds to the energy content of plasma (in J/m^3). This implies that (a) similar to kinetic instabilities the onset of MHD instabilities depends on the heating rate of electrons and (b) increasing the magnetic field strength i.e. operating the ion source in "high-B mode" [12] allows one to reach higher plasma density without suffering from instabilities or, alternatively, to mitigate instabilities at given plasma density. In practice it has been observed that magnetic mirror confinement structures start exhibiting MHD instabilities when the particle pressure reaches ~ 1% of the magnetic pressure [13].

The increase of the beam current oscillation frequency with microwave power suggests that the fluctuation

Copyright © 2012 CC-BY-3.0 and by the respective authors

ISBN 978-3-95450-123-6

mechanism is related to the rate of energy transfer to plasma electrons. On the other hand, the decrease of the beam current oscillation amplitude at high mirror ratio suggests that the magnetic field configuration plays a crucial role. In this view it is especially important to increase the radial field to minimize the volume where the radial decrease of the solenoid field overcomes the radial increase of the sextupole field. Dedicated experiments addressing this point could be conducted in the future with the VENUS ion source operating at 18 GHz. MHD-instabilities could be presumably eliminated by developing an ECRIS based on a true minimum-B configuration, e.g. the proposed ARC-ECRIS reviewed in Ref. 14.

In this study the focus has been in understanding the nature of the instabilities and the examples shown do not represent the optimum stabilities that can be achieved with careful tuning of VENUS or the JYFL A-ECR. Our future plans include measuring the effect of beam current stability on the transmission of the beam line and cyclotron at JYFL [15], studying the distribution of beam current oscillations in the beam, studying the stability of heavier element beams and correlating the beam current oscillations with plasma instabilities through different diagnostics.

REFERENCES

[1] D. Leitner, C. M. Lyneis, T. Loew, D. S. Todd, S. Virostek, and O. Tarvainen, Rev. Sci. Instrum., 77, 03A302 (2006).
[2] H. Koivisto et al., Nucl. Instr. and Meth in Phys. Res., B 174, (2001), p. 379.
[3] J. Benitez et al., Rev. Sci. Instrum., 83, 02A311, (2012).
[4] V. Toivanen, unpublished, executable program available online at http://users.jyu.fi/~vialtoiv/shared/beam-n-spectr/
[5] G. S. Taki, P. R. Sarma, A. G. Drentje, T. Nakagawa, P. K. Ray and R. K. Bhandari, High Energ. Phys. Nuc., Vol. 31, Supp. I, (2007), p. 170.
[6] A. G. Shalashov, A. V. Vodopyanov, S. V. Golubev, A. G. Demekhov, V. G. Zorin, D. A. Mansfeld, and S. V. Razin, JETP Letters, 2006, Vol. 84, No. 6, pp. 314–319
[7] Golubev S. V., Shalashov A. G. Phys. Rev. Lett. 99, 205002, (2007).
[8] J. Berkowitz, K.O. Friedrichs, H. Goertzel, H. Grad, J. Killeen and E. Rubin, in Peaceful Uses of Atomic Energy, Proc. 2nd Intl. Conf. (Geneva, 1958), Vol. 31, UN, New York, (1958), p. 171.
[9] M.S. Ioffe, R.I. Sobolev, V.G. Tel'kovskii and E.E. Yushmanov, Sov. Phys. - JETP 12, (1969), p. 1117.
[10] J.B. Taylor, Phys. Fluids, 6, (1963), p. 1529.
[11] I. Izotov et al. submitted to Phys. Plasmas, (2012).
[12] T.A. Antaya and S. Gammino, Rev. Sci. Instrum., 65 (5), (1994), p. 1723.
[13] M. Tuszewski, D. Price, M.A. Lieberman, R. Bravenec, K. Doniger, C. Hartman and A.J. Lichtenberg, Nucl. Fusion, 19, (1979), p. 1244.
[14] H. Koivisto, P. Suominen, O. Tarvainen and P. Spädtke, Rev. Sci. Instrum. 83, 02A312, (2012).
[15] V. Toivanen et al. to be submitted, (2012).

ISBN 978-3-95450-123-6

Copyright © 2012 CC-BY-3.0 and by the respective authors

TWO-FREQUENCY HEATING TECHNIQUE FOR STABLE ECR PLASMA

A. Kitagawa, T. Fujita, M. Muramatsu, NIRS, Inage, Chiba 263-8555, Japan
S. Biri, R.Racz, ATOMKI, Debrecen, Hungary
Y. Kato, K. Yano, Osaka Univ., Suita, Osaka 565-0871, Japan
N. Sasaki, W. Takasugi, Accelerator Engineering Corporation (AEC), Inage, Chiba 263-0043, Japan

Abstract

Two frequency heating technique was studied to increase beam intensities for highly charged ions. The observed dependences on microwave power and frequency suggested this technique improves plasma stability but it requires precise frequency tuning. Although the mechanism is not clear, a high power travelling tube amplifier is promising for more improvement.

INTRODUCTION

In order to accelerate various ion species for basic experiments in e.g. biomedical and material science, physics and chemistry, two ECR ion sources and one PIG ion source are installed in the Heavy Ion Medical Accelerator in Chiba (HIMAC) at the National Institute of Radiological Sciences (NIRS)[1]. Efforts to extend the range of ion species are continuously devoted, but more intense beams in excess of the present performance are desired for heavier ions like Xe or ions made from solid materials like Sn. In addition, a few carbon-ion radiotherapy facilities plan uses of some different ion species for fundamental researches. Since such experiments will be given a lower priority than the treatment, the diversion of existing hardware is expected. In the case of a typical hospital-specified facility, a charge-to-mass ratio as the injection condition into a linac is around 1/3. It means higher charge state ions are also required. For example, Ar^{13+} is required for some biological experiments.

Feeding RF power into an ECRIS at two frequencies was initiated by ECR pioneers Jongen and Lyneis in Berkeley, and some years later more successfully by Xie and Lyneis again in Berkeley[2]. So-called 'Two-frequency heating technique' has advantages; it is effective for any kinds of ion species, no modification of existing structure is necessary, and it is coexistent with almost other techniques. In early stages of our development, the enhancement of plasma region at different ECR zones was observed by the shapes of visible radiations[3]. The output currents had great dependence on additional microwave frequency[4]. However, the limited maximum power and bandwidth of an additional microwave constricted more detailed experiments.

A travelling wave amplifier system (TWT) recently has a capacity to feed larger power. A TWT with the frequency range from 17.75 to 18.25GHz and the maximum power of 700W was added to an 18 GHz ECR ion source called 'NIRS-HEC' with a krystron amplifier system (KLY) with a maximum power of 1500 W in 2007, then we studied the phenomena of two-frequency heating[5]. Table 1 shows maximum records of output currents of NIRS-HEC without two frequency heating technique. The underlined output currents were obtained with the afterglow technique. The output currents for ion species indicated in Italic have not routinely achieved the intensity requirement. The details of development on NIRS-HEC had been described in Ref. [6]

Table 1: Output Currents of the 18 GHz ECR Ion Source, NIRS-HEC Without Two Frequency Heating Technique

Ion	Ar		Fe	Co	Ni	*Ge*	*Kr*	*In*	*Xe*
m	40		56	59	58	74	84	115	132
q	8	13	9	9	10	28	15	20	21
I (eμA)	1100	20	400	160	100	*50*	*200*	*140*	*200*

DEPENDENCE ON MICROWAVE POWER

Dependence of Plasma Stability on Microwave Power

A beam intensity of highly charge state ions usually depends on the microwave power under a well-optimised condition. However, when the power increases, the plasma shows instability and it is difficult to keep. Figure 1 shows an example of plasma instability in the pulse shape of an extracted beam of Xe^{21+}. The left, centre, and right figures are obtained at the microwave power of 480, 720, and 960 W by KLY, respectively.

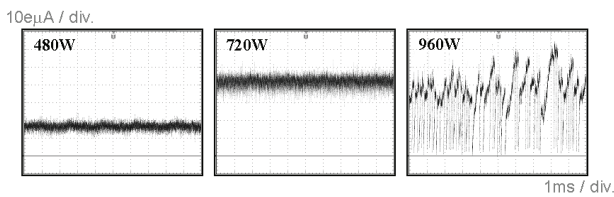

Figure 1: Example of plasma instability in the pulse shape of an extracted beam.

When an additional microwave is added in the above situation, the plasma instability is improved at larger microwave power obtained by the mixture of two different frequency microwaves.

Dependence of Beam Intensity on Microwave Power

Figure 2 shows the dependence of the beam intensity of Ar^{13+} on microwave power. A triangle, rectangle, and

Copyright © 2012 CC-BY-3.0 and by the respective authors

ISBN 978-3-95450-123-6

circular symbols mean a single KLY, a single TWT, and a sum of KLY and TWT, respectively. At first, all operation parameters like the mirror magnetic fields, the gas flows of Ar and O_2, the extraction voltage and distance of electrodes, the biased disk voltage, and so on were optimised by the single KLY. Then the microwave from TWT was added and the frequency of additional microwave was precisely optimised under the fixed conditions. The total of microwave power mostly dominated the beam intensity. It seems that the balance of KLY and TWT is not so effective. 792 W by the single KLY, 802 W by the sum of 602 W KLY and 200 W TWT, and 793 W by the sum of 552 W KLY and 241 W TWT gave almost same currents, 21.0, 17.7, and 19.5 eμA indicated in the dotted ellipse in Figure 2.

At the small KLY power, the measurement value is decreased from the proportional line. It is reasonable that the optimised additional frequency is not suitable for the single operation.

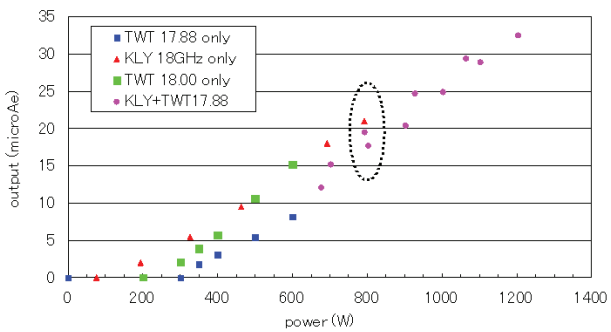

Figure 2: Dependence of beam intensity on microwave power.

DEPENDENCE ON MICROWAVE FREQUENCY

Dependence of Beam Intensity on Microwave Frequency

Figure 3 shows the dependence of the beam intensity of Ar^{13+} on microwave frequency in the same condition as Figure 2. The dependence on the frequency of single microwave by TWT makes a peak at 18 GHz. The result suggests the source was well optimised at 18 GHz. The dependence on the frequency of additional microwave by TWT has some peaks. Figure 2 was measured at 17.88 GHz. It is noted that the mixture of 18GHz KLY and 18GHz TWT gave no improvement and the power exceeded by the power limit by the single KLY also showed instability.

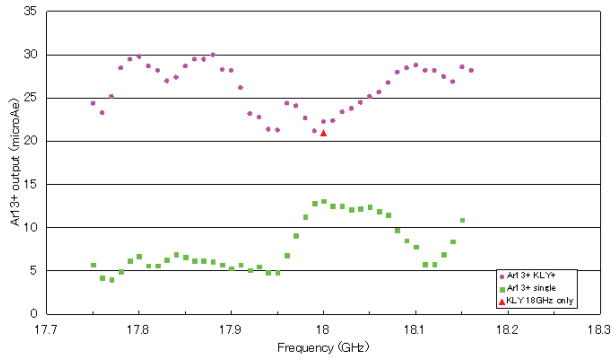

Figure 3: Dependence of the beam intensity on microwave frequency.

When the operation parameters are changed, it is guessed that the coupling efficiency between the microwave and the plasma is changed. It is natural that the optimised frequency of additional microwave is also changed. We searched another optimum condition (B) from the original condition (A) and measure the dependence on microwave power and frequency. Figure 4 shows both of dependences at the condition (A) and (B). The major difference between (A) and (B) was the mirror magnetic field. The mirror field at the extraction side of (B) was about 2.5 % lower than (A). The maximum currents of Ar^{13+} were same as both conditions. However, the optimum frequencies were different at 17.88 GHz for (A) and 18.08 GHz for (B).

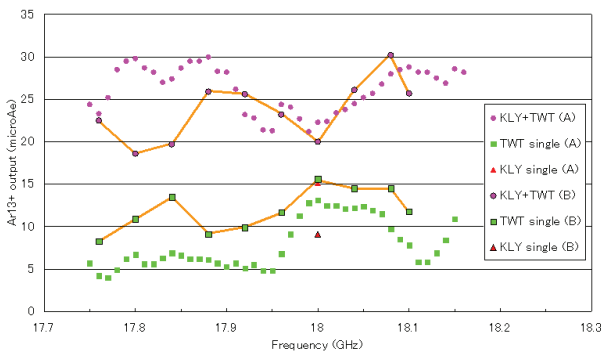

Figure 4: shows both of dependences at the condition (A) and (B).

The dependence on the microwave power under (B) shows the left figure of Figure 5. The large difference from (A) is that the beam intensity of the single KLY were lower than one of the single TWT. It seems that the coupling efficiency of 18GHz KLY microwave and the plasma under (B) decreased from (A) almost 50 %. If this efficiency coefficient is taken account, the tendency is similar as the previous one shown in the right figure of Figure 5.

Copyright © 2012 CC-BY-3.0 and by the respective authors

ISBN 978-3-95450-123-6

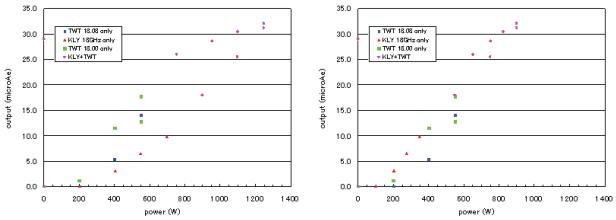

Figure 5: Dependence of beam intensity on microwave power.

In order to obtain better improvement, the larger microwave amplifier with enough wide bandwidth is necessary. Since a few % of bandwidth is required from our experiences, a klystron amplifier is not suitable as an additional microwave amplifier. The performance of a solid state amplifier is increasing year by year, but it still does not have enough cost effectiveness. A travelling wave tube amplifier is only a solution of two frequency heating technique at present. In our situation, the existing 700 W system is not enough for almost cases. So we are developing a new amplifier with a maximum power of over 1 kW. The amplifier will be installed in March 2013.

DISCUSSION

It is usually considered that the plasma instability of ECR heating plasma with a minimum B structure is not magnetohydrodynamic instability called 'macroscopic instability', but 'microscopic instability' like velocity space instability. Especially, in an ECR ion source for the production of highly-charged ions, a great deviation of electron energy distribution from Maxwell-Boltzmann distribution and anisotropy of its velocity distribution may adversely affect the plasma stability. The additional microwave with a different frequency may cause various modes of waves and also causes unexpected resonant absorptions as an origin of microscopic instability. For example, when the 14 GHz microwave penetrated through the 18 GHz resonance zone which surrounded 14 GHz plasma, the plasma instability grew with increasing 18 GHz microwave power. It is likely that the 14 GHz microwave was disturbed by the dense plasma maintained with 18 GHz microwave. In the case of lower 18 GHz microwave power, a similar phenomena was not appeared. Although the interference in two far discrete frequency microwaves shows the complex phenomena, it is curious that an additional microwave with a well-tuned close frequency supports the stability of plasma.

Many reports pointed the importance of fine tuning of microwave frequency, for example in Ref. [9]. A detailed study on frequency tuning effects was performed by INFN, GSI, and JYFL group[10-13]. Here the emphasis in the explanation was set to the RF properties of the plasma chamber. The authors' another work also gave similar results for more simple system[14]. On the other hand, a typical ECR ion source has a steep gradient of magnetic field. One percent of frequency change gives almost no spatial difference less than one mm. It suggests that the optimising frequency of additional microwave displays behaviour different from the cavity mode of chamber in the case of two frequency heating technique. From the comparison between the X-ray photographs and spatial distribution of the simulated warm electron component of the plasma, the highly charged ions probably occupy much larger volume around the resonance zone than the ionising electrons [15] and collect cold electrons due to quasi-neutrality. In the future these spatial distributions will be taken into account for the frequency tuning. If it is supposed that the coupling of additional frequency alleviates the deviation and anisotropy and results in the improving the instability, it is expected that optimised multiple frequencies make more favourable condition.

REFERENCES

[1] A. Kitagawa *et al.*, Rev.Sci.Instrum. **83**, 02A332 (2012).
[2] Z. Q. Xie *et al.*, Proc. of the 12th International Workshop on ECRIS, Wako, INS-J-182 (1995), p.24.
[3] A. Kitagawa *et al.*, Rev.Sci.Instrum. **71**, 1061 (2000).
[4] A. Kitagawa *et al.*, Proc. of European Particle Accelerator Conf., Wien, 2000, p.1607.
[5] A. Kitagawa *et al.*, Proc. of the 18th International Workshop on ECRIS, Chicago, 2008, p.92.
[6] A. Kitagawa *et al.*, Proc. of the 14th International Workshop on ECRIS, Geneva, 1999, p.23.
[7] M. Muramatsu *et al.*, Rev. Sci. Instrum. **76**, 113304 (2005).
[8] A.G. Drentje, *et al.*, IEEE Trans. Plasma Sci., Vol.**36**, No.4, 1502 (2008).
[9] P. Sortais, *et al.*, Proc. of the 12th International Workshop on ECRIS, Wako, 1995, p.44.
[10] L. Celona, *et al.*, Rev. Sci. Instrum. **79**, 023305 (2008).
[11] V. Toivanen, *et al.*, Rev. Sci. Instrum. **81**, 02A319 (2010).
[12] D. Mascali, *et al.*, Rev. Sci. Instrum. **81**, 02A334 (2010).
[13] F. Maimone, *et al.*, Rev. Sci. Instrum. **82**, 123302 (2011).
[14] Y. Kato, *et al.*, Rev. Sci. Instrum. **75**, 1470 (2011).
[15] R. Racz, *et al.*, Plasma Sources Sci. Technol. **20**, 025002 (2011).

Copyright © 2012 CC-BY-3.0 and by the respective authors

ISBN 978-3-95450-123-6

EXPERIMENTAL STUDY OF TEMPERATURE AND DENSITY EVOLUTION DURING BREAKDOWN IN A 2.45 GHz ECR PLASMA

O.D. Cortázar*, Universidad de Castilla-La Mancha, ETSII, 13071 Ciudad Real, Spain
A. Megía-Macías and A. Vizcaíno-de-Julián, ESS Bilbao, Landabarri 2, 48940-Leioa, Spain

Abstract

An experimental study of temperature and density evolution during breakdown in off-resonance ECR hydrogen plasma by time resolved Langmuir probe diagnostic is presented. Under square 2.45 GHz microwave excitation pulses with a frequency of 50 Hz and relative high microwave power, unexpected transient temperature peaks that reach 18 eV during 20 μs are reported at very beginning of plasma breakdown. Decays of such peaks reach final stable temperatures of 5 eV at flat top microwave excitation pulse. Microwave coupling times are also measured in connection with plasma parameters evolution as function of duty cycles and incoming microwave power for two hydrogen working pressures.

INTRODUCTION

Understanding plasma physics processes during breakdown and decay in pulsed plasma sources is of special interest for many application fields as particle accelerator science, nuclear fusion reactors and plasma processing industry [1, 2]. An extensive research on this subject was conducted by different researchers with electrical probes, spectroscopy and radiation diagnostics under a wide range of parameters for different plasmas. Processes involved during breakdown should be determining for monocharged beam current optimization as well as the improvement of multiple charged ion production efficiency, both cases of great interest and under deep study in the ECRIS community [3, 4, 5]. In this work we present a study of breakdown process in off-resonance ECR hydrogen plasma by means of time-resolved Langmuir probe diagnostics and incoming and reflected microwave power measurements. The main goal is to improve our knowledge about evolution of plasma parameters during pulse mode operation helping to the design of ion sources at ESS Bilbao.

EXPERIMENTAL SETUP AND PROCEDURE

Measurements are made in a plasma reactor driven by a 3 kW adjustable output power magnetron of 2.45 GHz that is operated at 50 Hz in pulsed mode. Four coaxial coils with typical circulating currents of 10 amps produce an axial 120 mT off-resonance magnetic field. Such coils have a positioning mechanism to adjust the magnetic field distribution. On chamber diagnostic side a lid including pumping port, a fused silica observation window and a vacuum feed-through for probes are mounted. Such lid is placed where plasma electrode and extraction system would be placed in case of using this reactor as an ECRIS. Clearly our plasma reactor is an ECRIS reproduction without extraction electrodes. Fig. 1 shows a view of the experiment where the magnetic field system and diagnostic port side can be appreciated in first plane. The idea is to have a closed reproduction of ISHP ion source under development at ESS Bilbao [6] to use it as test bench for plasma research and optimization.

As is well-known in plasma community, Langmuir probes are used immersed in plasmas for acquiring characteristic I-V curves which permit to estimate plasma electron temperature and density. Time needed to make voltage sweep with acquisition of current values is always a limitation for time resolved measurements. However, several instrumentation companies have developed Langmuir probe systems that permit making transient studies of repetitive pulsed plasmas with some tens of ns resolution. These systems take first I-V point at one pulse; second one at following and so on, completing the voltage sweep in a predetermined number of pulses. In other words, each point at I-V curve belongs to different consecutive plasma pulses. When synchronization is carefully made checking during process if jitter is low enough, it is possible to have a good estimation of electron density and temperature at a precise predefined instant. In our case the system acquires an I-V point during 62.5 ns and after approximately 14.6 μs (time necessary for digitalizing and storing data) is ready to take

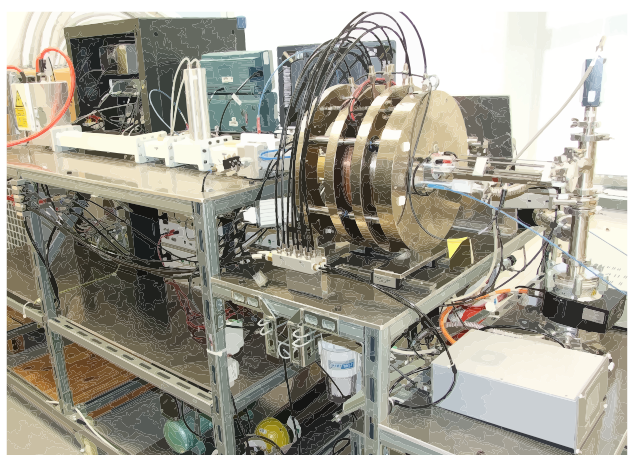

Figure 1: View of the experiment where the plasma reactor, magnetic coils and diagnostic port are shown in first plane.

* dcortazar@essbilbao.org

ISBN 978-3-95450-123-6

Copyright © 2012 CC-BY-3.0 and by the respective authors

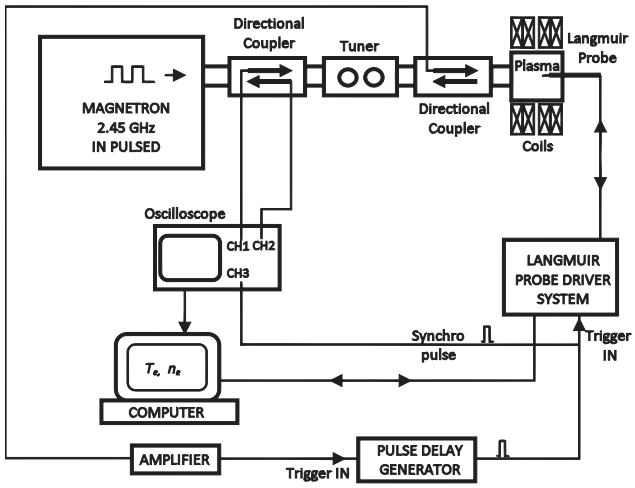

Figure 2: Experimental arrangement for time resolved density and temperature measurements during breakdown with a resolution of 200 ns.

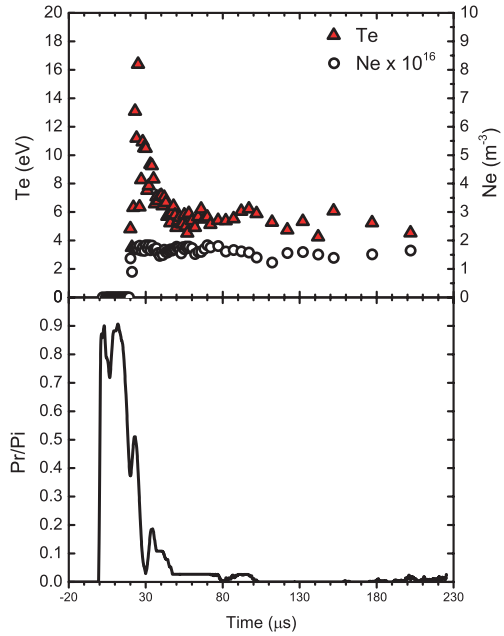

Figure 3: Upper window: Plasma temperature and density evolution during breakdown. Lower window: ratio of reflected power and incoming power *Pr/Pi*.

the following one under TTL trigger order. This process is averaged twenty times before moving to the next I-V point. Applying this method, time resolved I-V curves can be obtained by synchronizing Langmuir probe trigger driver and magnetron via a delay generator. Fig. 2 shows the experimental set-up. A Langmuir probe made of tungsten wire 6 mm long and 0.5 mm diameter is placed in the middle of plasma chamber (r = 0 and z = 46 mm). The Langmuir probe driver consists in ESPION system made by Hiden Analytical LTD. Jitter is carefully checked obtaining a value lower than 200 ns in order to obtain an acceptable measurement time resolution. By modifying Langmuir probe trigger delay, it is possible to obtain the time evolution of electron temperature and density during the breakdown. Typical I-V curve obtained during experiments show that ion saturation current increases following negative voltage. For low plasma densities and small probes the sheath expansion produces an increase in the collected current because effective area for particle collection is the sheath area and not the geometric probe area [7, 8]. Such situation is reflected by ion currents that do not show clear saturation values increasing gradually with increasing negative voltage. The slope in the I-V curve ion current branch is an unequivocal sign of low density plasma always with values under critical density. Considering such fact, density calculations were carried out by modeling the left branch or I-V curve using the numerical results of Laframboise [9].

RESULTS

The study of plasma parameters evolution during breakdown was conducted for two hydrogen working pressures taking measurements every $1\,\mu s$ followed by points every 10 and $20\,\mu s$ on the microwave pulse flat top. Fig. 3 shows a typical evolution of measured parameters for hydrogen pressure of 3.8 x 10^{-3} mb, 1500 W peak microwave incoming power and 90% duty cycle. Upper window shows evolution of electron temperature and density during the breakdown process until reaching flat top microwave excitation pulse. Lower window shows evolution of reflected/incoming power ratio *Pr/Pi* on same time-base. It shows that at the very beginning of the pulse the electric field inside the chamber is much higher than later during steady-state when plasma damps microwave and electric field drops. Such behavior reflects the interplay between the electric field strength and plasma load of the cavity during the ignition transient[5] showing microwave coupling time as directly the width of the *Pr/Pi* pulse. Note in the upper window that a temperature peak reaching almost 20 eV is observed in coincidence with a drastic reduction of reflected power during microwave coupling process. Such peak is followed by a decreasing behavior that reaches about 5 eV as final steady state temperature, remaining practically constant during flat top microwave pulse. Electron density reaches stable values about 1.5 x $10^{16} m^{-3}$ at the time when temperature peak is produced, fact that suggests this process as deeply associated to plasma evolution during breakdown. The error bar in temperature measurement is estimated below 5% , reaching 1 eV at high values during peak and 0.25 eV during steady state. Accuracy in electron density is estimated lower than 0.5 x 10^{16} m^{-3}.

Low Pressure Regime (3.8 x 10^{3} mb)

Fig. 4 shows temperature and density temporal evolution for three cases with hydrogen pressure maintained at 3.8 x 10^{-3} mb and the magnetic field at 120 mT as function of duty cycle and incoming power. Fig. 4(a) is a duty cycle

Copyright © 2012 CC-BY-3.0 and by the respective authors

ISBN 978-3-95450-123-6

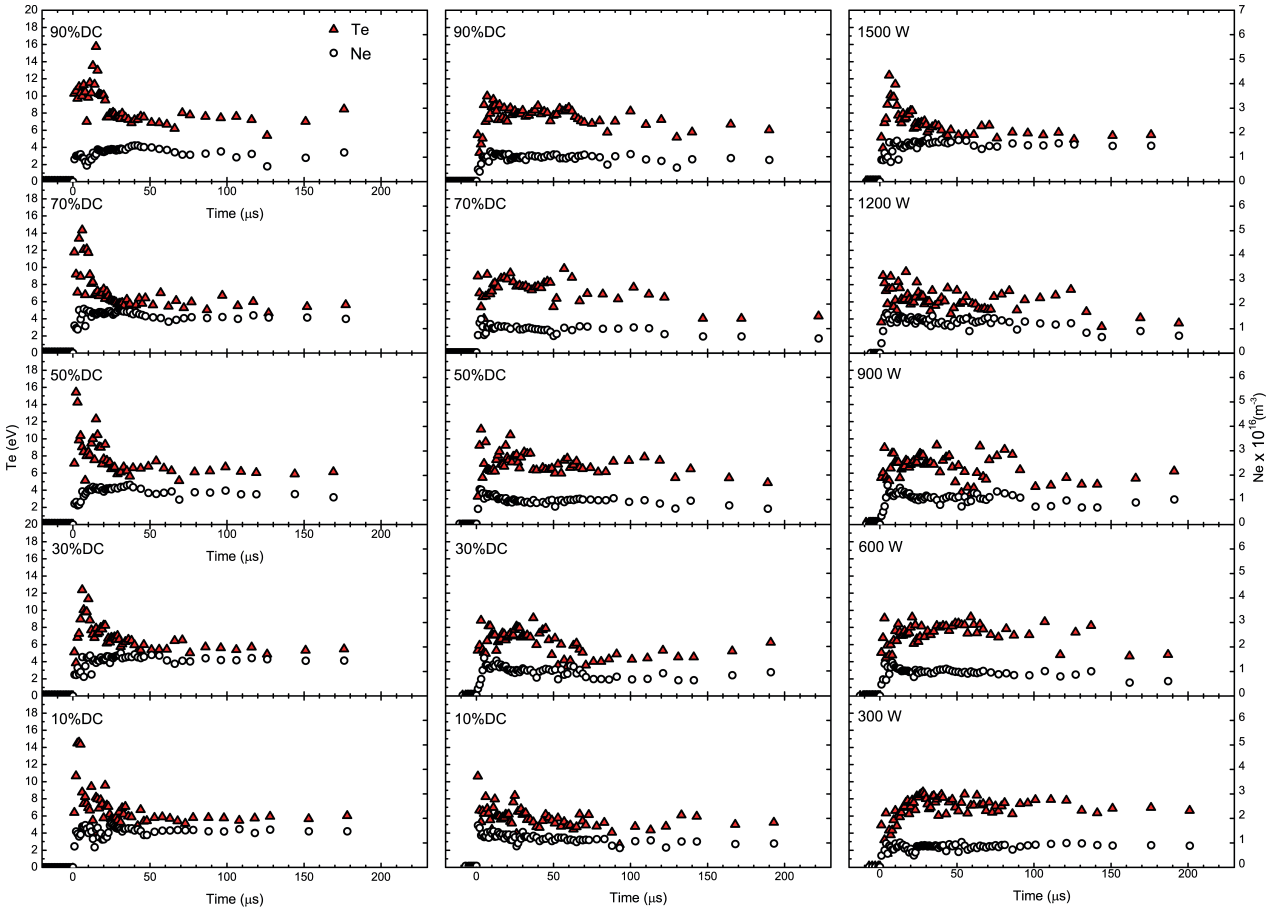

(a) 1500W (b) 900W (c) 30% DC

Figure 4: Temperature and Density evolution during breakdown process for a hydrogen pressure of 3.8 x 10^{-3} mb and 120 mT Bz magnetic field. (a) Constant power at 1500 W. (b) Constant power at 900 W. (c) Constant duty cycle at 30%.

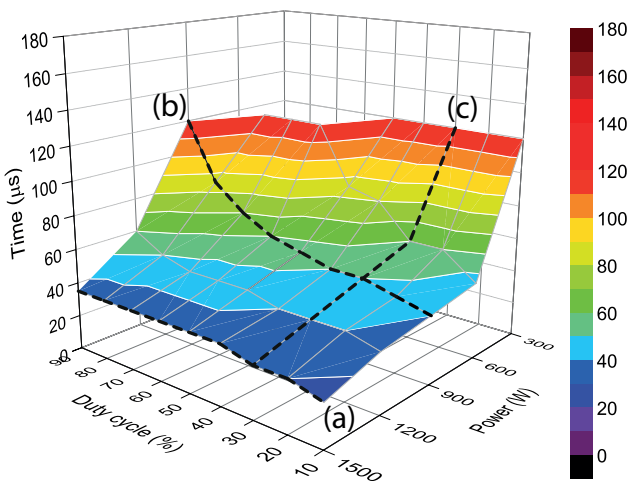

Figure 5: Microwave Coupling time as function of incoming power and duty cycle for low pressure regime (3.8 x 10^{-3} mb).

scan at 1500 W of power, Fig. 4(b) is a duty cycle scan at 900 W of power and Fig. 4(c) is a power scan at 30 % of constant duty cycle.

In all theses cases the beginning of temperature and density pulses are coincident with *Pr/Pi* pulse fall as is shown in Fig. 3. On the other hand, the microwave coupling time can be estimated by measuring the width of such *Pr/Pi* pulse. Theses measurements are represented as a surface obtained by linear interpolation between measured points as function of MW incoming power and duty cycles in Fig. 5. Note that this figure shows an empty area in the corner of low powers and high duty cycles corresponding to a high jitter measurement zone where is not possible to take data. As can be seen in this surface, the level curves of 1500 W (a), 900 W (b) and 30 % of duty cycle (c) are marked as doted lines and they correspond to measurements represented in Fig. 4(a), Fig. 4(b) and Fig. 4(c) respectively. It is interesting to compare Fig. 4 with Fig. 5 because some connection can be found between microwave coupling time and plasma parameters evolution. For example,

ISBN 978-3-95450-123-6

Copyright © 2012 CC-BY-3.0 and by the respective authors

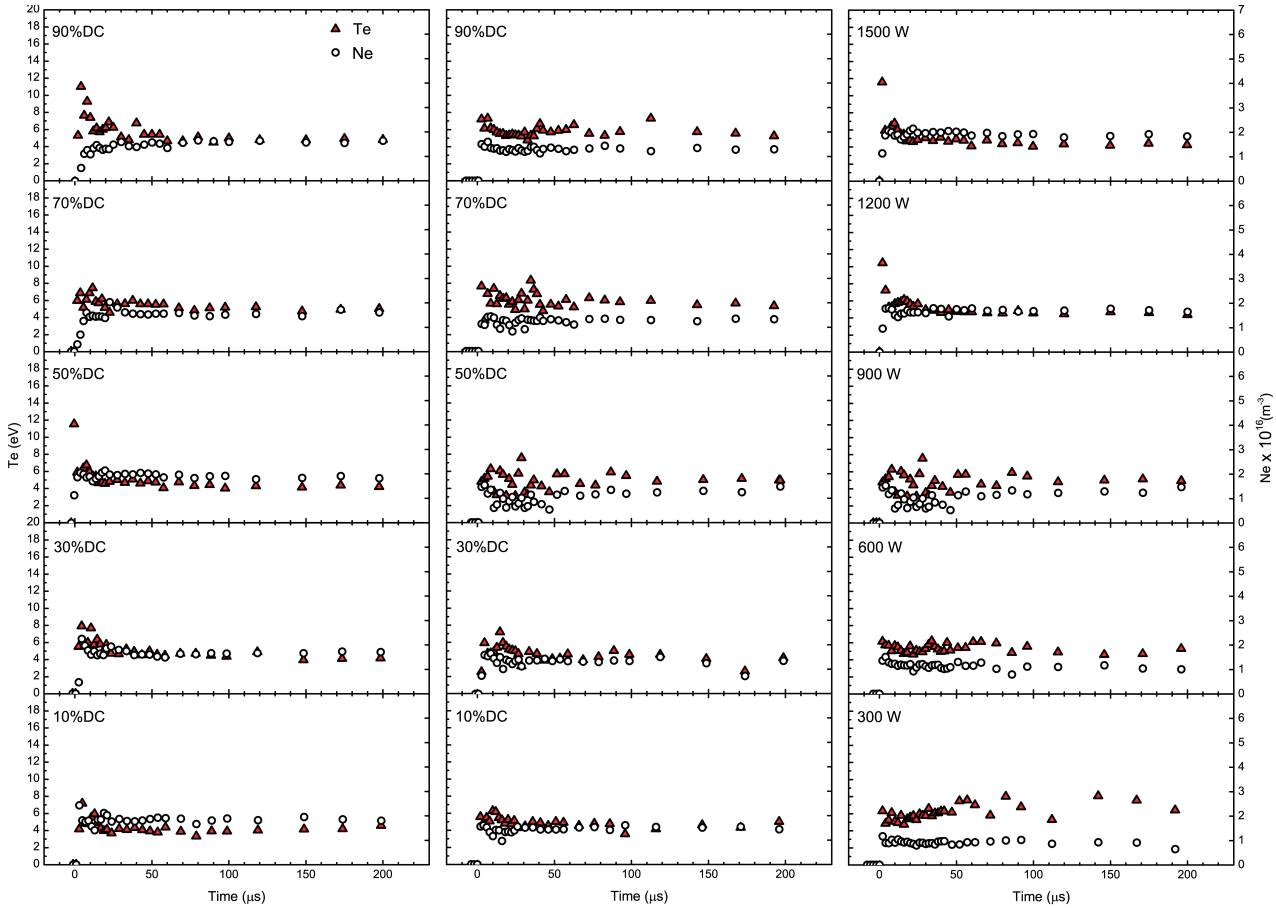

Figure 6: Temperature and Density evolution during breakdown process for a hydrogen pressure of 6.2 x 10^{-3} mb and 120 mT Bz magnetic field. (a) Constant power at 1500 W. (b) Constant power at 900 W. (c) Constant duty cycle at 50%.

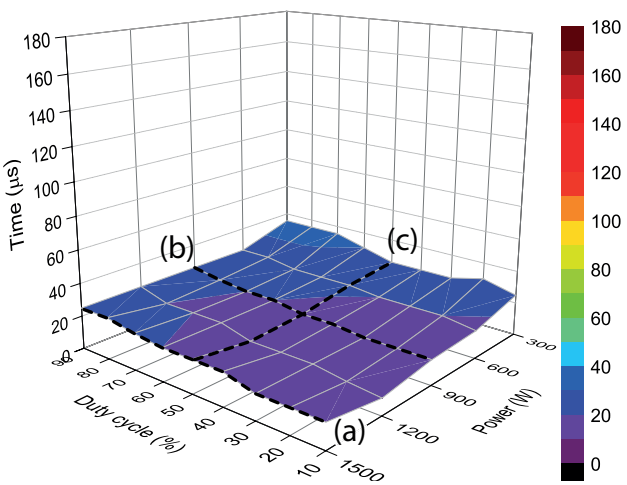

Figure 7: Microwave Coupling time as function of incoming power and duty cycle for high pressure regime (6.2 x 10^{-3} mb).

keeping incoming power constant at 1500 W as indicated in level curve (a) in Fig. 5, practically constant microwave coupling times are observed with values around of 35 μs for all range of duty cycles studied. The corresponding plasma parameters evolution in Fig. 4(a) also shows non relevant differences along all the studied range. Temperature and density evolution suggest that this case is characterized by sharp temperature peaks of 16-18 eV followed by decays to final temperature steady state around 5 eV. However, the case of constant power at 900 W that is indicated as level curve (b) in Fig. 5 shows a remarkable coupling time tendency to increase when duty cycle is also increased, starting at values of 40 μs at 10 % of duty cycle and reaching 120 μs at 90 %. The corresponding plasma parameters evolution in Fig. 4(b) shows that plasma temperature evolves by decreasing temperature peaks values and increasing final temperatures at plasma steady state. In this case the relationship between microwave coupling times and temperature evolution indicates that for longer coupling times, longer and lower temperature pulses are observed with slight higher final temperatures. The last case where duty cycle is kept constant at 30 % is indi-

Copyright © 2012 CC-BY-3.0 and by the respective authors

ISBN 978-3-95450-123-6

cated as level curve (c) in Fig. 5 for power ranging between 300W and 1500W. Microwave coupling times show the tendency to grow when power decreases and the corresponding plasma parameters evolution in Fig. 4(c) shows how temperature pulse decrease with power and it practically vanishes at low powers. On the other hand, electron density show a general behavior characterized by a practically no dependence of duty cycle and a slightly tendency to grow with incoming power. Higher values reach 2 x $10^{16}m^{-3}$ at 1500 W and lower values of 0.8 x $10^{16}m^{-3}$ are registered at 300 W.

High Pressure Regime (6.2 x 10^{3} mb)

The same scheme of previous section is conducted for a relative higher hydrogen working pressure. Fig. 6 shows three cases of temperature and density evolutions for different values of incoming power and duty cycles maintaining hydrogen pressure at 6.2 x 10^{-3} mb and magnetic field at 120 mT. Fig. 7 shows the microwave coupling times obtained for such experimental condition keeping the same representation scale of Fig. 5 in order to facilitate comparisons. Note that measured times are shorter and practically constant during the studied interval with values between 20 and 35 μs showing a slight tendency to grow for lower power inputs and high duty cycles. Cases shown in Fig. 6 are represented on the surface as level curves (a), (b) and (c) for 1500 W, 900 W and 50 % of duty cycle respectively. Such data show that temperature peaks reach lower values respect to the previous low pressure regime suggesting that incoming power is the predominant factor for its increment. Specially interesting is the the case of Fig. 6(a) where the influence of duty cycle is remarkable for our maximum power input value under study. On the other hand, electronic densities show higher values reaching 2 x $10^{-16}m^{-3}$ following the relative increment for this pressure regime.

REMARKS

Evolution of plasma parameters for a 50 Hz pulsed off-resonance 2.45 GHz ECR plasma at two hydrogen working pressures (3.8 and 6.2 x 10^{-3} mb) during breakdown is reported . For low pressure regime, different plasma parameter evolution is observed depending of incoming power and duty cycle in connection to microwave coupling times. Under relative highly power conditions where short microwave coupling times are recorded, high temperature peaks are observed during microwave coupling process at very beginning of plasma breakdown. However, for lower incoming powers, temperature evolution shows a slow tendency to reduce the peak values by evolving gradually towards a higher final temperature without peaking. On the other hand, when pressure is increased to the high regime the peaking behavior turns less notorious keeping the dependence with incoming power and duty cycles while electron densities reach higher values of typically 2 x 10^{16} m^{-3}. In general terms, the temperature peaks duration seems to be related to microwave coupling quality in terms of the time needed to establish a good power transfer to plasma. For the high pressure regime, where microwave coupling times are short and practically uniform over all our studied range, temperature evolutions show lower peak values and shorter duration. However, for the low pressure regime where microwave coupling times show a strong dependence of power and duty cycle, a significant evolution of peaking behavior is observed. This effect suggest that the temperature peaking could be strongly related to plasma formation process and how the microwave interaction with neutral gas and a very low dense plasma evolves during the early breakdown stage. The influence of seed electrons remaining in the neutral gas between pulses[10], could be a factor to have into account to explain the dependence observed with duty cycle at relative high power. Finally, the early instant when temperature peaks are observed in our experiment suggests that may be interesting to conduct this diagnostic on others ECR plasmas of higher frequencies in order to see possible connections with the ECRIS preglow [11, 12].

ACKNOWLEDGMENT

The authors would like to thank to F.J. Bermejo for his continuous support, O. Tarvainen and S. Gammino for useful discussions.

REFERENCES

[1] Gammino S, Celona L, Ciavola G, Maimone F and Mascali D 2010 *Rev. Sc. Instrum.* **81** 02B313

[2] Pelletier J and Anders A 2005 *IEEE Trans. Plasma Sci.* **33** 1944–1959

[3] Tarvainen O, Ropponen T, Toivanen V, Ärje J and Koivisto H 2009 *Plasma Sources Sci. Technol.* **18** 035018

[4] Bäcker H, Bradley J W, Kelly P J and Arnell R D 2001 *J. Phys. D: Appl. Phys.* **34** 2709–2714

[5] Lyneis C, Benitez J, Leitner D, Noland J, Strohmeier M, Koivisto H and Tarvainen O. *Proceedings of ECRIS 2010* (Grenoble, France) pp 162–164

[6] Cortázar O D, Megía-Macías A and Vizcaíno-de Julián A 2012 Technical Report PLAB-00-0002-ESS.00-TR ESS Bilbao

[7] Merlino R L 2007 *Am. J. Phys.* **75** 1078–1085

[8] F F Chen 1965 *Plasma Diagnostics Techniques* edited by R. H. Huddlestone and S.L Leonard (New York: Accademic Press)

[9] Tuszewski M and Tobin J A 1996 *Plasma Sources Sci. Technol.* **5** 640–647

[10] Tarvainen O, Ropponen T, Thuillier T, Noland J, Toivanen V, Kalvas T and Koivisto H 2010 *Rev. Sc. Instrum.* **81** 02A303

[11] Melin G, Bourg F, Briand P, Debernardi J, Delaunay M, Geller R, Jacquot B, Ludwig P, N'Guyen T, Pin L, Pontonnier M, Rocco J and Zadworny F 1990 *Rev. Sc. Instrum.* **61** 236–238

[12] Thuillier, T and Lamy, T and Latrasse, L and Izotov, IV and Sidorov, AV and Skalyga VA and Zorin, VG and Marie-Jean, M 2008 *Rev. Sc. Instrum.* **79** 02A314

ISBN 978-3-95450-123-6

Copyright © 2012 CC-BY-3.0 and by the respective authors

CONTROL OF THE PLASMA TRANSVERSAL LOSSES, CAUSED BY MHD INSTABILITIES, IN OPEN MIRROR MAGNETIC TRAP OF THE ECRIS: RECENT EXPERIMENTS ON SMIS 37 SETUP

A. Sidorov[1,2], I. Izotov[1], S. Razin[1], V. Skalyga[1,2], and V. Zorin[1]
[1]Institute of Applied Physics, RAS, 46 Ul`yanova st., 603950 Nizhny Novgorod, Russia,
[2]Lobachevsky State University of Nizhni Novgorod (UNN), 23 Gagarina st., 603950, Nizhny Novgorod, Russia
P. Bagryansky[3]
[3]Budker Institute of Nuclear Physics, SB RAS, 11 Lavrent'eva st., 630090 Novosibirsk, Russia

Abstract
This work is a continuation of the experiments described in [1, 2] and aimed at the investigation of the new conceptions of MHD stabilization of plasma in open axisymmetric traps, specifically, it is aimed at the investigation of the shear flow influence on the transport control in open mirror traps. As in previous experiments, shear flow was created by limiter-electrode with bias potential according to the vacuum chamber. Plasma density structure in radial and azimuthal directions was studied. Mode structure of the perturbations was investigated. Substantial sharp shift of the plasma density maximum to the system axis with bias potential growth was demonstrated. It was shown, that the value of the bias potential that corresponds to the plasma density profile shift grows with the magnetic field growth that can be interpreted as the electron temperature growth.

INTRODUCTION

Creation of the new generation of the ECR ion sources now is connected with an increase in the heating radiation frequency up to 56 GHz. In this case, the required value of the magnetic field in the trap can reach a value of 5 Tesla. The minimum B magnetic field configuration, which is traditional for the ECR ion sources, in the case of high values of the magnetic field is quite complicated, and now its creation requires a lot of efforts, whereas creation of a strong magnetic field in the axisymmetric magnetic trap is not a problem. That is why the stabilization of MHD perturbations in axisymmetric magnetic traps seems to be perspective. The advance in plasma stabilization using the shear flows achieved on the GDT (GasDynamic Trap, described in details in [3]) setup allows one to assume the same result in the case of the non-equilibrium plasma of the ECR ion sources. The essence of the method developed in Budker Institute consists in creation of a differential rotation zone at the periphery of the plasma column. It is obtained by the creation of the special (step-like) form of the radial profile of the plasma potential, which is achieved by using a system of special electrodes: radial limiters and bit-slice plasma receivers placed in the plasma expansion zone after the magnetic trap plug. This method now allows one to confine the plasma with $\beta \sim 0.6$ in the GDT in the stationary regime with a negligible level of the transverse losses.

In papers [1-2] mentioned method was for the first time tested for the plasma of the ECR discharge created by 37.5 GHz radiation (SMIS 37 setup, see Fig.1) in an axisymmetric magnetic mirror trap of multicharged ion source. A limiter with bias potential was set inside the vacuum chamber for plasma rotation. The limiter construction and the optimal value of the potential were chosen according to the results of the preliminary theoretical analysis. The increase in the limiter's potential up to the values of 70–100 V leads to a substantial (by approximately 3.5–4 times) increase in the entire amount of the ions leaving the trap through the magnetic plugs during one working pulse. That is the result of the increase in the plasma density and, probably, in the electron temperature in the trap. So, the confinement became better, which was interpreted as substantial suppression of the transverse losses. Measurements of ion spectra showed that the increase in the ion current couldn't be a result of additional flux of contaminations from chamber walls. Investigation of the time dependences of the ion current in the plasma decay regime demonstrated the decay time increase from 60 μs to 110 μs for the regime with improved confinement. This work is a continuation of the previous researches [1-2] and aimed on the further investigation of the shear flow influence on the transport control in open mirror traps of the ECR ion sources.

SMIS 37 EXPERIMENTAL FACILITY

The experimental investigations presented here were carried out on the SMIS 37 setup, which was described in details in [4]. The scheme of the setup is shown in Fig. 1. A gyrotron with the 100 kW power at 37.5 GHz, pulse duration up to 1.2 ms, and linear polarization of the radiation was used as an RF heating source. The plasma was confined in an axisymmetric open mirror trap. The pulsed magnetic field was created by two groups of solenoids. The duration of a current pulse with its form being close to a half-period of the sinusoid was 14 ms; the change in the value of the magnetic field during an RF pulse was less than 3%. The distance between the plugs was about 35 cm, and the mirror ratio was close to 5. The value of the magnetic-field intensity was 1.5-1.9 T at the

Copyright © 2012 CC-BY-3.0 and by the respective authors

ISBN 978-3-95450-123-6

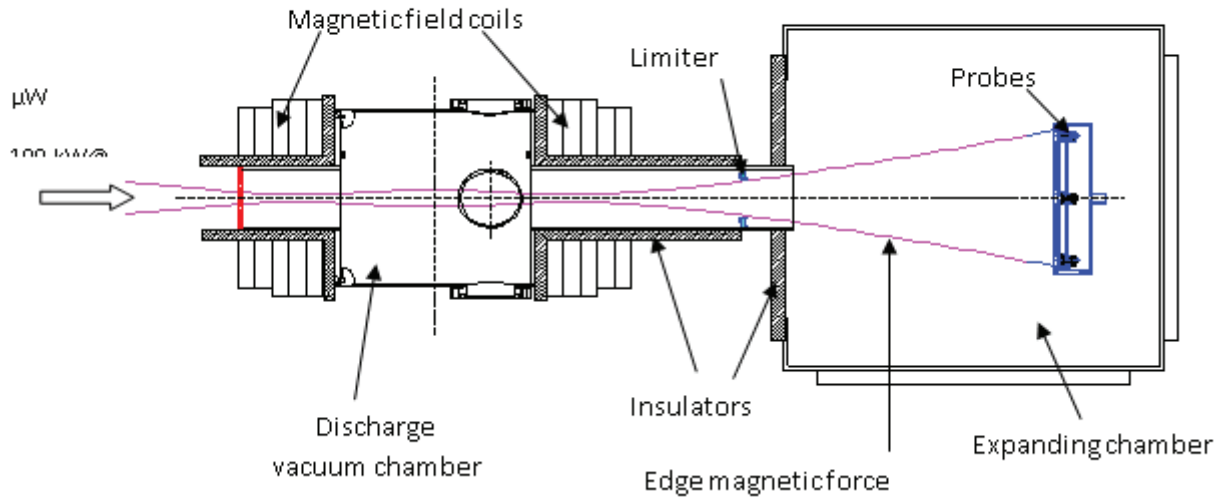

Figure 1: SMIS 37 experimental setup.

plug in most experiments. The gas (at the most part of the experiments we used helium) was injected to the vacuum chamber through a quartz pipe soldered at the center of the RF inlet quartz window.

The typical plasma parameters were as follows: an electron density of $10^{12}\div10^{13}$ cm^{-3}, an electron temperature of 50÷100 eV, and a plasma chord radius of ~ 1 cm. Under such conditions, the frequency of electron-ion collisions is rather high, the loss cone is filled with electrons, and quasi-gas-dynamic confinement is realized with a confinement time of about a few tens of microseconds.

An electrode limiter designed for the control of the electrical-potential profile was set in the vacuum chamber (Fig. 1). The negative electrical bias potential applied to the limiter with value ranged from 0÷200 V.

Plasma created into the trap spread into the expanding chamber where 8 electrical probes, intended for spatial distribution of the ion flux from the plug research, were placed. Position of the probes system is shown on the Fig. 1. Probes were operated in the ion current saturation regime. One of them was placed into the center of the system, three – along the radius and another 4 – along the azimuth at the maximum radius position at the points of 22.5^0, 45^0, 90^0, and 180^0 as it shown on the Fig. 2.

There were the steel mask-disk in front of the probes with 12 mm holes and the glass disk with same holes. Each of the probes was provided with measuring line and analog-to-digital converter (ADC) channel for pulse form registration.

The studying the spatio-temporal dynamics of the discharge optical radiation was made by streak camera.

RESULTS

Radial Profile Dynamics

The main purpose of the experiments was to investigate the structure of the plasma flux from the trap along the system axis under the conditions of the regime with improved confinement. The structure of the flux was studying by use the system of Langmuir probes placed into the expanding chamber (see. Fig.1).

Probes 1 – 4 placed along the radial coordinate (on the Fig. 2 they placed along the horizontal line) allowed one to investigate the dynamics of the plasma flux radial profile. The change of the shape of this profile with the change of the value of the bias potential on the limiter is shown on the Fig. 3 (the value of the magnetic field at the plug in this case was 1.7 T).

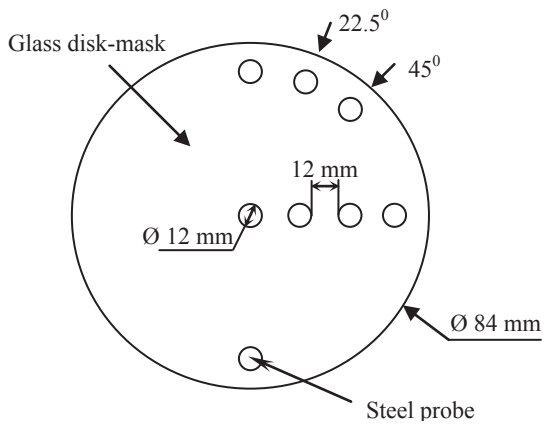

Figure 2: Scheme of the probes positioning in the probe's system.

Copyright © 2012 CC-BY-3.0 and by the respective authors

ISBN 978-3-95450-123-6

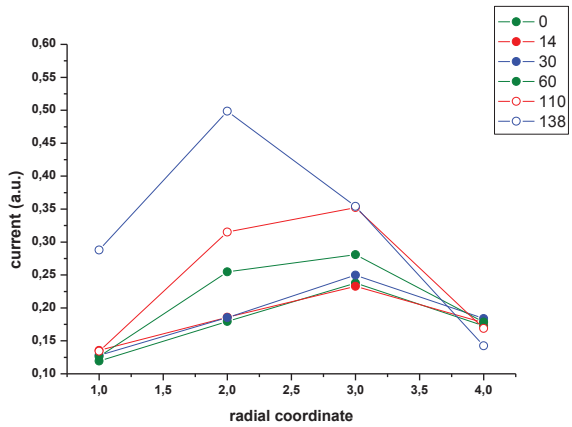

Figure 3: Dependence of the plasma flux radial profile on the value of the biased potential for the value of the magnetic field at the plug of 1.7 T. Radial coordinate 1 corresponds to the 1st probe, 2 – for second, etc.

As one can see at the value of the voltage more then 110 V there is the substantial shift of the profile maximum from the 3rd probe to the second. At the same time the increase of the total current to the probes was observed as it had been at the previous experiments (see [1-2]). For the lower value of the magnetic field at the plug (1.5 T) we observed the same situation but the shift was noticed at the lower value of the biased potential at the limiter (see Figure 4).

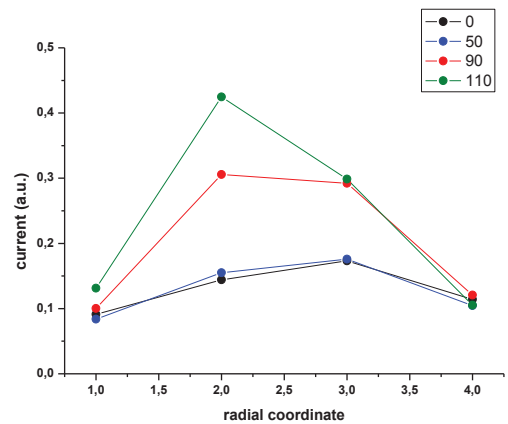

Figure 4: Dependence of the plasma flux radial profile on the value of the biased potential for the value of the magnetic field at the plug of 1.5 T. For this case the shift of the profile maximum observed at the value of the voltage close to the 90 V.

When the value of the magnetic field at the plug was even less (1.3 T, it have to be noted, that this value is lower then the resonance one for the 37.5 GHz, 1.34 T) the shift was observed at the 50 V. Moreover in this case it was possible to shift the profile maximum closer to center (1st probe) at the potential value of about 170 V.

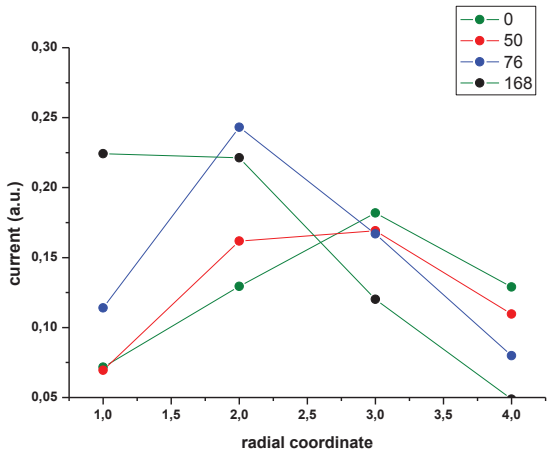

Figure 5: Dependence of the plasma flux radial profile on the value of the biased potential for the value of the magnetic field at the plug of 1.3 T.

We associate observed shift of the profile maximum from the periphery to the center with the switch to the regime with improved confinement (regime with transversal losses suppression). The fact, that even in the case of better confinement, the maximum of the density profile in spite of the shift is still not at axis of system we explain by the presence of the high azimuthal modes in the spatial structure of the plasma flux. The presence of the higher azimuthal modes (m=2, 3) in case of the ECR ion source was demonstrated in previous papers [1-2, 5] theoretically and experimentally and can be explained by the low value of the ion temperature ($T_i << T_e$) in ECRIS plasma.

As it was shown in paper [6] theoretically, the switch to the regime with improved confinement occurs at the value of bias potential proportional to the electron temperature. Specifically, for the SMIS 37 facility parameters (for helium plasma) $\varphi \sim 1.2 \cdot T_e$. And as it was shown above experimentally, the value of the bias potential, which corresponds to the switch to the regime with improved confinement, grows with the value of the magnetic field. That fact from the one hand could serve as the additional proof of the fact that in ECR ion sources electron temperature grows with the value of the magnetic field. On the other hand, if you accept the fact the temperature increases with increasing magnetic field as given, it may serve as a confirmation of the fact that the threshold value of bias potential grows with the electron temperature.

Spatio-Temporal Dynamics of the Discharge Optical Radiation

Studying of the spatio-temporal dynamics of the discharge optical radiation was made by streak camera. This camera was placed in front of the optical flange of the discharge vacuum chamber. treak camera images for the different values of the bias potential on the limiter (0 V, 120 V, and 180 V) are shown on the figures 6-8.

Copyright © 2012 CC-BY-3.0 and by the respective authors

ISBN 978-3-95450-123-6

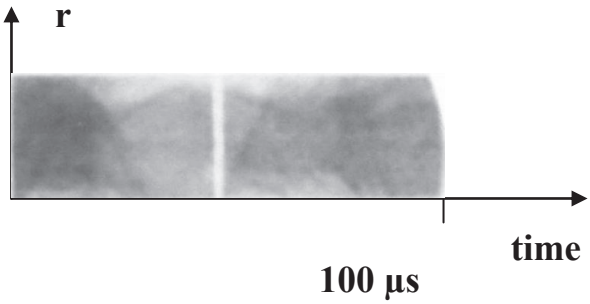

Figure 6: Streak camera image for the limiter potential of 0 V.

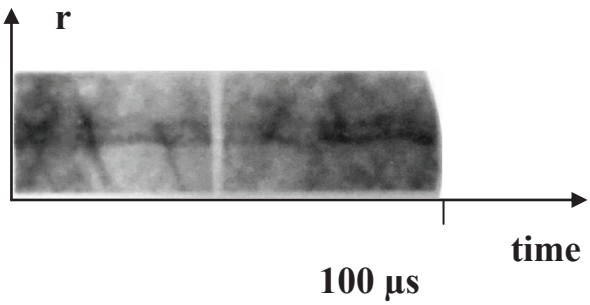

Figure 7: Streak camera image for the limiter potential of 120 V.

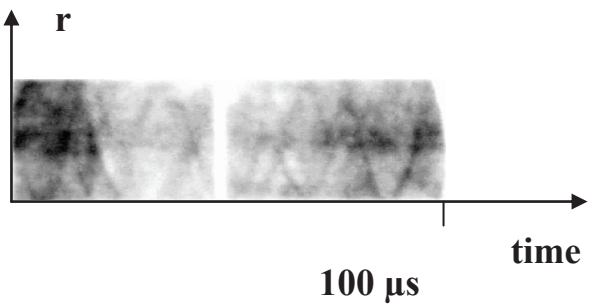

Figure 8: Streak camera image for the limiter potential of 180 V.

The value of the magnetic field at the plug was of about 1.7 T. At the high values of the potential (more then the threshold one) it is noticeable the creation of the plasma core (due to the shift of the plasma density maximum to the center) and the creation of the rotating layer, which is noticeable by its helical trajectory. When the rotation velocity is higher (compare 120 V case and 180 V), the pitch of the helix becomes shorter that confirms our expectations that the greater potential drop will result in a greater rotation speed.

CONCLUSION

The experimental results presented in this paper along with the results had been obtained earlier [1, 2, 5] demonstrated that the effective control of the transversal losses in non-equilibrium plasma of ECR discharge is possible by using shear flows, driven by biasing limiter. We suppose that these results may be useful in developing a new generation of ECR ion sources based on axisymmetric open magnetic traps.

ACKNOWLEDGMENTS

Work was supported by RFBR grant # № 12-02-31457-mol_a. Work was performed in frame of realization of federal targeted program “Scientific and pedagogical labor force for an innovative Russia” for 2009 – 2013 yy.

REFERENCES

[1] A.V. Sidorov, P.A. Bagryansky, A.D. Beklemishev et al. Trans. Fusion Sci. and Technology, **59**, 112, (2011).
[2] I. V. Izotov, S. V. Razin, A. V. Sidorov et al. Rev. Sci. Instrum., **83**, 02A318 (2012).
[3] P.A. Bagryansky, A.A. Ivanov, E.P. Kruglyakov, A.M. Kudryavtsev, Yu.A. Tsidulko, A.V. Andriyash, A.L. Lukin and Yu. N. Zouev, Fusion Engineering and Design, **70**, 13 (2004).
[4] V. Skalyga, V. Zorin, I. Izotov, S. Razin, A. Sidorov, A. Bohanov, Plasma Sources Science and Technology, **15**, 727 (2006).
[5] A.V. Sidorov, P.A. Bagryansky, A.D. Beklemishev, I.V. Izotov, V.V.Prikhodko, S.V.Razin, V.A. Skalyga and V.G. Zorin, *ECR Plasma Confinement Improvement in the Axisymmetric Mirror Magnetic Trap*, Preprint IAP RAS № 804, 2010 (in russian).
[6] Beklemishev, A. D. Shear Flow Effects in Open Traps. Theory of Fusion Plasmas, AIP Conference Proceedings, **1069**, 14 (2008).

Copyright © 2012 CC-BY-3.0 and by the respective authors

ISBN 978-3-95450-123-6

SECONDARY-ELECTRON-ENHANCED PLASMA AS AN ALTERNATIVE TO DOUBLE/VARIABLE-FREQUENCY HEATING IN ECRIS

K. E. Stiebing, L. Schachter[#], and S. Dobrescu[#],
Institut für Kernphysik der Goethe-Universität, Frankfurt/Main, Germany
[#] National Institute for Physics and Nuclear Engineering, Bucharest, Romania

Abstract

"Double Frequency Heating" (DFH) now has become the method of choice to optimize the output from the newest generation ECRIS installations. It was a challenge to compare this method with the comparatively cheap method of "metal dielectric" (MD) structure introduced into the plasma chamber, which has also proven to strongly enrich the plasma with electrons that are effectively trapped and heated. At the 14GHz ECRIS installation at Frankfurt, we have carried out a series of experiments using the two available RF-transmitters to launch two different frequencies into the IKF ECRIS. Due to restriction in the available frequency difference, the source could not be operated in real DFH-mode but was operated in "Frequency Tuning Mode" (FTM), for which also positive results are reported in literature. It turned out that the double RF-injection does not change the source performance substantially. The measured effects are in the order of 20% to 30% as reported elsewhere. In contrast to this, the enhancement gained by the MD method is much higher. The measured enhancement ratios even surpass those, reported for real double frequency heating.

INTRODUCTION

In order to increase the output, in particular of highly charged ions, from an ECRIS a number of techniques have been developed. One of these methods, DFH, is particularly suited for modern high power ECRIS installations with their ability to vary both the magnetic solenoid and multipole field of the source in a range appropriate to allow for resonance zones for both frequencies. First experiments with DFH were realized with second generation sources and were successful [1,2]. In order to apply DFH e.g. in a 14GHz source the RF-difference should be as large as 2 GHz. If the frequency difference is less than this value, one refers to this mode as "Frequency Tuning" (FT). Pioneering work on FT has been done by L. Celona, who developed FT as a powerful method to optimize the performance of electron cyclotron resonance ion source.[3]

At the 14GHz ECRIS of the Institut fuer Kernphysik Frankfurt (IKF), we have introduced the MD method to increase the output of highly charge ions from an ECRIS substantially [4,5]. The MD method is based on a development made at the Institute of Physics and Nuclear Engineering (INFIN), Bucharest, Romania.It consists in the production of metal-dielectric (MD) structures (Al-Al_2O_3 transitions) by a special electrochemical treatment of pure aluminium plates. The structures are characterised by high yields of secondary-electron emission under bombardment by charged particles (electrons/ions) from the plasma. The installation of MD-structures as wall coating into the plasma chamber therefore significantly enhances the density of plasma electrons n_e by injecting cold electrons to the plasma. At the same time the ion dwell times (ion confinement) are increased by blocking compensating wall currents, hence restoring the plasma ambipolarity. Due to this reduction in wall currents the method has also been shown to drastically reduce Bremsstrahlung radiation from the source, a limit that becomes more and more a problem in modern high power ECRIS devices.

In IKF we have two RF-transmitters available allowing to run the source in FT-mode. It therefore was a challenge to compare these two methods and in particular the possible benefit of FT-mode in an ECRIS with MD-configuration.

EXPERIMENT

The 14 GHz IKF ECRIS was operated in two different configurations, the standard (all stainless steel) mode of configuration, and the MD-mode, where the plasma chamber of the source was equipped with two MD-structures of 1 mm thickness. In MD-mode one structure (MD-liner) was installed in the stainless steel plasma chamber symmetrically with respect to the hexapole magnet for the radial plasma confinement. It covered the radial walls at a length of 150 mm (i.e. roughly 3/4 of the whole radial plasma chamber walls). The other structure (MD-electrode) covered the entire stainless steel extraction electrode of the source. The emissive layers of both structures faced towards plasma.

Wave-guides for both available RF-transmitters have been launched to the injection plug of the source. The transmitters are a wider bandwidth TWT-amplifier and the narrow bandwidth Klystron-amplifier. In this configuration the minimum RF-difference of ~2 GHz, required for full DFH, could not be reached. Therefore the source was operated in FT-mode. The source geometries and the main electrical parameters were kept unchanged during all measurements. The extraction voltage was 15 kV and measurements were performed at RF power levels of 200 W to 1000 W. Tests were also performed up to 1500 W. Pure Argon was used as working gas. For the experiments reported here, the ion optical elements of the

Copyright © 2012 CC-BY-3.0 and by the respective authors

ISBN 978-3-95450-123-6

LEBT were optimized for the transport of Ar^{14+} ions to clearly focus on highly charged ions.

Charge state distributions, taken at the Faraday cup after the 90° analyzing magnet are reported and discussed. The frequency difference for FT-mode was tuned to optimize the output of Ar^{14+} ions. Typical values of the vacuum during operation of the source were at the injection (1. - 5.) x 10^{-7} mbar and (7. - 8.) x 10^{-8} mbar at the extraction. A biased stainless steel electrode was located at the injection side of the plasma chamber. Axial position and voltage of this electrode were adjusted by optimizing the extracted ion current.

RESULTS

Quite generally, the output of highly charged ions form an ECRIS can be optimized by carefully tuning RF-frequency and magnetic field. The installation of the TWT wave-guide provided the possibility to test this in a wider range of RF-frequencies. In Fig. 1 the influence of the "single"-frequency-tuning by changing the RF-frequency of the TWT on the CSD is shown for the reference and the MD configuration of the source. For each CSD, the magnetic field was tuned to optimize the output of highly charged ions (Ar14+). The RF power was 600 W for all frequencies. Two distinct features stand out. One is the well-known shift of the CSD towards higher charge states when a MD-configuration is installed. The output of all high charge states is enhance by roughly one order of magnitude, the CSD is wider representing a hotter and better confined plasma as already derived in other experiments [6,7,8]. The second distinct feature is that the frequency tuning leads to marked improvement for the standard source while it has very little influence on the CSD taken with MD-configuration. This second behavior becomes clearer in Fig. 2. Here the same data are analyzed as a function of frequency for three selected charge-state groups, low (averaged over q=2-4), mediate (q=6-9) and high (q=12-14) charge states. The data are shown in terms of relative gain factors $g(\nu) = I(\nu) / I(\nu = 13{,}38\ \mathrm{GHz})$, i.e. normalized at the lowest frequency. In addition, also three data points for Ar^{16+} in MD-configuration are shown. As no signal could be analyzed for the lowest frequency in this case, these data points are normalized to the MD-data point at 14,16 GHz. It is evident that, while the intensity of highly charged ions can be increased by a factor of 3 to 4 for the standard configuration, the effect for the MD configuration is strongly reduced to only a factor of 1,5. The data also show that, quite generally, the output of highly charged ions increases with RF-frequency as expected from the general scaling laws formulated by Geller [9]. This increase is limited in this experiment by the magnetic field configuration of the source, which for the last two frequencies was already in saturation.

While this increase is reduced for the MD-configuration, due to its much better confinement and plasma stability the increase for Ar^{16+} indicates that the scaling law is also valid for this configuration. This general behavior supports earlier conclusions that an MD configuration changes the plasma electron density of any standard 14 GHz - ECRIS into that of an 18 GHz - ECRIS.

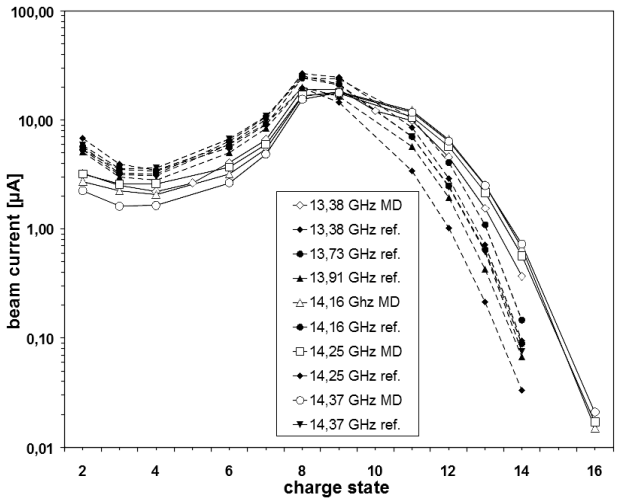

Figure 1: Optimizing single frequency for the standard ECRIS (closed symbols dashed lines) and for the ERCIS with MD configuration (open symbols solid lines).

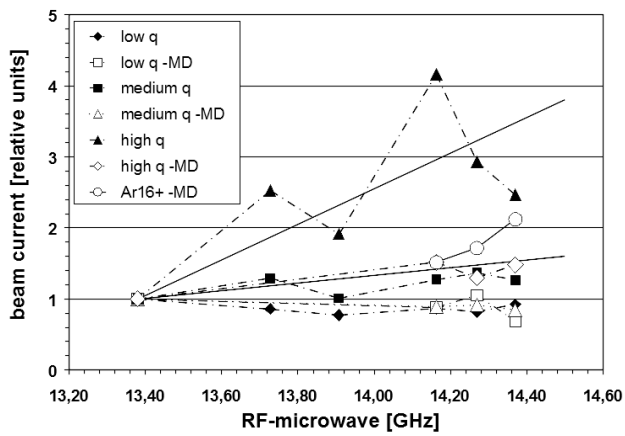

Figure 2: relative intensities as function of RF-frequency for selected charge-state groups (see text).

In Fig. 3 a collection of CSD taken with FT-mode are displayed. All spectra are optimized for the production of Ar^{14+}. Despite of the complexity at first glance, three different groups may readily be identified. First group (dashed dotted lines): CSD taken with reference source at RF-powers between 600 and 800 Watt, second group (dashed lines): CSD taken with reference source at RF-powers at 1 kW to 1,1 kW, third group (solid lines open circles): CSD taken with MD-configuration at a RF Power of 800 Watt.

It is evident that by changing the frequency and the power ratio $P_{Klystron}$ / P_{TWT} within the groups a moderate modification of the CSD is obtained, however at a level of normal parameter tuning of the source. In particular the

ISBN 978-3-95450-123-6

Copyright © 2012 CC-BY-3.0 and by the respective authors

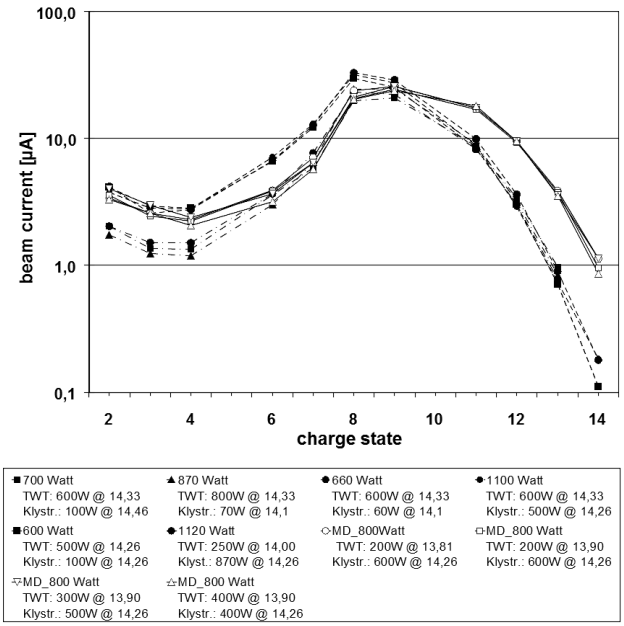

Figure 3: Optimized CSD for FT-mode. Reference-ECRIS (solid symbols), MD-ECRIS (open symbols).

power scaling still is stronger than the FTM-effect and more ions are created at higher input powers, however at low charge states. Most prominent, however, is the MD-effect, which changes the form of the CSD completely, indicating the strong improvement of the plasma parameters by this method.

FT-mode in MD-configuration does not change the CSD significantly. In this configuration the plasma volume, created by the RF-frequency and the magnetic trap of the source is best optimized by the mechanisms, which are due to the MD effect. Injection of a broader RF-Band into the source generally will enhance the resonance volume in the source, however, for optimized performance, this effect has to be accompanied by a better confinement and supply of cold electrons. MD exactly affects these changes, demonstrating that heating is not the limiting factor for the source performance here. This may be due to the restricted volume of this second generation ECRIS and does not allow to draw conclusions about the effect of DFH in large-volume superconducting sources, which provide the capability to adjust the magnetic field in a much wider range than in the case given here.

Table 1: Comparison to other Experiments

METHOD	INTENSITY GAIN				REFERENCES
	Ar^{12+}	Ar^{13+}	Ar^{14+}	Ar^{16+}	
DFH / SFH	-	**1.13**	**1.38**	**1.6**	**[1]** (10+14.5) GHz/ 14.5 GHz
DFH / SFH	**1.74**	**2.02**	**1.07**	-	**[2]** (10+14.5) GHz/ 14.6 GHz
FT(MD) / SFH(MD)	**1.038**	**1.055**	**1.0**	-	**IKF** this experiment
SFH(MD) / standard	**5**	**10**	**20**	-	**IKF** best results, good MD perform.
DFH / SFH	Xe^{30+}	Xe^{31+}	Xe^{35+}	Xe^{38+}	**[10]** (24+18) GHz/ 24 GHz
	1.55	**2.44**	**1.42**	**1.33**	

CONCLUSION

Frequency tuning is a method applied to enhance the output of highly charged ions from modern high-performance ECRIS installations. Some of the values reported in literature are compared in Table 1 to results using the ECRIS in MD-mode to enhance the highly charged ion production. It is obvious that the gain factors for the MD configuration with only single frequency injection, are by far higher than the gain factors reached by the quite involved injection of two frequencies, which for optimized conditions also demands for the ability to adjust the fields of the magnetic structures to the injection conditions. Like all methods that really improve the production of highly charged ions, DFH and MD lead to more stable plasma. However, taking into account that only the MD drastically reduces the x-ray emission from the source (by more than an order of magnitude), the MD method could be a real alternative to the double frequency plasma heating, taking also in account the much lower costs.

ACKNOWLEDGEMENT

We acknowledge financial support of the European Union 7th Framework Program FP7/2007-2013-Grant Agreement No. 262010-ENSAR. The EC is not liable for any use made on the information contained herein.

REFERENCES

[1] Z. Q. Xie, C. M. Lyneis, Rev. Sci. Instrum., 66, 8, 1995.
[2] R. C. Vondrasek, R. Scott, R. C. Pardo, Rev. Sci. Instrum. 77, 03A337, 2006.
[3] Celona et al... Rev. of Sci. Instrum., 79, 2, 2008.
[4] L. Schachter, K.E. Stiebing, S. Dobrescu, Al. I. Badescu-Singureanu, S. Runkel, L. Schmidt, and H. Schmidt Bocking, Rev. Sci. Instrum. 71,2 .918, 2000.
[5] L. Schachter, K.E. Stiebing, S. Dobrescu, Al. I. Badescu-Singureanu, S. Runkel, L. Schmidt, and H. Schmidt Bocking, Rev. Sci. Instrum. 71,2 .918, 2000.
[6] L. Schachter, S. Dobrescu, K.E. Stiebing, J.D. Meyer, Rev. Sci. Instrum. 75,5,1511, 2004.
[7] L. Schachter, K. E. Stiebing, S. Dobrescu, T. Thuiller, T.Lamy, Rev. Sci. Instrum. 79,2, 02A 329, 2008.
[8] K. E. Stiebing, L. Schachter, S. Dobrescu, Rev. Sci. Instrum., 83, 2, 2012.
[9] R. Geller, Electron Cyclotron Resonance Ion Sources and ECR Plasmas; IOP, Bristol, 1996.
[10] H. W. Zhao, W. Lu, X. Z. Zhang, Y. C. Feng, J. W. Guo, Y. Cao, J. Y. Li, X. H. Guo, S. Sha, L. T. Sun and D. Z. Xie Rev. Sci. Instrum. 83, 02A320 (2012).

Copyright © 2012 CC-BY-3.0 and by the respective authors

ISBN 978-3-95450-123-6

NEUTRAL GAS TEMPERATURE MEASUREMENTS OF A RADIO FREQUENCY MICRO-THRUSTER

A. Greig#, C. Charles, R. Boswell, R. Hawkins, Space Plasma, Power and Propulsion Laboratory, Research School of Physics and Engineering, Australian National University, Canberra, Australia
M. Bowden, Y. Sutton, Open University, Milton Keynes, UK

Abstract

A radio frequency (13.56 MHz) capacitively coupled cylindrical argon plasma discharge was analysed using optical emission spectroscopy (OES) for various powers and pressures in the ranges 5 W to 40 W and 0.5 Torr to 4 Torr. Trace amounts of nitrogen were added to the discharge to estimate the temperature of the neutrals using rovibrational band matching of the 2nd positive system of nitrogen. Comparing simulated computer generated spectra of these bands to experimentally measured spectra determined preliminary results for the rotational and vibrational temperatures of the nitrogen gas, from which the temperature of the neutrals was inferred by assuming the rotational temperature was the same as the neutral gas temperature.

INTRODUCTION

The development of increasingly smaller satellites and spacecraft has in turn developed a need for micro-thrusters that have low mass, volume and power consumption. Electric propulsion is favourable in such circumstances as the specific impulse is much higher than conventional chemical rockets [1]. Hall and gridded ion thrusters are current highly developed electric propulsion systems, however, these systems lose efficiency when scaled down [2]. Alternate options for electric micro-thrusters include resistojets and arcjets [1], hollow cathode thrusters [1,3] and radio frequency (RF) capillary discharge [4].

Another possible micro-thruster electric propulsion system consists of a capacitively coupled RF discharge (13.56MHz) within a tube with a 4.2mm inside diameter and 20mm length known as Pocket Rocket [5]. Gas, usually argon, is introduced to the system via an upstream plenum chamber with pressures around a few Torr. Electrodes placed around the Pocket Rocket tube create a cylindrical plasma discharge which is expanded into a vacuum. The discharge is weakly ionized (less that 1%) due to the higher pressures [6], therefore direct thrust from ion acceleration is negligible. However, the ions would typically reach a Bohm velocity in the order of 3000ms^{-1}, much greater than a typical thermal gas velocity of 300ms^{-1}. Charge exchange collisions between ions and neutrals may therefore result in neutral gas heating within the discharge and the thrust produced by the device will be increased over a cold gas thruster. Increased thrust from neutral gas heating makes Pocket Rocket a potentially viable micro-thruster for micro-satellites.

Previous experiments performed using a Langmuir Probe to determine the electron temperature of the Pocket Rocket discharge estimate the neutral gas temperature as 3200K at 10W and 1.5 Torr [6]. In the same paper, power coupling calculations relating the input power to discharge velocity estimated the neutral gas temperature for the same conditions much lower at 1430K.

To determine the temperature of the neutrals in the discharge, a non-invasive spectroscopy method was used where a small amount of nitrogen gas added to the discharge produces rovibrational spectral bands. The measured bands can be compared to simulated spectra to determine the rotational and vibrational temperature of the nitrogen molecules, from which the neutral gas temperature is inferred as the rotational temperature. This technique has been previously used to determine the temperature of similar discharges [7,8].

EXPERIMENTAL SETUP

The Pocket Rocket device, as shown in Figure 1(a) consists of a 4.2mm inside diameter, 1.3mm thick, 20mm long alumina tube. Argon gas is introduced to the system through an upstream plenum chamber with a diameter of 40mm and a length of 12mm. A 6mm wide copper electrode surrounds the tube at the midway point with two 3mm wide copper grounded electrodes placed either side at a distance of 3mm, creating a capacitively coupled discharge inside the tube. The discharge expands into a 750mm long, 50mm diameter evacuated glass tube which is itself attached to a vacuum chamber (160mm diameter, 300mm length) equipped with a primary rotary oil pump. A Convectron gauge measures the pressure in the upstream plenum, while a Baratron gauge measures the pressure in the vacuum chamber. The base pressure in Pocket Rocket is in the order of 10^{-3} Torr. Operating pressures measured in the plenum chamber ranged from 0.5 Torr to 4 Torr, resulting in vacuum chamber pressures approximately 2.2 times lower, from 0.2 to 1.8 Torr.

Power from an RF generator (13.56MHz) ranging from 5-40W is coupled to the system through a pi-matching network. The current and voltage supplied to the electrode are measured using a Rogowski coil and a 1/1000 high voltage probe respectively. In addition, a Bird power meter and standing wave ratio (SWR) meter are inserted between the RF generator and the matchbox to measure the forward and reflected power.

#amelia.greig@anu.edu.au

ISBN 978-3-95450-123-6

Copyright © 2012 CC-BY-3.0 and by the respective authors

The spectroscopy system, as shown in Figure 1(b), consists of a SPEX 500M monochromator with 500mm focal length, 50mm slit widths and a 1200 groove/mm grating is used in conjunction with a 4mm diameter, bifurcated fused silica fibre-optic bundle to direct light from the discharge onto a Hamamatsu C1053 photomultiplier tube (PMT). A specially designed Labview program is used to scan the monochromator over the wavelength region from 365nm to 392nm (with the data later trimmed to 365nm-381nm), simultaneously recording the data from the PMT. 12000 samples taken at 12000Hz were recorded and averaged using a PMT bias voltage of 900V.

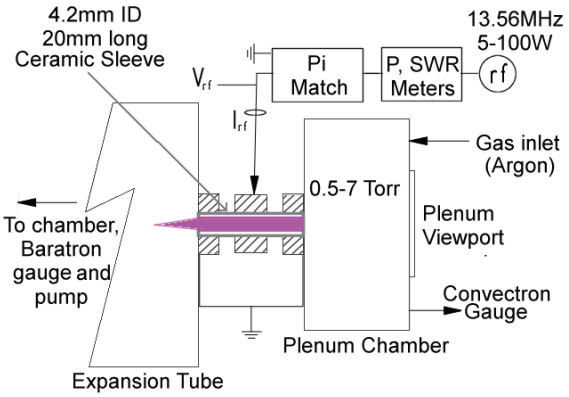

(a)

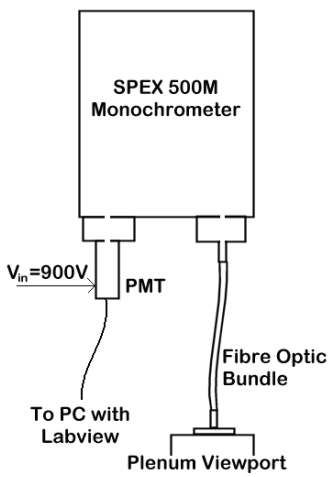

(b)

Figure 1: Experiment setup (a) Pocket Rocket System and (b) Spectroscopy equipment setup

SIMULATED SPECTRUM

As nitrogen (N_2) is a diatomic molecule it can undergo rotation and vibration as well as translation. The molecule can only exist in discrete energy levels for both rotation and vibration corresponding to the quantum numbers, denoted by J and v respectively. Transitions from an upper energy level (denoted by `) to a lower energy level (denoted by ``) release energy packets in the form of photons with different wavelengths depending on the transition. The intensity of the photons emitted depends on the rotational and vibrational temperature of the molecule. Therefore, using optical emission spectroscopy (OES), the wavelengths of the emitted light and the respective intensities can be used to determine the rotational and vibrational temperature of the molecule, and from that the neutral gas temperature implied.

The second positive system of nitrogen ($C^3\Pi \rightarrow B^3\Pi$) in the wavelength region from 365-381nm was chosen for this experiment. This wavelength region presents minimal interference from strong argon lines and the required constants are readily available as this system has been used in multiple previous works [7,8,9]. The vibrational transitions used were (0,2), (1,3), (2,4) and (3,5). For each vibrational transition, 100 J values were used.

The method of deriving the following equations will not be covered here but Herzberg [10] and Barrow [11] cover the procedure very well.

The vibrational and rotational energy of a diatomic molecule can be inferred from a quantum mechanical analysis of a non-rigid rotor (rotational) and anharmonic oscillator (vibrational) [10,11]. The resulting allowed energies for a nitrogen molecules rotation (E_J) and vibration (E_v) truncated to include only second order terms are

$$E_{J'} = hcB_{v'}J'(J'+1) + hcD_vJ'(J'+1)^2$$

$$E_{v'} = hc\omega_e(v'+1/2) - hc\omega_e x_e(v'+1/2)^2$$

where h is Planck's constant, c is the speed of light in vacuum, B_v and D_v are rotational constants taken from Herzberg [10, pg 106-107 and 12, pg 418] and ω_e and $\omega_e x_e$ are vibrational constants also taken from Herzberg [12, pg 418]

The wavelength (λ) of each transition is found using the basic relation $\frac{1}{\lambda} = \frac{\Delta E}{hc}$. Taking into account coupling of rotational and vibrational energies [12] the resulting equation becomes

$$\lambda^{Cv'J'}_{Bv''J''} = \left\{ n_a \sum_{pq} Y^C_{pq}(v'+1/2)^p[J'(J'+1)]^q - Y^B_{pq}(v''+1/2)^p[J''(J''+1)]^q \right\}^{-1}$$

where n_a is the refractive index of air. The subscripts p and q refer to the powers of the vibrational and rotational quantum numbers respectively. The constants Y_{pq} are Dunham coefficients and are amalgamations of the various constants resulting from the energy coupling for each of the power terms [13]. These were taken from Bai *et al.* [8] for values of p from 0 to 5 and q from 0 to 2.

The next step is to determine the intensity of the spectrum for each wavelength. It is assumed that the N_2 gas can be described by a Maxwell-Boltzmann distribution about a single rotational and vibrational temperature. Therefore, the intensity of the spectral line at each wavelength is given by

$$I^{Cv'J'}_{Bv''J''} = \frac{D}{\lambda^4} q_{v',v''} e^{\frac{-E_{v'}}{kT_v}} S_{J',J''} e^{\frac{-E_{J'}}{kT_r}}$$

where D is an arbitrary constant depending on the equipment used, $q_{v`,v``}$ are the Franck-Condon factors

Copyright © 2012 CC-BY-3.0 and by the respective authors

ISBN 978-3-95450-123-6

taken from Zare [14] and $S_{J',J''}$ the Holn-London factors calculated from Herzberg [10, pg 208].

Finally, to make the simulated spectrum match the observed spectrum a line broadening factor is included, determined by the particular spectroscopy apparatus used. The line broadening term used in this work was taken from Phillips [9] as

$$g(\Delta\lambda) = \frac{a-(2\Delta\lambda/W)^2}{a+(a-2)(2\Delta\lambda/W)^2}$$

where W is the full width half maximum and the wings extend to $\pm\frac{1}{2}Wa^{1/2}$. Values for a and W were determined experimentally by measuring the Hg546nm line.

Monte Carlo Markov Chains were used for fitting the measured and simulated data, resulting in a range of credible values for T_r and T_v. From the distribution of the returned values, a 95% credibility range for the temperature can be stated.

RESULTS

The raw spectral data obtained from the PMT tube was affected by relatively large background noise. A Matlab program was written to remove the noise using a smoothing function and subtract the baseline from the data. In addition, some argon peaks visible in the region of interest, identified by recording the spectrum of an argon only plasma to determine the wavelength and intensities of the relevant lines, were removed from the final nitrogen spectrum. The large amount of post-processing may affect the accuracy of the experimental data and reduce the accuracy of the gas temperature determined. However, the preliminary experimental data obtain is sufficient to demonstrate the validity of matching a simulated spectrum to the experimental data for this discharge and provide preliminary results regarding the neutral gas temperature of the discharge and the related trends with pressure and power.

An example of the experimentally determined spectrum is shown in Figure 2, for a 10 W, 1.5 Torr argon-nitrogen plasma discharge. The simulated spectrum overlaid with the same measured data is shown in Figure 3. The resulting temperatures determined were $1605 \pm 15K$ for rotational and 3905K for vibrational, inferring a neutral gas temperature $T_g = 1605 \pm 15K$. This value is within the order of the temperature estimates from the power coupling and Langmuir probe estimates discussed in the introduction, of 1430K and 3200K respectively [6].

Two independently developed codes were also used to check the measured and simulated spectra, one from the Open University in the United Kingdom and the other from the York Plasma Institute at the University of York. The Open University code compared the measured and simulated data over all four bands, determining temperatures of $T_v = 4050K$ and $T_r = 1570 \pm 75K$. The University of York code compared only the highest intensity band around 380nm to determine a rotational temperature of $T_r = 1530 \pm 25K$.

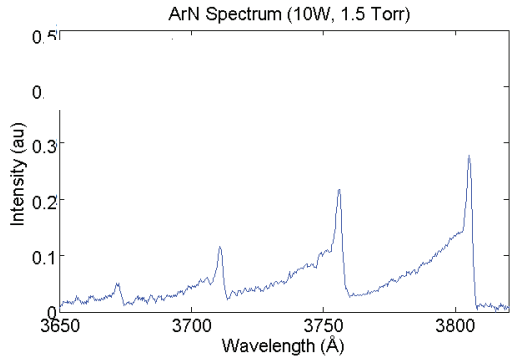

Figure 2: Measured spectrum for a 10W, 1.5 Torr argon nitrogen plasma.

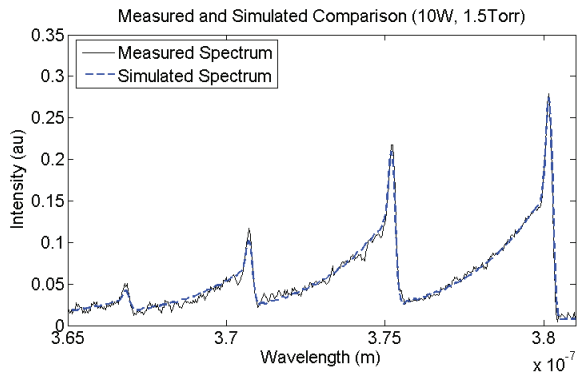

Figure 3: Measured and simulated spectrum for a 10W, 1.5 Torr argon nitrogen plasma.

The range of temperatures determined with this simulated spectrum is completely within the range of temperatures determined using the Open University code. As these codes were developed independently, the overlap demonstrates the simulated spectrum code is producing expected values. The temperature range found by the York Plasma Institute is slightly lower. However, the York code only analysed one band of the spectrum and would therefore be expected to produce slightly different results.

Measured spectra were taken for discharges ranging from 5W to 40W and 0.5 Torr to 4.0 Torr allowing analysis of the gas temperature for various operating conditions. The estimated neutral gas temperatures over the range of operating conditions and corresponding trends for changing power and pressure are shown in Figure 4. These preliminary results show power has an inverse effect on the neutral gas temperature and pressure has a large non-linear effect.

The main method for transferring energy to the neutrals, thereby producing neutral heating, occurs through ion-neutral collisions. The amount of energy transferred, therefore the temperature attained by the neutrals, is directly related to the Bohm velocity of the ions, $v_{B=}\left(\frac{eT_e}{M_i}\right)^{\frac{1}{2}} \approx 2700ms^{-1}$, where T_e is the electron temperature, e is the charge on an electron and M_i is the mass of the ion [15]. The higher the Bohm velocity, the

ISBN 978-3-95450-123-6

Copyright © 2012 CC-BY-3.0 and by the respective authors

more energy is available for transfer and the higher the resulting neutral gas temperature.

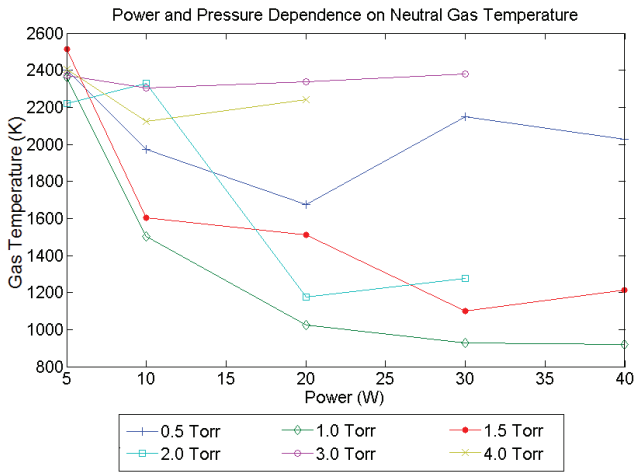

Figure 4: Neutral gas temperatures for an argon nitrogen plasma discharge for input powers of 5-40W and upstream pressures of 0.5-4.0Torr.

The change in neutral gas temperature with power is an inverse relationship with a large decrease at lower powers, tapering off to a more linear relationship as power increases. Changes to the input power of a capacitively coupled plasma have been shown to have little effect on the electron temperature [16,17]. As Bohm velocity is directly proportional to the square root of electron temperature, this would result in relatively constant neutral gas temperatures with increasing powers. However, as power increases the mode of excitation of the nitrogen molecules changes from rotational to vibrational. The rotational modes, which are the modes directly related to the translational temperatures, require lower energies to reach excited states than the vibrational modes. As the power increases, the main excitation mode shifts from rotational to vibrational, resulting in a decrease in rotational temperatures and an increase in vibrational temperatures. This is supported by the measured trends between rotational and vibrational temperatures for various powers, shown for 1.0 Torr as an example in Figure 5.

There are two main parameters affecting the relationship between neutral gas temperature and pressure. Firstly, increasing pressure decreases the electron temperature with an inverse relationship [16]. Therefore, increasing the pressure will decrease the Bohm velocity and the neutral gas temperature. However, the mean free path between charge exchange collisions is $\lambda_{cx} = \frac{1}{n_g \sigma_{cx}}$, where n_g is neutral gas density and σ_{cx} is the charge exchange cross section [15]. An increase in neutral gas density resulting from higher pressures, decreases the mean free path between charge exchange collisions and the number of collisions will increase. A higher number of collisions results in a higher transfer of energy and a higher neutral gas temperature.

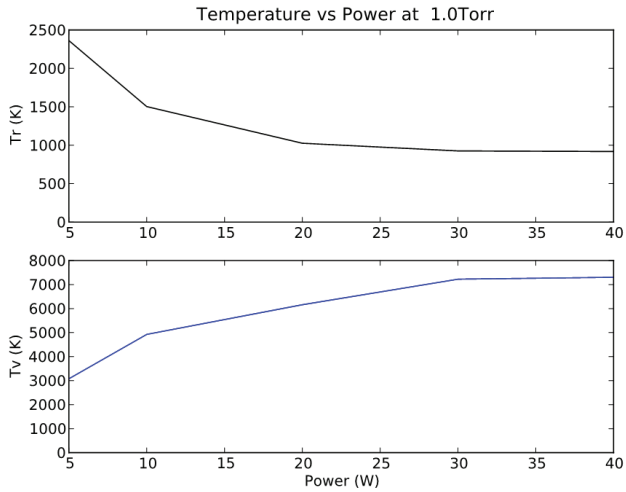

Figure 5: Change in rotational and vibrational temperature with power for a 1.0 Torr argon-nitrogen plasma.

These two aspects combined may explain the non-linear trend between neutral gas pressure and temperature. Further investigations into these results is needed to better understand the findings.

To enable a strong enough nitrogen signal to be detected with the current equipment setup, the argon-nitrogen plasma contained 90% argon and 10% nitrogen. With 10% nitrogen in the mixture the plasma properties are different from a pure argon plasma. For example, mixtures of nitrogen over a few per cent will decrease the plasma temperature [18]. To enable a more accurate estimate of the gas temperature the percentage of nitrogen in the discharge needs to be reduced. Additionally, the relatively large background noise levels in the raw measured data that lead to large amounts of post processing should be reduced. In order to improve both these issues, a charged-couple device (CCD) array will be used to repeat this experiment, allowing for a lower nitrogen per cent in the plasma and lower background noise levels.

CONCLUSION

Preliminary measurements of the neutral gas temperature of a radio-frequency capacitively coupled cylindrical argon plasma discharge, for use in a plasma micro-thruster, were determined using OES. Measurements were made for pressures between 0.5 Torr and 4.0 Torr and powers between 5W and 40W. Neutral gas heating was shown to occur for all pressures and powers tested. It was determined that gas temperature was dependent on both pressure and power. Knowledge of the effect of power and pressure on the gas temperature of the discharge will allow optimisation of the micro-thruster properties.

While the method of matching a simulated spectrum to experimentally determined data has been shown to be viable in this situation, to obtain more accurate results

Copyright © 2012 CC-BY-3.0 and by the respective authors

ISBN 978-3-95450-123-6

using the current method, the experimental data capture method needs to be refined to reduce the background noise level. Reducing the background noise level will allow for more accurate determination of the neutral gas temperature and measurements of error on the experimental data as well as the matched spectrum.

Future works on this theme will investigate different gases used for the discharge, such as pure nitrogen and carbon dioxide, to determine the effect of discharge species on the gas temperature.

ACKNOWLEDGMENTS

Aspects of this research made use of software developed by the Inversion Laboratory (ilab). Ilab is part of the Auscope AGOS project - an initiative of the Australian Government funded through the Education Investment Fund.

A special thanks also to Kari Niemi at the York Plasma Institute, University of York, for providing an additional temperature fit estimate for one of the spectrum.

REFERENCES

[1] D.M. Goebel and I. Katz, *Fundamentals of Electric Propulsion,* (Los Angeles: JPL, 2008), 1-10.
[2] A. Smirnov et al., J. App. Phys. 92 (2002)
[3] X. Gaungqing et al., Tsinghua Sci. Technol. 14 (2009)
[4] A. Dunaevsky et al., Appl. Phys. Letters. 88 (2006)
[5] R. Boswell et al., IEEE Trans. Plasma Sci. 39 (2011)
[6] C. Charles et al., Plasma Sources Sci. Technol. 21 (2012)
[7] X. Huang et al,. Physics of Plasmas. 15 (2008)
[8] B. Bai et al,. J. App. Phys. 99 (2006)
[9] D.M. Phillips, J. Phys. D: Appl. Phys. 8 (1975)
[10] G. Herzberg, *Spectra of Diatomic Molecules,* (New Jersey: Van Nostrand, 1950)
[11] G.M. Barrow, *Introduction to Molecular Spectroscopy,* (New York: McGraw-Hill, 1962)
[12] K.P. Huber and G. Herzberg, *Constants of Diatomic Molecules,* (New York: Van Nostrand, 1979)
[13] J.L. Dunham, Physical Review. 41 (1932)
[14] R.N. Zare et al., J. Mol. Spectrosc. 15 (1965)
[15] M.A. Lieberman and A.J. Lichtenberg, *Principles of Plasma Discharges and Plasma Processing,* (New Jersey: Wiley, 2005)
[16] T.E. Sheridan, J. App. Phys. 106 (2009)
[17] K. Wüst, Rev. Sci. Instrum. 63 (1992)
[18] M.H Abdullah and J.M. Mermet, J. Quant. Spectrosc. Radiat. Transfer, 19 (1977)

Copyright © 2012 CC-BY-3.0 and by the respective authors

ISBN 978-3-95450-123-6

DETAILED INVESTIGATION OF THE 4D PHASE-SPACE OF AN ION BEAM

H. R. Kremers#, J.P.M. Beijers, S. Brandenburg,V. Mironov, S. Saminathan*

KVI, Groningen, The Netherlands

Abstract

A second order transfer matrix is calculated, which is used in the calculation of a 4D phase-space distribution of a 24.6 keV He^{1+} beam. The calculated distribution matches a 4D phase-space distribution measured with the KVI pepper pot emittance meter. The pepper pot emittance meter is installed in the image plane of a dipole magnet acting as a charge-state analyser directly downstream the KVI AECR ion source. From the second order transfer matrix simple analytical equations are derived by retaining the terms for angular coefficients. These simple equations describe the main features of the phase-space correlations in the image plane. The equations show also that the subset of the 4D phase-space distribution, selected by one pepper pot aperture, results in multiple beam-lets. Due to this successful matrix modelling we conclude that the 4D phase-space distribution measured is fully determined by the ion-optical properties of the magnet.

INTRODUCTION

At KVI we have investigated the low transmission efficiency of the low-energy injection beam line of the superconducting cyclotron AGOR. For this investigation a pepper pot emittance meter [1] has been developed. With such an instrument the 4D phase space distribution was measured of a 24.6 keV He^{1+} beam in the image plane of the dipole charge-state analyzing magnet of the AECR ion source. In the measured response distribution multiple beam-lets were seen. Using second order matrix calculations of the setup a method has been developed to describe the measured phase-space distribution in a simple way. In the section 'transfer matrix' the Taylor expansion into second order is presented which can be written as an second order matrix. In the section 'simplification' simple analytical expressions are derived which reproduce the main features of the correlations. In the section 'measurements' we shown that the simple expressions describe the distributions in the projections of the measured 4D phase-space.

TRANSFER MATRIX

For the determination of the second order matrix we use the COSY Infinity 9.1 [2] code. The code is based on the principle that Taylor expansion coefficients are calculated to describe the action of ion optical elements on the phase-space coordinates in a curvilinear coordinate system. The code includes the technique of differential algebra in the numerical integrations, which permits the computation of Taylor expansions coefficients into arbitrary order. With the code a second order expression (see Eq. 1) is derived which maps the 4D state vector (x, x', y, y') of the beam from point A in an object plane to a position B in the image plane.

$$\begin{aligned}\theta_1 &= (\theta|x)x_0 + (\theta|x')x'_0 + (\theta|y)y_0 \\ &+ (\theta|y')y'_0 + (\theta|xx)x_0^2 + (\theta|xx')x_0x'_0 \\ &+ (\theta|x'x')x'^2_0 + (\theta|xy)x_0y_0 + (\theta|x'y)x'_0y_0 \\ &+ (\theta|xy')x_0y'_0 + (\theta|x'y')x'_0y'_0 \\ &+ (\theta|yy)y_0^2 + (\theta|yy')y_0y'_0 + (\theta|y'y')y'^2_0\end{aligned} \quad (1)$$

In this expression the θ_1 can be replaced by the coordinate x_1, x'_1, y_1 and y'_1 in the image plane. The terms within the bracket are the expansion coefficients. The values of these coefficients are calculated with COSY Infinity 9.1 and are shown in Table 1. They depend on drift spaces, dipole geometry and fringe fields. The dimensions of the experimental setup and main features of the magnet are described elsewhere [3].

As initial conditions in the transformation, the ions start from a small point source (ø 2mm) in a virtual object plane under random angles r'_0 with the beam axis not exceeding 64 mrad. This angle r'_0 represents the initial transversal momentum of an ion.

$$r'^2_0 = x'^2_0 + y'^2_0 \quad (2) \qquad E_t = \tfrac{1}{2}mr'^2_0 \quad (3)$$

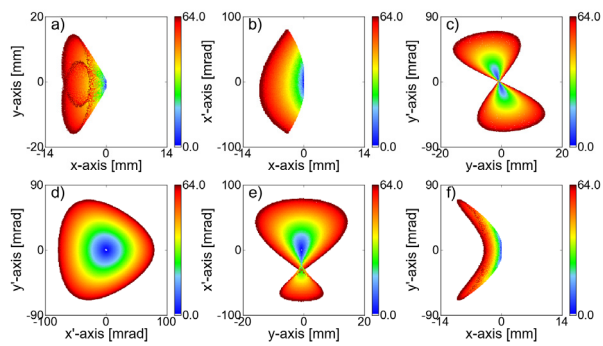

Figure 1: Calculated correlations of the initial transversal momentum r'_0 and the following combination of phase-space coordinates in the image plane: a) x-y, b) x-x', c) y-y', d) x'-y', e) y-x', e) x-y'. The colour code represents the initial transversal momentum r'_0.

email: kremers@kvi.nl
* present address: TRIUMF, 4004, Wesbrook Mall, Vancouver, CANADA

Copyright © 2012 CC-BY-3.0 and by the respective authors

ISBN 978-3-95450-123-6

Table 1: Expansion coefficients of the overall transfer matrix in COSY Infinity notation with each individual significance in percentage of the contribution to the final value normalized to 1 mm and 64 mrad (spatial units in [m] and angular units in[rad]).

$\Theta_1 = x_1$	%	$\Theta_1 = x'_1$	%	$\Theta_1 = y_1$	%	$\Theta_1 = y'_1$	%	ID coeff
0.82648	-6.2	2.26816	3.7	0	0	0	0	(θ/x)
1.668E-06	0	1.20995	125.1	0	0	0	0	(θ/x')
0	0	0	0	-0.85078	-3.1	-1.258137	2.4	(θ/y)
0	0	0	0	9.100E-02	21.2	-1.040819	126	(θ/y')
-1.3220	0	-0.84624	0	0	0	0	0	(θ/x^2)
-2.0211	1	-1.6758	-0.2	0	0	0	0	(θ/xx')
-0.94047	28.9	-1.1015	-7.3	0	0	0	0	(θ/x'^2)
0	0	0	0	1.96766	0	-3.98394	0	(θ/xy)
0	0	0	0	3.85987	0.9	-3.84397	0.5	(θ/x'y)
0	0	0	0	5.16242	1.2	5.65309	-0.7	(θ/xy')
0	0	0	0	5.34891	79.8	3.59906	-27.8	(θ/x'y')
-3.35827	0	-5.66803	0	0	0	0	0	(θ/y^2)
-3.03125	1.5	-6.27946	-0.6	0	0	0	0	(θ/yy')
-2.43596	74.8	-3.12330	-20.7	0	0	0	0	(θ/y'^2)

These simple initial conditions describe in a general way the back projection of a simulated emittance described elsewhere [3]. This simulated emittance is the result of a LORENTZ3D transport-simulation where ions start from a simulated spatial distribution in a virtual extraction aperture of a ECR ion source.

The phase-space coordinates of 10^6 ions are transformed from the object plane to the image plane using Eq.1 which results in a calculated 4D phase-space distribution in the image plane. From this 4D phase-space distribution six correlations are visualized (see Fig. 1). In Fig. 1 the colour represents the value of the initial transversal momentum r'_0 of the ion. In Fig. 1a the correlation between r'_0 and the spatial phase-space coordinates in the image plane are shown. In Fig. 1b,1c the correlation is shown of r'_0 and the x-x' and y-y' phase-space coordinates. Figure 1d shows how the angular distribution is organized around the beam axis correlated to the initial transversal momentum.

SIMPLIFICATION

The second order equation Eq.1 is a simplified expression as a mono-energetic beam is assumed. The terms with Δp/p are not printed. It is a reasonable assumption as the energy spread measured by Rodrigues et all. [4] is in the order of 14-24 eV/q with respect to an applied extraction voltage of 24.6 keV and the expansion coefficient (x|p) which is 5.4mm / %Δp/p.

In order to better understand the six correlations visualized in Fig. 1 , Eq.1 is simplified further and stripped from the terms which are not significant. The significance can be determined by normalizing the equation for a maximum in starting conditions which we have set on spatially 1 mm and angular 64 mrad. Given the small object size only the terms for the angular coordinates in Eq. 1 need to be retained. The resulting equations for the phase-space coordinates are then:

$$x_1 = (x|x'x')x'_0\,x'_0 + (x|y'y')y'_0\,y'_0 \quad (4)$$

$$x'_1 = (x'|x')x'_0 \quad (5)$$

$$y_1 = (y|y')y'_0 + (y|x'y')x'_0\,y'_0 \quad (6)$$

$$y'_1 = (y'|y')y'_0 \quad (7)$$

Two main effects can been seen. The first effect is a correlation between x_1 coordinate in the image plane and the initial transversal velocity and the second effect is a cross correlation between x'_0 and y'_0. The first effect can be seen after the introduction of a polar coordinate system where $x'_0 = r'_0 \cos\alpha$ and $y'_0 = r'_0 \sin\alpha$. After substitution of the polar coordinates in Eq.4 one finds relation Eq.8.

$$\frac{x_1}{r'^2_0} = (x|x'x') + \big((x|y'y') - (x|x'x')\big)\sin^2\alpha \quad (8)$$

In Eq.8 one can see that the ratio x_1/r'^2_0 is constant for α close to zero. Furthermore, $\sin^2\alpha$ is always positive and the coefficients are negative (see Table.1). Therefore, all ions arrive in the image plane at a negative x_1 coordinate. (see Fig. 1a). This is caused by the fact that ions with larger initial transversal velocity have lower longitudinal velocity and consequently are bend over a larger angle than 110 degrees. Furthermore, if we substitute (5) and (7) in (4) a description of an ellipsoid in the x'_1-y'_1 phase-space coordinates is found. The size of the ellipsoids increases as a function of x_1. The major and minor axes of these ellipsoid are given by:

$$a = \sqrt{|x_1|}(x'|x')/\sqrt{(x|x'x')} \quad (9)$$

$$b = \sqrt{|x_1|}(y'|y')/\sqrt{(x|y'y')} \quad (10)$$

ISBN 978-3-95450-123-6

Copyright © 2012 CC-BY-3.0 and by the respective authors

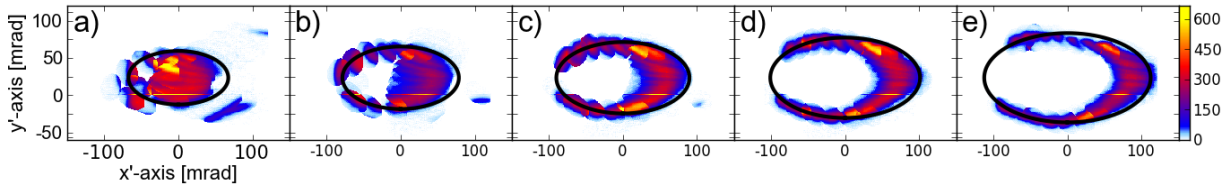

Figure 2: Measured sliced x′-y′ projection as function of five scan positions: a) x_1= -2 mm, b) x_1 = -3.5 mm, c) x_1= -5.0 mm, d) x_1 = -6.5 mm, e) x_1 = -8.0 mm. Black lines are from Eq.5 and Eq.7 substituted in Eq.4.

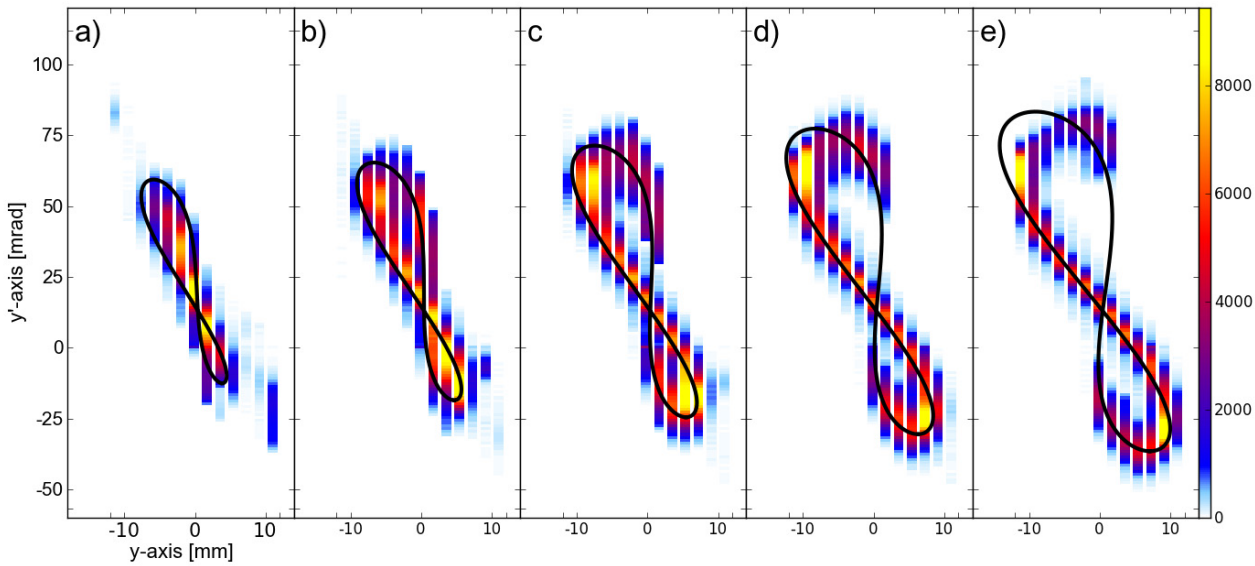

Figure 3: Measured sliced y-y′ projection at five different scan positions: a) x_1= -2 mm, b) x_1 = -3.5 mm, c) x_1= -5.0 mm, d) x_1 = -6.5 mm, e) x_1 = -8.0 mm. Black lines are from Eq.11 and Eq.7 in polar coordinates.

The second effect of the cross correlation can be seen in Eq.11 which results when Eq.6 is rewritten in polar coordinates. A closer look at Eq.11 shows that the term with ‘sin(2α)‘ generates the ‘figure eight’ distribution (see Fig. 1c).

$$y_1 = (y \mid y')r'_0 \sin\alpha + (y \mid x'\,y')r'^2_0 \cdot \tfrac{1}{2}\sin 2\alpha \quad (11)$$

The coefficient (y|x′y′) describes the ‘strength’ of the ‘figure eight’ in the distributions. This term is also responsible for the multiple beam-lets as for some values of y_1 one finds four different values of y'_1.

MEASUREMENTS

The two effects described in section above are clearly visible in the projections of the measured 4D phase-space distribution of the 24.6 keV He^{1+} beam. First, effect as describe earlier, can be observed in the measured x′-y′ projection (see Fig. 2) at five different x_1 positions. Each distribution separately is described by an ellipsoid derived from the Taylor expansion with values for major and minor axis derived from the expansion coefficients.

The second effect identified as a cross correlation between x′ and y′ is also observed in the measurements. In Fig. 3 the measured y-y′ projection of the 4D phase-space distribution is shown for five x_1 positions. The measured distributions are well described with the curves defined by Eq.7 and Eq.11.

CONCLUSIONS

The measured 4D phase-space distribution of an ion beam is successfully calculated with the help of a second order transfer map developed with COSY Infinity 9.1. The beam characteristics behind the magnet are fully determined by the ion-optical properties of the magnet. Further, the structure of the phase-space distribution is clarified with a simple model extracted from the second order transfer map.

ACKNOWLEDGMENT

This work is part of the research program of the “Stichting voor Fundamenteel Onderzoek der Materie” (FOM) with financial support from the “Nederlandse organisatie voor Wetenschappelijk Onderzoek” (NOW). It is supported by the University of Groningen and by “Gesellschaft für Schwerionenforschung GmbH” (GSI), Darmstadt, Germany. We acknowledge the financial support of the European Union Seventh Framework Program FP7/2007- 2013 under Grant Agreement n° 262010 - ENSAR.

Copyright © 2012 CC-BY-3.0 and by the respective authors

ISBN 978-3-95450-123-6

REFERENCES

[1] Kremers, H.R., J.P.M. Beijers, and S. Brandenburg, A Versatile Emittance Meter and Profile Monitor, in DIPAC07. May 2007: Venice, Italy. p. 195-197.
[2] Makino, K. and M. Berz, COSY INFINITY Version 9. Nuclear Instruments & Methods in Physics Research Section a-Accelerators Spectrometers Detectors and Associated Equipment, 2006. 558(1): p. 346-350.
[3] Saminathan, S., et al., Optimization of a charge-state analyzer for electron cyclotron resonance ion source beams. Review of Scientific Instruments. 83(7): p. 073305 (6 pp.)-073305 (6 pp.).
[4] Rodrigues, G., et al., Effect of source tuning parameters on the plasma potential of heavy ions in the 18 GHz high temperature superconducting electron cyclotron resonance ion source. The Review of scientific instruments. 83(3): p. 033301.

Copyright © 2012 CC-BY-3.0 and by the respective authors

ISBN 978-3-95450-123-6

NEW EXTRACTION DESIGN FOR THE JYFL 14 GHz ECRIS*

V. Toivanen†, T. Kalvas, H. Koivisto, J. Komppula and O. Tarvainen
JYFL, Jyväskylä, Finland

Abstract

A new extraction system has been designed and constructed for the JYFL 14 GHz ECRIS at the Department of Physics, University of Jyväskylä (JYFL). The goal of the new design was to improve the performance of the ion source and increase the transmission efficiency of the low energy beam transport and the accelerator by being able to handle higher beam currents, yield better beam quality and offer more tuning flexibility. The design is based on simulations with the IBSimu code. The suitability of the code for this task was verified by simulating the old extraction system resulting to good agreement between simulations and measurements. The new design, simulations and the first experimental results are presented.

INTRODUCTION

In order to improve the "ion source-to-target" performance at JYFL (Department of Physics, University of Jyväskylä), the low energy beam transport (LEBT) section of the beam line from the JYFL 14 GHz ECRIS [1] to the K-130 cyclotron will be upgraded in intermediate steps. The first section of the JYFL LEBT is presented in Fig. 1. Designing and constructing a new extraction system for the JYFL 14 GHz ECRIS is the first step of the project. This upgrade aims to make the ion source extraction more flexible and offer better ion beam starting conditions to facilitate further beam line modifications. Better beam quality and overall performance of the ion source, especially with high extracted total beam currents, are also desired.

SIMULATIONS

The new extraction system was designed by computer simulations with the IBSimu code [2] developed at JYFL. The code is capable of modeling extraction of multiple ion species in the presence of external magnetic field and strong space charge, which are the conditions normally present with ECR ion sources. However, the positive plasma model used by the code does not exactly match the complicated plasma conditions of ECR ion sources, a feature that has proven challenging for simulation codes. To study the feasibility of the code for ECRIS conditions the old extraction geometry was first modeled with IBSimu and the results were compared with measurements.

* This work has been supported by the EU 7th framework programme "Integrating Activities - Transnational Access", project number: 262010 (ENSAR) and by the Academy of Finland under the Finnish Centre of Excellence Programme 2006 - 2011 (Nuclear and Accelerator Based Physics Research at JYFL). VT acknowledges the support of the Ehrnrooth foundation.

† ville.toivanen@jyu.fi

Copyright © 2012 CC-BY-3.0 and by the respective authors

ISBN 978-3-95450-123-6

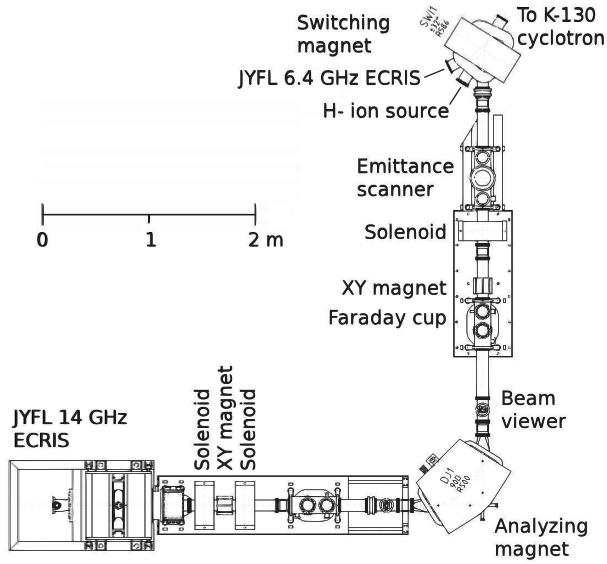

Figure 1: First section of the JYFL LEBT beginning from the JYFL 14 GHz ECRIS.

Old Extraction Design

Figure 2 shows simulation result of the original extraction geometry of the JYFL 14 GHz ECRIS with 1 mA of argon beam and optimum tuning. The beam includes charge states 1+ to 16+ with their ratios taken from measured charge state spectrum. Charge states 17+ and 18+ are omitted due to negligible beam currents. According to the simulations, the extraction system is barely able to handle the extracted beam. The outermost parts of the beam are collimated at the puller face and at the last grounded electrode of the Einzel lens. The beam exiting the extraction ($x = 0.525$ m in Fig. 2) is large, about 65 mm in diameter (FWHM of the profile) and rather divergent with maximum half-axis divergence of about 60 mrad. These values match well with the (64 ± 1) mm diameter and (60 ± 10) mrad half-axis divergence measured at the same location after the extraction with identical settings.

Increasing the current extracted from the plasma increases the simulated beam size due to space charge growth, leading to increased beam losses and a substantial drop in transmission through the extraction region (see Fig. 3). As a consequence, the total beam current leaving the extraction remains roughly constant at the level of $\sim$1 mA but the beam quality and profile are degraded. These results agree well with the experimental observation of degraded beam transmission with high total extracted currents in excess of 1 mA [3]. The collimation of the beam has been

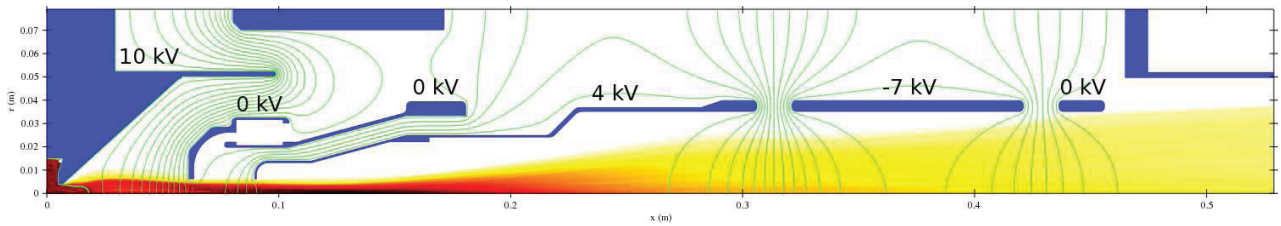

Figure 2: Simulation result (logarithmic trajectory density) for the old extraction system with 1 mA of argon beam, charge states 1+ . . . 16+, tuned for optimum performance. From left to right, plasma electrode (10 kV), puller electrode (0 kV), grounded puller holder, deceleration electrode (4 kV), Einzel electrode (-7 kV) and Einzel ground electrode.

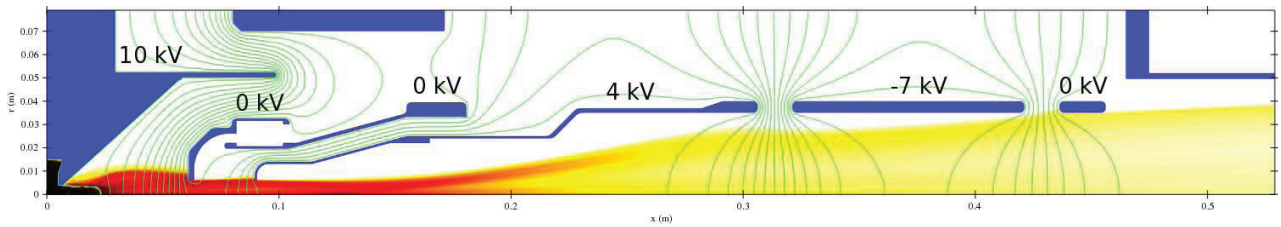

Figure 3: Simulation result for the old extraction system with 3.0 mA of argon beam with same settings as in Fig. 2. Varying electrode voltages shifts beam losses between electrodes, leading no insignificant improvements in the extracted beam.

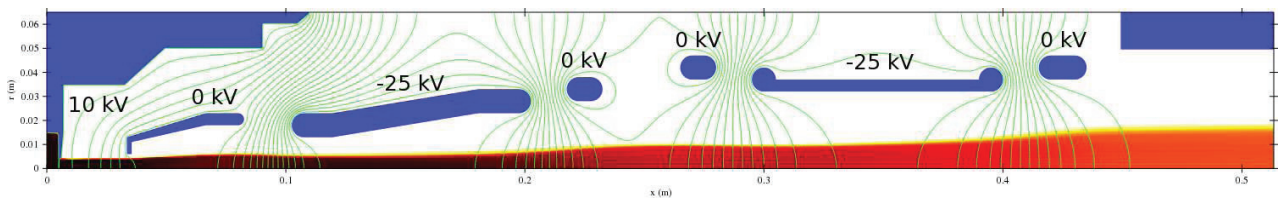

Figure 4: Simulation result for the new extraction system with 1.5 mA of argon beam, charge states 1+ . . . 16+, tuned for optimum performance. From left to right, plasma electrode (10 kV), puller electrode (0 kV), first Einzel (-25 kV), Einzel lens ground electrodes, second Einzel (-25 kV) and Einzel ground electrode.

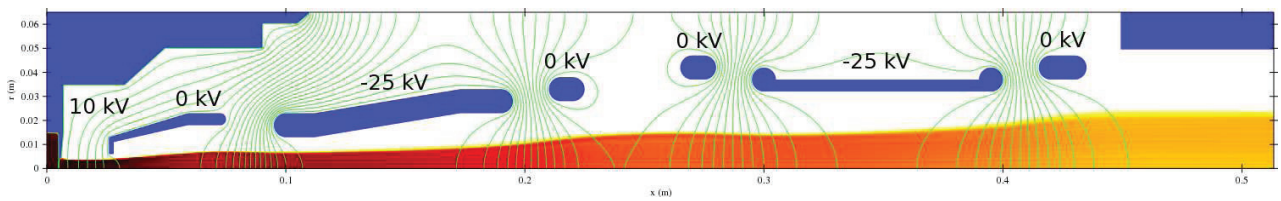

Figure 5: Simulation result for the new extraction system with 3 mA of argon beam with same settings as in Fig. 4.

verified by inspecting the puller face, which shows clear evidence of beam bombardment.

The main limitation of the JYFL 14 GHz ECRIS extraction is the low source potential, normally around 10 kV, dictated by the cyclotron injection. Hence, the beam energies are relatively low and the space charge effects are strong, i.e. slowing the beam further is undesirable. The old extraction design includes a decelerating positive electrode (see Fig. 2), use of which is inevitable in order to achieve reasonable extracted beam currents. However, this leads to emittance growth and decrease of beam quality. Also, the single accelerating Einzel lens, operated at low voltages (below extraction voltage) due to lens geometry limitations (high voltage sparking), can not provide enough focusing power to handle the diverging beam.

In the old extraction geometry the plasma electrode has a strongly conical shape, as shown in Figs. 2 and 3. As a result, the acceleration gap length between the plasma and puller electrodes increases towards the optical axis. This leads to weakening of the electric field at the extraction aperture and subsequent decrease in the Child-Langmuir limit for the maximum space charge limited current.

New Extraction Design

In the new design the decelerating electrode is removed and the beam transport is optimized with two accelerating

ISBN 978-3-95450-123-6

Copyright © 2012 CC-BY-3.0 and by the respective authors

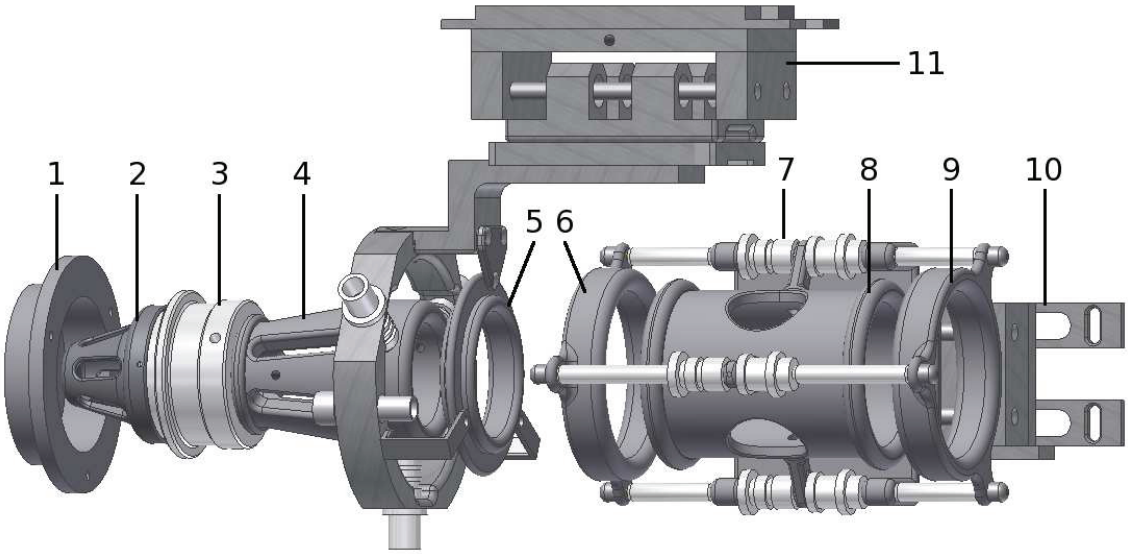

Figure 6: The new extraction system with a plasma electrode (1), a puller electrode (2) and two Einzel lenses (2-5 and 6-9). Macor and alumina are used as insulating materials (e.g. 3, 7). Lense positions can be varied independently (10, 11).

Einzel lenses to provide enough focusing power and flexibility. Accelerating Einzel lenses are more challenging to design than decelerating ones due to higher operating voltages but they offer clear advantage for low energy beams, as the energies of ions passing through the lens are not reduced below their initial values, which would increase the space charge effects. Also, unlike decelerating Einzel lenses, the accelerating ones do not act as electron collectors reducing the space charge compensation degree of the ion beam. Compared to decelerating Einzel lenses, the accelerating ones cause less spherical (smaller beam size inside lens) and chromatic (decreased $\Delta E/E$ inside lens) aberrations [4].

As the flexibility of the extraction system and extracted beam properties are very important features for the future LEBT upgrades, both Einzel lenses were designed to be movable. The puller electrode was designed to be part of the first Einzel lens, replacing the first grounded electrode, to simplify the design and to provide adjustable acceleration gap length.

To improve the electric field structure at the acceleration gap the new design includes an almost flat plasma electrode. To achieve this the extraction aperture position was shifted 12 mm outwards. The magnetic iron ring surrounding the extraction was modified to match the magnetic field maximum at the new aperture location.

Simulation results of the new extraction design for 1.5 mA and 3 mA argon beams are shown in Figures 4 and 5. The results implicate that the new design is capable of handling considerably higher beam currents than the old one and still provide good beam quality and small beam spot size. The beam diameter (FWHM of profile) and maximum half-axis divergence after the extraction (at $x = 0.513$ m in Figs. 4 and 5) are 32.5 mm and 40 mrad for the 1.5 mA case and 45 mm and 60 mrad for the 3 mA case. The performance of the new design with different acceleration voltage was studied by varying the source potential between 8 – 18 kV. Good results were achieved and no notable performance degradation was observed even with highest voltages. The simulations were performed with full space charge (worst case scenario) and the space charge compensation effects were evaluated by altering the total extracted beam current.

Table 1: Transmission results with old and new extraction systems (ES). I_{ECR} and I_{ACC} are beam currents measured after the ECRIS and the cyclotron (in μA), T the transmission efficiency (in %) and $\epsilon_{\mathrm{rms}}^{\mathrm{norm}}$ the normalized 1-rms emittance (in mm mrad).

Beam	ES	I_{ECR}	I_{ACC}	T	$\epsilon_{\mathrm{rms}}^{\mathrm{norm}}$
$^{40}Ar^{8+}$	Old	90	2.3	2.6	0.127 ± 0.004
$^{40}Ar^{8+}$	Old	138	3.1	2.3	0.126 ± 0.004
$^{40}Ar^{8+}$	Old	170	3.6	2.1	0.095 ± 0.003
$^{40}Ar^{8+}$	New	84	3.7	4.4	0.101 ± 0.004
$^{40}Ar^{8+}$	New	102	4.1	4.0	0.097 ± 0.003
$^{40}Ar^{8+}$	New	132	6.0	4.6	0.053 ± 0.002
$^{40}Ar^{8+}$	New	187	7.4	4.0	0.074 ± 0.003
$^{84}Kr^{16+}$	Old	31	1.6	5.0	-
$^{84}Kr^{16+}$	Old	60	2.6	4.3	-
$^{84}Kr^{16+}$	Old	30	1.6	5.3	-
$^{84}Kr^{16+}$	New	40	3.1	7.8	-
$^{84}Kr^{16+}$	New	30	3.1	10.3	-

Copyright © 2012 CC-BY-3.0 and by the respective authors

ISBN 978-3-95450-123-6

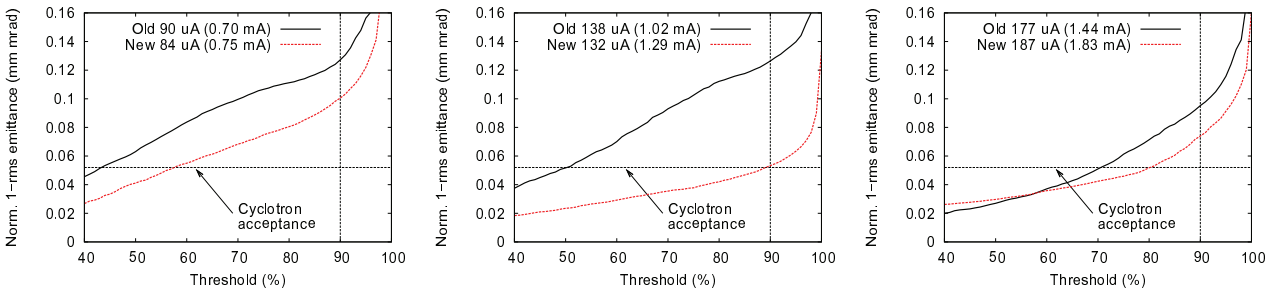

Figure 7: Emittance threshold analysis of $^{40}Ar^{8+}$ for various beam currents. Total extracted current in parenthesis. The 90 % threshold value, used for emittance comparisons, and the K-130 cyclotron acceptance (0.052 mm mrad) are indicated with dashed lines.

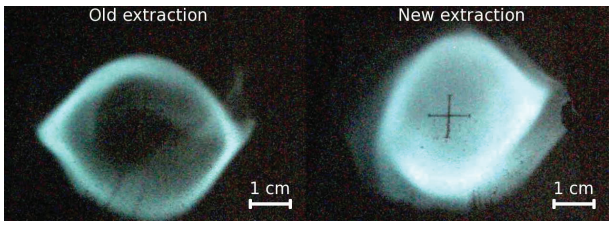

Figure 8: $^{40}Ar^{8+}$ profiles measured after mass separation with old and new extraction designs. Total extracted beam ∼1 mA and mass separated beam current ∼130 μA in both cases.

FIRST RESULTS WITH THE NEW EXTRACTION DESIGN

The mechanical design of the new extraction system is presented in Fig. 6. The performance of the new extraction was tested by running a series of transmission measurements for $^{40}Ar^{8+}$ and $^{84}Kr^{16+}$. The results for both systems are presented in Table 1. For $^{40}Ar^{8+}$ the total transmission through the cyclotron averaged over the data points in Table 1 increased from 2.3 % to 4.2 %. The average transmission of the LEBT increased from 23.0 % to 32.8 % and the transmission of the K-130 cyclotron from 10.0 % to 12.9 %. For $^{84}Kr^{16+}$ the total transmission increased from 4.9 % to 9.0 %. The new extraction yields lower emittance values, as shown in Table 1, indicating better beam quality. The emittance threshold analysis, presented in Fig. 7, shows that with the new extraction a higher fraction of the beam particles are within a given emittance, accounting for the improved transmission.

Figure 8 shows comparison of typical $^{40}Ar^{8+}$ beam profiles measured with KBr scintillation screen after the mass separation (see Fig. 1). The beam profiles measured with the new extraction system tend to be more uniform compared to the beams measured with the old extraction, however still exhibiting some degree of hollowness. This indicates that phenomena outside the extraction region, such as the magnetic solenoid focusing scheme before mass separation and the initial ion disribution extracted from the plasma, still contribute to the hollowness.

DISCUSSION

The new extraction system has been designed, constructed and installed successfully. The first tests and delivered ion beams show improved performance compared to the earlier system. In the presented measurements the optimum performance was achieved with lower Einzel lens voltages than used in the simulations, usually around -10 . . . -15 kV. This can be related to the space charge compensation present in the extraction region, leading to decrease in the required focusing power. Also, the matching of the extraction to the following beam line ion optics plays an important role in determining the lens voltages. As the operation experience increases the matching of the new extraction system to the existing beam line optics is expected to improve, leading to a further improvement in the overall performance of the ion source, LEBT and the cyclotron.

REFERENCES

[1] H. Koivisto, et al., Nucl. Instrum. Meth. Phys. Res. B 174, 379-384 (2001).

[2] T. Kalvas, et al., Rev. Sci. Instrum. 81, 02B703 (2010).

[3] H. Koivisto, et al., Rev. Sci. Instrum. 79, 02A303 (2008).

[4] H. Liebl, Applied Charged Particle Optics, Springer, 2008 (ISBN: 978-3-540-71924-3).

ISBN 978-3-95450-123-6

Copyright © 2012 CC-BY-3.0 and by the respective authors

SPACE CHARGE COMPENSATION MEASUREMENTS OF MULTI-CHARGED ION BEAMS EXTRACTED FROM ECR ION SOURCES

D. Winklehner#, D. Leitner, G. Machicoane, F. Marti, D. Cole, L. Tobos, NSCL/MSU, East Lansing, USA

Abstract

In this contribution, we present measurements of the beam potential performed after the extraction region of ECR ion sources in dependence of the base pressure in the beam line and other parameters, e.g. total extracted current, using a Retarding Field Analyzer (RFA). If the beam current and the beam profile are known, it is possible to infer the level of space-charge compensation from the measured beam potential distribution. Preliminary results are discussed and compared to simulations.

INTRODUCTION

Space-charge compensation in beam lines due to the interaction of the beam with residual gas molecules is a well-known phenomenon for high current injector beam lines. When the beam interacts with the residual gas in the beam line, electrons are separated from gas molecules by charge-exchange processes and accumulate inside the beam envelope, while the ions created in the process are expelled by the positive beam potential. This lowers the space-charge potential of the beam and is called space-charge compensation or - neutralization. In [1], Soloshenko investigates the simple case of space charge compensation for the stable stationary beam. A steady-state is defined for the beam, where the rates of electrons created/entering the beam and leaving the beam are equal. Electrons captured inside the beam may gain enough energy to leave through Coulomb collisions with the beam ions themselves and through collective processes. Considering also the energy balance of the electrons, Soloshenko arrives at the following expression for the potential difference of beam center and and beam edge ($\Delta\phi = \phi_{center} - \phi_{edge}$):

$$\Delta\phi = \sqrt{3\mathcal{L}}\left(\frac{M}{m}\right)^{1/2}\left(\frac{\varphi_i}{V_0}\right)^{1/2} n_+^{1/2}\left(\frac{1}{n_0\sigma_e}+\frac{v_+\sigma_i r_0}{2v_i\sigma_e}\right)^{1/2}\cdot e$$

Where $\mathcal{L} = 2\pi\Lambda$ with Λ a Coulomb logarithm, r_0 the beam radius, φ_i the gas ionization potential, M the beam ion mass, eV_0 the beam ion energy, $v_{i/+}$ the plasma ion/beam ion velocities, $\sigma_{i/e}$ the ion/electron originating cross-sections and $n_{0/+}$ the residual gas/beam ion densities. By investigating the balance of the two terms in the sum he concludes that for low pressures we can expect a decrease in $\Delta\phi$ with increasing pressure, whereas for high pressure, $\Delta\phi$ reaches its minimum and becomes essentially independent of the pressure (see [1] for more details).

winklehner@nscl.msu.edu

In addition, ions hitting apertures, charged electrodes, ion optics elements and beam line coatings can influence the creation and loss of compensation electrons greatly and have to be taken into consideration.

For beam lines using mostly magnetic focusing elements and for pressure around 10^{-5} Torr, almost full compensation has been predicted [1] and observed [2]. However, due to the low pressure (typically 10^{-7} to 10^{-8} Torr) required for the efficient transport of high charge state ions, ion beams in ECRIS injector lines may be only partly neutralized and space charge effects may be present. With the dramatic performance increase of the next generation Electron Cyclotron Resonance Ion Sources it is possible to extract tens of mA of beams from ECR plasmas [3]. In this high current regime, non-linear defocusing effects due to the space-charge potential of the beam become more and more important. In order to develop a realistic simulation model for low energy beam transport lines, it is important to estimate the degree of space charge compensation along the Low Energy Beam Line (LEBT).

HARDWARE

ECR Ion Sources

This type of ion source is described in great detail elsewhere [4]. One point to be made, though, is that the plasma from which the ions are extracted is confined by a strong magnetic field, which is usually a superposition of a solenoid field (longitudinal confinement) and a sextupole field (radial confinement). For special applications, however, (e.g. high currents of protons) it is preferable to use only the solenoid magnets (e.g. LEDA source, see below). In this context it is important to mention that the sextupole field has great influence on the shape and behavior of the extracted beam. While beams from sources using only solenoids are typically radially symmetric (uniform or Gaussian beam profile), ECR beams from sources using sextupoles exhibit a triangular or star-shaped cross-section [5, 6]. The triangular shape and intrinsic sextupole moment of the beam has been subject to research for many years now and has to be taken into account when designing the LEBT of an ECRIS. It might also influence the measurement of beam neutralization with an RFA as will be seen later.

SuSI

The Superconducting Source for Ions is one of the injector sources of the Coupled Cyclotron Facility at the National Superconducting Cyclotron Laboratory (NSCL) at Michigan State University. As the name suggests, the magnetic fields are provided by a set of superconducting

Copyright © 2012 CC-BY-3.0 and by the respective authors

ISBN 978-3-95450-123-6

magnets. The position (about 46 cm downstream of the extraction aperture) at which the measurements have been conducted can be seen in figure 1. The Einzel Lens that is used to match the SuSI beams into the analyzing beam line section was turned off for these measurements. Oxygen and argon beams with total extracted currents of up to 3 mA were used in these measurements.

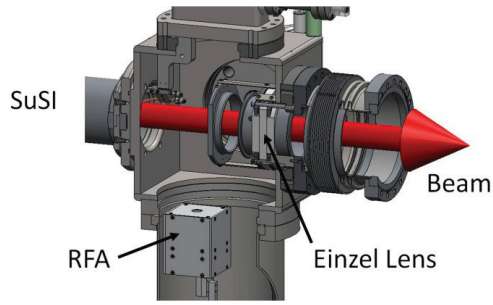

Figure 1: RFA in SuSI LEBT – diagnostic box 1. The Einzel Lens was turned off during measurements.

Artemis A

Artemis A is the second injector source used at the NSCL and is based on the design of the AECR-U source at Lawrence Berkeley National Laboratory [7]. The solenoid magnets are room temperature magnets and the radial confinement field is provided by a permanent magnet sextupole [8]. Oxygen and argon beams with total extracted currents of up to 2.8 mA were used in these measurements. The RFA was mounted in a 6-way cross in a vertical beam line between the source and the analyzing magnet, right after an electrostatic quadrupole doublet, looking at the beam from the side. The 6-way cross also held a faraday cup for measuring the beam current at that position and a turbo molecular pump as well as a needle valve for adjusting the beam-line pressure.

LEDA Source

Developed at Chalk River Laboratories, a high current proton source was extended as the Low-Energy Demonstration Accelerator (LEDA) injector source in Los Alamos and recently moved to the NSCL, where the presented measurements have been conducted. The LEDA source does not have a sextupole magnet and thus produces to first order round beams. Microwave powers of 500 to 700 W were used to produce 2-10 mA proton beams with a small contribution of H_2 ions. The ratio of H^+ to H_2^+ for this source is measured to be ~9:1 [9]. The RFA was mounted in a box approx. 50 cm after the plasma aperture looking at the beam from the side.

Retarding Field Analyzer (RFA)

The RFA consists of three parallel meshes housed in a grounded box with a set of two apertures for collimation of the secondary ions upon entering the detector (see figure 2). Mesh 1 is grounded at all times and helps providing a uniform retarding field together with mesh 2 which is set to the retarding potential (-100 V to +200 V). Mesh 3 is typically set to -450 V and acts as an electron repeller, both to keep electrons from the outside out and to turn back electrons produced upon impact of the measured ions on the collector. The collector is a copper plate.

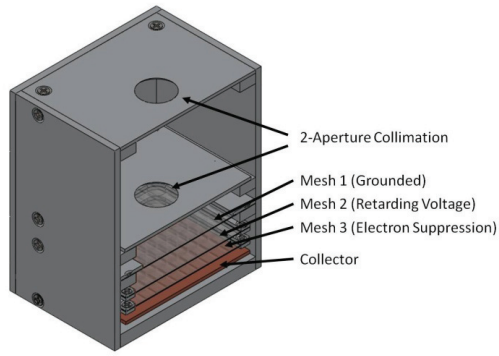

Figure 2: Cut isometric view of the RFA.

Extensive simulations using SIMION 8.1 [10] have been undertaken in order to determine the theoretical resolution of the device. In these simulations randomly generated monoenergetic particles filling the maximum acceptance of the detector were sent into the detector and the measured energy distribution was analyzed. The FWHM of the distributions were ~0.55 eV with a base width of 1.2 V. Together with a stability of the power supplies of better than 0.1 V a conservative estimation of the resolution of <1 eV can be made.

Alternative designs were considered, like giving the meshes a curvature to ensure maximum energy loss even for particles entering under an angle, but simulations showed negligible change in the resulting spectra.

Initial measurements without the double aperture system showed long tails on both, the high and the low energy side. Those could be mostly suppressed by adding the apertures, albeit thereby reducing the maximum current reaching the collector plate.

Data acquisition is managed by a computer program setting the voltage on mesh 3 and reading the current from an in-house fabricated BCM (beam current monitor) via EPICS/PLC communication.

MEASUREMENTS

Analysis Method

For the round beams from the LEDA source, we assume that the beam is a uniformly charged cylinder and the ions are created inside this cylinder through charge exchange processes. They are then expelled by the positive beam potential and carry a kinetic energy depending on the radial distance from the beam center at the time of their separation from the gas molecule. This is a good approximation, as has been seen in previous measurements with a similar device [2]. The potential difference between center and edge of the beam is then given by:

ISBN 978-3-95450-123-6

Copyright © 2012 CC-BY-3.0 and by the respective authors

$$\Delta\phi = \frac{I \cdot (1-f)}{4\pi \cdot \varepsilon_0 \cdot \beta c}$$

Where I is the total beam current, ε_0 the vacuum permittivity, βc the velocity of the beam, and f the neutralization factor between 0 and 1.

The potential difference $\Delta\phi$ can be obtained from the RFA spectrum by taking the derivative dI/dV which yields the energy distribution of the ions. $\Delta\phi$ is then given by the base width of the distribution (method 1) minus the base resolution of 1.2 V (method used in [2]). On the other hand, at the low currents that we are measuring, other effects like the initial random motion of the gas molecules, collisions, or the presence of a beam halo can add to the spectrum and round off the edges or even produce long tails. This widens the base of dI/dV. As a second method of analyzing the spectra, we suggest fitting with three straight lines and taking their crossing points as ϕ_{center} and ϕ_{edge} (method 2). An example of both methods for a typical spectrum can be seen in figure 3.

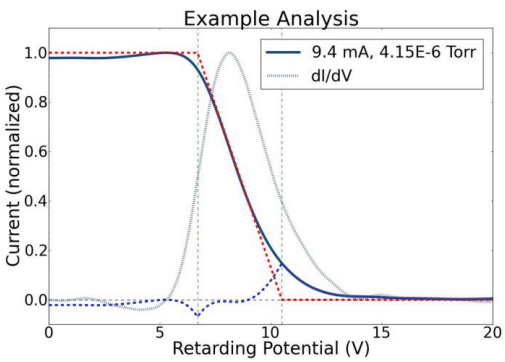

Figure 3: LEDA, Example Analysis of a LEDA ion source neutralization spectrum. The solid blue line is the normalized spectrum, the dotted line is dI/dV and the dashed red lines are the fit according to method 2. Method 1 would use the base width of dI/dV as $\Delta\phi$. $\Delta\phi_{meth.1}$ = 4.6 V, $\Delta\phi_{meth.2}$ = 3.8 V and f_{e1} = 78.4%; f_{e2} = 83.0%.

Measurements with Artemis A

The first measurements were obtained on the Artemis A line. In this setup, the RFA was operated with a larger aperture (r = 1.1 cm) and without the second collimation aperture. Following [2] we tried to relate the saturated RFA current $(I_{RFA})_s$ to theoretical predictions based on the 1-D continuity equation:

$$(I_{RFA})_s = \frac{{r_a}^2 \cdot T \cdot I \cdot \left(\sum n_g \sigma_i\right)}{2d}$$

with r_a the RFA entrance aperture radius (1.1 cm), d the distance from aperture to beam axis (10 cm), σ_i the ion production cross-section, n_g the gas density, T the grid material transparency, and I the ion beam current. The σ_i were calculated for the different beam components (multi-species beam) individually according to an empirical formula [11]. Predictions compared to measurements can be found in figure 4. A transparency factor of T = 0.4 (40% transmission) gave good agreement.

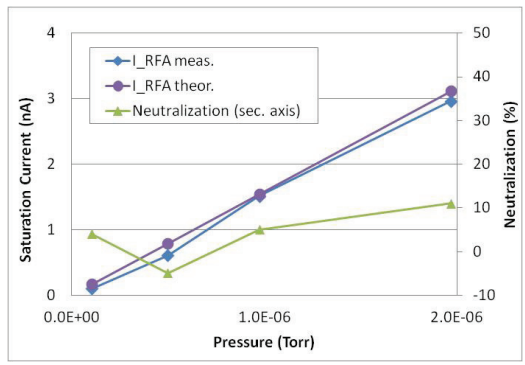

Figure 4: Artemis: Oxygen beam, pressure variation.

The neutralization values obtained with the aforementioned analysis method are also displayed in figure 4. They are distributed around 0 % with an overall tendency to increase slightly with pressure, indicating that in this region of the beamline no space charge compensation occurs. This might be due to the presence of the electrostatic quadrupole doublet, although the measurement was taken approx. 20 cm after the exit of the quadrupole. One of the values is slightly negative, stemming from the $\Delta\phi$ in the spectrum being larger than the theoretical prediction for the completely uncompensated beam. See SuSI measurements below for a discussion.

Measurements with the LEDA Source

Measurements in the LEDA source were taken with both RFA apertures in place (as depicted in figure 2) and their radius decreased to 0.88 cm. The distance d is now 31.7 cm. The comparison of saturation current with theory is shown in figure 5. Here we had to decrease the transmission factor to T = 0.1 to match the experimental values. This is a factor 4 lower than for Artemis without the inner aperture. Several reasons are conceivable:

- A known misalignment of the LEDA beam.
- Longitudinal velocity components of the created ions (see *Measurements with SuSI* below for discussion).
- Aspect ratio of the ARTEMIS beam.
- Uncertainties of the absolute beam line gas pressure and composition.

But further investigation is necessary.

Despite the small collector currents, it was possible to obtain neutralization spectra for different beam currents (see figure 6) and different beam-line pressures (see figure 7). No significant change in neutralization with increasing current was observed. The neutralization for 3-10 mA lies between 60% and 80% (depending on the analysis method) at a pressure of 4.2E-6 Torr.

This is lower than the reported neutralization factors for high current operation with the LEDA source, but as shown in figure 8 the neutralization factor increases to 89% at higher beam line pressure (which are present at

Copyright © 2012 CC-BY-3.0 and by the respective authors

ISBN 978-3-95450-123-6

high current operations). It has also been reported previously [2] that for lower currents the neutralization factor is dependent on total beam current and drops with current.

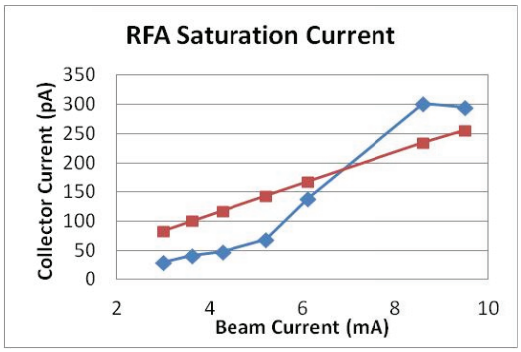

Figure 5: Blue diamonds: RFA saturation current on collector, red squares: Calculation with continuity equation using T = 0.1 (cf. Text).

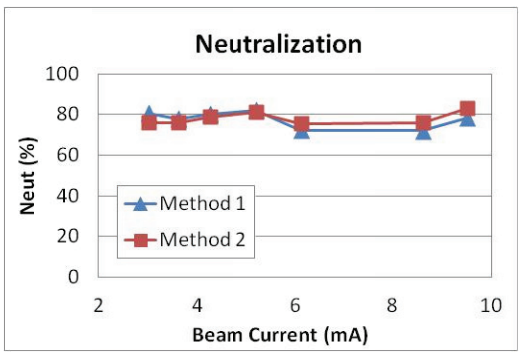

Figure 6: Neutralization level vs. beam current. The pressure in the beam line was 4.2E-6 Torr. For a description of methods 1&2 cf. text.

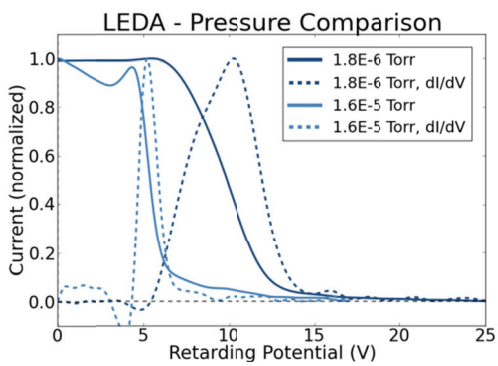

Figure 7: Measured beam potential for two different Ar pressures in the beam line. Beam current = 6.2 mA. The spectrum on the left was taken at the higher pressure. The neutralizations were about 64% for the lower pressure and 89% for the higher pressure.

Measurements with SuSI

When we apply the same analysis methods as in the LEDA source to the spectra obtained with the RFA positioned in the SuSI LEBT (as seen in figure 1), we immediately notice, that the simple assumptions are no longer valid. As an example, figure 8 shows saturation current and calculated neutralization factors as a function of pressure. Larger $\Delta\phi$ as theoretically predicted (with the simple model) for an uncompensated beam lead to slightly negative values for the neutralization at lower pressures. Obviously the round uniform beam approach is over-simplified. What we can conclude with these preliminary measurements, however, is that at this particular location of the SuSI beamline the space charge compensation is very low. We will continue the study, but are also planning to move the detector to a different location on the beam line in the near future.

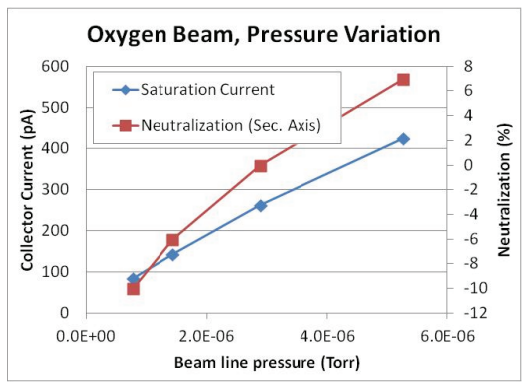

Figure 8: SuSI, oxygen beam, pressure variation. total beam current ~2 mA.

As a first step, the influence of the detector position perpendicular to the beam was investigated. For a round, centered beam, the saturation current should be symmetric about the center position and simulations showed that the neutralization obtained from the spectra should be more or less independent of the position. As can clearly be seen in figure 9, for the SuSI diagnostic box 1 this is not the case. The saturation current peaks at an offset of ~ -15 mm.

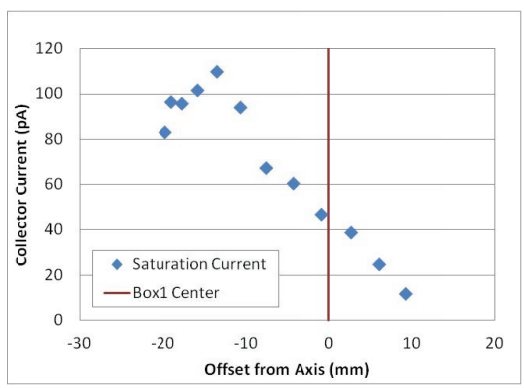

Figure 9: SuSI: RFA saturation current as a function of offset from the chamber center.

The situation in the diagnostic box right after SuSI's extraction system as it is seen in figure 1 is more complex as for the LEDA source. For one, there is a lot less space. Half of the box is filled with the first segment of an

Copyright © 2012 CC-BY-3.0 and by the respective authors

ISBN 978-3-95450-123-6

Einzel Lens (the lens is switched off during the measurements). This changes the longitudinal space-charge potential distribution created by the beam. It actually has a maximum shortly after entering box 1, as can be seen in figure 10 in a potential map created with SIMION's Poisson-solver. This changes the expelled ion's trajectories and consequently the obtained signal.

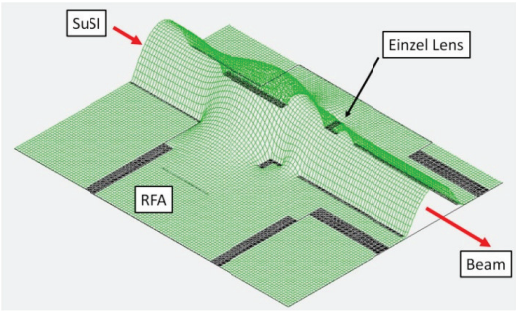

Figure 10: Potential map of beam space-charge potential. The cut is made vertically at the beam-line center.

On the other hand, as mentioned earlier, ECRIS beams from sources using a sextupole magnet have an intrinsic triangular structure and so great care has to be taken to determine whether or not the approximation of a uniformly charged cylinder can be made for these beams. Using SIMION's Poisson solver, a triangular charge distribution can easily be created and used as the beam's space-charge potential as experienced by the secondary ions. Figure 11 shows a simulated RFA spectrum for an oxygen beam with 2 mA total beam current and 25% neutralization as well as a round beam without neutralization compared to a measurement. The triangular beam seems to reproduce the shape of the spectrum better than the round one.

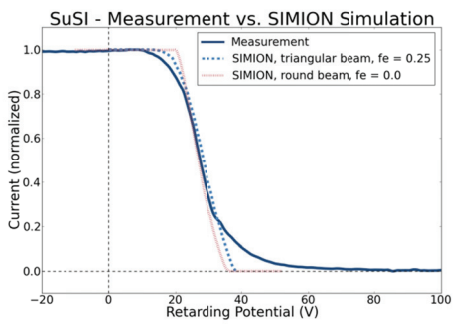

Figure 11: Comparison of a spectrum obtained with SuSI and SIMION simulations. Solid line: Measurement. Dashed line: Assuming triangular beam and 25% neutralization. Dotted line: Assuming round beam without neutralization. Both simulations used the same parameters otherwise.

Finding the right parameters (size, orientation of the triangle, neutralization factor), unfortunately, is a tedious and time-consuming work and we hope to come up with a simpler and faster method to analyze RFA spectra obtained in those problematic measuring locations.

CONCLUSION

Measurements of the beam space-charge compensation for ECR-type ion sources have been conducted using a newly-developed retarding field analyzer (RFA). These measurements have been performed at 3 different ECRIS low energy beam transport (LEBT) systems (ARTEMIS, LEDA, SuSI) for typical pressures and beam currents. The influence of a two-aperture collimation system for a more focused view of the beam on the saturation current $(I_{RFA})_s$ has to be investigated further, as it seems to reduce the $(I_{RFA})_s$ more than expected. Data obtained for a solenoid-only ECR source (LEDA injector source) agrees reasonably well with data presented in [2]. Data obtained for Artemis A and SuSI, the two injector sources of NSCL's coupled cyclotron facility indicate low to no neutralization at those particular measurement positions in the beam line. The influence of the beam shape (triangular) and intrinsic multi-component nature of ECR beams has been observed and will be subject to further investigation as well as it can have significant influence on the neutralization levels obtained from the data. In the future we are hoping to combine these measurements with beam cross-section measurements at the RFA location.

ACKNOWLEDGEMENTS

The authors would like to acknowledge the excellent support from the NSCL's electronical engineering department and the machine shop.

D. Winklehner would also like to thank the Michigan Institute for Plasma Science and Engineering (MIPSE) for providing the MIPSE fellowship that made it possible for him to attend the ECRIS workshop this year.

This work was funded by the Michigan State University and the National Science Foundation.

REFERENCES

[1] I. A. Soloshenko, Rev. Sci. Instrum. 67(4) (1996).
[2] R. Ferdinand et al., PAC'97 (1997).
[3] D. Leitner et al., Cyclotrons'07, (2007).
[4] R. Geller, Electron Cyclotron Ion Sources and ECR Plasmas, (London, IOP Publishing, 1996).
[5] D. S. Todd et al., Rev. Sci. Instrum. 77 (2006).
[6] D. Winklehner et al., Rev. Sci. Instrum. 83 (2) (2012) 02B706.
[7] Z. Q. Xie, Rev. Sci. Instrum. 69 (1998) 625.
[9] J. D. Sherman, LINAC'96 (1996) THP23.
[10] SIMION® 8.1 Ion and Electron Optics Simulation Software http://www.sisweb.com/simion.htm
[11] A. Müller, E. Salzborn, Physics Letters 62A, 6 (1977).

Copyright © 2012 CC-BY-3.0 and by the respective authors

ISBN 978-3-95450-123-6

QUANTITATIVE DETERMINATION OF ^{146}SM/^{147}SM RATIOS BY ACCELERATOR MASS SPECTROMETRY WITH AN ECR ION SOURCE AND LINEAR ACCELERATION FOR ^{146}SM HALF-LIFE MEASUREMENT

N. Kinoshita[1], M. Paul[2], P. Collon[3], Y. Kashiv[3], D. Robertson[3], C. Schmitt[3], X. D. Tang[3], B. DiGiovine[4], J. P. Greene[4], D. J. Henderson[4], C. L. Jiang[4], S. T. Marley[4], R. C. Pardo[4], K. E. Rehm[4], R. Scott[4], R. Vondrasek[4], C. M. Deibel[4,5], T. Nakanishi[6], A. Yokoyama[6]

[1]Research Facility Center for Science and Technology, University of Tsukuba, Japan
[2]Racah Institute of Physics, Hebrew University, Jerusalem, Israel 91904
[3]Department of Physics, University of Notre Dame, Notre Dame, IN 46556-5670
[4]Physics Division, Argonne National Laboratory, Argonne , IL 60439
[5]Joint Institute for Nuclear Astrophysics, Michigan State University, East Lansing, MI 46624
[6]Faculty of Chemistry, Institute of Science and Engineering, Kanazawa University, Japan

Abstract

The alpha-decaying ^{146}Sm nuclide is used for chronology of the Solar System and silicate mantle differentiation in planets. We performed a new determination of ^{146}Sm half-life by measuring ^{146}Sm/^{147}Sm alpha activity and atom ratios in ^{147}Sm activated via (γ,n), (n,2n) and (p,2$n\varepsilon$) reactions and obtained a value (68 Myr), smaller than that adopted so far (103 Myr), with important geochemical implications. The experiment required determination of ^{146}Sm/^{147}Sm ratios by high-energy (6 MeV/u) accelerator mass spectrometry to discriminate ^{146}Sm from isobaric ^{146}Nd contaminant. Activated Sm targets were dissolved, chemically purified and reconverted to metallic Sm. Sputter cathodes, made by pressing the Sm metal into high-purity Al holders, were used to feed the Argonne Electron Cyclotron Resonance (ECR) ion source. ^{146}Sm^{22+}, ^{147}Sm^{22+} ions were alternately injected and accelerated with the ATLAS linac by proper scaling of ion source and accelerator components. A tightly-fitted quartz cylindrical liner was inserted in the ECR plasma chamber to reduce contamination from the walls. ^{146}Sm ions were eventually counted in a gas-filled magnet and ^{147}Sm ions either measured as charge current or counted after proper attenuation.

INTRODUCTION

The extinct p-process nuclide ^{146}Sm ($t_{1/2}$= 103 ± 5 Myr [1,2]) was live in the early Solar System, as established through isotopic anomalies of its α daughter ^{142}Nd, first observed in meteorites [3]. The data have been used to estimate a time interval (≈ 70 Myr) between isolation of the Solar Nebula from the insterstellar medium and the start of formation of the Solar System [4]. ^{146}Sm acts also as an important geochronometer for the early silicate differentiation in planetary bodies (meteorite parent bodies, Earth, the Moon and Mars, see [5] for a recent review of the field).

The ^{146}Sm half-life which is a crucial component in these applications has been measured four times with values of ~50 Myr [6], 74 ± 15 Myr [7] and 103 ± 5 Myr [1,2]. Considering the range of these values, we have performed a new determination of ^{146}Sm half-life [8] by measuring both the α activity ratio (A_{146}/A_{147}) and the atom ratio (N_{146}/N_{147}) in samples prepared from activated ^{147}S material. The half-life ($t_{1/2}^{146}$) is obtained through the expression

$$t_{1/2}^{146} = \frac{A_{147}}{A_{146}} \times \frac{N_{146}}{N_{147}} \times t_{1/2}^{147},$$

where $t_{1/2}^{147}$ denotes the α-decay half-life of naturally occurring ^{147}Sm ($t_{1/2}^{147}$ = 107 ± 0.9 Gyr, [9]). The ratio measurement eliminates most systematic α-activity uncertainties due to detector efficiency and geometrical acceptance. We focus in this contribution.on the use of the ECR ion source at the ATLAS facility for accelerator mass spectrometry (AMS) in order to measure N_{146}/N_{147} atom ratios. The high charge states produced in the ECR ion source allow us to accelerate Sm ions at energies of about 6 MeV/u with the ATLAS superconducting linear accelerator for unambiguous ion identification and also eliminates any stable molecules in the injected beam, two basic properties of AMS [10]. Ion identification was considered important in this experiment because of the need of ^{146}Sm discrimination against stable isobar ^{146}Nd.

EXPERIMENTAL SETUP

Samples of ^{146}Sm to be used in the AMS measurements were prepared from three different activations of enriched ^{147}Sm targets (^{147}Sm(γ,n)^{146}Sm, ^{147}Sm(p,2$n\varepsilon$)^{146}Sm and ^{147}Sm(n,2n)^{146}Sm, see [11,12] for details). Following the measurement of the α activity, the sources were dissolved and quantitatively diluted with high-purity ^{nat}Sm to obtain ^{146}Sm/^{147}Sm ratios in the range 10^{-7}-10^{-9}.

ISBN 978-3-95450-123-6

Copyright © 2012 CC-BY-3.0 and by the respective authors

The solutions were purified of Nd impurities by repeated liquid-chromatography steps using a lanthanide-specific resin (Ln resin, manufactured by Eichrom Ltd.). The samples were eventually reduced to high-purity Sm metal, observed to have higher ionization yields in the Electron Cyclotron Resonance (ECR) ion source. This was performed by the following steps for each individual sample: (*i*) Sm hydroxide was precipitated with an ammonia solution and evaporated to dryness; (*ii*) ignition to oxide in a quartz crucible at 600°C; (*iii*) the oxide was thoroughly mixed with freshly filed Zr powder and pressed to 3mm diameter pellets; (*iv*) the pellets were introduced in a tightly fitting cylindrical tube made of 0.1 mm thick Ta having a 1 mm diameter orifice; (*v*) the sealed tube was then placed in a high-vacuum (10^{-5} Pa) evaporator and resistively heated to ~1300°C; (*vi*) reduced and evaporated metallic Sm was collected by distillation on a water-cooled Cu collector placed just above the 1-mm orifice. The Sm sample was eventually pressed in a holder made of high-purity Al to be used as sputter cathode in the ECR ion source. In order to reduce background of parasitic ions, the chamber walls were lined with a closely fitted cylinder made of quartz (Fig. 1), transparent to the microwave radiation (~100W at 14 GHz) which ignites and maintains the plasma.

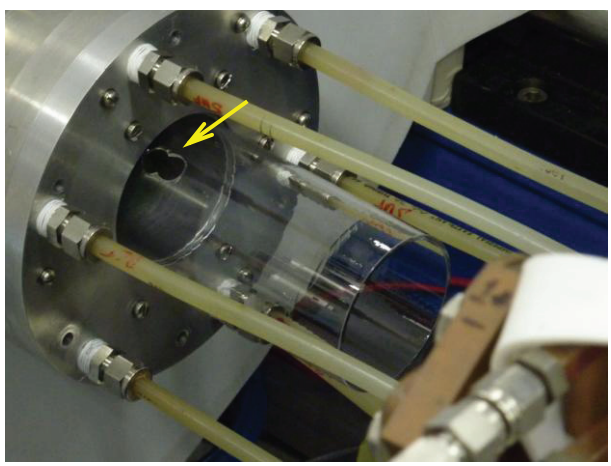

Figure 1: Quartz liner tube is inserted in the ECR chamber, tightly fitted to the chamber cylindrical wall, to reduce contamination from ion source structural materials. An orifice (see arrow) allows the sputter cathode to be radially inserted flush to the walls and sample material to feed the plasma in the quartz tube.

$^{146}Sm^{22+}$ and $^{147}Sm^{22+}$ ions, alternately selected by magnetic analysis, are bunched and accelerated to a final energy of 6 MeV/*u* in the superconducting linear accelerator. Acceleration of neighboring isotopes such as ^{146}Sm and ^{147}Sm, both in 22+ charge state, requires adjustment of resonator field amplitudes and ion-optical elements by scaling a master tune according to the *m/q* ratios of the atomic mass and charge state of the ions, in order to conserve an exact velocity profile. The accelerator system acts then as a high-energy accelerator mass spectrometer and its abundance sensitivity (defined as the abundance ratio of two resolvable neighboring isotopes) before the detection system was shown [10] to be ~5×10^{-12} for Pb isotopes, separating in the present experiment ^{146}Sm from ^{147}Sm. The reliability of the *m/q* scaling procedure to transport alternately $^{146}Sm^{22+}$ or $^{147}Sm^{22+}$ from the ECRIS to the detection setup was checked by measuring the ratio of charge currents for $^{147}Sm^{22+}$ and $^{152}Sm^{22,23+}$. The measured $^{152}Sm/^{147}Sm$ (1.8±0.2), after correcting when necessary for the 23+/22+ population ratio (measured experimentally), is consistent with the natural abundance ratio 1.78 (Fig. 2)

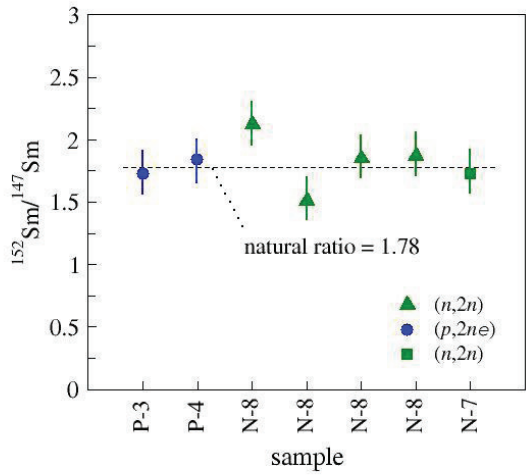

Figure 2: Stable $^{152}Sm/^{147}Sm$ isotopic ratio measured by scaling the ECR and ATLAS elements, based on the mass-to-charge ratio of the isotopes. The symbols P-x and N-x on the x-axis represent samples prepared from the proton-activated and neutron-activated ^{147}Sm targets, respectively. The measured ratio is consistent with the natural abundance ratio of 1.78.

Isobaric separation of ^{146}Sm from residual ^{146}Nd ($(m/q)/\delta(m/q)\sim2.4\times10^6$), beyond the separation power of the accelerator, is achieved in a gas-filled magnetic spectrograph (GFM). The ions are physically separated in the GFM owing to their (Z-dependent) mean charge state in the gas and are unambiguously identified by measurement of their position and differential energy loss in a focal-plane detector (see Fig. 3 and [12] for details). The AMS determination of the atom ratio ($^{146}Sm/^{147}Sm$ in this case) is normally performed in our setup by alternate measurements of the ^{146}Sm (accelerated as $^{146}Sm^{22+}$) count rate in the focal plane detector and the charge current of the stable isotope $^{147}Sm^{22+}$. The ^{147}Sm beam current is measured in an electron-suppressed Faraday cup positioned in front of the spectrograph. The atom ratio was also measured as the ratio of $^{146}Sm^{22+}$ counts in the focal-plane detector (see Fig. 3) to $^{147}Sm^{22+}$ counts in the same detector, after quantitative attenuation of the $^{147}Sm^{22+}$ beam [13], avoiding systematic effects of ion-transmission efficiency between the Faraday-cup and the detector.

Copyright © 2012 CC-BY-3.0 and by the respective authors

ISBN 978-3-95450-123-6

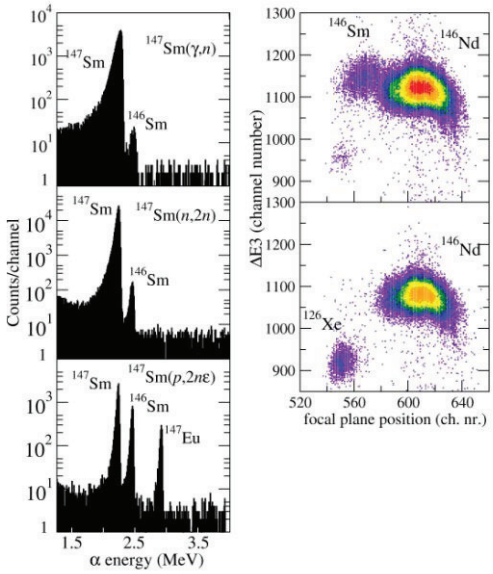

Figure 3: (left panel) Alpha energy spectra measured for (top to bottom) the gamma, neutron and proton activated samples, determining their (A_{146}/A_{147}) activity ratios; (right panel) Ion identification spectra of differential energy loss versus position along the focal plane of the gas-filled magnet. The groups corresponding to ^{146}Sm and stable isobaric ^{146}Nd (from chemical impurities) for the *n*-activated sample are indicated. The lower spectrum corresponds to an unactivated Sm sample.

RESULTS AND DISCUSSION

The results for the different samples are shown in Fig. 4 as the double ratio of N_{146}/N_{147} measured by AMS to the same ratio as expected from the α-activity, using the presently adopted half-lives for ^{146}Sm (103 My) and ^{147}Sm (107 Gy). The double ratio is equal to the ratio of the determined ^{146}Sm half-life for each sample to the value adopted in the literature (103 My), with an overall unweighted mean and standard deviation of 0.66 ± 0.07. The mean value of the measured half-life is 68 ± 7 My, substantially (34%) shorter than the literature value. This lower value implies a shorter time interval between (1) isolation of the Solar Nebula from the Interstellar Medium and formation of the Solar System, and (2) formation of the Solar System and planetary silicate differentiation events in the early Solar System, as inferred from ^{146}Sm-^{142}Nd systematics (see [8] for details).

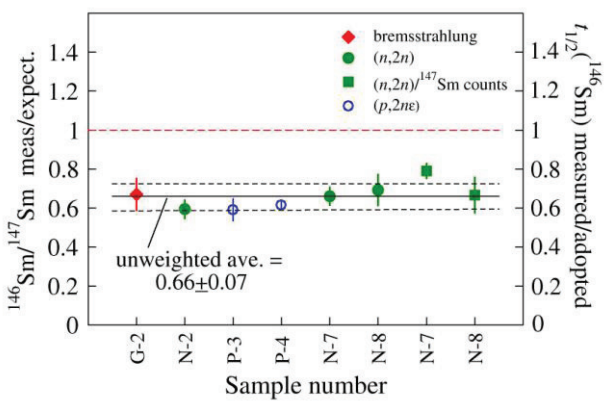

Figure 4: Double ratios of N_{146}/N_{147} atom ratios measured by AMS to those expected from the α activity ratioa of the different samples. G-x, N-x and P-x represent the gamma, neutron and proton activated samples. The double ratios are equal to the ratios of the determined half-life for each sample to that adopted in the literature.

ACKNOWLEDGMENT

This work was supported by U.S. DOE, Office of Nuclear Physics, contract No. DE-AC02-06CH11357, NSF JINA Grant Nr. PHY0822648 and Science Research Prog. of Japan Society for the Promotion of Science (20740161).

REFERENCES

[1] A.M. Friedman *et al.*, Radiochim. Acta **5,** 192 (1966).
[2] F. Meissner, W.-D. Schmidt-Ott & L. Ziegeler, Z. Phys. *A* **327,** 171 (1987).
[3] G.W. Lugmair & K. Marti, Earth Planet. Sci. Lett. 35, 273 (1977).
[4] G.J. Wasserburg, M. Busso, R. Gallino & K.M. Nollett, K. M., Nucl. Phys. A 777,5 (2006).
[5] G. Caro, Annu. Rev. Earth Planet. Sci., 39 31 (2011).
[6] D. C. Dunlavey & G. T. Seaborg, Phys. Rev. 92, 206 (1953).
[7] M. Nurmia, G. Graeffe, K. Valli & J. Aaltonen, Ann. Acad. Scient. Fenn. A.VI.148, 1 (1964).
[8] N. Kinoshita et al., Science 334, 1614 (2012).
[9] K. Kossert, G. Joerg, O. Naehle, C. Lierse & C.L. v. Gostomski, Appl. Rad. Isot. **67,** 1702 (2009).
[10] M. Paul *et al.*, Nucl. Inst. Methods Phys. Res. B **172,** 688 (2000).
[11] N. Kinoshita et al., J. Nucl. Radiochem. Sci. 8, 109. (2007).
[12] N. Kinoshita et al., J. Phys. G: Nucl. Part. Phys. 35, 014033 (2008).
[13] N. Kinoshita *et al.*, Nucl. Inst. Methods Phys. Res. B, in press; doi:10.1016/j.nimb.2012.01.013.

Copyright © 2012 CC-BY-3.0 and by the respective authors

ISBN 978-3-95450-123-6

INTEGRATION OF A THIRD ION SOURCE FOR HEAVY ION RADIOTHERAPY AT HIT

T. Winkelmann, A. Büchel, R. Cee, A. Gaffron, T. Haberer, J. Mosthaf, B. Naas, A. Peters, J. Schreiner, Heidelberger Ionenstrahl-Therapie Centrum (HIT), D -69120 Heidelberg, Germany

Abstract

HIT is the first European hospital based facility for scanned proton and heavy ion radiotherapy. In 2009 the clinical operation started, since then more than 1000 patients were treated in the facility.

In a 24/7 operation scheme two 14.5 GHz electron cyclotron resonance ion sources are routinely used to produce protons and carbon ions.

In the near future a helium beam for regular patient treatment is requested. The modification of the low energy beam transport line (LEBT) for the integration of a third ion source into the production facility was done in winter 2011. For beam quality improvement with a smaller emittance at the same current we designed and tested a new extraction system at the testbench and equipped the source for protons and helium with this optimized system. This paper will present results of the LEBT modification and give an outlook to further enhancements at the HIT ion source testbench.

INTRODUCTION

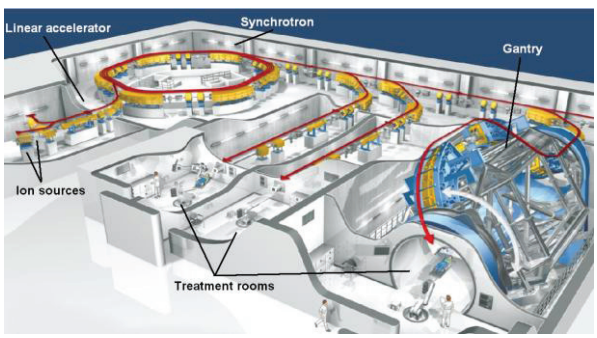

Figure 1: Overview of the HIT facility.

Since November 2009 more than 1000 cancer patients have been treated at HIT (see Fig.1) with carbon ions and protons [1, 2]. The increasing interest in the treatment with helium ions, especially for paediatric tumours [3], in addition with the requirement for fast switching between carbon ions, protons and helium ions triggered the design of a third independent spectrometer line and a new ion source.

LEBT MODIFICATION

The motivation for the new design of the LEBT beam line is based on the desire for higher beam brilliance and thus increased intensities for the upcoming clinical applications. The geometry of the available LEBT-room and the necessary space for a third source was an additional reason. Figure 2 and 3 is the status shown before winter 2011.

Figure 2: The existing low energy beam line (LEBT) before winter 2011.

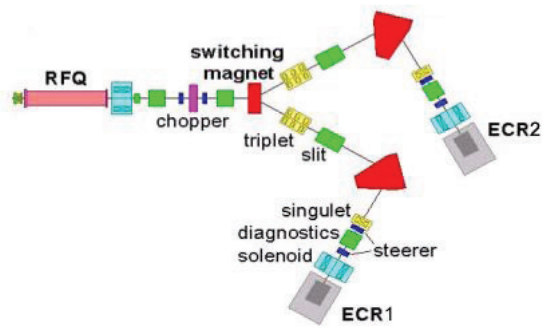

Figure 3: Schematic drawing of the LEBT before winter 2011.

The major improvement is motivated by the large emittance and the resultant poor transmission for the low LET beams especially protons through the LEBT.

TESTBENCH

To improve and test the possible LEBT setup with the requirement to integrate a third ion source in the production facility we build up a testbench with the following setup (Fig. 4): ECR ion source with extraction system (einzel lens), horizontal/vertical pair of steerers, 90° double focusing analyser dipole, beam diagnostics chamber with profile grid and Faraday cup, DC transformer, emittance measuring system (slit/grid) and Faraday cup. The emittance measurement analyser is a

Copyright © 2012 CC-BY-3.0 and by the respective authors

ISBN 978-3-95450-123-6

loan of GSI Darmstadt and consists, amongst the data acquisition electronics and software, of two chambers, the first one housing the slits, the second one the profile grids. It is capable to measure the horizontal as well as the vertical beam emittance [1, 2]; [4, 5].

Without a magnetic focusing element between source and analyser dipole the plasma lens (extraction aperture) is placed in the focus of the dipole a difference to the existing (long) LEBT with a solenoid generating a beam focus in this section.

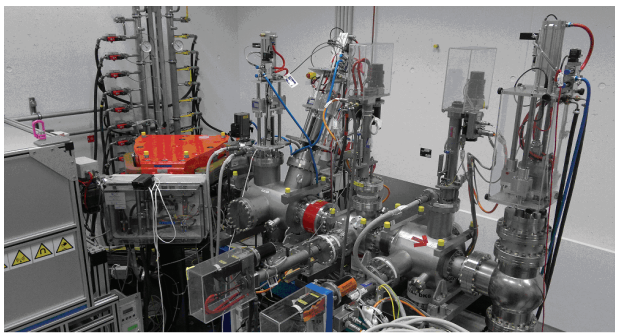

Figure 4: Test bench setup with a slit grid emittance measurement device.

We also integrate in the extraction system a fourth extra electrode with an independent power supply to accelerate or decelerate the ions in the puller-electrode gap. This fourth electrode improves the beam brilliance caused by a clearing effect (electrons) in this very "sensitive" area (Table 1). The beam line contraction between ion source and spectrum magnet optimized also the space charge compensation.

Table 1: Emittance and beam current output setup with the fourth electrode and without (in brackets).

Ion	Emittance [π ·mm·mrad]		Current [eμA]
	Horizontal	Vertical	
H_2^+	133 (147)	124 (160)	927 (902)
H_3^+	65 (85)	77 (103)	1490 (779)
$4He^{2+}$	64 (65)	64 (72)	746 (577)
$12C^{4+}$	98 (67)	110 (92)	166 (206)
$16O^{6+}$	74 (102)	53 (86)	188 (165)

LEBT MODIFICATION (STEP 1)

To realize the LEBT modifications during the operation we divided the mechanical work in two steps (Fig. 5 and 9). At the first step we change the 90° double focusing analyser dipole in the beam line to ECR 1 with a new dipole. These magnets get in addition to the same optical characteristic for the deflection angle of 90° (ECR 1) the possibility to pass the beam straight through (T_ Magnet).We contract also in the winter 2011 the LEBT for ECR 2 and remove the quadrupol Singulett, one pair of steerer, the diagnostic box and the solenoid. After this we installed the ion source (ECR2) with the implemented einzel lens extraction system.

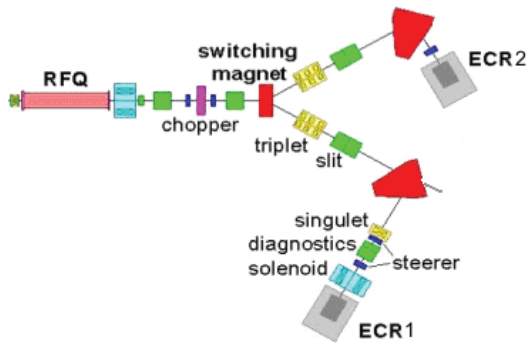

Figure 5: Schematic drawing of the LEBT after winter 2011.

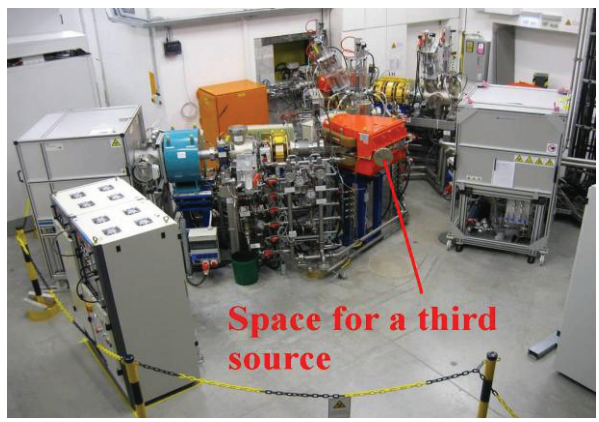

Figure 6: The low energy beam line (Step 1).

OPERATION EXPERIENCE AND RESULTS OF THE LEBT MODIFICATION

During the first five years of operation mainly carbon ions were used by 59 %, followed by hydrogen (39 %), helium (1 %) and oxygen (1 %). The continuous operation runtime of the two sources are 330 days per year 24h-operation!

The operation-statistics (see Fig. 7) since summer 2007 of the two ion sources are: 98.75% of the time in operation, 1.2% of the time for planed maintenance shifts and 0.05% of the time are the "off time" caused by multiple RF-amplifier breakdowns in the first two years.

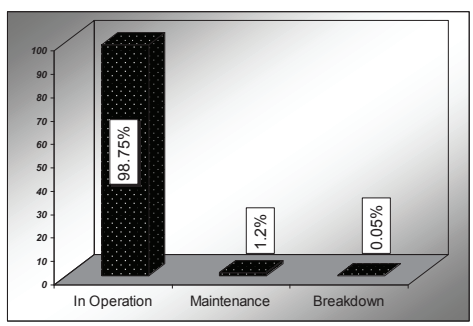

Figure 7: operation-statistic of the two ion sources at HIT, since summer 2007.

ISBN 978-3-95450-123-6

Copyright © 2012 CC-BY-3.0 and by the respective authors

With the new set-up we reach nearly 100% transmission through the LEBT, and we have now the ability to operate the ion source gently to reach the same requested H3+ intensity behind the LEBT. That leads to a reduction of the extraction current from 7mA to 2,5mA. The benefit of that are lower wasting and a longer durability especially for the ceramics in the ion source. The beam shapes are comparable to measurements that we have done at the testbench [5] and looks much smaller than the shapes in the "old" set-up (see Fig. 8).

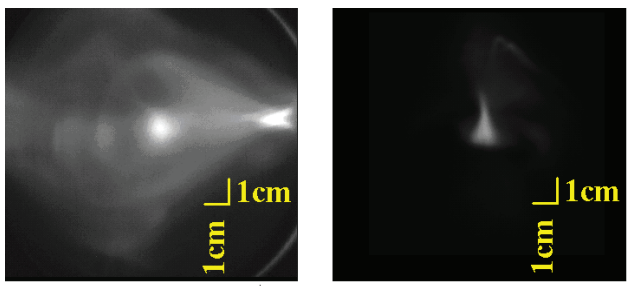

Figure 8: Shape of H_3^+ beam at a glass viewing screen (Herasil) behind the switching magnet. Left figure: Before LEBT modification (2emA) - Right figure: Status now (700eμA).

LEBT MODIFICATION (STEP 2)

The start of the third source implementation in the LEBT room starts in winter 2012.

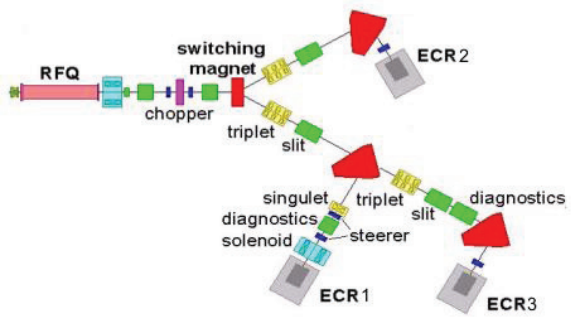

Figure 9: Considered design of the LEBT including three ion sources (planned in winter 2012) (Setup 2).

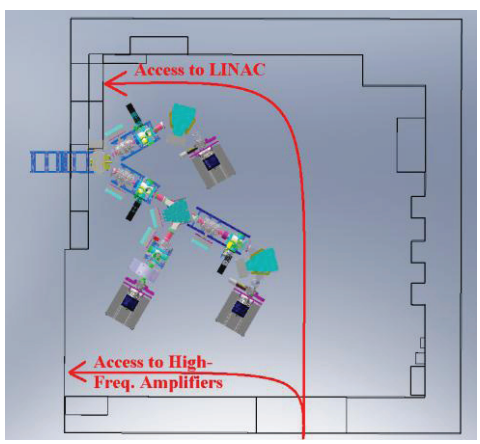

Figure 10: Considered design of the LEBT including three ion sources in the LEBT room.

OUTLOOK

The next measurement campaign takes place at the moment to analyse the poor RFQ transmission. The test bench configuration is installed and contains the LEBT, including quadrupole triplet, macro pulse chopper, solenoid, and the RFQ with a dedicated test beam line at the high energy end. These beam diagnostic components are: three phase probes, an AC transformer, a viewing target, a profile grid and a pepper pot screen with mirror plus CCD-camera and a Faraday cup in the end (see Fig. 11).

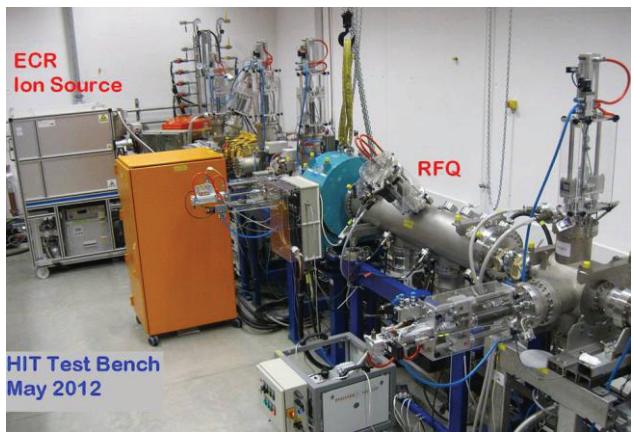

Figure 11: Test bench set up to analyse the RFQ output parameter.

REFERENCES

[1] A.D. Jensen, M.W. Münter, J. Debus, "Review of clinical experience with ion beam radiotherapy" British Institute of Radiology, doi:10.1259/bjr/71511359; Publ. 03/2011.

[2] A. Peters et al., "Five years of operation experience at HIT", IPAC'12, New Orleans, USA, May 2012, TUOAB03.

[3] T. Haberer "Charged particle therapy steps into the clinical environment" Int. J. Modern Physics E, Vol.16.

[4] R. Cee et al., "Status of the Ion Source and RFQ Test Bench at the Heidelberg Ion Beam Therapy Centre",IPAC'11, San Sebastian, Spain, September 2011,WEPS044, p. 2586 (2011).

[5] T.Winkelmann et al., "Test Bench to Commission a Third Ion Source Beamline and a New Designed Extraction System", ICIS'11, Catania, Italy, September 2011, Rev. Sci. Instrum. **83**, 02B904 (2012).

Copyright © 2012 CC-BY-3.0 and by the respective authors

ISBN 978-3-95450-123-6

DESIGN OF A COMPACT ECR ION SOURCE FOR VARIOUS ION PRODUCTION

M. Muramatsu, A. Kitagawa, T. Fujita, Y. Iwata, S. Sato, S. Hojo,
Y. Sakamoto, K. Katagiri, and A. G. Drentje,
National Institute of Radiological Sciences, 4-9-1 Anagawa, Inage, Chiba 263-8555, Japan

Abstract

Carbon ion therapy facilities need not only carbon ions for medical use but also other ions for research. Ion source is required: 1) H to Fe ion production, 2) enough intensity of various ions for medical use and research, and 3) low cost. Our previous compact ECR ion sources (Kei series) are optimized for carbon ion production. In order to produce various ion beams, we design a new compact ECR ion source, named Kei3, based on previous Kei series. Manufacturing of the Kei3 will be finished in end of this year.

INTRODUCTION

Carbon ion radiotherapy is started in 1994 by the Heavy Ion Medical Accelerator in Chiba (HIMAC) at the National Institute of Radiological Sciences (NIRS). The total number of patients reached to 6,500 and various types of tumor have been treated. NIRS carried out R&D studies for various components and designed a hospital-specified carbon ion radiotherapy facility [1]. The construction of the Gunma University Heavy Ion Medical Centre (GHMC [2]) was funded by the Japanese government and Gunma prefecture beginning in 2006, and construction started in 2007 at the Centre site in Maebashi, Gunma. The technologies concerned were transferred from NIRS to Gunma University. Gunma University already started a clinical trial since March 2010.

Compact ECR ion source with all permanent magnets, named Kei2, was developed for high energy carbon ion therapy facility at NIRS. Kei2 source was designed for producing enough intensity of carbon ion for medical treatment. A compact ECR ion source for GHMC, the KeiGM, is also based on the development of the compact ECR ion sources (Kei series) at NIRS [3]. These ECRISs are developed for production of C^{4+} ions for medical treatment. Table 1 shows beam intensity of H_3^+, $^{11}B^{4+}$, $^{12}C^{4+}$, $^{16}O^{6+}$, $^{40}Ar^{11+}$, and $^{56}Fe^{13+}$ ions by prototype Kei2 source at 30 kV extractions. Ion source parameters (microwave power and frequency, gas flow, biased disk voltage and position) were tuned for each ion. In the case of bigger q/A than 1/3, beam intensity was reached requirement value. However, in the case of smaller q/A than 1/3 and molecule ions, sufficient intensity was not obtained. Kei series were designed for production of C^{4+} ions. Therefore, it is difficult to produce enough intensity of heavier ions and molecule ions.

Some carbon ion radiotherapy facilities need to use H to Ne ion beam for biological experiment like irradiation of mouse, Ar and Fe beam for irradiation of cells and physical experiment. In order to produce various ion beams, we design a new compact ECR ion source, named Kei3. Kei3 is designed based on previous Kei series. Target ion species are molecule hydrogen to iron. Charge to mass ratio of ion is up to 1/3, because, we don't want to change the injector linac. Therefore, ion source has to produce H_3^+ to Fe^{19+} ions.

Table 1: Beam Intensity of Various Ions at Kei2

Ion	Required intensity [eμA]	Kei2 intensity [eμA]	Material
H_3^+	500	270	H_2 gas
$^{11}B^{4+}$	100	120	$C_2H_{12}B_{10}$
$^{12}C^{4+}$	200	680	CH_4 gas
$^{16}O^{6+}$	100	60	O_2 gas
$^{40}Ar^{11+}$		2.5	Ar + O_2 gas
$^{56}Fe^{13+}$		0.5	Metal iron +He gas

DESIGN OF THE KEI3

There are five important points for improvement from Kei2: 1) Same magnetic field and microwave system will be used for easy maintenance and the cost effectiveness, 2) Improve the vacuum in the plasma chamber and extraction region for production of heavier ion and increase the extraction voltage, 3) Movable beam extraction system for various extraction current densities, 4) Biased disk method and double frequency heating method for heavier ions, and 5) An evaporator and MIVOC method for production of ion from solid materials and metal. Figure 1 shows schematic drawing of Kei3 source. The Kei3 has an outer diameter of 280 mm and a length of 1120 mm. Kei3 consists of injection side vacuum chamber, permanent magnets and plasma chamber, and extraction side vacuum chamber with extraction system. The magnetic field was copied from Kei2 [4]. Magnetic field of upstream mirror peak, downstream peak and minimumB are 0.877 T, 0.579 T and 0.26 T, respectively. Based on experimental studies with a conventional 10 GHz ECR source [5] at HIMAC, the field distribution of the mirror magnet for compact source was designed so that a charge distribution of carbon ions was optimized at 4+. Radial magnetic field by hexapole magnet on the plasma chamber wall is 0.757 T.

ISBN 978-3-95450-123-6

Copyright © 2012 CC-BY-3.0 and by the respective authors

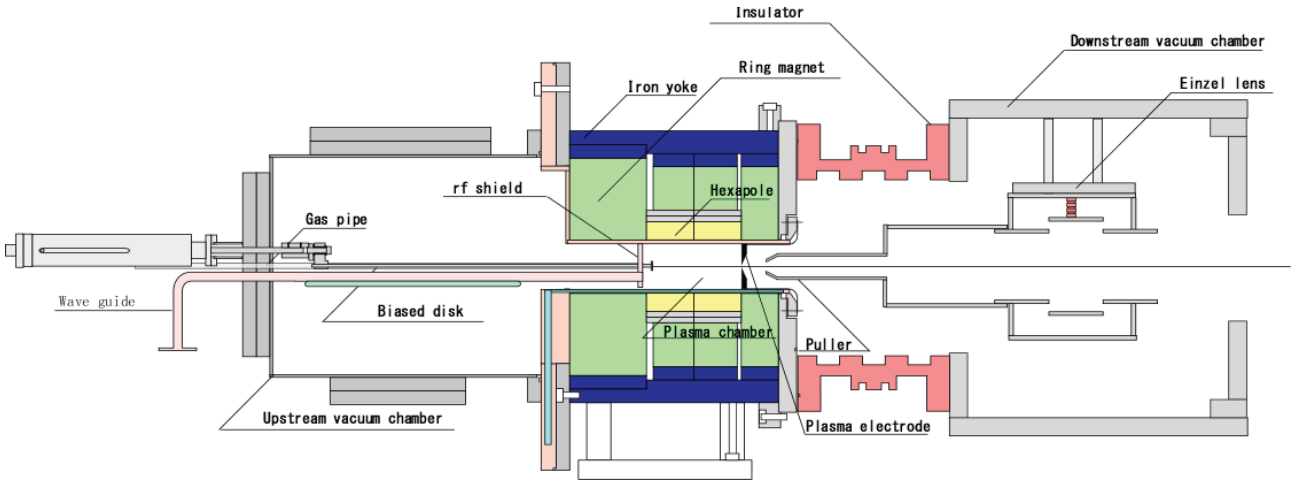

Figure 1: Schematic drawing of Kei3 source.

A microwave source with the traveling-wave-tube (TWT) was adopted, with a frequency range and maximum power of 9.75 - 10.25 GHz and 750 W, respectively. Microwave power is fed into the plasma chamber through a rectangular wave guide from the axial direction. The plasma chamber is made of copper for a good cooling efficiency, in order to avoid a decrease in the magnetic field due to high temperature. The plasma chamber has an inner diameter of 50 mm. Inner diameter of the insulator is larger than the Kei series for improve the vacuum for production of heavier ion and higher voltage extraction. Movable extraction system is used for various extraction current densities. We can change the distance between puller and plasma electrode 0 to 50 mm.

Figure 2 shows the Kei3 with high voltage platform. Extraction voltage is applied to high voltage platform with ion source, microwave system, vacuum pump, gas bottle, and control system. 300 l/sec and 500 l/sec Turbo-Molecule-Pumps (TMP) connect to the injection side and extraction side of the vacuum chamber, respectively.

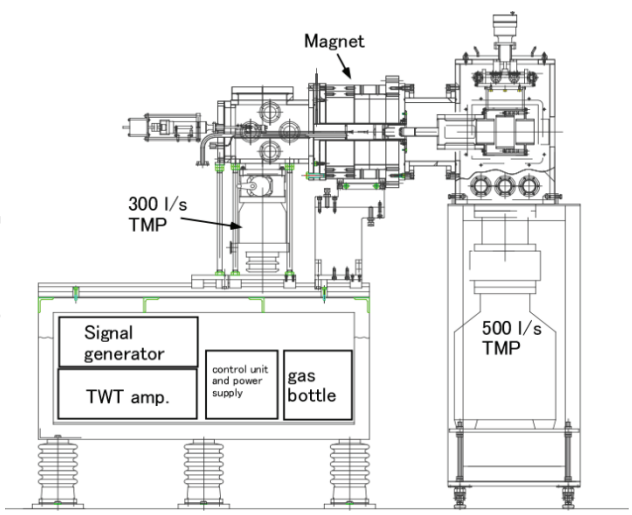

Figure 2: Kei3 with high voltage platform.

In order to obtain enough heavier ion intensity, we will use three methods: 1) biased disk method, 2) gas mixing method, and 3) two frequency heating method. Biased disk was already used Kei series. It is effective for production of highly charged ion (HCI). Gas mixing method is also useful method for production of HCIs. Moreover, we want to test double frequency heating method. Some groups already test this method. We expect that this method is also useful for production of HCI production. On the other hand, an evaporator and MIVOC method are used for production of ion from solid materials and metal.

REFERENCES

[1] K. Noda, et al., J. Radiat. Res. 48: Suppl. A A43 (2007).
[2] Satoru Yamada, Ken Yusa, Mutsumi Tashiro and Kota Torikai, Proceedings of NIRS-Etoile Joint Symposium 2009 on Carbon Ion Radiotherapy, Lyon, France, NIRS-M-218, 170 (2009).
[3] M. Muramatsu et al., Rev. Sci. Instrum. 81, 02A327 1-3 (2010).
[4] M. Muramatsu et al., Rev. Sci. Instrum. 76, 113304 1-6 (2005).
[5] A. Kitagawa et al., Rev. Sci. Instrum. 65, 1087 (1994).

Copyright © 2012 CC-BY-3.0 and by the respective authors

ISBN 978-3-95450-123-6

CHARGE-BREEDING AT THE TEXAS A&M UNIVERSITY CYCLOTRON INSTITUTE *

D.P. May, G. Tabacaru, Cyclotron Institute, Texas A&M University, College Station, TX 77845, USA
J. Arje, Accelerator Laboratory, University of Jyväskylä, Finland

Abstract

The Cyclotron Institute of Texas A&M University is currently involved in an upgrade that is intended to produce beams of radioactive ions suitable for injection into the K500 superconducting cyclotron. As an integral part of this upgrade an electron-cyclotron-resonance ion source (CB-ECRIS) has been specially constructed for charge-breeding. This CB-ECRIS incorporates a hexapole of the Halbach style. Since radial injection of microwave power is ruled out, this presents special problems for the axial injection of low-charge-state ions for charge-breeding. In preparation for the injection of radioactive ions, low charge-state rubidium ions have been successfully charge-bred and subsequently accelerated by the cyclotron.

INTRODUCTION

Reference 1 gives a complete description of the Texas A&M upgrade. As part of the upgrade the K150 cyclotron has been re-commissioned to use as a driver for the production of radioactive ions. The primary method is to first stop radioactive products from beam-target collisions in a helium-filled cell and then to transport them as low-charge-state ions. For products resulting from K150 light-ion beams, Texas A&M is developing a suitable light-ion guide (LIG). For products resulting from K150 heavy-ion beams, a heavy-ion guide (HIG) based on the ion-guide program at Argonne National Laboratory is also being developed. These low-charge-state ions will be injected into an ECR ion source (CB-ECRIS) for charge-breeding to higher charge states. A beam of ions of one selected charge-state will then be transported to the injection line of the K500 superconducting cyclotron and finally accelerated by the K500. Figure 1 illustrates the scheme including the driver K150 cyclotron.

CHARGE-BREEDING

Charge-breeding of ions injected into an ECR ion source presents special problems. The goals are first efficiency and second fast breeding times, holding radioactive species in mind. Efficiency depends upon, among other things, matching the injected beam to the optical acceptance of the source. Also, as when in our case injection occurs opposite to extraction in the ECRIS, efficiency depends upon minimizing losses due to charge-bred ions lost to extraction back along the injection path. For acceptable efficiencies optical matching and minimizing losses must be made compatible.

*Work supported by U. S. Dept. of Energy Grant DE-FG02-93ER40773

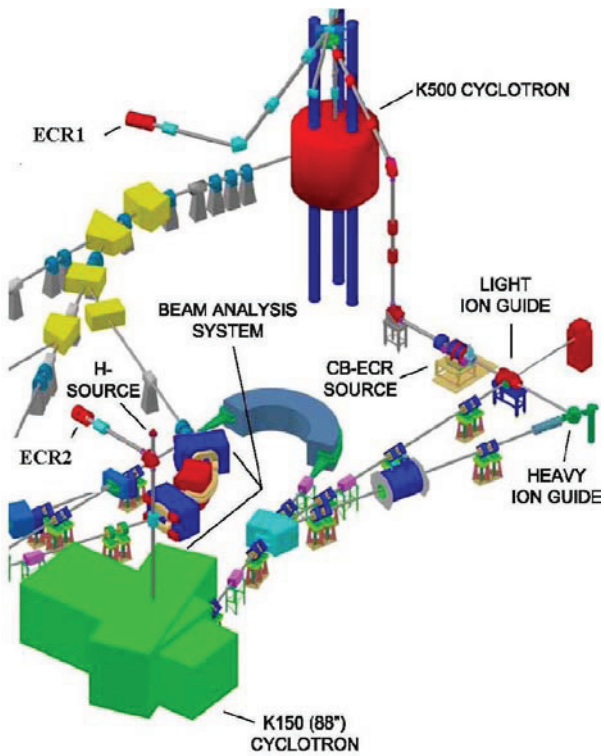

Figure 1: Layout of the Texas A&M Radioactive Beam Facility.

CB-ECRIS

The 14.5 GHz CB-ECRIS was designed and built by Scientific Solutions of San Diego, California with a Phase I and a Phase II Small Business Innovative Research grant from the U. S. Department of Energy [2] and first operated in 2009 [3]. The 9 cm ID, aluminum plasma chamber is surrounded by a Halbach style, NdFeB, permanent-magnet hexapole with a peak field of 1.1 Tesla at the inner wall. The two copper axial coils are encased in steel yokes and are capable of producing peak confinement fields of 2.5•B(ECR) at 500 A of excitation.

Injection of Singly-Charged Ions

At present an aluminosilicate ion gun manufactured by HeatWave Labs, Inc. for the production of a low intensity beam of singly charged alkali ions is being used to test charge-breeding. In the injection path are an electrostatic x-y steerer [4], an Einzel lens, a Faraday cup, a grounded, funnel-shaped tube and a separately biased tube

ISBN 978-3-95450-123-6

Copyright © 2012 CC-BY-3.0 and by the respective authors

positioned immediately before the plasma-chamber entrance aperture (Fig. 2).

In initial efforts to observe charge-breeding the injection geometry has been changed somewhat. A 12 mm aperature was added to the biased tube near the plasma-chamber entrance, and the original 6 mm diameter plasma-chamber aperature was widened to 19 mm. Not illustrated in Fig. 2 is a grounded tube on axis before the Einzel lens. This tube was recently added and proved necessary to shield the injected beam from the gas-feed tube held at the extraction voltage of the CB-ECRIS. Figure 3 is a detail of a simulation of the path of the injected ions including their deceleration into the plasma chamber.

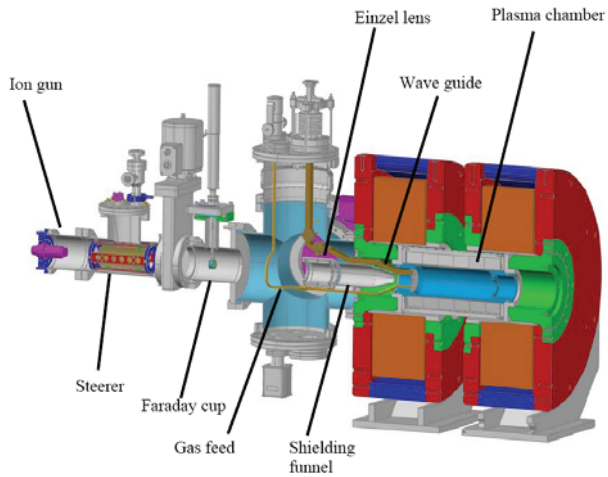

Figure 2: Injection Line into the CB-ECRIS.

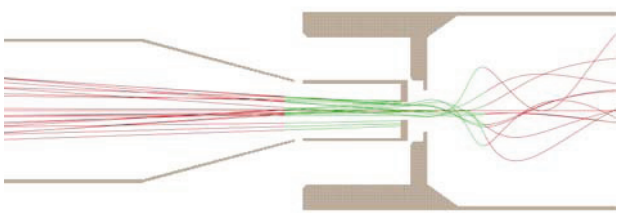

Figure 3: SIMION calculation of injection.

First Results

A 1+ rubidium beam was first transported through CB-ECRIS with coils and high voltage, but not microwaves, energized. As much as 50% could be transported in this manner. With microwaves energized the voltage difference between the two ion sources ($\Delta V=V_{ion\ gun}$ - $V_{CB\text{-}ECRIS}$) was adjusted to maximize the rubidium peaks. These were verified as resulting from charge-breeding and not rubidium build-up in the plasma chamber by switching the alkali source on and off and also by electrostatically deflecting the injected beam and by blocking the injected beam with the Faraday cup. ΔV has been between +35 and +50 volts depending on CB-ECRIS conditions.

Figure 4 shows superimposed spectra with the rubidium beam injected and not injected. The double peaks of ^{85}Rb and ^{87}Rb are clear, with 17+ being the most dominant. The large peaks are due to the oxygen support gas and to carbon and nitrogen contaminants

For best results the tube immediately preceding the plasma chamber is now being held at ground potential. This tube is necessary to prevent the injected beam from being deflected by the electric field of the microwave guide at source potential. Since this tube acts as a puller a large back-current is presumably extracted as evidenced by a large vacuum rise and beam discoloration in the injection region. Since the plasma-chamber aperature is at the peak of the axial magnetic field, this position should enhance the back-extracted beam. When any bias is supplied to the tube, however, charge breeding disappears, perhaps due to a mismatch of the injected beam to the plasma chamber. Also the microwave power has been kept low to less than 100 watts up to now as higher power still causes significant out-gassing and a degradation in charge-breeding.

Conclusions

The power supplies, transmitter and remote controls for the CB-ECRIS and the power supplies and remote controls for the HeatWave ion gun have only recently been installed on the shielding above the ion-guide cave, so little time has been available up to this point for this investigation.

The efficiency of charge breeding into any one rubidium charge-state has not been measured accurately, but probably is less than 1%. The large back-extracted current may indicate that there is significant loss through this mechanism. Also, the microwave power has been low up to now, so the plasma density may be lower than ideal for efficient stopping. More optimization is clearly necessary for charge-breeding of radioactive ions. This will be pursued with more modifications to the injection design and with higher microwave input. Specifically, the micowave guide will be separately shielded so that the biased tube can be spaced further from the peak of the plasma-chamber entrance aperature, and this aperature can be moved to ouside the peak of the axial magnetic field. The clear signals of charge-breeding should aid in this optimization.

Meanwhile, the injection line from the CB-ECRIS to the K500 cyclotron has been completed. Beams of 10 AMeV and 15 AMeV rubidium charge-bred to 15+ and 17+, respectively, have been injected into, accelerated by and extracted from the K500 cyclotron. Preparations are underway for injection of radioactive products from the

Copyright © 2012 CC-BY-3.0 and by the respective authors

ISBN 978-3-95450-123-6

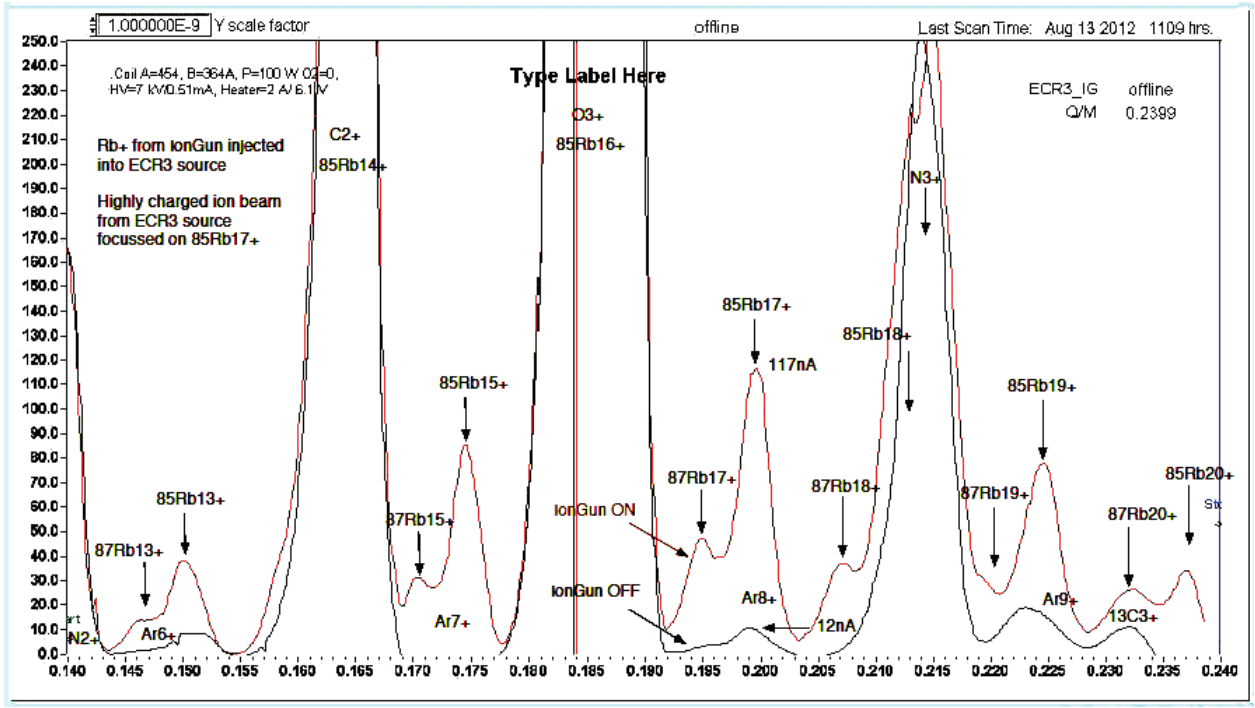

Figure 4: Superimposed spectra with the rubidium beam injected and not injected. The lower scale is charge-to-mass ratio, and the left-hand scale is intensity in nanoamperes.

light-ion guide into the CB-ECRIS. The first ions will originate from a radioactive source placed within the LIG stopping cell before attempting injection of beam-derived radioactive products.

ACKNOWLEDGMENT

The authors wish to acknowledge Dr. Wayne Cornelius of Scientific Solutions for the design and construction of the Texas A&M CB-ECRIS.

REFERENCES

[1] G. Tabacaru, D. P. May, J. Arje, G. Chubarian, H. Clark, G. J. Kim, and R. E. Tribble, Rev. Sci. Instrum. **83,** 02A905 (2012).

[2] W. D. Cornelius, Proceedings of the 18th International Workshop on ECR Ion Sources, Chicago, IL, 185 (2008).

[3] D. P. May, G. Tabacaru, F. P. Abegglen and W. D. Cornelius, Rev. Sci. Instrum. **81**, 02A901 (2010).

[4] R. C. Vondrasek, J. R. Carr, R. C. Pardo, R. H. Scott, Proceedings of the 18th International Workshop on ECR Ion Sources, Chicago, IL, 184 (2008).

Copyright © 2012 CC-BY-3.0 and by the respective authors

ISBN 978-3-95450-123-6

DESIGN OF THE AISHA ION SOURCE FOR HADRON THERAPY FACILITIES

L. Celona#, G. Ciavola, S. Gammino, L. Andò, D. Mascali
INFN-LNS, Via. S. Sofia 62, 95123 Catania, Italy

Abstract

Different facilities for hadrontherapy have been built or designed in the recent past and Italy is present in the field either with synchrotron-based and with cyclotron-based facilities. For both types of accelerators the availability of high brightness multiply charged ion beams is essential and R&D efforts in this subject are increasing. At CNAO, proton and carbon ion beams will be accelerated up to 400 AMeV by a synchrotron and the beam injection is guaranteed by two identical ECR sources of the SUPERNANOGAN family modified according to the specifications we set. Optimisation of beam emittance and intensity is of primary importance to obtain the necessary current in the RFQ-LINAC and future facilities may require much better performances in terms of beam brightness than the ones provided by such commercial ECRIS. A hadron therapy center is going to be built in Catania and the R&D related to the injector has already started within the frame of a collaboration between the Sicilian Authority and INFN. The design of a relatively compact ECR ion source operating at 18 GHz, named AISHa, has been completed recently and the construction will start at the end of 2012.

INTRODUCTION

The AISHa ion source has been designed by keeping in mind the typical requirements of hospital-based facilities, where the minimization of the mean time between failures (MTBF) is a key point together with the maintenance operations which should be fast and easy. Therefore, a so-called 3rd generation ECR ion source is not suitable, being quite complex for unskilled operators.

The new AISHa source is designed to be an intermediate step between the 2nd generation ECRIS (unable to provide the requested current and/or brightness) and the 3rd generation ECRIS (too complex and expensive).

It is intended to be a multipurpose device, operating at 18 GHz instead of 14 GHz in order to achieve higher plasma densities. It should provide enough versatility for future needs of the hadron therapy, including the ability to run at larger microwave power to produce different species and higher charge states than it is now for C^{4+}. At the same time, the electrical power to be installed for its operation will be kept below 50 kW, for possible installation on high voltage platforms. This demand implies also the simplification of all ancillary systems including an oven for metallic ion beams, which is interesting for new beam for hadrontherapy and for other applications.

The AISHa source is funded within the framework of the program of Sicilian Government named PO FESR 2007-2013 and a pool of Sicilian SME is associated with INFN for this project. The source is potentially interesting for the hadrontheraphy center to be built in Catania (call in progress) and for the CNAO (Pavia), which is the only operational Italian center for deep hadrontherapy at this date. In fact, it aims to offer treatments with active scanning both with proton and carbon ion beams, accelerated up to 400 MeV/amu by a synchrotron. Actually, at CNAO two ECR sources of the SUPERNANOGAN type (built by the Pantechnik company according to specifications set by INFN) are used. The factory tests confirmed the fulfilment of the specifications in terms of beam current and emittance. A further increase of accelerator reliability involves the improvement of the beam brightness, which can be achieved with the design and construction of this new ECR ion source.

MECHANICAL DESIGN AND BEAMLINE

The plasma chamber design is particularly important because its dimensions determine the plasma dynamics and the microwave coupling, while on the other way its larger dimensions may increase dramatically the construction costs. Since highly charged ions are not required to be produced (highest charge state requested do not exceed 6^+), the source can be designed with a short plasma chamber.

This will also reduce the number of high energy electrons, with a general improvement of source stability and reliability. Mechanics is essential for reliable operations; the perfect water-cooling permits to avoid hot spots which deteriorate the vacuum, making the beam less stable and the emittance larger and variable with the time.

The plasma chamber will be stainless steel made and it should operate at a maximum power rate of 2 kW by using double wall water-cooling . The insulation will be adapted to 40 kV operation by means of a 4 mm thick PEEK tube surrounding the hexapole, keeping magnets and yoke at ground potential. Polishing of any surface is requested in order to avoid sparks. This value of insulation will permit to adapt the AISHa source to other facilities (e.g. the high voltage platform for INFN-LNL). A new type of dc break has been designed to permit reliable operation even at 40 kV. The layout of the source is shown in Fig. 1.

celona@lns.infn.it

Copyright © 2012 CC-BY-3.0 and by the respective authors

ISBN 978-3-95450-123-6

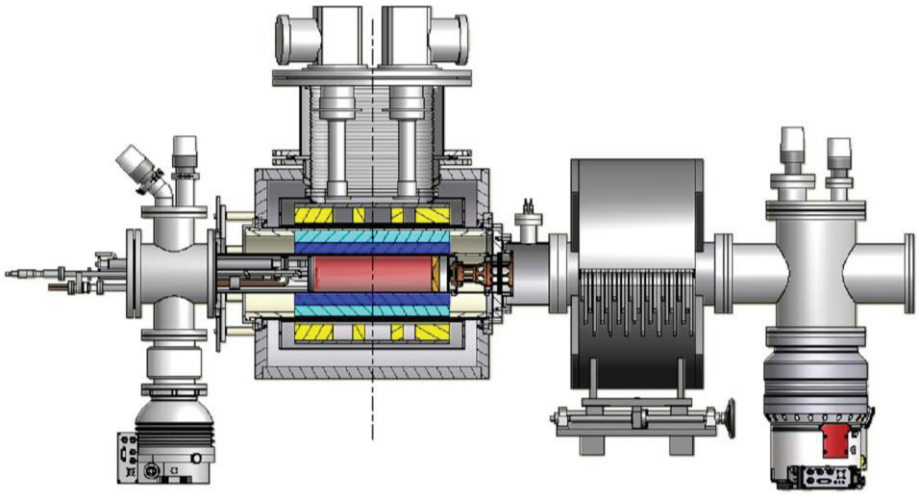

Figure 1: The layout of the AISHa source.

MAGNETIC SYSTEM DESIGN

The AISHa source will be based on a hybrid magnetic system able to confine the plasma radially by means of a permanent magnet hexapole, providing a maximum field of 1.3 T in the plasma chamber; the axial confinement will be given by a set of superconducting solenoids, enclosed in a compact cryostat. The cryostat will include two cryocoolers that permit to the equipment to run in LHe-free configuration. Studies have been carried out for two different configurations, with 3 or 4 solenoids to generate the mirror field, but the solution with 4 solenoids seems to be preferable for its versatility, even if it increases slightly the construction cost. The use of two middle coils instead of one may allow to finely tune the mirror ratio that is deemed to improve the ECR heating process according to recent achievements [1].

The hexapole demagnetization due to the superconducting solenoidal field has been carefully take into account in the OPERA calculations: Fig.3 shows the resultant of H_x and H_y over the hexapole surface due to the SC coils. The red parts indicate where the absolute value of the demagnetization vector is greater than the coercitivity; such calculations permitted to appropriately choose the permanent magnet materials and to define the final hexapole structure. The magnetic field values obey to the so-called ECRIS standard model for the operational frequency of 18 GHz. The peak field at the injection side is around 2.6 T and at the extraction side it should be about 1.7 T, with a minimum value so low as 0.4 T, about 60% of the ECR resonance field. This design should maximize the plasma density with a moderate microwave power and with a set of magnets that do not present any criticality. The cryostat has quite compact dimensions (its total length is 620 mm and its diameter 550 mm); the ECR region may be sufficiently long to facilitate the production of multiply charged ions; by changing the current in the two middle coils the ECR region may extend it up to 100 mm. The position of the ECR region is a crucial parameter as it strongly influences the electron heating: the tunable magnetic profile allows to improve the heating efficiency, suppressing the production of quasi-collisionless high energy electrons.

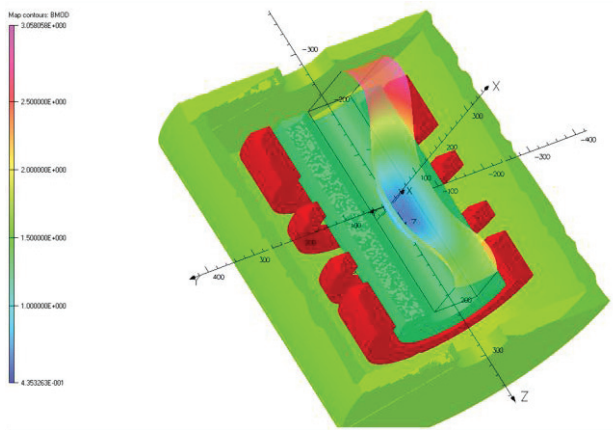

Figure 2: A 3D view of the entire magnetic system.

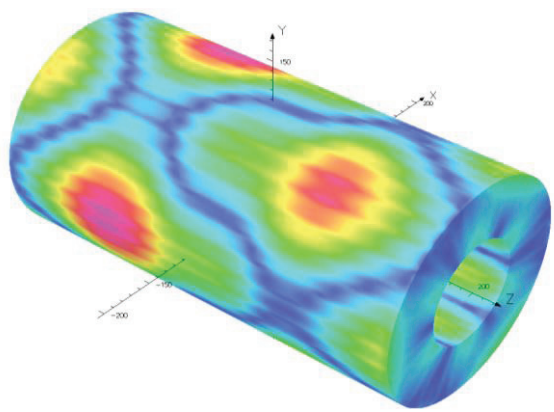

Figure 3: The resultant of Hx and Hy over the hexapole surface.

ISBN 978-3-95450-123-6

Copyright © 2012 CC-BY-3.0 and by the respective authors

The permanent magnet hexapole is made of NdFeB and it has a total length of 331 mm, slightly longer than the plasma chamber, which length is 300 mm, roughly corresponding to the distance between the two maxima of the mirror field. The superconducting solenoids are NbTi made and they are surrounded by an iron yoke, 30 mm thick, with 50 mm thick end plates on both sides. The current density in the four coils is 145, 121,120 and 121 A/mm^2 respectively, with the second and third coil current running in opposite direction with respect to the injection and extraction coil. The maximum axial gradients is about 13 T/m, enough to run the plasma in "strong gradient regime" [1,2] even for moderate microwave power (500 W to 1 kW).

MICROWAVE SETUP

The microwave injection system is the key element of the AISHa source design, according to our recent studies [1-2]. The source will use the frequency tuning effect with two electromagnetic waves of different frequencies injected in the chamber through separate input. The chamber dimensions have been chosen as a compromise between compactness and frequency gap between the modes in vacuum in the range 17.3-18.1 GHz. The position of the input waveguides was determined on the basis of the field pattern for the different modes. An estimation was performed on the maximum intensity of the modal electric fields excited in a vacuum filled cylindrical cavity, representing the plasma chamber. Simple considerations indicated that a position close to the value of 0.6r is the best choice.

The two frequency heating has been largely used to generate moderate currents of the highest charge states, but it has never been used to optimize the beam brightness. It may be helpful whether both the frequencies would be separately tuneable. In this way the electron energy distribution function may be optimized for the ionization of a definite charge state. Two 'traveling wave tube' (TWT) amplifiers will be used and their microwaves frequencies may be determined numerically, to use a maximum power much lower than it is for fixed frequency generator (at INFN-LNS a factor two or three difference was measured in similar experiments). Even from the point of view of the loss cone, the so-called 'plug-in' mechanism is enhanced in such a way and a larger number of electrons is confined, which improves the stability and reliability of the source. A "multi-frequency heating" has been also studied but the improvement does not balance larger cost and complexity. The microwave injector is shown in Figs. 4 and 5.

EXTRACTION SYSTEM

The extractor is an important element in the coupling between the ECR source and the following accelerator as it determines the shape and the width of the beam in the real space and in the phase space.

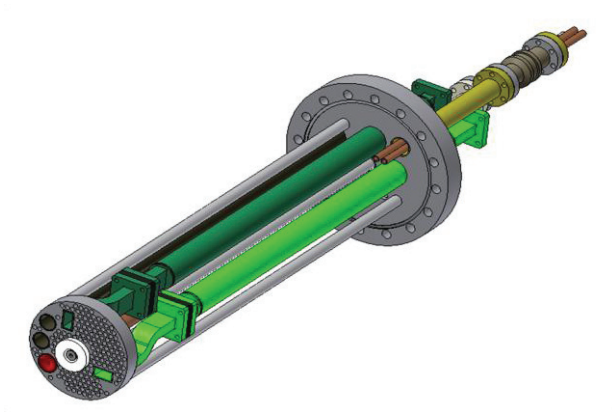

Figure 4: The injection system.

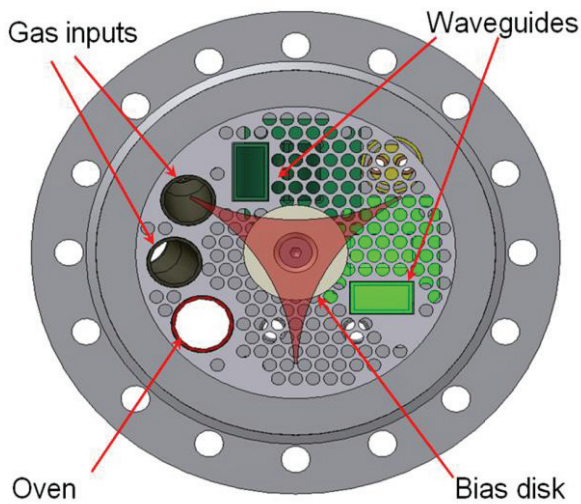

Figure 5: The injection flange.

The SUPERNANOGAN CNAO extractor was optimized by taking into account the constraints of the existing design, that permitted a limited increase of beam brightness. A further step is possible and it is under way with the design of the AISHa extraction system. At this moment the study is not yet complete, it will be defined as soon as the effective fringing field of the magnetic trap will be available for the KOBRA3D simulations.

ACKNOWLEDGEMENTS

The contribution of L. Allegra, G. Gallo, S. Passarello F. Chines, S. Marletta, M. Castro is gratefully acknowledged.

REFERENCES

[1] S. Gammino et al, Plasma Source Sci.&Tech. 18 (2009) 045016.
[2] S. Gammino, et al., IEEE Trans. on Plasma Science, (2008) vol. 36, 4 part II, 1552.

Copyright © 2012 CC-BY-3.0 and by the respective authors

ISBN 978-3-95450-123-6

OPERATIONAL EXPERIENCE WITH THE GTS-LHC ION SOURCE AND FUTURE DEVELOPMENTS OF THE CERN ION INJECTOR

D. Küchler, G. Bellodi, A. Lombardi, M. O'Neil, R. Scrivens, J. Stafford-Haworth,
CERN, BE/ABP/HSL, 1211 Geneva 23, Switzerland

R. Thomae, iThemba LABS, P.O. Box 722, Somerset West 7130, South Africa

Abstract

Since 2010 the GTS-LHC source delivers lead ions for heavy ion physics at the LHC. Several modifications allowed the improvement the source reliability and the beam stability. The attempts to improve the beam intensity were less successful. The different modifications and actual performance figures will be presented in this paper.

In addition to the heavy ion physics program of the LHC new ion species will be requested for different experiments in the future. The fixed target experiment NA61 requires primary argon and xenon beams. And a future biomedical facility asks for light ions in the range helium to neon. Approaches to prepare these beams and to modify the ion injector towards a light ion front end are presented.

INTRODUCTION

The GTS-LHC source was installed and commissioned in 2005. It delivered the Lead ion beam needed for the commissioning of the heavy ion injector chain: Linac3 - Low Energy Ion Ring (LEIR) - Proton Synchotron (PS) – Super Proton Synchotron (SPS). For the very first setting up of LEIR also an oxygen ion beam was used.

In 2010 and 2011 the LHC used the lead beam for heavy ion collisions at a momentum of 1.38 A TeV/c. In parallel NA61 used the beam for fixed target physics [1].

HEAVY ION OPERATION

The GTS-LHC ECR Ion Source was built by CEA, Grenoble, and installed at Linac3 in 2005. It uses three warm electromagnet solenoids to generate a minimum B configuration, and a permanent magnet hexapole for radial plasma confinement. The source is injected with 14.5 GHz microwaves, typically using 10 Hz repetition cycles of 50 ms pulse length. Lead is introduced through a resistively heated micro-oven and mixed with oxygen gas. The source uses the afterglow technique to increase the intensity of high charge state ions for injection into the LEIR synchrotron, extracting Pb^{29+} with a voltage of 18.8 kV. More information can be found in [2]

The GTS-LHC source and Linac3 were running about 26 weeks in 2011. Most of the time was used for setting up the injector chain. 778 hours beam time was taken for physics. During the physics period a total of 45 hours were needed for two oven refills and 2.4 hours the source was down due to failures. Since then the oven refills could be optimized. Now it takes in average 8-10 hours from the stop of the source until a stable beam is available again.

For the year 2011 several improvements on the source were done:

- The gas injection feedback loop was sensitive to the microwaves injected into the source. This has been improved with a different gauge type (IMR265 by Pfeiffer) installed close to the gas injection valve that could be used for the feedback loop (see Figure 1). This eliminated the sensitivity to the microwave and in addition it smooths out any (fast) pressure fluctuations in the source.

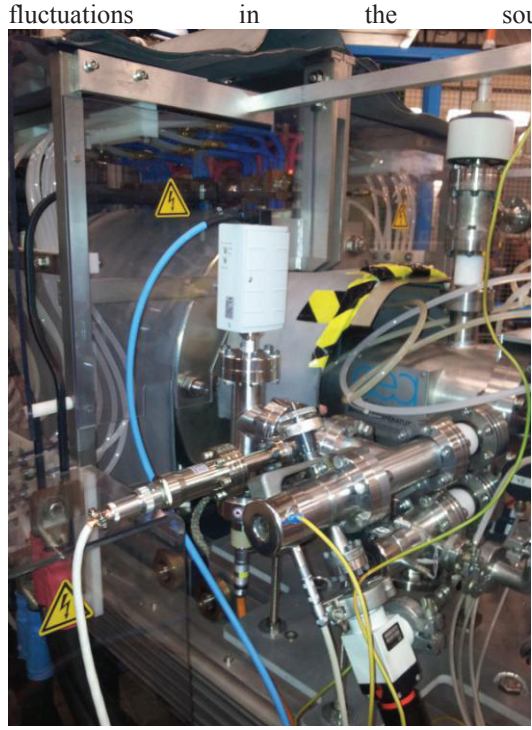

Figure 1: Gas injection with new gauge (in the center of the picture) for gas injection feedback loop.

- The electrical connection of the intermediate electrode failed regularly in previous years. The connection wire had a direct view of the beam, and the kapton insulation was eroded over some period which resulted in a short circuit. An additional insulation with a kapton tubing and a shielding with a wire mesh (braid) was made (see Figure 2), and inspection after the run showed no damage this time.

ISBN 978-3-95450-123-6

Copyright © 2012 CC-BY-3.0 and by the respective authors

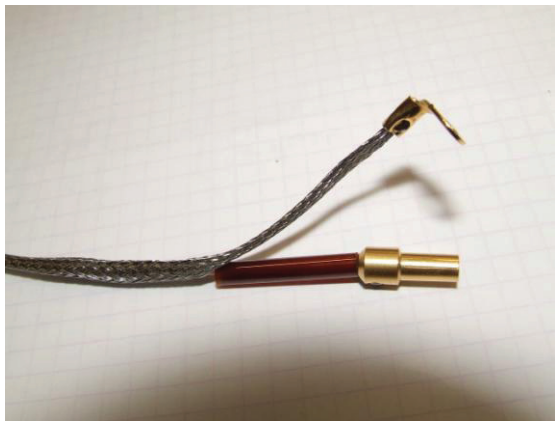

Figure 2: Modified electrical connection for the intermediate electrode.

To improve the amount of lead available from the source an attempt was made to fill the sample with liquid lead. But it turned out that for the operation a higher oven power was needed and that the output hole of the oven became clogged much faster with lead oxide (see Figure 3), actually leading to a reduction in lifetime. So this was discarded for the operation.

Figure 3: Oven tip clogged with lead and lead oxide.

The source delivered 80-130 eμA of Pb^{29+} out of the RFQ, which correspond to 20-22 eμA of Pb^{54+} at the end of the linear accelerator (after stripping). These are not record intensities as this time the source was tuned for stability.

When the source was commissioned the first time a plasma chamber made of aluminium was used. The beam intensity with this chamber was good but the beam stability over a long period was not acceptable. After a long period of operation some traces of damage were found inside the chamber. To avoid any problem during the physics run the chamber was replaced by a new one made of stainless steel. The performance was similar but the beam stability was noticeably improved. The only difference in the tuning of the source between aluminium and stainless steel chamber is the required microwave power. One needs roughly a factor three more power in the stainless steel chamber.

An explanation for the different beam stability could be the stiffness of the chamber. It was noticed that the aluminium chamber is less stiff and reacts on changes of the cooling water pressure and temperature with small changes in the source vacuum pressure (opening and closing leaks due to distortion of the chamber by the water temperature and pressure). These small leaks influence the ion production in the plasma. To test this hypothesis a stainless steel chamber coated on the inside with a thin layer of aluminium is in preparation.

The 18 GHz Tests

Following the results presented in [2] some more tests were done to improve the source performance using a microwave frequency of 18 GHz. Almost no improvement of the intensity of the Pb^{29+} ion could be found. There are several possible explanations for this result:

- The low energy beam transport line (LEBT) following after the source cannot transport the complete beam and losses reduce the extracted beam intensity. If the beam is scraped before entering the Faraday cup higher extracted currents are not visible.
- Pb^{29+} is only a medium charge state. For higher charge states some higher beam currents for 18 GHz compared to 14.5 GHz could be seen, but for operation the particle current is the figure of merit (the beam is stripped at the end of the linear accelerator).
- One test gave a hint that the maximum available microwave power at 18 GHz (2.4kW) may not be sufficient for optimal beam production.

As no improvement could be found after several attempts, it was decided to convert the 18 GHz generator to a 14.5 GHz generator to have a hot spare for operation.

LIGHT IONS FOR THE FIXED TARGET PHYSICS

Another client of ion beams at CERN is the experiment NA61 (see Figure 4) which is situated in the North Area of the SPS. This fixed target experiment studies phase transitions in strongly interacting matter (quark-gluon plasma). Up to now protons, indium and lead primary beams were used. Beryllium was created as a secondary beam from a lead primary beam.

Copyright © 2012 CC-BY-3.0 and by the respective authors

ISBN 978-3-95450-123-6

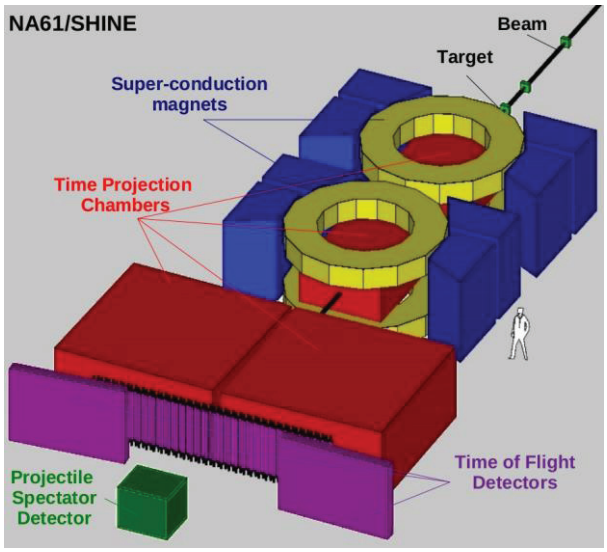

Figure 4: Scheme of the NA61 experiment.

Scaling the SPS energy and with different projectile ions the properties of the transition can be studied, and therefore argon and xenon were requested as primary beams.

In order to set up the injector chain with new ions, and make the physics run, more than 20 weeks of beam time is needed, and hence the source must also be quite stable over this period, testing the stability is one of the driving factors on the length of the required time to set up the source. Due to the limited time the source and Linac3 are available for tests, a collaboration with iThemba LABS in South Africa was signed. The advantage is that iThemba LABS has an identical source and the results gained there [3] can be used directly at the GTS-LHC source.

The argon beam will be studied at Linac3 in 2013.

A FUTURE BIOMEDICAL FACILITY

A meeting with potential users in June 2012 showed a big interest within the user community to have a dedicated facility for basic research related to hadron therapy for cancer. Light ions from protons up to neon at an energy of up to several 100 MeV/u are requested. These beams would mainly be used to irradiate cell cultures to study the biological effect of light ions onto cancer cells.

The main idea is to use the LEIR synchrotron which is part of the LHC ion injector chain, and would be able to deliver stacked, cooled and accelerated ions in the requested energy range. The ion beam for LHC is only required for part of the year, and even then only for studies, and during the LHC injection process, so Linac3 and LEIR would be available for such a biomedical facility during the rest of the time.

At the moment a study is under way to review the modifications needed in Linac3 and LEIR to be able to create, accelerate and extract light ions of the requested beam types, with the boundary condition that lead operation for LHC must not be perturbed, and switching from LHC lead operation, to medical ion operation should only take a few minutes.

For the light ion front end three options are under discussion.

1. An extension of Linac3 with a new source, a new RFQ and a switchyard to connect the new line with the present linear accelerator. The drawback is that some of the infrastructure work and installation can only be done when the present Linac3 does not run for heavy ion physics.
2. A complete new linear accelerator. A first estimate of these two options showed a very long schedule which is not very attractive for the user community that is already gaining momentum.
3. A commercial cyclotron with an external source.

Towards the end of this year a decision should be made based on schedule, budget and manpower on one of these options for further studies.

The source for this project has to deliver high currents of the requested ions for periods of several days to some weeks with a high stability and reliability. The type of source is not yet chosen, but for first estimations of the beam performance a commercial ECR source was used.

The source extraction voltage affects the current that can be extracted from the source and the beam transport until the RFQ. But a too high injection energy into the RFQ makes this device very long. Several injection energies were studied and 5 keV/u and 7.5 keV/u were found to be a good compromise between high source extraction voltage and the length of the RFQ. Detailed studies will concentrate on these values.

CONCLUSIONS

The GTS-LHC source delivered successfully Lead ions for the heavy ion physics at the LHC and for the fixed target experiment NA61. Several modifications improved the reliability of the source and lead to a better beam stability and higher up time for physics. As next the beam intensity has to be improved, but without jeopardizing the stability.

New ion beams have to be studied and to be made available for the users.

Future machine extensions could extend the catalogue of available ion species for a new user community.

ACKNOWLEDGMENTS

The authors like to thank S. Bertolo, Ch. Mastrostefano and M. O'Neil for their help during the operation.

The discussions with Ch. Carli and M. Dosanjh helped a lot to develop the first ideas for the light ion front end.

REFERENCES

[1] D. Manglunki et al., "Performance of the CERN heavy ion production complex", Proc. IPAC2012, New Orleans, Louisiana, USA, May 20-25, 2012.

Copyright © 2012 CC-BY-3.0 and by the respective authors

ISBN 978-3-95450-123-6

[2] D. Küchler, M. O'Neil, R. Scrivens, "First experience with the operation of the GTS-LHC ion source at 18GHz", proc. 18th International Workshop on ECR Ion Sources (ECRIS'08), Chicago, Illinois, USA, 15-18 September, 2008.
[3] R. Thomae, J. Conradie, D. Fourie, D. Küchler, „Beam experiments with the Grenoble Test Electron Cyclotron Resonance Ion Source at iThemba LABS", this conference.

Copyright © 2012 CC-BY-3.0 and by the respective authors

ISBN 978-3-95450-123-6

DESIGN OF WEB-BASED INTERFACE TO RIKEN 28 GHZ SUPER-CONDUCTING ECR ION SOURCE AND THE FUTURE PLAN

A. Uchiyama, The Graduate University for Advanced Studies (SOKENDAI), Tsukuba, Japan,
SHI Accelerator Service, Ltd., Shinagawa, Tokyo, Japan
K. Furukawa, High Energy Accelerator Research Organization (KEK), Tsukuba, Japan
Y. Higurashi, K. Ozeki, M. Komiyama, T. Nakagawa, RIKEN Nishina Center, Wako, Japan

Abstract

A new RIKEN 28GHz superconducting ECR ion source (28GHz-ECRIS) was constructed in 2009 in order to increase the intensity of Uranium ion beam for RIKEN RI beam factory project (RIBF) [1]. For effective and stable operation of the 28GHz-ECRIS, its operational software should have a user-friendly man-machine interface. The ECRIS control system was constructed with the Experimental Physics and Industrial Control System (EPICS) as well as RIBF control system. As a result, it was successful to provide the useful software, such as the operation GUI panels, the XY chart application, and the data acquisition system in EPICS-based system. On the other hand, to keep beam quality from 28GHz-ECRIS for a long beam service term, it should be possible to operate the 28GHz-ECRIS by members of the ion source team at any time. In order to relieve concern in the overseas business trip of members, we designed a real-time web-based client operational software using WebSocket, which is a new protocol presented by Internet Engineering Task Force (IETF) [2].

INTRODUCTION

The control system for RIKEN 28GHz-ECRIS was built with using EPICS which is the same as that for RIKEN RIBF [3]. The TCP/IP network was used for the communication with between local controller and client system. For manipulation of the main parameters of the ion source (gas pressure, current of the super-conducting solenoid coils, etc), F3RP61-2L was adopted, which was manufactured by Yokogawa Electric Corporation and was a CPU module of FA-M3 Programmable Logic Controller (PLC) without a ladder program. As the Linux runs on the F3RP61-2L, it can work as an EPICS Input/Output Controller (IOC). Similarly, the vacuum control system and beam diagnostic system were constructed by using EPICS, and Linux-based IOCs connected with N-DIMs, which were developed originally in RIKEN, over the Ethernet. On the other hand, for the 28GHz-ECRIS operational software, two Microsoft Windows XP PCs were used both in RIKEN linear accelerator (RILAC) and RIBF cyclotron control rooms. The PCs, in which X Window System is installed, have six displays using a multiple-display environment. And the web-based system is used for reading and writing of electric-log book and data archive viewer system for 28GHz-ECRIS.

MAIN CONTROL PANEL

The main panel to manipulate the gas pressure, extraction voltage, power supplies of the magnets and the X-Y plot of the spectrum of charge state distribution were developed with using the EDM [4]. EDM is one of the motif-based display managers provided by EPICS collaboration in order to develop the client operational software with GUI. The main panel GUI and plotter GUI are shown in Fig. 1 and 2, respectively. We adopted the Cygwin-X as an X-server, because the EDM is displayed on the X-window system.

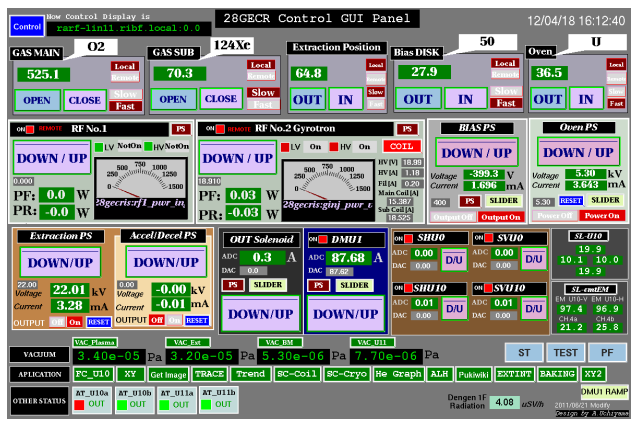

Figure 1: Main control panel constructed with EDM for 28GHz-ECRIS.

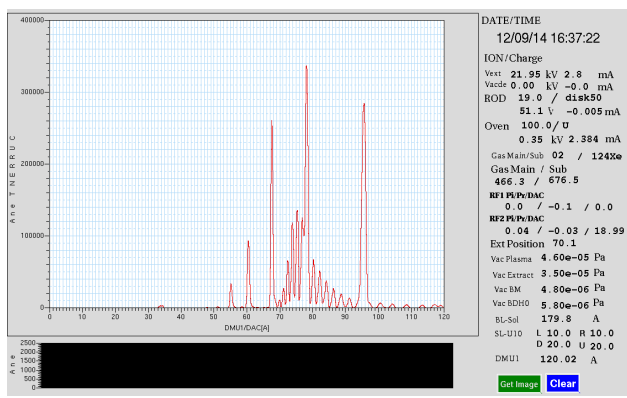

Figure 2: XY plotter chart constructed by using EDM for 28GHz-ECRIS operation.

#a-uchi@riken.jp

ISBN 978-3-95450-123-6

Copyright © 2012 CC-BY-3.0 and by the respective authors

PRESENT WEB-BASED SYSTEM

The Advantage of Web-based System

In today's society, Web and Internet access means one of the infrastructures. It is available to get various kind of information from Internet by using not only PC, but also mobile phone, TV and tablet. Therefore, the client system is not confined to the platform as long as corresponding to the Web. Besides, it is possible to reduce the cost of replacement of the client system significantly, so that it is not necessary to setup the dedicated client PCs.

Electric Log System

We obtained the log by hand-writing the numerical value indicated on the panel conventionally. However, it is not effective to obtain it, when we have many parameters. To make up for the disadvantages, we implemented the web-based Wiki instead. The Wiki is the system that one can edit the Hypertext Markup Language (HTML) on the web server by using Web browser.

To save the 28GHz-ECRIS parameter effectively, we planned to construct a paperless log system using Wiki (See Fig. 3). Recently, various kinds of Wiki are being used with a growing rate of Internet accesses around the world. In our system, open-source PukiWiki [5] was installed in the server. Simultaneously, we developed a program for the client, it dumps image files from these GUIs, and then it pastes the image file into PukiWiki page automatically. As a result, it was useful to adopt the electric log system using the Pukiwiki instead of writing the numerical value on the notebook. In the actual operation, the ion source operators obtained the log by using the method described above without any problems. Furthermore, it was useful to take over the condition of the ion source to the operators who work in the next shift.

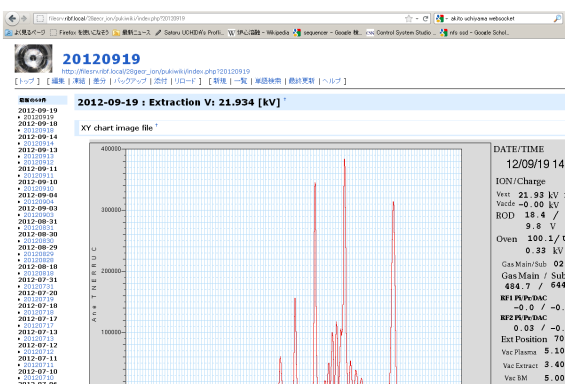

Figure 3: Wiki page with an image dump file for 28GHz-ECRIS XY plotter chart.

Archive Viewer

Using MyDAQ2 [6] developed at JASRI/Spring-8 as the data archive system in 28GHz-ECRIS, EPICS record value such as vacuum, extraction current and RF power were recorded into MySQL database. In our system, an EPICS Channel Access (CA) client for data collection was developed. The data is inserted into MySQL database with socket connection to the server running MyDAQ2 every ten seconds. Since the plot and the text are displayed on the Web browsers with ease, the web applications have user-friendly interface as well as Wiki-based system. The data archive system using MyDAQ2 is an effective method in order to shorten turnaround time in the system construction process.

NEW SYSTEM AND FUTURE PLAN

WebSocket Protocol

As described above, we used Web-based system in the electric–log and archive viewer which is the sub part of the ion source control system. Generally, we used a method for GUI development, such as the display applications coded in C/C++, Python and Java or used with EDM/MEDM [7]/CSS [8] for EPICS-based main control panel, because it is required to ensure ergonomic interactivity for beam operation. Actually, traditional Web application was not suitable to operate the main parameters of 28GHz-ECRIS, such as gas pressure control, in the lack of interactivity.

On the other hand, the engineers in the SPring-8 proposed the development methods of GUI using the WebSocket and made a prototype implementation [9]. The prototype system was constructed using MADOCA-based system that has been developed in the SPring-8 and was different from the EPICS-based system. For these important advantages of the system and Web application using WebSocket, we developed WebSocket server and implemented Web applications using WebSocket for control system of 28GHz-ECRIS with EPICS.

WebSocket is a new protocol to achieve the bidirectional communication between Web server and Web browser. Initially, the WebSocket was the part of the HTML5. It was formulated as a RFC6455 by the ITEF in Dec. 2011. The overview of the protocol is as follows.

1. A Web browser sends the handshake request to the server for connecting to the WebSocket.
2. Server returns a response of handshake after approval.
3. After the establishment of the handshake, the protocol switches to the WebSocket, and then the bi-directional communication is done between the Web server and Web browser.

Conventionally, the Web-based client system has ever been implemented, however, only for the monitoring system where a fast control response is not required. It is difficult to ensure the interactive response like the native application because of the difficulty of bi-directional communication between the server and client using the

Copyright © 2012 CC-BY-3.0 and by the respective authors

ISBN 978-3-95450-123-6

conventional HTML/HTTP technology. Since it is possible to make a bi-directional communication while keeping the connection between server and client, the problems described above can be solved by using WebSocket. Actually, it was found that the behaviour is comparable to the EDM when we used the WebSocket to obtain the data which change the numerical values in the period of ~100 ms. The problem is that it is not compatible with the all Web browsers (ex. Internet explorer (IE) 9). However, it is scheduled that the next version IE10 will support the WebSocket [10].

Developments Method

We used the Node.js [11] and its library (Socket-IO [12]) for development of the WebSocket server. Node.js is one of the server-side JavaScript language developed based on the Google V8 JavaScript Engine [13]. It must be available to use the EPICS CA protocol in the node.js for implementation of WebSocket server in the Node.js. Therefore, we developed add-on of Node.js (NodeCA) which interfaces to EPICS CA using EPICS base library.

Client-Side Application

The text update can be done by the description of DOM (Document Object Model) written in JavaScript. For visualization of the information, we adopted the jsgauge [14] and flot [15] which is the JavaScript library based on the jQuery [16].

Overview of the System

The overview of the whole system is shown in Fig. 4. One can obtain the data from the EPICS IOC by sending the custom events (caPut, caGet, caMonitor) to the WebSocket server from client-side JavaScript.

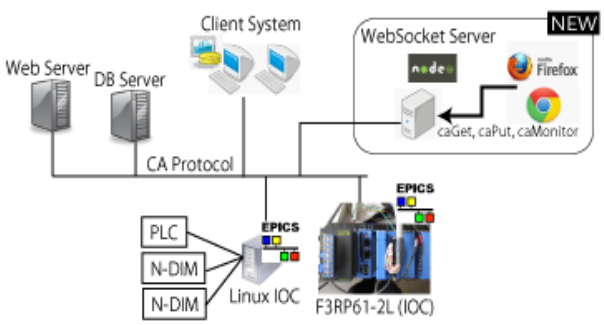

Figure 4: System overview of 28GHz-ECRIS control system and Web-based system.

System Implementation

We confirmed that it is possible to get the numerical value from the CA through WebSocket and indicate it by the iPhone 4S (See Fig. 5) and Android mobile. When implementing the application for the iPhone 4S, it is not easy to install the application developed their own without passing through the apple store. However, it is not needed in case of Web application developed by us.

At present, we are implementing it for controlling the 28GHz-ECRIS at RIKEN RIBF on a trial bases. We already checked that we had good response for monitoring the vacuum of the plasma chamber and controlling the gas-valve and so on. We continuously develop it to the actual operation.

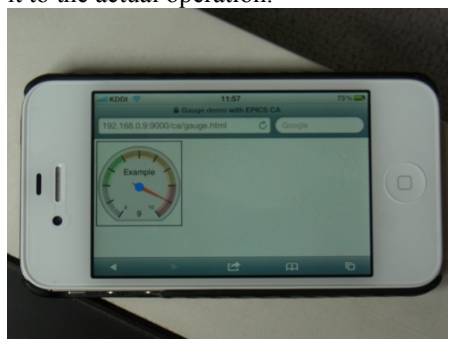

Figure 5: WebSocket-based Web application displayed on iPhone4S.

CONCLUTION

We developed the server which makes it possible to connect with EPICS CA by WebSocket. It enabled to display the information of the accelerator's conditions and to control it using the Web browser in real time. It makes possible to call CA API from Node.js by developing the add-on to interface for CA. At present, toward the full scale operation of 28GHz ECRIS control system, we released the first version and then we implement and control it on a trial bases. We confirmed that we can control and monitor a part of the main parameters for 28GHz-ECRIS as well as traditional EPICS-based application. It lay out on the table to make an access policy for implementation of access from WAN in the future.

REFERENCES

[1] T. Nakagawa et al., Review of Scientific Instruments, Vol. 79, Issue. 2, P.02A327, (2008).
[2] I. Fette and A. Melnikov. The WebSocket Protocol, IETF HyBi Working Group. 2011.
[3] M. Komiyama et al., Proc. ICALEPCS09, Kobe, Japan, (2009), P. 277
[4] http://ics-web.sns.ornl.gov/edm/
[5] http://pukiwiki.sourceforge.jp/ (in Japanese)
[6] T. Hirono et al., Proc. PCaPAC08, Ljubljana, Slovenia, (2008), P.55
[7] http://www.aps.anl.gov/epics/extensions/medm/
[8] J. Hatje et al., Proc. ICALEPCS07, Knoxville, Tennessee, USA, 2007, MOPB03.
[9] Y. Furukawa et al., Proc. ICALPECS2011, Grenoble, France, 2011, WEMAU010
[10] http://msdn.microsoft.com/en-us/library/ie/
[11] http://nodejs.org/
[12] http://socket.io/
[13] http://code.google.com/p/v8/
[14] http://code.google.com/p/jsgauge/
[15] http://code.google.com/p/flot/
[16] http://jquery.com/

ISBN 978-3-95450-123-6

Copyright © 2012 CC-BY-3.0 and by the respective authors

DEVELOPMENT OF INTENSE PROTON ECR ION SOURCES AT IMP*

Z.M. Zhang#, Z.W. Liu, H.W. Zhao, X.Z. Zhang, L.T. Sun, W.H. Zhang, Q. Wu, Y. Yang, H.Y. Ma, X. Fang, Institute of Modern Physics, CAS, 730000, China

Abstract

Since 1997, there have been two ECR ion sources for producing intense proton beam developed at Institute of Modern Physics (IMP). In 1999, a high current 2.45 GHz ECR proton source for Lanzhou university neutron generator, was constructed and tested at IMP. A mixed ion ($H_1^+ + H_2^+ + H_3^+$) beam current of 110 mA with CW mode was delivered from a single aperture of 6mm diameter with microwave power of 600W at the extraction voltage of 22 KV. Recently a new pulsed proton source has been designed and built at IMP for the CPHS (Compact Pulse Hadron Source) facility in Tsinghua University. Till now the commissioning of this source has been finished for 60mA pure proton beam with 50keV energy at Tisinghua University. The long time running stability and beam emittance have been tested and the results are well up to the requirements of CPHS. In this paper, the design of the proton ion source and the LEBT for the Chinese ADS project is also discussed.

INTRODUCTION

As an effective candidate, light ion Electron Cyclotron Resonance (ECR) source is always chosen to be the injector for proton accelerators. Different to the high charge state ECR ion source, which has more complicated magnetic field configuration and is driven by more than 10 GHz microwave with up to even more than 10kW power, the light ion ECR source is only considered by the simple axial magnetic field distribution and fed with 2.45 GHz microwave from magnetron of no more than 2kW power. Either electro-magnet or permanent magnet could be adopted to form the magnetic field. The ion source with all permanent magnet is very suitable to work on high voltage platform.

Today more and more proton accelerators have been, is and will be constructed for scientific research, industrial application and cancer therapy. High performance proton source is needed to satisfied different requirements. In china, there are some proton accelerator projects, such as Compact Pulsed Hadron Source (CPHS) project of Tsinghua University [1] and the china accelerator drive system (ADS) called for by Chinese Academy of Science (CAS) [2]. IMP undertook the task of proton source and LEBT for these two projects.

FIRST PROTON SOURCE AT IMP

1997, we started the research of producing high intensity proton beam from a compact ECR source for Lanzhou university neutron generator [3]. Fig.1 shows the source structure with the extractor and a near faraday cup. The necessary magnetic field is mainly formed by a set of permanent magnet rings of NdFeB material. The outer jacket of the source is made of iron to return the path of magnetic field. In order to get a better result, three auxiliary coils, which are water-cooled in directly through the copper sheets on the surface, are used to tune the magnetic field precisely in a small range. The water-cooled plasma chamber is made of copper with both diameter and length of 70mm. The ion extraction and beam pre-focusing are realized by a three-electrode system whose tips are made of TZM alloy. The gaps are 6mm and 3mm in the accelerating and decelerating regions respectively.

With a very simple microwave feeding system, a mixed ion ($H_1^+ + H_2^+ + H_3^+$) beam current of 110 mA with CW mode was delivered from a single aperture of 6mm diameter with microwave power of 600W at the extraction voltage of 22 KV.

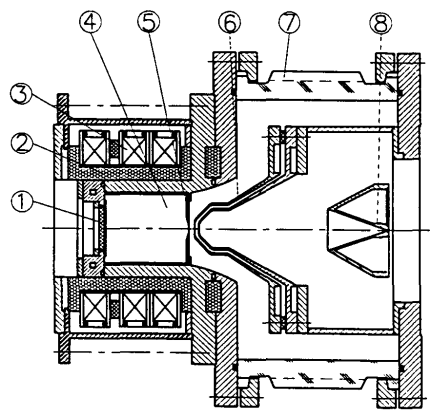

1. Microwave window;
2. Permanent magnets;
3. Coils;
4. Plasma chamber;
5. Plasma electrode;
6. Accel-decel electrodes;
7. Ceramics;
8. Faraday cup

Figure 1: Layout of papers.

PROTON SOURCE FOR CPHS

In 2009 a new project for the construction of a Compact Pulsed Hadron Source (CPHS) was approved on Tinghua University [1], which consists of a proton linear accelerator, a neutron target station, and beam lines for neutron and proton applications. In this system, a high intensity current ECR proton source and a low energy

*Work supported by NSFC (No. 91126004)
#zzm@impcas.ac.cn

Copyright © 2012 CC-BY-3.0 and by the respective authors

ISBN 978-3-95450-123-6

proton beam transport line (LEBT) are included. The 50-keV proton beam is extracted from the ion source, after the line LEBT transmission, focusing to match with the RFQ before injecting into it. Table 1 shows the primary parameters of the proton source and LEBT in CPHS.

Table 1: Design Parameters of Proton Source

Parameters	Request	Status
Microwave power (kW)	<1.5	<0.6
Beam energy (keV)	50	50
Peak current (mA)	60	70
Repeat frequency (Hz)	50	50
Pulse width (ms)	0.5	0.5
Rise time (μs)	100	80
Proton fraction	>85%	to be measured
$\varepsilon_{RMS,\ nom}$ (π.mm.mrad)	0.2	0.18
Reliability (hr)	120	140

To meet the requirements of the CPHS, the proton source and LEBT (shown in Fig. 2) are designed together with the colleague of Tsinghua University. Proton source is connected to the LEBT via a 150mm long high voltage column, in which a three-electrode extraction system is included. The whole length of LEBT is only 1283mm from source extraction hole to the RFQ entrance. Two solenoid magnets with two-direction steering magnets inside are used to focus the beam and match the Courant-Snyder parameters to the RFQ.

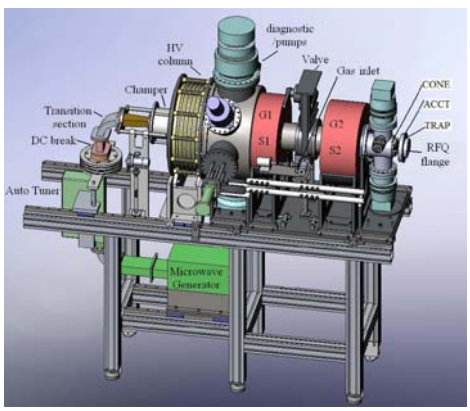

Figure 2: Layout of the proton source and LEBT.

Source Description

Similar to the first proton source of IMP, this source is also ECR type and uses the permanent magnets to form the needed magnetic field with slightly adjusting from two auxiliary coils. The schematic structure of the source is shown in Fig. 3 and Fig. 4 shows the simulated magnetic field distribution. The copper plasma chamber is cylindrical, with a 60 mm diameter and a 60 mm length. Both ends of the plasma chamber are lined with 2 mm thick boron nitride discs. To enhance the proton fraction, an aluminium tube with inner diameter of 50 mm is inserted the chamber. The microwave is produced by a 1.2 kW magnetron source at 2.45 GHz and is fed into the source via standard rectangular waveguides with a three-stub tuning unit. A three section ridged waveguide transition is placed between the plasma chamber and the cooled bend to enhance the axial RF field. The RF window is located on the front end of the chamber closed to first BN disk.

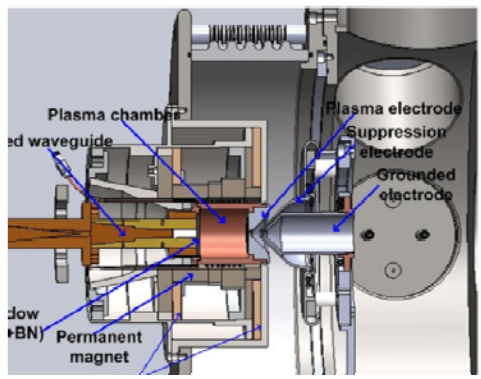

Figure 3: CPHS proton source with 3-electrode extraction.

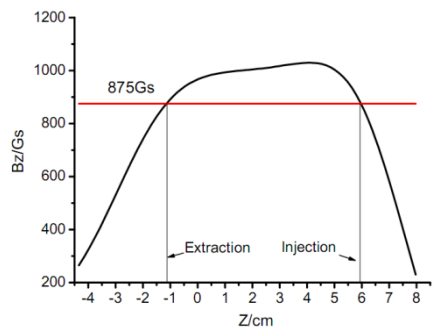

Figure 4: Simulated magnetic field of SPHS Proton Source.

Extraction System Design

In the previous design, this source is equipped with a three-electrode extraction system (shown in Fig. 3). All of the electrodes have 45° shape for high current extraction focalization. The aperture diameters are 6mm, 8mm and 8mm for plasma electrode, suppression electrode and ground electrode respectively. The gap between plasma electrode and suppression electrode is 12mm and one between suppression electrode and ground electrode is 4mm. Fig.5a shows the simulation result by IGUN program. The beam extraction and transmission look very good, but there are very frequent sparks occurring in two gaps during the commissioning of the source with required 50kV high voltage and 60mA pure proton beams. To deal with this problem, we developed a new 4-electrode extraction system and its simulation result by IGUN is shown in Fig. 5b. Compared with 3-electrode system, one additional ground electrode is inserted between plasma electrode and suppression electrode. The gaps are 10mm, 3mm and 3mm respectively from plasma

ISBN 978-3-95450-123-6

Copyright © 2012 CC-BY-3.0 and by the respective authors

electrode to the second ground one. The final experimental result proves that the new extraction system is more reliable for long term running.

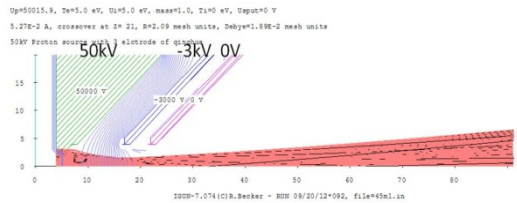

Figure 5a: Simulation result of 3-electrode extraction.

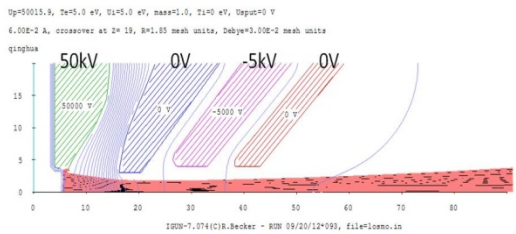

Figure 5b: Simulation result of 4electrode extraction.

Testing and Results

This proton source was tuned in pulse mode by modulate the rf signal before fed into ion source. The waveform of the beam pulse detected at the exit of LEBT is shown in Fig. 6. The rise time is about 100μs, which is less than the requirement. The beam emittance near the RFQ entrance plane was also measured by an ESS detector. Here the normalized rms Emittance is about 0.18 π.mm.mrad. Fig. 7 gives the image of emittance.

Figure 6: Beam pulse waveform.

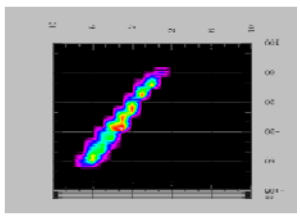

Figure 7: Emittance image.

It is not difficult for this source to produce more than 100 mA pulsed proton beam. But the long-term reliability is the key issue. More than 60mA beam current of pure proton was measured at the end of LEBT by a Faraday cup and ACCT. Long time monitoring of ion source and LEBT running were also implemented. The problem we met at the beginning is the reliability for running long time with 3-electrode extraction system. There are frequent sparks when proton beam reaches more than 50mA with 50kV extracting voltage. The discharge occurring in extraction area does not become better when decrease the extraction voltage. To deal with this problem, we developed a new 4-electrode system described in previous section. Then we got a very good result with new extraction system. Fig. 8 gives the monitoring result of 150 hr testing. There are only a few beam breaks during the running. In the graph we took the total beam current instead of the proton beam current because of the faraday cup insulation problem. The total beam current is really proportional to the proton beam current. That means the pure proton beam current was always more than 60mA during the operation.

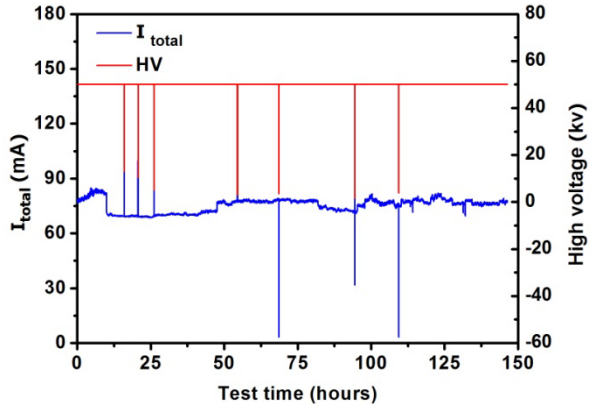

Figure 8: Long time running test of the proton source.

PROTON SOURCE DESIGN FOR C-ADS

To meet the great demand of nuclear transmutation and power generation, the Chinese government is setting off the C-ADS project, which is aiming at constructing a 15 MW CW proton linac of 1.5 GeV and about 10 mA. The C-ADS project is structured into three stages from 2011 all the way to 2030s. The first step completes the main parts of two independent injectors to higher than 5 MeV by 2013, which include ion sourced and its LEBT, RFQ and super-conducting cavities, and the whole system should be running at CW mode. Table 2 shows the requirements of proton source for C-ADS project.

Table 2: Required Parameter of CADS Proton Source

Parameters	Request
Beam energy (keV)	35
□E/E	0.1%
Proton current (mA)	15 (CW)
Proton fraction	>85%
$\varepsilon_{RMS,\ nom}$ (π.mm.mrad)	<0.2
Reliability (hr)	300

For designing this proton source, there are some key points to follow: 1). very compact source body; 2). all permanent magnet without any coils; 3). 4-electrode extraction system; 4). no tunable units on high voltage terminal. Fig. 9 shows the preliminary design of the source. We would like to make the magnetic field distribution similar to CPHS one. The simulation result suggests the magnetic field be provided by five permanent rings and be a little different to CPHS one by removing the auxiliary coils. The same extraction system

Copyright © 2012 CC-BY-3.0 and by the respective authors

ISBN 978-3-95450-123-6

as CPHS one was selected, but the diameter of extraction hole changed from 6mm to 4mm to minimize the beam emittance. Furthermore, the size of acceleration column will be much smaller than the previous one to enhance the vacuum pumping efficiency on this region. This proton source and its LEBT will be constructed and tested on the end of 2012.

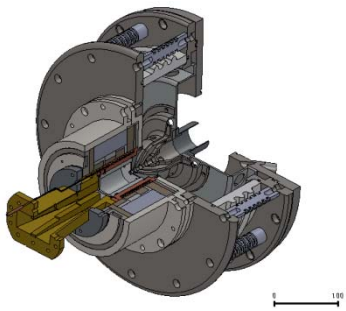

Figure 9: Schematic view of C-ADS proton source.

ACKNOWLEDGMENT

The authors would like to thank Dr. Gobin from CEA/Sarcly and Dr. Peng from Beijing University who participated in the discussion about the discharge problem of CPHS proton source.

REFERENCES

[1] Xialing Guan, et al., "LINAC for the compact pulsed hadron source project at Tsinghua University Beijing", proceeding of IPAC2011, San Sebastian, Spain, 2607-2609, 2011.

[2] Hesheng Chen, et al., "ADS Accelerator Program in Chian", IHEP-FNL Workshop on Proton Accelerator, Beijing, February 15-16 2011.

[3] Z.W.Liu, et al., "A Compact ECR Source At IMP", Proceeding of the 14th International Workshop on ECR Ion Sources, 1999, CERN, Geniva, Switzerland, 62-64.

Copyright © 2012 CC-BY-3.0 and by the respective authors

ISBN 978-3-95450-123-6

BEAM EXPERIMENTS WITH THE GRENOBLE TEST ELECTRON CYCLOTRON RESONANCE ION SOURCE AT ITHEMBA LABS

R. W. Thomae#, J. L. Conradie, D. T. Fourie, iThemba LABS, P.O. Box 722, Somerset West 7130, South Africa
D. Küchler, CERN, BE/ABP/HSL, 1211 Geneva 23, Switzerland

Abstract

At iThemba Laboratory for Accelerator Based Sciences (iThemba LABS) a new electron cyclotron ion source (ECRIS) was installed and commissioned. This source is a copy of the Grenoble Test Source (GTS) for the production of highly charged ions. The source is similar to the GTS-LHC at CERN and named GTS2. A collaboration between the Accelerators and Beam Physics Group of CERN and the Accelerator and Engineering Department of iThemba LABS was proposed in which the development of high intensity Argon and Xenon beams is envisaged. In this paper we present beam experiments with the GTS2 at iThemba LABS, in which the results of CW, pulsed and afterglow operation are compared.

INTRODUCTION

iThemba LABS is administered by the National Research Foundation (NRF) of South Africa. It provides accelerator and ancillary facilities for: research and training in the physical, biomedical and material sciences; treatment of cancer patients with energetic neutrons and protons and related research; production of radioisotopes and radiopharmaceuticals for use in nuclear medicine, industry and related research. At the heart of the iThemba LABS accelerator complex is the variable-energy, separated-sector cyclotron, which provides beams with a maximum energy of 200 MeV for protons. Beams are directed to vaults for the production of radioisotopes, proton and neutron therapy and nuclear physics experiments as shown in figure 1. Light ions, pre-accelerated in the first solid-pole injector cyclotron (SPC1) with a K-value of 8 are used for therapy and radioisotope production. For radioisotope production and neutron therapy a high-intensity 66 MeV proton beam is used, while a low-intensity 200 MeV beam is used for proton therapy. The second solid-pole injector cyclotron (SPC2) with a K-value of 10 is used for pre-acceleration of light and heavy ions as well as polarized protons from the three external sources [1]. In 2006 the decision was made that, due to the requirements of nuclear physics for new ion species and higher particle energies, a new ECRIS should be procured. A source, based on the design of the Grenoble Test Source (GTS) [2], which is similar to the GTS-LHC at CERN, has been constructed and installed. It is a room temperature source that uses two microwave frequencies, 14.5 GHz and 18 GHz, to deliver highly-charged ions of sufficient intensity to be accelerated in the separated-sector cyclotron to energies in the GeV range. At the same time a 14.5 GHz ECRIS4 that was designed and constructed by Grand Accelerator National d'Ions Lourds (GANIL) [3] and originally built for the Hahn-Meitner-Institute (HMI) in Berlin [4], with its beam line elements, was donated to iThemba LABS and is in operation since 2009.

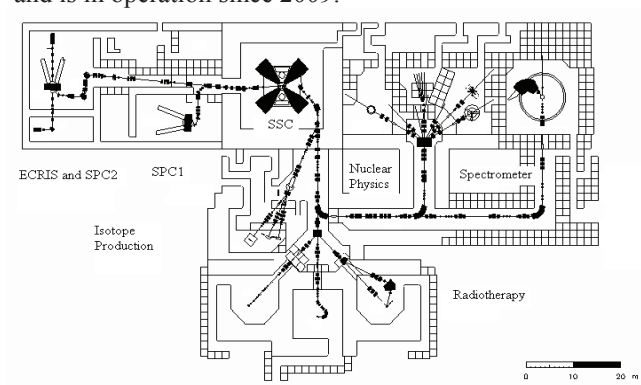

Figure 1: Layout of the iThemba LABS facility

The NA61 experiment at CERN studies the production of quark-gluon plasma. The light ion beam for the reaction is produced via the fragment method in which the primary lead beam hits a target which releases the secondary beam of lighter ion fragments. For experiments with heavier ions like Argon which are planned for 2014, a direct beam from the SPS is needed [5]. This beam is to be produced in the GTS-LHC and injected into LINAC3 which operates at a pulse length of 200 µs with a maximum repetition frequency of 5 Hz. Direct injection into the RFQ requires $^{40}Ar^{11+}$ ions from the source with a source potential of 9.6 kV.

THE GTS2 ECRIS

The coils, the permanent magnet assembly, the plasma chamber and all mechanical parts of the GTS2 were manufactured by different companies in Europe, which were also involved in manufacturing the GTS-LHC. For the vacuum system of the source three 700l/s turbo pumps (one at injection and two at extraction), one 70l/s turbo pump for the oven system and two dry roughing pumps are used. The longitudinal magnetic field is produced by three coils, namely the injection-, centre-, and extraction coil. The power supplies for the injection- and extraction coil can deliver 1300 A at 60 V leading to a maximum B-field of 1.6 T. A 600 A bipolar power supply is connected

#rthomae@tlabs.ac.za

Copyright © 2012 CC-BY-3.0 and by the respective authors

ISBN 978-3-95450-123-6

to the centre coil. The permanent magnet array in the Halbach configuration produces 1.27 T at the plasma wall surface [6]. Two 2.3 kW micro wave generators operating at 14.5 and 18 GHz are connected to the source via WR62 wave guides. The active plasma chamber volume which is manufactured from Aluminium is 1430 cm^3 at an active length of 30 cm and a diameter of 7.8 cm. The triode extraction system consists of a plasma electrode which is positioned at the end of the permanent magnet array in the plasma chamber, an intermediate electrode at a distance of 30 mm to the plasma electrode, and a ground electrode at 8 mm distance to the intermediate electrode. The aperture diameters of the electrodes are 12, 17, and 17 mm, respectively. The source can be operated with two resistive ovens which were not installed during the experiments. The bias disc (BD) has a surface of approximately 12 cm^2 and is positioned at 189 mm distance from the injection chamber exit flange which roughly corresponds to a position at the beginning of the permanent magnet array in the plasma chamber. Figure 2 shows a schematic of the source set-up.

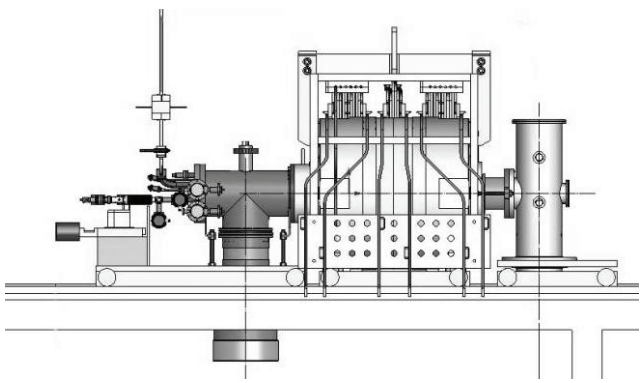

Figure 2: Schematic drawing of the set-up of the GTS2. On the left side the injection chamber with the micro wave guides, the oven feed through, and gas inlet systems are shown. The centre part contains the three coils for the generation of the longitudinal field. On the right side the extraction chamber concludes the set up.

The source is connected to the transfer beam line via a 104^0 bending-magnet. This set up of the beam lines in the ECRIS vault with the new diagnostic beam line for the GTS2 allows for simultaneously operation, i.e. the required beam for cyclotron acceleration will be delivered from one source, while the second source can be used for beam development. The diagnostic beam line of the GTS2 has an einzellens which focuses the beam on the double-focusing distance in front of the 90^0 magnet. Behind the magnet a horizontal slit is installed on the double-focusing distance to ensure sufficient mass resolution. The diagnostic line is completed with a chamber containing a slit-harp emittance device for both transversal planes and a Faraday cup. The set-up of the two sources in the ECR vault is shown in Fig. 3.

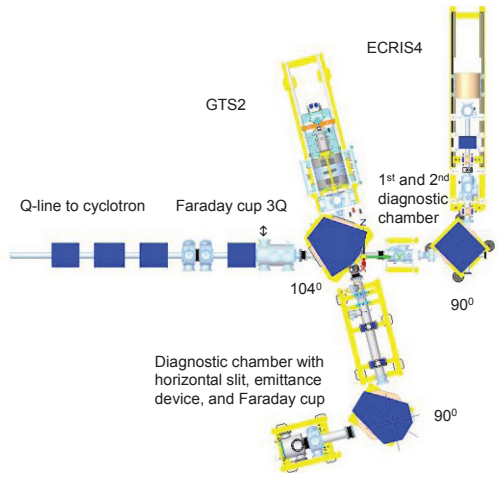

Figure 3: Layout of the beam lines in the ECR vault, in addition the position of Faraday cup 3Q is indicated.

ARGON BEAM MEASUREMENTS

After conditioning the source experiments in CW operation were performed which are important for the injection into the injector cyclotron SPC2. The Argon charge state spectrum was measured in the first Faraday cup (3Q) in the Q beam-line behind the 104^0 bending magnet (see Fig. 3).

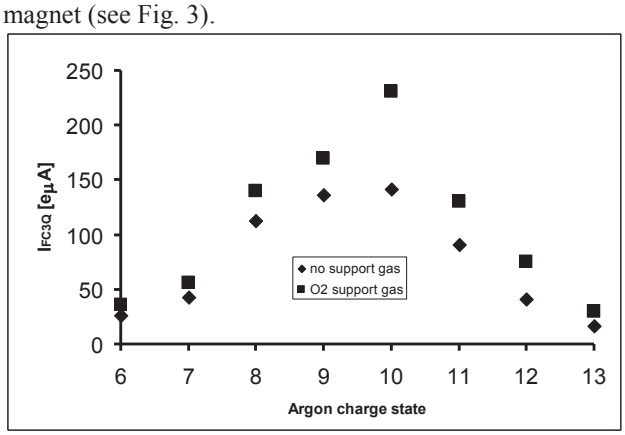

Figure 4: The Argon charge state distribution for CW operation with and without O_2 supporting gas. Note that the Ar^{10+} intensity includes O^{4+}.

The source was optimized for charge state 11+ for all measurements. Fig. 4 shows the measured spectrum. Typical values of the source parameters are: Extraction voltage U_{ex}=9.6 kV, Intermediate electrode voltage U_{int}=-2 kV, Bias disc voltage U_{BD}=-200 V, Injection coil current I_{inj}=1100 A, Centre coil current I_{cen}=300 A, Extraction coil current I_{ext}=1050 A, and Argon gas flow F_{Ar}=1.1 ml/h producing a pressure at the injection side of the source of $p_{inj}=2*10^{-7}$mbar and at the extraction side of $p_{ext}=3*10^{-7}$mbar, 14.5 GHz RF power P_{rf}=500 W. A current of 90 eμA for Ar^{11+} was obtained. The maximum of the distribution is around charge state 9+ to 10+. The figure shows further the influence of Oxygen supporting

ISBN 978-3-95450-123-6

Copyright © 2012 CC-BY-3.0 and by the respective authors

gas (gas flow F_{O2}=1.5cm^3/h). The intensity of the beam for the different charge states is increased by approximately 40 %.

In pulsed operation of the source (no supporting gas) with a duty cycle of 50% (50ms RF pulse on, 50ms RF pulse off) the current of the Ar^{11+} ions was slightly increased to 110 eμA during the pulse compared to CW operation.

For the injection into the RFQ accelerator at CERN, pulses with a pulse length of only 200 μs at a maximum repetition frequency of 5Hz are required which can be produced from the source in the afterglow regime.

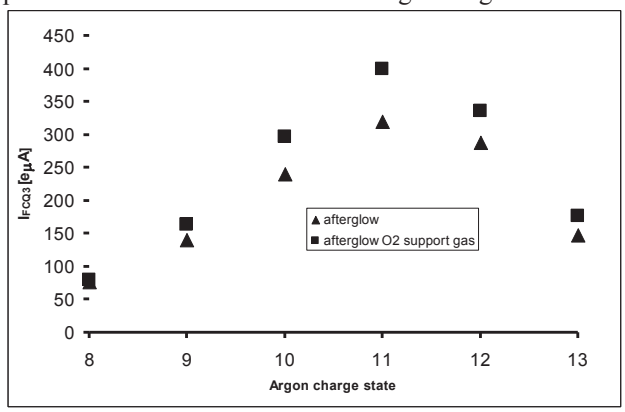

Figure 5: The Argon charge state distribution for after glow operation. Compared are the results without and with Oxygen as supporting gas.

For the afterglow operation the plasma was generated with 50 % duty cycle (RF power 50 ms on, 50 ms off) for thermal stability reasons. The bias disc was pulsed with pulse lengths between 1 and 3 ms. The pulse were delayed with respect to the end of the RF pulse between -1 and +3 ms. The best results (pulses which are stable in intensity and repeatability) were obtained for a delay time of 0.5 ms and a pulse length of 1 ms (see Fig. 6). In this mode an intensity of 320 eμA without supporting gas and 400 eμA with Oxygen supporting gas was achieved. It is also clear from Fig. 5 that the maximum of the distribution is shifted to higher charge states compared to CW operation. The source parameters were chosen to ensure stable operation over several hours. Fig. 6 shows a picture taken from the oscilloscope for afterglow operation with Oxygen supporting gas. Traces 1 and 2 show the end of the RF pulse. Trace 4 shows the pulse for the bias disc switch (delay 0.5 ms, pulse length 1 ms) and trace 3 shows the Faraday cup signal measured across 1 kΩ. In this example the current amounts to 80 eμA during the RF pulse. When the RF is switched off, the current increases linearly to 130 eμA over 0.5 ms. At the instant the bias disc voltage is applied the current increases to 400 eμA in 0.1 ms and stays constant during the bias disc pulse length. Experiments carried out without bias disc potential and with bias disc potential in DC operation resulted in much lower intensity compared to pulsed operation.

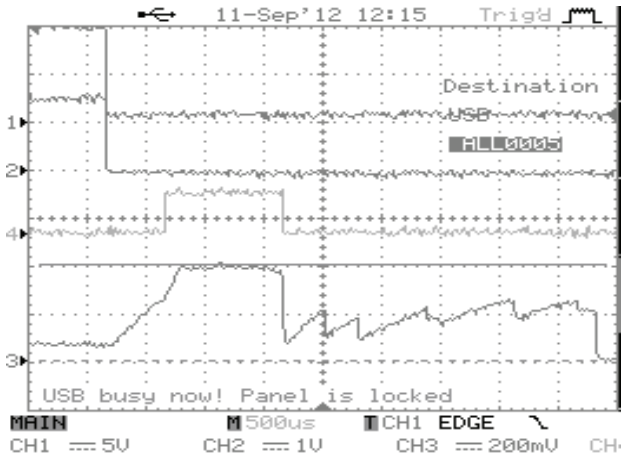

Figure 6: The oscilloscope signal for afterglow operation. Trace 1 shows the end of the RF trigger pulse. Trace 2 is the read back of the RF generator (1 V corresponds to 240 W). Trace 4 shows the pulse for the bias disc switch (delay 0.5 ms, pulse length 1 ms) and trace 3 shows the Faraday cup signal measured across 1 kΩ.

Experiments with Helium as supporting gas resulted in the same beam intensities for the different charge states, but the pulse stability was noticeably reduced.

Experiments using the new diagnostic beam line showed that the transmission decreases when compared to the transmission into the Q-line. This effect needs further investigation.

CONCLUSION

The experiments with the GTS2 show its capability to produce intense Ar^{11+} beams. The source parameter for stable beam generation in different operation modes could be determined and the influence of He and O_2 supporting gas was studied. The experiments will be continued to further optimize the source performance.

ACKNOWLEDGMENT

The authors like to thank their colleagues at iThemba LABS for their support.

REFERENCES

[1] J.L. Conradie et al., Proceedings of Cyclotrons'07, Catania, October 2007, p. 140.
[2] D. Hitz et al., Proc. 10th Int. Conf. on Ion Sources, Dubna, September 2003, Rev. Sci. Inst., 75, 1403, 2004.
[3] P. Sortais, Nucl. Instr. and Meth. B98, 1995, p. 508.
[4] H. Waldmann and B. Martin, Nucl. Instr. and Meth. B98, 1995, p. 532.
[5] M. Gazdzicki, J. Kochanowski, P. Seyboth, and J. Kochanowski, CERN COURIER, Januar 2012.
[6] R. Thomae et al., Rev. Sci. Instrum. **83**, 02A323, 2012.

Copyright © 2012 CC-BY-3.0 and by the respective authors

ISBN 978-3-95450-123-6

INSTALLATION AND OPERATION OF A 28 GHz GYROTRON FOR THE RIKEN SUPERCONDUCTING ECR ION SOURCE

J. Ohnishi, Y. Higurashi, T. Nakagawa,
RIKEN Nishina Center, Wako, Saitama, 351-0198, Japan

Abstract

We introduced a 28 GHz gyrotron with a maximum output power of 10 kW as a microwave source for the RIKEN superconducting ECR ion source. In its first test, large power ripples were observed in the output microwaves, and its operation was difficult at a power less than 1 kW. These ripples could be reduced by increasing the electric capacitance in the rectified circuit of the cathode power supply. In October 2011, the ion source could be continuously operated with the 28 GHz gyrotron for two months, and it supplied U and Xe beams to the experiments at the RI-Beam Factory. In this period, we observed fluctuations of 20-30% in the beam current from the ion source, which were correlated with the RF power. As a result of these investigations, the cause of these fluctuations was found to be attributed to the current in the solenoid coil of the gyrotron. These fluctuations could be reduced to within 7-8% of the total RF power by exchanging the solenoid power supply with new one with a current stability of less than 1×10^{-5} per day.

INTRODUCTION

At the RI-beam factory (RIBF) at RIKEN, all atomic elements up to uranium can be accelerated to an energy of 345 MeV per nucleon by a cascade of a heavy ion linac and four ring cyclotrons. Experiments in nuclear physics using secondary beams produced from these intense primary beams are being performed intensively. Because U beams have a large cross-section to generate many isotopes of interest, an increase in the beam intensity is of great need. In order to increase the intensity of U^{35+} used for beam acceleration at the RIBF, we have been developing a superconducting 28 GHz ECR ion source [1, 2]. This ion source uses a 28 GHz gyrotron. The gyrotron is produced by Mitsubishi Electric Corporation and has a maximum output power of 10 kW. The first test at the RIKEN site was performed with a dummy load in September 2010, and after improvement to its power supply, the superconducting ECR ion source was operated with the gyrotron in April 2011. Moreover, the 28 GHz ion source supplied U and Xe beams to the RIBF experiment successfully for two months from October to December of 2011 [3].

28 GHz GYROTRON

The newly developed 28 GHz superconducting ion source uses a gyrotron microwave source. Figure 1 shows the schematic drawing of this gyrotron, and its parameters are listed in Table 1. Electron beams produced from a magnetron-type electron gun are injected into an open resonator along solenoid fields, producing 28 GHz microwaves by electron cyclotron resonance in the cavity. The maximum acceleration voltage and current of the electron beams are 22 kV and 1.6 A, respectively. The gyrotron uses cathode and filament power supplies along with two dc power supplies for the solenoid coils, as shown in Fig. 1. Figure 2 shows a diagram of the electric circuit of the cathode power supply. The AC input power is controlled with thyristors at low voltage, and it is rectified into direct current after it is boosted up with a transducer. The cathode power supply also has a protection circuit with a three-gap device in order to protect the gyrotron from an arc event. The output RF power is controlled by the current and voltage of the electron beam. Figure 3 shows the relationship between the cathode voltage and the RF power for a fixed beam current of 1.2 A. The RF power was measured from the temperature rise of a dummy load. Each point in Fig. 3

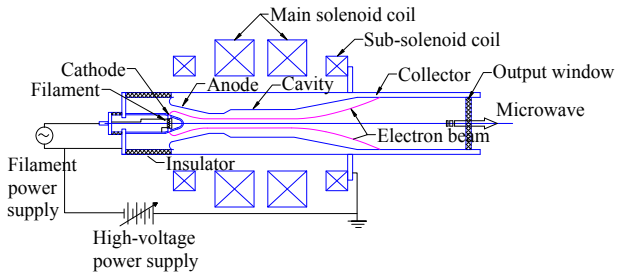

Figure 1: Schematic drawing of the 28 GHz gyrotron.

Table 1: Parameters of the Gyrotron

frequency	28±0.1 GHz
Mode	TE02
Electron beam voltage (max.)	22 kV
Electron Beam current (max.)	1.6 A
Input power (max.)	60 kW
Main Solenoid current (typ.)	195 A
Sub Solenoid current (typ.)	18.5 A
Output power (max.)	10 kW

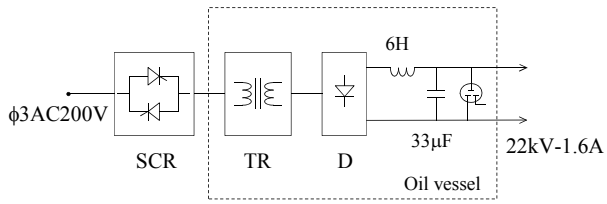

Figure 2: Electric circuit of the cathode power supply.

Copyright © 2012 CC-BY-3.0 and by the respective authors

ISBN 978-3-95450-123-6

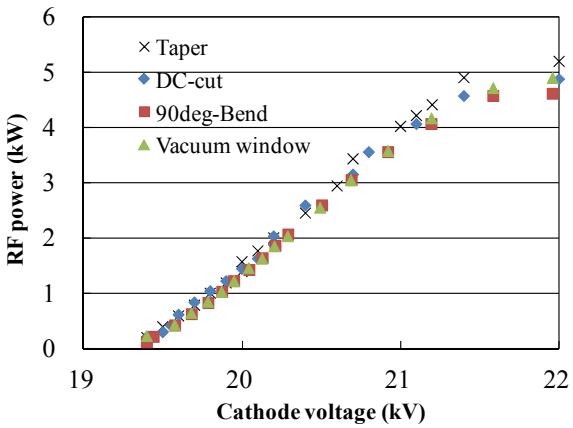

Figure 3: RF power versus cathode voltage.

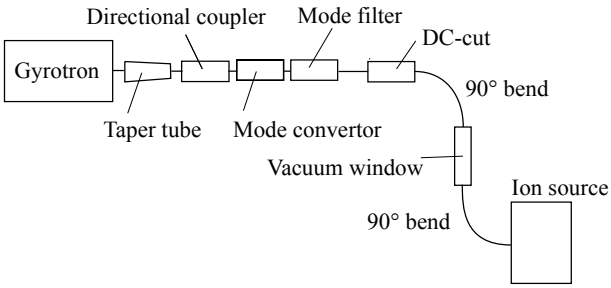

Figure 4: Microwave transmission line.

corresponds to a case where the dummy load was placed just behind the corresponding component indicated in the legend.

TRANSMISSION LINE

Figure 4 shows a drawing of the microwave transmission line. The gyrotron produces TE_{02}-mode microwaves, which are converted into the TE_{01} mode by a mode converter and a mode filter after passing through a taper tube and a directional coupler. The microwaves are then transmitted to the ion source via a DC-cut, two 90° bend tubes, and a vacuum window. The size of the output window of the gyrotron is ϕ63.5 mm, and the tubes downstream of the directional coupler have an inside diameter of ϕ32.512 mm. The directional coupler detects forward and reflected microwaves. The coupling is 50 dB and the diode detectors (DS2640, Herotek Inc.) are used to measure the power. The output voltages in the diode detectors have been calibrated to the power obtained from the temperature increase in the cooling water of a dummy load. Initially, the output of the detector was not stable at a power greater than 5 kW. Because the temperature of the directional coupler exceeded 50°C, we replaced the directional coupler with a water-cooled one. Figure 5 shows the diode voltage for the forward and reflected microwaves as a function of the RF power. Each point corresponds to the position of the dummy load. The voltages for the reflected waves represent only the relative power because setting level of an attenuator is

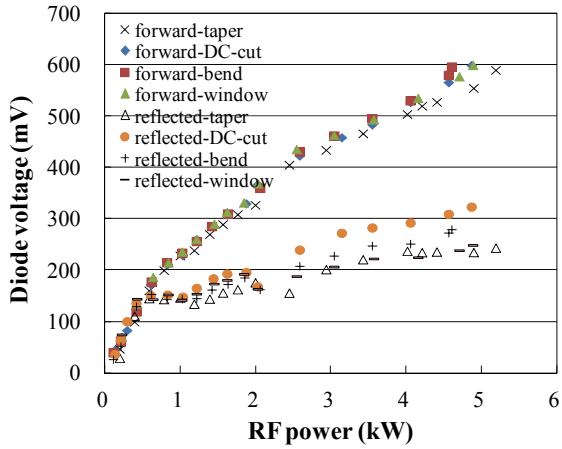

Figure 5: Output of the diode detector.

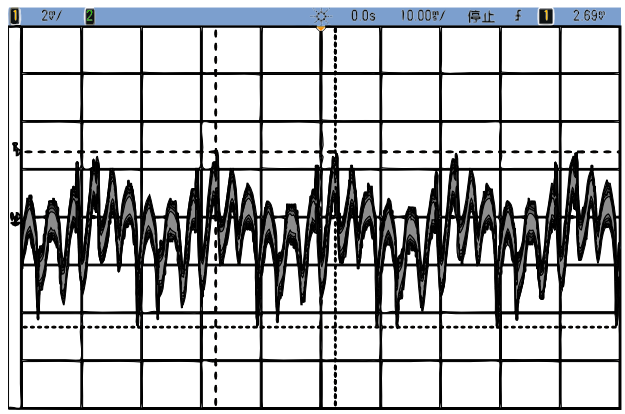

Figure 6: Waveform from the diode detector before improvement. Scales are 10 ms/div and 5 mV/div.

different from that in the forward wave, and most of the voltages seem to originate in the forward wave owing to the poor directivity. The mode converter changes the TE_{02} mode into the TE_{01} mode with an efficiency of 95%. The mode filter absorbs microwaves with modes other than the TE_{01} and TE_{02} modes.

REDUCTION OF THE RIPPLES IN THE RF POWER

The first test of the gyrotron was performed at RIKEN in September 2010 using a dummy load. Ripples of 300-500 W in the output power from the gyrotron were observed, making stable operation in the low-power region (<1 kW) difficult. The ripple waveform of the detector diode is shown in Fig. 6. The cathode voltage, beam current, and RF power were 22 kV, 1.5 mA, and 7.5 kW, respectively. The main component in the ripple frequency is at 300 Hz, and the magnitude of the ripple is approximately equivalent to the RF power of 400 W. Moreover, ripples of approximately 220 V were also observed in the cathode voltage. Even though we are operating at full power, the magnitude of both ripples did not change much, even at lower power.

Copyright © 2012 CC-BY-3.0 and by the respective authors

ISBN 978-3-95450-123-6

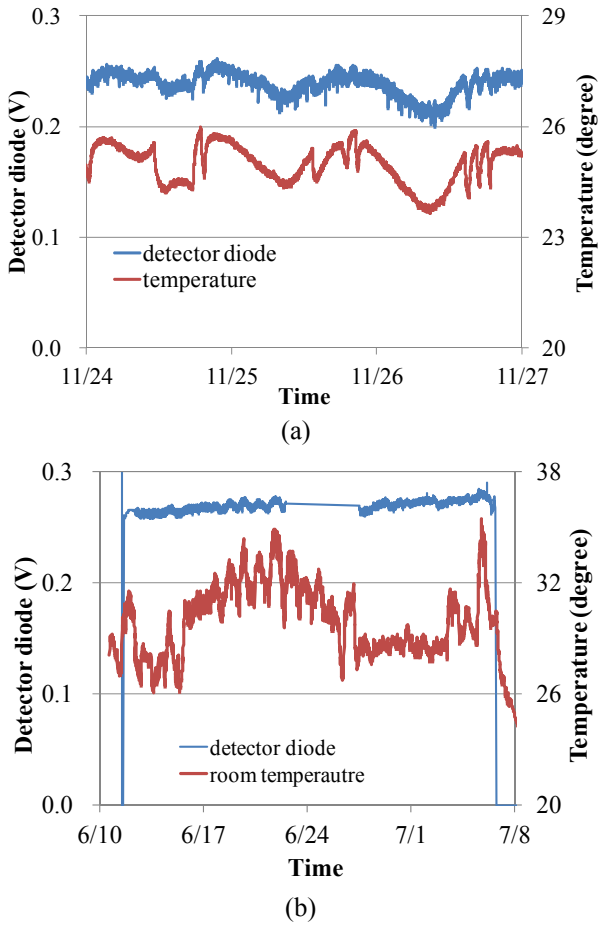

Figure 7: Detector diode voltage for the RF power and the room temperature during operation as a function of time (a) before and (b) after the stabilization of the output RF power.

Initially, the rectification circuit shown in Fig. 2 for the cathode power supply consisted of a 6 H inductor and a 3 μF capacitor. To reduce the voltage ripples, we increased the capacitance tenfold by adding four 7.5 μF paper capacitors with a maximum rated voltage of 37.5 kV. As a result, the ripples in the cathode voltage and RF power were reduced to approximately 15 V and 100-150 W, respectively, and operation below 500 W became possible. However, the reason why the ripples in the RF power did not decrease as compared to those in the cathode voltage is not clear.

STABILIZATION OF THE RF POWER

The ECR ion source with the 28 GHz gyrotron was operated from October to December 2011 in order to supply U and Xe beams to the RIBF experiments. During this period, 24-h operation was successfully achieved for a total of 70 days, except for two one-day breaks for the exchange of a uranium rod. Figure 7(a) shows the voltage change in the detector diode attached to the directional coupler for three days of machine time. The fluctuation in the diode voltage corresponds to a fluctuation in the RF power of approximately 300 W. This fluctuation seems to be correlated with the temperature of the room in which the power supplies are housed, as shown in Fig. 7(a). We investigated this phenomenon intensively because any fluctuation in the microwave power would influence the beam currents. As a consequence, we found that the RF power is very sensitive to the current in the main solenoid coil and that the current changes slightly, on the order of 1×10^{-4}/°C with the temperature of the room. In order to reduce this power fluctuation, we replaced the main solenoid power supply with another with a current stability of less than 1×10^{-5} per day. As a result, the RF power could be stabilized to within 7-8% of the total power in one month, as shown in Fig. 7(b).

REFERENCES

[1] T. Nakagawa et al., Rev. Sci. Instrum. 81 (2010) 02A320.
[2] Y. Higurashi et al., Rev. Sci. Instrum. 83 (2011) 02A308.
[3] Y. Higurashi et al., "Recent RIKEN 28 GHz SC-ECRIS Results," THXO03, these proceedings.

Copyright © 2012 CC-BY-3.0 and by the respective authors

ISBN 978-3-95450-123-6

DECRIS-5 ION SOURCE FOR DC-110 CYCLOTRON COMPLEX RESULTS OF THE FIRST TESTS

V.V. Bekhterev, S.L. Bogomolov, A.A. Efremov, Yu.E. Kostukhov, A.N. Lebedev, V.N. Loginov, N.Yu. Yazvitsky, FLNR JINR, Dubna, Russia
V. Mironov, KVI, Groningen, Netherlands

Abstract

The project of the DC-110 cyclotron facility to provide applied research in the nanotechnologies (track pore membranes, surface modification of materials, etc.) has been designed by the Flerov Laboratory of Nuclear Reactions of the Joint Institute for Nuclear Research (Dubna). The facility includes the isochronous cyclotron DC-110 for accelerating the intensive Ar, Kr, Xe ion beams with 2.5 MeV/nucleon fixed energy. The cyclotron is equipped with system of axial injection and ECR ion source DECRIS-5, operating at the frequency of 18 GHz. The main parameters of DECRIS-5 ion source and results of the first tests are presented in this report.

INTRODUCTION

The project of the DC-110 [1] cyclotron facility to provide applied research in the nanotechnologies (track pore membranes, surface modification of materials, etc.) has been designed by the Flerov Laboratory of Nuclear Reactions of the Joint Institute for Nuclear Research (Dubna). The cyclotron has 2m pole diameter, and to provide the energy of 2.5 Mev/nucleon the accelerated ions should have the mass to charge ratio about of A/Z = 6.6, that is 40Ar6+, 86Kr13+ and 132Xe20+. The parameters of the source are determined mainly by required intensity of the 86Kr13+ and the 132Xe20+ ion beams at the level of 200 eμA and 150 eμA correspondingly. The prolonged beam stability (few hours) is also important during the track pore membrane irradiation.

In recent years ECRIS has made considerable progress with the continuing increase of extracted ion beam intensity in which the fully superconducting ECRIS and hybrid ECRIS take the leading role. At the same time a room temperature ECRIS has the advantages of easy operation and lower cost in comparison to a SC ECRIS but with lower performance. Taking into account the operating conditions and that the production of very high charge states is not required the use of RT ECRIS in our case is more preferable.

A room temperature (RT) ECRIS consists of a set of water cooled resistive solenoids and a permanent sextupole magnet. To meet the requirement of an optimum 3D confinement magnetic field configuration the GTS-type [2] magnetic structure was chosen. This kind of magnetic structure provides a high enough level of an injection magnetic field keeping the reasonable ac power consumption.

DESCRIPTION OF THE SOURCE

The new 18 GHz RT ECRIS DECRIS-5 was constructed and built at FLNR JINR, Dubna, Russia. The magnetic structure of the source is composed by three independent copper coils. The injection and extraction coils are enclosed in soft iron yokes. By adding an iron plug at the injection side, which is situated directly inside the discharged chamber, the injection magnetic field can be effectively increased. At full excitation of the injection solenoidal coil, the injection magnetic field can be as high as 2.25 T. The calculated axial magnetic field distribution and the scheme of the magnetic structure are shown in the Fig.1 and Fig.2 correspondingly. The maximal current of the power supplies for the injection and extraction coils is 1200 A, for the middle coil – 800 A. The power consumption of the coils is about of 150 kW.

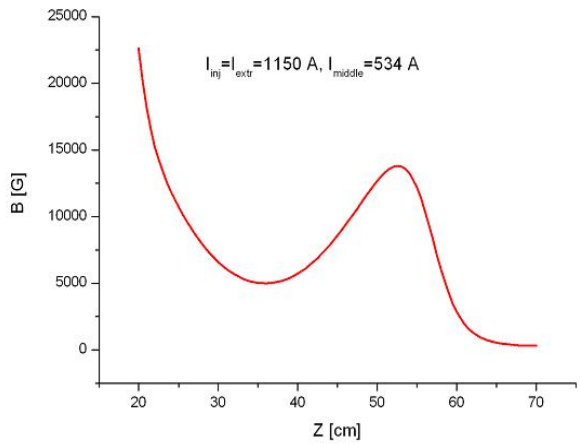

Figure 1: The axial magnetic field distribution.

The new hexapole for DECRIS-5 ion source (Fig.3) for radial confinement of plasma has a Halbach structure. It consists of 36 permanent-magnet identical trapezoidal sectors with the corresponding easy axis direction. In order to obtain a smooth magnetic field distribution along the pole an each sector was made from the whole piece of the magnetic material. This technology allows to eliminate some failings in magnetic field distribution near permanent magnet junctions. The inner diameter, the outer diameter, and the length of the hexapole are 86 mm, 230 mm, and 300 mm, respectively. Fig.4 shows the measured radial magnetic field strength on the plasma chamber wall in front of each pole. The comparison between radial field distributions of sectional hexapole for

Copyright © 2012 CC-BY-3.0 and by the respective authors

ISBN 978-3-95450-123-6

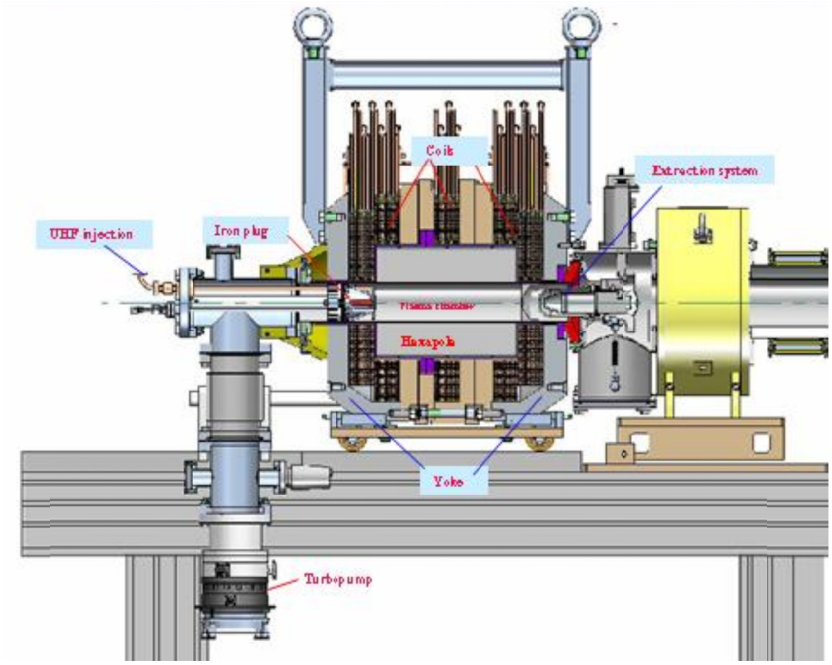

Figure 2: The cross-sectional view of the DECRIS-5 ion source.

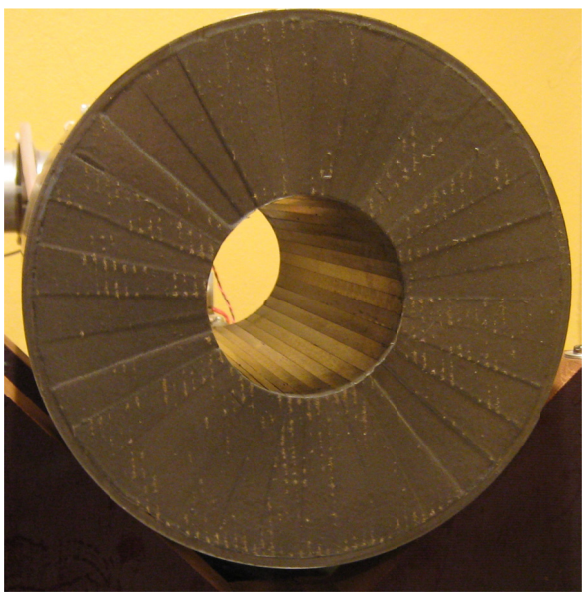

Figure 3: The new hexapole.

DECRIS-SC ion source (consists of 7 sections) and new hexapole is shown in Fig.5.

The stainless-steel plasma chamber is made as a water-cooled double wall tube. To enhance the ion source performance the internal diameter of the plasma chamber was increased up to 80 mm. On the injection flange there are mounted soft iron plug, water cooled standard waveguide, gas feeding tubes. Biased electrode is made from Ta and mounted on the soft iron plug. The shape and size of the bias electrode was designed to protect the iron plug from a direct interaction with plasmas.

The working gases (Ar, Kr, Xe) and support gas (O2) are fed into the source chamber by two double channel piezoelectric valves.

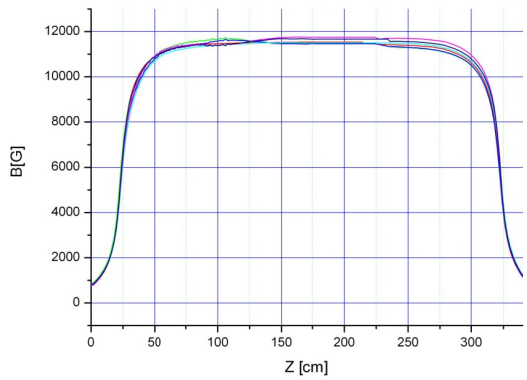

Figure 4: The measured radial magnetic field.

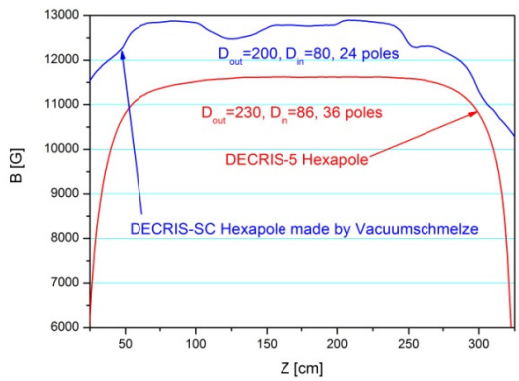

Figure 5: Comparison of sectional and new hexapoles.

ISBN 978-3-95450-123-6

Copyright © 2012 CC-BY-3.0 and by the respective authors

The source is pumped by 150 l/s turbopump from injection side, from the extraction side it is pumped by 150 l/s turbopump and 800 l/s cryopump.Subsection headings should not be numbered.

The source is equipped with three electrode extraction system, shown in Fig. 6. The plasma electrode aperture is 10 mm in diameter. The negatively biased extraction electrode is water cooled, and position of the whole assembly can be adjusted manually without breaking vacuum.

The main parameters of the DECRIS-5 ion source are collected in Table 1.

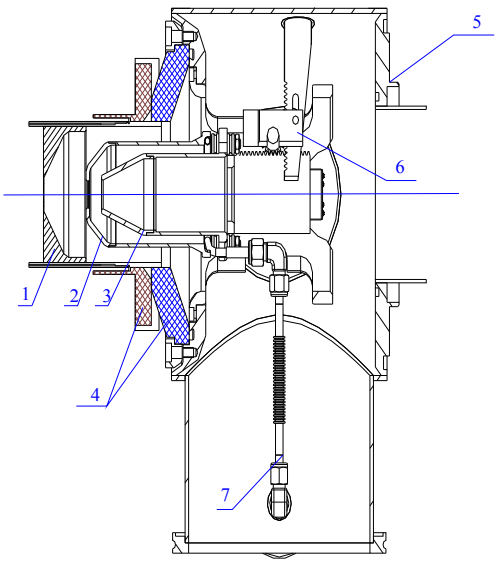

Fig.6 The extraction system of DECRIS-5 source.

Table 1: Main Parameters of DECRIS-5

UHF Frequency	18 GHz
Injection side magnetic field	2.25 T
Extraction side magnetic field	1.35 T
Radial magnetic field	1.15 T
Plasma chamber inner diameter	80 mm
Power consumption of the coils	150 kW

RESULTS OF THE TESTS

The test of the source was performed during December 2011 – February 2012. For the tests the source was assembled with the part of the axial injection beam line of DC-110 cyclotron. The main optical elements of the system are the analyzing magnet IM90, solenoid and two dipole correcting magnets. In the diagnostic box after analyzing magnet a Faraday cup and 30 mm diaphragm were installed. All elements are movable with pneumatic actuators. The vacuum system provides background vacuum about 2×10-8 torr in the extraction and diagnostics boxes.

The source was tested with the temporary mounted water cooling system. The cooling power of that system was lower than required. As a result the input water temperature was about of 30 ^{0}C when coils were exited with the maximum current. For this reason the time of continuous operation was limited (about of 30 min). With the nominal current) and the input UHF power was no more than 700 W.

The ion source was tested for production of Ar, Kr and Xe ion beams. The production of required intensity of the Ar^{6+} beam should present no problem. During the tests the operation of the DECRIS-5 ion source was very stable and reproducible. For the Ar^{8+} ion beam with the intensity of about 1 mA the measured beam stability reaches the value of 10^{-3} (20 min.). Fig. 7 shows the Ar charge state distribution when the source was tuned to maximize Ar^{8+}. The results, obtained during the tests are summarized in Table 2.

Table 2: Ion Yields from the DECRIS-5 Ion Source

Z	8	9	11	15	18	19	20
Ar	1200	750	300				
Kr				320	180	120	70
Xe							200

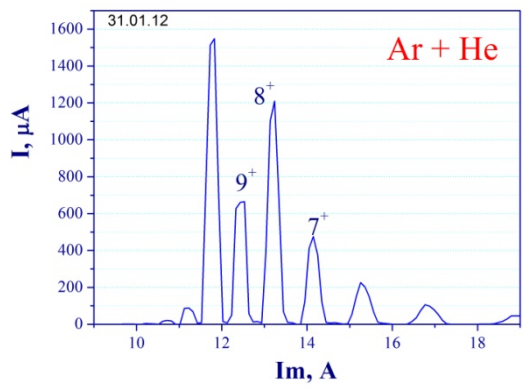

Figure 7: Charge state distribution for Ar. The source was tuned to maximize Ar^{8+}.

REFERENCES

[1] Gikal B.N. et al. The Project of the DC-110 Heavy Ion Cyclotron for Industrial Application and Applied Research in the Nanotechnology Field. Particle and Nuclei, Letters, V 7, N 7. p. 891 (2010).

[2] D. Hitz et al., Rev. Sci. Instr. 75, N 5, (2004) 1403.

Copyright © 2012 CC-BY-3.0 and by the respective authors

ISBN 978-3-95450-123-6

RECENT DEVELOPMENTS AND ELECTRON DENSITY SIMULATIONS AT THE ATOMKI 14.5 GHz ECRIS

S. Biri[1#], R. Rácz[1], Z. Perduk[1], I. Vajda[1] and J. Pálinkás[2]
[1]Institute of Nuclear Research (ATOMKI), Hungary, H-4026 Debrecen, Bem tér 18/c
[2]University of Debrecen, Hungary, H- 4010 Debrecen, Egyetem tér 1.

Abstract

The 14.5 GHz ECR ion source of ATOMKI is a standard, room-temperature ECRIS for plasma diagnostic studies, for atomic physics research and also serves as a low-energy particle source with wide range of elements for surface treatments. Recently the original NdFeB hexapole was exchanged by a new one and, consequently, new iron plugs were calculated, designed and installed at the injection side of the source. The resulted stronger magnetic trap has shown significant effect on the beam intensities and on the charge states distributions. The new magnetic configuration was re-calculated by the TrapCAD code developed by our group. The spatial positions and energy structure of 3 million electrons were calculated. A post-simulation energy filtering carried out on the non-lost (plasma) electrons reveals numerous interesting and important information in 3D.

INTRODUCTION

The 14.5 GHz ATOMKI ECR ion source celebrates its 20 years anniversary in 2012 because the basic financial contract was signed in 1992. The first plasma was generated in 1996 and the ion source delivers beams since 1997. During the past two decades continuous technical developments characterize the source itself and its surroundings called ECR Laboratory [1].

In a recent paper the status in 2011 and the special features of our ECRIS were shown in full detail [2]. Since then the magnetic trap was significantly strengthened by exchanging the hexapole magnet and the iron plugs. The computer control system was also changed and the new one is being tested and developed promisingly. All these technical upgrades are summarized in the first part of this paper.

The new magnetic trap significantly changed the structure of the magnetic field inside the plasma chamber. The magnetic system was re-calculated and then the electron cloud in the new trap was simulated by our TrapCAD code [3, 4]. Meanwhile TrapCAD itself was also slightly upgraded. The results of the simulation are shown in the second part of the paper.

UPGRADED MAGNETIC TRAP

The mechanical, electrical and microwave structures of the ATOMKI-ECRIS are not fixed: depending on the actual experiment they have several configurations. In Fig. 1 the basic (most frequent) setup is shown. The magnetic trap consists of two identical room-temperature solenoid coils with 5 cm thick iron yoke and of a permanent magnet hexapole. The coils-generated axial magnetic field peak values are 0.95 Tesla at both sides without the optional soft iron plugs at the injection side.

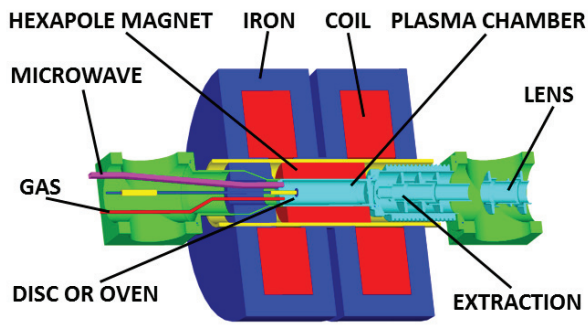

Figure 1: The most frequent mechanical and magnetic configuration of the ATOMKI-ECRIS.

In 2012 the 15 years old hexapole was exchanged by a new one. Table 1 summarizes the geometrical and magnetic features of the original and new hexapoles. The radial pole field of the old hexapole at the plasma chamber internal wall (R=29 mm) was 0.95 Tesla at the beginning and this value gradually decreased between 1996 and 2007 year by year by a yearly factor of about 2%. In 2008 however, a sudden and still un-understable big decrease occurred resulting a much weaker magnetic field strength of 0.7 Tesla at R=29 mm. Between 2008 and 2012 the ECRIS mainly operated at lower frequencies with the weakened hexapole in order to reach an acceptable mirror ratio. In 2012 the hexapole was exchanged by a new one. Its external diameter could be enlarged by a small re-designing of the surrounding pieces. Now the magnetic field in the plasma chamber is about 1.2 Tesla i.e. much stronger than ever it was with the old hexapole.

When the new hexapole was installed the soft iron magnetic plugs at the injection side had to be re-designed, manufactured and installed. The goal of this change was double. We wanted to increase the peak magnetic field at the injection side inside the plasma chamber as high as possible. The second gal was to minimize the force to the plugs and thus to minimize the opposite direction force to the basic structure of the ion source. Both goals were achieved and now the peak axial magnetic field at the injection side is almost 1.3 Tesla while it remained less

#biri@atomki.hu

ISBN 978-3-95450-123-6

Copyright © 2012 CC-BY-3.0 and by the respective authors

than 1 Tesla at the extraction side. One of our next plans within the development activities is to design and install iron plugs to the extraction side, as well.

	Old hexapole	New hexapole
Material	NdFeB (490i/400i)	NdFeB (N45H)
Segments	24	24
Lengths (mm)	200	200
ID (mm)	65	65
OD (mm)	135	155
B-field at R=29 mm (Tesla)	0.95 (0.7)	1.2

Table 1: Summary of the two hexapoles. R=29 mm is the internal radius of the plasma chamber.

The new hexapole and iron plugs (see Fig. 2) significantly effected on the charge state distribution of the plasma. So far the effect was tested mainly for oxygen and argon and a prompt 10-50 % increase was observed for all charge states. The beam tests will be continued for other elements.

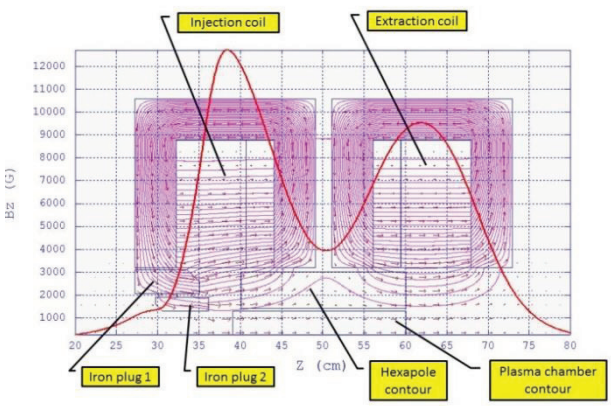

Figure 2: The upgraded magnetic system (Superfish calculation) with field lines and with the axial magnetic field distribution.

The ion choice of the ATOMKI-ECRIS recently increased due to new the requirement from our users. Gold and calcium beams were produced by the sputtering method using oxygen base plasma. While the peak intensities for both elements are not high yet (1-2 microampere) the CSD for gold is satisfactory. The highest peak was 20+ and charge states up to 26+ were observed in the first experiment.

The old computer control system (Pentium-1 motherboard, Windows-95) served well during the last 15 years. Recently a new NI-PXI hardware was installed. The development of the Labview-based control software is under way. At that moment all the functions operated under the old control system work at the same level or better in the new configuration. The final goals are to include majority of the ECRIS setting tools (digital and analogue inputs/outputs, GPIB and RS232 interfaces, stepping motors etc.) and to shorten the tuning and beam transport times.

PLASMA ELECTRONS SIMULATIONS

The modifications in the magnetic system involved that the simulation of the plasma in the upgraded magnetic trap is the next logical and useful step to understand the operation of our ECRIS. For the simulations the TrapCAD code was used which is described in details elsewhere [3, 4]. TrapCAD was made to visualize the magnetic trap of ECR and other ion sources and to follow the paths and the energy evolution of the electrons in this magnetic trap by including the electron-cyclotron-resonance phenomena. The magnetic field distribution is calculated by freeware or commercially available pre-processing codes (e.g. PoissonSuperfish). TrapCAD is a "limited-3D" code, the magnetic system must have some regularities (cylindrical axial field, multipolar radial field), but the resulting motion is implemented in 3D.

The spatial and energy structure of the non-lost electrons in the new magnetic trap of the ATOMKI-ECRIS were calculated. TrapCAD was used within a timescale such that the particle–particle interactions are neglected. A high number of independent electrons are energized by stochastic resonance heating process. All the initial particles were located at the resonance surface. A recent small upgrade in TrapCAD resulted that the initial electron density on the surface of the resonance zone (RZ) is more equal than before. Another modification accelerated the running time of the code. Now the simulation of one million electrons is possible in reasonable time (a few tens of hours CPU time on a PC with i5 processor). In the simulation the initial conditions were as follows.

- **Geometry.** Calculation took place in the cylindrical plasma chamber of the ATOMKI-ECRIS, diameter is 58 mm, length is 210 mm.
- **Magnetic field.** As described in the previous section, calculated by PoissonSuperfish. Mesh size is 1 mm in each directions.
- **Electrons**. 3 million electrons were placed with equal density into a thin layer developed by the resonance field (B=5200 gauss closed magnetic surface for 14.5 GHz microwave frequency). The basic condition was that the magnetic field can differ by less than 100 gauss from the resonance value. Electrons thus started from positions where the magnetic field was between 5100 and 5300 gauss. This corresponds to a layer with about 0.6 mm thickness. The starting energy of the electrons was a random value between 1 and 100 eV for both (parallel and perpendicular) components.

Copyright © 2012 CC-BY-3.0 and by the respective authors

ISBN 978-3-95450-123-6

- **Microwave**. A circularly polarized plane wave propagates along the plasma chamber axis. The electric vector of this type of wave is rotating in the perpendicular plane. The initial phase difference between the rotating electric field and velocity vector of the particle is a random value. Thus the electrons are heated up by stochastic resonance heating process. In this calculation 14.5 GHz frequency and 1000 watt power were applied.
- **Simulation time.** In order to neglect the electron-electron and electron-ion collisions (not included in TrapCAD) the simulation time was chosen to be 200 nanoseconds. In real (CPU) time the calculation lasted for 127 hours.
- **Overall result.** At the end of the simulation 49% (1.46 million) of the electrons were still remained in the plasma and 51% lost on the chamber wall. The average energy of the non-lost (plasma) electrons increased from 100 eV up to 3330 eV by the ECR heating process. In Fig. 3 the energy distribution curve of the non-lost (plasma) electrons is shown.
  According to our recent study [5] the electron component of the plasma may artificially be grouped into sub-populations (see Fig. 3):
  - E<200 eV: cold electrons.
  - 200 eV < E < 3 KeV: intermediate electrons.
  - 3 KeV < E < 10 KeV: warm electrons.
  - E>10 KeV: hot electrons.

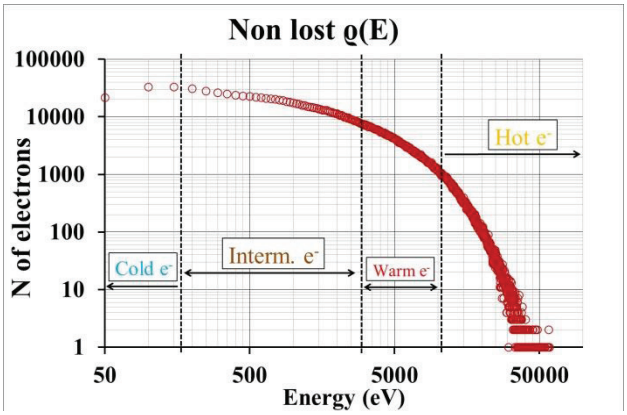

Figure 3: Simulated energy distribution curve of the non-lost electrons in the Atomki-ECRIS.

For the point of view of HCI production, the most important group is the warm electrons. In [5] was shown that for the case of argon plasma mainly the 3-10 KeV energy (warm) electrons carry out the step-by-step ionization. By comparing the simulation results with X-ray photos of argon ions the spatial positions of these two particle clouds were very similar. Based on this result, any spatial information to be obtained for the warm electrons from this simulation, can be used (with some limitations) for the plasma ions.

After 200 nanosecond simulation time the final energy and positions of all the electrons are saved. The non-lost electrons are filtered by their energies according to Fig. 3.

The electron density distribution along the plasma chamber axes demonstrates the significant difference between the electron populations. In Fig. 4 cold electrons are found all along the plasma chamber – according to the many visual observations (cold electrons excite atoms which emit visible light photons). The warm (ionizing) electrons concentrate much more around the resonance zone (RZ). They are two order of magnitude less near the chamber end-plates (z=1 and z=20) than the cold electrons. The ion density should also much higher near the RZ than at the ends. It does not mean of course, there are no electrons or ions close to or at the end-plates. The well-known triangles are always formed from both low charged and higher charged lost ions as it was shown in [6]. The density of the hot electrons outside the RZ is more than 3 orders of magnitude less than near the RZ. For all energy components however a general conclusion is valid: the electrons separate into a high density inner plasma (developed by the RZ) surrounded by a lower density halo. The same observation was found and proved in [7].

To get 3D-impression on the main components of the plasma it is useful to visualize "plasma-slices" along the Z-axes. In Fig. 5 one centimetre thick plasma-slices of three electron populations (intermediate, warm, hot) are shown. These populations are the most interested in the point of view of ions. Z=11-12 cm means the middle plane of the plasma chamber; here the plasmas consist of 6 identical clouds in the 6 magnet gaps. The Z=8-9 and 14-15 cm positions are at the two ends of the RZ. The transformation of the 6-pole structure gradually changes into triangles toward both directions. The differences between the 3 populations at the same axial position are also well visible. Note the different intensity scale for each sub-pictures (and for Fig. 6 and 7, later on). In the most right column the superposition of all the plasma slices are shown. The warm electrons sub-picture is very much similar to those X-ray plasma photos. Figure 6 shows the projection of the cold, intermediate, warm and hot electrons from side directions.

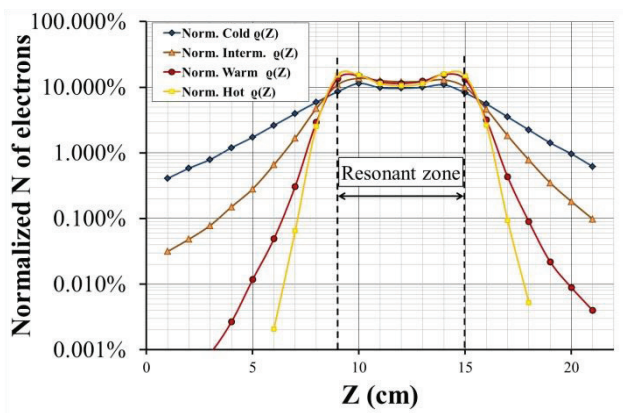

Figure 4: Normalized electron density distributions along the plasma chamber axes (z-axes).

Copyright © 2012 CC-BY-3.0 and by the respective authors

ISBN 978-3-95450-123-6

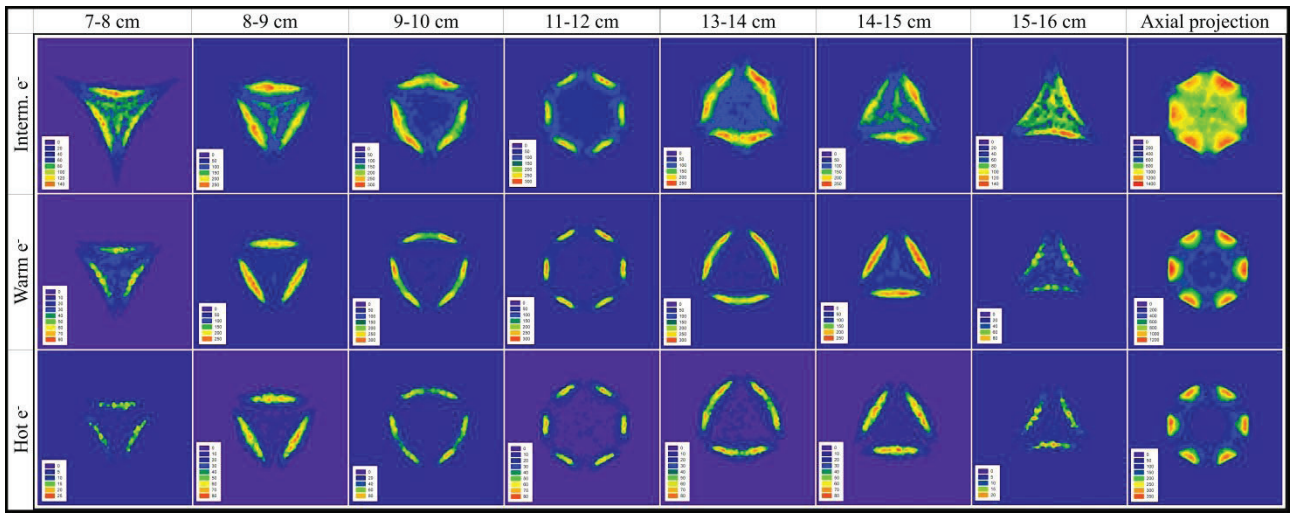

Figure 5: Plasma slices formed by electrons with different energy. In the right column: the superposition of all electrons from axial view.

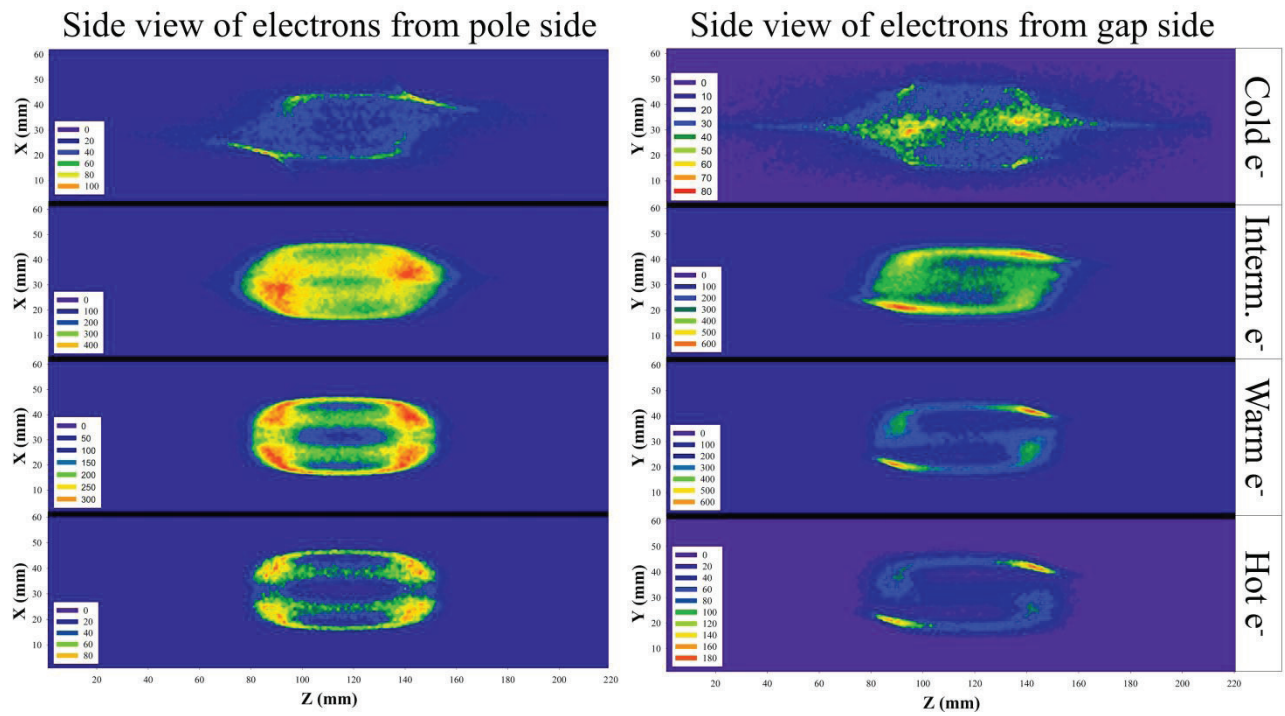

Figure 6: Side view projections of the cold, intermediate, warm and hot electron parts of the plasma from pole (left) and gap (right) direction.

In Fig. 7 the spatial distribution of the 3-10 KeV warm electrons are drawn in the extraction "third" of the plasma chamber (z-positions: 13-21 cm). Assuming that extraction of ions mainly takes place from these regions this double filtering may serve as starting data for extraction simulation codes (see e.g. [8]). In these extraction codes individual ions can be started from the appropriate x-y-z coordinates where the ion density (i.e. warm electron density) is the highest. Another way might be to construct a 3D density matrix by the TrapCAD output files (number of electrons in each cubic mm) and to use these position-dependent density values for the ions extraction simulations.

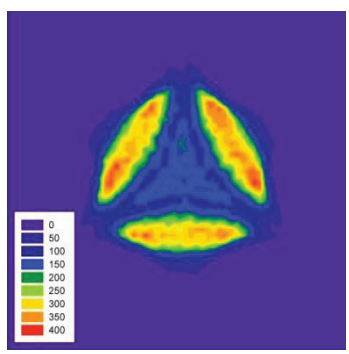

Figure 7: Axial projection of the warm electrons in the extraction side of the plasma chamber.

Copyright © 2012 CC-BY-3.0 and by the respective authors

ISBN 978-3-95450-123-6

ACKNOWLEDGEMENTS

The research leading to these results has received funding from the European Union Seventh Framework Program FP7/2007-2013 under Grant Agreement n° 262010 - ENSAR. The EC is not liable for any use that can be made on the information contained herein. This work was also partly supported by the Hungarian TAMOP 4.2.1./B-09/1/KONV-2010-0007 project which is co-financed by the European Union and European Social Fund.

REFERENCES

[1] http://www.atomki.hu/ECR
[2] S. Biri, R. Rácz and J. Pálinkás, Review of Scientific Instruments 83 (2012) 02A341
[3] S. Biri, A. Derzsi, É. Fekete and I. Iván, High Energy Physics and Nuclear Physics - Chinese Edition Supplement 31 (2007) 165-169
[4] S. Biri, R. Rácz, J. Imrek, A. Derzsi and Zs. Lécz, IEEE Transactions on Plasma Science 39 (2011) 11:2474-2475
[5] R. Rácz, S. Biri and J. Pálinkás, Plasma Sources Sci. and Tech. 20 (2011) 025002(7)
[6] J. B. M. Beijers and V. Mironov, Review of Scientific Instruments 83 (2012) 02A307
[7] D. Mascali, S. Gammino, L. Celona, G. Ciavola, Review of Scientific Instruments 83 (2012) 02A336
[8] P. Spädtke, R. Lang, J. Mäder, F. Maimone, J. Roßbach and K. Tinschert, Rev. Sci. Instrum. 83, (2012) 02B720

Copyright © 2012 CC-BY-3.0 and by the respective authors

ISBN 978-3-95450-123-6

NUMERICAL MODELING OF ION PRODUCTION IN ECRIS BY USING THE PARTICLE-IN-CELL METHOD

V. Mironov, J.P.M. Beijers
Kernfysisch Versneller Instituut, University of Groningen, The Netherlands

Abstract

To better understand the physical processes in ECRIS plasmas, we developed a Particle-in-Cell Monte-Carlo Collisions code that simulates the ionization and diffusion dynamics. The ion production is modelled assuming that the ions are confined by a ponderomotive barrier formed at the boundary of the ECR zone. The main features of ECRIS performance are reproduced, such as the saturation and decrease of highest charge state currents with increasing gas pressure, as well as response to an increase of injected RF power.

INTRODUCTION

The ponderomotive force plays an important role in the ECRIS plasmas [1]. Electrons are partially expelled by a gradient of the microwave electric field from a thin layer around the ECR zone, giving rise to a positive potential that confines the ions. The height of this ponderomotive barrier (PB) is difficult to estimate: it depends on the power density of the microwave radiation, on the gradient of the magnetic field at the resonance, on the plasma density and other factors. Taking the PB height as a free parameter in our calculations, we suppose that it goes to zero when the plasma density approaches the cut-off value because of reflections of the microwaves from the ECR zone boundary and absorption in the plasma.

The ECRIS plasma potential is experimentally known to be positive and around 20-50 V. Roughly half of the potential drop from the plasma to the walls occurs in a thin sheath area (extending a few Debye lengths from the walls), the remaining drop is in a pre-sheath further inside the plasma. The extension of the pre-sheath is unknown, but we here assume that it is located between the ECR zone and the wall sheath. Then, neglecting the PB width, the PB mimics the potential dip, often assumed to be a reason for ion confinement in ECRIS.

The PB confinement of the plasma is accompanied with the gas-dynamics confinement, where the ion pressure gradients govern the rate of ion diffusion to the walls and to the extraction area [2]. The length of the ion production volume defines the ion confinement times, which were found to be linear proportional to the ion charge state [2]. Here we present numerical simulations of the ECRIS plasma combining both confinement models.

CODE DESCRIPTION

The main features of our PIC-MCC code have been described elsewhere [2]. The calculations were done for neon as a feeding gas; the magnetic field and geometry of the source are those of the KVI-AECRIS [3]. The magnetic fields were calculated with POISSON-SUPERFISH, the hexapole component was calculated analytically, neglecting edge effects.

The elastic ion-ion collisions are modelled using the energy-and-momentum conserving Takizuka-Abe scheme [4], the rates of charge-transfer collisions and elastic collisions between ions and neon atoms are adopted from [5] with linear scaling of the rates as a function of the ion charge state (Z). The charge-transfer reactions for the multiply charged ions result in Coulomb repulsion of the colliding particles and we estimate the Q-value of these reactions to be 10 eV independent of the charge state. Then, even if the rates are relatively small ($\sim 3\times10^{-10}\times Z$ cm^3/sec) compared to the ionization and ion loss rates, and the neutral density in the chamber is much smaller than the plasma density, the influence of these collisions on the plasma behaviour is not negligible.

Heating due to electron-ion collisions is modeled by kicking the ions at each computational step in a random direction with the velocity diffusion coefficient corresponding to an electron temperature T_e of 1 keV. The ionization rates are calculated according to [6]. The recombination processes can be neglected in our conditions because of their low rates for this T_e.

The static electric field inside the ECR zone is set to zero, and arbitrary set to 1 V/cm along the magnetic field lines outside the zone. The pre-sheath electric field can be varied in a wide range without changing the computational results, as long as there is no backward influence of the pre-sheath area on the main production volume, but the ions are just moving toward the chamber walls and into the extraction aperture.

When hitting the walls, the ions are neutralized and scattered back with an angular distribution according to the cosine-law and with a Gaussian distribution of energies (FWHM=10 eV, peak energy of 10×Z eV [7]). In collisions with the walls, the neutralized particles loose their energy with a thermal accommodation coefficient taken from [8] for Ne on an Al surface. For initial energies above a few eV, this coefficient is relatively high (~0.5) while it goes to almost zero for energies in the meV range. The result is that the kinetic energies of the neutral atoms inside the source chamber are quite high (~0.25 eV) and are in the same range as the ion temperatures in the plasma.

When a computational macro-particle hits the extraction aperture (of 0.8 cm diameter), it is injected back into the volume from the injection side with an energy taken from a Maxwell-Boltzmann distribution at room temperature. The total number of computational macro-particles is conserved. Calculations are done until a steady state is reached. Transient processes are not properly calculated in such a scheme. In equilibrium, the

Copyright © 2012 CC-BY-3.0 and by the respective authors

ISBN 978-3-95450-123-6

ion flux that goes to the extraction is nearly equal to the gas flow into the chamber, because the ion flux is much higher than the neutral losses to extraction in most cases (ion-pumping effect).

When an ion crosses the ECR resonance surface, its velocity along the magnetic field line is calculated. If the velocity is smaller than a certain value (scaled as $\sqrt{Z}$), the ion is reflected back to the ECR zone, if not, it is accelerated by the pre-sheath electric field and goes to the walls/extraction. In our model, there are no spatial variations of the height of the PB, and the PB dependence on the plasma density is a step-like function. When the maximal electron density exceeds the limit of 2.5×10^{12} cm^{-3} (cut-off plasma density for 14 GHz microwaves), the PB value is set to zero, and otherwise it is an input parameter that is varied from 0 to 1 V in our calculations. If the PB value is set to zero, plasma decays and the plasma density falls below the cut-off; after that, ion accumulation begins again. Another way to ensure the saturation of plasma density is an introduction of anomalous ion heating above the cut-off, and it was shown in our calculations that the outputs of both approaches are basically the same.

RESULTS

The positions where the ions hit the extraction/injection plates of the source form the characteristic three-arm stars. The localization of HCI on axis is observed as a result of the ion-ion collisions and the radial gradients of ion densities – the well known effect of the inward transport of the highest charge states. The higher the neutral/ion temperatures, the more pronounced this localization is. The hollow profiles of the ion beams at the extraction were observed when setting the thermal accommodation coefficient to a high value with relatively small ponderomotive barriers.

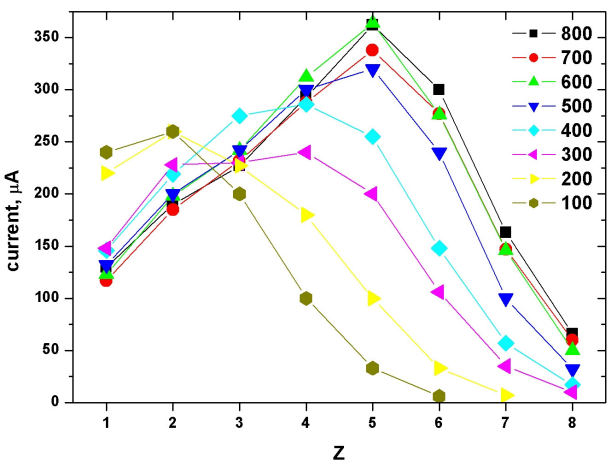

Figure 1: Experimentally observed spectra of extracted neon ions for different RF powers.

The experimental spectra of neon ions extracted from KVI-AECRIS are shown in Fig. 1 as a function of the injected RF power for comparison with simulation results.

The gas flow into the source was fixed at the optimal level for Ne^{6+} production. The total ion flux into the extraction zone is nearly constant (~500 pμA) for all spectra. Saturation of the source output is observed at RF powers above 800 W.

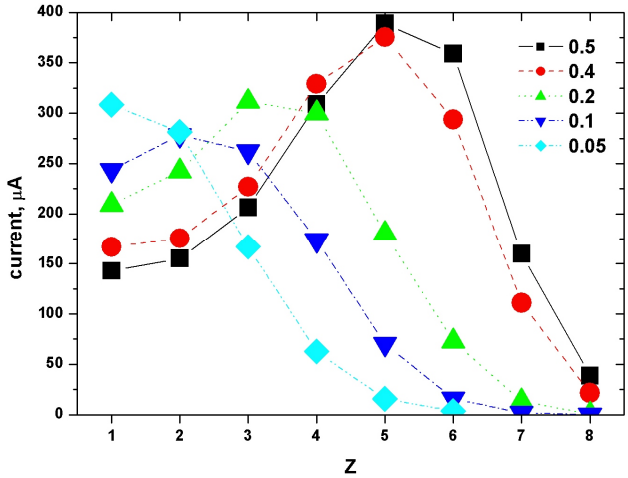

Figure 2: Simulated spectra of extracted neon ions for different ponderomotive barrier values.

The simulated spectra of extracted currents are shown in Fig. 2 for different values of the ponderomotive barrier indicated in the graph. The gas pressure in the chamber was varied for each PB by changing the statistical weight of the computational particles to keep the total flux of ions to the extraction aperture close to 500 pμA. The general experimentally observed features are well reproduced and we observe a linear correspondence between injected RF power and the PB height.

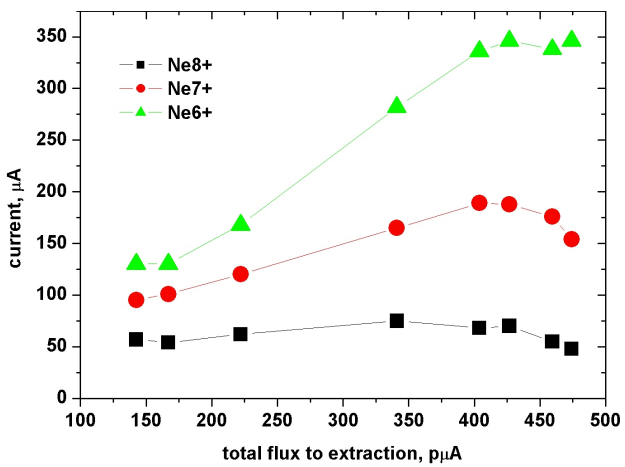

Figure 3: Experimental dependence of the extracted neon currents on the total flux of ions into the extraction (gas flow into the chamber).

In Fig. 3, the measured extracted ion currents of Ne^{6+-8+} are shown as a function of the total extracted ion current. The spectra were measured for an injected RF power of 800 W. The typical saturation of the currents of highly charged ions with increasing total flux is visible, followed

ISBN 978-3-95450-123-6

Copyright © 2012 CC-BY-3.0 and by the respective authors

by a drop at still higher total output. Also, the lower the lower the total extracted ion flux, the higher is the mean charge state. For gas flows above the value that corresponds to 500 pμA total output current, mode jumps in the source performance were observed that make it difficult to compare the extracted currents with the spectra at the lower pressures.

The simulated dependencies are shown in Fig. 4. The PB height was set at 0.5 V, and the gas pressure was varied by changing the statistical weight of the computational particles.

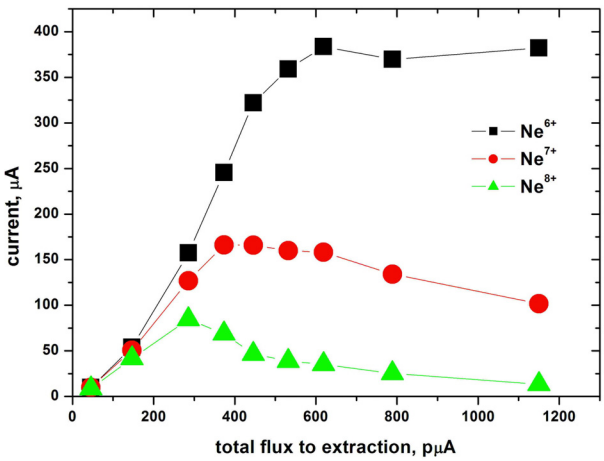

Figure 4: Simulated dependence of the extracted neon currents on the total flux of ions into the extraction (gas flow into the chamber).

It is seen that the currents of Ne^{6+-8+} ions saturate at gas flows that are close to the experimentally observed ones. Though some deviations are seen, the general behavior is well reproduced.

The gas mixing effect was modeled by running simulations with equal numbers of Ne and He macro-particles in the plasma chamber. The currents of neon ions were not observed to be substantially higher in a comparison with no gas-mixing. Ion current saturation and drop occurred at lower gas flows. When switching off Ne-He ion collisions, thus prohibiting thermalization between ions of different elements, the He^{2+} current almost doubled in agreement with the well-known performance degradation when heavier elements are present in the source volume.

Ion confinement times increase with increasing PB height and lower gas flows. The typical dependence of the confinement times as a function of the ion charge state is shown in Fig. 5 for PB=0.5 V and total ion fluxes as indicated in the graph. Ion confinement times are taken as the time difference between the moment of Ne^{1+} creation and the moment when the Ne^{Z+} ion is extracted [2].

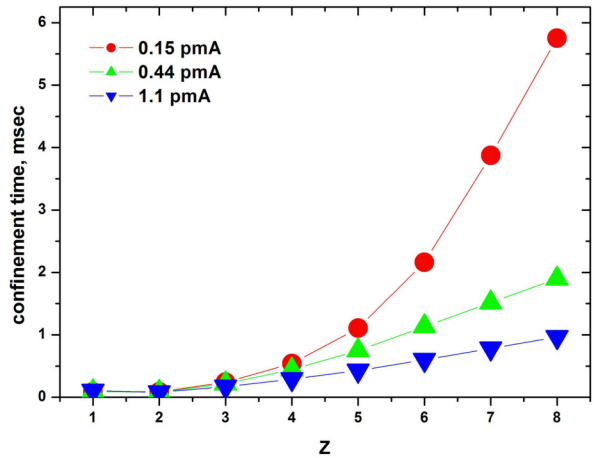

Figure 5: Simulated dependence of the ion confinement times on the ion charge state for different ion fluxes.

For the highest charge states, the dependencies are nearly linear in accordance with the measurements [9].

ACKNOWLEDGMENTS

This work is part of the research program of the "Stichting voor Fundamenteel Onderzoek der Materie" (FOM) with financial support from the "Nederlandse organisatie voor Wetenschappelijk Onderzoek" (NWO). It is supported by the University of Groningen and by the "Gesellschaft für Schwerionenforschung GmbH" (GSI), Darmstadt, Germany.

REFERENCES

[1] R. Geller, Electron Cyclotron Resonance Ion Sources and ECR Plasma (Bristol: Institute of Physics), 1996.
[2] V. Mironov and J. P. M. Beijers, Phys. Rev. ST Accel. Beams 12, 073501 (2009).).
[3] H.R. Kremers, J.P.M. Beijers, and S. Brandenburg, Rev.Sci.Instrum. 77, 03A311 (2006).
[4] T. Takizuka and H. Abe, J.Comp.Phys. 25, 205 (1977).
[5] D. Piscitelli, A.V. Phelps, J. de Urquijo, E. Basurto, and L.C. Pitchford, Phys.Rev.E 68, 046408 (2003).
[6] P. Mazzotta, G. Mazzitelli, S. Colfrancesco, N. Vittorio, Astron. Astrophys., Suppl. Ser., 133, 403 (1998).
[7] J.W. Cuthbertson, W.D. Langer and R.W. Motley, J.Nucl.Mater. 196-198, 113 (1992).
[8] F.O. Goodman and H.Y. Wachman, J.Chem.Phys. 46, 2376 (1967).
[9] G. Douysset, H. Khodja, A. Girard and J.P. Briand, Phys.Rev.E 61, 3015 (2000).

Copyright © 2012 CC-BY-3.0 and by the respective authors

ISBN 978-3-95450-123-6

PROTON BEAMS FORMATION FROM DENSE PLASMA OF ECR DISCHARGE SUSTAINED BY 37.5 GHZ GYROTRON RADIATION

V.Skalyga[1,2], I. Izotov[1], S. Razin[1], A. Sidorov[1,2], V. Zorin[1,2]
[1]Institute of Applied Physics, RAS, 46 Ul`yanova st., 603950 Nizhny Novgorod, Russia,
[2]Lobachevsky State University of Nizhni Novgorod (UNN), 23 Gagarina st., 603950, Nizhny Novgorod, Russia
T. Kalvas[3], H. Koivisto[3], O. Tarvainen[3]
[3]Department of Physics, P.O. Box 35 (YFL), 40500 Jyväskylä, Finland

Abstract

Formation of hydrogen ion beams with high intensity and low transverse emittance is one of challenging tasks determining success in the field of accelerator research for last tens of years. Now there are a few modern projects like ESS and IFMIF whose requirements for the ion beam could not be fulfilled with the most advanced proton (or deuteron) sources.

Present work is devoted to experimental investigation of proton beams production from dense plasma (Ne>1013 cm-3) of ECR discharge sustained by 37.5 GHz, 100 kW gyrotron radiation at SMIS 37 facility at IAP RAS. Extraction systems with different configuration were used. It was demonstrated that ultra bright proton beam with 4,5 mA current and 0.1 π·mm·mrad normalized emittance (corresponding brightness is 45 A/(π·mm·mrad)2) can be formed with single-aperture (1 mm in diameter) extraction.

For production of high current beams a 13-hole extractor was used. 200 mA and 1.1 π·mm·mrad normalized emittance proton beam was obtained. A possibility of further beam parameters enhancement by developing of extraction system and its power supply is discussed.

INTRODUCTION

Operation of modern high power accelerators often requires production of intense beams of hydrogen ions. H+ (proton) beams are utilized or envisioned for use in linear accelerators e.g. the future European Spallation Source under design [1], H- ions are favored in applications based on charge exchange injection into storage rings or circular accelerators, e.g. the US Spallation Neutron Source [2] and some special applications such as the IFMIF project [3], require D+ (deuteron) ion beams. Requirements for the brightness of such beams grow together with the demand of accelerator development and arising experimental needs. New facilities aiming at outperforming the previous generation accelerators are usually designed for higher beam currents. Enhancing the hydrogen beam intensity and maintaining low transverse emittance at the same time is, however, becoming increasingly difficult. The most modern accelerators require hydrogen ion beams with currents up to hundreds of mA (pulsed or CW), and normalized emittance less than 0.2-0-3 π·mm·mrad [1, 3] to keep the beam losses at high energy sections of the linac below commonly imposed 1 W/m limit.

This paper is devoted to investigating the generation of high current proton beams at SMIS 37 facility [4] at the Institute of Applied Physics (IAP RAS). SMIS 37 has been constructed for production of high current beams of multicharged ions. However, due to the substantial potential exhibited by the setup, we found it reasonable to test its capabilities for proton beam production.

SMIS 37 EXPERIMENTAL FACILITY

The experimental research presented in this work was carried out on the SMIS 37 shown schematically in Fig. 1. A gyrotron generating a Gaussian beam of linearly polarized radiation at the frequency of 37.5 GHz, with the power up to 100 kW, and pulse duration up to 1.5 ms was used as a source of pulsed microwave radiation. The microwave radiation is launched into the plasma chamber through a quasi-optical system consisting of 2 mirrors, quartz (vacuum) window and a special μW-plasma coupling system shown on the left in Fig. 1. The setup has been designed for efficient transport of the radiation avoiding parasitic resonances and plasma flux impinging the quartz window. A simple mirror trap was used for plasma confinement. The magnetic field in the trap was produced by means of pulsed solenoids, spaced 15 cm apart. The current pulse with the shape close to half period of a sinusoid had the duration of 11 ms with the magnetic field variation during the microwave pulse being less than 3%. Magnetic field in the mirror was varied from 1.4 to 4 T (ECR for 37.5 GHz is 1.34 T). Ratio of the maximum and minimum magnetic fields of the trap was equal to 5 (i.e. Bmax/Bmin). The hydrogen inlet into the source was realized through an opening incorporated with the microwave coupling system.

ISBN 978-3-95450-123-6

Copyright © 2012 CC-BY-3.0 and by the respective authors

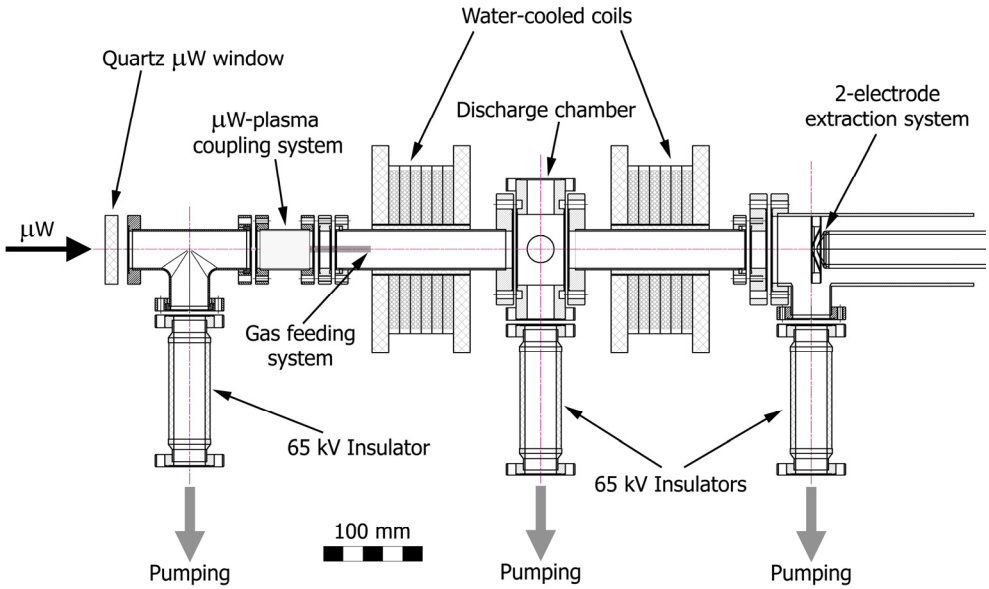

Figure 1: SMIS 37 experimental setup.

The delay between hydrogen injection and subsequent microwave pulse (300-3000 μs) as well as gas pulse duration (about 5 ms) were adjusted for each experimental condition in order to maximize the beam current and optimize the temporal shape of the extracted current pulse.

Ion extraction and beam formation were realized by two-electrode, i.e. single gap plasma electrode - puller electrode, system. In the experiments two different configurations were used: single-aperture system (see Fig.2-a) and 13-hole system (see Fig.2-b). Plasma electrode is 7 cm in diameter and puller diameter is 3 cm and length is 10 cm. The extraction was placed in the range of 10 to 15 cm downstream from the magnetic mirror to limit the extracted flux of ions as described in [5], which helps improving the beam transport through the puller. The density of outgoing plasma flux on the downstream side of the magnetic mirror decreases proportionally to magnetic field and therefore, the extracted current density can be tuned by moving the extraction system. Positioning the extraction at lower magnetic field helps to limit the emittance of the extracted beam, which theoretically depends almost linearly on the magnetic field at the extraction (assuming low ion temperature) [6, 7]. The position of the extraction can also help mitigating beam current fluctuations as shown in [8] where the oscillation of beam current was compensated by tuning the beam divergence angle.

The maximum available high voltage level, limited by the power supply or the voltage holding capability of the extraction during beam pulses, was 55 kV for single-aperture and 47.5 kV for multi-aperture system. A Faraday cup was placed just behind the end of puller electrode to measure the total beam current passing through the extractor. A traditional magnetostatic analyzer (bending magnet was placed in 1 m from extraction) and another Faraday cup located at the end of the beam line (1 m behind the magnet) were used for studying the species fraction of the extracted ion beam.

Emittance of the extracted beam (all species together) was measured with “pepper-pot” method [9], which has been successfully tested earlier at SMIS 37 [10]. “Pepper-pot” plate was placed 1 mm downstream from the puller with another 55 mm gap before a CsI scintillator for beam imaging.

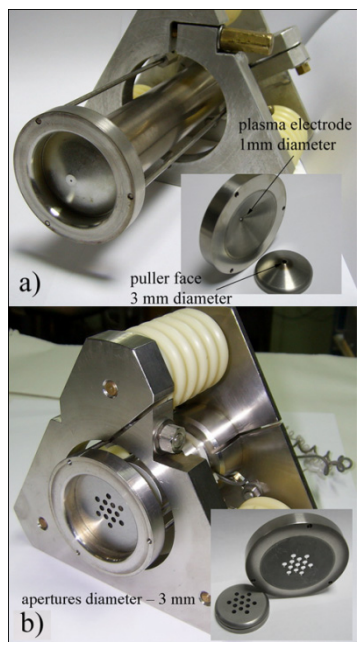

Figure 2: Extraction systems: (a) single-aperture extraction, (b) multi-aperture extraction with13 holes. The plasma and puller electrodes are shown separately on the lower right corner.

Copyright © 2012 CC-BY-3.0 and by the respective authors

ISBN 978-3-95450-123-6

RESULTS

Single-Aperture Extraction System

During the experiments the configuration, i.e. distance between electrodes, and positioning of the extraction system was optimized to achieve maximum beam current. In the case of single-aperture extraction the optimal distance of the puller, measured from the magnetic mirror of the trap, was 80 mm and distance between electrodes 5 mm, respectively. An example of typical beam current oscillogram is shown in Fig. 3. It takes about 200 µs to reach the saturation level of the beam current, which is quite typical for pulsed proton/deuteron sources [11, 12] operating with 2.45 GHz microwaves. The dependence between the Faraday cup current and extraction voltage is plotted in Fig. 3. The maximum achieved current was 4.5 mA at 50 kV source potential, which corresponds to current density of 570 mA/cm2 transported through the extraction. According to our knowledge the result obtained with SMIS 37 is a record for ECR ion sources. It is evident from Fig. 4 that the beam current is not limited by the plasma density but, instead, the extraction voltage. The amplitude of the beam current fluctuation after reaching the saturation is approximately 10-15 %. For comparison it is noted that the amplitude of beam current oscillation is typically 5 - 20 % for minimum-B ECR ion sources operated in CW mode [13].

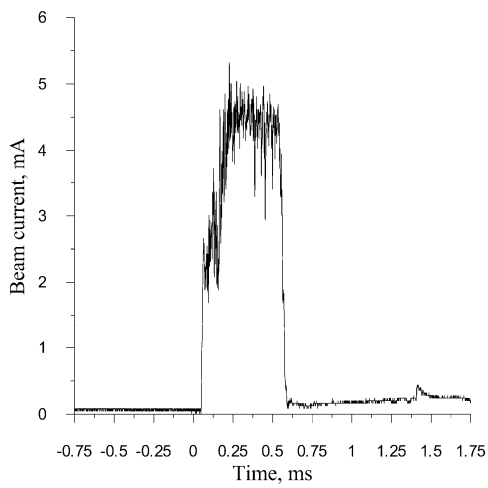

Figure 3: Typical oscillogram of hydrogen beam current obtained with the single-aperture extraction.

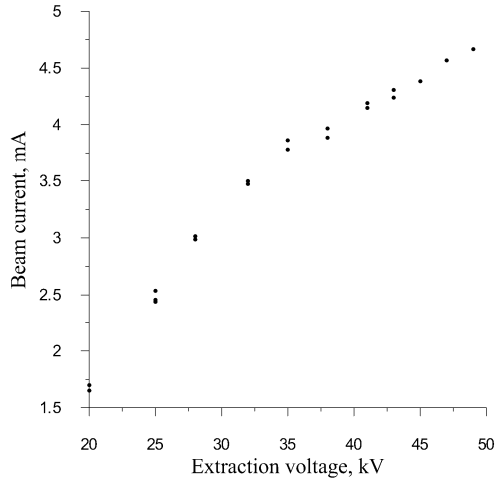

Figure 4: Beam current dependence on the extraction voltage for the single-aperture extraction.

The value of the hydrogen beam emittance was estimated by using "pepper-pot" method [9]. The normalized emittance of the beam is 0.03 π mm mrad and the brightness 5 A/(π·mm·mrad)^2.

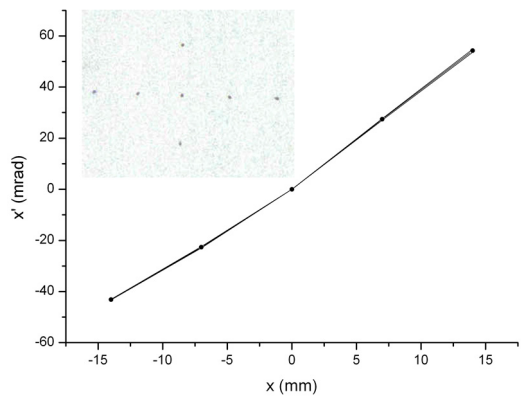

Figure 5: An example of the phase space distribution of the beam for single-aperture extraction. The corresponding scintillator luminescence image is shown on the upper left corner.

Multi-Aperture Extraction System

In the case of multi-aperture extraction system the optimal distances from the magnetic mirror and electrode spacings were 160 mm and11 mm respectively. The maximum Faraday cup current achieved was 200 mA at 46 kV, corresponding to 220 mA/cm2 current densities transported through the extraction. The dependence of the Faraday cup current on the source potential for the 13-hole extraction system is presented in Fig. 6. Again, the beam current is not limited by the plasma density but the extraction voltage. A representative oscillogram of the current pulse is shown in Fig. 7 for the 13-hole extraction system. The given example featuring saturation current of about 200 mA was measured with 46 kV extraction voltage. Reaching this current level takes about 150 µs, the amplitude of current fluctuation being 10-25 % after the fact.

ISBN 978-3-95450-123-6

Copyright © 2012 CC-BY-3.0 and by the respective authors

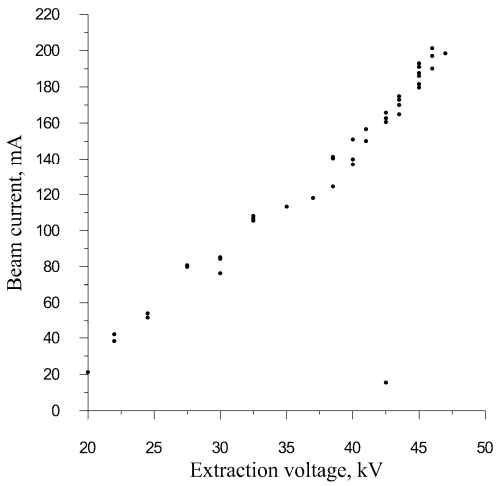

Figure 6: Dependence of the Faraday cup current on the source potential for the 13-hole extraction system

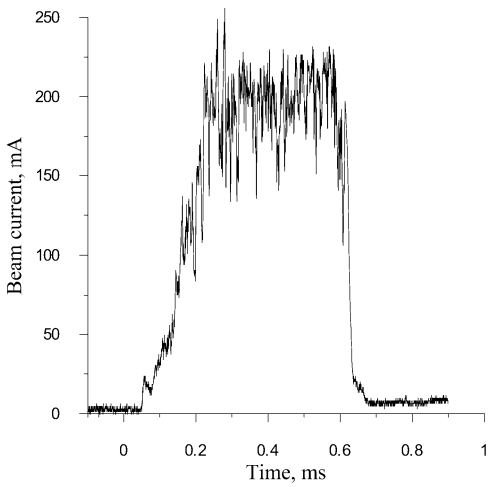

Figure 7: Oscillogram of the current pulse for the 13-hole extraction system.

The emittance of the beam produced by the multi-aperture extraction was also estimated using the "pepper-pot" method. A picture of the scintillator luminescence screen obtained with 45 keV, 200 mA beam is shown in the upper left corner of Fig 8. Nine sets of beamlets each consisting of 13 spots are clearly visible. The sets correspond to the holes in the pepper-pot and the spots correspond to the plasma electrode apertures. The reconstructed x-x' phase space for all 13 holes is shown in Fig. 8. The normalized emittance corresponding to 200 mA beam is 1.1 π·mm·mrad.

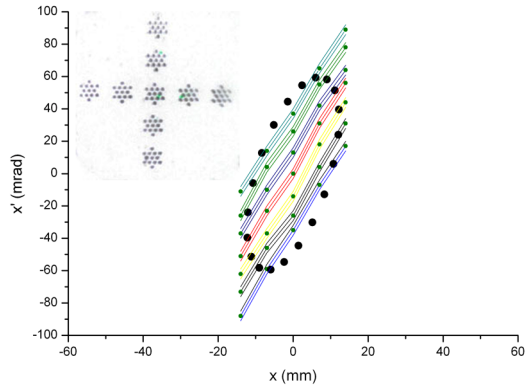

Figure 8: Phase space presentation and emittance diagram of the beam in the case of 13-aperture extraction. Corresponding scintillator luminescence image is shown in the upper left corner.

Ion Beam Spectrum

The fraction of atomic to molecular hydrogen (H^+/H_2^+) in the extracted beam was studied with all afore-mentioned extraction systems by measuring the ion beam spectrum with the bending magnet. No significant differences were found between the extraction systems. A typical spectrum is presented in Fig. 11. The data is normalized with respect to the total hydrogen beam current measured with the Faraday cup downstream from the bending magnet. In this case H_2^+-current is less than 6 % of the total hydrogen current. Only trace amounts of H_3^+ were observed. The proton fraction of about 94 % is slightly better than typically achieved with 2.45 GHz microwave ion sources [14, 11] being the state-of-the art proton sources for various applications.

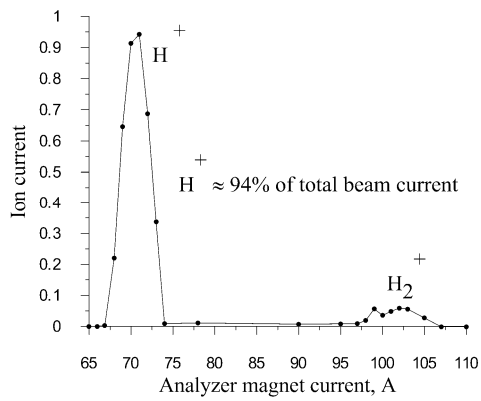

Figure 11: Mass-analyzed ion beam spectrum normalized to the total hydrogen beam current.

CONCLUSION

The experimental results described in the present paper demonstrate the feasibility of high power millimeter wave quasi-gasdynamic ECR ion sources for the production of high brightness proton beams with favorable species fraction. With all extraction geometries the maximum

Copyright © 2012 CC-BY-3.0 and by the respective authors

ISBN 978-3-95450-123-6

beam current was limited by the extraction voltage. The extracted beam current could be improved further by moving the plasma electrode inwards closer to the magnetic mirror and scaling the extraction voltage and geometry appropriately. This is because the plasma density on the downstream side of the mirror scales with the magnetic field [5]. It is also shown in the table that the current measured from the puller electrode is rather high i.e. a significant portion of the beam intercepts with the puller (up to 35 % of the puller current is estimated to be due to secondary electrons [15]). This demonstrates that improving the extraction geometry and its voltage holding capabilities could help improving the proton current density transported through the extraction by several tens or percent. The possibility of increasing the beam current of SMIS 37 by using a 3-electrode extractor has been demonstrated in [5] for multicharged nitrogen ion beams. Optimizing the extraction system for protons, i.e. maximizing current and minimizing emittance growth, requires dedicated simulation effort, which is out of the scope of this feasibility study.

A possible future step of this investigation is construction of a CW gasdynamic proton source based on 24 GHz, 10-15 kW gyrotron. It is expected that with an optimized extraction geometry such a source would match or even exceed the performance of the current SMIS 37 setup in terms of proton beam production. Obviously the maximum value of plasma density in this case would be lower in comparison to 37.5 GHz source but it is plausible to claim that it would still be able to produce plasma flux densities up to 1 A/cm^2. Such a versatile high brightness proton source would be useful as an injector for accelerators as well as for specific applications.

ACKNOWLEDGMENTS

Work was supported by RFBR grant # 11-02-97056. Work was performed in frame of realization of federal targeted program “Scientific and pedagogical labor force for an innovative Russia” for 2009 – 2013 yy.

Work was supported by the Academy of Finland under the Finnish Centre of Excellence Programme 2012-2017 (Nuclear and Accelerator Based Physics Research at JYFL) and researcher mobility grants 253482 and 253173.

REFERENCES

[1] S. Gammino, L. Celona, R. Miracoli, D. Mascali, G. Castro, G. Ciavola, F. Maimone, R. Gobin, O. Delferrière, G. Adroit, F. Senée, Proc. Linear Accelerator Conference LINAC2010, Tsukuba, Japan, THP116, available online at jacow.org.

[2] M.P. Stockli, B.X. Han, T.W. Hardek, Y.W. Kang, S.N. Murray, T.R. Pennisi, C. Piller, M. Santana, and R. Welton, Rev. Sci. Instrum., 83, 02A732 (2012).

[3] R. Gobin, G. Adroit, D. Bogard, G. Bourdelle, N. Chauvin, O. Delferrière, Y. Gauthier, P. Girardot, P. Guiho, F. Harrault, J. L. Jannin, D. Loiseau, P. Mattei, A. Roger, Y. Sauce, F. Senée, and T. Vacher, Rev. Sci. Instrum., 83, 02A345 (2012).

[4] S. Golubev, D. Mansfeld, S.V. Razin, V. Skalyga, A. Vodopyanov, V. Zorin, R. Geller, T. Lamy, P. Sortais, T. Thuillier, V. Murugov, A. Senik, A. Kravchenko, D. Litvin, V.Misko, S. Petrov. Progress Report of Investigations on Gyrotron ECR Ion Source SMIS 37. Proc. of the 15th International Workshop on ECR Ion Sources (ECRIS’02). Jyväskylä , Finland, June 12 – 14, 2002, p. 21-24.

[5] A. Sidorov, I. Izotov, S. Razin, V.Skalyga, V. Zorin, A. Balabaev, S. Kondrashev, A Bokhanov. Beam Formation from Dense Plasma of ECR Discharge. Review of Scientific Instruments. v.77, n3, p. 03A341-1 – 03A341-4 (2006).

[6] Z.Q. Xie, Thesis, Michigan State University, MSU CP-60, p. 58 (1989).

[7] M.A. Leitner, D.C. Wutte, C.M. Lyneis, Proc. 2001 Particle Accelerator Conference (PAC’01), Chicago, IL, USA, MOPB004, IEEE 0-7803-7191-7/01, available online at jacow.org

[8] A. Sidorov, M. Dorf, V. Zorin, A. Bokhanov, I. Izotov, V. Skalyga, A.Vodopyanov, Noise Suppression And Stabilization Of An Ion Beam Extracted From Dense Plasma, Journal of Applied Physics, Vol.102, No.5, p. 054504 (2007).

[9] Applied Charge Particle Optics.// Edited by A. Septier. New York: Academic Press, p. 214 (1980).

[10] A. Sidorov, M. Dorf, A. Bokhanov, I. Izotov, S. Razin, V. Skalyga, V. Zorin, A. Balabaev, P Spädtke, J. Roßbach. Multi-aperture ion beam extraction from gas-dynamic electron cyclotron resonance source of multicharged ions. Review of Scientific Instruments, 79, 02A317 (2008).

[11] R. Xu, J. Zhao, S.X. Peng, Z.X. Yuan, Z.Z. Song, J.X. Yu, and Z.Y. Guo, Rev. Sci. Instrum., 79, 02B713 (2008).

[12] R. Gobin, P.-Y. Beauvais, D. Bogard, G. Charruau, O. Delferrière, D. De Menezes, A. France, R. Ferdinand, Y. Gauthier, F. Harrault, J.-L. Jannin, J.-M. Lagniel, P.-A. Leroy, P. Mattèi, J. Sherman, A. Sinanna, P. Ausset, S. Bousson, and B. Pottin, Rev. Sci. Instrum., 73, 2, p. 922 (2002).

[13] Geller R. Electron cyclotron resonance ion sources and ECR plasmas. // Institute of Physics. Bristol (1996).

[14] J.D. Sherman, T.L. Figueroa, L.D. Hansborough, D.M. Kerstiens, J.D. Schneider, H.V. Smith, Jr., M.W. Stettler, R.R. Stevens, Jr., M.E. Thuot, D.S. Warren, T.J. Zaugg, A.A. Arvin, A.S. Bolt and J.E. Boers, Rev. Sci. Instrum., 73, 2, p. 917 (2002).

[15] L.N. Large and W.S. Whitlock, Proc. Phys. Soc., Vol. 79, p. 148 (1962).

ISBN 978-3-95450-123-6

Copyright © 2012 CC-BY-3.0 and by the respective authors

EFFECT OF SOURCE TUNING PARAMETERS ON THE PLASMA POTENTIAL OF HEAVY IONS AND ITS INFLUENCE ON THE LONGITUDINAL OPTICS OF THE HIGH CURRENT INJECTOR

G.Rodrigues*, P.S.Lakshmy, Y.Mathur, ,A.Mandal,D.Kanjilal, A.Roy,
Inter University Accelerator Centre, Aruna Asaf Ali Marg, New Delhi, India
R.Baskaran, Indira Gandhi Centre for Atomic Research, Kalpakkam, Tamilnadu, India

Abstract

Plasma potentials for various heavy ions have been measured using the retarding field technique in the 18 GHz High Temperature Superconducting ECR ion source, PKDELIS [1]. The influence of various source parameters viz., RF power, gas pressure, magnetic field, negative DC bias and gas mixing on the plasma potential is studied. It is observed that the plasma potentials are decreasing for increasing charge states and a mass effect is clearly observed for the ions with similar operating gas pressures. In the case of gas mixing, it is observed that the plasma potential minimises at an optimum value of the gas pressure of the mixing gas and the mean charge state maximises at this value. The energy spread arising from the plasma potential influences the longitudinal optics of the High Current Injector in terms of increased phase spread which deteriorates the transmission through the RFQ. Details of the measurements carried out as a function of various source parameters and its impact on the longitudinal optics are presented.

INTRODUCTION

Plasma potentials are one of the important figures of merits of an ion source and depicts the degree of stability of a plasma. The ion source stability is one of the main criteria for application in accelerators an ion implanters, besides other applications. In the context of electron cyclotron resonance ion sources, the improved stability results from a lower plasma potential and determines a good confinement of the plasma resulting in a higher mean charge state distribution [2]. On the other hand, if the plasma potential is high, sputtering to the wall is highly probable that results in an unstable plasma. Therefore, the confinement properties of the plasma are worsened and the resulting charge state distribution is a lower mean charge state. The main goal is to tune the source such that that plasma potential is as low as possible, which manifests itself in a stable operation mode. Measurement of plasma potentials is therefore important to get an idea of the source operating conditions. This in turn can be used to infer another important figure of merit called the 'energy spread'. A quick online estimate would suffice to further improve the source tuning and especially for delivering beams to experiments which require good timing information. The importance of the plasma potential shows up in the estimation of the energy spread which is crucial for timing measurements in nuclear physics experiments and other experiments where the pulse width of the bunched beam is of extreme importance. At the Inter University Accelerator Centre, a High Current Injector (HCI) is being installed for delivering a wider mass range of ions with relatively higher beam intensities into the superconducting linear accelerator (SC-LINAC) than what is presently available from the Pelletron-SC-LINAC combination Fig. 1. Due to the wide available mass range, there is a wider charge state distribution and the energy spread of the ion beam will depend on the charge state being delivered. In our earlier experiments, the emittance of various ion beams from an ECR ion source were measured [3] to obtain inputs in the design of beam transport and to match the acceptances of the downstream radio frequency quadrupole (RFQ) and drift tube LINAC (DTL) accelerators of the high current injector being developed [4]. For subsequent acceleration through the RFQ and DTL, the dc beam from the ECR needs to be pulsed and the longitudinal emittance depends on the energy spread of the beam. Due to the pulsed nature of the beam, the timing resolution is very important for various experiments. Since a significant energy spread can influence the longitudinal optics, it was felt necessary to measure the plasma potentials for various ions and its dependence on source tuning parameters. O.Tarvainen et al.,[6] have measured plasma potentials using the retarding field technique and observed the plasma potentials to increase with RF power and gas pressure and the values changed when the negative DC bias was varied. They [7] also measured the effect of the gas mixing technique on the plasma potential, energy spread and emittance of the beam under various source conditions. They estimated that the energy spread due to the plasma potential can influence the emittance of the beam to several tens of percent in the bending plane of the dipole magnet. In Ref 8., they compared the measured values of the emittance and plasma potential using single frequency and double frequency heating modes. In this study we carried out a systematic measurement of the plasma potential and the worst possible energy spread to study the influence on the longitudinal optics. Various methods have been used in the literature to measure the plasma potential. We have used the retarding field method and the instrument used is similar to the one used by the Jyvaskyla group [6] and is described in detail in [12]. In

*gerosro@gmail.com

Copyright © 2012 CC-BY-3.0 and by the respective authors

ISBN 978-3-95450-123-6

our previous experiments, we have measured the effect of the negative bias voltage on the x-ray bremstraahlung and beam intensities of medium and highly charged ions of argon [5] keeping all other source parameters fixed. In this experiment, various source parameters like DC bias voltage, magnetic field, gas pressure, gas mixing [11] and rf power have been tuned to study the influence on the plasma potential. From the measurements, we have estimated the value of the energy spread for the heaviest ion and studied its influence on the longitudinal optics of the High Current Injector. A corresponding energy spread of 0.11 % from the ion source increases the phase spread at the entrance of the radio frequency quadrupole (RFQ) accelerator and thus limits the transmission efficiency through the RFQ to 84 %.

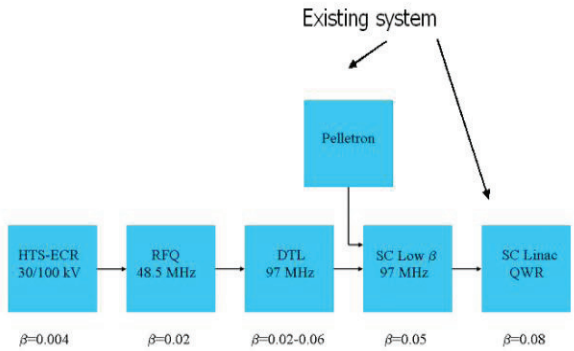

Figure 1: Schematic of the High Current Injector with respect to the existing Pelletron-SC LINAC accelerators.

EXPERIMENTAL METHOD

The compact instrument used for measuring the plasma potential was built in-house. The decelerating system geometry was optimised using TOSCA assuming the system was placed at the image plane of the bending magnet to further minimise the beam blow-up due to deceleration and to filter out unwanted beams. The model further showed that the beam had to enter parallel to the axis of the retarding system to obtain better energy resolution. Details of the system are further explained in [12]. The plasma potential measurement system was installed at the image position of the analysing magnet after the simulations confirmed the validity of the model. The error in the measurements was measured to be +/- 2 V and the repeatability in the measurements was found to be +/- 0.8 V. A typical retardation curve is shown in Fig. 2. The derivative of this current voltage distribution is shown in the inset graph depicting the energy spread information.

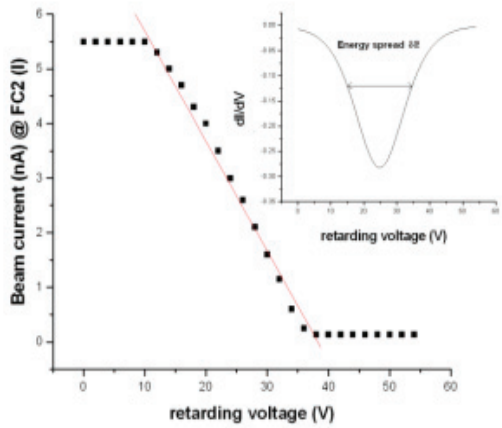

Figure 2: Typical retardation curve and it's derivative ; the inset graph shows the energy spread at FWHM.

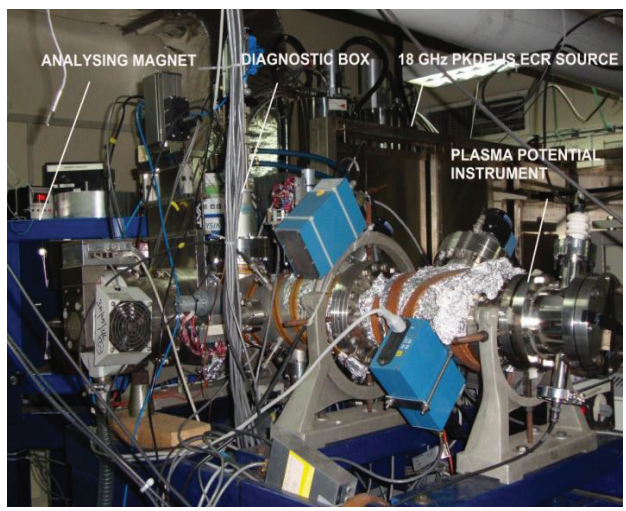

Figure 3: View of the 18 GHz HTS-ECRIS, PKDELIS and low energy beam transport.

EXPERIMENTAL RESULTS

The experimental set-up for measuring the plasma potential is shown in Fig. 3, where the decelerating system was installed at the image plane of the analysing magnet. The measurements have been carried out for oxygen, argon and xenon beams. The influence of the source parameters like rf power, DC bias voltage, magnetic field, gas pressure and gas mixing on the plasma potential has been measured. All the measurements have been recently reported in [12]. Few figures of the measurements will only be shown due to space constraints. In Fig. 4, the plasma potential is shown as a function of charge states of xenon, argon and oxygen, keeping the rf power (500 W), magnetic field (B_{min}/B_{ecr} =0.63) and gas pressure (4.9 x 10^{-6} mbar) fixed. In all the measurements, the dc bias was kept fixed at -100 V, except in the case of Xe where two values of the dc bias

ISBN 978-3-95450-123-6

Copyright © 2012 CC-BY-3.0 and by the respective authors

viz., -100 V and -500 V were used. A mass effect was clearly observed showing that the plasma potential is lower for the lighter mass ions under same source conditions. O.Tarvainen et al., also reported that the plasma which contain lighter mass ions have lower plasma potential [13]. It should be noted that in the present measurements, the plasma potential monotonically decreases with increase of charge states of argon in contrast to that obtained by Higashijima et al [14], where the potential was found to be constant above charge state 5+. A similar variation of the potential was also observed for other ions though it follows the general trend of increase of the plasma potentials for the lower charge states in comparison to higher charge states as observed by others [14,15]. In the case of Xe, application of a higher dc bias voltage of -500 V reduces the plasma potential further, as shown in Fig. 4. The higher dc bias reflects a large number of the electrons which otherwise would be lost, resulting in the decrease of the plasma potential [16]. The plasma potentials of $Xe^{17+,}$ Ar^{9+} and O^{6+} were measured as a function of B_{min}/B_{ecr} with RF power 500W, DC bias -100 V and fixed gas pressure. The plasma potential of $Xe^{17+,}$ Ar^{9+} and O^{6+} decreases with higher values of B_{min}/B_{ecr} up to ~ 0.63 to 0.65 while the normalised beam current is maximum for all three beams in the same range of B_{min}/B_{ecr} due to the increasing value of the electron temperature according to the calculations reported in [17]. Due to the lower gradient at the resonance zone, the electrons gain higher energies resulting in higher beam intensities. It should be noted that the plasma became unstable beyond the value of B_{min}/B_{ecr}=0.73. Our earlier measurements [5] also showed that at a similar field setting of B_{min}/B_{ecr}=0.65, the beam intensities of medium and highly charged ions of argon were maximized. The increase of plasma potential with increase in RF power is consistent with the calculations reported in Ref. 17. This is probably due to the increase of plasma density and density gradients with RF power which results in higher loss of electrons to the wall of the chamber. Therefore, a higher plasma potential is required to compensate the loss rates of electrons and ions [10]. The plasma potential of i) O^{6+} , ii) O^{6+} with gas mixing using He and iii)mean charge state variation of O_2 with gas mixing was measured. In the case of oxygen-helium mixing, the oxygen gas pressure was fixed at 3.5 x 10^{-6} mbar while helium was fed into the plasma. Similarly, the plasma potential of i) Ar^{9+} , ii) Ar^{9+} with gas mixing using O_2 and iii)mean charge state variation of Ar with gas mixing were also measured Fig. 5. In the case of gas mixing studies using the argon-oxygen combination, the argon gas pressure was fixed at 4 x 10^{-6} mbar while oxygen gas was fed into the plasma. The plasma potential increases with gas pressure for O^{6+} and Ar^{9+} due to the decrease in the electron temperature and ion confinement times [17]. The mean charge state variation (open symbols) is shown in Fig. 5 using gas mixing [11] where there is an optimum maximum value corresponding to lowest value (filled symbols) of the plasma potential. It means that the ion confinement time (τ_i) is longer corresponding to higher mean charge state <q> given by ~ $n_e \tau_i$, where <q> denotes the mean charge state and n_e is the electron density. If we compare our experimental result of the plasma potential variation with the mean charge state to the theoretical model developed by N.K.Bibinov et al., [18], and assume cold electron temperatures in the range of few tens of eV with the additional assumption of a Maxwellian electron distribution function (EDF), our experimental values of the plasma potential are of the same order of magnitude as per the calculated values given by the equation U_{pl} = (kTe/2e)(5.67- ln<q/M>) where U_{pl} is the plasma potential, k is the Boltzmann constant, Te is the cold electron temperature and <q> is the mean charge state. The plasma potential as a function of gas injection pressure for Xe^{17+} with and without gas mixing were measured, when the dc bias was kept at -500 V. In the case of gas mixing, the xenon gas pressure was fixed to 4 x 10^{-6} mbar while oxygen was added as a mixing gas. The normalized beam current maximises when the plasma potential attains a lower value. In Fig. 5, it is shown that the addition of a lighter mixing gas lowers the plasma potential and improves the beam intensities and the mean charge state of ions, which has also been observed by Higashijima et al [14] in the case of argon. In our earlier experiments, the emittance measurements using gas mixing [3] also shows that gas mixing reduces the beam emittance of the beam gas and increases the beam emittance of the mixing gas thus demonstrating the ion cooling mechanism [19]. Hence, the reduction of the plasma potential and the beam emittance due to gas mixing are signatures of the ion cooling mechanism.

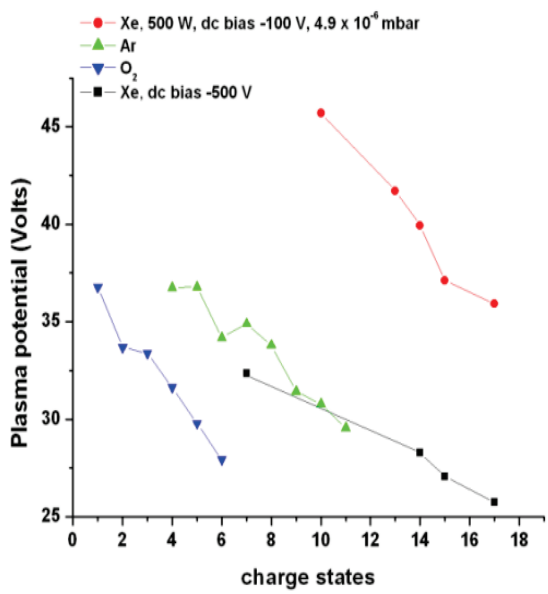

Figure 4:Plasma potentials for various charge states of xenon, argon and oxygen, keeping the rf power, gas pressure and magnetic field fixed.

Copyright © 2012 CC-BY-3.0 and by the respective authors

ISBN 978-3-95450-123-6

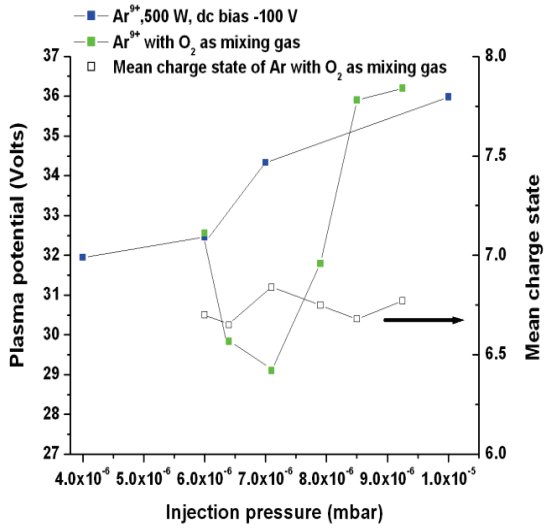

Figure 5: Plasma potentials of i) Ar^{9+}, ii) $Ar^{9+}$with gas mixing using O_2, and iii) variation of mean charge state of Ar with gas mixing using O_2.

LONGITUDINAL OPTICS OF THE HIGH CURRENT INJECTOR

The energy spread of ions coming from an ion source is an important parameter which can influence the bunched width of the beam since ions leaving the ion source with different energies will arrive at the target at different times thus decreasing the effectiveness of bunching. The maximum possible energy spread determined from the plasma potential in the ECR source will therefore have a corresponding influence on the longitudinal optics through the High Current Injector (HCI). The High Current Injector is designed for accelerating beams having A/q ~ 6 and to match to the velocity regime β ~ 0.08 in the main SC-linac. It mainly consists of the HTS-ECR source (PKDELIS), 48.5 MHz Radio Frequency Quadrupole (RFQ) and 97 MHz Drift Tube Linac (DTL) accelerators. In order to improve the longitudinal emittance of the RFQ, the adiabatic buncher is replaced with external discrete buncher. The transmsision of the RFQ is then equal to that of a conventional RFQ with adiabatic bunching, further reducing the length of the RFQ substantially. Due to this, stability requirement of the pre-injector voltage increases by an order of magnitude and therefore the rf defocussing in the buncher may be significant and use of grids may be necessary or a small beam size should be maintained in the buncher.The dc beam from the source will be accelerated to 8 keV/u using a 100 kV high voltage platform, bunched using a 12.125 MHz multi-harmonic buncher (MHB) before further acceleration by the RFQ to 180 keV/u and finally by the DTL to 1.8 MeV/u. The multi-harmonic buncher used for pre-bunching before the RFQ serves two purposes ; a) most of the DC beam from the source gets bunched close to the entrance of the RFQ to improve the capture efficiency, and b) the growth of the longitudinal emittance at the exit of the RFQ is minimised, following the proposal by J.Staples [20]. The beam having an energy of 1.8 MeV/u will be transported through the SC-LINAC for further acceleration to β ~ 0.08 In Fig.6, the FWHM of the energy spread at the exit of the ECR source is shown as a function of rf power, calculated from the derivatives of the current versus voltage distribution function of Xe^{17+}. Considering the worst possible case of the heaviest ions being accelerated through the High Current Injector ($^{238}U^{40+}$), an energyspread, ΔE, of 0.11 % would result in a corresponding phase spread, Δϕ, given by the equation $\Delta v/v = \Delta\phi\beta\lambda/\pi h L_{drift}$ at the entrance of the RFQ (where L_{drift}, distance of 4.0 m from the MHB, considering the length of the MHB and the harmonic number, h = 4) [20]. The model calculations by TRACK [21] using the value of energy spread from the ECR source showed that a significant phase spread Δϕ ~ +/- 22.5° arising from the energy spread, would need to be accomodated by the RFQ phase acceptance ellipse. The complete beam-line layout of the High Current Injector is shown in Fig. 7. In Fig.8, the longitudinal phase space plots at the entrance and exit of the RFQ are shown. The calculations show that the transmission through the RFQ is reduced by 16 % due to the energy spread in the beam. The deterioration in the energy spread after the RFQ is minimal and it is expected that the final injection into the main linac would not pose problems for phase matching through the next accelerating elements of the DTL. Since adjustment of the source parameters like gas pressure and rf power play a critical role in deciding the energy spread of the ion beams extracted, it would be necessary to optimise these parameters as determined from the present study for good transmission of the ion beams through the High Current Injector.

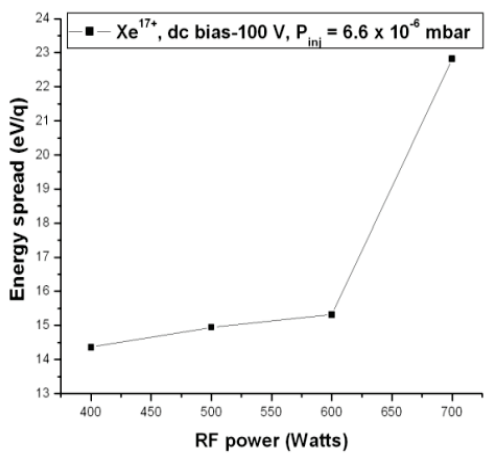

Figure 6: Energy spread at FWHM as function of rf power, calculated from the derivatives of the current versus voltage distribution function for Xe^{17}.

ISBN 978-3-95450-123-6

Copyright © 2012 CC-BY-3.0 and by the respective authors

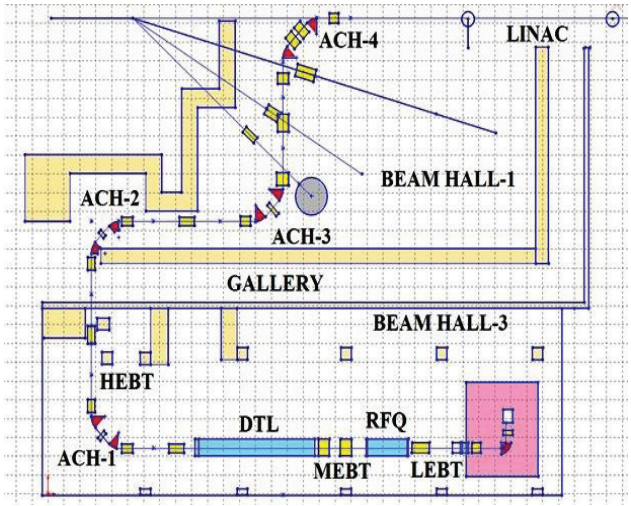

Figure 7: Complete beam-line layout of the High Current Injector.

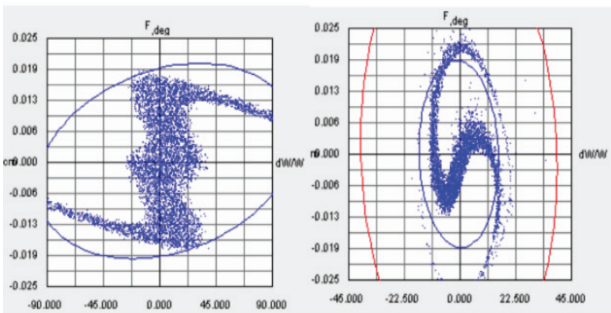

Figure 8: Longitudinal phase space at the entrance and exit of the RFQ situated 4.0 m downstream from the multi-harmonic buncher.

SUMMARY AND CONCLUSION

A systematic study has been undertaken to understand the variation of the plasma potential in an ECR plasma as a function of different source parameters and for several ion beams. These measurements show a mass effect. The measured values of the plasma potential variation with the mean charge state are in accordance with the theoretical model which assumes cold electron temperatures in the range of few tens of eV. The energy spread deduced from the plasma potential measurements influences the longitudinal optics of the High Current Injector in terms of increased phase spread which deteriorates the transmission through the RFQ. This study shows that the energy spread of the ions determined from the plasma potential measurements is a determining factor for the resultant time width of the beam bunches that would be accelerated further by the High Current Injector.

ACKNOWLEDGEMENT

One of the authors (G.R) would like to thank CSIR for supporting partial financial assistance for travel purposes.

REFERENCES

[1] C. Bieth, S. Kantas, P. Sortais, D. Kanjilal, G. Rodrigues, S.Milward, S. Harrison, and R. McMahon, Nucl. Instrum.Methods,B 235,498(2005) ;D.Kanjilal, G.Rodrigues, P.Kumar, A.Mandal, A.Roy, C.Bieth, S.Kantas, P.Sortais, Rev.Sci.Instrum.,77,03A317(2006).
[2] A.G.Drentje, A.Girard, D.Hitz and G. Melin, Rev.Sci.Instrum.,71,623(2000).
[3] G.Rodrigues, P.S.Lakshmy, Sarvesh Kumar, A.Mandal, D.Kanjilal, R.Baskaran and A.Roy, Rev.Sci.Instrum.,81,02B713 (2010)
[4] A. Roy, Curr. Sci.,76,149 (1999).
[5] G.Rodrigues, P.S.Lakshmy, R.Baskaran, D.Kanjilal, and A.Roy, Rev.Sci.Instrum.,81,02A323(2010).
[6] O.Tarvainen, P.Suominen and H,Koivisto, Rev.Sci.Instrum.,75, 3138 (2004).
[7] O.Tarvainen, P.Suominen, T.Ropponen, T.Kalvas, P.Heikkinen and H,Koivisto, Rev.Sci.Instrum.,76, 093304 (2005).
[8] O.Tarvainen, P.Suominen, T.Ropponen and H,Koivisto, Rev.Sci.Instrum.,77, 03A309 (2006).
[9] J.A.Simpson, Rev.Sci.Instrum.,32, 1283 (1961).
[10] Z.Q.Xie and C.M.Lyneis, Rev.Sci.Instrum.,65(9), 2947 (1994).
[11] A.G.Drentje, Nucl.Instrum.Methods,B 9, 526(1985).
[12] G.Rodrigues, R.Baskaran, S.Kukrety, Y.Mathur, Sarvesh Kumar, A.Mandal, D.Kanjilal and A.Roy, Rev.Sci.Instrum. 83,033301 (2012).
[13] O.Tarvainen, P.Suominen, T.Ropponen, H.Koivisto, R.C.Vondrasek and R.H. Scott, Proceedings of the 16th International Workshop on ECR ion sources, AIP Conference Proceedings, Melville, New York, Vol.749, 61(2005).
[14] H. Higashijima, W.Takai, T.Nakagawa,Y.Higurashi, M.Kidera and A.Goto, Rev.Sci.Instrum.,79,02B505(2008).
[15] P.R.Harris and F.W.Meyer, Rev.Sci.Instrum.,81, 02A310 (2010).
[16] V.Mironov, K.E.Stiebing, O.Hohn, L.Schmidt, H.Schmidt-Bocking, S.Runkel, A.Schempp, G.Shirkov, S.Biri, L.Kenez, Rev.Sci.Instrum.,73,623(2002).
[17] A.Girard, C.Lecot and K.Serebrennikov, J.Comput.Phys.,191,228 (2003).
[18] N.K.Bibinov, V.F.Bratsev, D.B.Kokh, V.I.Ochkur, K.Wiesmann, Plasma Sources Sci. Technol.,14,109 (2005).
[19] T.A.Antaya, J.Phys.(Paris), Colloq.,50, 707 (1989).
[20] John Staples, Particle Accelerators, Vol.47,191(1994).
[21] http://www.phy.anl.gov/atlas/TRACK/

Copyright © 2012 CC-BY-3.0 and by the respective authors

ISBN 978-3-95450-123-6

THE EINZEL LENS LONGITUDINAL CHOPPER

Ken Takayama[1,2,3]*, Leo Kwee Wah[1,2], and Toshikazu Adachi[1,2]
[1]High Energy Accelerator Research Prganization (KEK), Tsukuba, Ibaraki, Japan
[2]The Graduate University for Advanced Studies, Hayama, Kanagawa Japan
[3]Tokyo Institute of Technology, Nagatsuda, Kanagawa, Japan

Abstract

This paper describes the Einzel lens beam chopper that has been newly developed for the KEK digital accelerator (DA) project. Function of beam chopping is added to the Einzel lens used as a transverse focusing device for a low energy ion beam. Its idea and operational chopping performance are discussed in details.

INTRODUCTION

The KEK digital accelerator (DA) is a small-scale induction synchrotron without a high-energy injector [1]. The concept of an induction synchrotron was experimentally demonstrated in 2006 [2] by utilizing the KEK 12 GeV Proton Synchrotron. Instead of an RF cavity, an induction cell is employed as the acceleration device. It is simply a one-to-one transformer, which is energized by a switching power supply generating pulse voltage. Two types of induction cells for acceleration and confinement are employed. An injected beam pulse is captured by the barrier bucket and accelerated with pulse voltages. It is a crucial point of the induction synchrotron that voltage timing is controlled by a gate signal of solid-state switching elements based on bunch signals detected at the bunch monitor. This operational performance enables acceleration of ions from extremely low velocities, and is the reason why the DA does not require a high-energy injector. It is understood from these properties that the DA is capable of accelerating any species of ion, regardless of possible charge state.

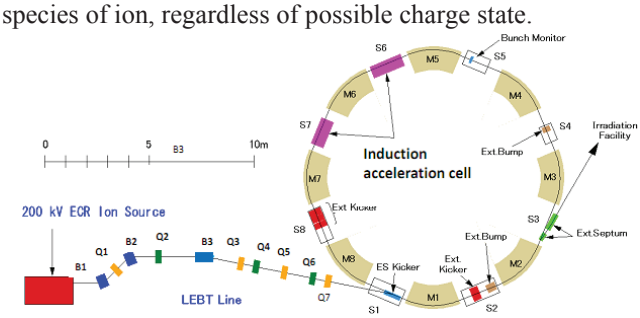

Figure 1: Outline of the KEK Digital Accelerator.

In the KEK DA, schematically shown in Fig. 1, a 5 msec long ion beam is created in the electron cyclotron resonance ion source (ECRIS) and chopped by the newly developed Einzel lens chopper in 5 μsec and post-accelerated in the acceleration column attached with the 200 kV high-voltage platform (HVP), after which it propagates through the low-energy beam transport line (LEBT) to be injected into the ring with the electrostatic injection kicker. The electrostatic kicker voltage is turned off before the injected beam pulse completes a single turn in the DA ring, which is a rapid-cycle synchrotron. The injected beam is captured with a pair of barrier voltage pulses and accelerated with pulse voltages.

The single turn injection scheme limits on the maximum beam length. On the other hand, beam production in most of ion sources requires a finite time period due to a principle mechanism of plasma formation. A beam chopper which can provide a desired pulse length is indispensable. In this paper, its main argument will be focused on how a necessary beam length can be generated and key features of its operational performance are summarized.

* takayama@post.kek.jp

ACCELERATOR COMPLEX

Permanent Magnet ECRIS [3]

The ECRIS is embedded on the DC 200 kV HVP. In order to minimize the consumed electric power and avoid troublesome of water cooling on the high voltage platform, the permanent magnet ECRIS being operated in the pulse-mode (10 Hz and 2-5 msec) has been developed. This ECRIS driven by a 9.35 GHz TWT with a maximum output power of 750 W is capable of producing from hydrogen ion to Argon ion, which are extracted at 10 kV. The HVP including the Einzel lens chopper and the post-acceleration column is schematically shown in Fig.2.

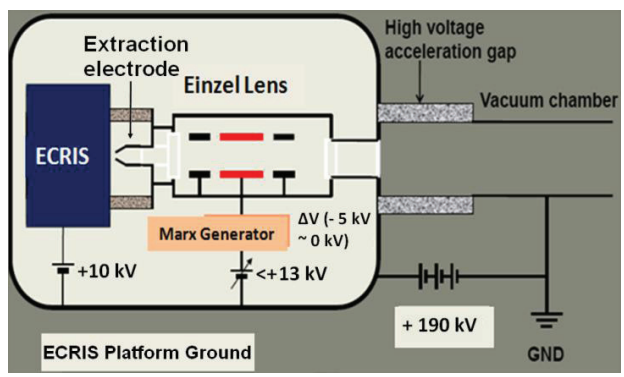

Figure 2: Schematic of the HVT and its contents.

Einzel Lens

The Einzel lens is located just after the ECRIS extraction electrode. Its middle electrode is sustained at an optimized voltage, which gives over-all transverse

ISBN 978-3-95450-123-6

Copyright © 2012 CC-BY-3.0 and by the respective authors

matching downstream. As described in details later, a function of beam chopping is added to this Einzel lens.

Low Energy Beam Transport (LEBT)

The LEBT consists of the momentum selector magnet (or charge state selector), other two bending magnets, 7 focusing quadrupole magnets, a few beam profile monitors, and additional steering magnets, the last four magnets (STH3,4 and STV3,4) of which are used for the purpose of injection error correction.

Accelerator Ring

The lattice consists of eight combined-function (FDF) magnets (M1~M8) symmetrically placed along the beam orbit. Eight straight sections are occupied by the electrostatic injection kicker (S1), extraction kicker (S2,S8), extraction septum magnets (S3), induction acceleration cells for beam confinement and acceleration (S6, S7), and vertical orbit correction magnets (S4, S5), position monitors (S2, S4, S5, S8), movable screen.monitor (S1), and bunch monitor (S5) Lattice/beam parameters are listed in Table 1.

Table 1: Lattice/beam Parameters

Circumference	C_0	37.7 m
Bending radius	ρ	3.3 m
Maximum B	B_{max}	0.84 Tesla
Bet. tune in x/y	Q_x/ Q_y	2.17 - 2.09/2.30 - 2.40
Transition energy	γ_T	2.25
Energy (Inj.)/ nucleon	E_{inj}	200 keV(Q/A)
Rev. frequency	f	~80 kHz – 3 MHz

Electrostatic Injection Kicker

From a simple reason that for handling of low velocity ions electrostatic fields are much suitable, the electrostatic injection kicker has been employed. Before the injection, two 80 cm long parallel plates are excited to 20 kV through a pulse forming network line, which is required to counter the injection angle of 11.25 degree. The high voltage is turned off by firing thyratrons, which allow charges on the capacitance including the electrode plates to quickly flow to the ground through the register. Actually the electrostatic kicker voltage was tuned off in a few μsec with dumped back-and force reflection noises.

LONGITUDINAL CHOPPER

As stated in the above introductive part, the revolution time-period of ions in the KEK-DA is around 10 μsec. The single-turn injection scheme requires a pulse length less than 10 μsec. A pulse chopper upstream is necessarily demanded. There are several possible schemes for a chopper. Is it a high energy type or low energy type? Is it a transverse type or longitudinal type? Beam-handling at a low energy stage is apparently preferable, leading to low yields of secondary electrons, small out-gassing, and low energy X-ray emission. Another important factor is cost. Careful considerations on a possible space and discharge in the high voltage post acceleration column and quality of chopper voltage have motivated us to develop the Einzel lens chopper, which works as a longitudinal chopper and demands only an additional power supply to control the gate voltage. Its conceptual idea is depicted in Fig.3.

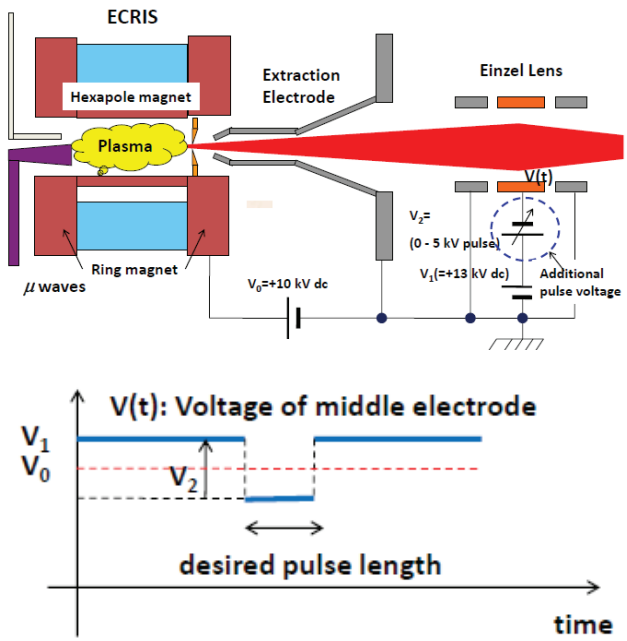

Figure 3: Idea of the Einzel lens chopper (upper) and Voltage profile of the Einzel lens V(t) (bottom).

In order to confirm the idea, IGUN simulations have been performed. The simulation results give us the necessary blocking voltage as well as the matching voltage. Figure 4 shows typical ion beam traces nearby the Einzel lens a s a function of V(t).

Copyright © 2012 CC-BY-3.0 and by the respective authors

ISBN 978-3-95450-123-6

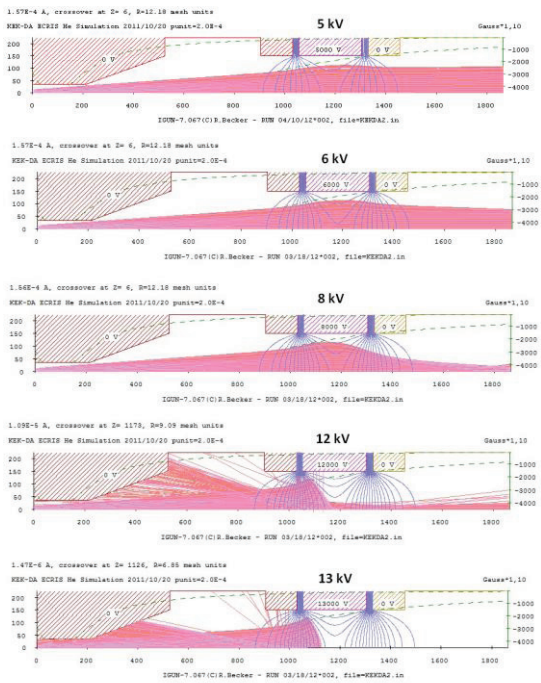

Figure 4: IGUN simulations for different Einzel lens voltages.

In addition, this prediction has been confirmed by experiments, where the current of ion beam is observed 2.5 m downstream by the Faraday cup for the different static Einzel lens voltages. The results are shown in Figure 5, which is fairly in good agreement with the simulation results.

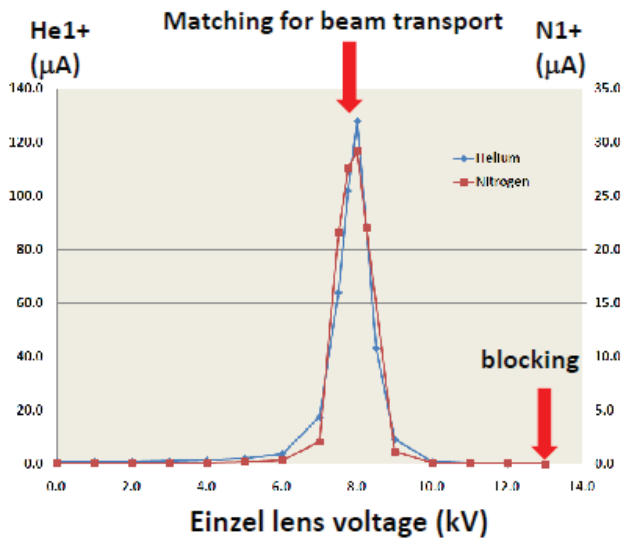

Figure 5: Beam Current for He1+ and N1+ vs. Einzel lens voltage.

To realize a fast pulse rising and falling time of the chopped pulse, the solid-state switch driven Marx generator has been developed. Expecting fast rising/falling in the pulse voltage, MOSFET devices have been employed as a switching element. The equivalent circuit is depicted in Figure 6 together with its photograph. Pulse profiles are shown in Figure 7, where one can realize a good agreement between the SPICE simulation and observed result.

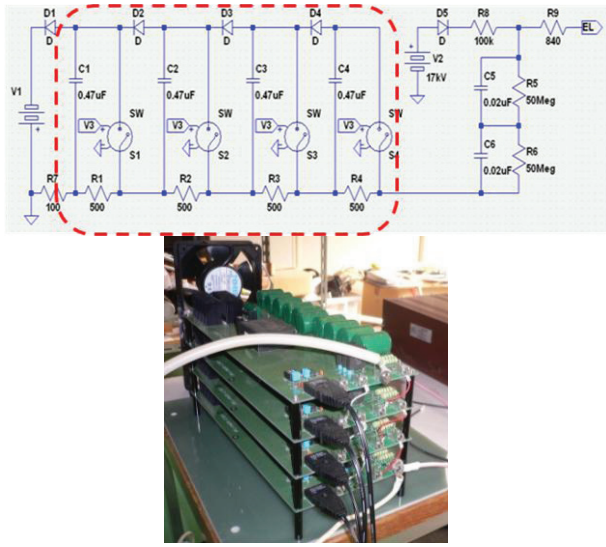

Figure 6: Equivalent circuit of the Marx generator and its photo.

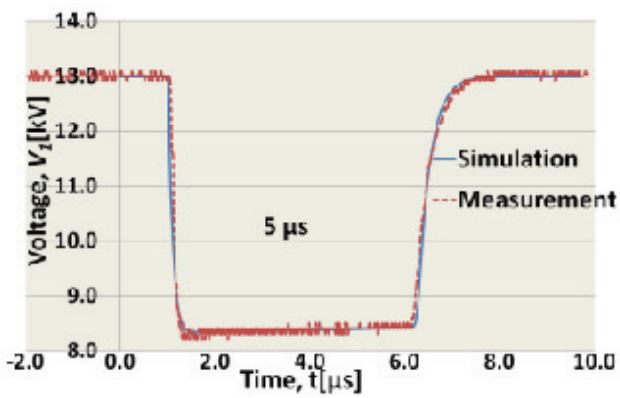

Figure 7: Pulse voltage for chopper performance.

A 5 μsec-long pulse of minus 5 kV generated by the Marx generator is superimposed on DC 13 kV of the middle electrode, which prevents ions to propagate downstream except for the gating time-period, as explained in Figure 3. The chopped pulse is immediately post-accelerated in the DC acceleration column of 190 kV to enter into the momentum selector or charge-state selector region.

Figure 8 shows the 5 μsec pulses chopped from the 5 msec He1+ beam at the timing of 0.4 and 3 msec from the pulse head respectively, which were measured by a Faraday cup (FC). The rising and falling time are determined by the circuit parameters of the diagnostics circuit system including the stray capacitance of FC.

ISBN 978-3-95450-123-6

Copyright © 2012 CC-BY-3.0 and by the respective authors

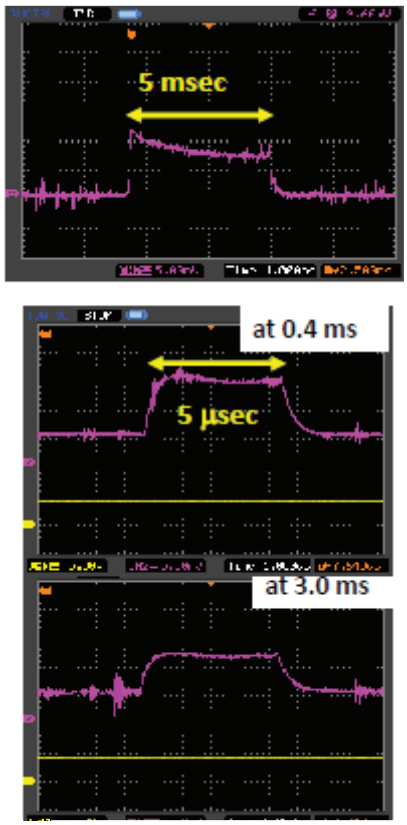

Figure 8: 5 µs chopped pulse profiles, which are chopped at different times from the pulse head of a 5 ms ion pulse.

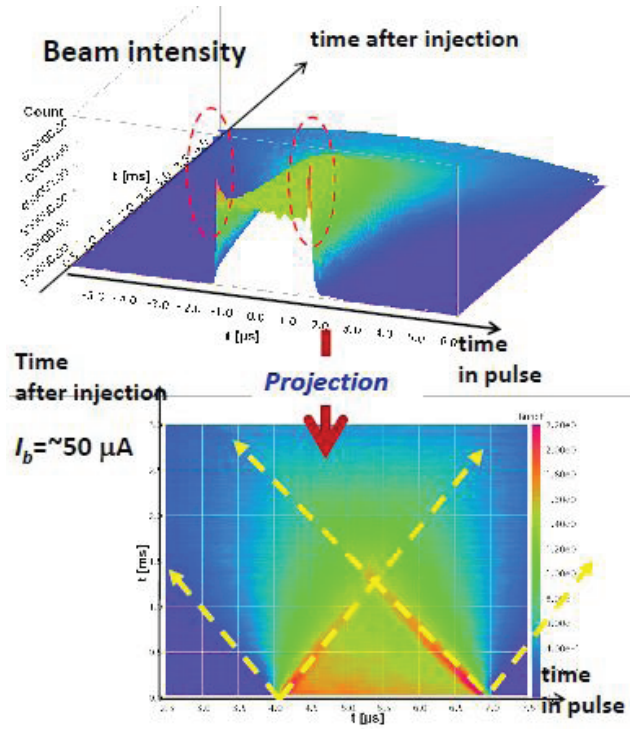

Figure 10: Mountain view of the freely circulating chopped pulse (top) and its projection on the time-turn plane (bottom).

QUALITY OF CHOPPED BEAM

Quality of a chopped beam is of our big concern. Especially, the longitudinal emittance of the chopped beam is an important parameter to capture in the barrier bucket of the digital accelerator. A distribution of chopped ions in the momentum space is crucial to determine the longitudinal emittance. In order to know precise information of the injected ion beam, a behaviour of free circulation in the ring has been carefully observed.

Free Circulation in the Ring

The injected bunch circulating in the ring without any longitudinal control has been observed by the bunch monitor. Mountain views in the time spaces and their projection on the time-turn plane as seen in Fig. 10 are quite useful for the present purpose. Sharp peaks at both edges of the injected pulse are notable.

Figure 10 strongly indicates that the injected beam pulse has a multiple momentum spectrum. Gradual diffusion in the time or on the orbit coordinate suggests a momentum spread of the injected bunch. Meanwhile, something like compression at the early stage of free circulation is visible. This suggests that the injected bunch has a negative momentum spread in the bunch head and a positive momentum spread in addition to an intrinsic momentum spread. It is suggested that the seed of this abnormal distribution in the phase space is created as transient effects in the chopper pulse shape. This view has motivated extensive studies to explore what happens in propagating through the chopper region [5,6].

Simulation

A macroparticle simulation code to analyze the particle motion in the longitudinal direction was written. The simulation has manifested that a large momentum deviation occurs at pulse head and tail timing, taking into account the temporal change in the chopper voltage pulse (see Fig.7). A typical example is shown in Fig. 11.

Copyright © 2012 CC-BY-3.0 and by the respective authors

ISBN 978-3-95450-123-6

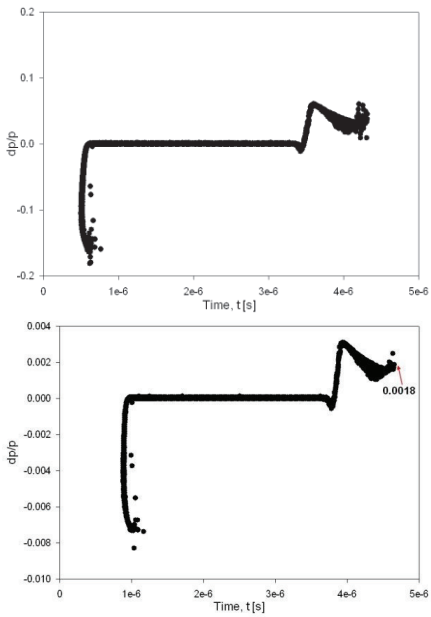

Figure 11: Phase space plot just after the Einzel lens (top) and the post acceleration column (bottom), where a relative momentum deviation is largely reduced due to acceleration from 10 keV to 200 keV, $(\Delta p/p)$=(-0.16)(10keV/200keV)=--0.008.

Since these momentum deviation survives even after injection into the ring, it turns out that the observed phenomena is understandable. Diffusion speed in the time-turn plane is consistent to the prediction from the momentum deviation observed in Fig. 11.

Physics Behind

This momentum deviation is qualitatively explained with the following simple model. Let consider three particles which enter into the gaps of the EL during a flat voltage region and the transient time regions that are depicted as colour zones in Fig.12. Magnitude of electric fields, E_1 and E_2 exerting on the particles at two gaps is different due to a finite transit time of a particle. This difference leads to the momentum deviation, that is,

for particle A, $|E_1|>|E_2|$, then $\Delta p/p < 0$,
for particle B, $|E_1|=|E_2|$, then $\Delta p/p = 0$,
for particle C, $|E_1|<|E_2|$, then $\Delta p/p > 0$.

This type perturbation on the momentum space is an intrinsic nature of the longitudinal chopper, where a rectangular pulse shape is not expected even if its net size can be reduced by improving the rising/falling time. The rising and falling time depends on a stray capacitance of the EL. Reducing of the stray capacitance as small as possible is effective to minimize the momentum deviation. The present magnitude of $(\Delta p/p)_{max}$~ 0.1% is still small and acceptable to the barrier bucket and the momentum aperture in the DA.

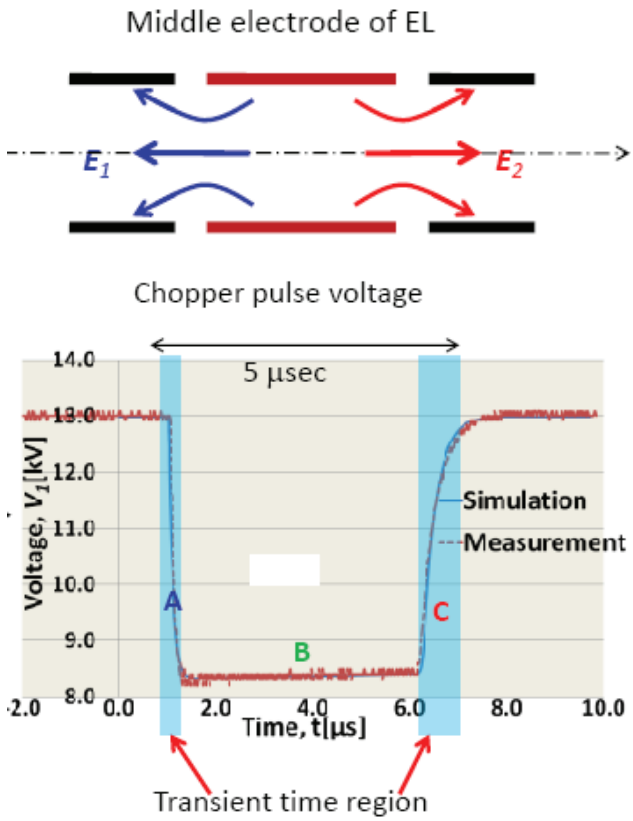

Figure 12: Model of the EL (top) and Typical chopper pulse with transient regions (bottom).

SUMMARY AND PERSPECTIVE

Intrinsic features in the operational performance of the noble longitudinal chopper have been described. The device has been operated more over one and half a year without any trouble. The system is quite reliable. Any required chopper length can be easily provided by simply changing gate timing of the MOSFETs for the Marx generator. It is noted that a whole story has been given in Reference 6. In the near future the EL chopper will be integrated with a laser ablation ion source under development in the collaboration between KEK, BNL, and RIKEN.

ACKNOWLEDGMENT

Authors acknowledge Prof. Jiang for introducing a solid-state Marx generator and A.Tokuchi for assembling the present Marx generator, and T. Arai for initiating IGUN simulations and developing the SPICE simulation model for the Marx Generator pulse power supply. The present work is supported by a Grant-In-Aid for Scientific Research (A) (KAKENHI No. 23240082).

Copyright © 2012 CC-BY-3.0 and by the respective authors

ISBN 978-3-95450-123-6

REFERENCES

[1] T. Iwashita *et al.*, "KEK Digital Accelerator", *Phys. Rev. ST-AB 14,* 071301 (2011).

[2] K. Takayama *et al*., "Experimental Demonstration of the Induction Synchrotron", *Phys. Rev. Lett*. **98**, 054801-4 (2007), "Induction Accelerators", K.Takayama and R.Briggs (*Eds.*) (Springer, 2010).

[3] Leo Kwee Wah *et al.*, "Permanent Magnet ECRIS for the KEK Digital Accelerator", *19th Int. Workshop on ECRIS*, August 23-26, Grenoble, France, TUPOT15 (2010).

[4] T.Adachi, T.Arai, K.W.Leo, K.Takayama, and A.Tokuchi, "A Solid-state Marx Generator driven Einzel Lens Chopper", *Rev. Sci. Inst.* **82**, 083305 (2011).

[5] Leo K.W., PhD Thesis, The Graduate University for Advanced Studies (2012).

[6] Leo K.W. *et al.*, "Einzel Lens Chopper and Behavior of the Chopped Beam in the KEK Digital Accelerator", submitted to *Phys Rev. ST-AB* (2012).

Copyright © 2012 CC-BY-3.0 and by the respective authors

ISBN 978-3-95450-123-6

EXPERIMENTAL RESULTS: CHARGE-STATE- AND CURRENT-DENSITY DISTRIBUTIONS AT THE PLASMA ELECTRODE OF AN ECR ION SOURCE

L. Panitzsch*, T. Peleikis, M. Stalder, R.F. Wimmer-Schweingruber
Institute for Experimental and Applied Physics (IEAP), University of Kiel, Germany

Abstract

We have measured the current-density distribution (CDD) in very close vicinity (15 mm downstream) of the plasma electrode of our hexapole-geometry electron-cyclotron-resonance ion source (ECRIS). For this, we equipped our 3D-movable puller electrode with a customized Faraday Cup (FC) inside. To achieve high spatial resolution we reduced the aperture of the puller electrode to only 0.5 mm. Thus, the source-region of the extracted ion beam is limited to a very small area of the plasma electrode's hole (d = 4 mm). The information about the charge-state distribution (CSD) and the current density in the plane of the plasma electrode is conserved in the ion beam and was scanned by remotely moving the small-aperture puller electrode (incl. FC) across the aperture of the plasma electrode. From additional m/q-measurements for the different positions we can deduce that different ion charge-states are grouped into bloated triangles of different sizes but with the same orientation in the plane of the plasma electrode with the current density peaking at the centre. This confirms simulations by various groups as well as some emittance measurements, but adds spatial resolution for the different charge-states.

INTRODUCTION

To further understand the processes within the plasma of ECR ion sources various groups have developed simulation tools to predict different plasma parameters or to benchmark them against existing ion sources. The parameters of importance usually are the extractable current, the achievable charge states, and the emittance of the beam at the extraction. The simulations also show the spatial arrangement of the different ion species and charge states. Here, the highly charged ions are concentrated closer to the axis of symmetry than the lower-charged ion species, but always arranged in characteristically shaped triangular stars [1, 2, 3] (if operated with a hexapole for radial plasma confinement). As a result the highly charged ions are expected to have a lower emittance. This was substantiated by emittance measurements using a bending magnet for ion separation [4, 5]. Unfortunately, using this technique the spatial information is lost. Therefore, we use a different approach to determine the spatially resolved CSD in the plane of the plasma electrode by experiment: We use our 3D-movable puller electrode to record the profile (or CDD) of the extracted beam at a distance of only 15 mm to the plasma electrode. Knowing the total CSD of the extracted beam and the axial magnetic fields we can conclusively show (by now for charge states 2+ to 4+) that the different charge states are grouped into triangular structures with the same orientation but different sizes in the plane of the plasma electrode. The current density peaks at the center.

* panitzsch@physik.uni-kiel.de

BEAM PROFILE MEASUREMENTS CLOSE TO THE EXTRACTION

To measure beam profiles at a distance of only 15 mm (!) downstream of the plasma electrode we take advantage of our 3D-movable puller electrode to scan the plasma electrode's aperture. It is equipped with a customized FC. The aperture which spatially limits the measured ions has a diameter of only 0.5 mm. The dimensions of the plasma electrode and the plasma chamber are shown in fig. 1. The geometrical dimensions of the FC and the use of a negatively biased repeller guarantee the suppression of secondary electron escape. Beam profiles have been aquired for two different source settings. By adding helium into the plasma chamber we changed the ion composition and the pressure inside the ECR zone. Therefore, we separate between the settings RG (residual gas at 5E-7 mbar) and RGHe (helium added until 1E-6 mbar) in the following paragraphs. The resulting beam profiles are shown in fig. 2. The figure shows the CDD for both settings (RG left and RGHe right) in the plane of the puller electrode at comparatively high resolution. The x- and y-axes denote the position in the plane of the plasma electrode with the origin being at beam center. The colour bars indicate the measured current densities. For both measurements we see similar tendencies: Areas with similar current densities can be grouped into bloated triangular-like structures with different orientations and sizes overlapping each other. The

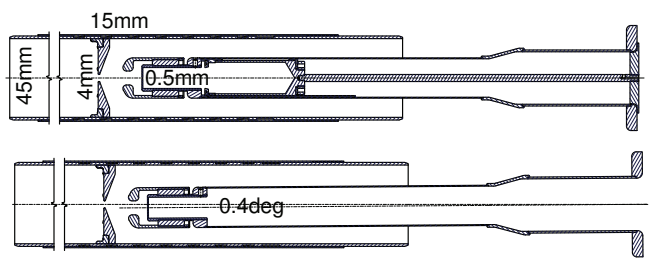

Figure 1: CAD-drawings of the plasma chamber, the plasma electrode, and the puller electrode for different settings: (1) central with implemented FC, (2) at the outmost position without the FC. Here the puller electrode is tilted by 0.4 °. The resulting shift is 2 mm.

ISBN 978-3-95450-123-6

Copyright © 2012 CC-BY-3.0 and by the respective authors

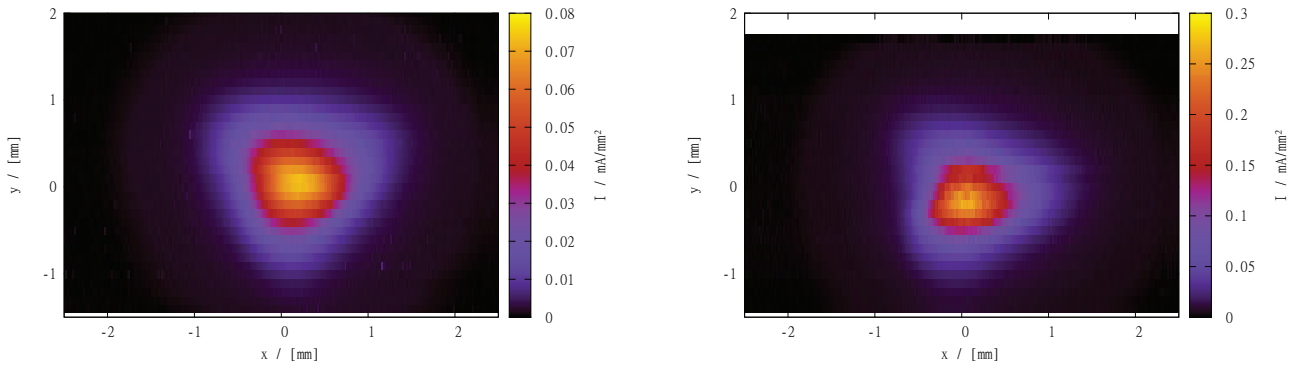

Figure 2: Measured current density distributions (CDDs or profiles) shortly behind the plasma electrode for settings RG (left) and RGHe (right). Note that the colour bars are scaled differently to match the particular intensity range.[2]

total current density is peaking at the center. In addition, the circular shape of the plasma electrode is clearly visible and its diameter can be verified to be 4 mm. Slight deviations from an ideal circle are supposed be caused by the end-position switch triggering the start signal of the current recordings. As we clearly can resolve the circular shape of the plasma electrode as well as the triangular structures we conclude that the ions passing through the tiny aperture are indeed extracted from a very limited region of the neutral plasma sheath only. If the ions were extracted from larger regions the resulting figures would be blurred and we would not be able to clearly resolve them. For the identification of the single structures we need further information about the CSD of the total extracted ion beam and the magnetic fields. With that, we will show that each of these triangular structures is dominated by ions of one m/q-ratio and that their orientation is equal directly at the extraction as predicted by the simulations referred above.

SPATIALLY RESOLVED CHARGE-STATE DISTRIBUTION (CSD)

To determine the spatially resolved CSD as observable from behind the sector magnet we again used the puller electrode with reduced diameter (but without the FC). We analyzed the m/q-spectra of the beams extracted from the different regions of the plasma electrodes aperture (and therefore the neutral plasma sheath) by the use of a sector magnet. The thus obtained spatially resolved CSDs for the most dominant ion species (N and O) are presented in fig. 3 for setting RG. We have to point out that these distributions are strongly influenced by the transmissivities of the particular charge states which was optimized before. All measurements were performed at an extraction voltage of 7 kV at an axially fixed position of the puller electrode (the puller electrode was only moved in the plane perpendicular to the beam axis, again). The results shown here have to be regarded as a 'snapshot' looked at from behind the sector magnet for the applied focussing only.

[2]Reprinted with permission from [6], Copyright 2011, American Institute of Physics

Figure. 3 shows the spatial distributions for the different nitrogen (left-hand) and oxygen (right-hand) charge states in the range from 1+ to 4+. Higher charged ion species were only found at the exactly central position. The intensities in the individual plots are scaled to the maximum measured intensity, I_{max}. I_{max} is indicated at the top of the individual plots and increases from low to high charge states. In both settings (RG and RGHe with only RG being shown here) the highest charge states only fill the central pixel and therefore seem confined to the very central region of the plasma electrode. As the emittances of the higher-charged ion species were measured to be smaller than for the low-charged ions (as referred to above, [4, 5]) we would expect the higher-charged ions to have a higher transmissivity also when being extracted from the non-central regions. Though, these ions are only present in the spectra recorded with the puller electrode at exactly central position. This, indeed, is a hint for them to be concentrated close to the axis of the source as observed in many simulations (again, as referred to before). With decreasing charge state the distribution broadens and nearly fills the plasma aperture for doubly charged ions. Obviously, the highest charge states clearly peak in the centre while lower charge states populate areas with larger radii around the centre. Also, the recorded current densities peak at the centre and decline with increasing radial distance for each ion species. The slope of the decline is distinctly steeper for more highly charged ions and more shallow for the lower charged species. From these spatially resolved CSDs we have calculated the total CSD of all extracted ions by summing up the currents for each particular ion species. The resulting CSDs for both settings (RG and RGHe) are presented in fig. 4. We observe a shift in the charge state with highest intensity from 2+ (for setting RG) to 3+ or 4+ for setting RGHe. This seems to be the effect of gas mixing. To validate these results we compared these calculated CSDs extracted with the puller electrode with reduced diameter with CSD measurements performed with our standard-sized puller electrode (not shown within these proceedings). The CSDs recorded with both different extraction techniques nicely show the same character-

Copyright © 2012 CC-BY-3.0 and by the respective authors

ISBN 978-3-95450-123-6

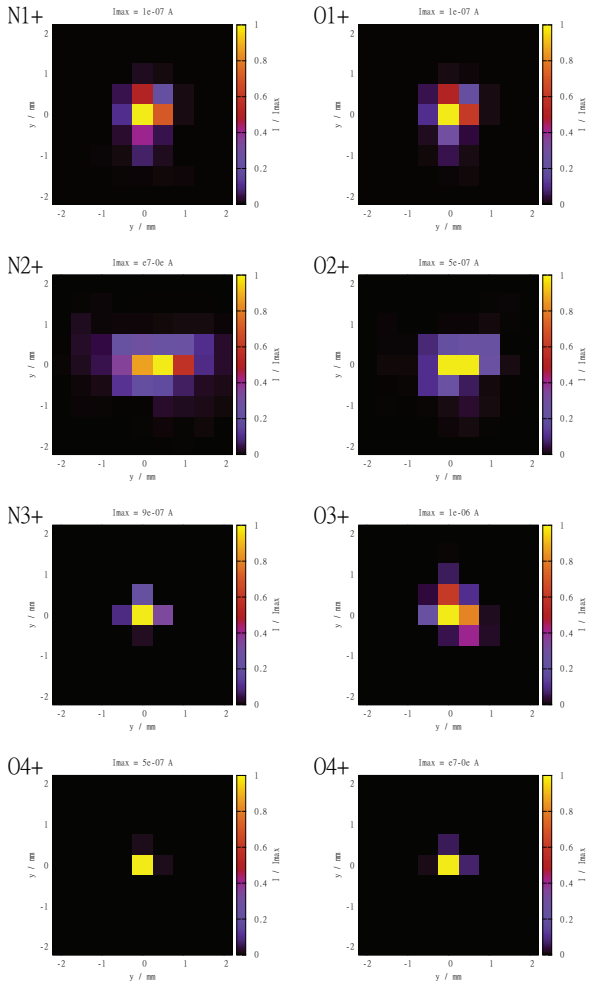

Figure 3: Measured charge state distributions at the plasma electrode as visible from behind the sector magnet for setting RG (residual gas only). The x- and y-axes denote the position in the plane of the plasma electrode with the origin being at beam centre. The colours show the measured current densities scaled to the maximum detected current, I_{max}, for each graph. This allows visualization of the entire distribution.[2]

istics/trends. Therefore, we can conclude that the transmissivity of the small-aperture puller electrode is not worse compared to the standard extraction and systematical ion-optical errors can be excluded. We even observed a 'multi-aperture-like' effect. Multi-aperture extractions are known to result in significantly increased total currents [7]. The added currents extracted with the puller electrode with reduced aperture at many different positions in the plane of the plasma electrode are higher than the currents detected with the standard-sized puller electrode (not shown in these proceedings, see [6] for reference). This trend was observed for all charge states higher than 1+.

[2]Reprinted with permission from [6],Copyright 2011,American Institute of Physics

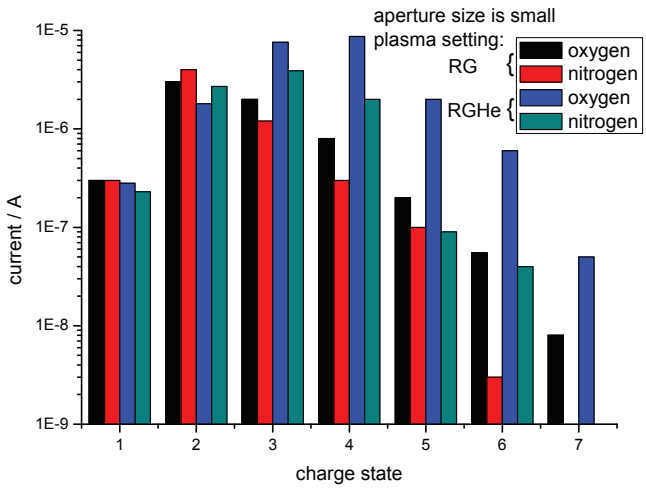

Figure 4: Comparison of the total charge state distributions for settings RG and RGHe. The distribution for the small sized aperture is calculated from the results of the CSD measurements by summing up the currents for each particular ion species. With helium as a mixing gas we see a shift of the maximum (2+ → 3+ or 4+) in the total charge state distribution and an increase of all higher charge states.[2]

COMBINATION OF THE PREVIOUS RESULTS

In this section we combine the results of the CSD measurements with the results of the CDD measurements. Taking the magnetic fields into account we are able to deduce the distribution of the different ion species directly at the extraction. We begin with a short discussion of systematic errors and the validity of the results: The CDDs are recorded using a FC inside the puller electrode. This results in a very short drift distance for the ion beam. For geometrical reasons the aperture size of the puller electrode in combination with the inner diameter of the FC guarantee the capture of the total beam passing through the aperture. The use of a repeller in front of the FC restricts secondary electrons from escape. A magnetic field-induced rotation has to be considered but generally we can exclude systematic errors for the CDD measurements. For the spatially resolved CSD measurements we have to point out limited validity. The presented CSDs portray only a 'snapshot' for the current focussing settings. They can be regarded as source regions in the plane of the plasma electrode for the different ion species effectively transmitted through the sector magnet under the particular focussing. A change in the extraction voltage will change the presented distributions due to ion-optical reasons. Therefore the calculated total CSDs (fig. 4) represent only the ion species that are transmitted through the sector magnet. They do not necessarily represent the real totally extracted CSD which we are interested in for our subsequent analyses. We know that the transmissivities for the standard and the tiny-sized apertures of the puller electrode are nearly identical (as

ISBN 978-3-95450-123-6

Copyright © 2012 CC-BY-3.0 and by the respective authors

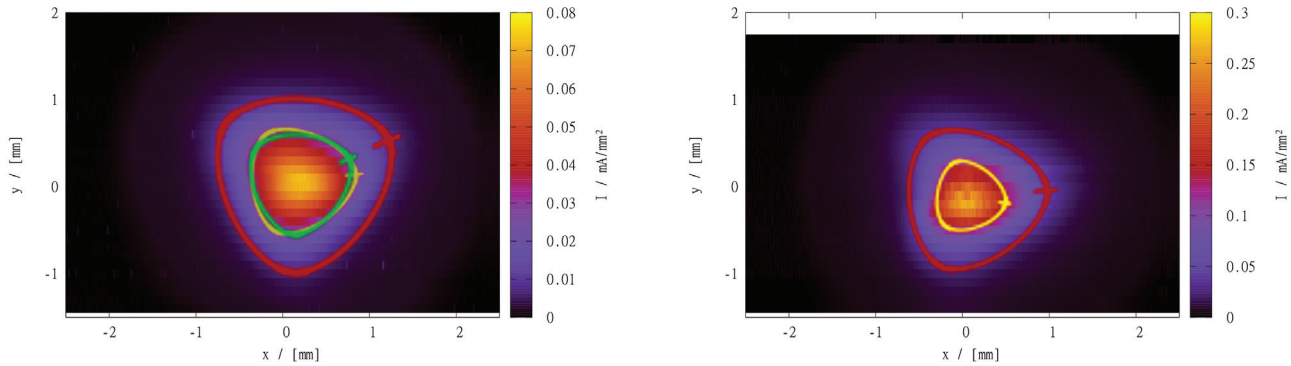

Figure 5: Measured CDD for settings RG and RGHe (compare caption of fig. 2 for details). Here the detected structures are framed with marked bloated triangles to guide the eyes. Note the different color scales.

mentioned above). Thus, we have determined multiple total CSDs for beams extracted with the large puller electrode while varying the extraction voltage. The spectra show that the main trends (especially the dominating ion species) within the recorded total CSDs do not differ significantly within the checked voltage range (4 kV to 11 kV) from these shown in fig. 4 (for 7 kV). Accordingly, we use the total CSDs already presented in fig. 4 for the following argumentation.

In fig. 2 the CDD in close vicinity of the extraction is shown. Here, bloated triangular structures of different sizes and orientations are clearly visible but no information about the ionic composition is present. To solve this we consult the (caluclated total) CSDs (fig. 4) obtained from the spatially resolved CSD measurements (fig. 3). The structures visible in fig. 2 should mainly be populated by the dominating ion species of the particular setting. For the analysis we make the assumption that higher charge states are concentrated closer to the axis. For setting RG the most dominant ion species are charged 2+ and 3+ with the 2+ component being slightly more dominant. Setting RGHe is dominated by charge states 3+ and 4+, respectively. Other ion species are too strongly suppressed to contribute significantly. For both settings two bloated triangles are found within the CDD. To guide the eyes we have framed the measured structures of fig. 2 by bloated triangles. These triangles have a mark to distinguish their orientation (see fig. 5). With this aid we are able to determine the angle of rotation of the different structures which is important for the analysis:

As for setting RG charge states 2+ and 3+ are dominant we assume that here the outer triangle (framed red, see fig. 5) is mainly populated by ions of charge state 2+. The orientation of the inner structure is more difficult to distinguish as different charge states (mainly 2+ and 3+) overlap each other. We are able to find two different orientations of the frames (green and yellow) that both well accentuate the inner structure(s?) of setting RG. A bloated structure in the center with the same orientation as the outer one (framed red, 2+) might still be caused by the 2+ component as for each charge state the current density is observed to peak at the center and that particular charge state is slightly dominant. On the other hand, there surely also is a strong 3+ component present in inner, central triangle. This 3+ component might be the reason for that second, differently orientated (yellow) inner frame. For setting RGHe we see the dominance of charge states 3+ and 4+. Again, according to the observation that higher charge states seem to be populated closer to the axis we assume the outer triangle (framed red) to mainly consist of ions of charge state 3+. Therefore, the inner triangle (framed yellow) is assumed to be dominated by the 4+ component. For the red-framed structure of setting RGHe (see fig. 2, right) two facts attract attention. It is rotated and its size appears to have decreased slightly compared to the red-framed structure of setting RG. The inner (yellow-framed) structure of setting RGHe (fig. 2, right) shows both, a further rotation together with a further decrease in size.

The beam is extracted in a region where the axial magnetic field peaks at roughly 1 T. This leads to a Lorentz-force-induced rotation of the beam. The angle of rotation Θ_{tot} can be calculated with the formula [8]:

$$\Theta_{tot} = \sqrt{\frac{q}{8mU_{extr}}} \cdot \int B_z dz \qquad (1)$$

with q, m, and U being the charge, the mass, and the extraction voltage respectively. The rotation of the beam that occurs after having passed the tiny aperture of the puller electrode does not affect the CDD measurements since all ions passing the aperture at its defined position will be collected by the FC. We summarize the information gained so far in table 1. For each resolved structure we denote the assumed dominating charge state as well as the observed orientation 15 mm downstream of the plasma electrode with the vertical plane denoting 0°. In addition, we line out the calculated rotation for the different charge states. The thus deduced orientation of the structures in the plane of the plasma electrode is given as the difference of both values. We see that the orientation of all structures calculated back to the plane of the plasma electrode shows the same value (≈13° ccw). This very well reproduces the orientation we observe for the sputter- and deposition marks at the inner

Copyright © 2012 CC-BY-3.0 and by the respective authors

ISBN 978-3-95450-123-6

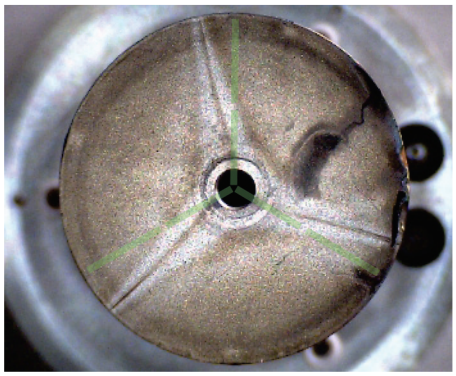

Figure 6: Sputter marks observed on the inner side of the plasma electrode. The tilt angle is ≈13° counter clockwise in relation to the vertical plane. This is in good agreement with the values for the original orientations calculated in table 1.

side of the plasma electrode itself (see fig. 6). This is a strong indicator that the dominating particles of the particular triangles shown in fig. 2 (or fig. 5, respectively) were assumed correctly. As a consequence we can draw the conclusion that indeed the different ion species are grouped in triangular structures of different sizes but same orientation in the plane of the plasma electrode and the current densities peak at the center. Thus, our measurements support the simulations of various groups who have predicted this behaviour.

CONCLUSIONS

We recorded beam profiles (CDDs) and spatially resolved CSDs in the closest vicinity of the plasma electrode we found in the literature (only 15 mm downstream). We combined both results in order to deduce for the CDD and the CSD directly at the extraction of a hexapole geometry ECR ion source. The results clearly show higher currents peaking at the center as well as the presence of (bloated) triangular structures. Each of these structures is dominated by ions of the same charge state. In the plane of the plasma electrode all the structures are orientated in the same direction determined by the magnetic field. The surface area of these structures differs from comparatively large for low charged ions and decreases rapidly for more highly charged ions. The higher/highest charge states clearly peak only in the centre and therefore populate the smallest effective radii. This is to our knowledge the first direct measurement of the CSD and the CDD at the extraction. The results in general conform to results from simulations and facts deduced from emittance measurements, both performed by other groups.

considered structure	suspected charge state	observed orientation	calculated rotation	original orientation
RG red	2+	-65°	-78°	+13°
RG green/yellow	2+/3+	-65°/-81°	-78°/-95°	+13°/+14°
RGHe red	3+	-81°	-95°	+14°
RGHe yellow	4+	-97°	-110°	+13°

Table 1: Summary of the information gained from the previous analyses. The observed orientation and the original orientation are given in relation to the vertical plane which denotes 0°. The original orientation is calculated as the difference of the observed orientation minus the calculated rotation.

References

[1] C. Pierret, L. Maunoury, S. Biri, J. Y. Pacquet, O. Tuske, and O. Delferriere. Preliminary results of the ion extraction simulations applied to the mono1000 and supershypie electron cyclotron resonance ion sources. *Review of Scientific Instruments*, 79(2):02B703, 2008.

[2] L. Maunoury, C. Pierret, and J.Y. Pacquet. Extraction from ECR ion sources: a new way to increase beam brightness. In *Proceedings of ECRIS08 18th International Workshop on ECR Ion Sources*, pages 224–228, 2008.

[3] J. P. M. Beijers and V. Mironov. Three-dimensional simulations of ion dynamics in an electron cyclotron resonance ion source. *Review of Scientific Instruments*, 81(2):02A307, 2010.

[4] D Wutte, M A Leitner, and C M Lyneis. Emittance measurements for high charge state ion beams extracted from the aecr-u ion source. *Physica Scripta*, 2001(T92):247, 2001.

[5] M.A. Leitner, C.M. Wutte, and Lyneis C.M. Design of the extraction system of the superconducting ecr ion source venus. In *Particle Accelerator Conference, 2001. PAC. IEEE*, 2001.

[6] Lauri Panitzsch, Thies Peleikis, Michael Stalder, and Robert F. Wimmer-Schweingruber. Spatially resolved charge-state and current-density distributions at the extraction of an electron cyclotron resonance ion source. *Review of Scientific Instruments*, 82(9):093302, 2011.

[7] R. Geller. *Electron cyclotron resonance ion sources and ECR plasmas*. Institute of Physics Pub., 1996.

[8] W. Glaser. *Grundlagen der Elektronenoptik*. Wien, 1952.

ISBN 978-3-95450-123-6

Copyright © 2012 CC-BY-3.0 and by the respective authors

ION BEAM EXTRACTION FROM MAGNETIZED PLASMA

P. Spadtke, K. Tinschert, R. Lang, J. Mader, F. Maimone, J. Roßbach, GSI Darmstadt

Abstract

By increasing the total extracted ion current, the optimization of the extraction system becomes more important for any ion source because of the space charge effect. Several attempts have been made in the past to simulate the extraction from an Electron Cyclotron Resonance Ion Source (ECRIS) in a correct way. Most of these attempts failed, because they were not able to reproduce the experimental results. The best model up to now is given by the following procedure:

- Tracing the magnetic field lines through the extraction aperture, looking where these field lines are coming from.
- Using these coordinates of the magnetic field line as starting points for ions to be extracted.
- The initial current of each trajectory is determined by theoretical assumptions about the plasma or by a plasma simulation.
- Childs law is applicable locally only in direction of the magnetic field, if no emission limited flow is present.

INTRODUCTION

This model assumes that ions travel through the plasma only influenced by the magnetic field. The positive ions inside the plasma chamber are assumed to be space charge compensated to a very high degree because of the presence of cold electrons, resulting in a small plasma potential. Collisions are neglected for the path of the ion, as well as diffusion effects inside the plasma. The radius of gyration for cold electrons is well within the μm range, and so the radius of gyration for ions is below the mm range. This is a necessary precondition to define the ECRIS plasma to be magnetized. The assumption that diffusion processes are playing also a minor role is supported by the experimental experience that plasma etching occurs only at places in the plasma chamber pronounced by the magnetic structure. The visible traces inside the plasma chamber and on both end plates of the plasma chamber (injection side plate and plasma electrode) are sharply limited. These effects confirm the validity of the model. Furthermore, with that model we are able to reproduce experimental results which we have obtained with viewing targets[1]. The different spatial distribution of starting conditions generates ions with different $\int Bds$ after extraction, which also degrades the beam quality.

BASIC PRINCIPALS

General Plasma Characteristics

Due to the condition of charge neutrality for any plasma, the number of electrons n_e and the number of ions $n_{i,a}$ with charge state a can be estimated by:

$$\frac{n_e - \sum_{a=1}^{qmax} a \cdot n_{i,a}}{n_e} << 1 \qquad (1)$$

The Debye shielding is deduced by solving Poisson's equation in a spherical coordinate system with the assumption, that there is no angular dependency[2]. This assumption is of not correct because of the magnetic field. If there would be no magnetic field, λ_D is given by:

$$\lambda_D = \sqrt{\frac{\varepsilon_0 k T_e}{n_e e^2}} = 7.43 \cdot 10^3 \sqrt{\frac{T_e[eV]}{n_e[m^{-3}]}} \qquad (2)$$

where k is Boltzman's constant, $T_e$is the electron temperature, respectively T_i the ion temperature, e the electron charge, and ε_0 the dielectric constant. The formulation of the Debye length λ_D is valid only, if the number of particles N_D within a sphere with radius λ_D is $>> 1$.

$$N_D = n_e \frac{4}{3}\pi \left(\frac{\varepsilon_0 k T_e}{n_e e^2}\right)^{3/2} = 1.72 \cdot 10^{12} \frac{T_e^{1.5}[eV]}{\sqrt{n_e[m^{-3}]}} \qquad (3)$$

This condition is fulfilled if we assume a typical particle number of $n_e = 10^{15..18} m^{-3}$, and a Debye length in the range of μm to mm, which means that the required conditions for a plasma are satisfied. However, the Debye length within the magnetic field is not isotropic any more. Equ. 2 might be valid in the direction of the magnetic field, but not perpendicular to it.

If dynamic shielding is investigated, the plasma frequency ω_p comes into consideration. For electrons it follows:

$$\omega_p = \sqrt{\frac{n_e e^2}{m_e \varepsilon_0}} = 56.5 \sqrt{n_e[m^{-3}]} \qquad (4)$$

The plasma frequency for ions with mass m_i and density $n_{i,\alpha}$ is derived by the same procedure as for electrons with mass m_e. Because the plasma frequency for ions is lower by the factor of $\sqrt{\frac{m_i}{m_e}}$, this frequency is not of importance for screening. Only electromagnetic fields with frequencies above the plasma frequency ω_p should be able to penetrate the plasma and to propagate through the plasma.

Copyright © 2012 CC-BY-3.0 and by the respective authors

ISBN 978-3-95450-123-6

According to [3] the mean free path length of collisions between electrons is comparable to the mean free path length of collisions between ions, if electron temperature T_e and ion temperature T_i are equal: $T_e = T_i$. In that case the mean free path length can be estimated with:

$$\lambda[m] \approx 2 \cdot 10^{16} \frac{T[eV]^2}{n[m^{-3}]} \tag{5}$$

If we assume an ion temperature of 1 eV and an ion density n_i of $10^{16}\,m^{-3}$ this length would be 2 m. Even that this number depends on unknown quantities, it seems to be larger than the dimension of the plasma chamber. This is why collisions will not contribute to the distribution function f_α in Equ. 13.

Motion of Charged Particles within a Magnetic Field

The equation of motion for a charged particle within a magnetic field is described by the Lorentz equation:

$$m\dot{\vec{\mathbf{v}}} = q \cdot \vec{\mathbf{v}} \times \vec{\mathbf{B}} \tag{6}$$

Because the force on the particle is perpendicular to $\vec{B}$, only the velocity perpendicular to $\vec{B}$ is affected. It can be shown, that this creates a motion of gyration. The electron cyclotron resonance frequency ω_{ce} can be calculated by:

$$\omega_{ce} = 1.76 \cdot 10^{11} \mathbf{B}[T] \tag{7}$$

respectively for ions with atomic mass z, ω_{ci} is:

$$\omega_{ci} = 4.11 \cdot 10^{9} \cdot \frac{\mathbf{B}[T]}{\sqrt{z}} \tag{8}$$

The Larmor radius for electrons $r_{L,e}$ is:

$$r_{L,e}[m] = 3.38 \cdot 10^{-6} \frac{\sqrt{T_e}[eV]}{B[T]} \tag{9}$$

respectively for ions $r_{L,i}$:

$$r_{L,i}[m] = 6.2 \cdot 10^{-3} z \frac{\sqrt{T_i}[eV]}{B[T]} \tag{10}$$

In addition to the Lorentz force another force might appear in the equation of motion.

$$m\dot{\vec{\mathbf{v}}} = \vec{\mathbf{F}} + q\vec{\mathbf{v}} \times \vec{\mathbf{B}} \tag{11}$$

If such an additional force is acting, closed circles are not possible for charged particles any more. In a mirror device, particles will be trapped if their magnetic momentum is less than the amount which would be necessary to leave the trap. Especially, if $\frac{d\vec{B}}{dt} = \frac{d\vec{E}}{dt} = 0$, the guiding center approach can be used.

$\vec{\mathbf{E}} \times \vec{\mathbf{B}}$ Drift If we assume the magnetic field mainly in longitudinal direction, and an ellipsoidal shape of the plasma (resulting in an electric field in radial direction), we should expect an azimuthal drift of that ellipsoid. The marks on each end of the plasma chamber could be explained with such a drift, see Fig. 1,2. Depending on the direction of the longitudinal magnetic field, the azimuthal rotation is either clock-wise or counter-clock-wise. The fact, that the observed rotation does not change its direction with increasing radius indicates that there is no change in sign of the electric field. The electric field depends on the plasma potential, which can be estimated using Bohm's sheath criterion, where the potential drop between the plasma chamber wall (on negative potential) and the plasma itself is:

$$\Phi = -T_e ln(\sqrt{\frac{m_i}{2\pi m_e}}) \tag{12}$$

For protons, plasma potential should be in the order of $2.8 \cdot T_e$, for heavy ions up to $5.5 \cdot T_e$[4]. For the electron temperature T_e only the cold electrons should be of importance, otherwise unrealistic high plasma potential would be estimated. The exact electron distribution over the full energy range would be required to solve that equation exactly.

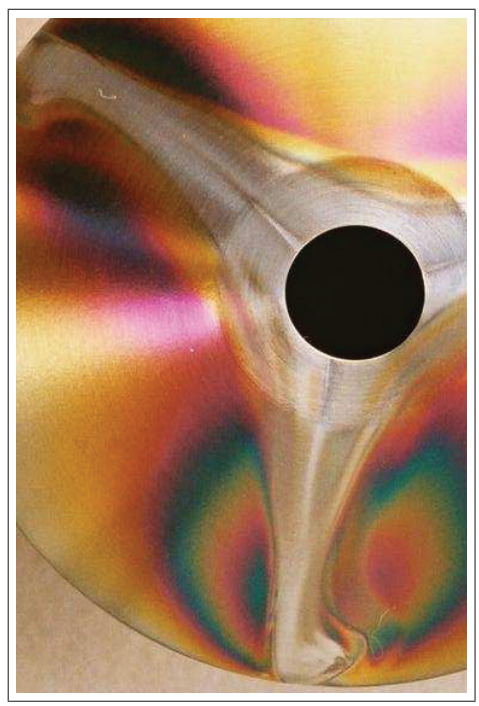

Figure 1: Plasma side of the extraction electrode showing the marks caused by the plasma. Two different traces are visible: a very thin groove, absolutely straight lined, and a more broaden structure, showing an azimuthal dependency.

Furthermore, assuming this kind of drift an explanation of the thin straight groove and the rotated erosion mark (see Fig. 1) can be given: whereas the thin groove is caused by the ions going into the loss cone at the position of the ex-

ISBN 978-3-95450-123-6

Copyright © 2012 CC-BY-3.0 and by the respective authors

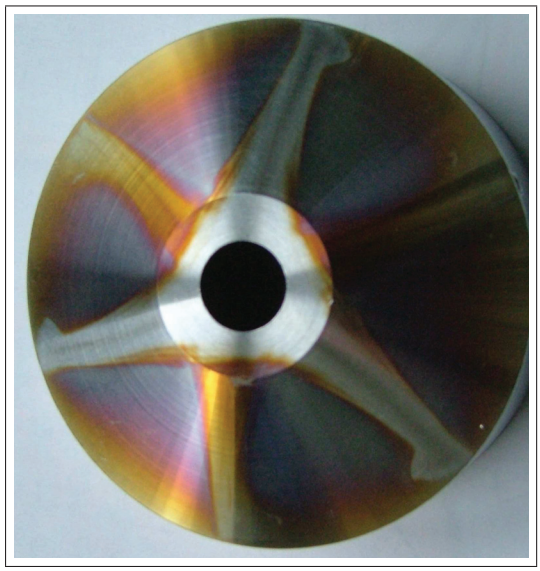

Figure 2: Extraction electrode used for ^{12}C. After some time of operation the polarity of magnetic mirror field has been reversed. The marks caused by the plasma are now orientated into the opposite azimuthal direction.

traction electrode, the larger mark is caused by the ions coming from different longitudinal positions by $\vec{\mathbf{E}}\times\vec{\mathbf{B}}$ drift.

Other forces causing a drift motion like diamagnetic drift, polarization drift, curvature drift, or $\nabla\vec{\mathbf{B}}$ drift beside the electric force can be neglected.

Fluid Model

Going from the description of single particle motion to the description of fluid motion, the distribution $\tilde{f}_\alpha$ of the particles has to be known. The tilde indicates that the distribution function is averaged and different distribution functions for different ions, indicated by α, might exist. This distribution function might be different for electrons, ions, and for the specific charge-to-mass ratios for different ions. Of course, the distribution function will depend on the external forces as well: magnetic flux density distribution, and the rf parameter, at least for the electrons.

$$\frac{\partial\tilde{f}_\alpha}{\partial t}+\vec{v}\nabla\tilde{f}_\alpha+\frac{q}{m}(\vec{E}+\vec{v}\times\vec{B})\nabla_v\tilde{f}_\alpha=\frac{\partial f_\alpha}{\partial t} \quad (13)$$

The homogeneous form of equ. 13 is the so-called Vlasov equation. This equation is solved with an iterative method by the program KOBRA3-INP©[5] used for simulation. The right hand side of this equation describes a collision term, negligible if the contribution of collisions is small. Note, that the left hand side contains averaged values $(\tilde{f}_\alpha)$ only.

Diffusion

Substituting Fick's law:

$$nu=-D\nabla n \quad (14)$$

into the continuity equation yield the diffusion equation for one specie:

$$\frac{\partial n}{\partial t}-D\nabla^2 n=0 \quad (15)$$

where n is the number of particles, v is the velocity, and D the diffusion constant.

Because of the magnetic field the diffusion coefficient D has to be modified for charged particles, using the mean radius of gyration r_L[4], instead of using the mean free path length λ.

$$D=\frac{\pi}{8}r_L^2 v_m \quad (16)$$

According Equ. 16 diffusion effects should decrease quadratically with increasing magnetic flux density. A more detailed derivation[6] shows that the diffusion constant for electrons in the direction of the magnetic field depends on density and temperature:

$$D_{\|e}=1.2\cdot 10^{22}T_e^{2.5}[eV]/n[m^{-3}] \quad (17)$$

whereas the diffusion coefficient perpendicular to the magnetic field shows a different behavior:

$$D_{\perp e}=4\cdot 10^{-22}\frac{n[m^{-3}]}{\sqrt{T_e[eV]}B^2[T]}. \quad (18)$$

For ions the perpendicular diffusion is larger by $\sqrt{m_i/m_e}$, while the diffusion parallel to the magnetic field scales with $\sqrt{m_e/m_i}$.

All experimental experiences indicate that diffusion effects are small, respectively can be neglected, see Fig. 3 to 5. Otherwise the clearly separated erosion marks from unaffected regions would not be possible. It even has been found very early, that additional holes in the extraction electrode can be used to improve the pumping speed from the plasma chamber, without contributing to the extracted ion current, however, only if the orientation of the plasma electrode is correct, see Fig. 5.

EXPERIMENTAL RESULTS

There are several experimental observations, which are similar for all existing ECRIS. The pattern on the plasma chamber wall (see Fig. 3), including both end plates (see Fig. 1,2) is one of them.

On the extraction electrode a pattern can be found, which needs clarification. Two different contributions are visible: one very thin groove, absolutely straight lined in radial direction (see Fig. 1), and another wider pattern showing some azimuthal movement, depending on the radius (see Fig. 2). This movement could be interpreted as consequence of an $\vec{\mathbf{E}}\times\vec{\mathbf{B}}$ drift. The direction of the azimuthal

Copyright © 2012 CC-BY-3.0 and by the respective authors

ISBN 978-3-95450-123-6

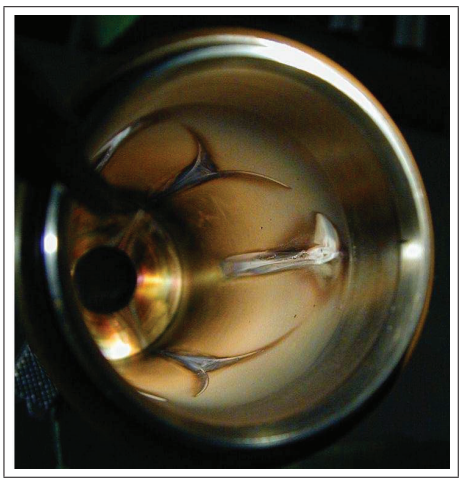

Figure 3: Plasma chamber showing the radial loss lines caused by the superposition of the magnetic mirror field and the hexapolar field.

movement can be found in both azimuthal directions, depending of course on the direction of the solenoidal magnetic field. No experimental result has been found where different directions were obtained simultaneously, indicating that the electric field would change sign.

This azimuthal movement is in addition to the one caused by the fringing field of the ion source solenoid.

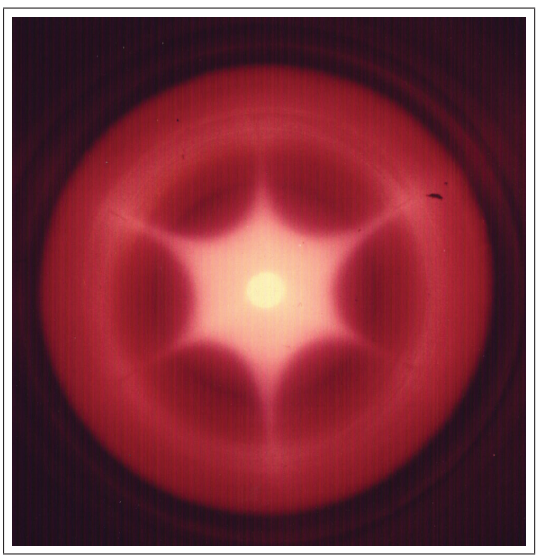

Figure 4: View into the plasma chamber with plasma. Extraction electrode has been removed for that picture [7].

The influence of different ion source parameters (gas pressure, magnetic flux density distribution, multiple frequency heating) on the local plasma density distribution is nicely demonstrated in a video produced by the ANL ECR group[8]. In that video the influence of different heating frequencies is demonstrated. Ramping individually the coils for the magnetic confinement, or ramping the gas pressure shows influence on the light, emitted from the plasma. Always a strong confinement dominates diffusion processes.

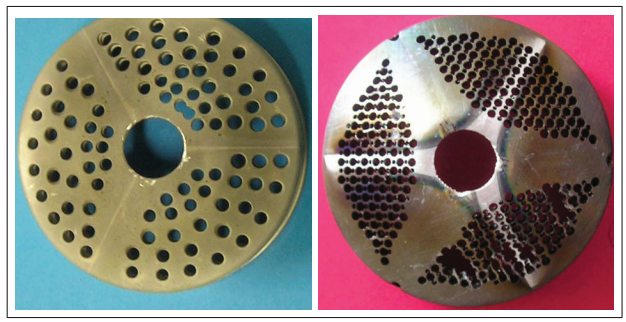

Figure 5: Extraction electrode with additional holes for pumping. No additional load for the extraction power supply caused by these additional holes has been observed (left). In case the plasma electrode is not aligned to the hexapolar pattern additional current load has been observed (right)[9].

SIMULATION

The magnetic field has been calculated using Vectorfield©[10] software. The flux density is than imported by KOBRA3-INP©. Figure 6 shows magnetic field lines going through the extraction aperture at a radius of 5 mm and an azimuthal increment of 1 degree (in total 360 magnetic field lines). When the magnetic flux density along the field line is larger than the flux density within the extraction aperture, starting coordinates for the ions are generated and the color of the field line changes to red. These ions are extracted and are shown for the case of Ar^{3+} in Figure 7 and for a certain distribution of different Argon charge states in Figure 8. The theory of Self [11] can be applied along the magnetic field line, to ensure space charge compensation close to the plasma potential.

Note, that the discrete distribution in radial direction is artificial and only for better understanding of the figures. It is caused by the fact that the analyzed magnetic field lines, going through the extraction aperture, have been analyzed by circles with 1 mm radial increment in between.

It should be pointed out, that this solution shows all possible trajectories. The particle distribution $\tilde{f}_\alpha$ at the beginning of the trajectory is still unknown. It could be demonstrated in experiment [8],[12] that this distribution will be influenced by rf-frequency, rf-power, magnetic field distribution, and gas pressure.

For the simulation the correct magnetic fields have to be used. More information about the initial particle density distribution functions $\tilde{f}_\alpha$ is required, only simulations are available[13].

ISBN 978-3-95450-123-6

Copyright © 2012 CC-BY-3.0 and by the respective authors

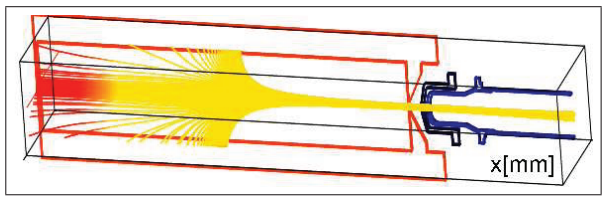

Figure 6: Magnetic field lines going through the extraction aperture on a circle of 5 mm. Depending on the azimuthal coordinate, the starting point of the field line could be located within the hexapole or at the center of the injection side.

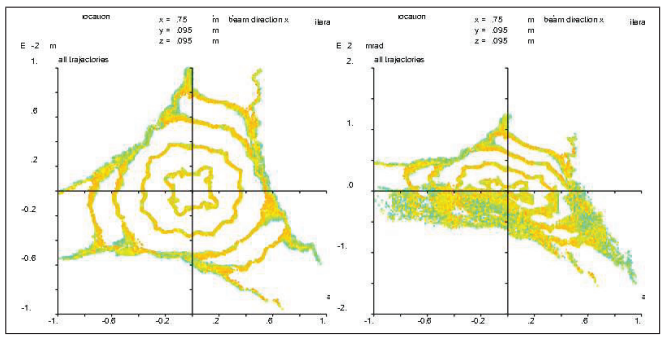

Figure 7: Real space (profile) and horizontal emittance directly behind extraction. Scale is ± 1 cm, respectively ± 200 mrad.

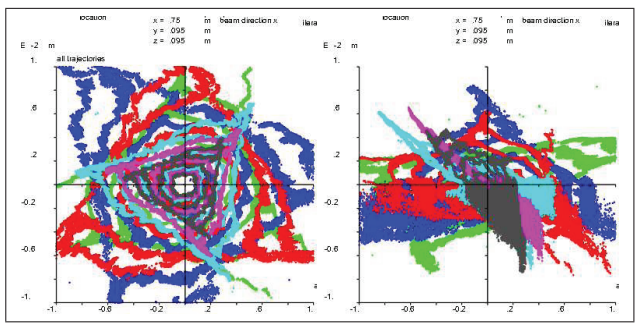

Figure 8: Real space (profile) and horizontal emittance at the same location as in Fig. 7. Blue: Ar^{+}, red Ar^{2+}, green: Ar^{3+}, light blue: Ar^{4+}, magenta: Ar^{5+}, grey: Ar^{6+}. The different focal lengths of different charge states are clearly visible.

REFERENCES

[1] P. Spädtke, K. Tinschert, R. Lang, J. Mäder, J. Roßbach, J.W. Stetson, L. Celona, RSI Vol. **79** No. 2, 02B716 (2008).

[2] E. Debye and E. Hückel, Z. Physik **24**, 185 (1923).

[3] Hartmut Zohm, Plasmaphysik, lecture notes, LMU Munich, 2010, in German.

[4] M.A. Lieberman, A.J. Lichtenberg, Principals of Plasma Discharges and Material Processing, John Wiley & Sons, Inc., (1994).

[5] INP, Junkernstr. 99, 65205 Wiesbaden, Germany.

[6] U. Stroth, Plasmaphysik, ISBN 978-3-8348-1615-3.

[7] Fred W. Meyer (ORNL), private communication.

[8] Video on YouTube produced by MikeBentrain ATLAS, Argonne National Lab, (2007).

[9] R. Geller, D. Hitz, private communication.

[10] Vectorfield Software, Cobham Technical Services, Brook Road, Wimborne, Dorset, UK.

[11] S.A. Self, Phys. Fluids 6, p. 1762, 1963.

[12] F. Maimone, L. Celona, R. Lang, J. Mäder, J. Roßbach, P. Spädtke, and K. Tinschert, Rev. Sci. Instrum. **82**, 123302 (2011).

[13] D. Mascali, S. Gammino, L. Celona, and G. Ciavola, Rev. Sci. Instrum. **83**, 02A336 (2012).

Copyright © 2012 CC-BY-3.0 and by the respective authors

ISBN 978-3-95450-123-6

STATUS OF THE SEISM EXPERIMENT*

M. Marie-Jeanne, J. Angot, P. Balint, C. Fourel, G. Freche, J. Giraud, J. Jacob, T. Lamy, L. Latrasse, P. Sole, P. Sortais, and T. Thuillier, LPSC UJF CNRS/IN2P3 INPG, Grenoble, France
F. Debray, C. Trophime, S. Veys, and C. Daversin, LNCMI CNRS UJF, Grenoble, France
V. Zorin, I. Izotov, and V. Skalyga, IAP, Nizhny Novgorod, Russia

Abstract

LPSC Grenoble has developed the first and unique confinement structure in the world that allows a closed 60 GHz ECR zone, using advanced magnet technology from Grenoble High Magnetic Field Laboratory (LNCMI). The magnetic structure was validated for 28 GHz resonance and a closed 1 T iso-B surface was measured. Discrepancies between calculated and measured field maps were extensively studied in order to determine a working range for 28 GHz plasma tests. A whole test bench, including high pressure water for helix cooling, intense currents (up to 15 kA) for helix powering and a beamline with mass separation is under construction at LNCMI. This contribution presents the status of the experiment.

SEISM MAGNETIC STRUCTURE

Initial Design

The SEISM prototype is based on a magnetic cusp, designed to reach 7 T at the injection, 3.5 T at the extraction and 4.5 T on the radial mirror [1]. A short axial mirror length (100 mm) is possible thanks to the use of polyhelix resistive coils developed by LNCMI Grenoble. Magnetic field measurements [2] confirmed that this configuration could produce a closed 1 T iso-B surface (see Fig.1), thus allowing the resonance at 28 GHz.

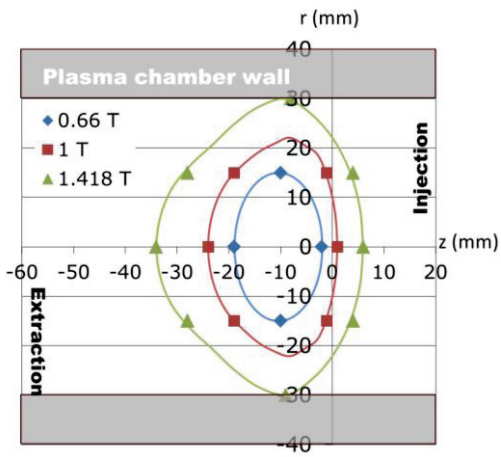

Figure 1: Iso-B map in the prototype at 15000 A.

However, one observed that the resonance zone had a 9 mm shift towards the extraction that remains unexplained. This shift was carefully investigated, as well as the consequences for the source design and operation.

Investigation of the Magnetic Shift

First, an independent measurement based on the magnetic field flux variation was performed with a 0.1 mm step along the central axis at low current (146 A). A 6 mm shift was found.

Then, both injection and extraction water tanks containing the helices were taken apart and their dimensions were checked with CAO drawings. No assembly error was found.

Finally, a new measurement was performed at low current (50 A and 100 A) after assembling the source parts between the tanks, and a 5 mm shift was found. This 5 mm shift is consistent with 2D simulations performed with FEMM software.

Consequences for the Source Design

Magnetic field configuration provides crucial information for the design of the plasma chamber and of the microwave injection.

Concerning the plasma chamber, such displacement of the magnetic field centre may cause energetic electrons crossing the resonance zone to hit and damage the plasma chamber walls. In the present case, plasma chamber dimensions are already constrained by the magnetic structure assembly. A solution was investigated to adjust the current ratio between injection and extraction coils in order to centre the resonance zone. For I_{inj}/I_{ext}=0.8, the cusp point is centred (see Fig. 2), which corresponds to 15 kA maximal intensity delivered by LNCMI power supplies on extraction coils and 12 kA on injection coils for 28 GHz resonance. In order to allow more flexibility on the coils current for the first beam tests, one decides to start with a 18 GHz plasma, which we expect to confine more.

*Work supported by EuroMagNET II under the EU contract number 228043.

ISBN 978-3-95450-123-6

Copyright © 2012 CC-BY-3.0 and by the respective authors

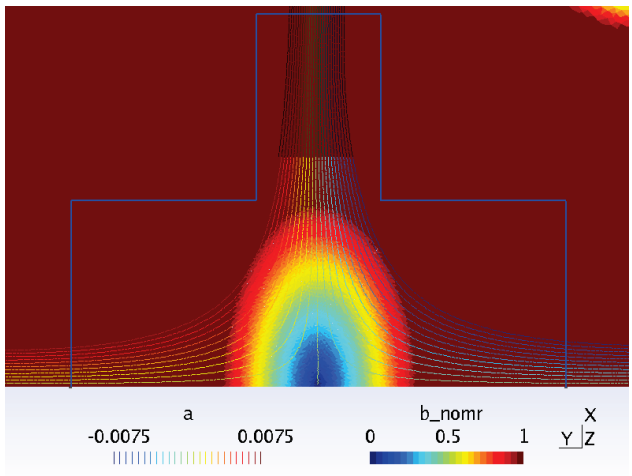

Figure 2: Magnetic field lines for a centred cusp in the prototype.

As for the microwave injection, one needs to avoid plasma flow into the waveguide, thus inducing undesirable discharge outside the trap. For first tests at 18 GHz and 28 GHz, microwave is injected off the source central axis, and the transmission window is protected by a turn of the injection waveguide. However, plasma chamber will be modified in order to connect the 60 GHz microwave launch.

SEISM BEAM TEST BENCH

Source Assembly

The plasma chamber was built according to initial design, with a 60 mm diameter and a 80 mm length. The 20 mm-wide shoulder at the centre allows magnetic field lines to pass from axial to radial mirrors through the resonance zone without touching the chamber walls. A polarized ring was added to prevent radial particle leaks. The plasma chamber is insulated by 2 mm thick PEEK parts. High-voltage (HV) is fed through the radiofrequency (RF) tube. As a first approach, conventional single-gap plasma and puller electrodes were designed, with respective extraction hole diameters of 8 mm and 13 mm. The gap can be varied between 17 and 54 mm.

Figure 3 shows the assembly of the source. Vacuum tests were performed on the source elements prior to assembly. The plasma chamber could be inserted without opening the helices cooling tanks.

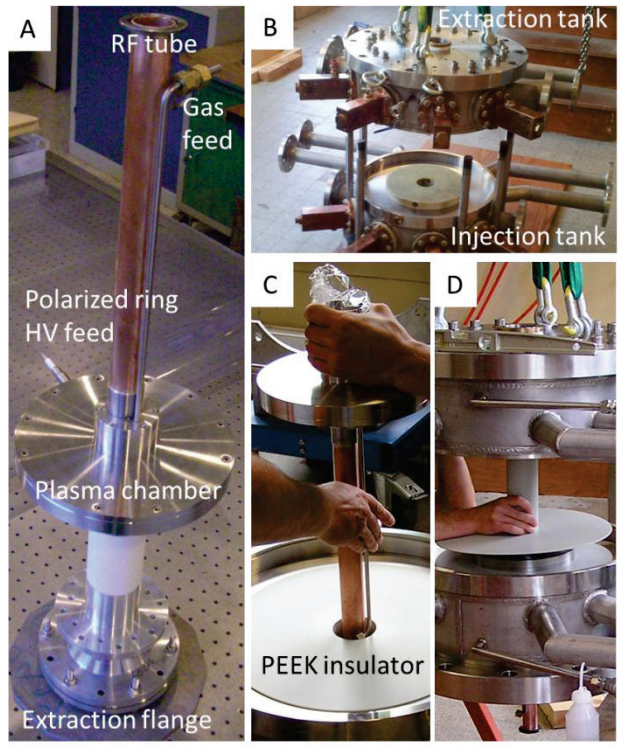

Figure 3: Steps for assembling the source, with (A) vacuum tests of the source parts, (B) taking apart injection and extraction tanks, (C) inserting the plasma chamber and (D) assembling both tanks. Puller electrode is inserted from the extraction flange side.

Beamline

A simple beamline was installed: the source is connected to a 102° magnetic dipole for mass selection and then to a water-cooled Faraday cup. Pumping is achieved by two 240 l/s turbopumps placed before and after the dipole. A 20 kV voltage is applied on the plasma chamber.

Argon gas is injected through a manually controlled grounded valve. Ion current is measured via a Keithley picoammeter.

Magnet Infrastructure

SEISM beam test bench was installed in a dedicated room at LNCMI, with direct hydraulic and electrical connections to the facility. A high de-ionized water flow (20 l/s) was delivered by the facility in order to cool the helices. Injection and extraction coils resistance were monitored to prevent any cooling problem. Injection and extraction coils were respectively connected to independent power supplies delivering up to 15 kA currents each. A scheme of the installation is shown in Fig. 4.

Copyright © 2012 CC-BY-3.0 and by the respective authors

ISBN 978-3-95450-123-6

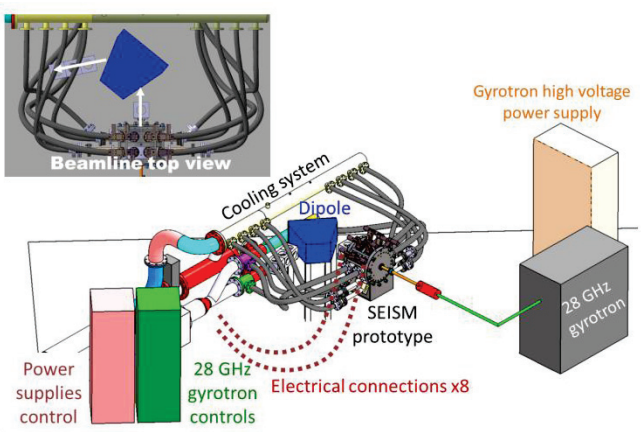

Figure 4: Schematic view of SEISM beam test bench at LNCMI.

TOWARDS 60 GHZ TESTS

Microwave Injection Design

A 60 GHz - 300 kW gyrotron was developped at IAP within an ISTC contract and should be delivered at LPSC-LNCMI in November 2012. Calculations were performed to adapt gyrotron launch to SEISM plasma chamber.

Suggested microwave-to-plasma coupling design intended to solve two problems simultaneously. The first one is feeding the cavity (which plasma chamber actually is) with microwave power with considerable transmission factor and localizing the electromagnetic field in the area where ECR surface would be located. Design shown in Fig. 5 is capable of delivering and focusing 96% of incident power to the ECR area.

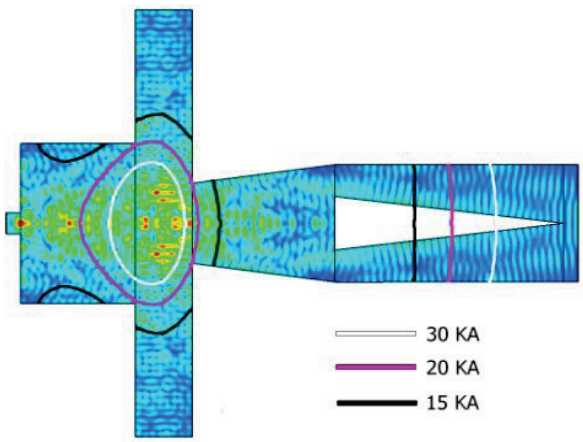

Figure 5: Simulated average microwave field in the whole system along with ECR surfaces plotted for three current settings. Red dots indicate maximal microwave incident power.

The second problem, which is solved by suggested coupling system, is necessity to avoid plasma flow into a waveguide, where the parasitic ECR surface is situated, thus avoiding undesirable discharge outside the trap. Configuration of the right side of the vacuum chamber is matched so it cuts field lines which go around microwave coupling wedge. Therefore, magnetic trap does not exist for field tubes, which are dangerous in the sense of parasitic ECR discharge in the waveguide.

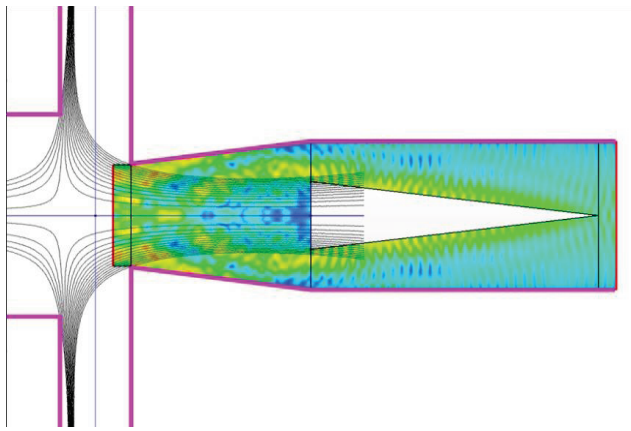

Figure 6: Microwave coupling field distribution plotted along with measured magnetic trap field lines. The pink line shows the new shape for the plasma chamber.

However, precise knowledge of real magnetic field distribution is crucial for suggested design of microwave-to-plasma. For example, in case of 9 mm cusp-point shift (see Fig. 6) microwave launch has to be redesigned due to significant distortion of field lines in comparison with 5 mm shift, which leads to plasma existence in the waveguide area.

Perspectives

Following beam tests at 18 GHz, the 60 GHz magnetic configuration for 30 kA current applied on the coils will be validated. The 60 GHz gyrotron operation will be tested on-site to check stability within the prototype fringe field.

Depending on SEISM beam characteristics, the pertinence of producing 60 GHz plasma with this first prototype will be evaluated.

ACKNOWLEDGMENT

We acknowledge the financial support of the European Community under the European Commission Framework Programme 7 Design Study: EUROnu, Project Number 212372. The EC is not liable for any use that may be made of the information contained herein.

REFERENCES

[1] L. Latrasse, M. Marie-Jeanne, T. Lamy, T. Thuillier, J. Giraud, C. Fourel, C. Trophime, F. Debray, P. Sala, and J. Dumas, Review of Scientific Instruments 81, 02A324 (2010).

[2] M. Marie-Jeanne, J. Jacob, T. Lamy, L. Latrasse, F. Debray, J. Matera, R. Pfister, and C. Trophime, in Proceedings of the XIXth ECRIS workshop (2011).

ISBN 978-3-95450-123-6

Copyright © 2012 CC-BY-3.0 and by the respective authors

DESIGN OF NEW 18 GHZ ECRIS FOR RIKEN RIBF

Kazutaka Ozeki#, Yoshihide Higurashi, Takahide Nakagawa and Jun-ichi Ohnishi,
RIKEN Nishina Center for Accelerator-Based Science, Saitama, Japan

Abstract

In RIKEN Radio Isotope Beam Factory (RIBF), we plan to install a new 18 GHz electron cyclotron resonance ion source (ECRIS), which supply an intense beam of highly charged heavy ions into the RIKEN linear accelerator (RILAC). By equipping the RILAC with two ion sources, we expect to be able to develop new beams while producing a beam for experiments at RIBF. Based on the structure of existing 18 GHz ECR ion source which have been developed at RIKEN, this ion source has the following additional features: (1) Three solenoid coils have been installed to enable B_{ext} to be adjusted while B_{min} is fixed at an optimum value. (2) A variable frequency RF power source has been adopted. Therefore, further enhancement of the beam intensity is expected because the frequency band that is suited to the size of a plasma chamber can be selected. (3) The structure of the chamber has been improved to simplify maintenance work.

INTRODUCTION

For RIKEN Radio Isotope Beam Factory (RIBF) project [1], we constructed and developed several high-performance electron cyclotron resonance ion sources (ECRISs) [2–5]. One of the ion sources is the RIKEN 18GHz ECRIS used as an external ion source for the RIKEN linear accelerator (RILAC) [5]. The main role of the ion source is to produce an intense beam of multi-charged medium-heavy ions (e.g., $^{40}Ar^{8+}$ $^{48}Ca^{10+}$, $^{70}Zn^{15+}$, $^{84}Kr^{18+}$) for the RIKEN RIBF and the super-heavy element search experiment. For this purpose, we have improved performance using various methods [5]. However, we recently needed to develop new beams to meet the requirements for new beams and to extend the irradiation time (longer than one month) of the heavy ion beam, particularly the metallic ion beam, on target for the RIBF. To meet these requirements, we needed a new ion source. By equipping the RILAC with two ion sources for the RILAC, we could develop new ion beams while producing a beam for the experiment. Furthermore, when faced with problems of the ion source during beam production for the experiment, we can immediately switch to another ion source for producing the beam. This means that we can extend irradiation time by using two ion sources. For these reasons, we started to design and construct the new 18 GHz ECRIS as an additional external ion source for the RILAC.

In the present paper, we describe the structure of the new 18 GHz ECRIS. We present the structure of the solenoid coils used for producing a magnetic mirror along the axis and a hexapole magnet, the design of the plasma chamber, and the traveling wave tube (TWT) amplifier for producing 18 GHz microwaves, in the following sections.

SOLENOID COILS AND HEXAPOLE MAGNET

Figures 1 (a) and (b) show schematic drawings of the new 18 GHz ECRIS. It consists of three solenoid coils that produce a mirror magnetic field along the axis. Figure 2 shows a typical magnetic field distribution along the axis. The main parameters of the solenoid coils are listed in Table 1. By using this magnet system, one can independently control the magnetic mirror ratio and B_{min}. As described in several papers [4, 6, 7], beam intensities of highly charged heavy ions are strongly dependent on B_{min}. The optimum value of B_{min} for maximizing the beam intensity is nearly constant (70%~80% of B_{ecr}) for the high-performance ECRIS [4]. This may be due to the effect of the magnetic field gradient and the ECR zone

Table 1: Specifications of the Mirror Coil

	Solenoids I & III	Solenoid II
Number of turns	296	60
Maximum current	660 A	300 A
Maximum voltage	105 V	10 V
Maximum intensity of the mirror magnetic field	>1.3 T	
Minimum intensity of the mirror magnetic field	<0.5 T	

Table 2: Specifications of the Hexapole Magnet

Material	Nd-B-Fe permanent magnet
Inner diameter	85 mm
Outer diameter	186 mm (magnet only), 210 mm (including a holding jacket)
Length	250 mm
Number of divisions	36
Magnetic field intensity	~1.3 T at the surface of the cylinder with the size of 79 mmϕ × 150 mm

#k_ozeki@riken.jp

ISBN 978-3-95450-123-6

Copyright © 2012 CC-BY-3.0 and by the respective authors

a)

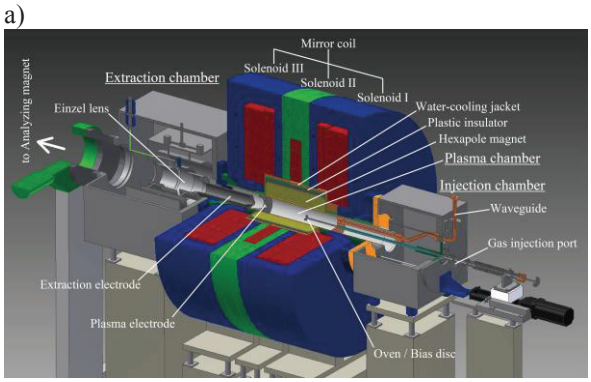

b)

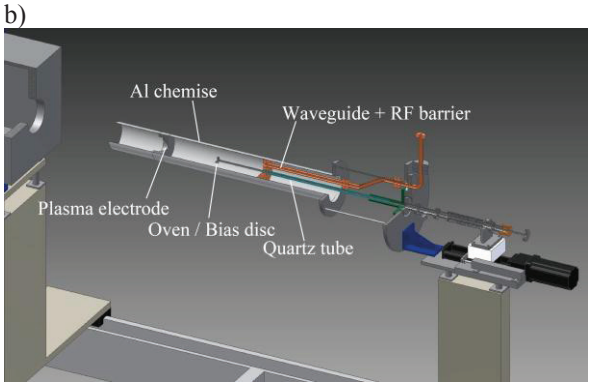

Figure 1: (a) Schematic drawing of the new 18 GHz ECRIS for the RIKEN RIBF. (b) Schematic drawing of the plasma chamber of the new 18 GHz ECRIS for the RIKEN RIBF.

size [8, 9]. On the other hand, the charge state in the plasma is dependent on the mirror ratio, because a longer confinement time for the plasma is obtained by a higher mirror ratio. To achieve these results, we can realize an optimum magnetic field distribution to maximize the beam intensity for the required charge state of the heavy ions as follows: (1) B_{min} should be maintained at 70%~80% of B_{ecr}, (2) the mirror ratio should be changed to maximize the beam intensity for the required charge state of the heavy ions while maintaining the optimum value for B_{min}.

In Fig. 3, the area enclosed by the blue line is the

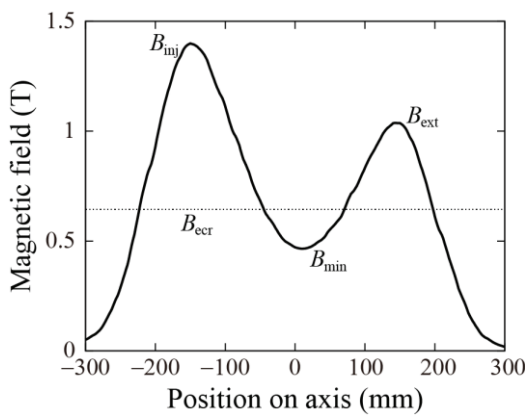

Figure 2: Typical magnetic field distribution along the axis.

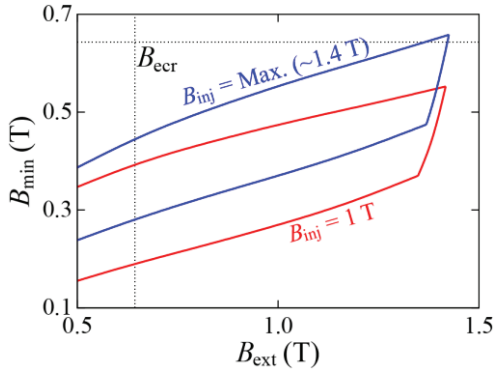

Figure 3: B_{min} vs. B_{ext}. Areas surrounded by the blue and red lines are the possible combination of B_{min} and B_{ext} for B_{inj} = 1.4 T (blue) and 1.0 T (red).

possible combination of B_{min} and B_{ext} when B_{inj} = 1.4 T is selected. In this figure, it is clear that B_{ext} can be changed from 0.8 to 1.3 T while maintaining B_{min} at 0.45~0.5 T.

Table 2 lists the main parameters of the hexapole magnet. The inner and outer diameters of the Hexapole are 85 mm and 186 mm, respectively. It consists of 36 segments of Nd-B-Fe permanent magnets (N48M, Shin-etsu Kagaku Co.). Figure 4 shows the schematic drawing of the hexapole magnet. The arrows in this figure show the direction of magnetization. The remanence (B_r) and coercivity ($H_{c,J}$) are 1.42~1.47 T and 16,000 Oe, respectively. The maximum energy product is 44~49 MGOe. The radial magnetic field strength at the inner surface of the plasma chamber (which is 79 mm in diameter) is ~1.3 T, which is sufficiently strong for 18 GHz microwave operation.

PLASMA CHAMBER

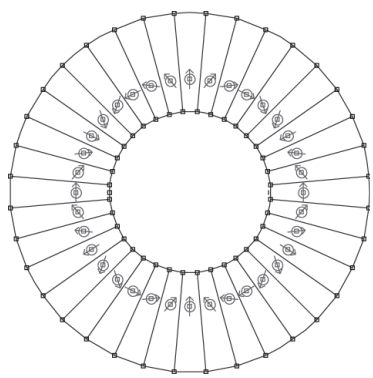

Figure 4: Schematic drawing of the hexapole magnet. Arrows indicate the direction of the magnetization.

The inner diameter of the plasma chamber is 79 mm, which is slightly larger than the old RIKEN 18 GHz ECRIS. There are two turbo-molecular pumps, ~500 L/s, placed at the RF injection side and beam extraction side to maintain a high vacuum in the plasma chamber (on the order of 10^{-8} Torr). The maximum extraction voltage is 20 kV. The position of the extraction electrode is remotely controlled to optimize the beam trajectory. The high-

ISBN 978-3-95450-123-6

Copyright © 2012 CC-BY-3.0 and by the respective authors

temperature oven is inserted from the RF injection side. To set the oven in the optimum position, its position is also remotely controlled. The position and negative voltage of the biased disc are important parameters for increasing the beam intensity of the highly charged heavy ions [5]. For this reason, we install a movable negatively biased disc in the plasma chamber. The position and disc voltage are remotely controlled.

The Nd-B-Fe permanent magnet is easily demagnetized by high temperature. For this reason, we must maintain it at a low temperature (i.e., at room temperature or lower) against the heat load from the ECR plasma. To maintain this temperature, the chamber consists of double-wall stainless steel tubing with a water cooling channel in the gap (~1 mm). The flow rate of the cooling water in the channel is ~6 L/min, which is sufficient to maintain the temperature against the heat load from the plasma when we inject an RF power of 700 W. The temperature of the injected cooling water is 20 °C.

To maintain the high voltage for the plasma chamber, 3 mm thick plastic insulators are placed between the chamber and the solenoid coils. The maximum extraction voltage is 20 kV. For example, the extraction voltage for a Zn^{15+} ion beam is 16.6 kV for the accelerator of RIKEN RIBF.

THE 18 GHZ MICROWAVE GENERATOR

Recently, changes in the ECRIS performances have been achieved by slightly varying the microwave feed frequency ("frequency tuning") [10, 11], which produces strong fluctuations in the beam intensities even for frequency variations in the megahertz range. Simulations based on the particle-in-cell code have shown that the ECR heating efficiency depends on the electromagnetic field distribution in the plasma chamber and on the electric field distribution on the resonance surface. It has been reported that the beam formation process and the beam shape are strongly affected by frequency variations. The explanation for these results is strictly linked to the electromagnetic field pattern inside the chamber; the heating and the ionization processes change with the electric field distribution on the resonance surface. In the case of strongly corrugated plasma surfaces, the scattering effect shortens the ion lifetime. In this case, the beam brightness decreases and is mostly populated by ions at low charge states. If we have "good" matching between the microwave frequency and the geometry of the plasma chamber and ECR zone, a smooth plasma surface can be created. In this case, the ion confinement time and brightness of the extracted beam are increased.

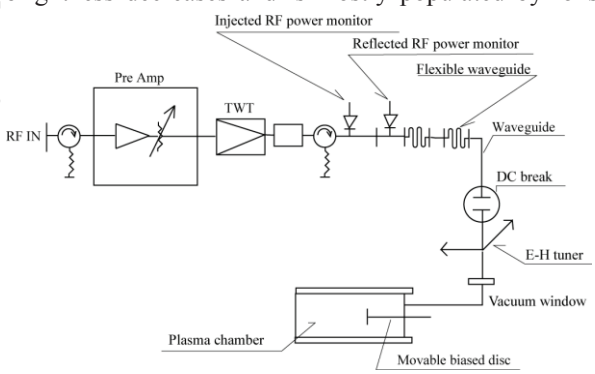

Figure 5: RF power line from the TWT amplifier to the plasma chamber of the ECRIS.

Following these experimental and theoretical results, we use the TWT amplifier for microwave generation to optimize the microwave frequency for the plasma chamber of the ion source. The frequency range is 17.2~18.4 GHz, and the maximum power is ~700 W. Figure 5 shows a schematic drawing of the RF injection system from the TWT to the plasma chamber. The rectangular waveguide is directly connected to the plasma chamber. We also use an E-H tuner to minimize the reflected power.

REFERENCES

[1] Y. Yano, Nucl. Instrum. Methods B 261 (2007) 1009.
[2] T. Nakagawa et al., Rev. Sci. Instrum. 81 (2010) 02A320.
[3] T. Kurita et al., Nucl. Instrum. Methods B192 (2002) 429.
[4] H. Arai et al., Nucl. Instrum. Methods A491 (2002) 9.
[5] T. Nakagawa, Nucl. Instrum. Methods B226 (2004) 392.
[6] H.W. Zhao et al., Rev. Sci. Instrum. 79 (2008) 2A315.
[7] D. Leitner et al., Rev. Sci. Instrum. 77 (2006) 3A302.
[8] Y. Kawai et al., Phys. Letter A371 (2007) 307.
[9] M. Lieberman, A. Lichtenberg, Principles of Plasma Discharge and Material Processing, John Wiley & Sons, Inc., 1994, New York.
[10] L. Celona, et al., Rev. Sci. Instrum. 81 (2010) 02A333.
[11] D. Mascali et al., Proceedings of 19th Int. Workshop on ECR Ion Sources (ECRIS '10), Grenoble, France, p. 165, http://www.jacow.org

Copyright © 2012 CC-BY-3.0 and by the respective authors

ISBN 978-3-95450-123-6

RECENT RESULTS OF PHOENIX V2 AND NEW PROSPECTS WITH PHOENIX V3*

T. Thuillier#, J. Angot, T. Lamy, M. Marie-Jeanne, LPSC, Grenoble, 38026, France
C. Peaucelle, IPNL, Villeurbanne, France
C. Barue, C. Canet, M. Dupuis, P. Leherissier, F. Lemagnen, L. Maunoury, B. Osmond, GANIL, Caen, France
P. Spädtke, GSI Helmholtzzentrum für Schwerionenforschung GmbH, Darmstadt, Germany

Abstract

The 18 GHz PHOENIX V2 ECRIS is running since 2010 on the heavy ion low energy beam transport line (LEBT) of SPIRAL2 installed at LPSC Grenoble. PHOENIX V2 will be the starting ion source of SPIRAL 2 at GANIL. The status and future developments of this source are presented in this paper. Recent studies with Oxygen and Argon beams at 60 kV have demonstrated reliable operation at 1.3 emA of O^{6+} and 200 eμA of Ar^{12+}. Metallic ion beam production has been studied with the Large Capacity Oven (LCO) developed by GANIL and 20 eμA of Ni^{19+} have been obtained. In order to improve further the beam intensities for SPIRAL2, an economical upgrade of the source named PHOENIX V3 has been recently approved by the project management. The goal is to double the plasma chamber volume from 0.6 to 1.2 liter by increasing the chamber wall radius, keeping the whole magnetic confinement intensity unchanged. The PHOENIX V3 magnetic design is presented along with a status of the project.

PHOENIX V2 RECENT RESULTS

The PHOENIX V2 source is an evolution of the former PHOENIX V1 source used to study intense pulsed afterglow Lead beams for the LHC [1,2,3]. Major improvement of V2 with respect to V1 are a higher voltage withstanding (60 kV) and a higher radial magnetic confinement (1.35 T instead of 1.2 T at plasma chamber wall); the drawback being a lower chamber volume (0.7 liter instead of 1.2). Information on the 3 PHOENIX version layout is reported in the next section for completion. PHOENIX V2 was installed at LPSC on the SPIRAL2 LEBT from December 2009 until June 2012 and allowed the successful beam line commissioning. Production tests of A/Q=3 beams have been performed with gas and metals in collaboration with IPNL and GANIL. The table 1 summarizes the results obtained. The beam results increased recently by 30% after the discovery and the fixing of a wrong mechanical part machining in the plasma chamber water flow circuit. Once fixed, the water flow reached its nominal value and the source immediately accepted much more RF power to produce further high charge states ions. The Fig. 1 presents a Ni spectrum obtained with the GANIL LCO. [4] The Ni consumption was 0.2 mg/h and beam featured stable behaviour for several hours. One should note the excellent charge state distribution peaked on the 19+ which was unexpected for such a compact source. The 20 μA Ni^{19+} was obtained at the upper LCO operation temperature and no intensity saturation was observed. So a higher Ni^{19+} current should be reached with 2 ovens set in parallel or a larger oven. Unfortunately, the 32 mm source radius is too small to allow this. The key to understand this high charge state distribution is likely the pressure decrease in the plasma chamber induced by the Ni vapor (Getter effect). Indeed, the plasma chamber is only pumped through the plasma electrode. The vapor to ion yield was measured to be ~10%. The LCO is located off axis with an angle that optimizes the vapor solid angle intersection through the ECR plasma.

Table 1: Intensities Produced by PHOENIX V2

Ion	Charge state	Intensity [μA]
He	2+	2400
O	6+	1300
	7+	250
Ar	12+	205
	14+	50
Ni	19+	20
	20+	11.5
	21+	5

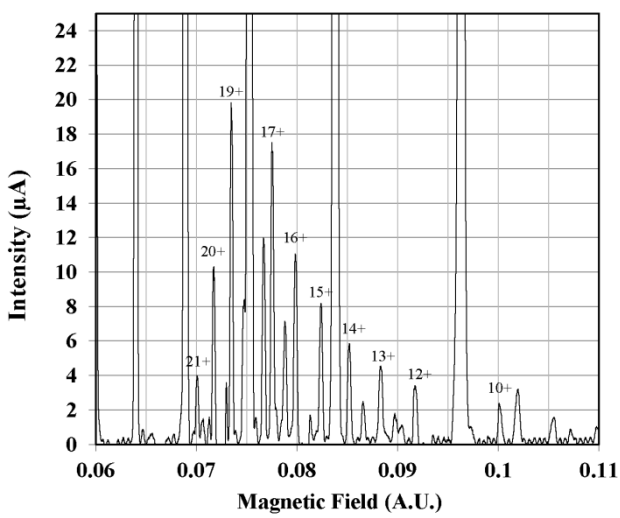

Figure 1: Nickel spectrum obtained with PHOENIX V2.

*Work partially funded by EU Grant Agreement 283745
#thuillier@lpsc.in2p3.fr

ISBN 978-3-95450-123-6

Copyright © 2012 CC-BY-3.0 and by the respective authors

PHOENIX SOURCES AND V3 UPGRADE

The PHOENIX Source Series

The PHOENIX source series have been developed at LPSC since 1997. The series is composed of PHOENIX BOOSTER, PHOENIX CERN (V1), PHOENIX V2; A-PHOENIX, and shortly PHOENIX V3. [1,2,3,5,6] The Table 2 presents the main parameters of these sources. Apart from A-PHOENIX, the room temperature PHOENIX series is based on the same axial coil geometry and high voltage isolation concept. A set of Axial coils and iron disks are stack together to reach the desired axial profile length and intensity, then clamped together with large threaded rods. A rigid 3 mm thick HV cylinder isolator is placed afterward in the resulting warm bore. The central HV core, composed of the permanent magnet hexapole, the plasma chamber and 2 clamped iron plugs, is inserted inside the insulator. Finally, two (or one for the BOOSTER) axial insulating rings are added at each end to clamp the inner HV core part to the outer grounded part (see [3]). The PHOENIX V2 sectional view displayed on Fig. 2 illustrates the unique PHOENIX geometry. In earlier time, the swapping of iron disks and coils set in the stack allowed studying the best experimental axial confinement configuration. Another advantage is the possibility to design new source core and replace it very quickly inside the source.

Table 2: PHOENIX Source Series

PHOENIX SOURCE	Magnetic Confinement		Plasma Chamber geometry			f_{ECR} [GHz]	High voltage
	Axial mirror [T]	Radial field at wall [T]	Length [mm]	Radius [mm]	Volume [liter]		
BOOSTER	1.2-0.4-1	0.8	300	36	1.2	14	25
CERN (V1)	1.6-0.7-1.3	1.2	300	36	1.2	28	55
V2	2.1-0.47-1.28	1.35	210	32	0.7	18	60
A-PHOENIX	3-0.7-3	1.55-2	400	32.5	1.3	18-28	60
V3	2.1-0.47-1.3	1.1-1.32	220	45	1.3	18	60

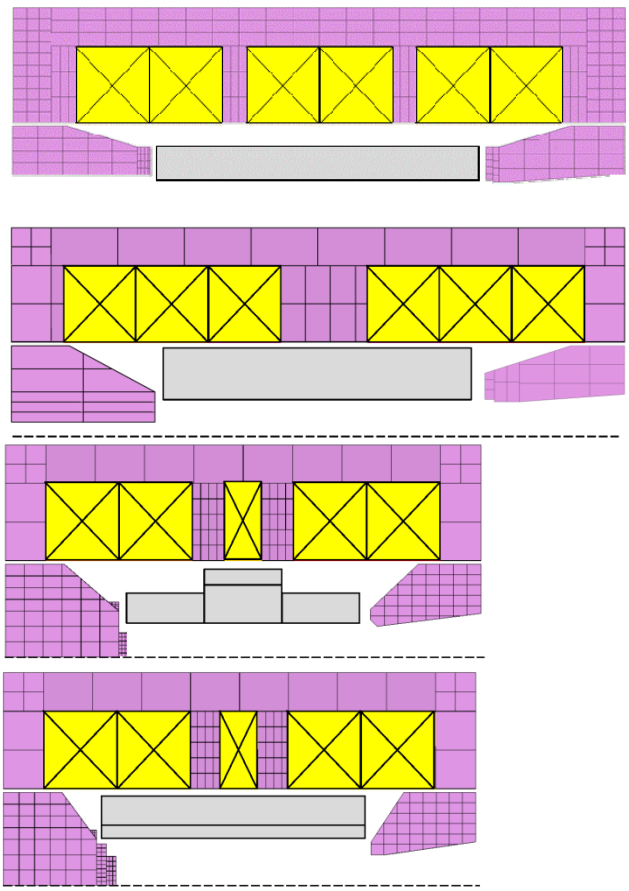

Figure 2: From top to bottom: sectional view of PHOENIX BOOSTER, CERN (V1), V2 and V3.

Volume Effect on A/Q=3 Beam Intensity

The Fig. 3 presents the evolution of O^{6+} and Ar^{12+} A/Q=3 ion beams as a function of several ion sources plasma chamber volume. [7,8] Apart from any ECR heating frequency consideration, a clear volume effect is visible in the plot. One should note firstly the results obtained for Ar^{12+} beams at 18 GHz for three different source chamber volume: PHOENIX V2 (0.66 l), GTS (1.5 l) and SUSI (3.3 l) featuring a linear increase of the beam intensity as a function of the chamber volume (see red dashed line). It is clear that at a given ECR frequency, a higher chamber volume with the appropriate magnetic confinement provides a larger ECR surface. For a given power density, the ion production rate is thus enhanced due to the higher ECR surface in a larger volume ECRIS. A large plasma chamber volume also provides a higher confinement time for both ions and electrons since the particle trajectories along field lines are longer from wall to wall. Consequently, the charge state distribution shifts to higher charge states, which favours A/Q=3 beam production. The larger volume sources points plotted corresponds to SECRAL and VENUS, operated at higher frequency (24-28 GHz) with possibly a double frequency heating. One can note that the A/Q=3 beam intensity results obtained for these latter sources are lower what the frequency scaling law predictions. For instance, the 700 µA Ar^{12+} beam obtained with SUSI would correspond to ~1700 µA at 28 GHz, while the best result obtained so far is 860 µA with the VENUS source operated at 18+28 GHz. A part of this intensity difference may come from the difficulty to manage the beam extraction and

Copyright © 2012 CC-BY-3.0 and by the respective authors

ISBN 978-3-95450-123-6

transport of such high intensity beams (present high voltage limitation of existing sources, power supply drain current limitation, RF power limitation, increase of magnetized beam emittance,etc.). Obviously, the know-how at 18 GHz operation is much developed than at higher frequency, and possible improvement at 24-28 GHz may occur in the future.

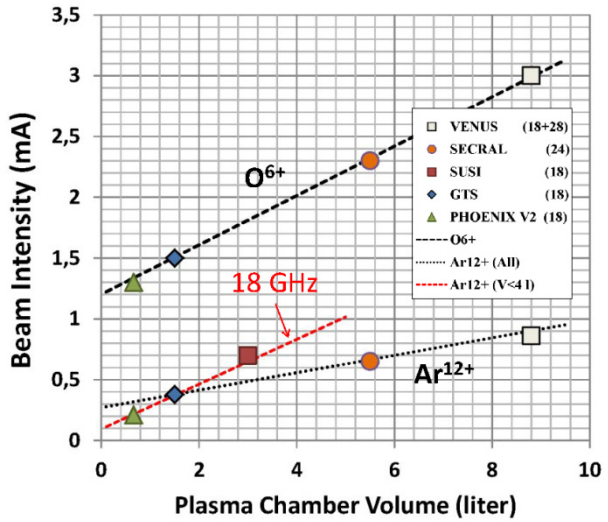

Figure 3: A/Q=3 beam current evolution for various ECRIS as a function of the chamber volume.

The PHOENIX V3 Upgrade

The prospect to improve the existing performance of the PHOENIX V2 source is of high interest for the SPIRAL2 physics experiments. Helped with the PHOENIX concept flexibility, a new serial source named PHOENIX V3 is under design to multiply the chamber volume by 2 with respect to the V2, keeping the magnetic confinement intensity at wall practically unchanged (see Fig. 2). The axial magnetic structure of the two series is practically identical in order to simplify the switch from V2 to V3. Thus, only the central HV core (composed of the two iron plugs, the hexapole and the plasma chamber) is changed. This will allow swapping the source core during operation, depending on the type of beam required by the physics: PHOENIX V2 for gas beams and PHOENIX V3 for metallic beams. The main difference between V2 and V3 is the inner radius of their permanent magnet hexapole (32 mm for V2 and 45 mm for V3). The two hexapole cross section views are displayed in Fig. 4. Both are classical Hallbach type hexapole with 36 magnets per turn. The V2 and V3 radial magnetic intensity at wall along the source axis z are plotted on Fig 4. The V2 hexapole features a hat sectional shape (see also Fig. 2) which delivers 1.35 T at the center and 1.1 T on both injection and extraction region. While the V3 profile is more homogeneous, with a flat intensity of 1.3T. The radial profile of V2 and V3 as a function of the radius is presented in the Fig. 6. the chamber walls are indicated by dashed lines for the two sources. One should note that the two hexapoles have the same outer diameter, since they both need to fit in the axial structure bore. The capacity to keep the V3 field intensity at R=45mm wall nearly identical to the V2's one at R=32 mm is obtained using the technique developed and checked on A-PHOENIX [6], technique in turn derived from the MMPS technique. [9] In V3, the inner stainless steel cylinder holding the permanent magnets is 1.5 mm thick and features 6 slits along the hexapole poles in which 6 mm large iron plates are welded. The iron plates fully saturate at 2.1 T and provide the requested 1.3 T intensity 2.5 mm away on the inner aluminum chamber cylinder wall as plotted on Fig.7. The plasma chamber cooling is performed by a water flow located between the two cylinders. A thin protection to prevent iron corrosion is foreseen. The inner aluminum cylinder would come apart for cleaning purpose. The V3 hexapole length is 270 mm, being 30 mm longer than the V2 one. The two axial iron plugs geometry has been modified accordingly to provide a higher radial intensity at wall at the axial peak fields locations (see Fig. 2 and 5).

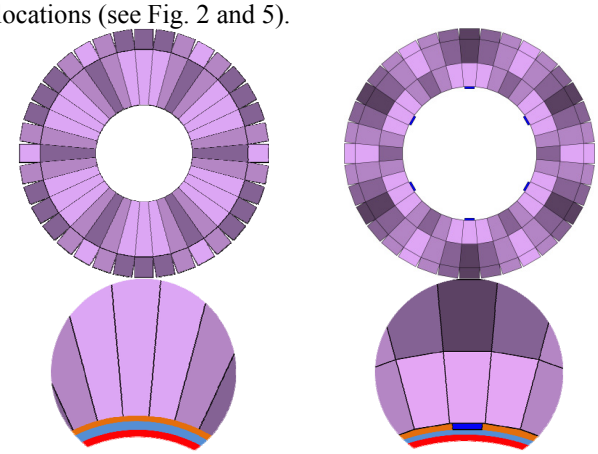

Figure 4: Up: Hexapole cross section of PHOENIX V2 (left) and V3 (right). Down: zoom on plasma chamber detail for V2 (left) and V3 (right).

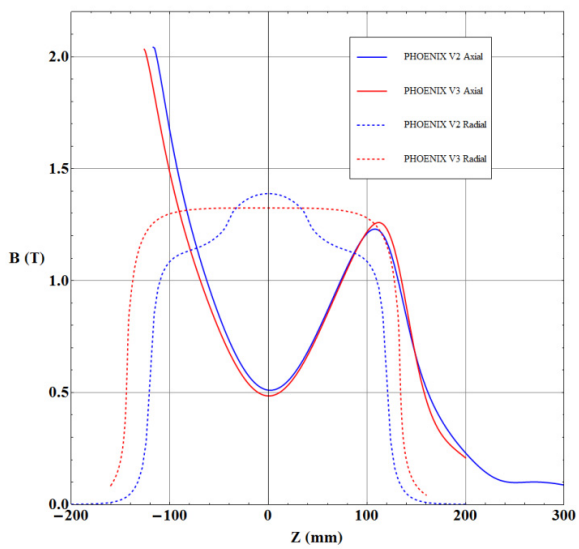

Figure 5: Axial (solid line) and radial (dashed line) magnetic field intensity along the source axis. Wall generated by the sole hexapole (dashed). Red and blue curves stand respectively for PHOENIX V3 and V2.

ISBN 978-3-95450-123-6

Copyright © 2012 CC-BY-3.0 and by the respective authors

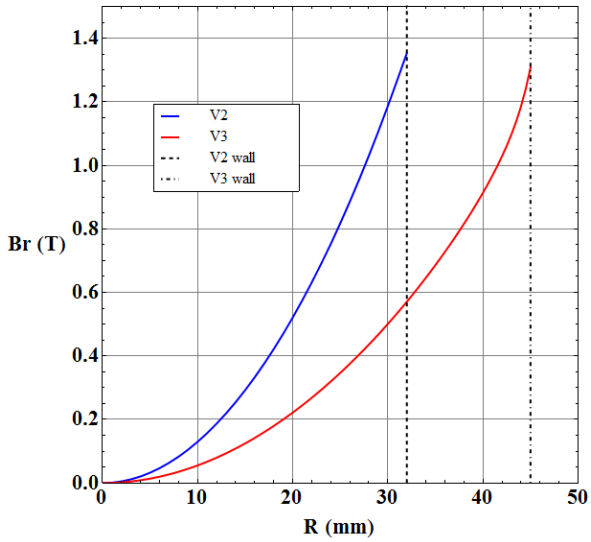

Figure 6: radial magnetic intensity in the center of the source generated by the hexapole as a function of the radius for PHOENIX V2 (blue) and V3 (red). Dashed lines stand for plasma wall position.

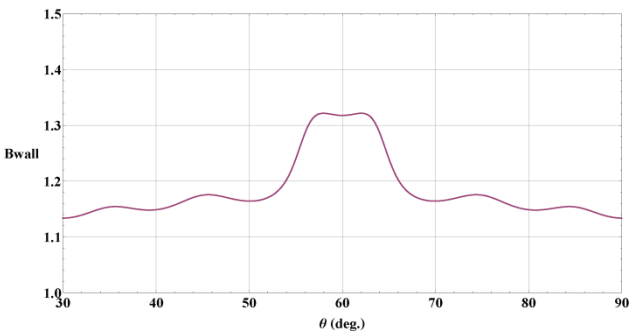

Figure 7: Magnetic boost along the wall induced by one the iron plates, as a function of the azimuthal angle (θ=60° is a main pole, next pole would be θ=120°, r=45 mm, Z=0 mm (centre of the source)).

FUTURE PROSPECTS

A comparison of the ability to produce and extract ions from both PHOENIX V2 and PHOENIX V3 will be performed by simulation in collaboration with GSI. This would give an interesting relative information on how the plasma chamber volume influences ion formation and extraction. The mechanical design study of PHOENIX V3 is foreseen to be completed by the first semester of 2013. The commissioning of the new source should begin during the second semester of 2013.

REFERENCES

[1] P. Sortais, J.-L. Bouly, J.-C. Curdy, T. Lamy, P. Sole, T. Thuillier, J.-L. Vieux-Rochaz, and D. Voulot, Rev. Sci. Instrum. **75**, 1610 (2004).

[2] T. Thuillier, T. Lamy, C. Peaucelle, P.Sortais, Rev. Sci. Instrum. **81**, 02A316 (2010).

[3] T. Thuillier, J.-L. Bouly, J.-C. Curdy, E. Froidefond, T. Lamy, C. Peaucelle, P. Sole, P. Sortais, J.L. Vieux-Rochaz, D. Voulot, Proc. of 8th European Particle Accelerator Conference, Paris, France, June 2002, www.jacow.org

[4] P. Lehérissier, F. Lemagnen, C. Canet, C. Barué, M. Dupuis, J. L. Flambard, M. Dubois, G. Gaubert, P. Jardin, N. Lecesne, R. Leroy, and J. Y. Pacquet, Rev. Sci. Instrum. **77**, 03A318 (2006).

[5] T. Lamy, J. L. Bouly, J. C. Curdy, R. Geller, A. Lacoste, P. Sole, P. Sortais, T. Thuillier, J. L. Vieux-Rochaz, K. Jayamanna, M. Olivo, P. Schmor, and D. Yuan, Rev. Sci. Instrum. **73**, 717 (2002).

[6] T. Thuillier, T. Lamy, P. Sortais, P. Suominen, O. Tarvainen, and H. Koivisto, Rev. Sci. Instrum. **77**, 03A323 (2006).

[7] T. Thuillier, J. Angot, C. Barué, T. Lamy, P. Lehérissier, F. Lemagnen, C. Peaucelle, Rev. Sci. Instrum. **83**, 02A339 (2012).

[8] G. Machicoane, Private communication during the 11th International Conference on Ion Sources, Giardini Naxos, 2011.

[9] H. Koivisto, P. Suominen, O. Tarvainen, and D. Hitz, Rev. Sci. Instrum. 75, 1479 (2004).

Copyright © 2012 CC-BY-3.0 and by the respective authors

ISBN 978-3-95450-123-6

RELATIONSHIP OF PERFORMANCE AND RF MODES IN ECR ION SOURCE

T. Hattori, A. Kitagawa, M. Muramatsu, National Institute of Radiological Science, Anagawa, Inage, Chiba-City, 263-8555 Japan
N. Hayashizaki, A. Takano, Tokyo Institute of Technology, Ookayama, Meguro-ku, Tokyo, 152-8550 Japan

Abstract

The performance of Electron Cyclotron Resonance (ECR) ion source depends on the operation frequency, the magnetic mirror field, the hexapole fields, the mirror ratio, the ECR zone. We studied the relationship of performance and operation frequency in ECR ion source. The performance (beam intensity of Ar^{9+} ion) was measured according to change of frequency from 9.7 to 11.7 GHz in fixed magnetic field of a new ECR (FM-ECR) ion source. We measured resonant frequencies of plasma chamber of the FM-ECR ion source in condition of no plasma (current of mirror coils is zero). The data of intensity of Ar^{9+} related to measured resonant frequencies. Their resonant modes were checked with a 3D electromagnetic simulator. As a result, it became clear that the performance of the ion source depends on electric field distribution of the RF resonant mode.

INTRODUCTION

We studied new ECR (Electron Cyclotron Resonance) ion source for production of full stripped heavy ion. This type ECR ion source is operated by high energy electron which is accelerated by same principle of frequency modulated (FM) Cyclotron. This ion source is named FM-ECR ion source. In experiment with this ion source, we fund that current of higher charge state ions depends on frequency of micro-wave. This phenomena is not so good for production of high energy electron in the FM-ECR ion source by input micro-wave power depending on frequency. Therefore an aim of FM-ECR ion source was not succeeded. Then, measurement of frequency dependence for production of high charge ion started with the FM-ECR ion source. Performance of ECR ion sources depends on the operation frequency, the magnetic field, the hexapole field, the mirror ratio, the magnetic profile and the length, surface and volume of ECR zone . Characteristic of RF modes in ECR ion source were not studied before for very complex mode. Simple RF modes were studied previously by LBL and Catania [1-3]. The relationship of frequency tuning and RF mode are studying several institute [4-6]. We studied relation of between currents of high charge ion and frequency of RF mode using the FM-ECR ion source.

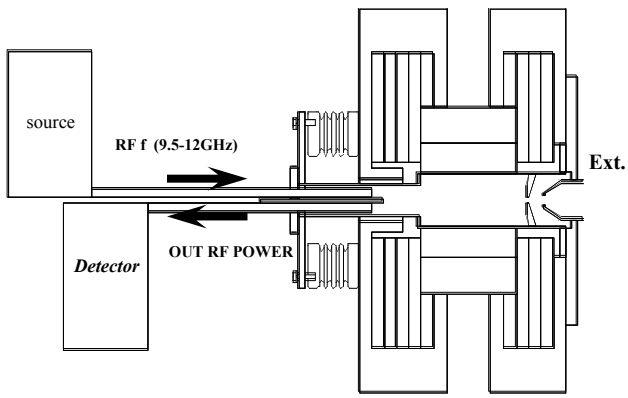

Figure 1: Experimental Apparatus and FM-ECR ion source.

Table 1: Main Parameters of FM-ECR Ion Source

	HiECR (Previous)	Present Status
Microwave Power source		
Frequency (GHz)	10-18	10-12
Power (W)	250	100/250
RF injection port	1	2
Diameter (mm) of Plasma Chamber		
RF injection side	38	
Extraction side	72	
Length (mm)		
RF injection side	77.5	
Extraction side	173.5	
Total length	251	
Hexapole Magnet		
Field on chamber (kG)	11.4	
Material	42N	
Inner diameter (mm)	76-82	
Length (mm)	145	
Mirror Field		
Maximum field on axis (kG)	9.6	7.8
Maximum coil current (A)	600	425
Maximum power (kW)	60	30

Copyright © 2012 CC-BY-3.0 and by the respective authors

ISBN 978-3-95450-123-6

FM-ECR ION SOURCE AND EXPERIMENTAL APPARATUS

The FM-ECR ion source is a miner change from HiECR ion source [7-9]. The FM-ECR ion source and experimental apparatus are shown in Fig. 1. Two microwave guides (19x9.5mm (WRJ 120)) of upper and lower side were connected flange of RF in jection. The flange has a quartz tube of gas feed in center.

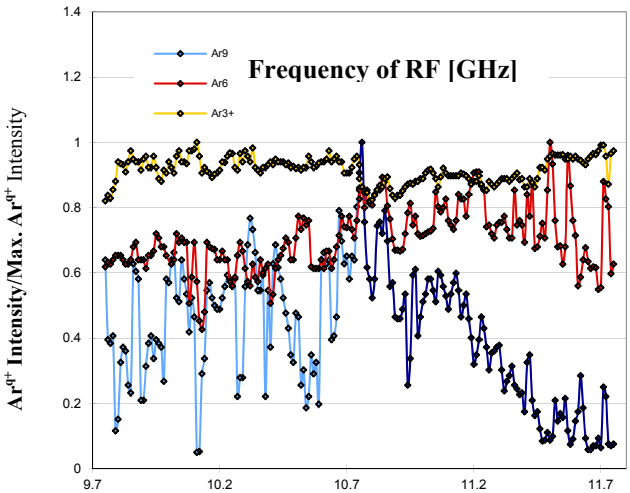

Figure 2: Ar^{q+} Intensity vs RF frequency (Ar^{q+}intensity (*normalized by maximum c urrent, respectively*) vs RF frequency).

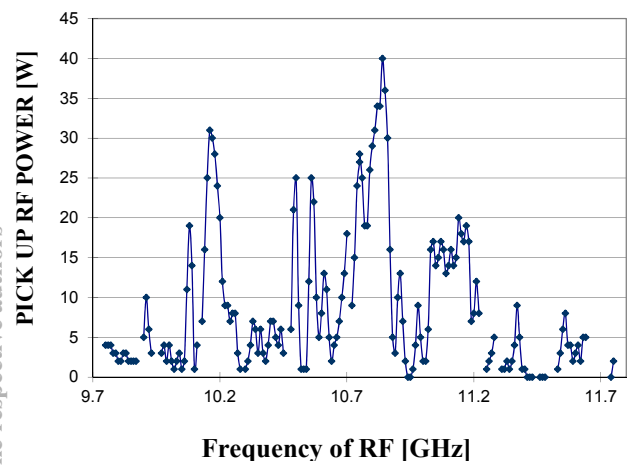

Figure 3: Measured pick up voltage strength of plasma chamber vs RF frequency.

(Measured beam intensity of Ar^{9+} (normalized by maximum current (peak4)) and resonance strength power (W) (normalized by maximum power (peak9)) of plasma chamber vs RF frequency.)

The RF power from microwave power source was transported with the upper waveguide. In resonant frequency measurement without plasma, the lower wave-guide was used as electro-magnetic pick up of the plasma coupler of microwave amplifier. Main parameters of this ion source are shown in Table 1. The e xperiments were studied in mirror coils condition of about 10.7 GHz operation.

EXPERIMENT AND DATA

Beam intensity of Ar^{9+}, Ar^{6+} and Ar^{3+} were measured according to change of frequency from 9.7 to 11.7 GHz produced by microwave amplifier from CPI Company in fixed magnetic field operation of the FM-ECR ion source by magnetic analyser. These data are shown in Fig. 2. The frequency deference of intensity is increased according as higher charge-state of Ar ion. Inte nsity of Ar^{9+} ion has many resonance peaks. This phenomena is very interesting problem. Output RF power of CPI amplifier depends on reflected power of plasma chamber and control it self. Th is control is v ery complex. Therefore, we measured again beam intensity of Ar^{9+} ion using microwave amplifier of Xicom Company which gives constant output power. Beam intensity of Ar $^{9+}$ is shown inside of Fig.3. The experiments were st udied in mirror coils condition of about 10.7 GHz operation.

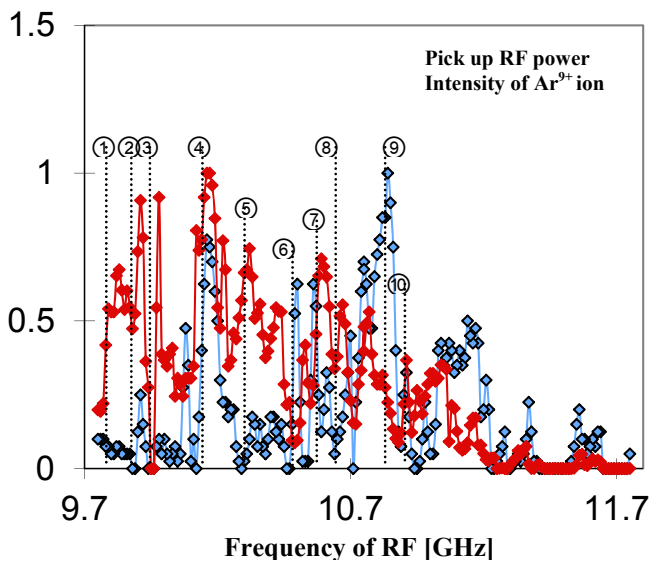

Figure 4: Measured Beam intensity of Ar^{9+} and Pick up voltage strength of plasma chamber vs RF frequency.

This phenomena is v ery interesting problem. Therefore, resonant frequency of the plasma chamber of FM-ECR ion source was measured without plasma (zero current ofmirror coils) by two wave-guide system as shown in Fig.1. RF power of 100 W from Xicom

Copyright © 2012 CC-BY-3.0 and by the respective authors

ISBN 978-3-95450-123-6

amplifier transported to chamber with upper wave-guide. And the pick-upped power with lower wave-guide is detected by directional-coupler of RF source. This RF pick-up method is ordinal measurement of RF characteristics of linear accel erator cavity. The value of pick-up means resonant strength of empty cavity of ECR ion source. M easured data are shown inside of Fig. 3. These resonant peaks are not sam e peaks of Ar^{9+} ion current. The intensity of Ar^{9+} ion and pick up RF power are in Fig. 4 on same frequency a xis. Typical peaks of intensity of Ar^{9+} and resonance strength of plasma chamber are labeled peak num ber for data analysis. Resonant peak of RF modes mean that electromagnetic field of the peak is high on constant injection RF power. Their resonant modes were checked with a 3D electromagnetic simulation (High Frequency Structure Simulator (HFSS)) program.

COMPARISON OF COMPUTER SIMULATION OF RF MODES AND EXPERIMENTAL DATA

Current intensity of Ar^{9+} and resonant frequencies were measured. But resonant peaks are not same peaks of Ar^{9+} ion current. Their resonant modes were c hecked with a 3D electromagnetic simulator HFSS(only electromagnetic program without plasma) program. The labeled peaks are assigned compare with elect ric field distribution of simulated RF resonant mode of near frequency. As a result, it beca me clear that the performance of t he ion source depends on electric field distribution of the RF resonant mode. Numbers of simulated resonance are about 200 in reason from 9.7 to 11.7 GHz.

In labelled peaks, relationship of peaks of Ar^{9+} intensity, pick up RF power and simulated resonant mode are shown in table 2. Characteristic of RF-mode of typical labeled peaks by HFSS calculation are show in Fig.4-6. We can't understand clearly now proof of that these frequency coincide with peaks Ar^{9+} intensity related ECR plasma and R F resonance characteristics of em pty chamber. But these frequencies coincide with Ar^{9+} intensity and simulated resonance mode by 3D electromagnetic simulator HFSS program.

A good electric field distribution of the RF resonant mode on ECR zone produces high current ion beams as shown in Table-2 and Fig.4-6. We measured higher Ar^{9+} currents for peaks (2), (3) and (4). The RF resonance strength for peak (4) is good, but for peaks (2) and (3) it is very low.

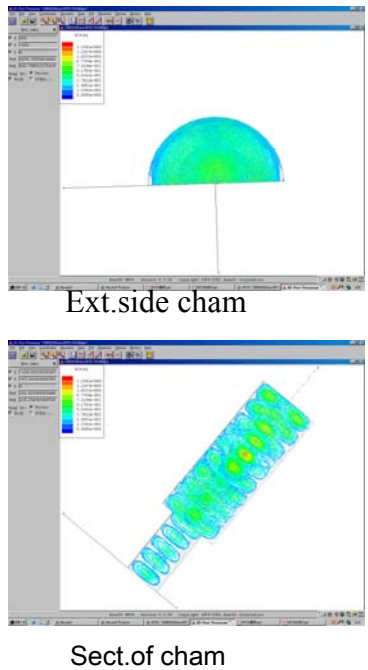

Figure 5: Electric Distribution of (2) HFSS
Detected RF resonance frequency : 9.91[GHz]
Ar9+ intensity peak frequency 9.91 [GHz]
HFSS simulated frequency 9.929[GHz]
Resonant mode:
Injection side:TE_{115}, Extraction side:TE_{115} andTE_{128}

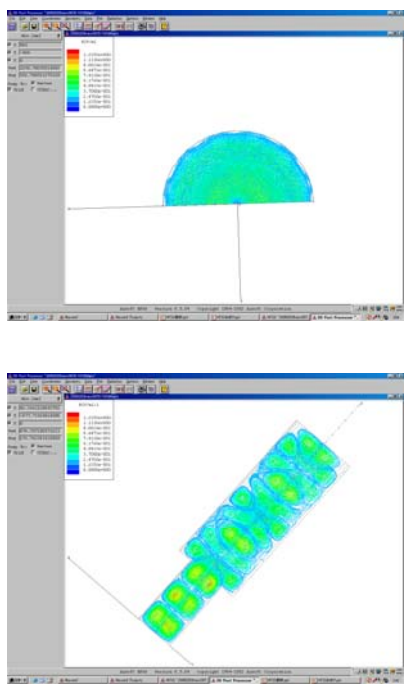

Figure 6:Electric Distribution of (4) HFSS
Detected RF resonance frequency : 10.16[GHz]
Ar9+ intensity peak frequency 10.165[GHz]
HFSS simulated frequency 10.166[GHz]
Resonant mode:
Injection side:TE_{013} Extraction side:TE_{01n} and TE_{02n}

ISBN 978-3-95450-123-6

Copyright © 2012 CC-BY-3.0 and by the respective authors

We think that resonance mode TE_1 or TE_2 of peaks (2) and (3) are better compared by resonance mode TE_0 of peak (4) for effective acceleration of electron (energy and intensity). If a plasma chamber having high resonance-strength similar resonance mode of peaks (2) and (3) is made, making ECR ion source of best performance will be succeeded input RF power of frequency of resonance mode TE_1 or TE_2. Best performance of ECR ion source must have two conditions (frequency of good electric field distribution of the resonance mode and high resonance-strength of plasma chamber). But above reason, good electric field distribution of resonance mode is more important condition. Therefore, peak (9) is not good performance as shown in Fig.3 and Fig.6.

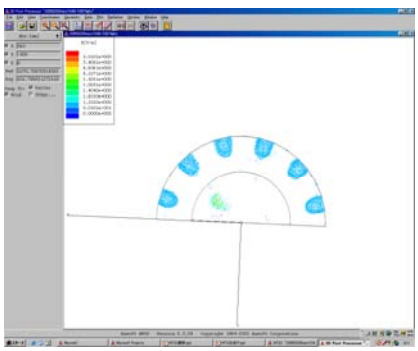

Ext.side cham.

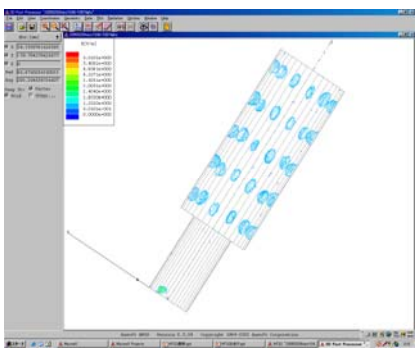

Sect. of cham.

Figure 7: Electric Distribution of (9) HFSS
Detected RF resonance frequency :10.84[GHz]
Ar9+ intensity peak frequency 10.82[GHz]
HFSS simulated frequency 10.874[GHz]
Resonant mode:
Injection side: no resonance Extraction side:TE_{614}

Table 2: Relationship of Peaks of Ar^{9+} Intensity, Detected RF Power and Characteristics of Resonance Modes

Peak(N) f(GHz)	Detected Pow.(W)	Ar^{9+} e10^{-6}A	1st ECR zone	Inj.cham. RF Mode	Ext. cham RF Mode
I 9.83	3	3.3	Yes	TE_{012}	TE_{01},TE_{02n}
2 9.92	10	4.45	Yes	TE_{115}	TE_{128}
3 9.97	4	4.5	Yes	TE_{214}	TE_{225}
4 10.16	31	4.9	Yes	TE_{013}	TE_{01},TE_{02n}
5 10.32	7	3.69	Yes	TE_{013}	TE_{025}
6 10.50	25	-	No	-	TE_{419}
7 10.56	25	-	No	-	TE_{614}
8 10.61	13	3.48	Yes	TE_{013}	TE_{026}
9 10.85	40	1.55	No	-	TE_{615}
10 10.91	13	1.8	Yes	TM_{114}	$TM_{12,11}$

SUMMARY

We studied the relationship of performance and operation frequency in ECR ion source. The performance of intensity of Ar^{9+} ion was measured according to change of frequency from 9.7 to 11.7 GHz in FM-ECR ion source. We measured resonant frequencies of plasma chamber of the FM-ECR ion source in condition of without plasma. Their resonant modes were checked with a 3D electromagnetic simulator (HFSS). As a result, it became clear that the performance of the ion source depends on electric field distribution of the RF resonant mode. If these phenomena are true, the resonance strength is strong, but in RF mode of not so good electric field distribution, the intensity of high charge ion is low. Electric field distribution of RF mode (main TE mode) is good and resonant strength is strong, performance of ECR ion source is best. Therefore we will be able to design good performance ECR ion source on these 2 conditions. But this condition depends on ECR zone and magnetic field. We will study relationship of performance, ECR zone and magnetic field.

REFERENCES

[1] C.M.Lyneis, Proc. of International Cnference on ECR Ion Sources and Applications, NSCL REPORT MSUCP-47 (1987) 47-56.
[2] C.M.Lyneis, LBL report, 32649,US413(1992)
[3] L. Celona, et al., Rev. of Sci. Instrum., 79, 023305 (2008)
[4] V. Toivanen, et al., Rev. of Sci. Instrum., 81, 02A319 (2010)
[5] D. Mascali, et al., Rev. of Sci. Instrum., 81, 02A334 (2010)
[6] F.Maimone, et al., Rev. of Sci. Instrum., 82, 12302 (2011)
[7] T.Hattori, T. Katayose et al., Proc. of the 12th International Workshop on ECR Ion Source, INS-J-182 (1995) 277-280.
[8] T.Katayose, T. Hattori, S. Yamada, K. Kitagawa and M. Sekiguchi, Proc. of the 12th International Workshop on ECR Ion Source, INS-J-182 (1995) 281-283.
[9] T.Hattori, T. Katayose et al., Rev. of Sci. Instrum., 67 (1996) 1186-1188.

Copyright © 2012 CC-BY-3.0 and by the respective authors

ISBN 978-3-95450-123-6

PLASMA INSTABILITY IN THE AFTERGLOW OF ECR DISCHARGE SUSTAINED IN A MIRROR TRAP

I. Izotov[1], D. Mansfeld[1], V.Skalyga[1], V. Zorin[1], T. Grahn[2], T. Kalvas[2], H. Koivisto[2], J.Komppula[2], P. Peura[2], O. Tarvainen[2] and V. Toivanen[2]
1 Institute of Applied Physics, RAS, 46 Ulyanov st., 603950 Nizhny Novgorod, Russia
2 University of Jyväskylä, Department of Physics, P.O. Box 35 (YFL), 40500 Jyväskylä, Finland

Abstract

The investigations of plasma decay in ECR heated discharges confined in a mirror magnetic trap is actively studied subject for many years. The motivation of this work is to study plasma instabilities causing perturbations of ion current during the plasma decay.

Present work is devoted to time-resolved diagnostics of non-linear effects observed during the afterglow plasma decay of an 14 GHz Electron Cyclotron Resonance Ion Source (ECRIS) at JYFL operated in pulsed mode. Plasma instabilities causing perturbations of extracted ion current during the decay were observed and studied. It is shown that these perturbations are associated with precipitation of high energy electrons along the magnetic field lines and strong bursts of bremsstrahlung emission. The effect of ion source settings on the onset of the observed instabilities was investigated. Based on the experimental data and estimated plasma properties it is assumed that the instabilities are of cyclotron type. The conclusion is supported by a comparison to another type of plasma devices (SMIS 37, IAP RAS) exhibiting similar characteristics but operating in a different plasma confinement regime.

INTRODUCTION

A number of studies have been devoted to the investigations of plasma decay in ECR heated discharges confined in a mirror magnetic trap (e.g. refs. 1-4). The motivation of this work is to study plasma instabilities causing perturbations of ion current during the plasma decay. The initial transient peak observed during the afterglow plasma decay has been successfully utilized for injection to circular accelerators of heavy particles[5]. The ejection of multicharged ions during the plasma decay is related with its strong nonequilibrium state. ECR plasma heating results to complex non-equilibrium velocity distribution of electrons. In addition, the electron and ion components of plasma are confined in the magnetic trap differently due to significant difference of collision rates. Plasma non-equilibrium state continues to grow after switching off the microwave pulse due to loss cone scattering depending on electron energy, which in particular can cause instabilities described e.g. in Refs. 6-9. Strongly non-equilibrium velocity distribution of electrons confined in mirror magnetic trap can be found in Earth's magnetosphere10 as well as in plasma generators driven by high frequency microwave radiation. Thus, the investigations described in the present paper have rather wide range of applications. The main focus of this work is determining the reasons of apparent perturbations of ion current extracted from plasma during the afterglow of ECR discharge. It is obvious that these perturbations are related to plasma instabilities. The temporal correlation of these perturbations and peaks of bremsstrahlung emission was suggested in ref. 11. Bremsstrahlung and characteristic X-rays are produced by collisions of fast electrons in plasma and with vacuum chamber walls, the latter being the dominant process. Ejection of electrons from the plasma to the walls is evidently related with changes in confinement of fast electrons whose lifetime in quiescent plasma amounts to seconds. Ejection of fast electrons (> 100 keV) from a mirror trap in afterglow mode has been studied in refs. 7 and 12. It was demonstrated that as a result of development of cyclotron instability fast electrons interacting with electric field of plasma waves could enter the loss cone and abandon the trap. The instantaneous current of such electrons, expelled in bursts of less than 200 ns, can be substantial. It is hypothesized in this paper that ion current perturbations, peaks of bremsstrahlung radiation and ejection of fast electrons from the trap are consequences of a single phenomenon, and are related with the evolution of cyclotron instability in strongly non-equilibrium plasma in afterglow of ECR discharge. To confirm this hypothesis a detailed study of temporal behavior of extracted ion currents, bremsstrahlung emission and fast electrons expelled from afterglow plasma was carried out.

EXPERIMENTAL SETUP

The experimental data were taken using the JYFL 14 GHz ECRIS[13]. The source uses an Nd-Fe-B permanent magnet sextupole arrangement and solenoid coils forming a minimum-B structure for confinement of the plasma. The strength of the sextupole field on the wall of the plasma chamber is 0.95 T. Plasma electrons are heated by 50 - 800 W of microwave power at 14.085 GHz. Typical operating neutral pressures are in the 10^{-7} mbar range. The main parts of the setup are a 14 GHz klystron amplifier with a rise and fall times of < 10 μs and < 40 μs, a fast RF-switch with a rise time of 40 ns controlling the incident power, dedicated electron detector with attenuating foils mounted downstream from the plasma electrode, Germanium x-ray/gamma ray detector equipped with a lead collimator structure, TNT2 digital signal processing unit[14]. The Ge-detector arrangement is suitable for studying the temporal behavior of

ISBN 978-3-95450-123-6

Copyright © 2012 CC-BY-3.0 and by the respective authors

bremsstrahlung emission but does not yield direct information on the plasma electron energy distribution. At a later stage of experiments the electron detector was removed to allow extracting ions and recording the temporal evolution of the charge state distribution.

A detector recording the current of electrons, escaping the magnetic confinement through the 8 mm extraction aperture, consists of an array of aluminum foils, each of them occupying a 10 mm aperture, suppression electrode and Faraday cup. The aluminum foils were assembled on a movable cradle whose position could be adjusted through a vacuum feedthrough. Foils of varying thickness were used for the experiments to provide a crude energy resolution for the detection of escaping electrons. The foil thicknesses and corresponding (approximate) energy thresholds for perpendicular angle of incidence are listed in Ref. 15.

The electron detector was positioned 205 mm downstream from the extraction aperture (location of the foil) where the magnetic field strength has decreased to approx. 4% compared to the extraction mirror. It can be assumed that the flux of magnetized electrons is reduced by a comparable factor. The effect of the magnetic field on electron trajectories and velocity components has been neglected when calculating the threshold energies. Consequently all the data were recorded using residual gas (mainly oxygen and nitrogen) mixed with a small amount of oxygen keeping the pressure constant at about $4 \cdot 10^{-7}$ mbar throughout the experiments. The bremsstrahlung radiation was measured radially from one of the magnetic poles of the sextupole structure. The detector line-of-sight was located between the solenoids. Thus, the bremsstrahlung observed by the Ge-detector is a mixture of thick target (wall) and plasma bremsstrahlung. Because the focus of the experiments was to study the temporal evolution of the bremsstrahlung, no special attention was paid in optimizing the collimator structure, which results to a significant contribution from Compton scattering. For this reason, only time-resolved (normalized) total count rates integrated over the energy range of the detected photons are presented in this article. During the analysis data from ~ 102 - 105 rf pulses were combined to gain statistics. The ion beam currents of different charge states of Oxygen were measured with a Faraday cup downstream from a bending magnet (M/Q analysis). An extraction voltage of 10 kV was applied. At the corresponding energy the ion time-of-flight from the ion source to the Faraday cup is on the order of 10^{-6}–10^{-5} s. The purpose of measuring the ion currents of various charge states was to study their (typical) temporal correlation with bremsstrahlung emission and escaping electron flux.

THE MAIN RESULTS

Figure 3 shows the temporal evolution of high charge state oxygen ion currents during the afterglow. Hereinafter t=0 corresponds to the end of microwave pulse. The given example was obtained with 500 W microwave power (2 Hz, 50 % duty factor), solenoid magnetic field profile (injection / minimum / extraction) of Binj = 1.95 T, Bmin = 0.32 T and Bext = 0.90 T and neutral oxygen pressure of $4.2 \cdot 10^{-7}$ mbar. Rather slow plasma decay with characteristic time of approximately 20 ms is interrupted by fast current drops with characteristic time less than 1 ms. Such temporal behavior of current could be related with a plasma instability resulting in abrupt change of lifetime and/or loss pattern of multicharged ions.

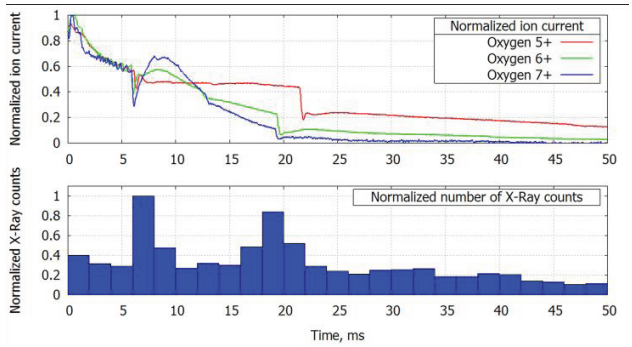

Figure 1. Ion currents of oxygen ions (upper curves) and normalized bremsstrahlung count rate (lower curve) during the afterglow plasma decay.

The figure also shows the temporal behavior of bremsstrahlung counts measured with the Ge-detector. The counts are summarized over 2 ms, averaged over 750 pulses in photon energy range from 30 keV to 1.2 MeV. It can be seen that significantly higher number of counts are detected during fast perturbation of ion beam current. Detected radiation is mainly related with collisions of fast electrons with vacuum chamber wall (wall bremsstrahlung). Formation of a fast electron population in magnetically confined ECR-heated plasma has been studied in number of articles (see, e.g., ref. 17) where it was demonstrated that under ECR heating energy of electrons may reach relativistic values. So, the abrupt peaks of bremsstrahlung are presumably related with pulsed ejection of energetic electrons as suggested in ref. 11.

Direct measurement of fast electron flux from the JYFL 14 GHz ECRIS was carried out first time with the combination of Faraday cup and set of aluminum foils. An example of corresponding temporal plot is shown on Figure 2. In this case the microwave power of 200 W was pulsed with 20 Hz / 50 % duty factor. The magnetic field profile and neutral gas pressure were Binj = 1.95 T, Bmin = 0.32 T and Bext = 0.90 T and 4.0·10-7 mbar, respectively. The data represents the time-average of 100 microwave pulses. After the microwave power is switched off the detected electron current first falls rapidly - in less than 1 ms - and then exhibits slower decay. The abrupt fall of the fast electron flux is very different from the behavior exhibited by ions extracted from the afterglow plasma. Short and repeatable peaks of electron signal with significant magnitude can be observed superimposed on the “background” of slow decay. Similar qualitative behavior was observed

Copyright © 2012 CC-BY-3.0 and by the respective authors

ISBN 978-3-95450-123-6

independent of the ion source settings. Only the number of periodic instabilities and their temporal spacing were affected by the source parameters. A single peak of afterglow fast electron burst measured without any foil and with high temporal resolution (across a resistor) is presented in Figure 3. The duration of the burst (FWHM) is on the order of 100 ns. The magnitude of the electron current has been normalized with respect to the saturation value obtained during the microwave pulse. The fine structure of the peak cannot be resolved due to limited bandwidth of the oscilloscope (100 MHz) and stray capacitance of the cables. Thus, the given width of the peak (100 ns) represents the upper limit of the duration of the electron burst.

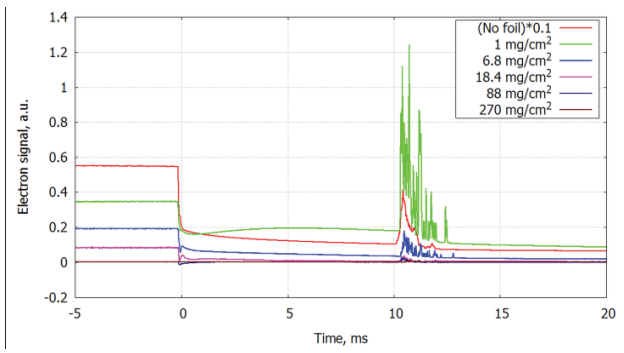

Figure 2: Electron current signal from the Faraday cup with different aluminum foils.

It can be observed that as the solenoid magnetic field strength is increased the first afterglow instability occurs closer to the trailing edge of the microwave pulse. Similar trend appears with increasing microwave power.

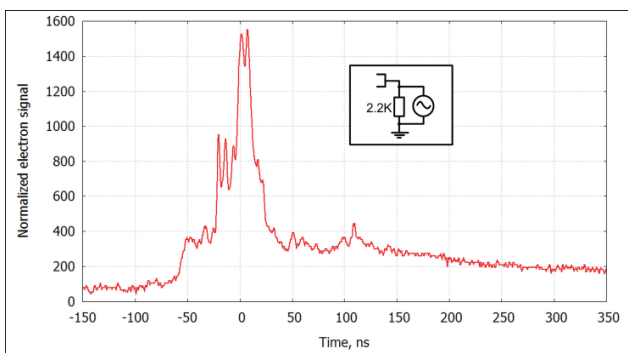

Figure 3: Afterglow electron burst signal with high temporal resolution. Acquisition method is shown in the figure schematically, t=0 corresponds to an oscilloscope trigger moment.

Escaping electron flux was also measured simultaneously with temporal behavior of bremsstrahlung radiation (count rate at energies ranging from 30 keV to 1 MeV). An example measured with 6.8 mg/cm^2 foil is presented in Figure 4. The electron signal has been normalized with respect to the value reached at the trailing edge of the microwave pulse. The corresponding ion source settings in this case were 200 W pulsed with 20 Hz, 50 % duty factor, $4.1 \cdot 10^{-7}$ mbar neutral gas pressure and magnetic field profile of Binj = 2.01 T, Bmin = 0.35 T and Bext = 0.95 T. Data in both plots were averaged over more than 105 pulses to gain statistics and achieve high temporal resolution. Due to a slight temporal shift of the onset of the instability from pulse to pulse, the duration of averaged pulse exceeds the actual duration of fast electron pulse. The figure highlights the coincidence of the bremsstrahlung and electron bursts.

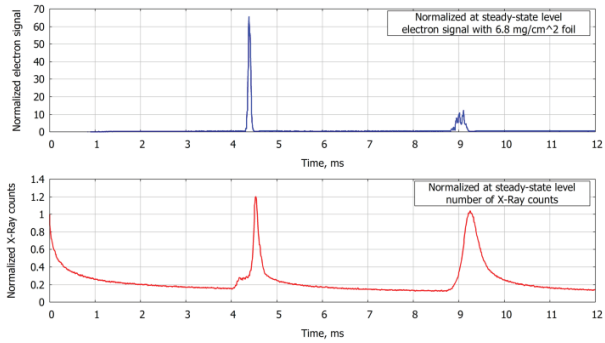

Figure 4: Temporal behavior of electron flux (upper curve) and bremsstrahlung (lower curve).

The energy of fast electrons was estimated from the difference of currents measured with the Faraday cup through various foils. Unfortunately, the signals associated with the electron bursts were strong enough to saturate the data acquisition system for the majority of the pulses. Thus, the lack of data at low electron energies prohibits plotting an energy spectrum. However, it can be estimated that the upper limit for the average electron energy within the instability peaks is in the range from 49 to 60 keV. The existence of relativistic electrons was observed as the Faraday cup current even with the thickest foil i.e. 270 mg/cm^2 / 570 keV threshold energy.

DISCUSSION

The observed particle ejections from the trap have much in common with pulsed precipitations of hot electrons from the decaying plasma of ECR discharge in a mirror magnetic trap described in previous studies (refs. 6-9). These experiments were carried out using 37 GHz 100 kW pulsed gyrotron with pulse duration up to 1 ms and simple mirror magnetic trap with maximum field Bmax=1.8 T and mirror ratio of 5, confining plasma in gas-dynamic (collisional) regime. Precipitations of hot electrons from the magnetic trap detected by pin-diode appeared 600 μs after MW trailing edge. Basically, the electron distribution function formed by ECR discharge can be considered to be comprised of at least two fractions: (1) less dense “hot” component with strongly anisotropic velocity distribution function, i.e. significantly higher transverse electron energy in comparison to longitudinal energy, and (2) dense “cold” component with lower level of anisotropy (or even isotropic, depending on plasma parameters). The dense plasma component determines dispersion relation and damping of propagating waves, which can resonantly interact with energetic electrons. The anisotropy of the hot component

ISBN 978-3-95450-123-6

Copyright © 2012 CC-BY-3.0 and by the respective authors

ensures the growth of electron cyclotron plasma instabilities. The precipitations of hot electrons, observed in ref. 9, were identified to be a consequence of cyclotron instability of a slow extraordinary wave propagating across the magnetic field. Interaction of hot resonant electrons with this electromagnetic wave, exponentially increasing at the linear stage of instability, reduces their transverse energy[18]. As a result, some hot electrons enter the loss cone and leave the trap. During ECR discharge these instabilities are suppressed by phenomenon referred in the literature as depression of cyclotron radiation at gyro-frequency in dense plasma (see e.g. ref. 19). After switching off the microwave pulse the density of the "cold" electron fraction decreases rapidly in the decaying plasma due to Coulomb collision induced loss cone scattering, while the hot electrons with an anisotropic velocity distribution function are confined in the magnetic trap much longer. Therefore, starting from a certain time, the density of the hot component can become equal to or even higher than the density of the cold component. The growth of instabilities becomes possible in rarefied plasma when the plasma density becomes low enough, so that the electron plasma frequency is much less than the electron gyro-frequency. The periodic excitation of electromagnetic waves at frequencies near the electron gyro-frequency which propagate perpendicularly to the magnetic field and cause precipitation of energetic electrons have been observed recently[9]. It seems logical to argue that pulsed electron precipitations described in refs. 6-9 and those observed in the present work are of the same origin as the characteristics of the oscillograms are similar: (i) electron precipitations are generated as pulses (bursts) with a duration of ~ 10^{-7} s, (ii) the delay between the trailing edge of the microwave pulse and the first electron burst exceeds the cold plasma confinement time, (iii) amplitude of the electron (and bremsstrahlung) signal during the instability often overcomes the steady-state value. It is of note that the experimental conditions in the two experiments (this paper and ref. 9) are significantly different, the most important distinction being the operational regime i.e. classical (collisionless) vs. gas-dynamic confinement. Thus, it has been experimentally shown that the nature of the described instability mechanism is rather universal. These facts let us assume that observed phenomena is the result of resonant interaction between hot electrons and electromagnetic waves in rarefied plasma.

Temporal coincidence of electron and X-ray bursts as well as ion current perturbations during the afterglow plasma decay indicates that all of them are driven by the same mechanism. The number of electrons, i.e. amount of negative charge, expelled by the instability-driven plasma waves could be sufficient to affect the ambipolar potential. It is straightforward to assume that as a result of the cyclotron instability this imbalance is momentarily amplified causing perturbations of ion currents. Identifying the exact mechanism of ion current fluctuation requires further research. However, it has been clearly demonstrated that the driving mechanism of afterglow plasma perturbations is the onset of cyclotron type electron instabilities resulting to transient peaks of electron flow from the trap, bremsstrahlung emission and fluctuation of ion current.

ACKNOWLEDGEMENTS

This work has been supported by the EU 7th framework programme "Integrating Activities - Transnational Access", project number: 262010 (ENSAR) and by the Academy of Finland under the Finnish Centre of Excellence Programme 2012-2017 (Nuclear and Accelerator Based Physics Research at JYFL) and researcher mobility grants 253482 and 253173. This work has also been supported by federal targeted program "Scientific and pedagogical labor force for an innovative Russia" for 2009 – 2013 yy and by Russian Foundation for Basic Research (RFBR), grant # 10-02-00646.

REFERENCES

[1] C J Lasnier, R F Ellis, G D Tsakiris, R A James and T A Casper. Plasma Phys. Control. Fusion **30**, 491 (1988).

[2] V. Guerra, F.M. Dias, J. Loureiro, Sa. Paulo Araujo, P. Supiot, C. Dupret, T. Popov. IEEE Transactions on Plasma Science, **31** (4), 542 (2003).

[3] V.V. Alikaev, V.M. Glagolev, S.A. Morosov, Plasma Phys. **10** (8), 753 (1968).

[4] R.C. Garner, M.E. Mauel, S.A. Hokin, R.S. Post and D.L. Smatlak, Phys. Rev. Lett. **59** (16), 1821 (1987). 11

[5] C.E. Hill and K. Langbein, Rev. Sci. Instrum. **69**, 643, (1998).

[6] A.V. Vodopyanov, S.V. Golubev, A.G. Demekhov, V.G. Zorin, D.A. Mansfeld, S.V. Razin, and A.G. Shalashov. JETP, **104** (2), 296 (2007).

[7] A.G. Shalashov, A.V. Vodopyanov, S.V. Golubev, A.G. Demekhov, V.G. Zorin, D.A. Mansfeld, and S.V. Razin. JETP Letters, **84** (6), 314 (2006).

[8] M.E. Viktorov, S.V. Golubev, E.D. Gospodchikov, I.V. Izotov, D.A. Mansfeld, A.G. Shalashov, A.V. Vodopyanov. Proceedings of 8th International Workshop "Strong Microwaves and Terahertz Waves: Sources and Applications", Nizhny Novgorod — St. Petersburg, 2011 (IAP RAS, N. Novgorod, 2011), p. 204.

[9] S.V. Golubev, D.A. Mansfeld, A.G. Shalashov, A.V. Vodopyanov. Proceedings of the 35th International Conference on Infrared, Millimeter and THz Waves, Houston, 2010. Available online at http://ieeexplore.ieee.org.

[10] Van Allen J.A., Frank L.A., Hills H.K. J.Geophys. Res. **69**, 2171 (1964)

[11] O Tarvainen, T Ropponen, V Toivanen, T Kalvas, J Ärje and H Koivisto, Plasma Sources Sci. Technol., **19**, 045027, (2010).

Copyright © 2012 CC-BY-3.0 and by the respective authors

ISBN 978-3-95450-123-6

[12] A.V. Vodopyanov, S.V. Golubev, A.G. Demekhov, V.G. Zorin, D.A. Mansfeld, S.V. Razin, and A.G. Shalashov. Journal of Experimental and Theoretical Physics, **104** (2), 296 (2007).
[13] H. Koivisto, P. Heikkinen, V. Hänninen, A. Lassila, H. Leinonen, V. Nieminen, J. Pakarinen, K. Ranttila, J. Ärje and E. Liukkonen, Nucl. Instr. and Meth. in Phys. Res. B, **174**, 379 (2001).
[14] L. Arnold, R. Baumann, E. Chambit, M. Filliger, C. Fuchs, C. Kieber, D. Klein, P. Medina, C. Parisel, M. Richer, C. Santos, C. Weber. IEEE Transactions on Nuclear Science, **53** (3), 723 (2006).
[15] http://www.nist.gov/pml/data/star/index.cfm
[16] T. Ropponen, O. Tarvainen, P. Jones, P. Peura, T. Kalvas, P. Suominen, H. Koivisto and J. Ärje, Nucl. Instrum. and Meth. in Phys. Res. A, 600 (3), 525 (2009).
[17] V.A. Zhiltsov, A.A. Skovoroda, A.V. Timofeev, K. Yu. Kharitonov, A.G. Sherbakov. Fizika Plazmy (in Russian), **17 (**7), 771 (1991).
[18] P.A. Bespalov and V.Yu. Trakhtengerts. Reviews of Plasma Physics, **10**, 155 (1986).
[19] V.V. Zheleznyakov, in *Radiation in Astrophysical Plasmas* (Kluwer Academic Publishers,Dordrecht/Boston/London, 1996), p. 215.1 2
[20] T Ropponen, O Tarvainen, I Izotov, J Noland, V Toivanen, G Machicoane, D Leitner, H Koivisto, T Kalvas, P Peura, P Jones, V Skalyga and V Zorin, Plasma Sources Sci. Technol. **20**, 055007 (2011).
[21] Golubev S.V., Shalashov A.G. Phys. Rev. Lett. **99**, 205002 (2007)
[22] Y. Jongen, Proceedings of 6th International Workshop on ECR Ion Sources, Berkley (LBNL, Berkley, California, 1985), p. 238.

Copyright © 2012 CC-BY-3.0 and by the respective authors

ISBN 978-3-95450-123-6

EMITTANCE MEASUREMENT FOR U ION BEAMS PRODUCED FROM RIKEN 28 GHZ SC-ECRIS

Kazutaka Ozeki#, Yoshihide Higurashi, Takahide Nakagawa and Jun-ichi Ohnishi,
RIKEN Nishina Center for Accelerator-Based Science, Saitama, Japan

Abstract

In order to investigate the ion optical parameters of the beam line of a new injector system for RIKEN RIBF, we measured the emittance of heavy ion beams from the RIKEN 28 GHz SC-ECR ion source. In the test experiments, we observed that the emittance of the U^{35+} beam was ~100π mm-mrad (4 rms emittance). The emittance with 28 GHz was almost the same as that with 18 GHz and independent of the injected RF power. The size of the emittance increased with the decreasing charge state. We also observed that the brightness of the U^{35+} ion beam increased with the increase in the negative bias voltage of the disc installed in the plasma chamber.

INTRODUCTION

At RIKEN, we commenced the construction of the new superconducting electron cyclotron resonance ion source (SC-ECRIS), which has the optimum magnetic field strength for the operational microwave frequency of 28 GHz to produce an intense beam of highly charged heavy ions for RIKEN RI beam factory project [1]. In the spring of 2009, RIKEN SC-ECRIS produced the first beam with 18 GHz microwaves [2]. Since then, we have conducted various test experiments with the aim of increasing the beam intensity of highly charged heavy ions [2]. In 2010, we started the injection of 28 GHz microwaves into the ion source and produced intense Xe and U ion beams [3]. For the external ion source of the heavy ion accelerator, it is important to not only increase the beam intensity but also improve the beam quality (emittance, brightness, etc.). Accordingly, several laboratories have systematically studied the effect of the main parameters (magnetic field distribution, gas pressure, RF power, etc.) of the ECRIS on the emittance. A simple method to increase the beam intensity is the "biased disc" method [4]. We employed this method and successfully increased the beam intensity of highly charged heavy ions [2]. Although it is natural to assume that a negatively biased disc would affect the beam quality, few experiments have so far been conducted for understanding the effect of a biased disc on beam quality. Hence, we started studying the effect of the biased disc.

In this paper, we report the experimental results of emittance measurements for the U ion beam produced from the RIKEN 28 GHz SC-ECRIS. The effect of a biased disc on the emittance is also described.

RIKEN 28 GHZ SC-ECRIS

The detailed structure and performance of the RIKEN SC-ECRIS with 28 GHz microwaves have been described in Refs. [2, 3]. Using six solenoid coils, RIKEN SC-ECRIS can produce various magnetic field distributions on the axis, which are both of the classical B_{min} and the so-called "flat B_{min}" [5]. The microwaves were generated by the 28 GHz gyrotron (Max. power of 10 kW) and injected into the RIKEN 28 GHz SC-ECRIS.

EXPERIMENTAL RESULTS AND DISCUSSION

In this experiment, the maximum mirror magnetic field strength at the RF injection side (B_{inj}), minimum strength of mirror magnetic field (B_{min}), the maximum mirror magnetic field strength at the beam extraction side (B_{ext}), and radial magnetic field strength at the inner wall of the plasma chamber (B_r) were fixed to 3.3, 0.6, 1.8, and 1.8 T, respectively, with 28 GHz microwaves. The extraction voltage was 22 kV. To produce a U ion beam, we used the sputtering method. Figure 1 shows the schematic illustration of the RF injection side of the plasma chamber. The sputtering voltage and the position of the U rod (L) were optimized to maximize the beam intensity of highly charged U ions. The typical sputtering voltage and L were 5 kV and ~140 mm, respectively. Figure 2 shows the typical charge distribution of the highly charged U ions. The RF power was ~1 kW.

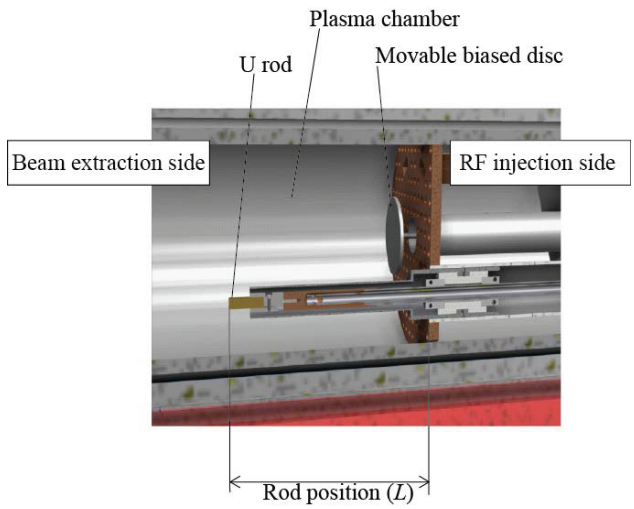

Figure 1: Schematic illustration of the RF injection side of the plasma chamber.

The root-mean-square (rms) emittance is defined as

$$\varepsilon_{x-rms} = \sqrt{\langle x^2\rangle\langle x'^2\rangle - \langle xx'\rangle^2}$$
$$\varepsilon_{y-rms} = \sqrt{\langle y^2\rangle\langle y'^2\rangle - \langle yy'\rangle^2}.$$

#k_ozeki@riken.jp

Copyright © 2012 CC-BY-3.0 and by the respective authors

ISBN 978-3-95450-123-6

In these formulae, the averages of the phase-space coordinates of the position (x, y) and the divergence (x', y') were weighted by the beam intensity [6].

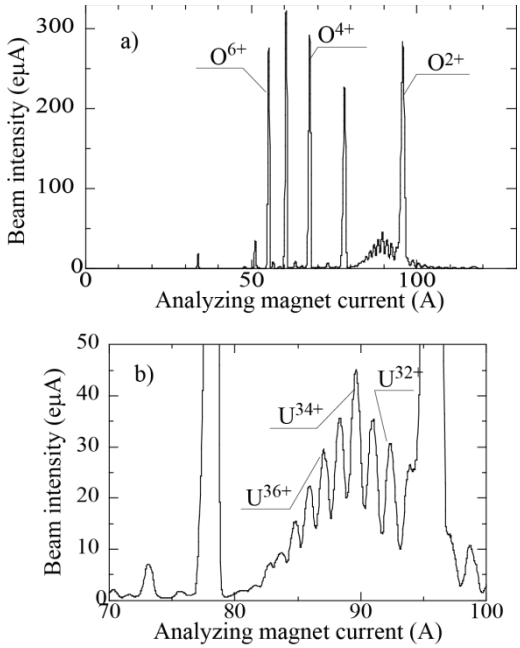

Figure 2: Charge state distributions for O and U ion beams.

Figure 3 shows the normalized x-emittance (rms) for U and O ions as a function of M/q, where M and q are, respectively, the mass and charge state of heavy ions. The emittances for these ions were measured at the same plasma and beam extraction conditions. The RF power was 1 kW. The gas pressure was ~4×10^{-7} Torr. The emittance for U ions gradually increased with the increase in M/q; on the other hand, the emittance for O ions is constant or even decreased. Furthermore, the emittance for O ions is significantly larger than that for U ions, which agrees with the results obtained at other laboratories [7]. According to the simple model calculation [8], the emittance is inversely proportional to M/q. In order to understand the difference between the model calculation and experimental results, further investigation is required.

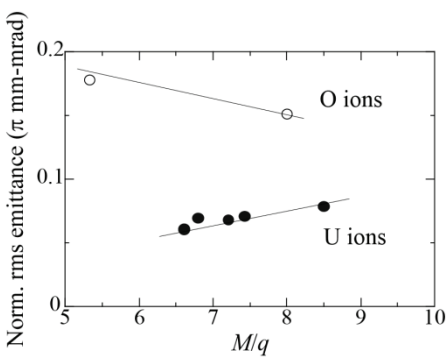

Figure 3: Normalized rms x-emittance for O and U ion beams.

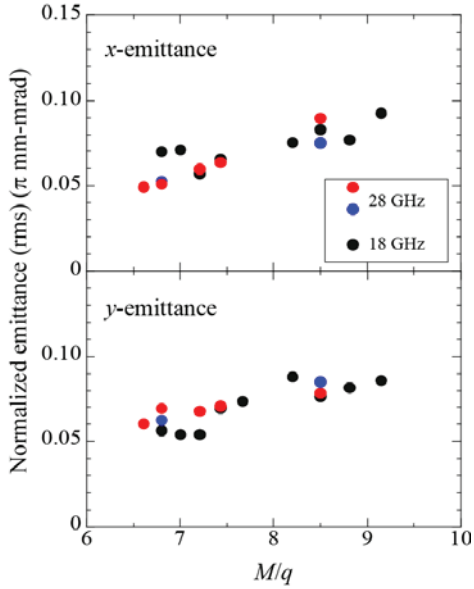

Figure 4: 4 rms emittance for highly charged U ion beams for 28 and 18 GHz microwaves (red and blue circles indicate the value obtained for 28 GHz microwaves for different measurement runs).

According to Ref. [8], the emittance becomes larger with the increase in B_{ext}. Practically, we use a high B_{ext} for a high microwave frequency to produce an intense beam of highly charged heavy ions. In this experiment, we set B_{ext} ~1.8 T for 28 GHz microwaves and ~1.2 T for 18 GHz microwaves. This implies that the emittance for 28 GHz may be 1.5 times larger than that for 18 GHz. For investigating this effect on the emittance of highly charged U ions, we measured the emittance for 28 and 18GHz microwaves. B_{inj}, B_{min}, B_{ext}, and B_r were fixed to 2.3, 0.5, 1.2, and 1.3 T, respectively, for 18 GHz microwaves. Figure 4 shows the emittance of U ion beams with 18 and 28 GHz microwaves as a function of the charge state of U ions. The emittances in the case of 28 GHz microwaves were almost the same as those in the case of 18 GHz microwaves. Increasing the beam brightness is advantageous, because, a high microwave frequency generally results in high intensity of the highly charged heavy ions. Figure 5 shows the emittance of U ions as a function of RF power. From this figure, it appears that the emittance is almost constant.

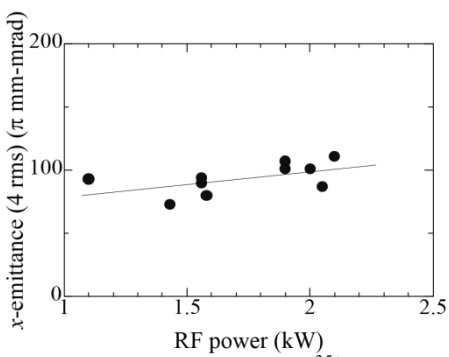

Figure 5: 4 rms x-emittance for U^{35+} ion beams as a function of RF power.

ISBN 978-3-95450-123-6

Copyright © 2012 CC-BY-3.0 and by the respective authors

Figure 6a) shows the beam intensity as a function of biased disc voltage. Two cases of the biased disc position are shown. The beam intensity increased with the increase in the negative disc voltage. Figure 6b) shows the brightness of the Xe^{19+} beam as a function of disc voltage. We observed that the brightness was almost constant and independent of the disc voltage. For example, the 4 rms *y*-emittance (non-normalized) changed from 140 to ~170π mm-mrad with the increase in the negative bias voltage from 0 to –500 V. We also measured the beam intensity of U^{35+} as a function of disc voltage. The beam intensity increased from 20 to 35 eμA with the increase in the negative bias voltage from 0 to –300 V (see Fig. 7a)). We observed the same tendency for the beam intensity as that for Xe^{19+} ions. However, the brightness of the U^{35+} beam increased with the increase in the negative voltage, as shown in Fig. 7b). The 4 rms *y*-emittance decreased from ~150 to ~100π mm-mrad with the increase in the negative bias voltage from 0 to –300 V. Although the mechanism of this phenomenon is unclear so far, practically, it is advantageous to increase the brightness of the beam. We require further investigation to understand the phenomenon.

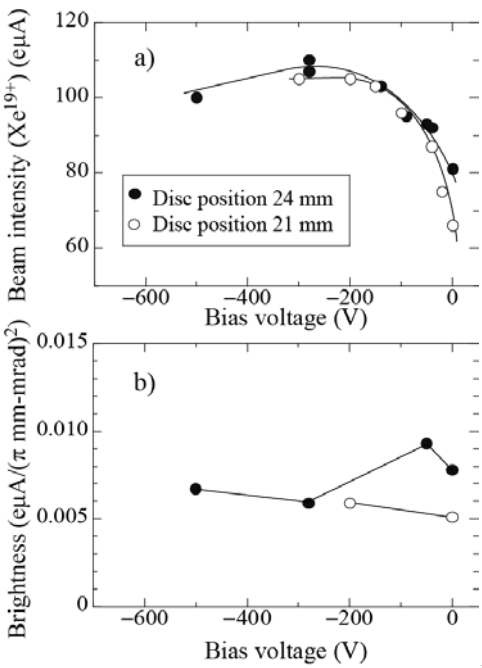

Figure 6: a) Beam intensity and b) brightness of Xe^{19+} ion beams as a function of disc voltage.

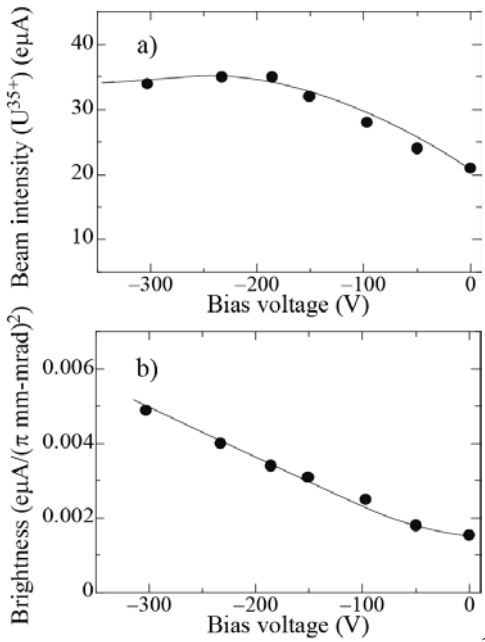

Figure 7: a) Beam intensity and b) brightness of U^{35+} ion beam as a function of disc voltage.

CONCLUSIONS

We measured the emittance of the RIKEN 28 GHz SC-ECRIS. The emittance of a highly charged U ion beam was smaller than that for an O ion beam at the same *M*/*q*. The emittance of the highly charged U ions for 28 GHz microwaves was almost the same as that for the 18 GHz microwaves and was independent of the RF power. We observed that the brightness for U^{35+} ion beam increased with the increase in the negative bias disc voltage.

REFERENCES

[1] Y. Yano, Nucl. Instrum. Methods B 261 (2007) 1009.
[2] T. Nakagawa et al., Rev. Sc. Instrum. 81 (2010) 02A320.
[3] Y. Higurashi et al., these proceedings.
[4] S. Biri et al., Nucl. Instrum. Methods B 152 (1999) 386.
[5] G. D. Alton, and D. N. Smithe, Rev. Sci. Instrum. 65 (1994) 775.
[6] I. G. Brown, The Physics and Technology of Ion Sources, Wiley, New York, 1989, p. 94.
[7] D. Wutte et al., Physica Scripta T92 (2001) 247.
[8] O. Trvainen et al., RSI 76 (2005) 093304.

Copyright © 2012 CC-BY-3.0 and by the respective authors

ISBN 978-3-95450-123-6

DEVELOPMENT UPDATE OF THE LECR4 ION SOURCE – DRAGON AT IMP*

W. Lu, D.Z. Xie, X.Z. Zhang, L.T. Sun, H. Wang, B.H. Ma and H.W. Zhao
IMP, Lanzhou 730000, China
B. Xiong and L. Ruan, IEE, Beijing 100190, China

[1] Also of the Graduate School of Chinese Academy of Sciences, Beijing 100049, P. R. China
[2] Visiting Scientist

Abstract

A room temperature ECR ion source, LECR4-DRAGON to operate at 18 GHz, is under development for the SSC-LINAC project at IMP. In comparison to other room temperature ECRISs, a unique feature of the LECR4-DRAGON is its plasma chamber of ID 126 mm that is the biggest chamber for a room temperature ECRIS and the same as the superconducting ECR ion source SECRAL. Because of the project funding agency requires study a different magnet cooling scheme, solid quadrate copper coils cooled by medium evaporation at about 50 ^{0}C are to be used to produce a maximum axial magnetic field of about 2.5 T at injection and 1.4 T at the extraction, which are similar to SECRAL operating at 18 GHz. Furthermore, a large bore non-Halbach permanent sextupole with staggered structure has been under fabrication which can produce a radial magnetic field reaching 1.5 T at the plasma chamber wall for operation at 18 GHz. The progress updates and discussions of this ion source will be presented.

INTRODUCTION

The LECR3 source, a room temperature ECRIS [1], is operating at IMP since 2003 and it has been delivering the most of light ion beams for the SSC cyclotron and CSR, whereas the SECRAL [2] ECR ion source has been mainly providing the highly charged heavy ion beams. To meet the demands of intense medium charge state heavy-ion beams, a research program, collaborating with IEE- Beijing, had been started two years ago. The goal of this program is to produce intense medium charge state heavy-ion beams with a room temperature ECR ion source, meanwhile testing an evaporative cooling technology [3] for potential applications to accelerator magnets. In comparison to a superconducting ECR ion source, a room temperature ECR ion source has the advantages of lower cost and easier operation but with lower performance due to the limitations on the magnetic field and ac power consumption. To date, all the room temperature ECR ion sources are built with a small plasma chamber of inner diameter less or equal to 80 mm producing a radial field of about 1.2 to 2.0 T [4]. The small plasma chambers are not optimal as evidenced by some outstanding SC ECRISs [2, 5] at about the same field profile with larger plasma chambers (ID > 120 mm). Thus a larger bore sextupole magnet has been chosen for the LECR4-DRAGON with its axial magnetic field modelling the SECRAL field profile operating at 18 GHz: 2.5 T at the injection and 1.3 T at the extraction region with a radial field of 1.4 T at the plasma chamber walls. The unique feature of LECR4-DARGON is that the solenoid magnet coils are fully immersed in and cooled with a 47.7 ^{0}C evaporative medium. Figure 1 shows the mechanical layout of the LECR4-DRAGON while Fig. 2 showing the computed axial magnetic field profile.

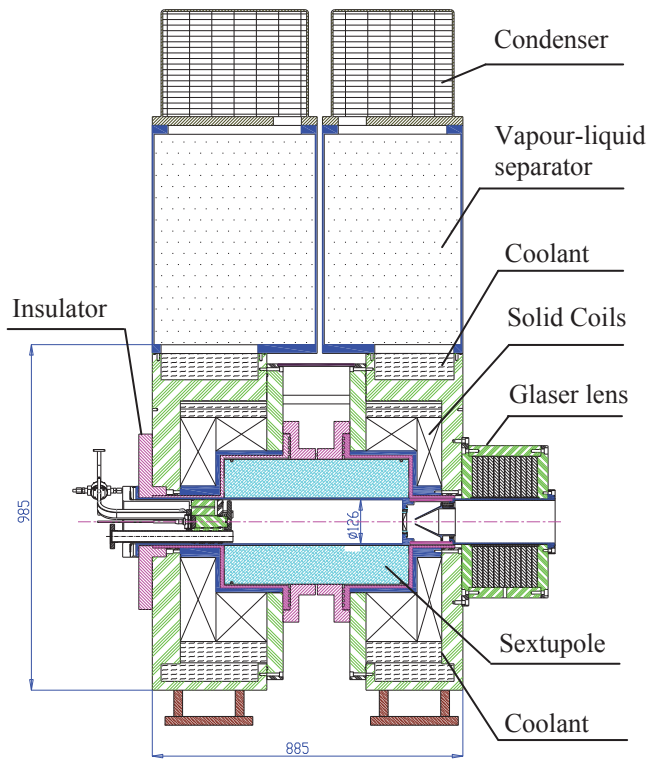

Figure 1: A schematic cross-section view of the LECR4-DRAGON. No mechanical pumping at the injection side for simplicity but may be added in the future.

Evaporative Medium Cooled Solenoid and Prototype Experiments

Institute of Electrical Engineering of Chinese Academy of Sciences (IEE) has been researching the evaporative

* This collaboration project was supported by the Research Foundation of Chinese Academy of Sciences.

ISBN 978-3-95450-123-6

Copyright © 2012 CC-BY-3.0 and by the respective authors

cooling since 1958 [3]. Based on its structure, there are three kinds of evaporative cooling schemes in the application to the large electrical equipment: pipe inner cooling, immersion cooling and mixed cooling. Through careful theoretical analyses and experimental evaluations, the immersion scheme has been chosen for cooling the LECR4-DRAGON solenoid magnets. Figure 3 shows a schematic layout of this cooling system consisting of two condensers, liquid transport pipes, immersion tank, gas-out tubes, etc. When the coils are excited, the boil-off medium vapour will carry away the heat by a phase transition with good latent heat absorption, just like the liquid helium cooling the superconducting magnet. The vapour in the immersion tank goes up into the condenser and gets liquefied there then flows back-down to the immersion tank. To date, a prototype of solenoid coil and condenser shown in Figure 3 have been built and tested. In order to increase heat transmit efficiency and simplify ECR ion source structure as well, an integrated structure has been fabricated and tested [6]. Using coolant with a boiling temperature of 47.7 ^{0}C, the testing has achieved excitation current up to 300A that is equivalent to a current density: 12.05 A/mm^2, slightly higher than using normal hollow copper conductor with pressurized water cooling at IMP. The experimental result is shown in Table 1 that shows the maximum temperature of copper coils reaching 77 ^{0}C after 3 hours of continuous operation. This maximum temperature is about 43% of its temperature limit (180 ^{0}C- depending up on the conducting insulation grade). At the stated excitations, the maximum temperature at the permanent sextupole location is 52 ^{0}C, that is about 43% of N48SH's maximum working temperature of 120 ^{0}C.

Table 1: The Experimental Results of Prototype Solenoid Coils (2012)

Measure position	Exciting current (A)	Average Temp. (^{0}C)	Maximum Temp. (^{0}C)
Coil1conducting wire surface	303.5	70	74
Coil2 conducting wire surface	300.2	70.5	77
Permanent magnet location	-	49.5	52

Large Bore Sextupole and Force Analysis

In general a room temperature ECR ion source uses a permanent sextupole to produce the needed radial field. Most of the existing conventional ECR ion sources use a Halbach-structure sextupole that is constructed with M equal-size sections in which the easy-axis rotating (N-1)∏/M from the section to the next [7]. Because of the superimposing magnetic fields, the Halbach structure has six potential de-magnetization regions when the field can approach dangerous de-magnetization strength. In addition, the fabrication of such a Halbach sextupole magnet requires very complex magnet-block cutting and assembling tools, especially for larger bore permanent sextupoles. To simplify the fabrications, a large bore non-Halbach-structure sextupole is used for the LECR4-DRAGON at a price of about 2% lower radial field at plasma chamber walls. The inner diameter of LECR4-DRAGON sextupole bore is 134.5 mm which is large enough to support a double-layer water-cooled plasma chamber of inner diameter of 126 mm. This large bore sextupole is made of N48SH permanent magnet blocks for its higher working temperature and possibly more resistant to the permanent magnet deteriorations with age. Figure 4 shows the cross section of the sextupole magnet and force analysis of one-sixth sextupole segment. Calculations show the maximum attractive force is up to 13000 N after assembling.

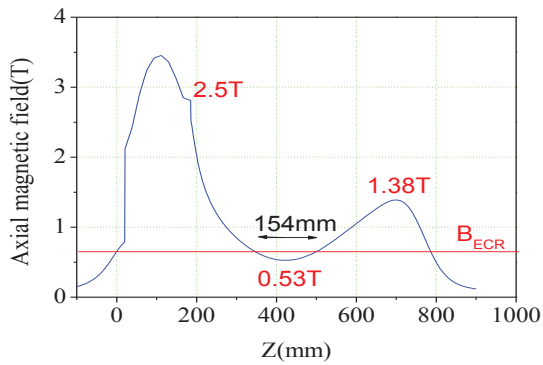

Figure 2: The axial field profile of DRAGON that is similar to the SECRAL operation at 18 GHz. With an iron plug field booster the maximum axial field reaches 2.5 T at the surface of the bias probe in the injection.

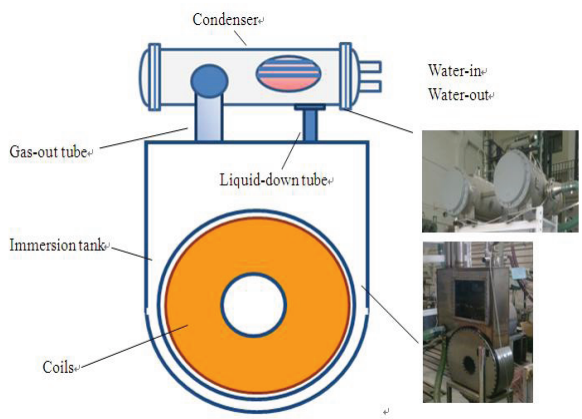

Figure 3: Schematic layout of evaporative cooling system for LECR4-DRAGON.

Copyright © 2012 CC-BY-3.0 and by the respective authors

ISBN 978-3-95450-123-6

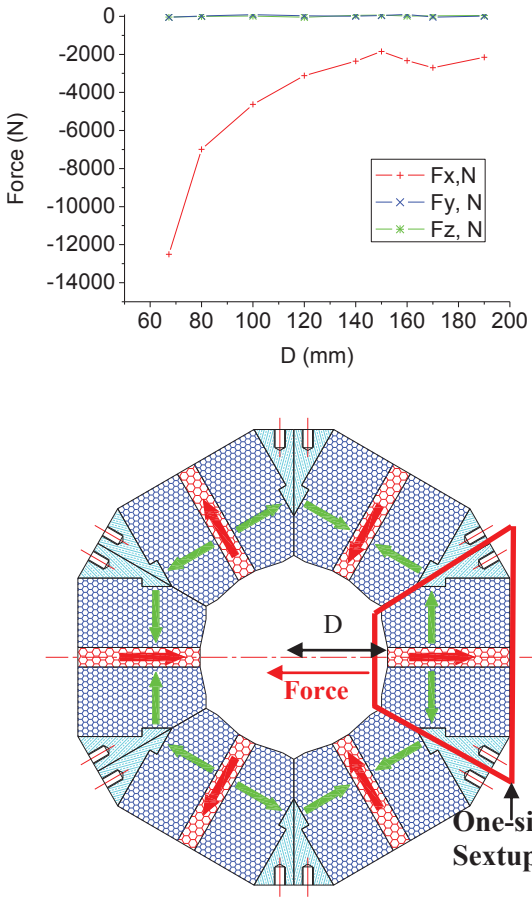

Figure 4: The layout of LECR4-DRAGON ECR ion source sextupole magnet and force analysis of one-sixth sextupole magnet.

High Voltage Beam Extraction

The beam transport line of LECR4-DRAGON is based on the one at the SECRAL beam line. It is designed to be able to transport 10-15 emA intense heavy ion beams with high efficiency and sufficient resolution. A Glazer lens and a 90^0 analyzing magnet have been chosen while the SECRAL beam line using an 110^0 analyzing magnet for slightly higher resolution. A turbo molecular pump is directly attached to the extraction box between the source and the Glazer lens to enhance the pump speed to reach higher vacuum. Pumping in the injection side is omitted for simplicity but could be added depending on the performance development. Slits and Faraday-cup are installed at the waist of extraction ion beams. LECR4-DRAGON will be insulated with 7 mm thick material hoping to achieve higher extraction voltage up to 50 kV. For simplicity a two-electrode extraction system is considered for the initial commissioning but three- and four-electrode will be explored later on. Figure 5 shows the layout of LECR4-DRAGON ECR ion source with its initial extraction system and the beam transport line.

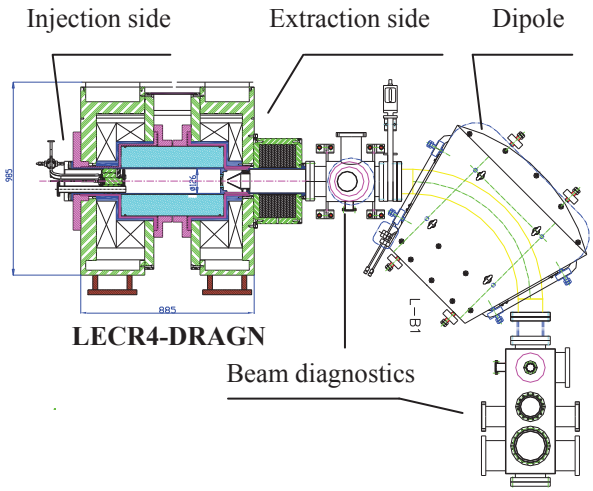

Figure 5: Layout of LECR4-DARGON ECR ion source and its beam transport line.

DISCUSSIONS AND CONCLUSIONS

The design and development of a large bore sextupole room temperature ECR ion source for the production of medium charge state heavy ion beams has been presented. The prototype of solenoid coils and the cooling condenser have been tested with satisfactory results. In order to support a large plasma chamber, a large bore non-Halbach-structure sextupole has been designed and fabrication is underway. Based on the progress, the detailed engineering design and component fabrication are underway.

REFERENCES

[1] H.W. Zhao *et al,* RSI, 75, 1410 (2004)
[2] H.W. Zhao *et al*, RSI, 81, 02A202 (2010).
[3] L. Ruan *et al*, "The comparison of cooling effect between evaporative cooling method and inner water cooling method for the large hydro generator", Proc. of ICEMS, p. 67 (2007).
[4] T. Thuillier *et al*, RSI, 77, 03A323 (2006).
[5] C. Lyneis *et al,* RSI, 81, 02A201 (2010).
[6] W. Lu *et al,* RSI, 83, 02A328 (2012).
[7] K. Halbach, NIM, 109, 187 (1981).

Copyright © 2012 CC-BY-3.0 and by the respective authors

ISBN 978-3-95450-123-6

ADVANCED INJECTION SYSTEM OF LIGHT IONS (AISLI) FOR DIELECTRIC WALL ACCELERATOR*

Shixiang PENG#, Haitao REN, Jie ZHAO, Pengnan LU, Jia CHEN, Yuan XU, Zhiyu GUO and Jia'er Chen
SKLNPT, Institute of Heavy Ion Physics, Peking University, Beijing 100871, China

Abstract

Dielectric wall accelerator (DWA) is a kind of acceleration system with high electric field gradients up to 400 MV/m and very compact dimension, for example ϕ 30 mm x 50 mm, which has the ability to accelerate the particles with any charge to mass ratio. To demonstrate the high gradient tiny acceleration system, a compact injector is required, which should deliver a 50 mA/40 keV pulsed H^+ converging beam to the entrance of DWA. Based on the experimental results obtained on the test bench, a six electrodes injector was developed at Peking University (PKU). In this paper we will describe the preliminary experimental results as well as the details of the new compact injector which named as Advanced Injector System of Light Ions (AISLI).

INTRODUCTION

Dielectric wall accelerator (DWA) is a new acceleration concept that can generate an extremely high gradient up to several hundred MV/m for a short pulse beam with any charge to mass ratio particle [1]. As mentioned in literature [2], a compact proton injector capable of delivering sub-ns proton bunches, and high gradient insulators (HGI) with high surface breakdown strength are two of the five essential elements to make a proton DWA accelerator compact. Sitting the HGI in oil tank is a solution to increase the HGI surface breakdown strength. A space between the proton injector and HGI for adaption is needed. To better understanding the DWA concept, a ϕ 30 mm x 50 mm HGI will be used to demonstrate its acceleration ability. Beam need for this HGI demonstration is a 50 mA/40 keV converging square pulse proton beam. Its repeat frequency is 50 Hz. The width of each pulse is 200 ns. Besides, the injector should be a very compact one so that it can match DWA's tiny features with reasonable dimension. Parameters of the injector are listed in table 1.

To meet the requirement of the tiny DWA, a 20 cm long proton injector including 8 cm adaption space for ion tank are developed at Peking University (PKU). It consist of on a permanent magnet 2.45 GHz Electron Cyclotron Resonance Ion Source (PMECRIS) [3] and an electrostatic focusing LEBT based on the preliminary experimental results obtained on PKU LEBT test bench. This injector is named as Advanced Injection System of Light Ions (AISLI). In part II, we will present the preliminary experimental results based on PKU ion source test bench. In part III we will give a description of AISLI, emphases are located on PBGUNS code simulation, methods for the beam producing, beam focusing, pulse shape controlling. At the end of this paper we will give a summary and anticipation.

Table 1: Proton Injector Key Performance Parameters Required by DWA

Peak Current	mA	50
Energy	keV	40
Emittance	π mm.mrad	≤0.2
Radius at entrance of HGI	mm	5
Frequency	Hz	50
Pulse width	ns	200
Space for adaption	mm	80

PRELIMINARY EXPERIMENT ON PKU ION SOURCE TEST BENCH

General Consideration

A proton injector is a facility to generate plasma, create an expected ion beam and transport it into accelerator. The core of it is an ion source and a low energy beam transport part (LEBT).

There are more than 50 kinds of ion source around the world. Scientists at LLNL chose a spark source to produce proton beam for their DWA [2]. At PKU a permanent magnet 2.45 GHz Electron Cyclotron Resonance Ion Source (PKU PMECRIS) has been chosen. This is not only because researchers at PKU are skillful on this kind of ECRIS [3-5], but also because the unique feature of it, high ion beam density, high reliability, ability to operate both in CW mode and in pulsed mode, good reproducibility and low maintenance and long lifetime. Because of those characteristic, 2.45 GHz ECRIS is popular as a high current ion source in the world [6-10]. By using permanent magnet to replace the solenoid, the ECR ion source body is about 100 mm, and even smaller.And accessories to support source operation on high voltage platform become less. This will benefit the miniaturization the whole injector.

*Work supported byNational Science Foundation of China No. 91126004, No.11075008 & No.11175009.
#sxpeng@pku.edu.cn

Copyright © 2012 CC-BY-3.0 and by the respective authors

ISBN 978-3-95450-123-6

LEBT is used to transport and to match the beam created and extracted from the ion source to accelerator. Beam focus can be done with electrostatic [10] or magnetic elements [6,8] within LEBT. The beam usually presents a cylindrical symmetry because of the geometry of the extraction system. In order to preserve this symmetry and to simplify the beam tuning, magnetic solenoid lenses or electrostatic einzel lenses are more commonly used than quadrupole lenses. During a high intensity beam LEBT designing, beam focus method selection should count seriously emittance growth, space charge effect, beam transmission efficiency [6,11]. In the meantime, the dimension of LEBT is also an important factor for this decision. Compared with a magnetic LEBT, the disadvantages of electrostatic LEBTs are obvious, no space charge compensation, intrinsical optical aberrations, beam halo creasing and beam divergence enlarging. All this shortcomings will lead beam emittance growth rapidly with its intensity (especially for current of several tens of mA). However, the design of electrostatic LEBTs is simplified by the fact that no repelling electrode for the neutralizing particle trapping. So the beam lines are very compact. As an example, the SNS injector is composed by an H- ion source with a 12 cm long LEBT equipped with two einzel lenses [10]. At PKU we choose an electrostatic type LEBT to match the proton beam with the HGI for this compactDWA.

Experiment Setup

When the frame of the proton injector used for DWA is fixed with electrostatic type, preliminary experiment is launcher to verify this scheme before the detail design on the proton injector done on PKU ion source test bench. Fig. 1 is the skeleton diagram of this test bench before modification. It consists of a permanent magnet 2.45GHz ECR ion source, a tri-electrode extraction system, a slit-grid emittance measurement device and an analysis magnet.

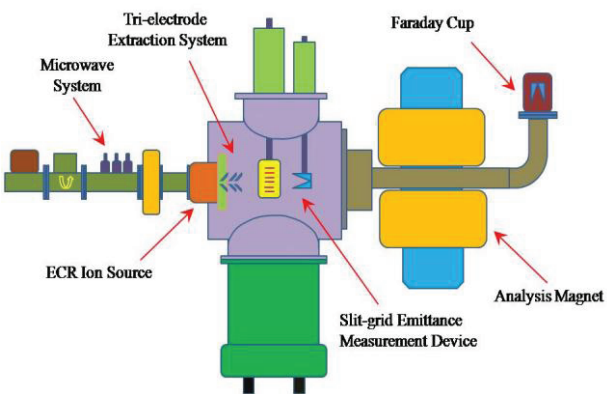

Figure 1: The skeleton diagram of PKU Ion Source Test Bench.

This ECR ion source on the test bench has the ability to produce 120 mA of H^+, 83 mA of D^+,50 mA of O^+, 63 mA of N^+, 70 mA of Ar^+ and 65 mA of He^+ ion beams with a ϕ6 mm extraction aperture at at 50 keV [5].

The distance between each two neighbor slits is 2 mm that locates 200 mm away from the ion emit aperture [12]. Modification will be done by insert an electrostatic lens between the suppressing electrode and the ground electrode.

Preliminary Experimental Results

Figure 2 is 50 mA/40 keV H+ beam transverse distribution obtained using slit-grid emittance measurement device on PKU ion source test bench. As shown in Fig. 2, the beam diameter is about 5 slits that equal to 10 mm, and its rms emittance is only about 0.1 π mm.mrad. This result proves that our preliminary experiment satisfies the requirement of DWA.

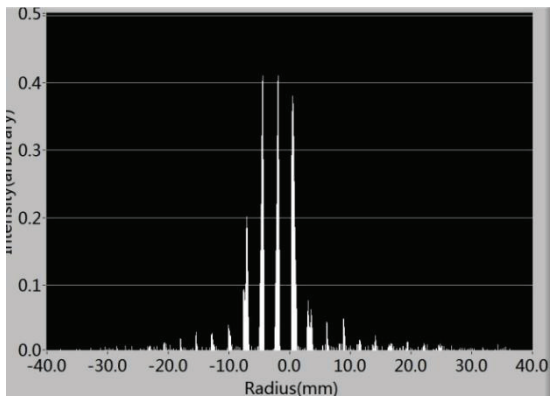

Figure 2: The transverse distribution of 50 mA/40 keV H^+ beam at the location of DWA entrance.

THE PROTON INJECTOR(AILIS) FOR DWA

Based on experimental results gained on the PKU Ion Source test bench, an H^+ injector consisted of the proton source and LEBT is shown in Fig. 3. The ion source is a PKU PMECRIS, just a copy of D^+ ion source developed for PKUNIFTY. The LEBT electrodes basically form two electrostatic einzel lenses that provide two-parameter matching into HGI at its entrance plane. The central electrode of the second lens is split into two isolated quadrants, and electrostatic voltages can be superimposed on the main potential to provide angular steering in the horizontal and vertical directions. Kicker that follows the second lens is used to chop the 50 Hz/0.5 ms H^+ beam generated by microwave power into 50 Hz/200 ns shape. The kick-off beam will be absorbed at the water-cooling flange just before the ion tank.

Preliminary study using the code PBGUNS [13] with 40 keV/50 mA proton beam transport is illustrated in Fig. 4.

Copyright © 2012 CC-BY-3.0 and by the respective authors

ISBN 978-3-95450-123-6

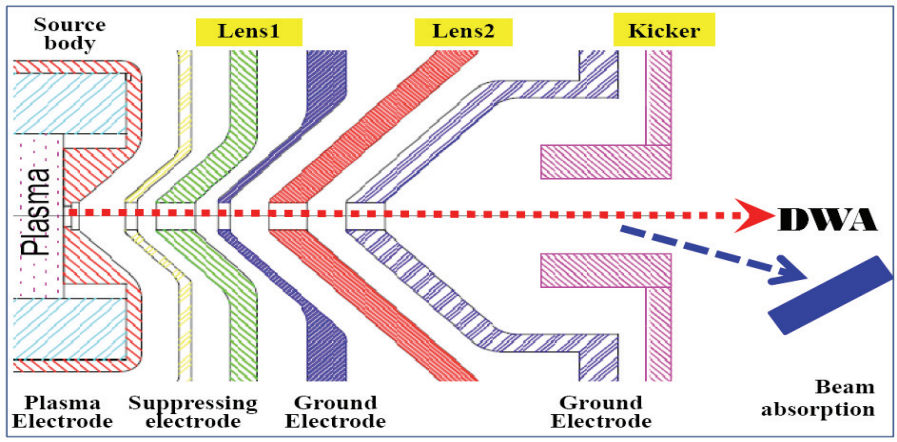

Figure 3: The schematic view of AISLI (un-scaled).

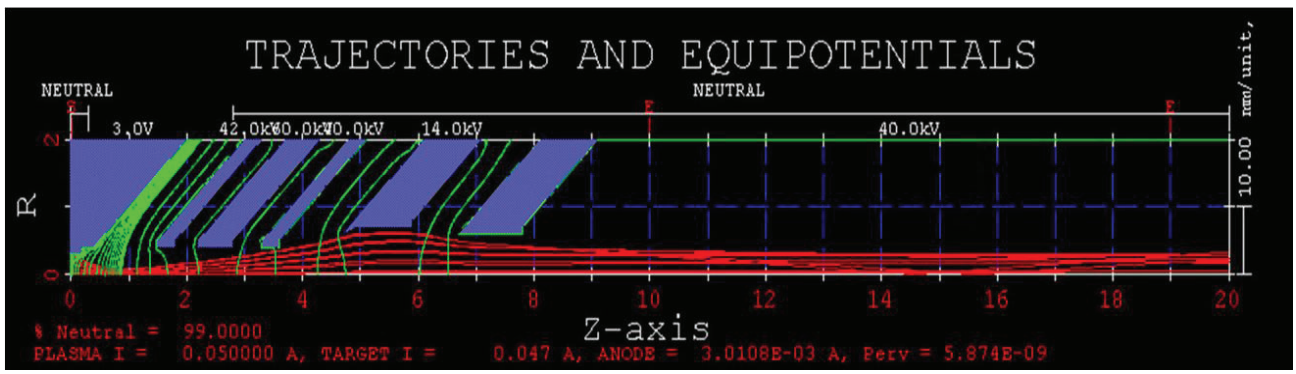

Figure 4: PBGUNS simulation of AISLI for 50 mA H^+ beam.

SUMMARY AND ANTICIPATION

According to the preliminary experimental results, a novel design of the proton injector (AISLI) for DWA has been developed. Two electrostatic einzel lenses are adopted to adjust the proton beam for matching with DWA. The commissioning of AISLI will be done in the near future, and we expect to obtain a 50 mm/40 keV proton beam with the diameter less than 10 mm at the entrance of the dielectric wall accelerator.

ACKNOWLEDGMENT

This work was supported by National Science Foundation of China No. 91126004, No.11075008 & No.11175009.

REFERENCES

[1] George J. Caporaso, Y-J. Chen, S. Sampayan, et al.,STATUS OF THE DIELECTRIC WALL ACCELERATOR.Proceedings of PAC09, Vancouver, BC, Canada, TH3GAI02.

[2] Y.-J. Chen, G. Guethlein, G. Caporaso, et al., COMPACT PROTON INJECTOR AND FIRST ACCELERATOR SYSTEM TEST FOR COMPACT PROTON DIELECTRIC WALL CANCER THERAPY ACCELERATOR. PAC09 Particle Accelerator Conference Vancouver, Canada, May 4, 2009 through May 8, 2009.

[3] S. X. Peng, Z. Z. Song, J. X. Yu, et al., STATUS OF THE HIGH CURRENT PERMANENT MAGNET 2.45GHZ ECR ION SOURCE AT PEKING UNIVERSITY. Proceedings of ECRIS10, Grenoble, France. TUCOCK02, August 23-26, 2010: 102-104.

[4] M. Zhang, S. X. Peng, H. T. Ren, et al., Upgrade of permanent ECR ion source and its extraction system , Review Science Instrument. 81, 02B715 (2010).

[5] H. T. Ren, S. X. Peng, P. N. Lu, et al., Intense beams from gases generated by a permanent magnet ECR ion source at PKU. Review Science Instrument.83, 02B905(2012).

Copyright © 2012 CC-BY-3.0 and by the respective authors

ISBN 978-3-95450-123-6

[6] H. T. Ren, S. X. Peng, P. N. Lu, et al., Deuteron injector for Peking University Neutron Imaging Facility project. Review Science Instrument.83, 02B711 (2012).
[7] L. Celona, G. Ciavola, S. Gammino, et. al., Rev. Sci. Instrum. 75, 1423 (2004).
[8] R. Gobin, P.-Y. Beauvais, O. Delferrière, et. al., Rev. Sci. Instrum. 79, 02B303 (2008).
[9] Gobin, R., Blideanu, V., Bogard, D., et. Al., Rev. Sci. Instrum.81, 02B301 (2010).
[10] M. P. Stockli, B. Han, S. N. Murray, T. R. Pennisi, M. Santana, and R. F. Welton, Rev. Sci. Instrum. 81, 02A729 (2010).
[11] N. Chauvin, O. Delferrière, R. Duperrier, R. Gobin, P. A. P. Nghiem, and D. Uriot, Transport of intense ion beams and space charge compensation issues in low energy beam lines.REVIEW OF SCIENTIFIC INSTRUMENTS 83, 02B320 (2012).
[12] S.X. Peng, P.N. Lv, H.T. Ren,etc., Methods to Reduce the System Error for High Power MSSW Emittance, proceedings of IBIC2012, TUPB64.
[13] J. E. Boers, PBGUNS Manual, available through Thunderbird Simulations, Garland, TX 75042.

Copyright © 2012 CC-BY-3.0 and by the respective authors

ISBN 978-3-95450-123-6

METAL ION BEAM PRODUCTION WITH IMPROVED EVAPORATION OVENS

K. Tinschert#, R. Lang, J. Mäder, F. Maimone, J. Roßbach, GSI, Darmstadt, Germany

Abstract

Most of the ion beams delivered by the ECR ion sources at the GSI accelerator facilities are produced from materials in the solid state, which must be transformed into the gaseous state to feed the plasma. The well established method of thermal evaporation has been used by means of two types of resistively heated ovens for metals and solid compounds. The main goal of development is to improve their versatility in terms of lifetime, durability, efficiency, and extended temperature range. Recent investigations and developments include the use of alternative materials for oven components. The main focus has been on the further development of the high temperature oven. A modular construction with improved mechanical dimensional accuracy for more precise and easier mounting has been established. Its optimization for stable long time operation has been continued leading to a lifetime of 6 days for evaporation of Ti at 1750°C. Furthermore the temperature limit could be extended to 2300°C. In addition to the improvements in evaporation technology the technique of microwave frequency tuning could be successfully applied for metal ion operation leading to enhanced ion beam intensities.

INTRODUCTION

A great variety of ion species is required at the GSI heavy ion accelerator facility. More than 85% of the natural elements are solid at room temperature and must be transformed into the gaseous state to feed the plasma. Several methods like thermal evaporation, plasma heating, ion sputtering, laser ablation or producing metal ions from volatile organic compounds (MIVOC) can be applied. At GSI the evaporation technique using ovens has been preferred because it resembles closely the operation with gases [1]. It has been used for two decades to produce ion beams from many different materials with the CAPRICE type ECR Ion Source (ECRIS). The basic requirements of operation are long time stability, long operation periods without maintenance, constant beam parameters and low material consumption when using rare isotope materials. According to semi-empirical scaling and experimental experience a vapour pressure of about 10^{-3} mbar is suitable for evaporation into the plasma and to extract stable ion beams of sufficient intensity.

STANDARD OVEN

The resistively heated standard oven (STO, Fig.1) is mostly used for the production of metal ion beams in routine operation with the ECRIS at GSI. The STO is optimized for temperatures between 300°C and 1500°C.

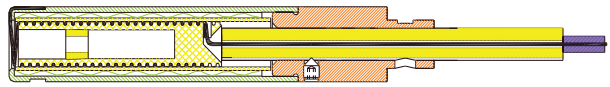

Figure 1: STO - GSI standard oven (yellow: Al_2O_3; green: Ta; orange: Mo; violet: CuBe2)

For $^{54}Cr^{8+}$ it was investigated whether the lifetime of the oven can be increased by increasing the initial amount of ^{54}Cr sample material. It turned out that the lifetime increases with the charge to some extent, however, the material consumption also increases. It became evident that an optimum charge of sample material exists giving the best compromise between oven lifetime and material consumption. The overall consumption of ^{54}Cr sample material was 4 mg/h on average with a range of fluctuation between 2 mg/h and 6 mg/h for the particular charges. Figure 2 shows a typical mass/charge spectrum of the extracted ion beam. Besides ^{54}Cr and He (auxiliary gas) it shows a very low amount of contaminations and confirms the very high degree of enrichment of the ^{54}Cr material.

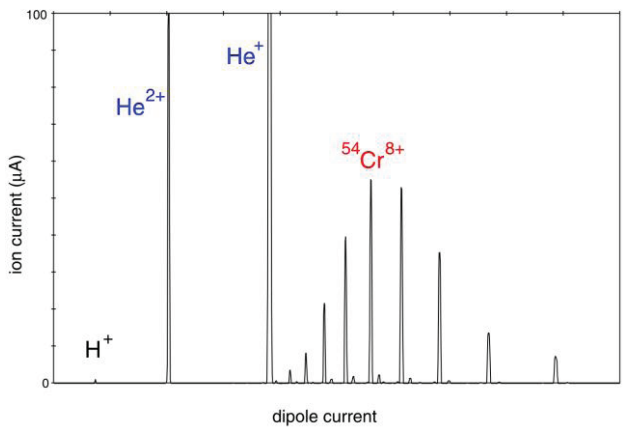

Figure 2: Typical mass/charge spectrum of ^{54}Cr.

TITANIUM BEAM WITH STO

The investigations on the development of a ^{50}Ti beam for experiments of the Super Heavy Element (SHE) program were extended by exploring 3 alternative approaches. Besides thermal evaporation of titanium with the STO another type of resistively heated oven was investigated. This type of oven had been developed for the thermal evaporation of materials at very high temperatures (HTO, Fig. 3) [1].

K.Tinschert@gsi.de

Copyright © 2012 CC-BY-3.0 and by the respective authors

ISBN 978-3-95450-123-6

Furthermore the evaporation of chemical Ti-compounds at low temperatures was explored but did not lead to a useful method.

The normal version of the STO is equipped with alumina (Al_2O_3) ceramics as support for the heating wire and as container for optional crucibles. However, alumina is not resistant against molten Ti and its vapour, which show very high chemical reactivity with almost any material. After exploring various oven configurations using different ceramics materials and refractory metals it turned out that only yttria (Y_2O_3) based ceramics can provide improved resistance. Commercially available yttria ceramics showed insufficient mechanical form stability at the required temperature. An optimization of the ceramics sintering processes including different ceramic stabilizers could considerably improve the durability. Thus the operating conditions of the modified STO for Ti could be improved. An improved thermal front shielding of the STO by multi-laminated and corrugated Ta foils led to an optimized axial temperature function, which lowered the heating power to achieve the same temperatures.

TITANIUM BEAM WITH HTO

Contrary to the STO the design of the HTO avoids any ceramics in the hot volume. Instead it utilizes a free heater helix supported only at its ends. All parts in the hot volume are made from Ta, W or W compounds. This circumvents the specific problems arising from the use of ceramics and so the application of the high temperature oven turned out to be the most promising approach. The disassembling of parts after operation with very high temperature leads to problems. In order to optimize the HTO for routine operation its modular construction was improved in mechanical dimensional accuracy for more precise and easier mounting and dismounting. The use of a special W compound containing 2% of La_2O_3 for crucibles and for furnace facilitates their ductility and machinability. However, its drawback is the evaporation of La out of the metal matrix at very high temperatures, which implies the use of W crucibles under such conditions.

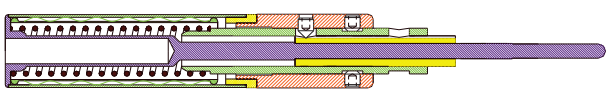

Figure 3: HTO - GSI high temperature oven (yellow: Al_2O_3; green: Ta; orange: Mo; violet: W).

Various experiments were performed with the HTO using natural Ti for most runs. For final confirmation, however, ^{50}Ti sample material had to be used. In addition the evaporation of TiO_2 was investigated, which avoids the problems related to the chemical reactivity of pure Ti at high temperatures. According to the required vapour pressure for the evaporation of TiO_2 the temperature limit of the high temperature oven could be successfully extended near to 2300 °C corresponding to 560 W of electrical heating power (Fig. 4).

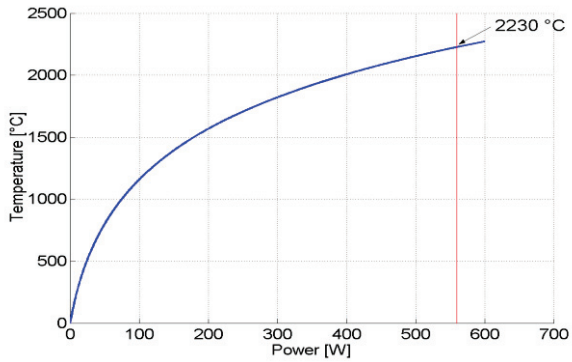

Figure 4: HTO temperature as function of heating power (measured up to 2050°C; extrapolated above 2050°C).

However, this high operating temperature reduces the lifetime of the oven. Therefore it appeared to be more favourable to use pure titanium as sample material at evaporation temperatures between 1750 °C and 1800 °C.

Several successful runs could be performed with natural titanium material and with enriched material. It could be demonstrated that the material processed in the GSI target laboratory by chemical reduction of enriched $^{50}TiO_2$ material is usable. The charge state distribution was optimized for Ti^{8+}, which is suitable for injection into the linear accelerator. The expected intensities of more than 50 µA could be easily achieved at high level of beam stability. Figure 5 shows a typical spectrum for a ^{50}Ti run.

The lifetime of the oven is related to the applied heating power, which is also of major influence on the average ion beam intensity. At a typical lower level of heating power of 250 W (corresponding to 1750 °C) a lifetime of 6 days is obtained. This value is reduced, when the heating power is increased. The high temperature oven in its present development status is prepared for routine operation at the accelerator.

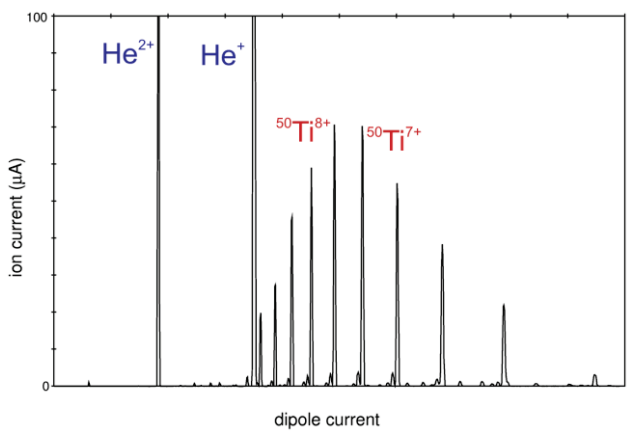

Figure 5: Typical mass/charge spectrum of ^{50}Ti.

Copyright © 2012 CC-BY-3.0 and by the respective authors

ISBN 978-3-95450-123-6

MICROWAVE TUNING

The new Facility for Antiproton and Ion Research (FAIR, [2]) that will be set up in the next years at GSI implies upgrades of the existing accelerator facility which will be used as injector machine for FAIR. For the ECRIS an increase of accelerated ion charge state is desired together with a considerable increase of ion beam intensity.

It has been demonstrated that a frequency tuning of the microwave injected into the ECRIS using a travelling wave tube amplifier (TWTA) can provide a considerable increase of the intensity of metal ion beams (at selected frequencies) like in the case of gaseous elements [3].

The test was carried out by replacing the Klystron microwave generator working at 14.5057 GHz by a TWTA driven by a frequency variable synthesizer. It was initially set at 14.5057 GHz and a power around 250 W was provided to the ion source. At a heating power of the oven of around 230 W a sufficiently stable ion beam of Ti^{8+} was obtained. Then the microwave frequency was swept in the frequency range from 12.5 to 16.5 GHz exhibiting a pronounced intensity variation of Ti^{8+} and Ti^{11+}, respectively.

The ion current of Ti^{11+} at the initial frequency was around 13 µA while during the sweep some frequencies were indentified where this current was increased. For instance at 13.725 GHz the current of Ti^{11+} was around 34 µA.

A comparison of the mass/charge spectra at these two frequencies shows a shift of the charge state distribution leading to a considerable intensity gain for the higher charge states. This is demonstrated e. g. for the ratio of Ti^{11+} and Ti^{8+} in Fig. 6 and Fig. 7, respectively. These spectra are obtained with identical source settings and oven heating. After almost 12 hours of operation at 13.725 GHz the beam was stable and the ion source worked continuously without any adjustment of the parameters with the exception of the oven power which was increased for compensating the consumed material. A frequency sweep was carried out again and it was possible to measure the highest intensity of Ti^{8+} current of more than 90 µA at 14.5438 GHz (Fig. 8).

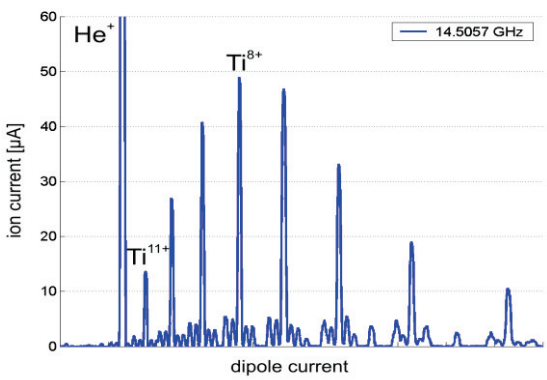

Figure 6: Mass/charge spectrum of natural Ti (forward power = 250 W; reflected power = 28 W; HTO heating power = 234 W).

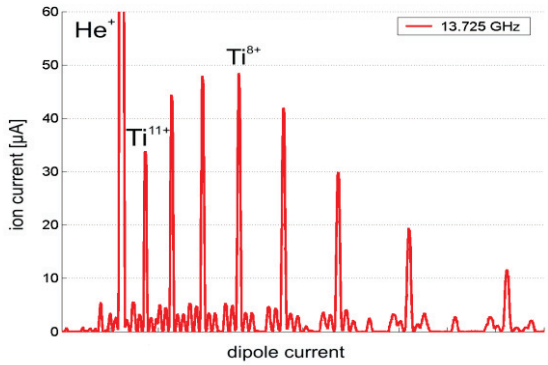

Figure 7: Mass/charge spectrum of natural Ti (forward power = 250 W; reflected power = 1 W; HTO heating power = 234 W).

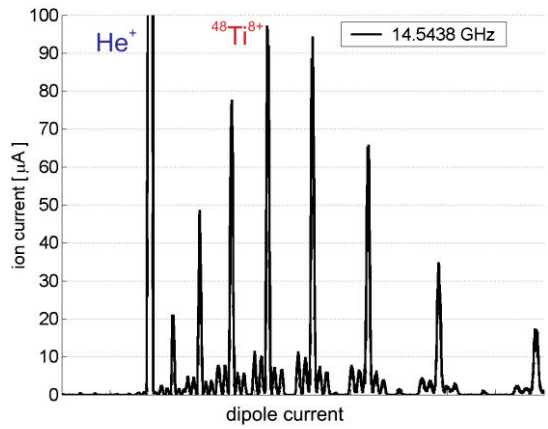

Figure 8: Mass/charge spectrum of natural Ti (forward power = 234 W; reflected power = 95 W; HTO heating power = 262 W).

These experiments demonstrated that frequency tuning can be a powerful method to increase the ion beam intensity of the highest charge states for metal ions.

ACKNOWLEDGMENT

We acknowledge the financial support of the European Union Seventh Framework Programme FP7/2007-2013 under Grant Agreement n° 262010 - ENSAR. The EC is not liable for any use that can be made on the information contained herein.

REFERENCES

[1] R. Lang, J. Boßler, H. Schulte, K. Tinschert, Rev. Sci. Instrum. 71, 651 (2000); R. Lang, J. Boßler, R. Iannucci, K. Tinschert, Proc. 15th Int. Workshop on ECRIS, University of Jyväskylä, Finland 180 (2002).

[2] http://www.fair-center.de

[3] F. Maimone, *Ph.D. thesis*, Università di Catania, 2012.

Copyright © 2012 CC-BY-3.0 and by the respective authors

ISBN 978-3-95450-123-6

EXPERIMENTAL STUDIES ON THE ALISES ION SOURCE AT CEA SACLAY

O.Tuske*, O. Delferrière, Y. Gauthier, R. Gobin, F. Harrault, J-.L. Jannin and S. Nyckees, Commissariat à l'Energie Atomique et aux Energie Alternatives, CEA/Saclay, DSM/Irfu, 91191-Gif/Yvette, France

Abstract

The ALISES ion source was originally designed to reduce beam emittance at RFQ entrance by shortening the length of the LEBT. A wide opened magnetic coil at ground potential produces the fringe field needed for the ECR heating at 2,45 GHz frequency. The first part will describe the commissioning of the source: Penning discharges inside the accelerating column make the high voltage power supply collapse. Experimental tests with kapton films while discharges occur and simulations with the OPERA-3D code have shown great similarities to detect the location of those discharges and allow us to make the ion source work. The second part of this paper will present the result of low intensity light ion beam production versus the plasma chamber length and radius. Those very preliminary tests give us indications to reduce the ion source dimensions.

INTRODUCTION

At CEA Saclay, light ion sources are generally designed for accelerator purpose. Since mid-90's ECR ion sources have been developed for high intensities: the SILHI source produces up to 100 mA of proton or deuteron beams routinely [1] for the IPHI accelerator and the IFMIF ion source [2] producing up to 120 mA of deuteron is under commissioning. Recently the need of smaller size ion sources had increased, capable to deliver 50 mA of proton beams with the lowest emittance. In order to work on this need, an internal R&D work was scheduled on several years to study several criterions: what are the relevant parameters that can reduce the size of an ion source?

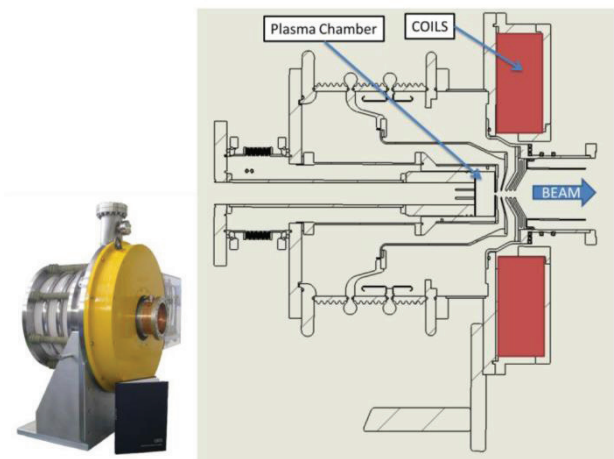

Figure 1: ALISES Ion Source, extraction side.

*otuske@cea.fr

This paper will show the first experimental results of the ALISES ion source installed on the BESTI test bench [3] and how we solved partially Penning discharges inside the source. The second part will show the preliminary results at low bias voltage for low extracted currents when changing the plasma chamber length and diameter.

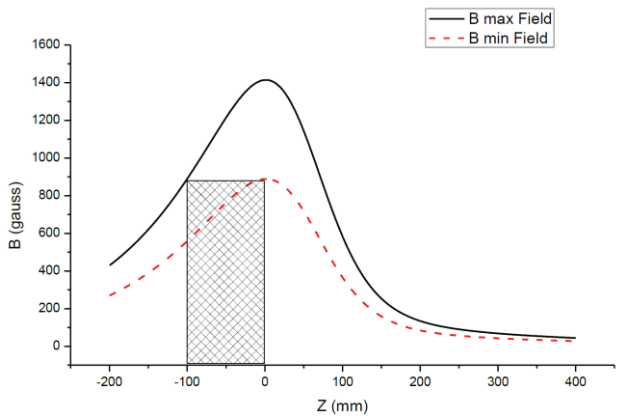

Figure 2: Fringe field of the source coil. The dash zone represents the plasma chamber

COMMISSIONING

The ALISES ion source has been described in ref [4] and [5]. This source is not intended to be a small size source but allows us to test several size parameters in order to miniaturize the next generation of ion sources. The ALISES concept consists in reversing the position of the insulating structure with the magnetic field generation material (coils or permanent magnets), in order to shortened the LEBT and keep the extracted beam focalized at source exit.

The commissioning of the ion source was made in several steps. First we applied 50 kV of bias voltage on the source body and the puller electrode independently in order to detect some grounding problem or sparking. No sparking was detected on either electrode. For the second step, we switched off all HV power supplies of the source and switched on the magnetic field of the source coil in order to produce the 875 Gauss resonance zone at 100 mm behind the plasma electrode. With a 3 sccm of H2 gas and 300 W of HF power delivered by the magnetron, a pink colored plasma was observed through a window along the LEBT axis, characteristic of the hydrogen Balmer lines.

When the electric and magnetic field were simultaneously on, the HV power supplies dropped down

ISBN 978-3-95450-123-6

Copyright © 2012 CC-BY-3.0 and by the respective authors

with a maximum current flow. This behavior occurs every time and is different than a spark. We suggest that it could be a Penning discharge occurring inside the accelerating column. With the OPERA-3D code [6] we could simulate the whole system, applying the right bias potential (40 kV on the plasma electrode and -2 kV on the repeller and ground potential on all the others) and the right magnetic field. We added also several free electrons (10-5eV of initial kinetic energy) in the space between electrodes. At several locations, electrons were accelerated up to several kilovolts and trapped by the combination of electric and magnetic field lines. Theses electrons have their energy and life-time increased and are able to ionize the residual gas, thus ignite a plasma: the Penning discharge.

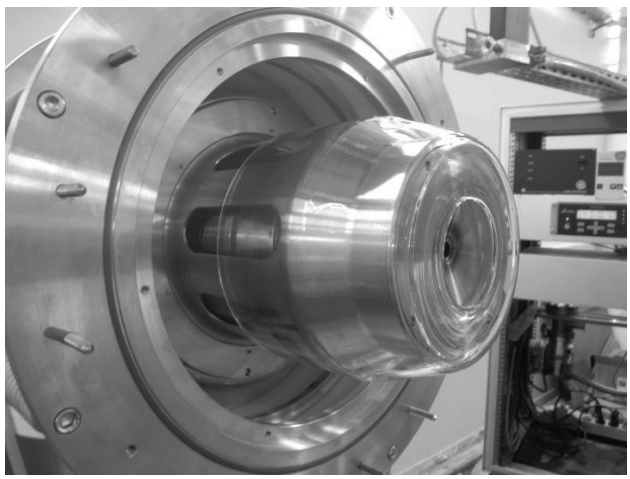

Figure 3: External glass-tube around the puller electrode.

To comfort our idea, we placed around the electrodes several foils of Kapton. We applied simultaneously the HV and the magnetic field several millisecond. We compared the locations of the marks on the foils with the trapped electrons zones simulated with the code: they showed a good agreement.

In order to reduce the Penning discharge occurrence, three tubes made of glass where positioned around the electrodes. That allowed us to apply simultaneously HV and magnetic field in order to ignite the ECR plasma and extract the H+ particles out of the source.

The gaps between electrodes were set for 23 kV (maximum potential reach with spark) of 20 mA beam extracted with a 6 mm diameter extraction hole. Now beam can be extracted at 23 kV and measurements with plasma chamber dimensions were started.

PLASMA CHAMBER REDUCTION

Plasma Chamber Length

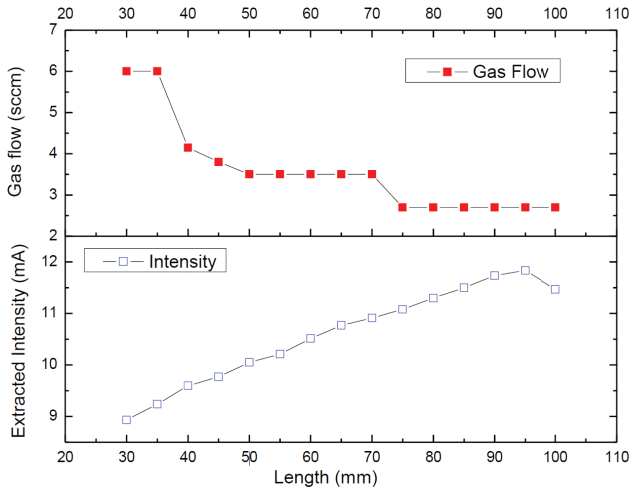

Figure 4: Intensity extracted and injected H_2 gas flow versus plasma chamber length.

The ALISES plasma chamber length can be modified from 100 mm to 30 mm. The extraction hole remains fix and the RF ridge part moves toward extraction hole. As the plasma chamber length get reduce, the intensity of the magnetic field produced by the source coil must also be decreased in order to keep the 875 Gauss at the ridge exit. On Fig.4 we report the optimized extracted intensity and the injected H2 gas flow rate versus the plasma chamber length. It shows that from 30 to 95 mm the intensity increases regularly as the gas flow decreases.

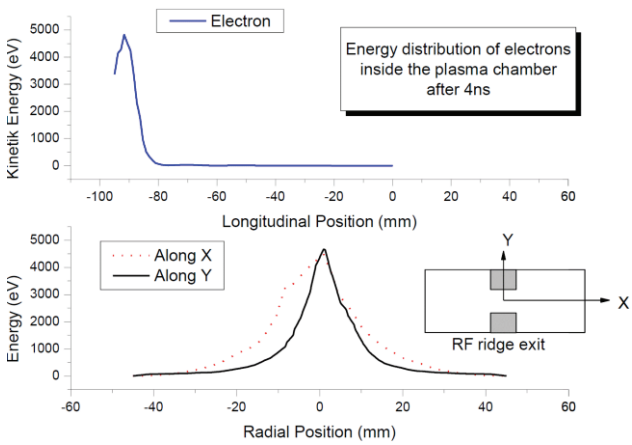

Figure 5: Spatial-energy distribution of electrons in the plasma chamber calculated with SOLMAXP.

One explanation of those behaviors can be advanced if we look at the longitudinal energy distribution of electrons in a 100 mm plasma chamber. This was simulated with SOLMAXP [7]. Highly energetic electrons are produced and concentrated around 10 mm of the ridge exit located at position -100 mm on Fig.5 upper curve.

The maximum of total cross section for producing H+ from H or H_2 by electron bombardment is around 60 eV

Copyright © 2012 CC-BY-3.0 and by the respective authors

ISBN 978-3-95450-123-6

[8-9], low value compare to the 5 keV of the hot electrons produced at the resonance zone. In order to lower the kinetic energy of those hot electrons, the gas in the rest of the plasma chamber is used as a "thermalizer". That explains also the behavior of the gas pressure to obtain the maximal value of extracted current for a shorter plasma chamber: as the thermalizer length is reduced the pressure must be increased to cool down with a better efficiency hot electrons in order to increase the cross section values for ionization.

Plasma Chamber Diameter

With ALISES ion source we can also reduce plasma chamber diameter by inserting a metallic tube and fix it on the RF ridge side of the plasma chamber. The nominal diameter of the chamber is Ø90 mm. Two metallic tubes of 100 mm long were manufactured with internal diameter of 45 and 30 mm. On the result Fig.6 the extracted current seems to be quite constant all over the 3 different diameter values.

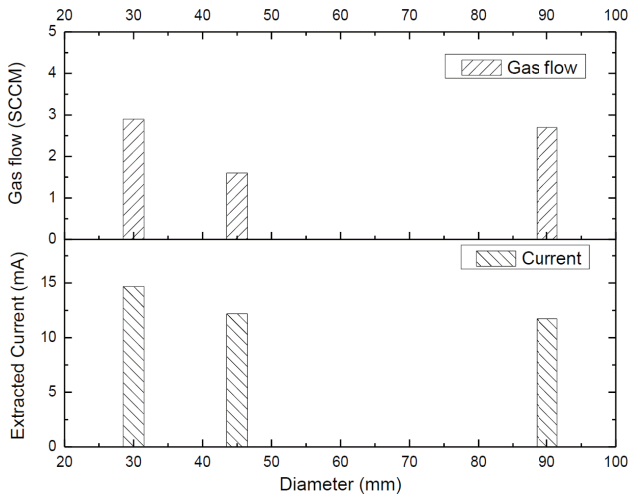

Figure 6: Extracted current intensity and injected gas pressure versus plasma chamber diameter.

On the lower part of Fig. 5 the radial simulation of kinetic distribution of hot electrons is centered on the ridge steps, where the electric field is concentrated. The radial dimensions of the distribution are around 20 and 30 mm respectively for vertical (Y) and horizontal direction (X). Compare to the waveguide dimension, the small distance between ridge steps in the vertical dimension (Y) makes the kinetic distribution narrower in this direction than in the horizontal plane: it seems evident that reducing plasma chamber radial dimension from 90 to 30 mm would not affect as much the heating zone where hot electrons are produced.

That means that plasma chamber internal diameter for future ion source can be reduced to 30 mm, giving the possibility of decreasing the dimension of the magnetic system and accelerating column radial dimension also.

This experiment was also carried out on the IFMIF ion source with a more intense proton beam, and gives the same results: for a 50keV of beam energy, extracted current intensity remains constant. For higher extraction potential a 10% decreased of current seemed to be observed as one reduces the internal diameter to 30mm.

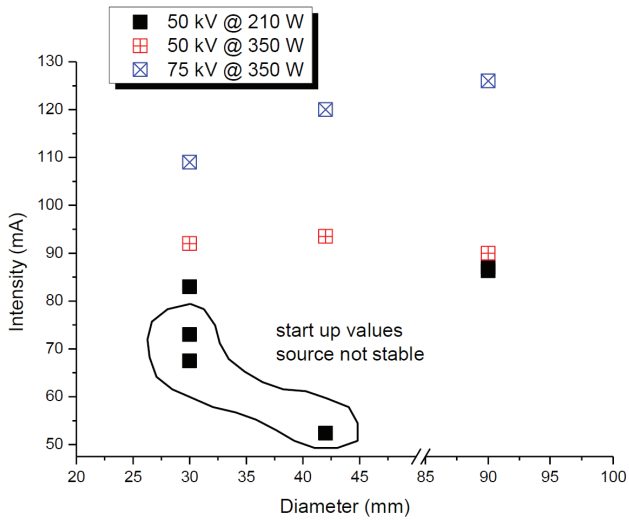

Figure 7: Preliminary results on IFMIF source, intensity vs plasma chamber diameter, bias voltage and bean extraction energy.

CONCLUSION

The commissioning of the ALISES ion source made us create a new tool to test our accelerating columns in order to find electrons traps that give rise to Penning discharges. This code was also tested on other source and helped us to understand some marks inside accelerating column of the IFMIF source for example.

Plasma chamber radial reduction on two ion sources (ALISES and IFMIF) showed the same behavior: up to Ø30mm internal diameter no dramatic changes on beams intensities were observed.

ALISES ion source Patent n°

REFERENCES

[1] R. Gobin, et al., Rev. Sci. Instrum. **81**, 02B301 (2010).
[2] R. Gobin, et al., Rev. Sci. Instrum. **83**, 02A349 (2012).
[3] O.Tuske, et al., Rev. Sci. Instrum. **79**, 02B710 (2010).
[4] O. Delferrière, et al., Rev. Sci. Instrum. **83**, 02A307 (2012).
[5] S. Nyckees, et al., Rev. Sci. Instrum. **83**, 02A349 (2012).
[6] Opera-3D, Cobham Technical Services 24 Bankside Kidlington, Oxford OX5 1JE, UK.
[7] The SolMaxP code, IPAC 2012, New Orleans (MOPPC056).
[8] Y.-K. Kim and M.E. Rudd, Phys. Rev. A **50**, 3954 (1994).(T).
[9] Y.-K. Kim and M. E. Rudd, Comments At. Mol. Phys. **34**, 293 (1999).

ISBN 978-3-95450-123-6

Copyright © 2012 CC-BY-3.0 and by the respective authors

A MULTI-SAMPLE CHANGER COUPLED TO AN ECR SOURCE FOR AMS EXPERIMENTS*

R. Vondrasek[a)], T. Palchan, R. Pardo, C. Peters, M. Power, R. Scott, Argonne National Laboratory, Argonne, IL 60439, U.S.A.

Abstract

A project using Accelerator Mass Spectrometry (AMS) at the ATLAS facility to measure neutron capture rates on a wide range of actinides in a reactor environment is underway. This project will require the measurement of a large number of samples previously irradiated in the Advanced Test Reactor at Idaho National Laboratory. The AMS technique at ATLAS is based on production of highly-charged positive ions in an electron cyclotron resonance ion source (ECRIS) followed by acceleration in the ATLAS linac. The sample material is introduced into the plasma via laser ablation. This should limit the dependency of material feed rates upon the source material composition as well as minimize cross-talk between samples. A new multi-sample changer has been constructed allowing rapid changes between samples. The sample changer has 20 positions and is capable of moving from one sample to the next in one minute.

INTRODUCTION

Accelerator mass spectrometry (AMS) is a sensitive technique for accurately measuring quantities of long-lived, rare isotopes in the presence of more abundant ones using very small amounts of material. The material of interest is introduced into the ion source of an accelerator, ionized, accelerated, and separated by electromagnetic means. Accelerators offer an advantage over conventional mass spectrometers owing to the total elimination of molecular interference due to the dissociation of the molecules in the ion source plasma. By accelerating the mass of interest to energies of a few MeV/U, it is often possible to use differences in rates of energy loss to separate the isobar constituents into their exact elemental groups resulting in a complete atom-by-atom unique identification over much of the periodic table [1, 2].

AMS often has a limited amount of material that can be provided for the measurement with sample sizes of at least a few mg mass required to be able to handle and control the delivery of the ions into the plasma (and hence to the detector). Also for oven evaporation or even sputtering, the form of the source material determines how easily this material can be introduced into the plasma. So in many AMS cases the success of the project can hinge on the choice of the material chemical form and either the dilution methods employed or the pre-AMS chemical separation techniques used to enrich the element of interest.

Oven evaporation and sputtering can indiscriminately deposit material into the source resulting in an accumulation of material on the source walls. This can lead to sample 'cross-talk' and elevated backgrounds. For many AMS experiments, it has been necessary to develop liners to shield the source plasma from the wall contaminations [3]. This can form the ultimate limitation to AMS sensitivity either because of an inability to discriminate isobar members adequately or due to sample cross-talk.

In an effort to reduce both the cross-talk problem and allow the use of small samples with minimal chemical processing and dilution, the laser ablation technique is being employed to introduce the sample material into the source in a very controlled and precise manner. Laser ablation was first developed at ATLAS [4, 5] and used as a plasma diagnostic tool and has since been used by a number of other labs to explore the coupling of laser produced ions into an ECR source [6, 7]. The controlled release of materials into the plasma by well-focused laser light will eliminate the significant material accumulation often seen in the region of the oven throat or beside the sputter samples. The inefficient and indiscriminate injection of material into the source using the sputter or oven methods reduces the total sensitivity of the AMS method and is a major source of cross-contamination between samples.

THE ANL ECR ION SOURCE

ECR2 is a room temperature ion source based upon the A-ECRU design [8] with the plasma excited with multiple frequencies between 10 and 14 GHz and a typical bias voltage of 14 kV. The source has radial access utilized for material introduction as well as pumping to the plasma region. Due to source space considerations as well as the desire to have the ablated material traverse as much of the plasma as possible, it was decided to pursue an axial ablation geometry. In this geometry the laser is mounted off of the source high voltage platform at ground potential. The beam is directed up to the high voltage platform through large diameter insulting pipes. The ablation sample is introduced on the injection side of the source with the laser beam entering the vacuum system through a port on the 0º line. The laser enters the ion source plasma chamber through the extraction aperture and strikes the target (Fig. 1).

For the initial on-line tests, the ablation sample was mounted on a simple linear motion feed through. The optimum ablation position during source operation was determined by varying the sample position and observing the intensity of the beam of interest. However, for the experimental program, a large number of sample positions were required with the ability to cycle rapidly between them.

Copyright © 2012 CC-BY-3.0 and by the respective authors

ISBN 978-3-95450-123-6

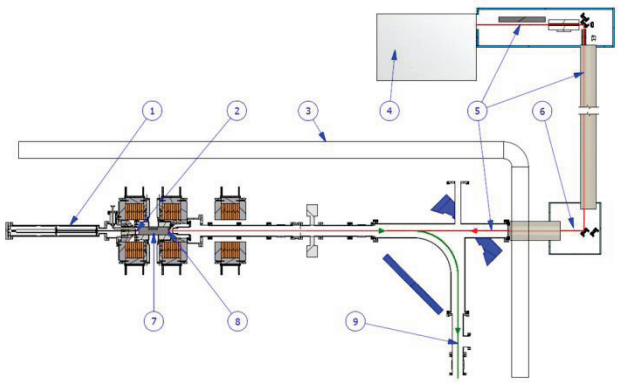

Figure 1: Installation of the laser ablation system at the ECR2 ion source. 1: sample changer chamber, 2: sample ablation position, 3: high voltage platform, 4: laser power supplies, 5: laser path, 6: wobbler mirror, 7: plasma chamber, 8: extraction aperture, 9: ion beam path.

SAMPLE CHANGER SYSTEM

The sample changer accommodates 20 sample positions and allows the experimental data system to remotely operate the system. The samples are mounted on the end of stainless steel rods 3.16 mm in diameter. The sample wheels are fabricated from PCTFE due to its low outgassing rate as well as its low surface coefficient of friction. The rods are arrayed around a central shaft which is manipulated with a stepper motor augmented with an absolute encoder. In this way, absolute position information is maintained even in the event of a loss of power. Sample position and composition information is entered into a computer data base and is accessible from either the accelerator control system or the experimental data system. The sample is moved into ablation position with a magnetically coupled linear drive which is also equipped with a stepper motor. A variable linear resistor provides position information and IN and

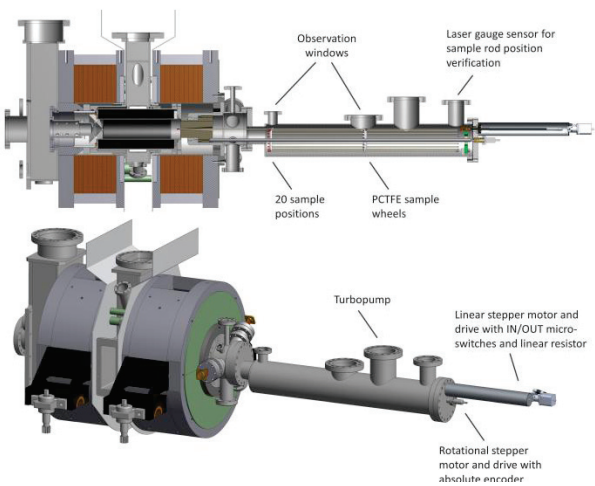

Figure 2: Schematic of ECR ion source with sample changer chamber and associated hardware.

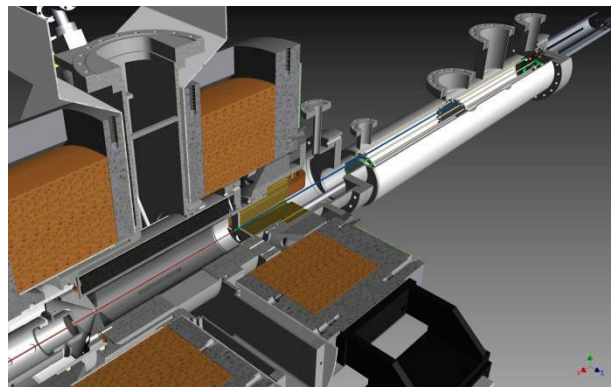

Figure 3: Cut- away view of ECR ion source with sample changer chamber. Sample is depicted in the fully inserted position with the laser beam shown in red entering the plasma chamber through the extraction aperture.

OUT position limit switches control motor power to prevent over driving of the feed through. As an added safe guard to verify that the sample rod is fully retracted before rotation, a laser gauging sensor is used to detect the fully retracted sample rod. Only when this circuitry is closed is power provided to the rotational stepper motor. Fig. 3 shows a cut-away view of the sample changer chamber installed on the ECR source. The sample is in ablation position and the laser beam is entering from the left through the extraction aperture.

A detail of the injection region is shown in Fig.4. One end of the central shaft is secured in the injection side iron with a CPVC bushing to facilitate smooth operation. The iron was modified with a taper to accommodate any positioning errors and has a coaxial section at the end of the taper to assure accurate and repeatable positioning of the sample on axis. A high intensity lamp in the injection region back lights the sample and allows visual verification of its position. Also seen in the figure are the samples, shown in red, mounted on the ends of the sample rods.

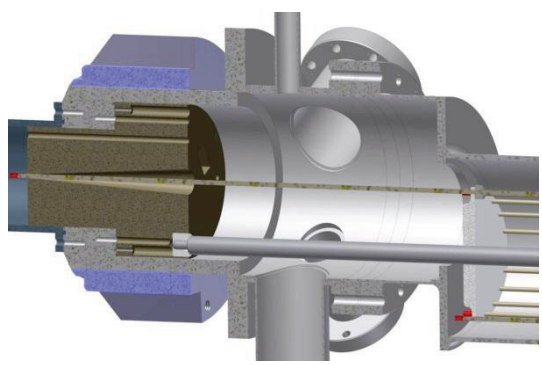

Figure 4: Detail of the taper in the iron plug and the spindle mount in the injection tank region. The RF and support gas also enter the source via this chamber.

ISBN 978-3-95450-123-6

Copyright © 2012 CC-BY-3.0 and by the respective authors

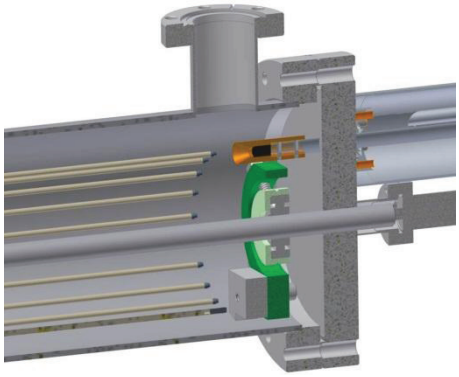

Figure 5: Detail of the spindle mount, the linear drive receptor with magnet, and the iron end tips on the sample rods. The linear drive pushes the sample into position. A permanent magnet allows retraction and decoupling from the sample rod at the full OUT position.

At the other end of the sample shaft is a mount which allows alignment of the overall device. Seen in Fig. 5 are the central shaft and the surrounding sample rods, the shaft mount, and the mounting flanges for the rotary feed through and the linear drive. At the end of the linear drive shaft is a receptor cup. The cup is tapered such that when it moves forward to push the sample into position any misalignment is compensated for with the taper. To secure the sample rod to the linear drive a permanent magnet is used. The magnet engages an iron end tip that is threaded onto the stainless steel sample rods. The magnet strength was specified such that during sample retraction the sample rod remains firmly engaged but once the end of the sample rod travel is reached the linear drive pulls away from the magnet allowing free rotation.

The sample holders are constructed of either stainless steel or high purity aluminium and are 3.16 mm in diameter. The sample volume is recessed so that there is less chance for the sample material to be transferred to source surfaces via direct contact. The interior is tapered such that it minimally intercepts the ablation plume while at the same time self-shielding the plasma chamber walls from the portions of the ablation plume which may not directly intercept the plasma.

Figure 6: Sample holder.

OPERATION AND PERFORMANCE

The sample changer has been operated on-line during source ablation tests. Samples of aluminum, aluminum oxide, iron oxide, and uranium oxide were ablated into the ECR source, ionized, and analysed.

During an ablation sequence, a sample is selected and the rotational motor moves it into position with the position being verified by the absolute encoder. The linear drive then pushes the sample into the ablation position, a total travel of 375 mm. The sample linear position is monitored by the linear resistor. After sample ablation, the linear drive retracts the sample with the magnetic coupling disengaging at the end of travel. The laser sensor verifies that the sample rod has been fully retracted before allowing rotation of the sample assembly. The total selection, insertion, and retraction time is one minute.

ACKNOWLEDGEMENTS

This work was supported by the U.S. Department of Energy, Office of Nuclear Physics, under contract number DE-AC02-06CH11357.

REFERENCES

[1] M. Paul et al.,Nucl. Instr. and Meth B 172,688 (2000)
[2] L.K. Fifield, A.P. Clacher, K. Moris, S.J. King, R.G. Cresswell, J.P. Day, F.R. Livens, Nucl. Instr. and Meth. B 123 (1997) 400
[3] P. Collon et al., Nuclear Instruments and Methods in Physics Research B 283 (2012) 77–83
[4] R. C. Pardo, R. Harkewicz, and P. J. Billquist, Rev. Sci. Instrum. 67, 1602 (1996)
[5] R. Harkewicz, J. Stacey, J. Greene, and R.C. Pardo, Rev. Sci. Instrum. 65, 1104 (1994)
[6] S. Gammino et al., Rev. Sci. Instrum. 73, 650 (2002)
[7] K. Sasa, I. Arai, M. Kurosawa, and T. Nakagawa, Rev. Sci. Instrum. 75, 1928 (2004)
[8] Z.Q. Xie and C. M. Lyneis, Rev. Sci. Instrum. 67, 886 (1996)

Copyright © 2012 CC-BY-3.0 and by the respective authors

ISBN 978-3-95450-123-6

OPTIMIZATION OF THE NEW SC MAGNETIC STRUCTURE DESIGN WITH A HYBRID MAGNET*

D.Z. Xie#, W. Lu, L.T. Sun, X.Z. Zhang, H.W. Zhao, M.Z. Guan, Q. Hu, T.J. Yang, L. Zhu, and L.Z. Ma, IMP, Lanzhou, 730000, China

Abstract

In the development of the next generation Electron Cyclotron Resonance Ion Source, so far either a set of full NbTi or Nb_3Sn magnets has been proposed to construct the magnet system. However, the single set of NbTi magnets may not be the optimum in terms of the field strength and configuration. An optimization of the new SC magnetic structure [1] with a hybrid magnet (NbTi and Nb_3Sn) is being investigated. With the hybrid magnet and other minor changes the optimized new magnetic system is capable of producing field maxima of 9.0 T on axis and 4.1 T at the plasma wall, which are about 30 and 5 percent higher than the new SC magnetic structure to be built with a set of full NbTi magnets. In addition, the axial length of the optimized magnetic structure has been slightly shrunk resulting in a less bulky system. This new magnetic field profile is high enough for operation frequency up to 56 GHz. The design features and the preliminary stress analysis of the optimized new SC magnetic structure will be presented and discussed.

INTRODUCTION

The significant performance enhancement of Electron Cyclotron Resonance Ion Source (ECRIS) in the last decade has demonstrated that operating with higher-field and higher-frequency remain to be the most effective and straightforward path to further improve the ECRIS performance [2-4]. To meet the increasing ion beam demands from the accelerators worldwide under construction or design, the next generation ECRISs of much higher-field and higher operating-frequency have been proposed to be built with either a set of full Nb_3Sn or a set of full NbTi magnets. As a continuation of the classical magnet structure, a set of full Nb_3Sn magnets would yield field maxima of 8.0 T on axis and 4.0 T at the plasma chamber walls [5]. The newly proposed magnetic structure (MK-I) would produce 7.0 T and 3.9 T with a set of full NbTi magnets, and 12.0 T and 6.0 T with a set of full Nb_3Sn magnets, respectively [1]. However, there are many uncertainties of the Nb_3Sn magnet to be used in ECRIS and which need thoroughly addressed before an ECRIS of Nb_3Sn can become a reality. On the other hand, the NbTi magnet has been fully proven its reliability in the present generation ECRISs, but the configuration of maximum fields of 7.0 T and 3.9 T may not be very satisfactory to support operations up to 56 GHz. Development has demonstrated that higher magnetic fields is the needed basis for a next generation ECRIS to achieve higher performance [6]. Therefore building an ECRIS with a set of full NbTi magnet may not be the best option in the near future and an exploration of any possible optimizations on the magnet system would greatly benefit the development.

*Work supported by China Nature Science Foundation under Contract No. 10921504
zqxie@impcas.ac.cn

A HYBRID MAGNET WITH THE NEW MAGNTIC STRUCTURE

Fabrication of a Nb_3Sn solenoid coil nowadays is a pretty straightforward process. In reference to the case of a set of full NbTi magnets (NbTi-I) with the MK-I magnet structure [1], the hybrid magnet (Hybrid-I) described here is such a set of magnets that injection solenoid is fabricated of Nb_3Sn wires but keep the rest coils of NbTi wires, as indicated in Fig. 1.

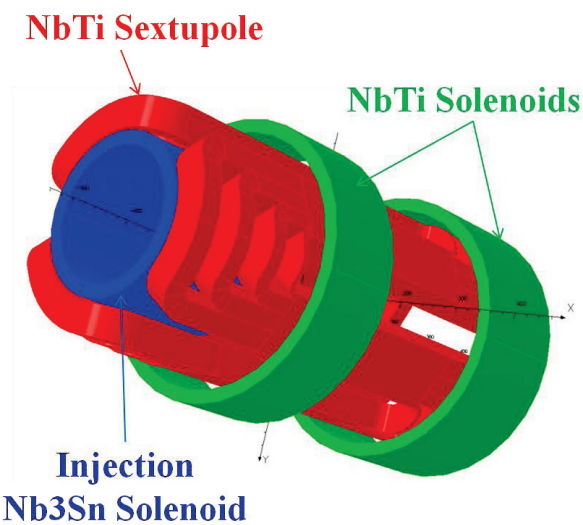

Figure 1: The hybrid magnet in the MK-I magnet structure in which the injection solenoid is made of Nb_3Sn wires and the rest of NbTi wires.

Other Optimizations

Since the Nb_3Sn wires can carry higher currents than the NbTi wires, thus the following optimizations are also exercised:

- Thinning the solenoid coil by keeping the outer diameter constant but increasing inner diameter by 24 mm so that there will be more space for inserting more injection components;

Copyright © 2012 CC-BY-3.0 and by the respective authors

ISBN 978-3-95450-123-6

- Shortening the extraction side of the sextupole magnet by 60 mm that results in an 800 mm long magnet, instead of the previous length of 860 mm;
- Replacing the intended EAS NbTi (F54) wires with the Supercon NbTi (56S53) wires of slightly higher critical currents in the sextupole magnet to obtain field increase of a few percent along the larger radius of the hexagonal plasma chamber.

Table 1 below lists the variations and comparisons of the mechanical dimensions and the system stored energy between the Hybrid-I and the NbTi-I. With these modifications, the Nb_3Sn injection solenoid and the NbTi sextupole excited respectively at 82% and 88% of its critical currents at 4.2 K as indicated in Fig. 2, the field maxima on the coils are 10.9 T at the inner surface of the injection solenoid and 8.15 T at the sextupole coil. These excitations of less than 90% of its critical currents should be achievable with careful coil winding and clamping as have demonstrated in SECRAL and other sources. Under these excitations, the Hybrid-I produces a peak field of 9.0 T on axis and a radial field of 4.1 T at the plasma chamber walls. These fields are about 30% and 5% higher in comparison to the 7.0 T and 3.9 T in the NbTi-I, as shown in Fig. 3 and Fig. 4. This field configuration of 9.0 T and 4.1 T should satisfactorily support operations with microwaves of frequency up to 56 GHz, based on the present design criteria.

Table 1: Magnet System Variations

	Hybrid-I	NbTi-I
Total Magnet Length (mm)	800	860
ID (mm) of the Injection Solenoid (OD = 240 mm)	200	176
Peak Axial Field/Radial Field at Chamber Walls (T)	9.0/4.1	7.0/3.9
Axial Peak Field Distance (mm)	612	644
System Stored Energy (MJ)	1.4	0.9

The 24 mm enlargement in the injection solenoid ID will increase the diameter of the injection snout accordingly which allows more space for wave guide insertions, easier wave mode conversion and oven ports. With more wave guides available it is easier to launch multiple-frequency plasma heating of various combinations of 14 to 56 GHz to explore any further performance enhancement other than two-frequency plasma heating [7]. More injection space will also allow easier wave conversions to investigate the wave-mode effects on plasma heating and source performance [8]. In addition, more oven ports would provide a better flexibility of solid-ion beams for daily operations with the accelerators. A shorter magnet length will lead to a less bulky source that would benefit the ion beam extraction, transport, vacuum pumping and somewhat lower cost, as the higher-field SC ECRIS becomes larger and bulkier.

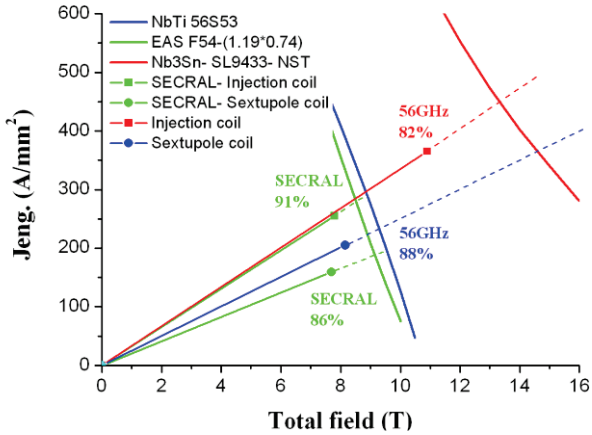

Figure 2: Magnet coil current loading at 4.2 K and comparison between the Hybrid-I and SECRAL.

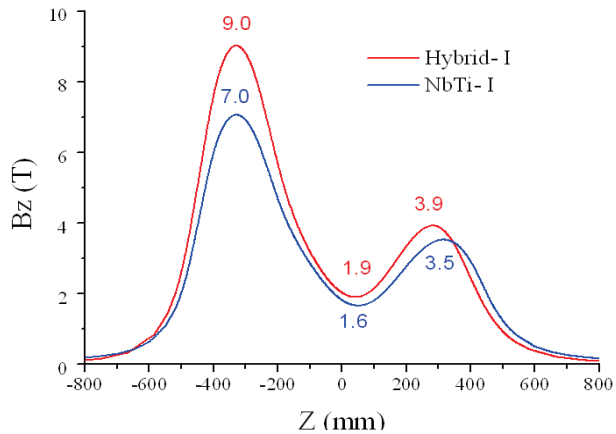

Figure 3: The Hybrid-I produces about 30% higher axial field (red line) and slightly shorter distance between the field peaks in comparison to the NbTi-I (blue line).

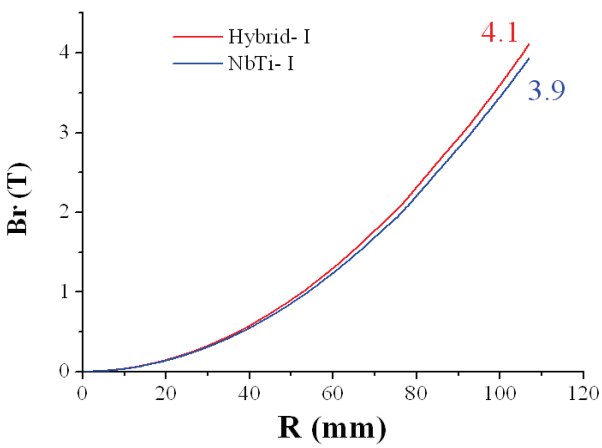

Figure 4: With the Supercon 56S53 wires the Hybrid-I produces slightly higher radial field (red line) than the NbTi-I with EAS F54 wires (blue line) at the plasma chamber walls.

Copyright © 2012 CC-BY-3.0 and by the respective authors

ISBN 978-3-95450-123-6

PRELIMINARY STRESS ANALYSIS

A full 3D ANSYS model has been developed for the stress analysis to verify the feasibility of the Hybrid-I design. In this preliminary analysis, the controlled pre-stress to the coils is omitted but real material properties were applied to the coils cooled down to 4.2 K. Fig. 5 shows the applied constraints assuming infinite rigid the cold iron segments. With the magnet coils were excited at the maximum design currents flowing at the same direction, the stress distribution has shown a maximum stress of 108 MPa at the inner surface of the injection solenoid, as shown in Fig. 6. The peak field at this location is of only 10.1 T computed by the ANSYS model but TOSCA calculations showing a field of 10.9 T. This field strength discrepancy could well be due to the mesh size of the ANSYS code is relatively coarse in comparison to TOSCA. In the future analyses, the e.m. forces should be imported from the 3D TOSCA model for better accuracy and consistency [5].

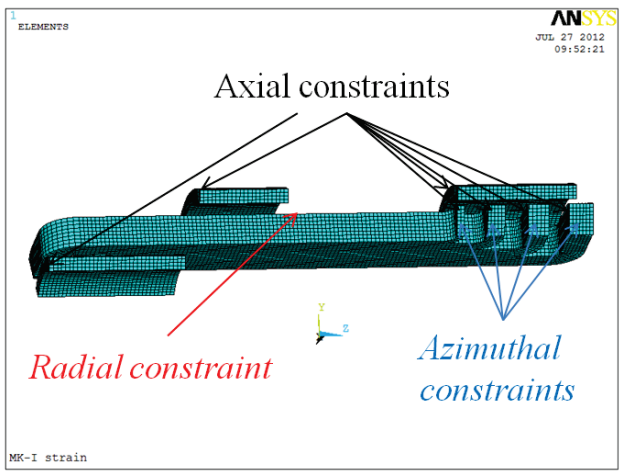

Figure 5: Constraints applied to the preliminary stress analysis in one sixth of the Hybrid-I model at 4.2 K. The same azimuthal constraints were applied to the other end of the sextupole but not graphically indicated in this figure.

Under the above stated excitations, all the e.m forces exert on the coils are both radially and axially outward, which is the characteristic of the MK-I and the non-classical magnetic structures. Fig. 7 indicates the likely maximum deformation could be of about 0.18 mm that occurs mostly in the axial direction at the inner side of the Nb_3Sn injection solenoid where there is a peak radial field from the sextupole magnet that has 3-fold of symmetry. So cares should be taken to well secure the injection solenoid to minimize the potential of quenching. The rest deformations at other places are pretty minimal, most of them in the orders of a few hundredths of one mm and that should be taken care by the cold iron segments without great difficulties.

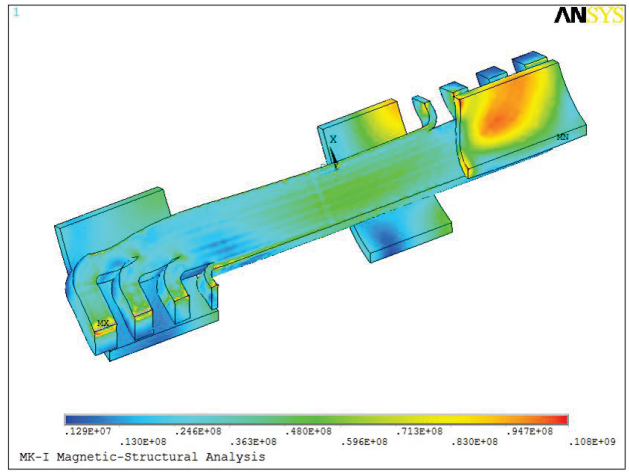

Figure 6: Stress distribution of the Hybrid-I with the applied constraints indicated in Fig. 5. In this preliminary analysis the maximum stress is of 108 MPa occurring at the inner surface of the Nb_3Sn injection solenoid which is within the stress limit.

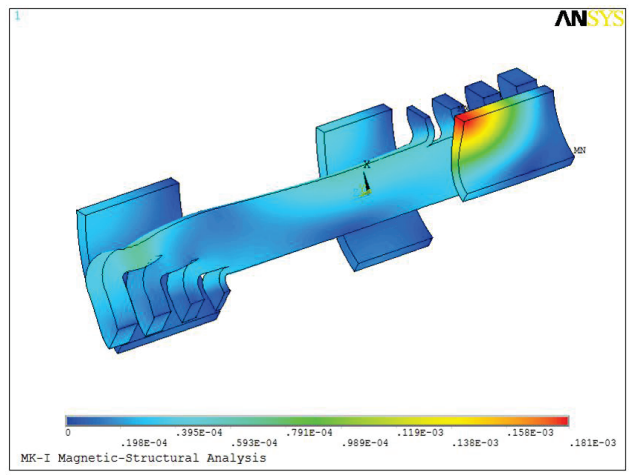

Figure 7: Distribution of the likely deformation of the Hybrid-I with the applied constraints indicated in Fig. 5. The maximum deformation occurs mostly in the axial direction at the inner side of the Nb_3Sn injection solenoid.

DISCUSSIONS

The studied optimizations have lead to a substantial axial field increase at the injection, more space for injection insertions and a less bulky magnet system that would accordingly result in a smaller cryostat. All of these features are very preferable for the next generation ECRISs. Without pre-stressing and at 4.2 K, the preliminarily analyzed peak stress of 108 MPa at the Nb_3Sn injection solenoid and about 80 MPa at the NbTi sextupole coil, which are well within the yield stress limits even taking into account that there is about 8% field underestimate by the ANSYS model. Though further stress analyses with controlled preload need performed in

ISBN 978-3-95450-123-6

Copyright © 2012 CC-BY-3.0 and by the respective authors

the near future, this study has established a base to start designing the detailed system clamping and supports, given that the one-body-wound NbTi sextupole can be fabricated.

The explored optimizations have shown that the Hybrid-I in many aspects is superior to the NbTi-I. Thus if a set of full Nb_3Sn magnets with the MK-I structure is not feasible in the near future, the Hybrid-I could well be a good option for the next generation ECRIS.

REFERENCES

[1] D.Z. Xie, Rev. Sci. Instrum. **83** 02A302 (2012).
[2] J.Y. Benitez et al., Rev. Sci. Instrum. **83** 02A311 (2012).
[3] H.W. Zhao et al., Rev. Sci. Instrum. **83** 02A320 (2012).
[4] L.T. Sun et al., "Intense Beam Production with SuSI," ECRIS'10, Grenoble, August 2010, MOCOAK02, p. 4 (2010); http://www.JACoW.org
[5] C. Lyneis, P. Ferracin, S. Caspi, A. Hodgkison and G.L. Sabbi, Rev. Sci. Instrum. **83** 02A301 (2012).
[6] R. Geller, F. Bourg, P. Brand et al., Proc. of the 8th ECR Workshop, E. Lansing, MI, USA, p. 1 (1987).
[7] Z.Q. Xie, C.M. Lyneis, Rev. Sci. Instrum. **66** (1995) 4218.
[8] C. Lyneis, proceedings of this workshop (Sept 2012).

Copyright © 2012 CC-BY-3.0 and by the respective authors

ISBN 978-3-95450-123-6

CURRENT DEVELOPMENTS OF THE VENUS ION SOURCE IN RESEARCH AND OPERATIONS *

J. Benitez#, K. Y. Franzen, C. Lyneis, L. Phair, M. Strohmeier, LBNL, Berkeley, CA 94720, USA
G. Machicoane, FRIB, East Lansing, MI 48824, USA
L.T. Sun, Institute of Modern Physics, CAS, Lanzhou 730000, China

Abstract

The VENUS ion source functions as a research and development tool in the ECR community as well as an injector for LBNL's 88-Inch cyclotron. In order to meet the needs of both the ECR community and users at the 88-Inch cyclotron, technology such as ovens and a sputter probe have been developed for introducing metals into the plasma. Using a modified high temperature oven, VENUS has produced 450eμA of $238U^{33+}$ and 400eμA of $238U^{34+}$, twice the required Uranium beam current needed for FRIB. In addition, after upgrading its high voltage capabilities VENUS produced 11emA of $4He^{2+}$, a capability that remains unparalleled by other ECR ion sources. In addition to its recent record high intensities VENUS is also being developed to deliver low intensity, ultra high charge state ions for the cocktails beams, where many species are produced simultaneously for use by the BASE Facility. $124Xe^{43+}$ is now in regular production for the 16MeV/u cocktail, and development of $209Bi^{56+}$ for the 10MeV/u cocktail is in progress and has been accelerated through the 88-Inch cyclotron. This paper presents the latest work towards integrating the VENUS ion source into our research and operational goals.

INTRODUCTION

During the last two years a lot of effort has gone into the integration of VENUS into the operation of the 88-Inch cyclotron as well as a continued effort to use it to push the limits of ECR's. To meet the needs of the 88-Inch cyclotron users VENUS should provide intense medium charge state beams for studies involving low-cross section reactions as well as several low intensity medium and high charge state ions simultaneously for the cocktails. A low temperature oven has been developed and work with the high temperature oven continues for the production of intense metal ion beams. To produce a variety of low intensity beams development of a sputter probe has begun and initial results are presented. In order to continue to explore the limits of ECR ion production capability we continue to work to make improvements. In this paper we discuss improvements in the VENUS high voltage capability as well as potential improvements to be made in the VENUS plasma chamber. The mechanical layout and specifics of the VENUS ECR ion source have been discussed at length previously and as such will not be done so here [1,2]. Table 1 provides key specifics.

* This work was supported by the Director, Office of Science, Office of Basic Energy Sciences, of the U.S. Department of Energy under Contract No. DE-AC02-05CH11231.
#jybenitez@lbl.gov

Table 1: Key Parameters of the VENUS ECR Ion Source

VENUS Key Parameters	Values
Maximum 18GHz/28GHz Power	2,000W/10,000W
Maximum INJ/ /EXT Fields	4.0T/3.0T
Maximum RADIAL Field at wall	2.2T
Superconductor	NbTi
Coil Structure	Sextupole in Solenoid
Plasma Chamber Volume	9L
Plasma Chamber Diameter/Length	14.4cm/50cm

SPUTTER PROBE DEVELOPMENT

A sputter probe being developed for use in VENUS is intended to be used to produce metal beams for the cocktails used by the chip testers at the BASE Facility [1]. Cocktail beams consist of ions from up to 14 different elements with similar mass-to-charge, M/Q, ratio which are all extracted from the ion source and delivered to the cyclotron simultaneously. The 88-Inch cyclotron then selects the ion to deliver to the user. Each ion has a different range or penetration depth and will deliver a different amount of energy to the tested part.

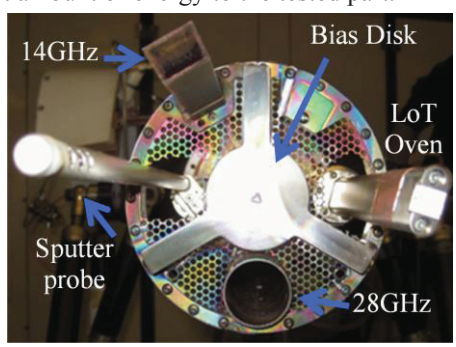

Figure 1: The VENUS injection is shown with the sputter probe and low temperature oven.

The sputter probe, shown in Figure 1, is inserted axially on a water-cooled support tube and a moveable bellows. The intention is to get the sputter probe, made to hold three metal samples, as close as possible to the plasma in order to take advantage of the high ion density regions since it is biased negatively from 0 to-3000V. Because it is inserted axially, placing the sputter probe at the maximum radial position closest to the wall will allow us to insert it further along the chamber in between the plasma flutes. Figure 2 shows the initial results when sputtering ^{181}Ta. At -2000V, 16eμA of 29+ was obtained.

ISBN 978-3-95450-123-6

Copyright © 2012 CC-BY-3.0 and by the respective authors

However, at its current radial position of 5.6cm, compared to the plasma chamber radius is 7.2cm, the sputter probe is too close to the plasma to operate without melting. Although positive results have been obtained, modifications are planned to place it at the maximum radius inside the plasma chamber.

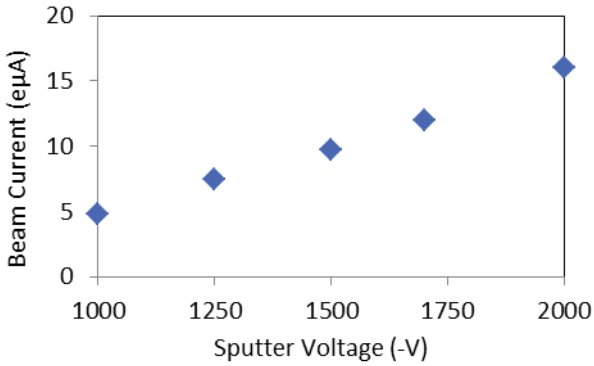

Figure 2: Initial sputter probe results producing $^{181}Ta^{29+}$.

LOW TEMPERATURE OVEN DEVELOPMENTS

Calcium Development

With the development of the low temperature oven [4], shown in Figure 1, several long term performance tests have been done. Because 48Ca is of particular importance to the 88-Inch cyclotron users, consumption measurements have been performed using 40Ca. During one test with the low temperature oven 40Ca was run for 94 hours with a consumption rate of 0.67mg/h, a 2% efficiency into the $^{40}Ca^{11+}$ charge state, and a total efficiency of 9% into all charge states. The 40Ca was run using 18GHz heating only at a typical 18GHz axial field configuration of 2.2T at injection, 1.5T at extraction, 0.3T at the center, and 1.3T radially at the wall.

Hot Liner Test

In an effort to further decrease the calcium consumption rate a test was performed using a hot tantalum liner as done by the Dubna group who showed the use of the hot liner covering the plasma chamber walls increases the ion source efficiency [5]. In the 14GHz AECR-U the use of the Ta liner decreases the consumption rate by a factor of 3. The VENUS liner test lasted 46 hours with a consumption rate of 0.73mg/hr and a 2.11% efficiency into the $^{40}Ca^{11+}$ charge state. The liner did not decrease the consumption rate as expected. As with the previous run only 18GHz was used with the same magnetic field configuration. The run started with an equivalent radial field of 1.3T at the wall but soon after the run commenced, Ta peaks began to appear in the spectra, disrupting the ^{40}Ca charge state distribution, and it was necessary to turn up the radial field to 2.2T which is usually used only for 28GHz operation. Figure 4 shows how quickly the Ta^{20+} peak corresponded with the radial field.

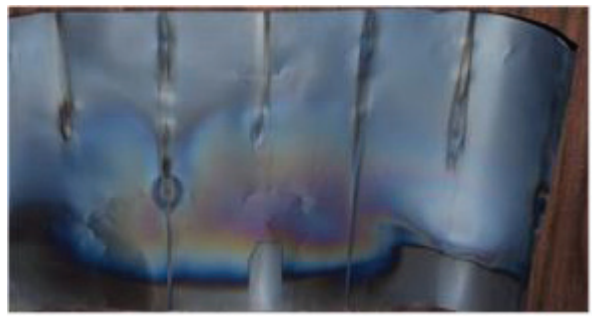

Figure 3: Innermost layer of the tantalum liner.

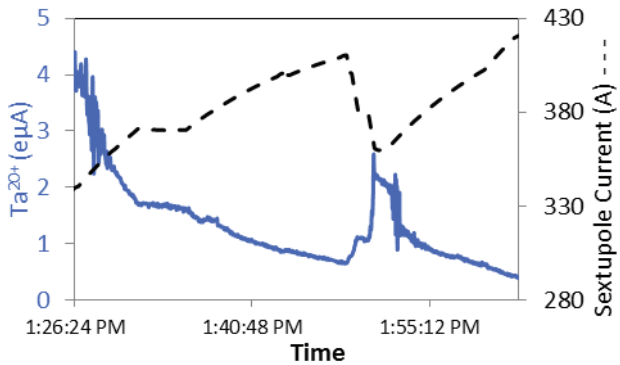

Figure 4: The graph shows the response of the Ta^{20+} peak, coming from the Ta liner, to the sextupole field.

The liner consisted of three individual Ta layers each 0.003" thick and was 12 inches long. Figure 3 shows the innermost layer of the liner after the test as well as the markings made by the plasma flutes. The plasma chamber length is about 20 inches long but the liner was placed at the injection side where the oven is located. When the liner was removed no layers where burned through but the innermost layer was dimpled at the locations where it saw the most hot electrons. It is interesting to note that little to no CaO was found on the liner when removed. This suggests that either little calcium makes it onto the wall or that it is efficiently re-circulated back to the plasma.

Bismuth Development

The VENUS low temperature oven allows for the development of new ions in the cocktail beams. Development has begun to add $^{209}Bi^{56+}$ or $^{209}Bi^{57+}$ to the 10MeV/u cocktail. The ion $^{209}Bi^{56+}$ would extend the Linear Energy Transfer in the 10MeV cocktail from 78 to 91 MeV/(mg/cm2) for silicon. In May of 2012, Bi^{56+}, B^{i57+}. and Bi^{58+} were accelerated and extracted from the cyclotron. The maximum $^{209}Bi^{56+}$ measured at cyclotron extraction on a Faraday cup was 0.08enA. $^{209}Bi^{57+}$ and $^{209}Bi^{58+}$ were only seen in trace amounts. Table 1 lists the important parameters of the VENUS tune when producing these high charge states of Bismuth. More cyclotron development time is needed to allow for tuning the VENUS ion source in conjunction with the cyclotron. With VENUS tuned for very high charge states, it produced 5.3eμA of Bi^{50+}.

Copyright © 2012 CC-BY-3.0 and by the respective authors

ISBN 978-3-95450-123-6

Table 1: Summary of Parameters used in High Charge State Production of Bismuth

VENUS Bismuth parameters	values
Extraction Voltage	12.5kV
Bi^{56+} at cyclotron extraction	0.08 enA
Bi^{50+} at source extraction	5.3 eμA
Bi Oven Temperature	605°C
18GHz/28GHz Power	2000W/4700W
INJ/MID/EXT Fields	3.4T/0.55T/2.2T
RADIAL Field at wall	2.2T
INJ/EXT Pressure	$1.3x10^{-7}/1.9x10^{-8}$ mbar

URANIUM RESULTS

Recently the high temperature oven used to produce uranium beams was modified to improve the water cooling of the current carrying leads, which allowed us to reach higher oven power [4]. This modification led to the successful production of high intensity uranium beams. To reach a vapor pressure of UO2 between 1x10-2 and 1x10-1mbar requires temperatures from 2000-2300°C [7]. UO2 has a melting point at about 2820°C. Two tests were done to produce uranium beams from UO2, one using a tungsten oven and one using a rhenium oven.

The first test, which was done using the tungsten oven, was unsuccessful in producing a stable and intense uranium beam. Figure 5 shows the resulting condition of the oven after the test and removal from VENUS. The tungsten oven's lower stem, in the presence of the strong axial magnetic field and resulting Lorentz force, traveled sideways in the soft copper housing. Poor contact between the lower stem and the copper housing may have resulted in a higher local temperature which allowed the stem to move in the then soft copper. The resulting contact between the oven body and the copper housing caused the oven to be electrically and thermally shorted. This was apparent during the run when the resistance of the oven became unstable.

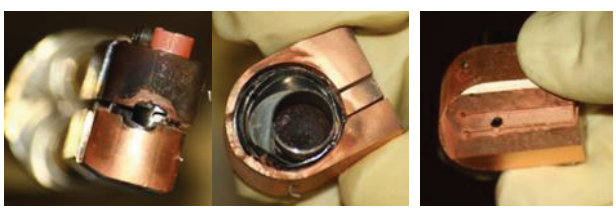

(a) (b) (c)

Figure 5: High temperature oven with the tungsten oven used in the first and unsuccessful uranium production test. (a) and (b) show that the tungsten oven moved off center within the copper housing. (c) shows the underside of the copper housing and the tungsten stem moved off from the center.

The second test, using the rhenium oven shown in Figure 6, successfully produced 450eμA of $238U^{33+}$ and 400eμA of $238U^{34+}$. Figure 7 shows the uranium spectrum. The source parameters for the high intensity tune are shown in Table 2. With this oven, tuning for high charge states of uranium was also done. We reached 13eμA of $238U^{50+}$ which required both a lower injection pressure of 1.8x10-7mbar and a lower oven power of 340W than the values used to produce the high intensity results. The high charge states were very sensitive to the oven power and, hence, the amount of uranium vapour introduced.

(a) (b)

Figure 6: (a) High temperature oven with the rhenium oven used in the second and successful uranium production test. (b) rhenium oven after the run shows a deformed body.

One factor contributing to the success of the rhenium oven is that the rhenium oven requires less current to reach the temperature at which UO_2 vaporizes due to its higher resistance than the tungsten oven. This is shown in Figure 8, which compares the oven power versus temperature for the tungsten, tantalum and rhenium axial ovens currently in use to produce various metal vapours. When the rhenium oven was removed from VENUS it was seen that the oven walls had slightly buckled but there was no damage to the stems and no indication of instabilities during the test. Approximately 179 mg of UO_2 was used over the course of about 29 hours, giving a consumption rate between 6-7mg/hr. The emittance of the uranium beams produced with the rhenium oven is discussed in reference [6].

Table 2: Summary of Parameters used in High Intensity Production of Uranium Beam with a Rhenium Oven

VENUS Uranium parameters	Values
Extraction Voltage	12.5kV
Bi^{56+} at cyclotron extraction	0.08 enA
Bi^{50+} at source extraction	5.3 eμA
Bi Oven Temperature	605°C
18GHz/28GHz Power	2000W/4700W
INJ/MID/EXT Fields	3.4T/0.55T/2.2T
RADIAL Field at wall	2.2T
INJ/EXT Pressure	$1.3x10^{-7}/1.9x10^{-8}$ mbar

ISBN 978-3-95450-123-6

Copyright © 2012 CC-BY-3.0 and by the respective authors

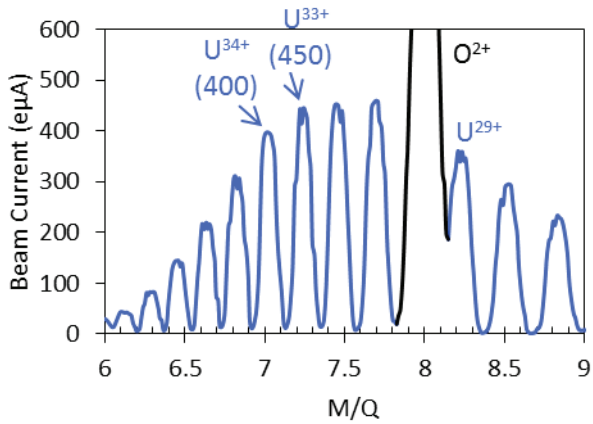

Figure 7: A high intensity Uranium spectrum produced using a rhenium high temperature oven.

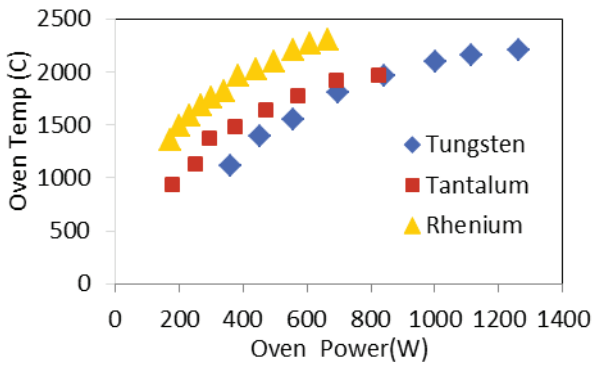

Figure 8: A comparison of the oven power required to reach a certain temperature for the axial ovens available for use in VENUS.

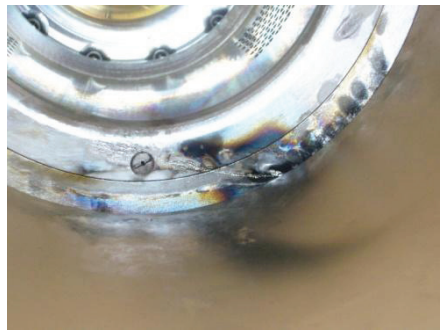

Figure 9: Damage caused by sparking between ground shield, that protects the 40kV insulator, and the high voltage surface. The ground shield is removed here, exposing the 40kV insulator.

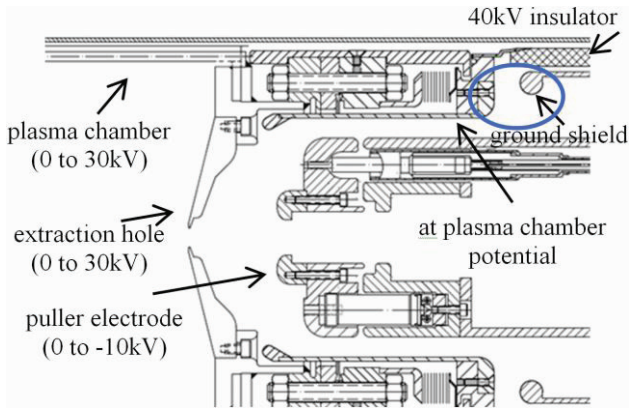

Figure 10: Drawing showing the extraction region of VENUS. The distance between the ground shield and the high voltage surface was increased and the surfaces cleaned, allowing VENUS to reach higher voltage.

HIGH VOLTAGE UPGRADE

In an effort to increase the maximum high voltage capability of VENUS, and increase transmission efficiency, several improvements were made to the source. One change was in the region after beam extraction. It was known to us that during operation there was sparking in the extraction region that prevented VENUS from holding more than 22kV.

An investigation of the extraction region revealed burn marks between the last high voltage surface and the ground shield that protects the 40kV insulator, as shown in Figure 9. Figure 10 is a mechanical layout of the extraction region and shows the region where the sparking occurred. In addition water damage to the surfaces, from an incident that occurred in 2004, was seen on the ground shield. The surfaces were cleaned and the ground shield was replaced. The distance between the high voltage surface and the ground shield was increased by 0.32" to a new distance of 0.75" with the installation of the new ground shield. This improvement has allowed VENUS to reach 30kV during operation and is currently limited by the 28GHz high voltage break.

High Intensity Helium

With the improvements to the VENUS extraction system a new record intensity for the production of helium was achieved. A total extracted current of 25.4emA was obtained with 9.3emA of He^{1+} and 11emA of He^{2+}. This was the upper limit of the power supply current capability and no saturation in extracted current was noted. With a higher voltage, higher current power supply we anticipate that VENUS can extract much more beam intensity. It is worth pointing out that the amount of current on the aluminium bias disk at the injection end was 57.5 mA, twice that of the total extracted current.

Table 3 lists the source settings used in the intense production of helium.

VENUS PLASMA CHAMBER

VENUS' large superconducting magnet structure allows for a large plasma chamber with a 9L volume. The increased plasma volume allows the absorption of larger amounts of microwave power. Most of the power heats the electrons, which are lost to the walls. Because of this

Copyright © 2012 CC-BY-3.0 and by the respective authors

ISBN 978-3-95450-123-6

it is important that there be adequate cooling of the chamber walls where the magnetic confinement field is weakest. These weak points are located where the solenoid field's radial component partially cancels out the radial field produced by the sextupole. In total, there are 18 water cooling channels, with the six wide supply channels oriented to the six plasma flutes, or loss lines. A CAD drawing of the plasma chamber is shown in Figure 11. The plasma chamber is aluminum and designed to have a wall thickness of 1.85 mm (0.073") at the water supply channels, with this being the thinnest region, and 3.50 mm (0.138") where there is no water channel. The inner diameter is 14.4 cm and the total length is approximately 103 cm, however the total length of the plasma chamber is 50cm.

Table 3: Summary of Parameters used in High Intensity Production of Helium Beam

VENUS Helium parameters	Values
Extraction Voltage	25kV
Total Extracted Current	25.4emA
He^{1+}	9.3emA
He^{2+}	11emA
18GHz/28GHz Power	1745W/1000W
INJ/MID/EXT Fields	3.4T/0.41T/2.1T
RADIAL Field at wall	2.2T
Bias Disk V/I	335V/57.5mA
INJ/EXT Pressure	$1.1x10^{-6}/8.7x10^{-7}$ mbar

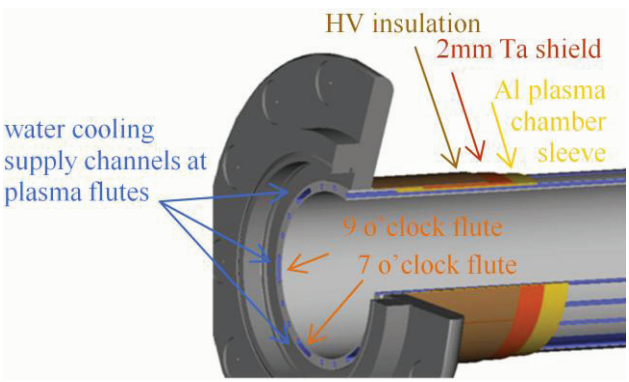

Figure 11: A CAD drawing of the VENUS plasma chamber. The water cooling supply channels are aligned with the plasma flutes. Towards the injection the flutes are located at 3, 7 and 11 o'clock.

Recently the VENUS plasma chamber developed a hole in the wall along one of the flutes. Figure 12 shows the hole which is located at the 7 0'clock position when looking from the injection towards extraction, along an injection flute line. The position of the hole has proved to be an exact point of localized heating of the plasma chamber in the past. Figure 12 shows the hole. After the hole occurred, the wall was inspected carefully. The thickness of the wall along this supply channel was only 0.053", 0.020" thinner than called for in the drawings. This is attributed to the complexity in machining and assembling the plasma chamber. It is also interesting to point out that the hole is located in approximately the same location as the first chamber failure in 2004. Figure 13 shows a side-by-side comparison of the holes when viewed with the outer layer cut away to expose the water channel and hole. Despite the location being the same, there is a significant difference in the heating pattern. The accident in 2004 was instantaneous and caused by a failure in the 28GHz gyrotron power control circuit where the power went to a full 10kW. The 2012 hole appears to be the result of long term heating.

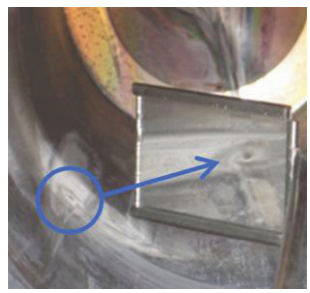

Figure 12: Location of the water leak along an injection flute line.

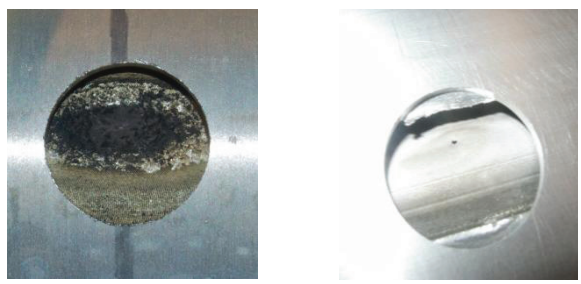

(a) (b)

Figure 13: The outer sleeve of the plasma chamber was cut to expose the water channel at the position of the hole in both pictures. (a) 2012 hole (b) 2005 hole.

The plasma chamber failure led us to study the magnetic fields in VENUS in detail. A magnetic field survey along each pole, at the plasma chamber wall, was done using the sextupole at 460A, with the solenoid field off. Figure 14 shows the magnitude of the maximum radial field for each pole, as indicated by the clockwise position of the pole, at r=7.2cm (at the wall) and at the location of the plasma chamber hole. It appears that there is a misalignment between the plasma chamber and the position of the sextupole magnets, which would increase

ISBN 978-3-95450-123-6

Copyright © 2012 CC-BY-3.0 and by the respective authors

the local heating at the location of the 2012 hole. Plans to improve the alignment of the plasma chamber and the magnetic field are under way.

SUMMARY

VENUS operated without any quenches or other cryogenic issues for 22 months. This was the longest period of cold operation and no degradation of the cooling capacity of the Gifford McMahan crycoolers was observed. During this time it produced a number of new beams, summarized in Table 4.

Improvements in the VENUS high temperature oven and the high voltage capability have allowed for new records. Development of the sputter probe continues as well as an investigation of improvements in the plasma chamber and alignment to the magnets.

Table 4: Summary of Recent High Intensity Beam Production Milestones for VENUS

Ion	Charge State	Intensity (eμA)
^{4}He	2+	11,000
^{16}O	6+	3,000
^{40}Ar	11+	860
^{209}Bi	31+	300
^{209}Bi	50+	5.3
^{238}U	33+	450
^{238}U	50+	13
^{40}Ca	11+	400

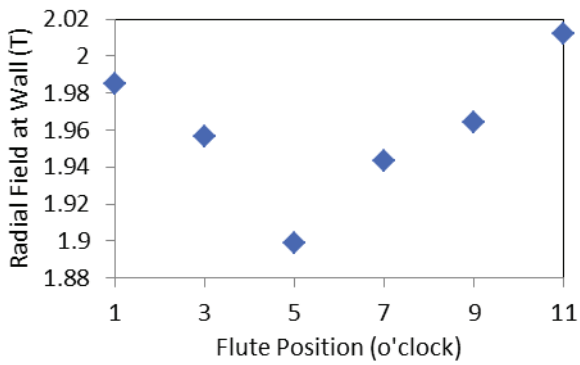

Figure 14: The maximum radial magnet field due to the sextupoles at each pole at the position where the plasma chamber was damaged.

REFERENCES

[1] M. Leitner, D. Leitner, S. Abbott, C. Taylor, C. Lyneis. (2002). Progress report on VENUS. Lawrence Berkeley National Laboratory: Lawrence Berkeley National Laboratory, 03 Sept 2002. 17 Oct. 2012. http://escholarship.org/uc/item/1x17d7tr.

[2] C. Lyneis, D. Leitner, M. Leitner, C. Taylor, S. Abbott. *The Third Generation Superconducting 28GHz ECR Ion Source VENUS*, Rev. Scient. Instrum., **81**, 2 (2010).

[3] M.A. McMahan. *The Berkeley Accelerator Space Effects (BASE) Facility-A new mission for the 88-Inch Cyclotron at LBNL*. Nucl. Instr. and Meth. in Phys. Res., B241, (2005), p. 409.

[4] J. Y. Benitez, A. Hodgkinson, M. Johnson, T. Loew, C. Lyneis, and L. Phair. *Recent Progress on the Superconducting Ion Source VENUS.* Rev. Scient. Instrum., **83**, 02A311 (2012). \

[5] V.B. Kutner, S.L. Bogomolov, A.A. Efremov, A.N. Lebedev, V.N. Loginov, A.B. Yakushev, and N. Yu. Yazivitsky. *Production of Intense 48Ca Ion Beam at the U-400 Cyclotron.* Rev. Scient. Instrum., **71,** 860 (2000).

[6] G. Machicoane, J. Benitez, N. Bultman, , C. Lyneis, G. Morgan, E. Pozdeyev, X. Rao, L.T. Sun. *Design Status of ECR Ion Source and LEBT for FRIB.* Proc. of the 20th International Workshop on ECR Ion Sources (ECRIS12), Sydney, Australia, 2012.

[7] C. Lau. Proceedings of the EURISOL target and ion-source working group, 2000.

Copyright © 2012 CC-BY-3.0 and by the respective authors

ISBN 978-3-95450-123-6

RECENT THE RIKEN 28 GHZ SC-ECRIS RESULT

Y. Higurashi#, J. Ohnishi, K. Ozeki, H. Haba, M. Fujimaki,M. Kidera, M. Komiyama and O. Kamigaito, RIKEN Nishina Center, 2-1 Hirosawa, Wako-shi, Saitama, JAPAN
T. Aihara, M. Tamura, A. Uchiyama, SHI Accelerator Service Ltd. 1-17-6 Osaki, Shinakagaw, Tokyo, JAPAN

Abstract

Highly charged uranium (U) and xenon (Xe) ion beams were produced by the RIKEN superconducting electron cyclotron resonance ion source (SC-ECRIS) using 28 GHz microwaves. The beam intensity of Xe^{25+} was about 250 eμA at an RF power of 1.7 kW. The sputtering method was used to produce a highly charged U ion beam. The beam intensity is strongly dependent on the rod position and sputtering voltage. We obtained ~60 eμA for the U^{35+} ion beam at an RF power of 2 kW.

INTRODUCTION

In the last decade, facilities for the production of radio isotope (RI) beams have been constructed worldwide.[1–4] In these facilities, intense heavy ion beams are needed to produce intense radioisotope (RI) beams. To meet this requirement, several super-conducting electron cyclotron resonance ion sources (SC-ECRISs) have been constructed to produce intense highly charged heavy ions. [5–8]

At RIKEN, we started to construct the new SC-ECRIS, which has an optimum magnetic field strength for 28 GHz microwaves to produce intense highly charged heavy ion beams for the RIKEN RI beam factory project [1]. In the spring of 2009, the RIKEN SC-ECRIS produced its first beam using 18 GHz microwaves.[5] In 2010, 28 GHz microwaves were injected into the new SC-ECRIS and obtained highly charged Xe ion beam. Since then, we have conducted various experiments and modifications to increase the beam intensity. In this paper, we present the modification of the ion source and recent results for highly charged U and Xe ion production.

RIKEN SC-ECRIS

The detailed structure and performance were described in Ref. 5. The RIKEN SC-ECRIS can produce various on axis magnetic field distributions using 6 solenoid coils, which include both the classical B_{min} and the so-called "flat B_{min}"[9]. The liquid He vessel for the ion source is cooled by two refrigerators, (a Gifford-McMahon refrigerator (maximum cooling power of ~1 W) and a Gifford-McMahon + Joule-Thomson refrigerator (maximum cooling power of ~4 W)).

#higurasi@riken.jp

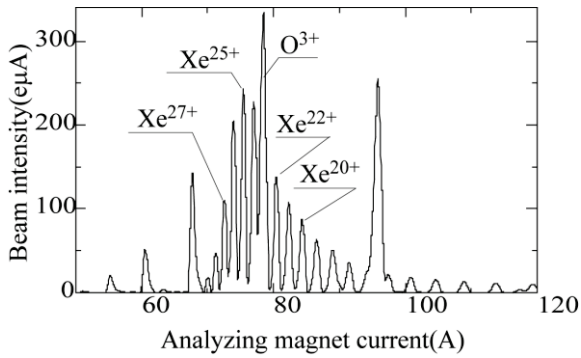

Figure 1: Charge state distribution of highly charged Xe ions at an RF power of 1.7 kW. The ion source was tuned to produce a Xe^{25+} ion beam.

RESULTS AND DISCUSSION

Xe Beam Production

In this test experiment, the maximum strength of the mirror magnetic field at the microwave injection side (B_{inj}), the radial magnetic field strength at the inner surface of plasma chamber (B_r), and the maximum strength of the mirror magnetic field at the beam extraction side (B_{ext}) were fixed to 3.2 T, 1.85 T, and 1.8 T, respectively. The extraction voltage was 22 kV, And the typical gas pressure was ~5×10^{-5} Pa. Figure 1 shows the charge distribution of highly charged Xe ions. The ion source was tuned to produce Xe^{25+} ions. Figure 2 shows the beam intensity of Xe^{25+} as a function of RF power.

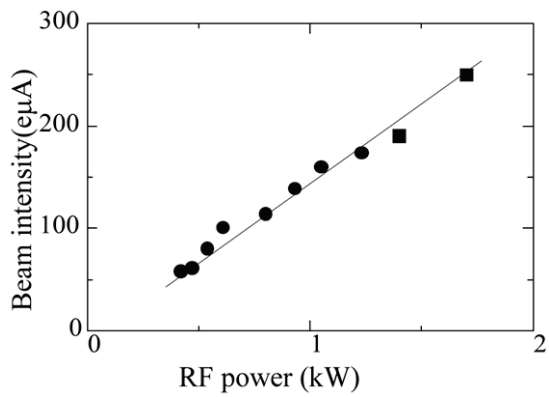

Figure 2: Beam intensity of Xe^{25+} ions as a function of RF power.

The beam intensity increased linearly and we obtained

ISBN 978-3-95450-123-6

Copyright © 2012 CC-BY-3.0 and by the respective authors

250 eμA at an RF power of 1.7 kW. We also measured the emittance and brightness of the Xe ion beam. We observed that the emittance of the Xe^{25+} ion beams were strongly affected by the biased disc voltage. The experimental results are described in Ref.10.

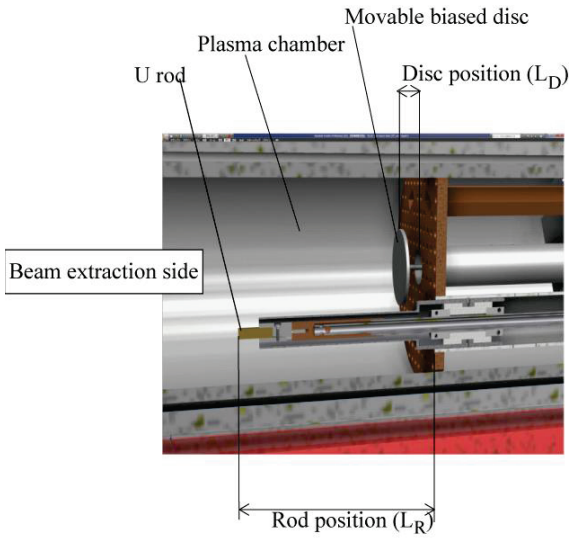

Figure 3: Schematic drawing of the RF injection side for the sputtering method.

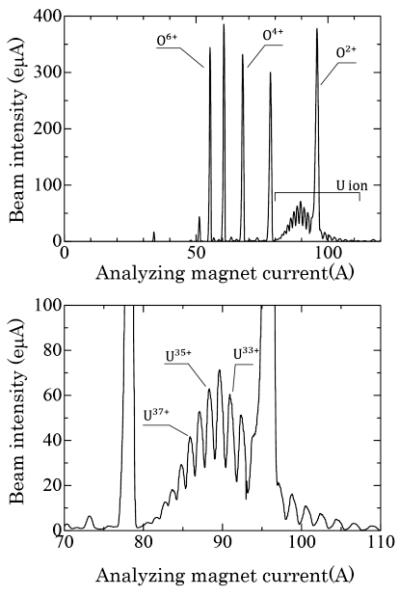

Figure 4: Charge state distribution of U ions. The ion source was tuned to produce a U^{35+} ion beam.

U Beam Production

To produce the U ion beam, we used the sputtering method. The detailed method is described in Ref. 11. Figure 3 shows the schematic drawing. The sputtering voltage and U rod position (L_R) were optimized to maximize the beam intensity of highly charged U ions. The rod position is shown in Fig. 3. The typical sputtering voltage and rod position (L_R) were ~5.5 kV and ~140 mm, respectively. Figure 5 shows a typical charge distribution of the highly charged uranium ions. The RF power was ~2 kW. The ion source was tuned to produce U^{35+} ions. The typical gas pressure was 3-5.5 × 10^{-5} Pa.

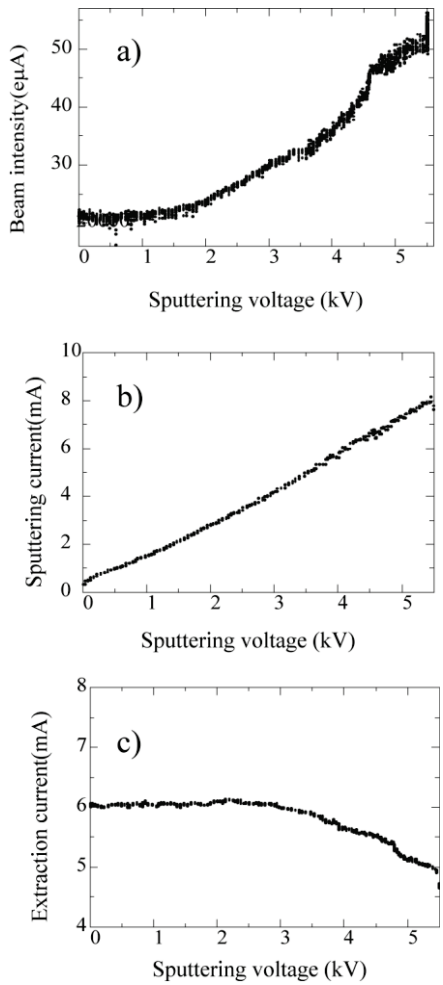

Figure 5: (a) Beam intensity of U^{35+} ions, (b) sputtering current, and (c) extraction current as a function of sputtering voltage.

The beam intensity of the highly charged U ions was strongly dependent on therod position, and sputtering voltage. In order to investigate the effect of these parameters on the beam intensity of U^{35+} ions, we measured the beam intensity as a function of rod position and sputtering voltage. Figure 5-(a) shows the beam intensity of U^{35+} ions as a function of sputtering voltage. The beam intensity increased with increasing voltage up to 5.5 kV. The sputtering current also increased linearly with increasing sputtering voltage as shown in Fig. 5-(b). However, the extraction voltage gradually decreased with increasing voltage as shown in Fig. 5-(c). Figure 6-(a) shows the beam intensity as a function of rod position

Copyright © 2012 CC-BY-3.0 and by the respective authors

ISBN 978-3-95450-123-6

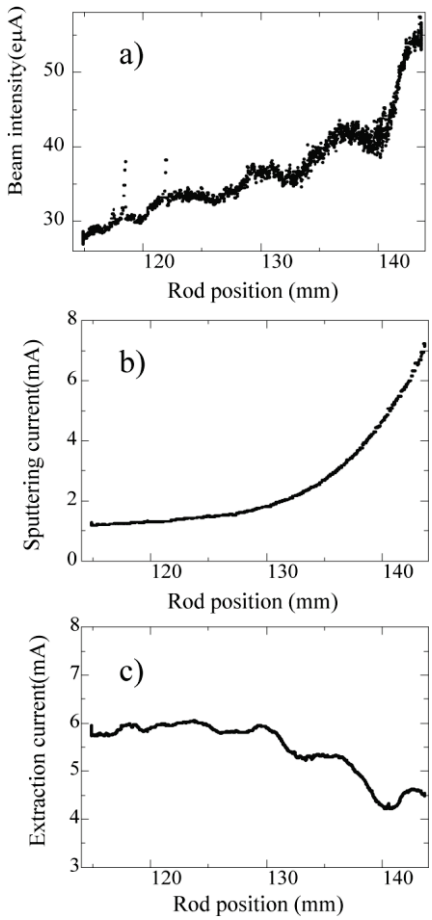

Figure 6: Beam intensity of U^{35+} ions (a), sputtering current(b) and extraction current(c) as a function of rod position.

(L_R). The sputtering voltage was fixed at 5.5 kV. The beam intensity increased with moving the rod toward the ECR zone and oscillated slightly as a function of rod position. Figure 6-(b) shows the sputtering current as function of rod position. The current suddenly increased at the rod position of $L_R \approx 135$ mm. We observed that the extraction current decreased with moving the rod toward the ECR zone.

The beam intensity was also strongly affected by the biased disc position as shown in Fig. 7. The disc position was defined in Fig. 3. The beam intensity of U^{35+} ions is strongly fluctuated by moving the disc. Figure 8 shows the beam intensity as a function of RF power which was calculated from the chamber cooling water temperature. The beam intensity increased linearly with increasing RF power up to 2 kW. We obtained ~60 eμA of U^{35+} and ~80 eμA of U^{33+} at an RF power of 2 kW. The emittance of the U^{35+} ion beam was measured under various conditions. We observed that the emittance of U^{35+} ions was ~100 πmm mrad (4 rms emittance) and independent of the RF power (1–2 kW). Furthermore, we observed that the brightness of the beam increased with increasing disc bias voltage. The detailed experimental results are described in Ref. 10.

Long-term stable beam production is a very important issue for the ion source at RIKEN RIBF. When producing a U^{35+} ion beam for a long time, we observed that the beam intensity fluctuated regularly which is mainly due to changing output power from the gyrotron. We found that the current to power supply for the solenoid coils fluctuated slightly with changing room temperature, and as a result, the output power of the gyrotron changed. To minimize this effect, we replaced the power supply with a more stable one. Using it, we obtained a stable beam with less than 10% fluctuation in long-term operation. The detailed results are described in Ref. 12.

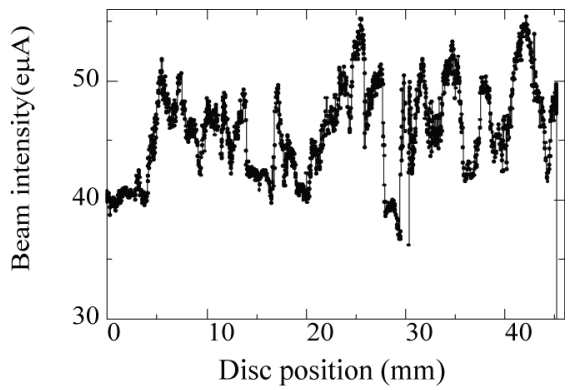

Figure 7: Beam intensity of U^{35+} ions as a function of biased disc position.

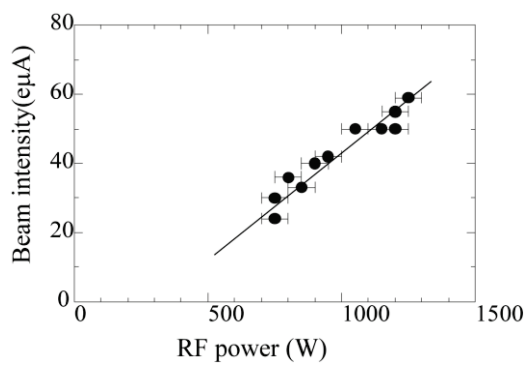

Figure 8: Beam intensity of U^{35+} ions as a function of RF power as calculated from chamber cooling water temperature.

CONCLUSIONS AND FUTURE PLANS

We measured the beam intensity of highly charged U and Xe ions with 28 GHz microwaves under various conditions. The sputtering method was used to produce U ion beams. The beam intensity of U^{35+} ions was strongly dependent on the rod position and sputtering voltage. The beam intensity of U^{35+} ions increased with increasing

ISBN 978-3-95450-123-6

Copyright © 2012 CC-BY-3.0 and by the respective authors

sputtering voltage and proximity of the rod to the ECR zone. The biased disc position strongly affected the beam intensity. Using the sputtering method, we obtained ~60 eμA of U^{35+} and ~80 eμA of U^{33+} at an RF power of 2 kW.

To increase the beam intensity, we will attempt to increase the injected RF power in a future work. Furthermore, we plan to use a high-temperature oven to obtain a higher vapor pressure of U next spring.

REFERENCES

[1] Y. Yano, Nucl. Instrum. Methods. B261 (2007) 1009.
[2] M. Thoennessen, Nucl. Phys. A 834 (2010) 688c.
[3] FAIR Baseline Technical Report, http://www.gsi.de/fair/reports/btr.html
[4] M. Leitowicz, Nucl.Phys. A 805(2008) 519c.
[5] T. Nakagawa et al., Rev. Sci. Instrum. 81 (2010) 02A320.
[6] D. Leitner et al., Proceedings 19th Int. Workshop on ECR ion sources, 2010, Grenoble, France, p. 11.
[7] H. Zhao et al., Rev. Sci. Instrum. 81 (2010) 02A202.
[8] T. Sun et al., Proceedings 19th Int. workshop on ECR ion sources 2010, Grenoble, France, p4.
[9] G. D. Alton and D. N. Smithe, Rev. Sci. Instrum. 65 (1994) 775.
[10] K. Ozeki et al., in these proceedings
[11] Y. Higurashi et al., Proceedings 19th Int. workshop on ECR ion sources 2010, Grenoble, France, p. 84.
[12] J. Ohnishi et al., in these proceedings.

Copyright © 2012 CC-BY-3.0 and by the respective authors

ISBN 978-3-95450-123-6

OPERATION OF AN ECRIS CHARGE STATE BREEDER AT TRIUMF

F. Ames, R. Baartman, P. Bricault, K. Jayamanna, A. Mjøs,
TRIUMF, 4004 Wesbrook Mall, Vancouver, BC V6T 2A3, Canada

Abstract

After initial commissioning of the charge state breeder for radioactive ions at the TRIUMF/ISAC facility further tests on the performance of the system have been done., One of the major problems found was the high background of stable ions from the ECR source. The main source of those is the residual gas and sputtered material from the plasma chamber wall and from the surrounding electrodes. Although, their intensity is small it can be orders of magnitude more than the intensity from the radioactive ions. Therefore, the original stainless steel plasma chamber of the Pantechnik PHOENIX ECR source has been exchanged to aluminium with a pure aluminium coating, all electrodes for injection and extraction of the ions have been replaced with aluminium and the iron joke at the extraction side, which is part of the vacuum system in the PHOENIX source has been coated as well. This combined effect has reduced the amount of background ions substantially. Together with some beam purification in the accelerator chain the background could be reduced to a level acceptable for experiments with radioactive ions. A low transport efficiency of ions with very high charge states can be explained by to charge changing collisions with residual gas

INTRODUCTION

Radioactive ions are produced at the ISAC facility at TRIUMF by bombarding solid targets with protons at 500 MeV and up to a current of 100 μA. The products diffuse out of the hot target into an ion source, are extracted at an energy of several 10 keV and mass separated. With ion sources robust enough to operate in this environment at high temperature and high radiation fields mainly singly charged ions are produced. The ions can be used directly in low energy experiments or they can be injected into a post accelerator for high energy experiments. The post accelerator at ISAC consists of a room temperature radio frequency quadrupole (RFQ) accelerator, a room temperature drift tube linear accelerator (DTL) and a superconducting linear accelerator (SClinac). The acceptance of the RFQ allows the injection of ions up to a mass to charge ratio of 30 amu/e at an energy of 2 keV/amu. It accelerates the ions to 150 keV/amu. The following accelerator sections can accelerate ions with a maximum mass to charge ratio of 7 amu/e. That means for most ions an increase in charge state is necessary. This is usually done by stripping in thin carbon foils after the RFQ. If ions with a mass greater than 30 amu are to be accelerated their charge state has to be increased already before the RFQ and in order to avoid further losses due to the stripping the mass to charge ratio should be below 7 amu/e. A modified charge state breeder PHOENIX electron cyclotron resonance (ECR) ion source from PANTECHNIK has been chosen as it is well adapted to the continuous mode of operation of the rest of the systems. The source has been installed and commissioned in 2010 and first results have been reported [1].

RESULTS

Already in the first experiments two problems have been found. It is the low transmission for very high charge state ions and the background from stable elements.

Charge Exchange

A reason for the low transmission is charge exchange along the beam transport. This process has been investigated earlier with the ECR source being installed at a test facility. Cross sections for the charge exchange in the relevant energy range from 10 -18 q keV have been determined for different ions with charge states up to 24+ [2]. In order to measure the charge state dependence of the transport efficiency $^{40}Ar^{7+}$, $^{56}Fe^{10+}$ and $^{133}Cs^{23+}$ have been selected after the charge breeder. They have been accelerated through RFQ and DTL and the total transmission has been determined. All those ions have a mass to charge ratio close to 5.7 amu/e, so possible mass dependencies in the accelerator are minimized. Table 1 gives the transmission for the different ions together with a theoretical transmission. It assumes charge exchange only in the low energy part with an average pressure of $2 \cdot 10^{-7}$ T over 25 m and 70% transmission of the accelerator. Cross sections from [2] have been used. Although, for the lowest charge state the measured value is close to the theoretical expectation for the higher charge states the transmission is less. This indicates that for those charge states charge exchange processes have to be considered as well for higher energies.

Figure 1 shows a beam profile from a $^{133}Cs^{23+}$ beam measured after an electrostatic bender in the low energy section. One can see that in the horizontal bending plane the beam splits in 3 components in this case: the main beam with charge 23+ and two more components with charge 22+ and 21+ respectively. The centre of the beam has been moved off the centre of the beam line for this picture.

ISBN 978-3-95450-123-6

Copyright © 2012 CC-BY-3.0 and by the respective authors

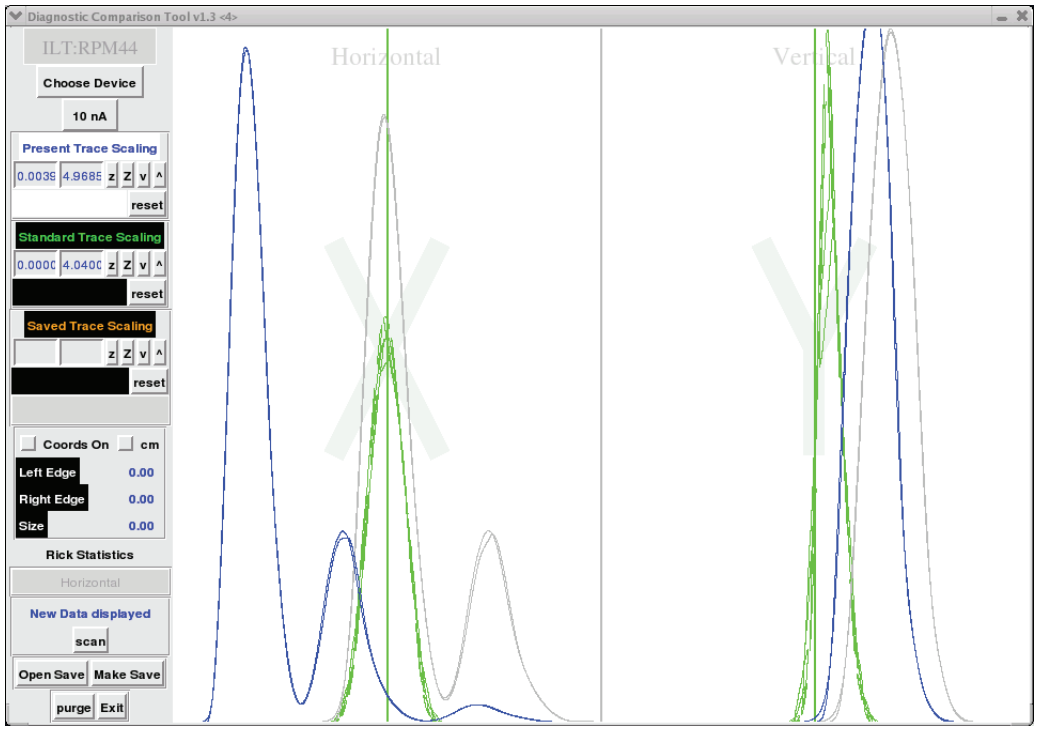

Figure 1: Cs^{23+} beam profile (blue) at the focal plane of first bender in front of the RFQ. The center of the beam has been moved in horizontal (x) direction to show more beam components.

Table 1: Measured and Theoretical Transmission from the Charge State Breeder to the End of the DTL

ion	measured transmission	theoretical transmission
$^{40}Ar^{7+}$	54.6%	56.2%
$^{56}Fe^{10+}$	37.2%	53.5%
$^{133}Cs^{23+}$	27.3%	43.3%

Background

Soon after the first test experiments with radioactive ions it became obvious that the background of stable ions with a mass to charge ratio close to the one of the charge bred radioactive ions is too high for most of the proposed experiments. At ISAC the typical yield of radioactive ions not too far off the region of stable isotopes is up to about 10^8/s and rapidly goes down when leaving this valley of nuclear stability. Thus, with charge state breeding efficiencies of several percent the number of highly charged radioactive ions will be 10^6/s or less. The total current extracted from the ECR source is typically at some 100 µA. It consists mainly of ions from the support gas, in our case helium, and from the residual gas: hydrogen, oxygen, nitrogen, carbon and some noble gases. The charge state of the radioactive ion has to be chosen in such a way, that the mass to charge ratio does not coincide with a charge state of one of those ions. Also the less abundant isotopes of these elements have to be considered. In some cases this may result in a lower efficiency if a non optimum charge state has to be chosen.

Other sources of background are sputtered ions from the material of the plasma chamber and the surrounding electrodes. Their intensity is usually much less, but can still reach several 10-100 pA, which in most cases is much higher than the current of the charge bred radioactive ions. Non-gaseous elements which could be clearly identified either by their mass to charge ratio or after acceleration by their energy are Si, Fe, Ni, Cr, Mo, Sn. All of those have several stable isotopes in their natural abundance and can form several charge states, which lead to mass to charge ratio in the interesting range below 7 amu/e.

In order to minimize the influence of the background, both the gas composition and the wall material should be as pure as possible. This will reduce the number of background ions and possibly open up some “clean” areas in the mass to charge ratio range. A background reduction by several orders of magnitude by grinding and carefully cleaning the surface of an aluminium plasma chamber has been reported by N. Imai et al. [3].

The residual gas pressure in the source is normally kept below $5 \cdot 10^{-8}$ T measured on both sides of the source. It is achieved by pumping with a combination of cryogenic and turbo pumps. As all vacuum seals are done by using Viton o-rings it is not possible to bake the system for a further reduction of the baseline pressure. The support gas is pure helium.

Copyright © 2012 CC-BY-3.0 and by the respective authors

ISBN 978-3-95450-123-6

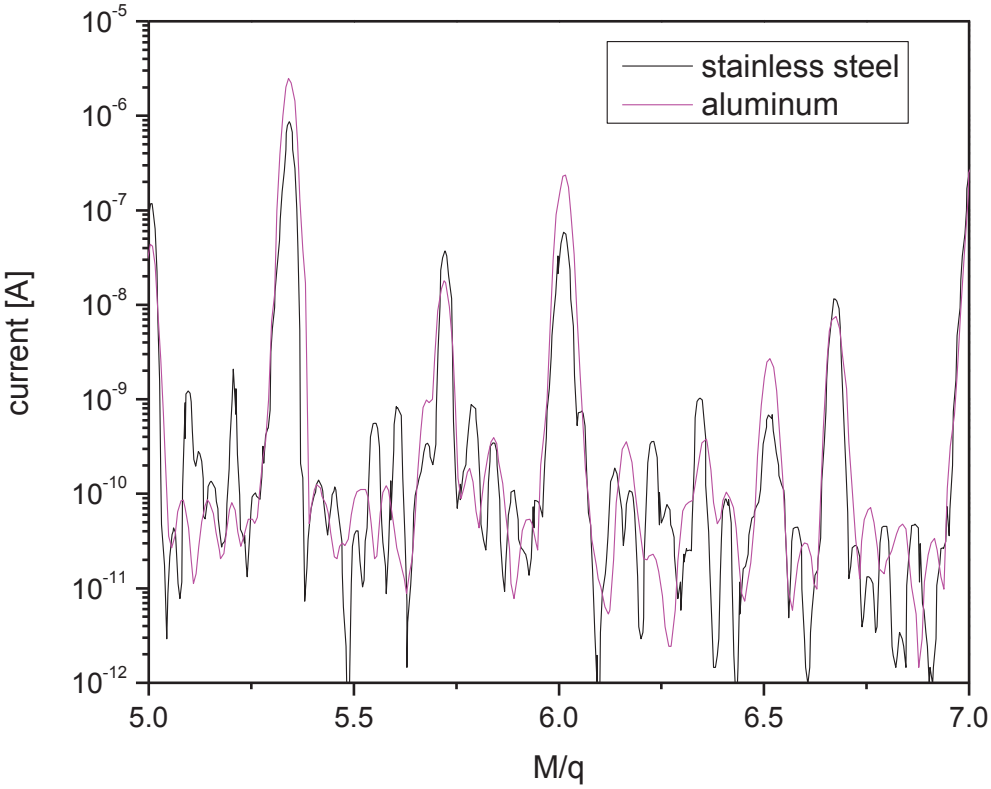

Figure 2: Ion current as function of M/q ratio for a stainless steel and aluminium plasma chamber.

The original PHOENIX source has been equipped with a plasma chamber made of stainless steel. The source has been modified by us to allow an easier adaptation of the ion energy in order to meet the velocity acceptance of the RFQ for different mass to charge ratios. On the injection side we have added a two step deceleration system also with stainless steel electrodes and on the extraction side a two step acceleration system made from copper and stainless steel components. On the extraction side the iron from the magnetic field coils is exposed to the vacuum as well.

To reduce the background from sputtered material the plasma chamber has been exchanged to one made of aluminium. This reduced the background by some small amount but the main components were still present. Therefore, in a second attempt the plasma chamber has been coated with pure aluminium, all electrodes at the injection and extraction side have been exchanged to aluminium and the magnet iron has been coated as well. The result can be seen in Figure 1. It shows a mass spectrum from the source with the stainless steel chamber and with the coated aluminium chamber. Although, the intensity of ions from the gaseous elements is about the same, the intensity of the other components has been reduced by about 2 orders of magnitude.

In the summer of 2012 this set up has been used the first time for a test with radioactive ions in 2 different runs with the acceleration of $^{76}Rb^{15+}$ and $^{94}Rb^{15+}$. Due to insufficient time for conditioning the efficiency in both cases was only about 1% resulting in some 10^5 highly charged ions per second. Background ions which could be identified from their total energy after the acceleration were in case of mass 76 $^{61}Ni^{12+}$ and the direct isobars $^{76}Se^{15=}$ or $^{76}Ge^{15+}$. For mass 94 the direct isobars Zr and Mo could be seen together with some $^{69}Ga^{11+}$ and $^{119}Sn^{19+}$. In both cases the total intensity of the background was several pA.

SUMMARY AND OUTLOOK

Two problems for the charge state breeding for the post acceleration of radioactive ions have been identified. The beam transport of the highly charged ions can be compromised by charge exchange in collisions with residual gas ions in the beam lines. Especially for very high charge states above 15+ not only the low energy part of the installation has to be taken into account, but also the high energy section.

ISBN 978-3-95450-123-6

Copyright © 2012 CC-BY-3.0 and by the respective authors

The second challenge is the background from an ECR charge state breeder, which originates from residual gas ions and sputtered material from the plasma chamber and its surrounding. It could be demonstrated that this background can be reduced by carefully choosing the materials, which may come into contact with the plasma or beam. Improvements of the vacuum and the purity of the support gas can reduce gaseous components in the extracted beam. The design of the PHOENIX charge state breeder allows only small improvements as it utilizes o-ring vacuum seals and does not allow baking at high temperature. Future sources for charge state breeding should be designed to comply with ultra high vacuum standards.

At ISAC additional cleaning techniques along the accelerator chain will be used for further purification of the beam. Although, it will be difficult to eliminate direct isobars the mass resolution of the accelerator chain can be increased by introducing additional slits and carefully reducing the acceptance in energy and mass by choosing relative phases in the RF fields of the different accelerator components. A mass resolving power of up to 1000 has been demonstrated. In some cases additional stripping at high energy may be used for beam purification. This will reduce the final beam intensity but the improvement in the ratio of desired ion to background ions may be essential for the experiment. Results on measurements dealing with the in flight purification of the beam and the tools developed for this will be published elsewhere [4].

ACKNOWLEDGMENT

TRIUMF receives federal funding via a contribution agreement through the National Research Council of Canada.

REFERENCES

[1] F. Ames et al. “Commissioning of the ECRIS Charge State Breeder at TRIUMF”, ECRI 2010, Grenoble, August 2010, WECOBK01, p. 178 (2010); http://www.JACoW.org
[2] F. Ames et al., High Energy Physics and Nuclear Physics 31 (2007) 211
[3] N.Imai et al., Rev. Sci. Instrum. 79, (2008) 02A906
[4] M. Marchetto et al., ‘In Flight Ion Separation using a LINAC Chain”, LINAC’12, Tel Aviv, September 2012, to be published in JACoW conference proceedings

Copyright © 2012 CC-BY-3.0 and by the respective authors

ISBN 978-3-95450-123-6

LPSC PHOENIX ECR CHARGE BREEDER BEAM OPTICS AND EFFICIENCIES

J. Angot, T. Lamy, M. Marie-Jeanne, P. Sortais, T. Thuillier, Laboratoire de Physique Subatomique et de Cosmologie, Université Joseph Fourier, CNRS IN2P3, Grenoble INP, 53 rue des Martyrs 38026 Grenoble CEDEX France

Abstract

The PHOENIX ECR charge breeder characteristics (efficiency and charge breeding time) were measured at CERN-ISOLDE and at the Laboratoire de Physique Subatomique et de Cosmologie (LPSC), they were considered as sufficient to allow its setup on various facilities (TRIUMF - Canada / GANIL - SPIRAL2 and SPIRAL1 – France / SPES/INFN). The developments performed at the Argonne National Laboratory (ANL) have shown that the ECR charge breeder efficiencies could be much higher than the ones obtained with the LPSC PHOENIX, without major differences between the two devices. We have tried to study the possible reasons of such different results in order to improve the PHOENIX charge breeder characteristics. The transmission value of the n+ beam line has been measured to be as low as 30%. Emittances of the total beam extracted from the source and of some analysed beams (after the magnetic spectrometer) have been measured and will be presented. Simulations have shown a too low vertical acceptance at the center of the magnetic spectrometer. Simulations and experimental results will be presented, they show how an additional Einzel lens, inserted just before the dipole, has drastically improved the beam transmission. The impact of this new beam transport on charge breeding efficiencies will be presented.

ANL AND LPSC CHARGE BREEDERS CHARACTERISTICS

The ANL charge state breeder has been extensively described in [1]. It is a modified ECRIS allowing the injection and slowing down of an ion beam close to the axis, through a 25.4 mm internal diameter movable transfer tube. Like performed at LPSC, the injection plug has been modified in order to symmetrize the magnetic field at the injection side [2]. The recent configuration and results are presented in [3]. The pressure in this charge state breeder is about $2x10^{-8}$ mb, the axial magnetic field values at the injection, in the middle plane and at the extraction of the source, are respectively B_{inj} = 1.16 T, B_{min} = 0.27 T and B_{ext} = 0.83T.

Concerning the LPSC PHOENIX charge state breeder a few modifications have been performed since 2008. For example, the plasma chamber was modified in order to have the possibility to insert a liner (no internal diameter change) and has been equipped with two waveguide ports. The magnetic field, at the injection, has been slightly increased and fully symmetrized by the addition of iron parts around the plasma chamber [4]; finally, the grounded transfer tube has been removed allowing a more stable operation of the source. The pressure at the injection is about $6x10^{-7}$ mb and the axial magnetic field values are equal to B_{inj} = 1.21T, B_{min} = 0.42T and B_{ext} = 0.82T.

Both the ANL and LPSC charge breeders have two waveguide ports, at ANL the plasma is excited by a 2kW, 10.44GHz klystron plus a 500W, 11 to 13GHz TWTA. At LPSC we use a 2kW, 14GHz klystron and performed experiments (in collaboration with the INFN Laboratori Nazionali di Legnaro, Padova-Italy) with an additional 500W, 13.75 to 14.5 GHz TWTA [5].

This description of the two charge breeders shows that their characteristics are very close, some results presented in 2011 by both laboratories [3], [6] are compared in Table 1 below.

Table 1: Some Performances of the ANL and LPSC Charge Breeders

Laboratory	Ion	Yield (%)	Global yield (%)
ANL	$^{129}Xe^{25+}$	13.4	64
LPSC	$^{132}Xe^{18+}$	6.31	Not measured
ANL	$^{85}Rb^{19+}$	13.7	77
LPSC	$^{85}Rb^{15+}$	6.5	32

We can see that the performances of the ANL charge breeder are much better in term of yields and charge states. Unfortunately, the final number of radioactive ions being the convolution between the charge breeding time and the efficiency, it is difficult to make a valuable comparison due to the lack of data concerning charge breeding times. However, the difference in the yields results is sufficient to expect an improvement of the characteristics of the LPSC charge state breeder. The next paragraphs of this publication will discuss the LPSC charge breeder setup characteristics.

N+ BEAMS CHARACTERIZATION AND BEAM LINE OPTICS AT LPSC

Extraction Conditions and Beam Line

A photo of the PHOENIX charge breeder extraction beam line is shown Fig. 1. The extraction holes diameters of the source are 8 mm for the plasma electrode and 18 mm for the puller, the distance between them is 42mm. The n+ ions are extracted at 20 kV, they enter a 120° magnetic spectrometer through a beam line equipped with

ISBN 978-3-95450-123-6

Copyright © 2012 CC-BY-3.0 and by the respective authors

an X-Y magnetic steerer and a Faraday cup (Extraction Faraday cup), the analysed ion beams are characterized in a 1.3 m long n+ beam line equipped with X and Y emittance scanners and a N+ Faraday cup.

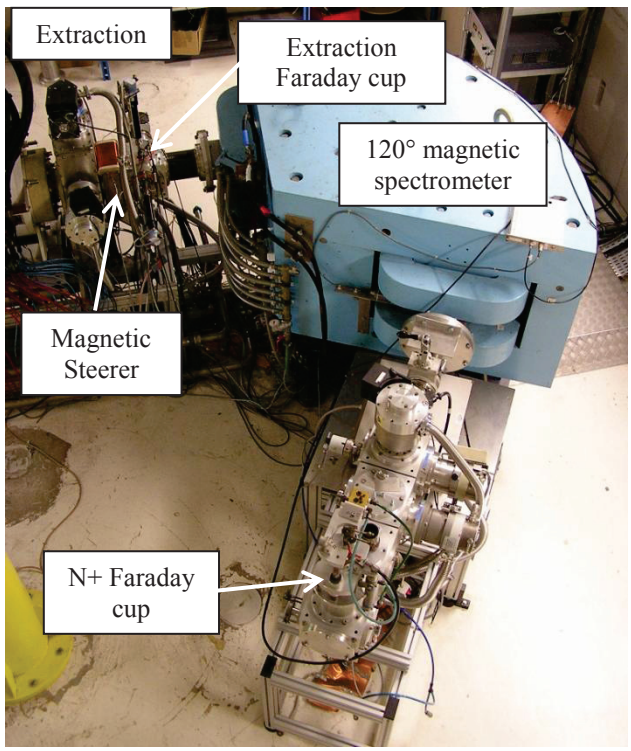

Figure 1: The LPSC charge breeder extraction beam line.

Last year, we noticed, on the LPSC PHOENIX ECR charge breeder, an excess of high voltage drain current with regard to the total current of a spectrum performed in the n+ Faraday cup. After, we disconnected the the 1+ source and the charge breeder ancillary equipment (to be sure that no parasitic current was flowing out), the excess drain current was still existing. This latter may have a few origins like: electrons produced at the extraction and accelerated towards the source; a transmission problem between the ion extraction and the final faraday cup placed after the magnetic spectrometer; for charge breeders, another origin of this current excess is due to the plasma leak occurring at the opened injection side, unfortunately this flow has not been carefully measured.

Let us consider three quantities: T_{glob}, T_{ext}, T_{tr} being defined as follows:

$$T_{glob} = \frac{\sum_i I_i}{I_{HV}}. \quad (1)$$

Where I_i is the ionic current of each peak analysed by the magnetic spectrometer and measured in the n+ Faraday cup, I_{HV} the drain current of the high voltage power supply,

$$T_{ext} = \frac{I_{axis}}{I_{HV}}. \quad (2)$$

Where I_{axis} is the total ionic current measured in a Faraday cup (Extraction Faraday cup on Fig. 1) placed just after the puller electrode before the magnetic spectrometer, and finally,

$$T_{tr} = \frac{\sum_i I_i}{I_{axis}}. \quad (3)$$

Even if we consider that the major part of the ions are extracted at the extraction side, to rigorously measure the global transport T_{glob}, one has to avoid the plasma leak at the injection side, this is performed by closing the plasma chamber, at the injection side, with a flange at the source voltage. In this configuration, we measured a global transport $T_{glob} \approx 0.3$ which is a low value potentially decreasing the measured 1+ → n+ efficiencies.

Diagnostic

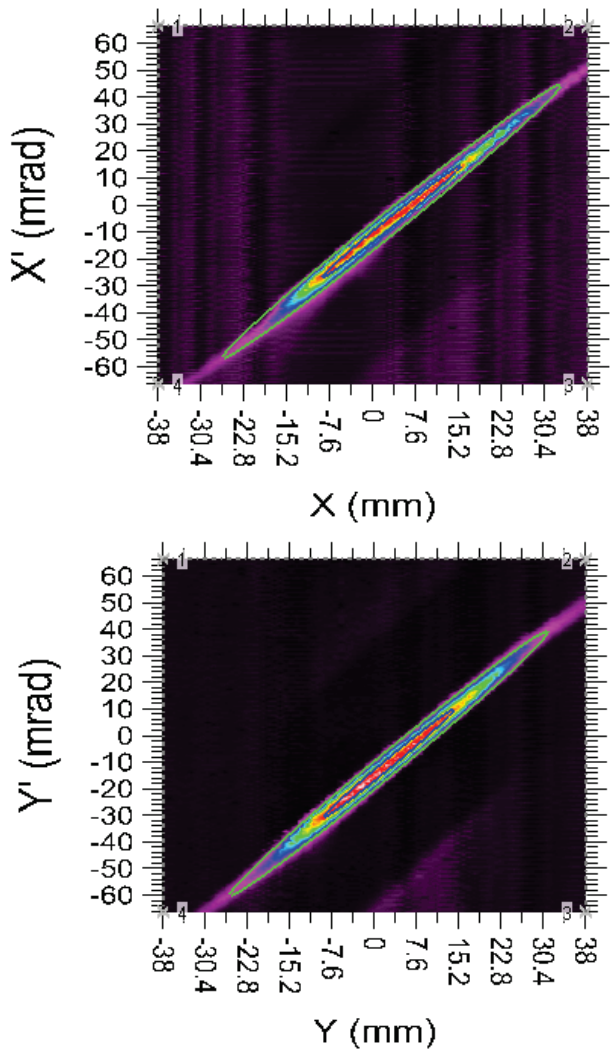

Figure 2: Horizontal (top) and vertical (bottom) emittances plots.

In order to determine the origin of this low global transmission, we have first characterized the total beam

Copyright © 2012 CC-BY-3.0 and by the respective authors

ISBN 978-3-95450-123-6

extracted before its entrance in the spectrometer, then we have measured its transmission through the 120° spectrometer. We have measured the two quantities T_{ext} and T_{tr}, to be respectively 0.91 and 0.32. These measurements clearly show that there is no electron production excess at the extraction itself, and that 70 % of the ions extracted from the charge breeder (when operated as a normal source) are lost in the magnetic spectrometer or the n+ beam line.

To characterize better this problem, and in order to have realistic experimental data input for N+ beam line optics simulations, we have measured the horizontal and vertical emittances of the total beam at the extraction of the charge breeder, these plots are presented Fig. 2. The emittance values are about 25 π.mm.mrad (RMS).

TRANSPORT SIMULATIONS IN THE N+ BEAM LINE

Initial Configuration Simulation

First we used the TRANSPORT code [7] and plotted X and Y beam envelopes (1σ), with the beam line acceptance on the same graph. The result is that the X envelope tangents the dipole vacuum chamber at its entrance and exit, and that the Y envelope is much bigger than the vertical size of this vacuum chamber all along the dipole.

In order to evaluate the transmission through the dipole we have used the SIMION code [8]. The model was simply composed of the vacuum chamber at the extraction (we did not simulate the beam extraction), the two magnetic poles of the dipole and a disc representing the Faraday cup. The experimental emittances were used to fly a 'realistic' beam of O^+ ions (during the emittance measurement, the average charge state was low), the space charge was neglected. The magnetic field has been computed using 'magnetic charges' on inclined surfaces (the magnet having a horizontal focalization index), and manually adjusted in order to direct the extraction axis ions at the center of the Faraday cup. With this simulation, we observed that about 50% of the ions were hitting the Faraday cup, the other ones being splashed on the upper and lower dipole vacuum chamber walls. The obtained trajectories are shown Fig. 3. With such a simple model, we find a difference with the experimental value T_{tr} = 0.32, but we have the confirmation of the loss in the vertical plane in the spectrometer.

Figure 3: Ion beam trajectories in the magnetic spectrometer after the extraction.

Technical Choice for Transport Improvement

We have planned to improve the charge breeder beam adaptation to the n+ beam line adding a lens just after the extraction. The use of a Glaser lens was discarded because it couldn't be easily implemented: modification of the extraction to insert the coil, installation of a power supply… So, as a first approach, we have installed a kind of Einzel lens, by inserting an 80 mm diameter and 135 mm long cylindrical electrode into the extraction chamber, using the vertical walls of the chamber as the grounded electrodes.

Einzel Lens Effect on the Simulated Beam

The electrode was added in the SIMION simulation and we checked if the assembly was acting as an Einzel lens. We plotted the focal length of the lens as a function of the cylindrical electrode voltage and deduced that the electrode setup was close to an Einzel lens configuration. By varying the cylindrical electrode voltage, we looked for the optimal beam transport to the Faraday cup and found an optimum value of 0.9 for T_{tr}, at -27kV and +15kV values.

IMPLEMENTATION

The cylindrical electrode was installed on an insulated support into the extraction chamber, no alignment system was present to help placing the electrode (see Fig. 4). In this configuration, we measured a global transport T_{glob} = 0.75 that could be optimized up to 0.82 using the magnetic steerer in the vertical plane. Finally, the magnetic steerer acting differently on different m/Q, its current intensity has been automatically adjusted to be optimized for each ion beam selected by the magnetic spectrometer. This latter servo control allowed us to reach a global transport T_{glob} = 0.84. With T_{ext} = 0.91, it gives a transport coefficient $T_{tr} = \frac{T_{glob}}{T_{ext}} = 0.92$. This value being close to 1 (and much higher than 0.32!), it has been decided to evaluate the impact of this improvement on the charge breeding efficiencies. So, the flange at the injection of the charge breeder was removed and the test bench reconfigured in the charge breeding configuration.

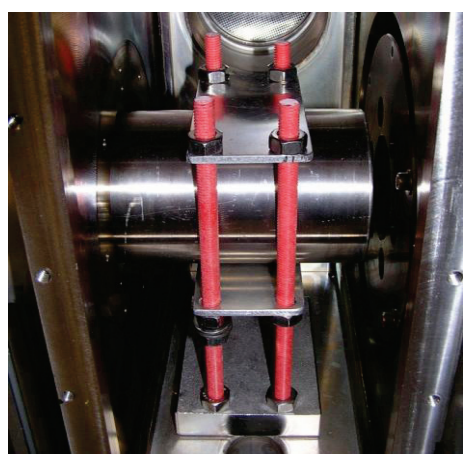

Figure 4: High voltage cylindrical electrode.

ISBN 978-3-95450-123-6

Copyright © 2012 CC-BY-3.0 and by the respective authors

EXPERIMENTAL RESULTS

Argon and Xenon

To test the new configuration, we first measured argon charge breeding. A 1µA Ar^{+} current was produced by the COMIC ion source [6] and injected into the charge breeder. With a usual charge breeder tuning, we obtained a maximum yield of 16.2% for $Ar^{1+} \rightarrow Ar^{8+}$, with a global capture of 75% (see Fig. 5) and a charge breeding time of 78ms (about 10ms per charge). For Ar^{8+}, it represents an increase of 17% compared with the previous maximum of 13.4% measured in April 2012, values reported in blue (Fig. 5).

When injecting a $^{132}Xe^{+}$ beam, we obtained a maximum yield of 10.9% for $^{132}Xe^{20+}$ with a global capture of 80% and a charge breeding time of 252ms for Xe^{21+} (12 ms per charge).

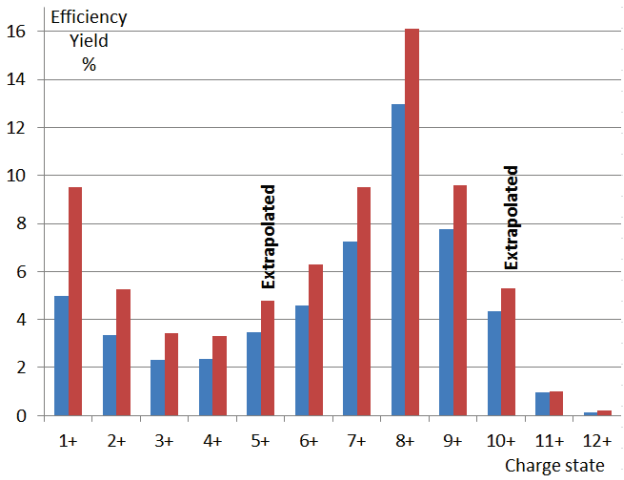

Figure 5: Argon charge state distribution extracted from the LPSC charge breeder.

Rubidium

To produce $^{85}Rb^{+}$, the COMIC source was replaced by a new 1+ ion thermo-ionic source based on the use of an alumina-silicate emitter. We designed a simple extraction optics formed by a set of three electrodes to produce the beam (Fig. 6).

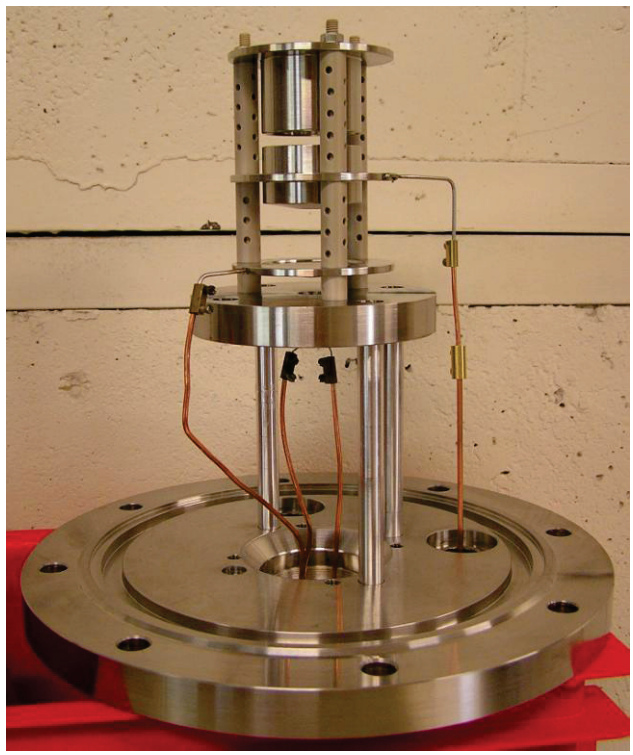

Figure 6: ion gun with its set of three electrodes.

The source was able to deliver a 300 nA $^{85}Rb^{+}$ beam within an horizontal emittance of about 2 π.mm.mrad, which is a reasonable value, even if much higher than the one get with the former source (0.6 π.mm.mrad) that was equipped with a sophisticated set of five electrodes. The tuning of the charge breeder led us to find a yield of 7.5% for $^{85}Rb^{+} \rightarrow {}^{85}Rb^{17+}$ with a charge breeding time of 226 ms (about 13 ms per charge). The charge state distribution is shown Fig. 6, the charges marked as extrapolated are superimposed with impurities, the 16+ is approximated to 8% in order to get a rather normal distribution, this leads to a global capture of about 55%. For this experiment with rubidium, it is more difficult to say that the efficiency yields increases are due to the transport improvement. One can see (with respect to our previous experimental data plotted as the blue bars Fig. 7), that the charge state distribution is shifted towards higher charge states, certainly due to an improvement of the pumping, leading to a lower pressure in the charge breeder.

Copyright © 2012 CC-BY-3.0 and by the respective authors

ISBN 978-3-95450-123-6

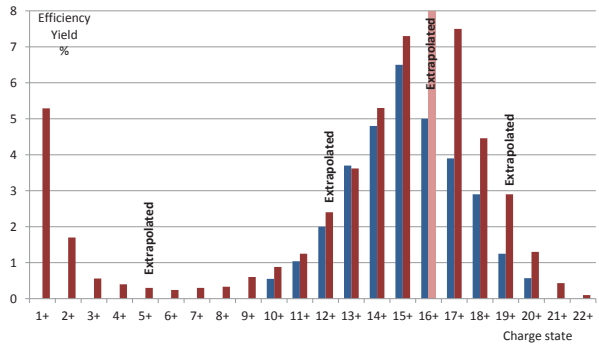

Figure 7: Rubidium charge state distribution extracted from the LPSC charge breeder.

Conclusion

The maximum efficiency yields obtained by the LPSC charge breeder have been improved by at least 15% after having solved a transmission problem observed in the vertical plane of the n+ line vertical plane. All the results we give are obtained with a charge breeding time of about 10 ms per charge, in order to avoid possible plasma modifications observed when tuning the charge breeder in a long confinement time configuration. This plasma modification systematically observed could lead to overestimated results. The improvement of the vacuum level clearly shows a shift of the charge state distribution and an improvement of the efficiencies, certainly due to a better confinement and a decrease of the charge exchange effect.

REFERENCES

[1] R.C. Vondrasek, R. Scott, J. Carr and R.C. Pardo
Rev. Sci. Instrum. 79,02A901 (2008).
[2] R. Vondrasek, A. Kolomiets, A. Levand, R. Pardo, G. Savard and R. Scott
Rev. Sci. Instrum. 82,053301 (2011).
[3] R. Vondrasek
Rev. Sci. Instrum. 83, 02A913 (2012)
[4] T. Lamy, J. Angot, C. Fourel, T. Thuillier
ECRIS 2008 proceedings (WECO-A01)
[5] T. Lamy, J. Angot, M. Marie-Jeanne, J. Medard, P. Sortais, T. Thuillier
ECRIS 2010 proceedings (WECOBK03)
[6] T. Lamy, J. Angot, P. Sortais, T. Thuillier and A. Galatà
Rev. Sci. Instrum. 83, 02A909 (2012)
[7] K.L. Brown et al CERN yellow reports CERN 73-16 (1973) and CERN 80-04 (1980)
[8] http://simion.com (Scientific Instrument Services, Inc. (SIS)

Copyright © 2012 CC-BY-3.0 and by the respective authors

ISBN 978-3-95450-123-6

DESIGN STATUS OF ECR ION SOURCE AND LEBT FOR FRIB*

G. Machicoane, N. Bultman, G. Morgan, E. Pozdeyev, X. Rao, FRIB, East Lansing, MI 48824, USA
J. Benitez, C. Lyneis, LBNL, Berkeley, CA 94720, USA
L.T. Sun, Institute of Modern Physics, CAS, Lanzhou 730000, China

Abstract

The Facility for Rare Isotope Beams (FRIB) at Michigan State University will provide intense beams of rare isotopes for research in nuclear physics, nuclear astrophysics and study of fundamental interactions. A Superconducting linac will accelerate the primary beam to energies beyond 200 Mev/u and is designed to reach a maximum beam power close to 400kW on the fragmentation target. In the case of Uranium about 13.3 pμA of U33+ are needed from the ion source to reach this maximum beam power on target. An ECR ion source operating at 28 GHz and based on the VENUS ion source developed at Lawrence Berkeley National Laboratory (LBNL) is currently being designed to meet the project intensity requirement and is presented in this paper. Although the intensity requirement from the ion source are very high for the FRIB project, new results have been obtained recently with VENUS that demonstrate that this ion source can actually produce close to 13pμA of U33+ within the emittance required by the accelerator. In addition an achromatic Low Energy Beam Line (LEBT) capable of transporting concurrently two charge states will be used to transport and accelerate the ion beam coming from the ion source.

INTRODUCTION

Michigan State University has been selected to build the Facility for Rare Isotope Beams (FRIB) in 2008 by the US Department of Energy (DOE). The FRIB driver accelerator consists of two Electron Cyclotron Resonance (ECR) ion sources located on a high voltage platform that will provide a large range of elements from Oxygen to Uranium at an initial energy of 12 keV/u, an achromatic low energy beam transport, a Radiofrequency Quadrupole (RFQ), a first linac segment with Quarter-wave Resonators (QWR) of β=0.041 and 0.085 accelerating the beam up to 20 MeV/u, a liquid lithium based stripper to reach higher charge states followed by two other linac segments with Half-wave Resonators (HWR) of β=0.29 and 0.53 accelerating the beam above 200 MeV/u. The third linac segment could be used for a future energy upgrade of the facility to 400MeV/u. The linac will be located about 10 meters underground and following the different linac segments a beam delivery system will transport the accelerated beam to the target. This latter is followed by a fragment separator that merges with the existing nuclear experimental areas of the NSCL laboratory. The facility is also designed to allow for the future implementation of an ISOL option. Figure 1 below show a section view of the driver linac with the different segments. The FRIB driver accelerator is described in more details in other publications [1]

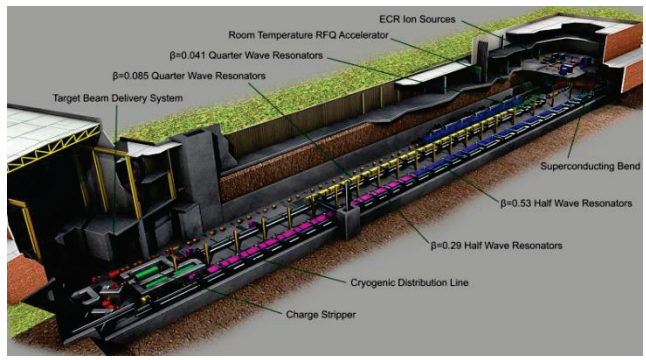

Figure 1: Layout of the FRIB driver linac. Ground level is shown in green at the top.

FRIB ECR ION SOURCES

To limit machine downtime during ion source development or possible breakdown, two ECR ion sources will be implemented for FRIB. Each source is located above ground primarily for radiation safety reasons. FRIB won't operate at full power initially but instead the accelerator will be first commissioned at low beam power and later followed by an operational phase where the beam power will be gradually ramped up to the maximum design value. Intensity required from the ion source during the commissioning will be much lower and a simpler source can be used during that phase. ARTEMIS-B developed in 2005 for offline development [2] and based on the design of the AECR-U of LBNL is available and will be sufficient for the commissioning need of the accelerator. Although, ARTEMIS-B was originally built to be operated vertically, the design has been recently modified to position the ion source horizontally. A temporary deck has been built as well as a new stand to support the ion source. Over the next year, the source will be reassembled and tested in this new orientation. Because, the ion source will be operated on a high voltage platform, the power supplies used for the solenoid coils have to be replaced with ones that are more efficient in order to be compatible with operation on the high voltage platform. The NdFeB based hexapole magnet of ARTEMIS-B will be also upgraded with a materials grade that has a higher energy product to increase the radial field.

The second ion source will be a high performance superconducting ECR ion source capable to operate at 28 GHz and based on the ion source VENUS developed at LBNL. The magnet system follows the conventional design of the sextupole inside the solenoids. The VENUS

*Work supported by the U.S. Department of Energy Office of Science under Cooperative Agreement DE-SC0000661
#machicoa@nscl.msu.edu

Copyright © 2012 CC-BY-3.0 and by the respective authors

ISBN 978-3-95450-123-6

magnet has been described extensively in previous publications [3],[4]. Calculations have been done with the commercial software LORENTZ regarding the magnetic field and match very closely the previous results obtained with VENUS. Table 1 summarizes the main parameters for the coils that are used to design the FRIB SC-ECR and the calculated magnetic field.

Table 1: FRIB SC-ECR Coil Parameters

	Solenoid Injection	Solenoid Middle	Solenoid Extraction	Sextupole
Turn #	6272	2208	4480	648
ID(mm)	340	340	340	200
OD(mm)	458	441	458	270
Max B (T) on conductor	6.14	4.22	5.47	7.3
Field(T) on axis	3.95	0.36	2.98	-
Field (T) Chamber wall	-	-	-	2.2
Operating I (A)	225	-240	225	450

PRELIMINARY DESIGN OF FRIB SCECR

Magnets for Superconducting ECR ion source are challenging because of the interaction forces between the solenoids and the sextupole coils. The design of the Superconducting Source for Ions (SuSI) built at MSU was also based on the VENUS ion source but has not been able to reach the field necessary for operation at 28 GHz and is instead limited to work at a maximum frequency of 22-24 GHz due to quenches in the sextupole coil when the solenoid are energized. Several differences were introduced in the design of SuSI that may explain the limitation of the magnet performance [5]. First, the NbTi conductor used with SuSI had different properties than the one used for VENUS and is discussed below. Second, the structural banding used to keep the sextupole tightly against the bore tube was not extended to the end regions of the coil for SuSI and the gap existing at this location was filled with soft material such as Kapton. Finally, the small gaps created between the coils and the bore tube after inflation of the bladders was not filled as it was for VENUS by vacuum impregnation. The approach for the VENUS project of using an aluminium structure around the sextupole coil (consisting of an aluminium sleeve followed by the thick solenoid bobbin) is necessary to ensure that the coils will be pre-stress in the radial direction during cool down before they are energized. This pre-stress has to be confirmed by measuring the contraction of the wire-epoxy composite during cool down to ensure that the aluminium contracts more. The bladders provide an elegant solution for the loss of stress in the azimuthal direction during cool down and will be used again for FRIB. More advanced techniques using water bladders and Keys have been developed at LBNL since the VENUS project and would certainly provide a better and more controlled clamping of the coil structure [6] which would especially be useful to reach magnetic field higher than required for operation at 28 GHz but would require substantial engineering and go beyond the scope of a project such as FRIB. The Bladders will be filled with indalloy which has a low melting point at 117F and does not change volume significantly after solidification. Calculations have been done with ANSYS to analyze the hoops stress and radial pressure resulting from the bladder inflation. Using an inflation pressure of 1500PSI for the bladders create a radial pressure of about 550PSI which is sufficient for the banding to yield and push the coils against the Aluminium sleeve.

The next step on the analysis of the pre-stress is to simulate the cool down and verify that the radial stress on the sextupole will increase. These calculations will be done using data available regarding the thermal contraction of the coils that was measured for VENUS [3] as well as the elastic modulus also measured for this type of conductor [7]. The last step of the analysis will be to include the impact of the Lorentz force when all coils are energized. The radial field experienced by the sextupole in the regions where the axial field profile is rapidly changing (B_r proportional to dB_z/dz) can be very significant. Depending on the polarity of the current in the sextupole coil, this field either reinforce or weaken the self field of the sextupole. This is illustrated in figure 2 where the top picture shows the sextupole self field only and the bottom picture the contribution of both the sextupole and solenoids on one of the sextupole coil. The field is oriented perpendicular to the plan shown.

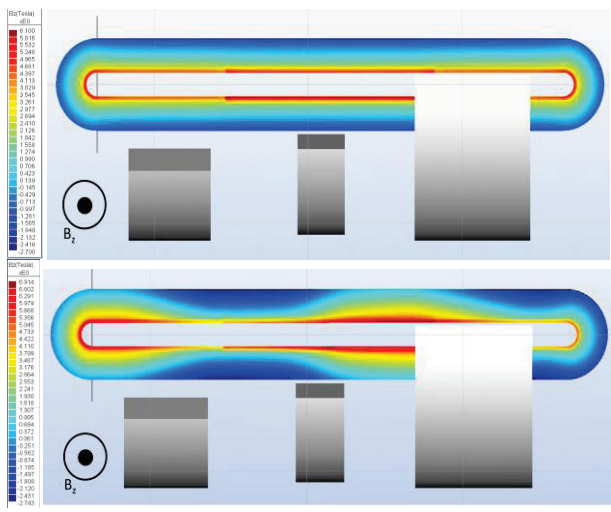

Figure 2: Magnetic field intensity along the radial direction. Top: self field of sextupole only. Bottom: Contribution from the solenoids is added. A section of the solenoids are shown in gray with the injection coil located to the right.

The additional contributions from the solenoids results in added azimuthal forces for the straight sections of the sextupole. They also modify the force in the longitudinal direction for the end sections where depending on the

ISBN 978-3-95450-123-6

Copyright © 2012 CC-BY-3.0 and by the respective authors

polarity the coil can be either stretched or compressed. In the end region, the field has also a significant component in the longitudinal direction (not shown here) resulting in radial force that tend to flex the ends either inward toward the bore tube or outward to the aluminium sleeve around the sextupole. In the case of SuSI, these forces in the end region may have been responsible for the movement of the coils due to the lack of banding and epoxy.

The design of the FRIB cryostat is progressing. The cryostat has been modified from the original VENUS cryostat to increase the cooling capacity at 4.2 K using a GM-JT cryocooler that has a cooling capacity of 5W. This cryocooler is also capable to condensate liquid helium. The design leaves open the possibility to add another one later on. In addition to the GM-JT cryocooler, two pulse tubes PT415 with a capacity of 1.5W of 4.2 K have been added. Pulse tubes require much less maintenance than a GM type cryocooler and several other projects at NSCL already use this type of cryocooler. Finally a single stage cryocooler AL330 with a large cooling capacity at 40K will be used to cool the cryostat shield and will be located close to the warm ends of the HTC leads. Heat load calculations have been done and demonstrate that this arrangement of cooler would be sufficient for the FRIB SC-ECR. The thermal shield in the lower part of the cryostat will be made of copper instead of Aluminum to improve the thermal conduction in this section which is far from the cryocoolers. To avoid that eddy currents generated during a quench along the copper surface would strain the shield, this latter will be made out of 2 sections separated by a small gap.

SELECTION OF NBTI CONDUCTOR

Because of the success of the VENUS project it was natural to select the NbTi conductor based on the conductor originally used for the construction of the magnet. However the sextupole conductor of VENUS was made in 1998 and was a special order from the Finnish manufacturer OUTOKUMPO. Custom orders are nowadays difficult from manufacturer of superconducting wire and it was not possible to order a conductor identical to the one used in VENUS sextupole. Extensive discussions let to prioritize the most important properties of the Superconducting wire for an ECR ion source. Beside the consideration of the critical current, the Copper to Superconducting ratio is a very important parameter in the selection of the conductor for an ECR magnet. Although many projects such as SuSI or MS-ECRIS or RIKEN SC-ECR have chosen conductor with a small Cu:Sc ratio (~1.3-1.6), VENUS sextupole used Cu:Sc ratio of 3 and for the solenoids a ratio of 4. NbTi conductors with a low Copper content are normally preferred due to the higher margin they offer to the critical current by lowering the current density. However it is known that larger copper content helps improve the stability of the coils by taking the excess heat away during micro-movements of the coils caused by magnetic force. Similarly larger Residual Resistivity Ratio (RRR) is an indicator of the quality of the stabilizer and smaller filament size also improves the stability of the conductor by better distributing the heat generated within a filament.

Table 2 below summarizes the characteristics of the conductor selected for FRIB ECR.

Table 2: NbTi Conductor Properties Selected for FRIB SC-ECR

	Solenoid	**Sextupole**
Solenoid Cu:Sc	4:1	3:1
RRR	60-70	>140
Filament Size (um)	<100	<50
Cross section	Rectangular	Rectangular
Filament size	1.57mm x 0.88mm	0.9mm x 1.8mm
Critical Current (A)	600 @6T	680 @7T

The sextupole for FRIB SC-ECR will operate nominally at about 75 % of the critical current.

URANIUM BEAM DEVELOPMENT

Transport and acceleration of heavier beams such as Uranium represents one of the most difficult challenges for an accelerator such as FRIB. To reach the nominal beam power of 400 kW on target requires an initial beam current of more than 13 puA from the ion source coming in a charge state of at least U33+. Uranium beam measurements with the ECR ion source VENUS at LBNL had shown that about only half of the current required for FRIB could be achieved for the charge state U33+ and U34+ [8]. This situation was resolved early on in FRIB by designing the LEBT and the linac to transport and accelerate two charge states. For the beam measurements done with VENUS, a compound of URe2 was used in a resistive Ta oven which provided U vapour at temperature between 1800C to 2000C. Beyond 2000C a phase transition in the compound would separate the Uranium from the Rhenium and would make the crucible unusable which ultimately limited the amount of Uranium vapour available during these measurements. After the measurements, it was also observed that the crucible stems were damaged by the action of the Lorentz forces. Recently, new measurements with VENUS have been done using Uranium oxide (U02) loaded respectively into a W and Re crucible. Uranium Oxide is very stable even at temperature well above 2000C (melts around 2700C) but require a temperature above 2000C to reach a sufficient vapour pressure (therefore somewhat higher than URe2). The initial measurements using the tungsten oven weren't very successful and only provided at best about 100euA of U33+.The production of the vapour was also quite instable. Although one cannot rule out that chemical reaction between the tungsten and the sample may have hinder the production of the Uranium vapour,

Copyright © 2012 CC-BY-3.0 and by the respective authors

ISBN 978-3-95450-123-6

an important difference of the Tungsten and Rhenium is the relatively lower resistivity of Tungsten compare to Rhenium which led to couple significantly more power on the Tungsten crucible (up to 700W) to reach the production temperature.

With such power, the voltage of the power supply feeding the oven was fluctuating which may have been caused by poor contact between the crucible stems and the oven at high temperature. In the case of the Rhenium crucible, the production was very stable and responded very well to increase in the oven current. Figure 3 below shows the measured ion beam current for U33+ and U34+ function of the current in the oven with the Rhenium crucible.

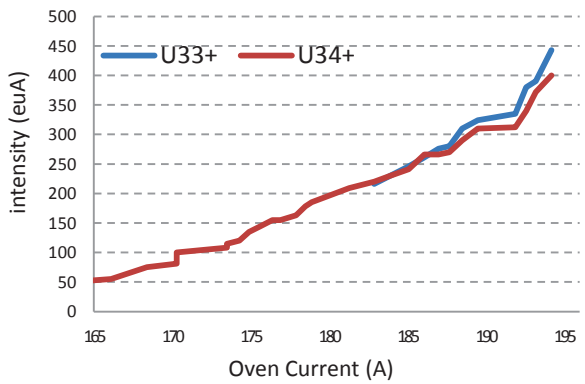

Figure 3: Uranium beam currents for the Rhenium crucible function of oven current

An important result for the FRIB project is that the maximum current reach for U33+ and U34+ exceeded 400euA. The charge state distribution obtained for Uranium is shown below in figure 4

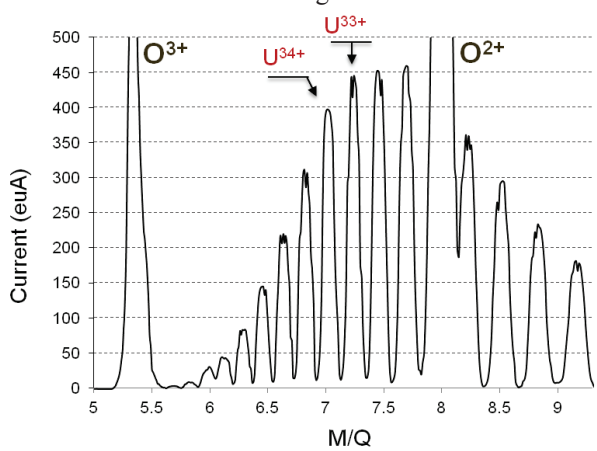

Figure 4: CSD of Uranium optimized for U33+ and U34+. Close to 450euA of U33+ was obtained. Power :1.8kW (18GHz) + 6.5kW (28 GHz). Drain current~9emA. Pext=4.8E-8 mbar.

The total injected power reached 8.3kW with 6.5kW coming from the 28 GHz gyrotron and the total extracted current was above 9emA. The VENUS LEBT line is not optimized to transport such a high current and the transmission measured by summing up the peaks of the CSD only reached about 55% of the drain current. One factor that limited the transmission of the beam was the extraction voltage of VENUS which was limited to 22kV. The high intensity (consistently above ~300euA) beam was maintained overall for about 10 hours. The power was not increased further by fear of damaging the ion source but the CSD was still very responsive to increase in microwave power or increase in the oven current when the CSD shown in figure 4 was obtained. It is likely that still better performance can be obtained be extraction at higher voltage and by coupling additional power.

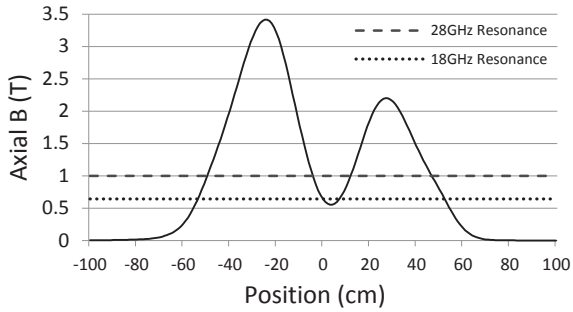

Figure 5: Axial magnetic field profile of VENUS used for the production of high intensity uranium beam.

The material consumption measured after the measurement was estimated to be over 9mg/hr. Finally the axial magnetic field profile used during the production of high intensity uranium is shown in figure 5 above.

The beam emittance of the uranium beam was measured for U 33+ and U 34+ and the result are summarized in table 3 below. In this case, the total extracted current was about 7.5emA.

Table 3: Measured Beam Emittance for U33+ and U34+ with VENUS

Beam	Plan	Current (euA)	εmittance - 1rms normalized	% of beam within 0.6 mm.mrad	% of beam within 0.9 mm.mrad
U33+	H	365	0.156	86	95
U33+	V	365	0.112	95	99
U34+	H	311	0.141	90	95
U34+	V	311	0.112	95	99

Emittance requirement for beam injected into FRIB linac are set to 0.6 pi.mm.mrad for the transport of two charge states and 0.9 pi.mm.mrad for single charge state acceleration. For this last case, the table shows that close to 95 % of the beam fall inside the emittance requirement for acceleration of a single charge state and therefore at least for U33+ these new results show that almost enough intensity is available from VENUS in one charge state for U33+ to reach FRIB goal of 400kW on the production target. However such conclusion would not be exactly correct as other parameters have to be considered in general to define the level of beam available for the accelerator such as time spent tuning the ion source, or higher losses than expected or stability of the beam. More experience is needed to operate high frequency ECR ion

ISBN 978-3-95450-123-6

Copyright © 2012 CC-BY-3.0 and by the respective authors

sources at high power to know what can be routinely achieved.

LEBT DESIGN

As mentioned previously, the LEBT was designed to be achromatic to transport two charge states simultaneously. To reduce cost, most of the focusing in the LEBT is done through electrostatic elements including quadrupoles and two 90° dipoles for the vertical line transporting the beam into the tunnel. The beam halo is collimated by several apertures in the LEBT in a process similar to the collimation channel developed for SuSI. A chopper is used to vary the duty cycle to control the pulse length from several hundreds of ns to CW and the pulse frequency from 0 to 30 kHz. The machine protection system is implemented in the LEBT by switching off very fast the voltage of one of the 90° dipoles. Due to the length of the LEBT, the vacuum requirement is very low (5E-9 Torr) throughout the LEBT to minimize losses through charge exchange especially for heavy elements. At the ion source extraction as well as in the charge selecting section, it is expected that the vacuum will be much higher however. Finally, The FRIB RFQ is a 4-vane structure to accelerate single and two-charge state beams from 12 to 500 keV/u with an estimated transmission efficiency above 80%. A layout of the FRIB front end beamline is shown in figure 6 below. More details on the LEBT and RFQ can be found in [9]

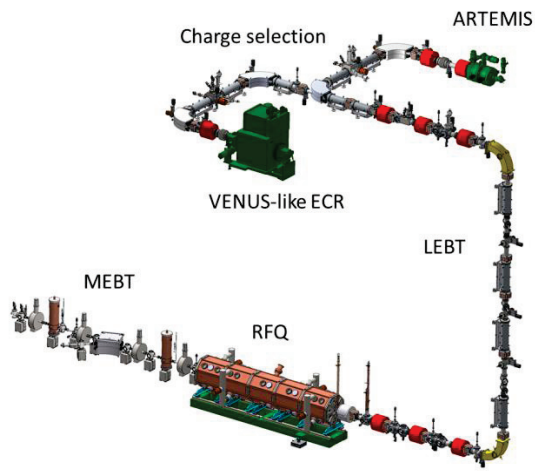

CONCLUSION

The design of the FRIB SC-ECR cold mass and cryostat are well advanced. The procurement of the NbTi conductor is being finalized and the conductor should be delivered at MSU in the spring 2013. Winding of the coils for the ion source will be done through an external vendor but the assembly and testing of the cold mass including the inflation of the bladders will take place at MSU and should be completed in 2014. The ion source with the cryostat is expected to be completed in 2016 and available for commissioning of FRIB in 2017. ARTEMIS-B will be first used for the accelerator in 2016.

REFERENCES

[1] J.Wie et *al*. Proceedings 26th international Linac conference, Tel Aviv, Israel (2012).
[2] G.Machicoane, D.Cole, J.Ottarson, J.Stetson, P.A.Zavodszky, Rev. Sci. Instrum. **77**, 03A322 (2006).
[3] C. Taylor, S. Caspi, M. Leitner, S. umdgren, C. Lyneis, D. Wutte, S.T. Wang and J. Y. Chen "Magnet system for an ECR ion source,"*IEEE Trans on Applied Superconductivity.,* vol. la, No. l ,pp. 224-227, March 2000.
[4] M.A. Leitner, S. A. Lundgren, C.M. Lyneis, C.E. Taylor, D.C. Wutte Proceedings of 14th international Workshop on ECR ion source,CERN, Geneva (1999).
[5] G.Machicoane, D.Cole, P.A.Zavodszky, proceedings of the 18th international workshop on ECR ion source, Chicago, USA (2008).
[6] S. Caspi, LBNL Engineering Note, SCMAG-706.
[7] K.Chow, LBNL Engineering Note, SCMAG-637.
[8] D. Leitner, M. L. Galloway, T. J. Loew, C. M. Lyneis, I. Castro Rodriguez, and D. S. Todd Rev. Sci. Instrum. **79**,02C710 (2008).
[9] E. Pozdeyev et *al*. Proceedings 26th international Linac conference, Tel Aviv, Israel (2012).

Copyright © 2012 CC-BY-3.0 and by the respective authors

ISBN 978-3-95450-123-6

PERFORMANCE OF ANL ECR BREEDER WITH LOW MASS BEAMS

R. Vondrasek, S. Kutsaev, R. Pardo, R. Scott, Argonne National Laboratory, Argonne, IL 60439, U.S.A.
P. Delahaye, and L. Maunoury, Grand Accélérateur National d'Ions Lourds (GANIL), CEA/DSM-CNRS/IN2P3, Blvd Henri Becquerel, 14076 Caen, France

Abstract

The CAlifornium Rare Isotope Breeder Upgrade (CARIBU) is a new radioactive beam facility for the Argonne Tandem Linac Accelerator System (ATLAS). The facility utilizes a ^{252}Cf fission source coupled with an electron cyclotron resonance (ECR) ion source to provide radioactive beam species for the ATLAS experimental program. The californium fission fragment distribution provides nuclei in the mid-mass range which are difficult to extract from production targets using the isotope separation on line (ISOL) technique and are not well populated by low-energy fission of uranium. To date the charge breeding program has focused on optimizing these mid-mass beams, achieving high charge breeding efficiencies of both gaseous and solid species including 14.7% for the radioactive species $^{143}Ba^{27+}$. In an effort to better understand the charge breeding mechanism, we have recently focused on the low-mass species sodium and potassium which up to present have been difficult to charge breed efficiently. Unprecedented charge breeding efficiencies of 10.1% for $^{23}Na^{7+}$ and 17.9% for $^{39}K^{10+}$ were obtained injecting stable Na^+ and K^+ beams from a surface ionization source.

INTRODUCTION

The development of ECR charge breeders is being pursued by many groups [1-8] with a particular concern being the efficient charge breeding of light ion species which up to present has been problematic [9,10]. The GANIL ion source group is pursuing a new 1+ to n+ charge breeding system for the SPIRAL project utilizing an ECR ion source with the efficient charge breeding of light nuclei being of high importance. Previously confined to gaseous elements, new versatile 1+ sources will be used to extend the range of elements available for post-acceleration to condensable elements. During on-line tests with such ion sources, radioactive isotopes of 9 new elements have already been ionized: isotopes of the alkali (Li, Na, K, Rb) metallic (Al, Fe, Cu, Mn) and halogen (Cl) elements were all produced from the FEBIAD ion source except for the alkali ion Li which was only surface ionized. While the new 1+ sources allow for the production of a wider range of elements, achieving a high charge breeding efficiency in the ECR remains a critical step. With this in mind, a new ECR charge breeder is being designed for the SPIRAL upgrade. The future ECR charge breeder will be based on an upgrade of an existing Phoenix ECR ion source which was formerly tested at ISOLDE, CERN [11,12]. The upgraded charge breeder will include a number of modifications inspired from the Argonne National Laboratory (ANL) ECR charge breeder: the injection of two RF frequencies (one fixed 14 GHz and one variable 8-18 GHz); complete cylindrical symmetry at the injection side; on-line adjustment of the grounded tube position; and a vacuum level around a few 10^{-8} mbar.

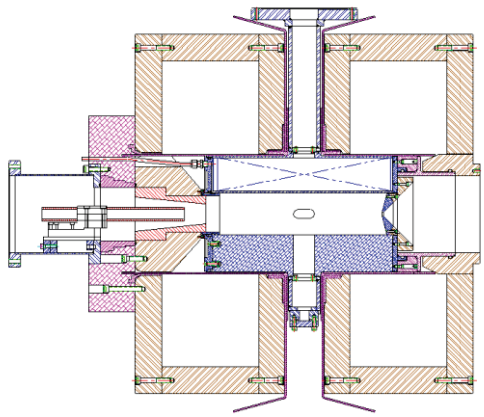

Figure 1: Schematic of the ANL ECR charge breeder. The 1+ beam is injected from the left through the grounded stainless steel tube. The tapered iron plug is highlighted with diagonal red hatching. The radial slots where the RF is launched are visible on the source mid-plane.

THE ANL ECR CHARGE BREEDER

In its final configuration, the CARIBU facility [13] will use a 1 Ci ^{252}Cf source to produce fission fragments which will be thermalized and collected by a helium gas catcher into a particle beam with a charge of 1+ or 2+. An ECR ion source functions as a charge breeder (ECRCB) [14,15] in order to raise the ion charge sufficiently for acceleration in the ATLAS linac.

The charge breeder is a room temperature ECR operating at 10-14 GHz with an open-structure NdFeB hexapole (see scheme in Fig. 1). The six radial ports which are each 17 x 41 mm in size act as pumping channels resulting in a plasma chamber pressure of 5 x 10^{-8} Torr. They also serve to introduce the RF and support gas into the plasma chamber. This eliminates the need for cut-outs in the injection side iron plug and results in a large peak and highly symmetric axial magnetic field where the ions enter the plasma. This scheme differs from other ECR charge breeders in existence which are closed hexapole devices with axial RF injection. For the ANL ECRCB, the low charge-state ions are introduced into the plasma through a grounded stainless steel tube mounted on a linear motion stage. The stage has a 30 mm range of

Copyright © 2012 CC-BY-3.0 and by the respective authors

ISBN 978-3-95450-123-6

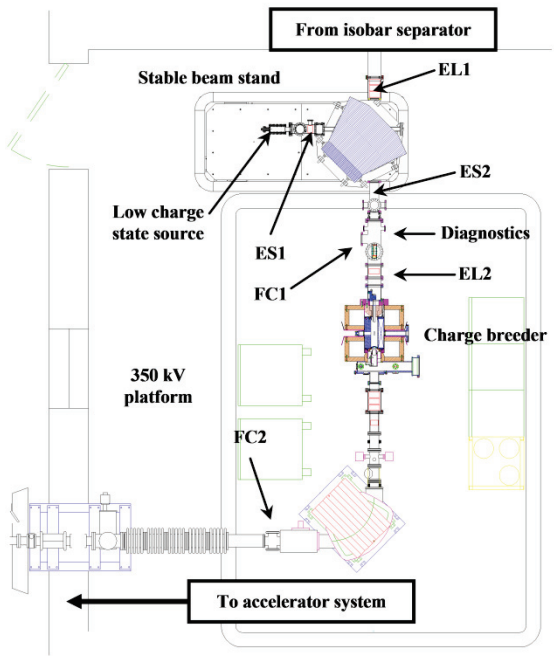

Figure 2: Floor plan of the charge breeder system showing the stable beam stand, the electrostatic steerers (ES1 & ES2), the einzel lenses (EL1 & EL2), the faraday cups (FC1 & FC2), the diagnostics location, and the ECRCB.

travel, and thus the deceleration point of the low-charge state ions can be adjusted on-line without disturbing the source conditions. The ECRCB is designed to operate at a 50 kV potential although for these tests the voltage was maintained at 30 kV.

CHARGE BREEDING RESULTS

Stable 1+ beams of sodium and potassium were produced by a surface ionization source with injected intensities ranging from 500 enA to as low as 2 enA. The transport system, shown in Fig. 2, consists of two electrostatic steerers, an einzel lens, a set of 4-jaw slits directly after the surface ionization source for controlling beam intensity, and a double set of 4-jaw slits at the image point of the 90 degree analyzing magnet spaced 16.5 cm apart. The slits serve to control the beam emittance and define the beam trajectory going into the ECRCB easing the transition between stable and radioactive beam breeding. The diagnostics region includes a fully shielded Faraday cup for measuring the 1+ beam (FC1) and a silicon surface barrier detector (SBD) for measuring radioactive beams via beta decay. After the 1+ beam has been injected into the charge breeder through the grounded tube, a ΔV voltage between the 1+ source and the ECRCB decelerates the ions into the plasma region where a sub-set of them are ionized and captured by the plasma [16].

Table 1: Summary of Charge Breeding Results for Mid-Mass Species

Ion	Charge state	Efficiency (%)	A/Q
^{84}Kr	17+	15.6	4.94
^{85}Rb	19+	13.7	4.47
^{129}Xe	25+	13.4	5.16
^{133}Cs	27+	13.0	4.93
^{143}Cs(1+) ($t_{1/2}$=1.79 s)	27+	11.7	5.30
^{143}Ba (2+) ($t_{1/2}$=14.3 s)	27+	14.7	5.30

After charge breeding, the intensity of the mass analyzed n+ ions is observed on either a Faraday cup (FC2) for the stable beams or a SBD at this same location for the radioactive beams. The breeding efficiency and time are determined by pulsing the incoming 1+ beam, using the electrostatic steerer (ES1) voltage, and measuring the n+ response on FC2. A summary of achieved charge breeding efficiencies for the mid-mass species is given in Table 1.

The first charge breeding test was with Rb-85 in order to establish a performance benchmark. While the best efficiency for $^{85}Rb^{20+}$ was 11.4% (lower than the record of 13.2%), the higher charge states performed well and surpassed the previous achieved efficiencies by a factor of 2 for 23+ through 25+ (shown in Fig. 3).

The first test of light element breeding was performed with a sodium pellet loaded into the surface ionization source. The system was checked for leaks and achieved a base pressure of 2.5 x 10^{-8} Torr without plasma. With the ECRCB running a base plasma of helium, the pressure increased to 6.6 x 10^{-8} Torr. A beam of Na^{+} with an intensity of 12.6 nA was injected into the ECRCB resulting in a $^{23}Na^{8+}$ breeding efficiency of 6.0%. The addition of oxygen to the plasma reduced the breeding efficiency to 5.0%.

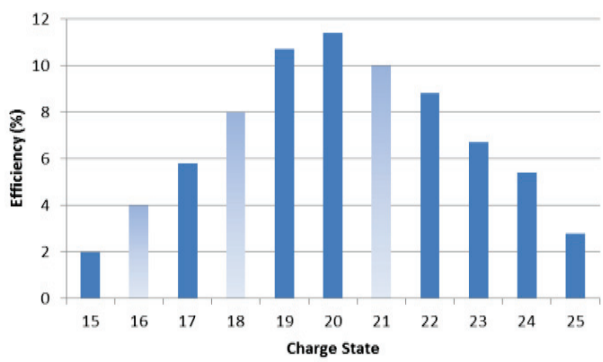

Figure 3: Efficiency of Rb-85 as a function of charge state. Charge states 16+, 18+, and 21+ were obscured by intense background peaks and their values have been extrapolated.

Copyright © 2012 CC-BY-3.0 and by the respective authors

ISBN 978-3-95450-123-6

A second test of the sodium breeding efficiency took place where the base plasma of He-4 was replaced with He-3. With a pure He-4 plasma, the source was producing $^{23}Na^{8+}$ with an efficiency of 7.6%. As only the gas mixture was altered such that the plasma was entirely He-3, the efficiency for $^{23}Na^{8+}$ remained at 7.6%. Further optimization of the injection optics, solenoid coils, gas pressure, and ΔV ultimately produced $^{23}Na^{8+}$ with a 8.1% efficiency and $^{23}Na^{7+}$ with a 9.0% efficiency. Further optimization on $^{23}Na^{7+}$ resulted in a breeding efficiency of 10.1%. Changing the base plasma back to He-4 produced no change in efficiency.

A potassium pellet was then installed in the surface ionization source. The ECRCB was restarted and immediately achieved a 4.2% breeding efficiency for $^{39}K^{10+}$ with 14.8 nA of K^+ injected into the source. As stated earlier, the 4-jaws after the surface ionization source are used to control the 1+ beam intensity and emittance. These slits also play a role in defining the beam trajectory. By adjusting these slits while observing the charge bred beam intensity, an optimum setting was found which produced a 13.8% breeding efficiency for $^{39}K^{10+}$ with 16.5 nA injected into the ECRCB. Further optimization of the optics elements, the support gas, and grounded tube position resulted in a maximum breeding efficiency of 17.9 % for $^{39}K^{10+}$. This represents the highest charge breeding efficiency to date for an ECR ion source. It is possible to achieve such high efficiencies due to the charge state distribution for the lower masses narrowing and resulting in an increase of the single charge state population. A complete list of the light element charge breeding efficiencies is shown in Table 2. The higher ^{39}K charge states were obscured by other stable beams and could not be reliably identified. As with sodium, it was observed that adding oxygen to the mixing gas was not beneficial. The breeding time for $^{39}K^{10+}$ was determined to be 160 msec from injection of the 1+ beam to full intensity of the 10+ beam and 150 msec for the $^{39}K^{9+}$ case.

Table 2: Summary of Charge Breeding Results for Sodium and Potassium

Ion	Charge state	Efficiency (%)	A/Q
^{23}Na	6+	6.6	3.83
	7+	10.1	3.29
	8+	8.6	2.87
	9+	3.4	2.56
^{39}K	7+	3.0	5.57
	8+	4.9	4.87
	9+	15.6	4.33
	10+	17.9	3.90

BEAM INJECTION SIMULATIONS

The work with the ANL ECRCB has shown that the large performance disparity between gaseous and nongaseous elements has been greatly diminished. For identical source conditions, the only difference between the two cases is the wall sticking coefficient. In the case of gaseous elements, many of the ions which hit the plasma chamber surfaces are quickly re-emitted into the plasma. In contrast, the solid elements condense onto the plasma chamber surfaces meaning that any incoming particles that do impact a surface are lost to the plasma. It can be surmised that the present injection optics and source conditions reduce the number of incoming ions lost to the plasma chamber surfaces before capture into the plasma.

One of the possible contributing factors to the high breeding efficiencies is the iron plug design. The lack of cut-outs in the iron plug results in a large peak magnetic field which is symmetric where the ions enter the plasma chamber. 3D magnetic field calculations of the ANL ECRCB using Computer Simulation Technology Electromagnetic Studio [17] were performed taking into account the coils, iron, and hexapole. The coil currents were set to the values used for charge breeding resulting in a peak axial field of 1.2 T. The hexapole wall field was measured to be 0.84 T. Two cases were evaluated – one for radial RF injection and one for axial RF injection which included cut-outs in the iron plug. The results were then plotted as horizontal planes passing through the charge breeder with the central axis of the source at the 0,0 coordinate. The view shown in Fig. 4 is the horizontal plane directly in front of the face of the iron plug. The simulations showed that the magnetic field for the case with the cut-outs was asymmetric with the magnetic field center offset from the ion source geometric center.

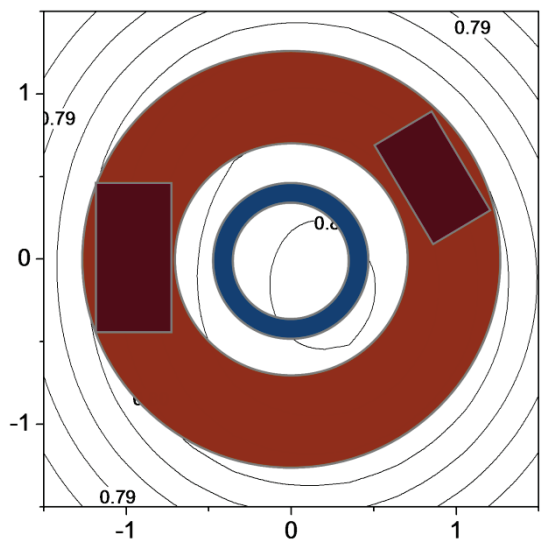

Figure 4: The magnetic field in the injection region with the waveguide cut-outs. The overlaid shapes show the position of the transfer tube in blue, the iron plug in brown, and the waveguides in red.

ISBN 978-3-95450-123-6

Copyright © 2012 CC-BY-3.0 and by the respective authors

While the simulations showed that the magnetic field was asymmetric, the effect on the incoming low charge state ions was not well established. Further simulations were performed with test particles of $^{133}Cs^{+}$ ions injected into the ECRCB using the full 3D magnetic and electric field configuration. The simulations assumed: injection of $^{133}Cs^{+}$ ions with an energy spread of 1 eV and emittance of 3 π mm mrad (the measured values of the beam coming from the CARIBU gas catcher), the running condition coil currents, and 30 kV injection with a ΔV of -20 V. Fig. 5 shows that in the case of the symmetric injection field, the 1+ ions penetrate deep into the plasma chamber almost reaching the extraction aperture. For the asymmetric case, the ions do not travel far into the plasma and hence capture into the plasma is diminished. The simulations were only intended to model the trajectories of the incoming 1+ ions and do not take into account any ion/plasma interactions.

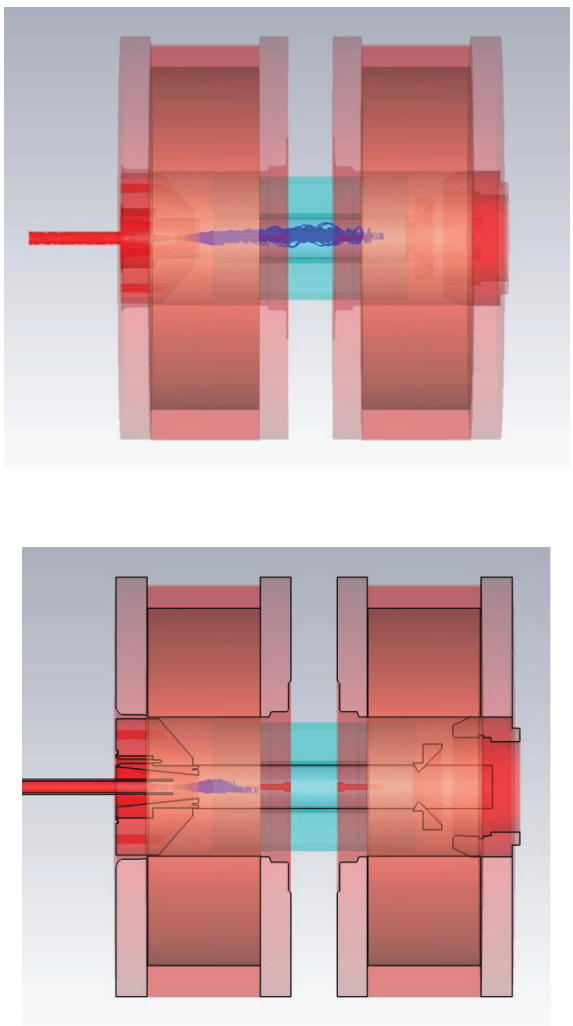

Figure 5: Simulation of $^{133}Cs^{+}$ injected into the ECRCB at 30 kV with ΔV of -20 V. The top figure is the case with radial RF injection and no cut-outs in the iron plug. The bottom figure assumes identical conditions except that the RF is now injected axial and the iron plug has cut-outs to accommodate the waveguides.

SUMMARY AND OUTLOOK

With the charge breeding efficiencies of ^{23}Na and ^{39}K meeting or surpassing that of the heavier elements, the previously observed trend of decreased performance for the light elements [18] is after a careful and complete parameter optimization not seen in this work. In [9], it was proposed that the incoming ions are slowed by elastic ion-ion collisions with the plasma ions. The optimum slowing down occurs when the incoming ions enter into the plasma with a velocity roughly equal to the average velocity of the plasma ions. A velocity mismatch will result in a weaker slowing down force and hence a lower breeding efficiency. Additionally, good beam optics are required for the efficient capture of the very low velocity incoming ions.

In the case of sodium, assuming an oxygen plasma with an ion temperature of 2 eV, the sodium ion energy required to match the ion velocities and attain the optimum slowing coefficient is 2.9 eV. In source tests with an oxygen plasma, the realized charge breeding efficiency of $^{23}Na^{8+}$ was 5.0%. It was only with a helium plasma that the quoted efficiency of 8.6% was achieved. In this case, the sodium ions would have an energy of 11.5 eV for optimum slowing, very similar to the rubidium case and requiring less stringent requirements on the beam optics due to the increased velocity.

Compared to the couple of percent obtained thus far with other charge breeders, the charge breeding efficiencies for light condensable ions have been dramatically enhanced during the course of these experiments, approaching efficiencies usually observed for noble gases. This tends to indicate that the relevant parameters – beam emittance and trajectory, gas mixing, magnetic field alignment and homogeneity - have been optimized. Further investigation will be performed at ANL with an emittance meter installed in the 1+ beam line. In light of these latest results, special care will be taken in the SPIRAL upgrade for the optimization and control of the 1+ ion source beam optics and emittance.

ACKNOWLEDGEMENTS

This work was supported by the U.S. Department of Energy, Office of Nuclear Physics, under contract number DE-AC02-06CH11357. The SPIRAL upgrade activities are supported by the European Union's Seventh Framework Programme under grant agreement n°262010 within the ENSAR project, and within ERA-NET NuPNET as part of the EMILIE project.

REFERENCES

[1] R. Vondrasek, A. Levand, R. Pardo, G. Savard, and R. Scott, Rev. Sci. Instrum. 83, 02A913 (2012).
[2] S.C. Jeong, M. Oyaizu, N. Imai, Y. Hirayama, H. Ishiyama, H. Miyatake, K. Niki, M. Okada, Y.X. Watanabe, Y. Otokawa, A. Osa, and S. Ichikawa, Rev. Sci. Instrum. 83, 02A910 (2012)
[3] T. Lamy, J. Angot, P. Sortais, T. Thuillier, and A. Galatà, Rev. Sci. Instrum. 83, 02A909 (2012)

Copyright © 2012 CC-BY-3.0 and by the respective authors

ISBN 978-3-95450-123-6

[4] Prospects for advanced electron cyclotron resonance and electron beam ion source charge breeding methods for EURISOL
[5] P. Delahaye, A. Galata, J. Angot, G. Ban, L. Celona, J. Choinski, P. Gmaj, A. Jakubowski, P. Jardin, T. Kalvas, et al, Rev. Sci. Instrum. 83, 02A906 (2012)
[6] G. Tabacaru, D. P. May, J. Arje, G. Chubarian, H. Clark, G. J. Kim, and R. E. Tribble, Rev. Sci. Instrum. 83, 02A905 (2012)
[7] F. Ames, R. Baartman, P. Bricault, K. Jayamanna, T. Lamy, and M. McDonald, Rev. Sci. Instrum. 81, 02A903 (2010)
[8] Damayanti Naika, Vaishali Naika, Alok Chakrabartia, S. Dechoudhurya, Sumanta Kumar Nayaka, H.K. Pandeya, Takahide Nakagawab, Nucl. Instrum. and Meth. A 547, 270 (2005)
[9] R. Geller, T. Lamy and P. Sortais, Rev. of Scient. Instrum. 77 (2006) 03B107
[10] F. Wenander, NIM B, 266 (2008) 4346-4353
[11] M. Marie-Jeanne, PhD thesis, Université Joseph Fourier (2009)
[12] P. Delahaye, C. J. Barton, K. Connell, T. Fritioff, O. Kester, T. Lamy, M. Lindroos, P. Sortais, G. Tranströmer, and F. Wenander, Rev. Sci. Instrum. 77, 03B105 (2006)
[13] R. Pardo, G. Savard, S. Baker, C. Davids, E. F. Moore, R. Vondrasek, G. Zinkann, NIM-B 261, Issues 1-2 (2007) 965
[14] R. C. Vondrasek, R. Scott, J. Carr, R. C. Pardo, Rev. Sci. Instrum. 79, 02A901 (2008)
[15] R. Vondrasek, A. Kolomiets, A. Levand, R. Pardo, G. Savard, R. Scott, Rev. Sci. Instrum. 82, 053301 (2011)
[16] R. Geller, Rev. Sci. Instrum. 71, (2000) 612
[17] Computer Simulation Technology Electromagnetic Studio, www.cst.com
[18] P. Delahaye, O. Kester, C. Barton, T. Lamy, M. Marie-Jeanne, F. Wenander, Eur. Phys. J. A 46, 421–433 (2010)

Copyright © 2012 CC-BY-3.0 and by the respective authors

ISBN 978-3-95450-123-6

HIGH INTENSITY BEAM PRODUCTION AT CEA/SACLAY FOR THE IFMIF PROJECT

R. Gobin*, G. Adroit, D. Bogard, N. Chauvin, O. Delferrière, Y. Gauthier, P. Girardot, F. Harrault, J.L. Jannin, D. Loiseau, P. Mattei, A. Roger, F. Senée, O. Tuske, Commissariat à l'Energie Atomique et aux Energies Alternatives, CEA/Saclay, DSM/IRFU, 91191 - Gif/Yvette, France

Abstract

At CEA/Saclay, IRFU institute is in charge of the design, construction and characterization of the 140 mA continuous deuteron Injector for the IFMIF project. This injector is composed of the source and the low energy beam line (LEBT) with its own diagnostics. The Electron Cyclotron Resonance (ECR) ion source operates at 2.45 GHz and the 2 m long LEBT is based on 2 solenoids. Krypton gas injection in the beam line is foreseen in order to reach a high level of space charge compensation for the beam matching at the RFQ entrance. During the last months hydrogen beam has been produced in pulsed and continuous mode and the beam diagnostics have been installed and commissioned. Recently a 125 mA-100 keV pulsed deuteron beam has been produced with a 1% duty cycle. In this article, the high intensity proton and deuteron beam characterization will be presented.

INTRODUCTION

For several decades numerous HPPA (High Power Proton Accelerator) projects are based on high intensity beam interaction with different targets, either for industrial applications or research facilities. Even if the IFMIF (International Fusion Materials Irradiation Facility) machine [1], dedicated to irradiation materials for future fusion reactors will accelerate deuteron instead of protons, this project is also ranked in the HPPA family.

The aim of the IFMIF machine is to produce a high flux of neutrons with energy spectrum comparable to next fusion reactors like DEMO. To reach this goal, the IFMIF layout is based on 2 deuteron accelerators able to simultaneously produce 125 mA at 40 MeV. The 2 combined beams will impact a liquid lithium target flowing down in front of the test cells where future studied materials will be installed for neutron irradiation.

The total power delivered in continuous mode by the accelerators at the target interaction will be 10 MW. Nevertheless, despite such high beam power, the maintenance of the machine leads to imperative very low beam losses. One could consider this machine as the accelerator of all the records: the highest intensity, the highest beam power, the highest space charge and the longest RFQ.

email: rjgobin@@cea.fr

That is why a prototype is presently under construction. This prototype consists of only the front end of one of both accelerators made of the ion source with its associated LEBT, a 10 meter long RFQ operating at 176 MHz and a first cyomodule with 8 HWR superconducting cavities. This cryomodule will allow reaching about 9 MeV beam energy.

Table 1: Summary of the IFMIF Injector Requested Parameters at the RFQ Entrance Flange

Requirements	Target value
Particles	D+
Output energy	100 keV
Output D+ current	140 mA
D+ fraction	99 %
Beam current noise	1 % rms
Normalized rms transverse emittance	0.25 π mm mrad
Duty factor	CW
Beam turn-off time	< 10 µs

To reach the requested beam intensity and considering a RFQ transmission of about 92 %, the deuteron beam at the RFQ entrance should reach a minimum of 140 mA with 100 keV energy. Table 1 summarizes the injector requests. Such demands are very challenging and push to a design based on the SILHI source operating at CEA/Saclay for more than 10 years [2]. A LEBT (Low energy Beam Transport) follows the source and will allow matching the beam at the entrance of the RFQ. As a consequence, like for other HPPA, while designing an injector, one has to consider the ion source, the extraction system and the LEBT as a whole [3].

ION SOURCE AND LEBT DESIGN

The source design is based on a 2.45 GHz frequency magnetron which transfers the RF power to the plasma chamber via waveguides and a RF window. A 3 step ridged transition located between the window (protected behind a bend to avoid backstreaming electron damages) and the plasma chamber. A boron nitride disk, located at the end of the ridged transition determines the barrier between the waveguide and the plasma chamber. The cylindrical plasma chamber, made of water cooled copper, is 90 mm inner diameter and 100 mm long. A second

Copyright © 2012 CC-BY-3.0 and by the respective authors

ISBN 978-3-95450-123-6

boron nitride disk covers the plasma electrode. In such high intensity source, the 2 boron nitride disks, bearing important impact of the plasma, are the only parts which need systematic change (roughly twice a year). Specific Boron Nitride has to be chosen to avoid high outgassing under plasma bombardment. For such a 2.45 GHz frequency, the electron resonance occurs when the magnetic field reaches 875 Gauss in the plasma chamber. The magnetic field is provided by 2 independently tuneable coil associated with iron shielding (Fig. 1).

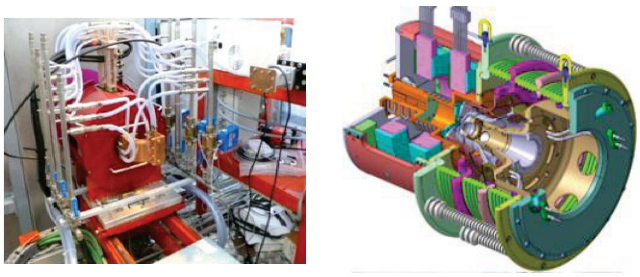

Figure 1: Picture and 3D view of the IFMIF injector ion source with coils and initial 4 electrode extraction system.

In order to minimize the beam divergence (by reducing the space charge effects) at the accelerator column exit, it has been initially decided at first to increase the plasma electrode aperture up to 12 mm. Then the overall extraction system length has been shortened by installing a 4 electrode accel-decel system. Such system allows keeping meniscus tuning with a puller for minimizing beam loses on the electrodes. Then the puller is followed by the electron repeller and the grounded electrode. Beam extraction simulations have been performed with the 2D Axcel code (Fig. 2) [4].

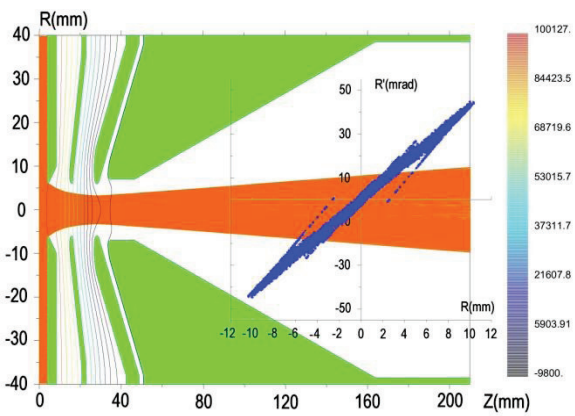

Figure 2: 140 mA D+@100 keV 4 electrodes extraction system Trajectories (r,r') beam emittance at z = 200 mm.

In the low energy transport line based on 2 solenoids, the space charge is partially compensated by the interaction of the beam with the residual gas. Secondary electrons are maintained into the beam core while secondary ions are repelled towards the walls. To minimize emittance growth in the LEBT, the length of the line has been reduced as short as possible. The use of short solenoids (310 mm long with shielding and H/V steerers located into the solenoids) allows limiting the total LEBT length at about 2.0 m. Beam transport simulations at low energy have been performed with the TraceWin code [5]. In addition, numerous simulations were performed with the SOLMAXP home-made code to better understand the space charge compensation evolution in the beam line and to improve beam transport simulations. Addition of heavy gas like krypton in the LEBT is expected for increasing the space charge compensation and for reducing emittance growth.

Along the 2 m long beam line, the following equipments have to be integrated: the accelerator column, the 2 solenoids and steerers, 2 pumping systems with their associated valves and gauges, diagnostics and security beam stopper, RFQ entrance cone, alignment devices and supports.

To characterize and to follow the beam evolution, free spaces allowing diagnostics installation are very limited. As a consequence, only several CID cameras, a deported spectrometer (using a radiation resistant fiberscope [6]), an Allison scanner emittancemeter, a ACCT and a movable beam dump are installed between the source and the RFQ entrance. The Allison scanner has been developed for being able to bear more than 15 kW continuous beam. Thermal simulations have been performed to design the thermal screen (which is used as entrance slit) made of tungsten tiles brazed on a water cooled copper block. Then a classical varying electric filed allows analysing the selected beamlet through a second slit.

EXTRACTED BEAM ANALYSIS

The first hydrogen plasma and the first beam were produced in May 2011 in pulsed mode [7]. Then up to 75 keV continuous beam has been extracted with intensity of about 100 mA through a 10 mm diameter aperture. With beam energy higher than 70 keV, the spark rate increases dramatically and X-ray production also increases.

After the Allison emittance scanner commissioning the first emittance measurements have been done between both solenoids with a 80 mA total hydrogen beam extracted at 50 keV. Emittance value reaches (rms norm.) 0.46 π mm mrad (Fig. 4a). Then after beam tuning in order to optimize the transmission through the RFQ entrance cone, only 42 mA of proton beam has been measured on the beam stop and the emittance value (rms norm.) reaches 0.29 π mm mrad (Fig. 4b). The low transmission through the cone may be due either to the poor proton fraction extracted from the source or to the high beam divergence at the source exit caused by the 8 mm plasma electrode diameter.

By changing the plasma electrode diameter from 8 to 10 mm, hydrogen beam has been produced in pulsed mode (10 % duty cycle and 10 Hz pulse repetition). In these conditions, up to 140 mA have been extracted at 50 keV while more than 80 mA were crossing the cone (Fig. 5).

ISBN 978-3-95450-123-6

Copyright © 2012 CC-BY-3.0 and by the respective authors

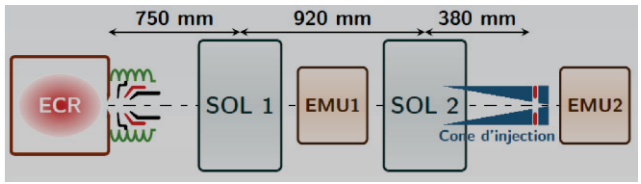

Figure 3: Both locations of the Allison emittance scanner (… diagnostic box between solenoids and after RFQ entrance cone).

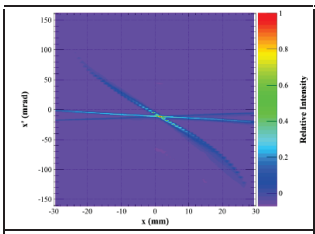

Figure 4a: emittance figure between both solenoids.

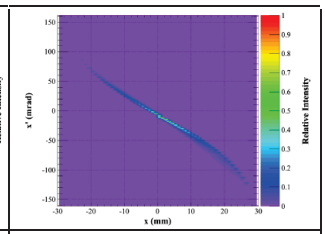

Figure 4b: emittance after RFQ entrance cone.

In addition, a pulsed Deuteron beam (125 mA) has also been produced at 100 keV with a 1% duty cycle. Up to now, with D^+ beam, the duty cycle is limited for neutron production and activation reasons.

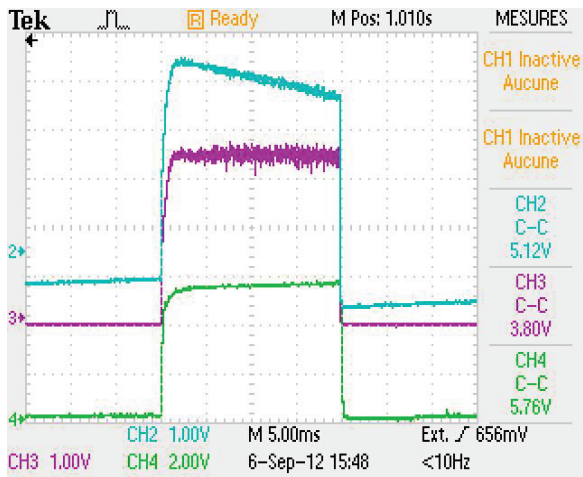

Figure 5: 50 keV extracted beam through a 10 mm diameter aperture i) green : 140 mA total hydrogen beam, ii) blue: 88 mA H^+ beam through the cone measured with ACCT, iii) magenta: 72 mA measured on beam dump.

FUTURE PLANS

As preliminary results demonstrated a quite high spark rate, the addition of a 5th electrode (as grounded electrode between puller and electron repeller) is presently underway. Figure 6 presents the recent simulations for the new extraction system. The addition of the 5th electrode would lead in higher beam divergence than with the initial 4 electrode extraction system.

This 5 electrode extraction system has been installed on the IFMIF injector mid of September 2012. As a consequence, after extraction gap conditioning, beam extraction and optimization will be performed within the next few weeks with hydrogen beams. Then, deuterium will be injected into the plasma chamber and beam characterization will be performed in pulsed mode before switching to continuous mode for a short period (neutron production limitation).

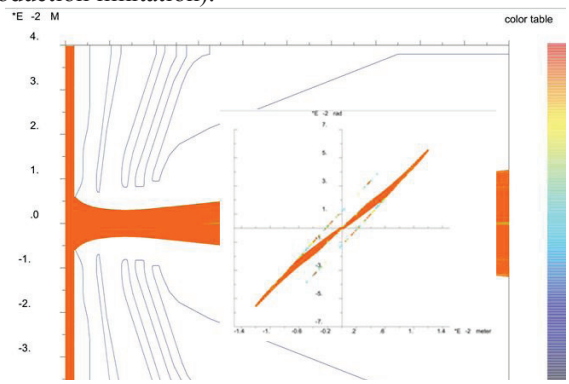

Figure 6: Simulations of beam trajectories with the new 5 extraction system.

Due to the high power beam, for use of interceptive diagnostics after the first accelerating cavities for machine commissioning, a slow chopper will be added between both LEBT solenoids.

CONCLUSION

The preliminary measurements performed with the IFMIF injector proton beams proved the expected challenges start immediately at source extraction and beam transport at low energy.

Important work still remains in beam optimization and understanding before reaching the requested beam performance at the RFQ entrance. This work will be performed at CEA/Saclay before the transfer of the whole injector on the Rokkasho site in Japan, foreseen in beginning 2013.

ACKNOWLEDGMENT

The authors would like to especially thank people who are involved for several years in the IFMIF project either at CEA/Saclay or in other European and Japanese institutes.

REFERENCES

[1] A. Mosnier et al., Proceedings of LINAC 2012 Conference, (TU1A01), Tel Aviv (Israel).
[2] R. Gobin et al., Rev. Sci. Instrum. **75** 1414 (2004).
[3] S. Gammino et al., Rev. Sci. Instrum. **81**, 02B313 (2010).
[4] O. Delferrière et al., Rev. Sci. Instrum. **79**. 02B723 (2008).
[5] N. Chauvin et al., Rev. Sci. Instrum. **83**, 02B320 (2012).
[6] F. Senée et al, "Beam species fraction measurement using Doppler shift method with FUJIKURA fiberscope for IFMIF-EVEDA Injector", Proceedings of the DIPAC 2011 Conference, Hamburg (Germany).
[7] R. Gobin et al., Rev. Sci. Instrum. **83**, 02A345 (2012).

Copyright © 2012 CC-BY-3.0 and by the respective authors

ISBN 978-3-95450-123-6

ALL PERMANENT MAGNET ECR ION SOURCE DEVELOPMENT AND OPERATION STATUS AT IMP

L. Sun#, X. Z. Zhang, J. Y. Li, Y. Cao, H. Wang, B. H. Ma, J. Q. Li, W. H. Zhang, H. W. Zhao, J. W. Xia, D. Xie

Institute of Modern Physics, CAS, 509 Nanchang Rd., Lanzhou 730000, China.

Abstract

All permanent magnet ECR ion sources have many advantages over traditional ECR ion sources composed of several axial room temperature solenoids and one permanent magnet hexapole magnet, which make them the first choice for many heavy ion facilities and platforms. At IMP, three all permanent magnet ECR ion sources have been built for different applications, i.e. the very compact ECR ion source LAPECR1 for intense mono or multi charge state ion beams' production, the LAPECR2 ion source installed on the 320 kV high voltage multidisciplinary platform, and the LAPECR3 ion source dedicated to C^{5+} beam production for the cancer therapy facility. In this paper, after a general discussion of the ion sources' design, the applications and the operation status of the IMP all permanent magnet ECR ion sources will be presented.

INTRODUCTION

Been widely used as Multiple Charge Ion (MCI) beam provider, ECR ion source is one of the best devices that can produce intense MCI beams. ECR ion source is actually a magnet field confined plasma machine, where the ion beams can be extracted. The confinement magnetic field is normally a so-called nested min-B magnetic field which is a superposition of radial multipolar field and axial mirror field. Generally, the axial field is supplied by superconducting magnet solenoids, room temperature magnet solenoids, or permanent magnet rings, while the radial field is supplied by either superconducting sextupole coils or Halbach structure permanent magnet hexapole [1] (other hexapole structures are also used). The different combination of the types of radial and axial field magnet gives the different species of ECR ion sources, i.e. fully superconducting ECR ion sources, such as VENUS [2] and SECRAL [3], hybrid ECR ion sources, such as SHIBA [4] and A-PHOEBIX [5], classical room temperature ECR ion sources, such as AECR-U [6] and GTS [7], and all permanent ECR ion sources, such as the Nanogan sources [8] and the BIE sources [9]. The first very successful modern ECR ion source, the so-called Caprice source [10], is a room temperature ECR source, which is still widely used in many labs. Fully superconducting ECR ion sources can provide the beam intensities and charge states that can't be met by other types of ECR sources, but based on the applications, all the four types of ECR ion sources can find the users if only the application needs can be met. All permanent magnet ECR ion sources have their special features and merits that make them extremely suitable for industrial applications and small experimental platform setup: (1) very compact device, (2) easy maintenance, (3) easy to operate, (4) low electricity consumption, (4) no needs for large volume LCW (Low Conductivity Water), and (5) most important of all, cost saving. But there also several intrinsic disadvantages of this type of devices mostly because of the all permanent magnet structure, such as: (1) inflexibility of the magnetic field, (2) low magnetic field strength and small plasma chamber size, and (3) therefore moderate MCI beam intensity.

IMP/CAS is an institute dedicated to nuclear physics and the associated multidisciplinary physics studies. The accelerator facility development is based on these needs and requirements. Three all permanent magnet ECR ion sources have been successively built at IMP for the facility's needs. The structure and the parameters will be discussed in the following content.

LAPECR1 SOURCE

Small experimental lab needs very compact experimental setups. This is the original reason to build the LAPECR1 source to deliver intense mono charge state ion beams, low intensity MCI beams and even some molecular ion beams. Table 1 gives the main parameters of this ion source. This ion source is designed with a very compact size which makes the source body weighs only 25 kg that can be easily moved around by an adult. Despite of the compactness, the source is equipped with a Ø40 mm ID plasma chamber that enables the direct microwave power feeding with a WR62 rectangular waveguide to simplify the injection plug structure. Iron plugs at both the injection and extraction sides have been incorporated to enhance the mirror peaks. The source is designed and operated at 14.5 GHz.

HIRFL accelerator needs intense proton and H_2^+ beams for ion beam injection. The room temperature LECR3 ion source, which is mostly used to deliver intense MCI beams like C^{4+}, Ar^{8+}, Kr^{18+}, Xe^{20+} and etc., can't be operated at the source potential higher than 25 kV, therefore a simple setup that can deliver intense proton or H_2^+ beams at the source potential of ~35 kV is proposed. In this project, LAPECR1 is floated on a G10 insulator plate which is covered with a plexiglass box. Because of the simple structure of LAPECR1, this setup composes a small HV platform that can be biased to more than 36 kV.

#sunlt@impcas.ac.cn

ISBN 978-3-95450-123-6

Copyright © 2012 CC-BY-3.0 and by the respective authors

28-35 kV has been tested for routine operation. This project has been completed by the end of July, 2012. With only tens of watts microwave power feeding, very stable intense ~emA proton and H_2^+ beams have been produced. Long term beam intensity fluctuation is observed to be reasonably good with a value of ~0.2%. Fig. 1 is the picture of the LAPECR1 source rested on the small HV platform.

Table 1: Main Parameters of LAPECR1

B_{inj}	1.0 T
B_{ext}	0.56 T
Hexapole pole surface	1.1 T
Plasma chamber ID	40 mm
f	14.5 GHz
Dimension	Φ102 mm×296 mm
Weight	~25 kg
Permanent material	N45M NdFeB
L_{mirror}	74 mm
L_{ECR}	55 mm
HV	30~50kV

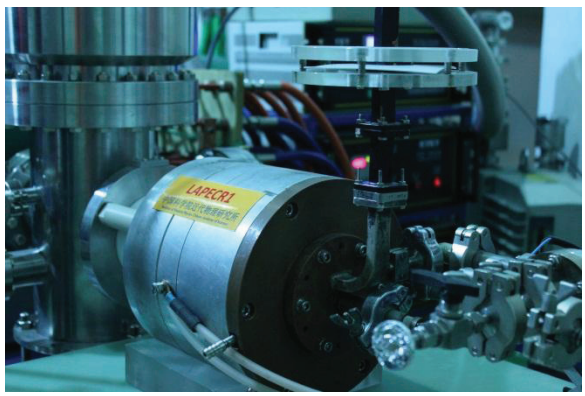

Figure 1: LAPECR1 source installed on a HIRFL injection beam line.

LAPECR2 SOURCE

The HIRFL accelerators can provide the beam energies covering several MeV/u to hundreds of MeV/u. Multidisciplinary physics research needs much wider energy range for various studies. A 320 kV HV platform was proposed in 2002 and completed in 2006. A high charge state all permanent magnet ECR ion source LAPECR2 has been built and installed on the platform to deliver intense ion beams. Based on the users' requirements, ion beam species from low to high charge states of gaseous or solid elements are required. For the purposes, the source was designed to operate at high magnetic field, high frequency mode. Table 2 lists the main parameters of LAPECR2 source in comparison with a classical room temperature LECR2 ion source [11] operated at the same frequency of 14.5 GHz.

LAPECR2 is designed with all permanent magnet structure. No iron plug has been used to boost the mirror fields because of the difficulties to handle the strong magnetic force during the installation. To produce intense high charge state ion beams, the plasma chamber is intentionally designed as big as possible. A tradeoff between the magnet compactness and the magnetic field strength makes Ø67mm the final plasma chamber ID value. The axial magnetic rings are specially designed with conical shape inner bore structure to achieve wanted axial field profile, and the hexapole magnet is also designed with conical shape on both sides to have sufficient radial confinement magnetic field inside the plasma chamber. For this design, there have been some difficulties and problems during the magnet fabrication, for example the edge of the conical shape magnet blocks are easily broken because the NdFeB magnetic blocks are very fragile and the edge is very sharp and flimsy. Nevertheless, the magnet has been successfully built and tested.

Table 2: Main Parameters of LAPECR2 in Comparison with LECR2 Ion Source

Parameters	LAPECR2	LECR2
Axial Mirror Peaks (T)	1.28, 1.07	1.5, 1.1
B_{min} (T)	0.42	0.39
B_{rad} (T)	1.21	1.0
Hexapole Material (NdFeB)	36-segmented N45M	24-segmented N42
μW Frequency (GHz)	14.5	14.5
μW Power Coupling Mode	Off-axial Direct	Coaxial
Lmirror (mm)	255	265
L_{ecr} (mm)	100	86
Plasma Chamber ID (mm)	67	70
Chamber Material	316 L SS	316 SS

During the machine commissioning, the source was fed with maximum 1.1 kW 14.5 GHz microwave power from a klystron amplifier to achieve high power density inside the plasma chamber. TWT microwave generator is of course a very good option that can provide flexibility in the microwave frequency tuning within a certain range to optimize source operation, which can compensate a little bit the magnetic field inflexibility disadvantage of an all permanent magnet structure source, but so far only 700W maximum output TWT machine is available, which is not enough for LAPECR2's Ø67mm ID plasma chamber. Both gaseous and solid materials have been fed into the plasma to produce intense medium charge state and high

Copyright © 2012 CC-BY-3.0 and by the respective authors

ISBN 978-3-95450-123-6

charge state ion beams. Promising results have been obtained with LAPECR2 ion source. Fig. 2 gives the typical intensities of xenon ion beams in comparison with other devices working at similar frequencies. The performance has demonstrated that LAPECR2 source a well performing ion source that is comparable to even high performance room temperature ECR ion sources working at 14.5 GHz [12].

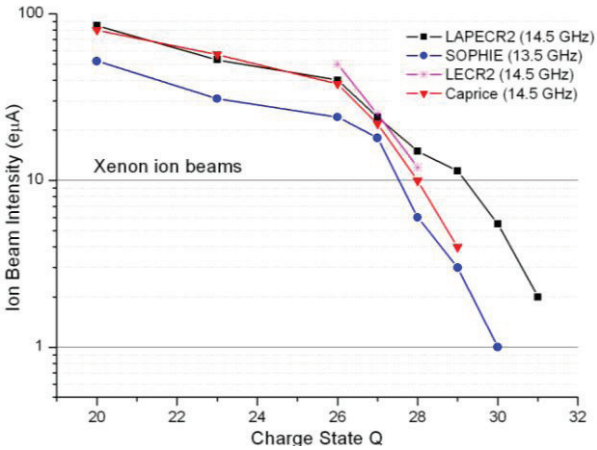

Figure 2: LAPECR2 xenon ion beam results in comparison with other 14.5 GHz ion sources.

LAPECR2 was put into operation on the 320 kV HV multidisciplinary platform in 2007. And it has been running on it to delivery various ion beam species for the 5 experimental terminals since then [13]. Fig. 3 is the picture of LAPECR2 source installed on the 320 kV HV platform. The HV platform has been tested to 395 kV, but for long-term operation stability and safety, the maximum allowed operation voltage is 320 kV. LAPECR2 together with the insulator support has been tested up to 28 kV, but due to the strong stray field and beam loss at source extraction side, the maximum safe operation voltage is lowered to ~23 kV for intense beam extraction. So, the nominal HV platform beam energy range is 5keV/q~340 keV/q which can cover a wide range of interesting physics. Till now, LAPECR2 has been used for routine operation more than 30,000 hours. Totally, 9 groups of gaseous elements including H, He, C, N, O, Ne, Ar, Xe, and Kr, and 9 groups of solid elements including Pb, bi, Fe, Eu, Mg, Cs, I, F and S ion beams have been delivered. Some of the results obtained during the experimental beam preparation are even much better than those obtained during the source commissioning test in 2006. Table 3 lists the typical beam intensities obtained during routine operation beam time. It is worth mentioning that most of the beam intensities were made with the microwave power of 400 W from a TWT microwave generator, since the footprint of a klystron amplifier is too big to be place on the HV platform.

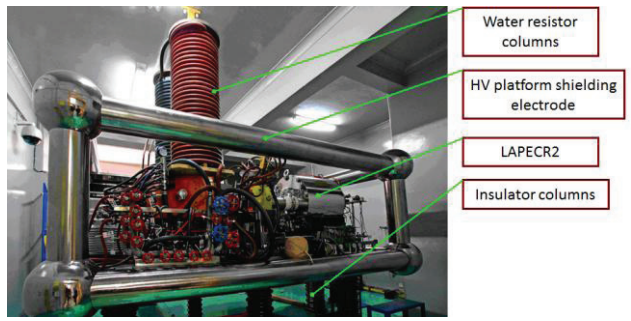

Figure 3: Picture of LAPECR2 ion source and the HV platform.

Table 3: Typical Delivered Ion Beam from LAPECR2 for Experimental Terminals

Ion Species	Results in 2006 (eμA)	During operation (eμA)
C^{5+}	/	190
Ar^{16+}	2	2
Kr^{23+}	/	15
Xe^{30+}	5.3	11
[a]I^{25+}	/	35
[a]Cs^{16+}	/	40
[a]Cs^{23+}	/	20
[b]Fe^{13+}	/	25
[b]Fe^{15+}	/	20
[a]Eu^{30+}	/	10
[a]Eu^{33+}	/	5
[a]Bi^{28+}	17	45
[a]Bi^{31+}	5	20
[a]Bi^{33+}	/	15
[a]Bi^{36+}	/	3

a) with resistor oven; b) with MIVOC ;

LAPECR3 SOURCE

Based on the existing technology and the experience with HIRFL-CSR, a new accelerator complex named HITFiL or Heavy Ion Therapy Facility in Lanzhou dedicated to hadron cancer therapy has been designed and is under constructing in Lanzhou by IMP staff. For the complementarity of proton and carbon ions in the performance of cancer therapy, HITFiL is designed to accommodate both proton and carbon ions. It is mainly composed of two ECR ion sources for beam shift, a Sector Focusing Cyclotron, a MEBT, a synchrotron, a HEBT and four treatment terminals. H_2^+ or C^{5+} beam produced by ECR source is pre-accelerated by the cyclotron to 7 MeV/u, and then stripped to H^+ or C^{6+}

ISBN 978-3-95450-123-6

Copyright © 2012 CC-BY-3.0 and by the respective authors

before the synchrotron injection point [14]. For the compactness, easy operation and maintenance, all permanent magnet ECR ion source is the best option for the complex's ion source choice.

For the project, 100eμA C^{5+} is desired for routine operation, therefore, the ion source should be capable of delivering more than 120eμA C^{5+} during source commissioning. Since C^{5+} is a comparably high charge state ion, especially in terms of the high beam intensity desired, very good plasma confinement must be provided by the permanent magnets. This ion source LAPECR3 has been designed and successfully built at IMP. As shown in Fig. 4, the ion source's magnet is mainly composed of the injection magnetic rings, extraction magnetic rings, middle magnetic ring and the 24-segmented Halbach structure hexapole magnet. An iron plug has been employed to boost the injection magnetic field peak to ~1.8 T which is essential for the high B mode operation for an ECR ion source at 14.5 GHz. Fig. 5 is the axial field distribution. The magnet design tricks utilized on LAPECR2 ion source have also been applied on LAPECR3, i.e. the hexapole magnet end toward the source extraction side has been designed with a conical shape to refine the total magnetic field configuration, and one of the extraction magnetic rings has been shaped to fit the hexapole magnet accordingly. The plasma chamber is originally designed with the ID of Ø50mm, which accordingly has the magnetic field of 1.14 T at the chamber inner wall. The glue problem eventually resulted in the shrinking-down of the hexapole magnet inner bore size. According to the magnetic field measurement, only ~1.0 T field strength has been obtained at the Ø47.5 mm ID plasma chamber inner wall. Table 4 gives the final key parameters of the ion source in comparison with the designed ones.

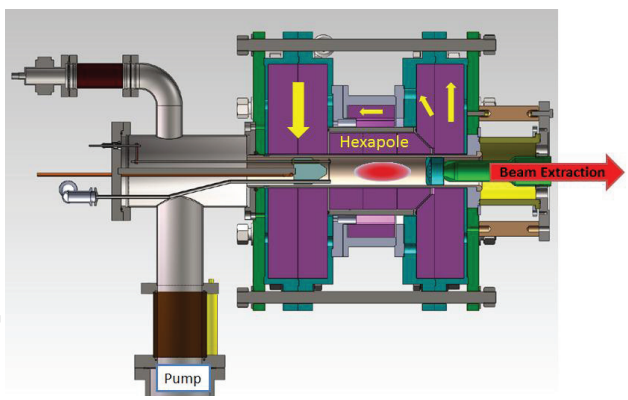

Figure 4: Sectional plot of the LAPECR3 ion source.

But to produce intense C^{5+} beam is still challengeable. The ionization potential of C^{5+} is ~400 eV, therefore, electron energy up to 1 keV is required to be optimum for the ion production. High microwave power heating and good plasma confinement are the necessities for the production of high charge state ions. However, the material feeding is a big issue. Since pure carbon normally exists in a solid state that needs a very high temperature to evaporate which is not applicable with ECR ion source in terms of reliability, especially for the cancer therapy purpose that needs a long-term stability of the ion beam. Gas feeding is so far the best solution. Carbon compound gas such as CO_2, CO, CH_4, C_2H_2, C_3H_8 and etc. have been already tried in many labs to produce intense carbon ion beams, and the work in NIRS has a more detailed investigation on the issues how to produce intense high charge state carbon ion beams, the gas choice and some other techniques [15]. Having in mind that the machine is going to be used as a turnkey device for cancer therapy treatment, cheap and easy handling gas such as CH_4 and C_2H_2 will be used as the feeding gas. Isotope gases can be used in study but not in this application. The ion source is already assembled and installed on the test bench. Once the beam line parts are connected, source conditioning will be started.

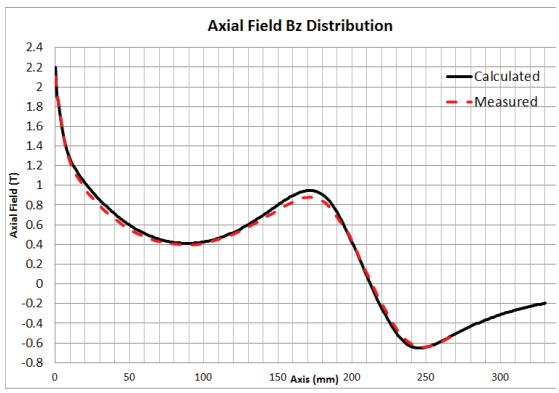

Figure 5: Axial magnetic field distribution (measured and designed results) of LAPECR3 source.

Table 4: Main Parameters of LAPECR3 Source

Parameters	Designed	Final specs.
Axial Field (T)	1.8-0.40-0.94	1.8-0.40-0.89
Field on Inner Chamber Wall -Br (T)	1.14	1.0
Mirror Length (mm)	170	172
ECR Length (mm)	64	~70
f (GHz)	13.75-14.5	13.75-14.5
Chamber ID (mm)	50	47.5
Effective Chamber Volume (L)	0.33	0.30
Max. Designed Operation HV (kV)	25	28
Max. Designed μW Power (kW)	0.70	0.70
Dimension (mm)	Ø450×380	Ø455×382
NdFeB Weight (kg)	157	157
NdFeB Type	N50M	N50M

Copyright © 2012 CC-BY-3.0 and by the respective authors

ISBN 978-3-95450-123-6

CONCLUSION

Three different design all permanent magnet ECR ion sources have been designed and built at IMP for multi-purposes. LAPECR1 source is now used as the HIRFL accelerator preinjector to deliver H^+ or H_2^+ beams. LAPECR2 source has been used on the 320 kV multi-disciplinary HV platform for 6 years. The ion source has produced different ion beams of 18 elements for the successive 5 experimental terminals for more than 30,000 beam hours. The latest built LAPECR3 source will be commissioned soon and once it is done, it will be removed and connected to the HITFiL complex to deliver intense H_2^+ or C^{5+} beams.

REFERENCES

[1] K. Halbach, Nucl. Instrum. Methods 169 (1980) 1.
[2] D. Leitner, C. M. Lyneis, T. Loew, D. S. Todd, S.Virostek, and O. Tarvainen, Rev. Sci. Instr. 77 (2006) 03A302.
[3] H. W. Zhao, et al., Rev. Sci. Instr. 83 (2012) 02A320.
[4] Tetsuro Kurita, et al., Nucl. Instr. and Meth. B 192 (2002) 429.
[5] T. Thuillier, T Lamy, L. Latrasse and J. Angot, Rev. Sci. Instr. 79 (2008) 02A330.
[6] Z. Q. Xie, Rev. Sci. Instrum., 69 (1998) 625.
[7] D. Hitz, et al., Rev. Sci. Instr. 75 (2004) 1403.
[8] P. Sortais, et al., "Development of Compact Permamnet ECRIS", Proceedings of 12th International Workshop on ECR Ion Sources, Tokyo, April 1996, p.44 (1995).
[9] Dan Z. Xie, Rev. Sci. Instrum. 73 (2002) 531.
[10] B. Jacquot and M. Pontonnier, "The New 10 GHz Caprice Source-Magnetic Structures and Performances", Proceedings of 10th International Workshop on ECR Ion Sources, Report ORNL CONF-9011136, p.133 (1990).
[11] H. W. Zhao, B. W. Wei, Z. W. Liu, Y. F. Wang, W. J. Zhao, Rev. Sci. Instr. 71 (2000) 646.
[12] L. T. Sun, et al., Nucl. Instr. and Meth. B, 263 (2007) 503.
[13] X. Ma, et al., Journal of Physics: Conference Series 163 (2009) 012104.
[14] Weiping Chai, Jiawen Xia, Jiancheng Yang, Youjin Yuan, Mingtao Song, Bing Wang, Jian Shi, Peng Li, "Study of Charge Exchange Injection in HITFiL", IPAC'11, San Sebastián, September 2011, THPS044, p. 3520 (2011); http://www.JACoW.org
[15] A. G. Drentje, A. Kitagawa, and M. Muramastsu, Trans. Plasma Sci. 36 (2008) 1502.

ISBN 978-3-95450-123-6

Copyright © 2012 CC-BY-3.0 and by the respective authors

LASER ABLATION OF ACTINIDES INTO AN ELECTRON CYCLOTRON RESONANCE ION SOURCES FOR ACCELERATOR MASS SPECTROSCOPY

T. Palchan[1], R. Pardo[1], F. Kondev[1], S. Kondrashev[1], C. Nair[1], R. Scott[1], R. Vondrasek[1], M. Paul[2], W. Bauder[3], P. Collon[3], G. Youinou[4], M. Salvatores[4,5], G. Palmotti[4], J. Berg[4], T. Maddock[4], and G. Imel[6]

[1] Physics Division, Argonne National Laboratory, 9700 S. Cass Avenue, Argonne, IL 60439 USA
[2] Racah Institute of Physics, Hebrew University, Jerusalem 91904, Israel
[3] Nuclear Structure Laboratory, University of Notre Dame, Notre Dame, IN 46556, USA
[4] Idaho National Laboratory, 2525 Fremont Avenue, Idaho Falls, ID 83415
[5] CEA-Cadarache, 13108 Saint-Paul-lez-Durance, France
[6] Idaho State University, 921 South 8th Avenue, Pocatello, ID 83209

Abstract

A project using accelerator mass spectrometry (AMS) is underway at the ATLAS facility to measure the atom densities of transmutation products present in samples irradiated in the Advanced Test Reactor at INL. These atom densities will be used to infer effective actinide neutron capture cross-sections ranging from thorium to californium isotopes in different neutron spectra relevant to advanced fuel cycles. This project will require the measurement of many samples with high precision and accuracy. The AMS technique at ATLAS is based on production of highly-charged positive ions in an ECRIS followed by injection into a linear accelerator. We use a picosecond laser to ablate the actinide material into the ion source. We expect that the laser ablation technique will have higher efficiency and lower chamber contamination than sputtering or oven evaporation thus reducing 'cross talk' between samples. The results of off-line ablation tests and first results of an accelerated beam generated by the laser coupled to the ECR will be discussed as well as the overall project schedule.

INTRODUCTION

Advanced nuclear fuel cycles are currently under evaluation in order to assess their potential to cope with new requirements of radioactive waste minimization, optimization of resource utilization and reduced risk of proliferation. This assessment should account for several key features of the fuel cycle, such as irradiated fuel processing, innovative fuel development and fabrication, waste characterization and disposal. In some cases, the impact of nuclear data and of their associated uncertainties can be crucial in order to assess further exploration. The need for accurate data has been pointed out in recent studies devoted to Generation-IV systems, see e.g. [1]. The very high mass actinides can play a significant role in the feasibility assessment of innovative fuel cycles. As an example, the potential build-up of ^{252}Cf when recycling all transuranics in a light water reactor, leads to increased neutron emissions that could impact the fuel fabrication process [2]. As a consequence, the poorly known nuclear data of higher mass transuranics need to be significantly improved.

At present, there is some information on these isotopes, but up to now, there has been little emphasis on the quality of these data and very little reliable uncertainty estimations have been provided. This situation is due to the difficulty to make both integral and differential cross section measurements for these isotopes.

The MANTRA (Measurements of Actinides Neutrons Transmutation Rates with Accelerator mass spectroscopy) project objectives are to obtain valuable integral information about neutron cross sections for actinides that are important for advanced nuclear fuel cycles. The proposed work takes advantage of two experimental facilities: the neutron irradiation capabilities of the Advanced Test Reactor (ATR) at the Idaho National Laboratory and the Accelerator Mass Spectrometry (AMS) capabilities of the Argonne Tandem Linac Accelerator System (ATLAS) at Argonne National Laboratory [3].

In this paper we will concentrate on the requirements of the AMS program and the novel aspects, specifically the laser ablation, that is implemented at the ECR ion source to carry out this research project. The requirements placed on the AMS measurements to be performed at ATLAS are quite challenging. These challenges include high-precision isotope ratio measurements, minimization of cross-talk between samples, efficient use of milligram samples, and the processing of an unprecedented number of samples for a facility as complex as ATLAS. Unique element (Z) identification is desirable, but is not expected to be possible except for specific cases.

The measurement configuration for ATLAS uses the ECR-II ion source [4], significantly modified as discussed below, as the source of ions. After acceleration and deceleration (increasing the accelerator m/q resolution but keeping the ion energy within acceptance range of analytical elements) in the ATLAS linac to approximately 1 MeV/u, the actinide ions of interest are counted in the focal plane of the Fragment Mass Analyzer (FMA) [5].

*Work supported by … U.S. Department of Energy, Office of Nuclear Physics, under contract No. DE-AC02-06CH11357

Copyright © 2012 CC-BY-3.0 and by the respective authors

ISBN 978-3-95450-123-6

Small Sample Size and Cross-Talk

A major feature of AMS is the ability to analyze small samples. At ATLAS the AMS activities are focused on samples of a few milligrams. For this project, an added complexity is the need to deal with many small samples. The smaller the samples, the less are the radiological problems associated with handling α-emitting actinides for ATLAS operation. The need to measure many small samples as quickly as possible pushes us to develop efficient sample changing techniques for the ECR source and material delivery techniques which minimize source contamination.

We believe the best approach for this situation is to develop laser ablation for the feeding of sample material into the source. With laser ablation a very small and controllable amount of sample material can be introduced into the source without introduction of extraneous material from the sample holder. Also the angular distribution of ablated material by laser irradiation tends to be strongly peaked around the normal to the surface [6] which is expected to improve the efficiency of capture of ions into the plasma and thereby reduce wall contamination. Finally, the form of the sample material (metal, oxide, etc.) is less critical than with the sputtering or oven technique.

The ECR-II source will also be equipped with a quartz liner. The quartz liner will keep the main body of the source relatively clean of actinides, thus simplifying clean-up. Furthermore, there is some operational evidence that cross talk among samples is reduced. This effect has been observed with other AMS projects at ATLAS [7]. A negative to using a quartz liner is that source performance, as measured by charge-state distribution and maximum beam intensity, is somewhat reduced. But the beam energy is limited by the bending power of the FMA system and use of high charge state ions is not required. A mass-to-charge ratio of ~8-9 will be quite adequate for these measurements.

LASER PARAMETERS

Laser ablation into an ECR source was first developed at ATLAS [8] and used as plasma diagnostic tool [9]. It has since been used by a number of other labs to explore the coupling of laser produced ions into an ECR source [10]. The technique has not been used routinely for ion production and requires development for this application. The controlled release of materials into the plasma by well-focused laser light will eliminate the significant material buildup often seen in the region of the oven throat or beside the sputter cones, two techniques widely used for sample feeding to the ECRIS. The inefficient, indiscriminate injection of material into the source with these older techniques not only reduces the overall sensitivity of the method but is a major source of cross-contamination between samples. Our experience with lasers in the past indicates that the laser ablation approach will be much cleaner, but must be shown to work for this application.

Laser ablation is a term used to describe removal of material by laser action and it is distinguished from evaporation in equilibrium conditions. In order to remove an atom from a solid by means of a laser pulse one should deliver an amount of energy that exceeds the binding energy of that atom. Therefore the absorbed energy density per atom in a laser-heated layer E_{abs}, should at least be comparable to the heat of vaporization in equilibrium;

$$E_{abs} = 2AF(t_p)/n_a l_s . \qquad (1)$$

here A is the absorption coefficient; F is the incident laser fluence, the energy per unit surface area during the pulse of duration t_p; n_a is atomic number density and l_s is the skin depth of the laser in the solid [11]. There are three regimes of laser ablation depending on the laser and target parameters: The thermal ablation, the non-equilibrium semi thermal ablation and the extreme non-equilibrium electrostatic ablation. In the thermal ablation the laser pulse is longer than the major relaxation routes in the irradiated material. Heat conduction and hydrodynamic processes cause the removal of the atoms from the solids. As a consequence the ablation is accompanied by the formation of a large heat- affected zone and throws out molten material [12]. The second regime, non-equilibrium and semi-thermal, is realized when electrons have enough time to transfer the energy to the lattice and the average energy of the ions (temperature) exceeds the binding energy but the distribution function is far from the equilibrium Maxwell distribution. In these conditions, the majority of ions escape the solid before the equilibrium distribution is established. The extreme ablation regime, electrostatic ablation, is completely non-equilibrium and non-thermal. This mode is realized when a short powerful pulse elevates average electron energy during the pulse in excess of the sum of the binding energy of the ions plus the energy necessary for the electron to escape from a solid. The lattice remains cold during the pulse. The energetic electrons escaping from a solid create a huge electrostatic field of charge separation, which pulls the ions out of the solid [13].

In order to avoid a flow of macroparticles or molten materials into the ECR ion source, we chose a laser with picoseconds pulse duration. The properties of the laser that we are using in this application are:

- λ =1064 nm
- 15 ps pulse width
- Repetition rate up to 400 Hz
- Pulse energy: variable, up to 5 mJ per pulse.
- Maximum, power of $3x10^8$W per pulse.

OFF LINE TEST SET UP AND RESULTS

For characterization of the laser and to acquire a better understanding of the laser ablated material coupling with the ECR ion source plasma we performed tests in an off line setup. The experimental set up is shown in Fig 1. A 4000mm focusing lens is placed at the entrance of a vacuum chamber to mimic the distances required at the ECR source. The result of the optical set up is a focal spot with a diameter of 450μm at the FWHM. The maximum laser intensity at the focal spot is $2x10^{11}$W/cm^2. An image of the focal spot is presented in Fig 1.

The laser-induced ablation creates a plasma plume which rapidly expands. Typically the plasma expansion

ISBN 978-3-95450-123-6

Copyright © 2012 CC-BY-3.0 and by the respective authors

speed is in the order of 10^6 cm/sec. During a picosecond ablation the number of ejected species is about 10^{13}atoms/pulse. The ion flux is about 1% [14]. Using a faraday cup located at a distance of 15.8cm from a solid Ti target we extracted the ion velocity by means of time of flight technique. The calculated averaged ion energy is 40±10eV. For Ti the corresponding velocity is $1.2x10^6$cm/sec. In addition we measured the ablating rates for different materials [15].

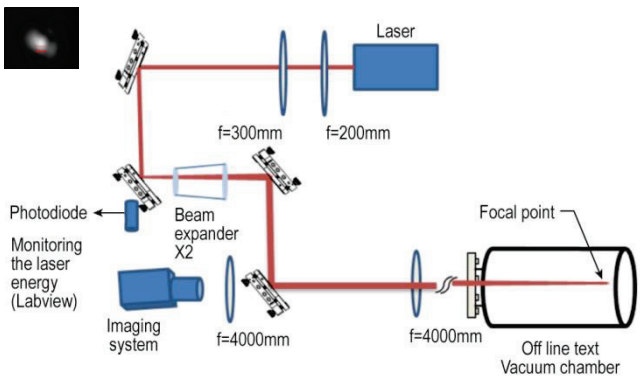

Figure 1: Off line test set up and the laser focal spot image.

These studies now provide us with the background information needed to better understand the laser/source performance when the laser is coupled to the ECR source.

INSTALLATION AT THE SOURCE

The installation of the laser at the source is shown in Fig. 2. The laser beam is delivered into the source through the extraction aperture. The ablation target is located at the rear of the ECR chamber near the edge of the plasma.

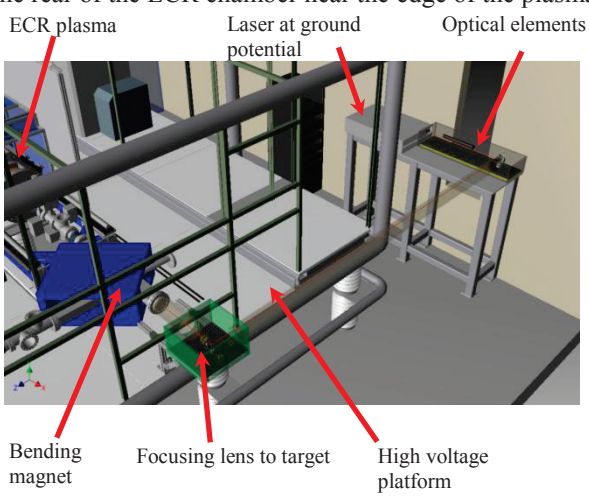

Figure 2: Drawing showing the laser ablation system relative to the ECR source HV platform.

Imaging of the Target Sample

In order to monitor the laser beam hitting the target samples, we developed an imaging system. The imaging system is located behind the last mirror that directs the laser beam into the source (see Fig 1). We installed a halogen light at the back of the iron taper, (see Fig 3). This way we can collect the scattered light behind the sample holder when it is in place. Using our imaging system we are able to image the outer edges of the sample holder. During a run, when the laser hit the sample we are able to identify where the laser hits the sample.

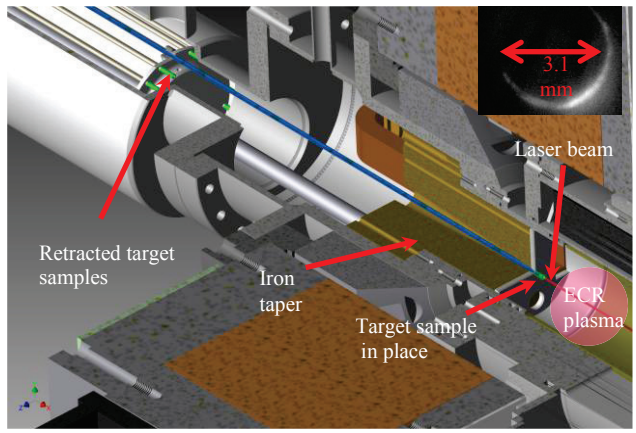

Figure 3: Multisample changer mounted on ECR source showing sample location with the back light.

Figure 3 shows the multisample changer interfaced to the source that we use in order to rapidly switch between the samples. See this proceeding for a detailed description of the multisample changer [16]. In addition the geometry of the laser beam relative to the plasma chamber is presented. The laser beam enters the plasma chamber on axis with the center axis of the plasma chamber. The target sample is inserted into the plasma chamber through the center of the bias disc.

ECR BEAM FROM ABLATED SAMPELS

Titanium Sample

Initial tests of the laser coupled to the ECR source took place with solid Ti sample. Fig 4 shows a Ti sample after irradiation. The laser parameters that we used during this test are 25Hz repetition rate and a variable energy of 0.5-1.5mj per pulse. The resulting peak intensity is $5x10^{10}$w/cm^2. The overall consumption rate was 0.3mg/hour.

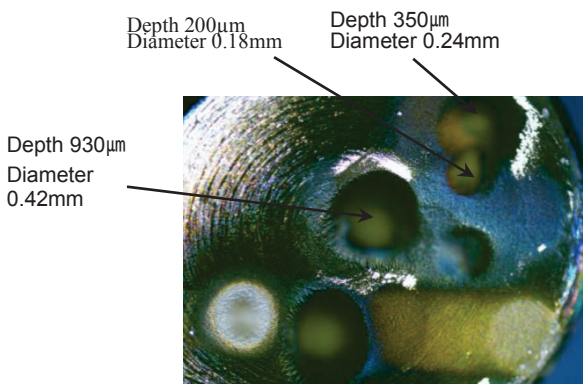

Figure 4: Ti sample after laser irradiations.

Copyright © 2012 CC-BY-3.0 and by the respective authors

ISBN 978-3-95450-123-6

By means of laser ablation on a Ti sample we were able to generate a high charge state beam. The charge state distribution is shown in Fig 5. From the charge state distribution, it is clearly evident the beam production drops to a very low level of 0.1μA when the laser is off compared to 1μA when the laser is on.

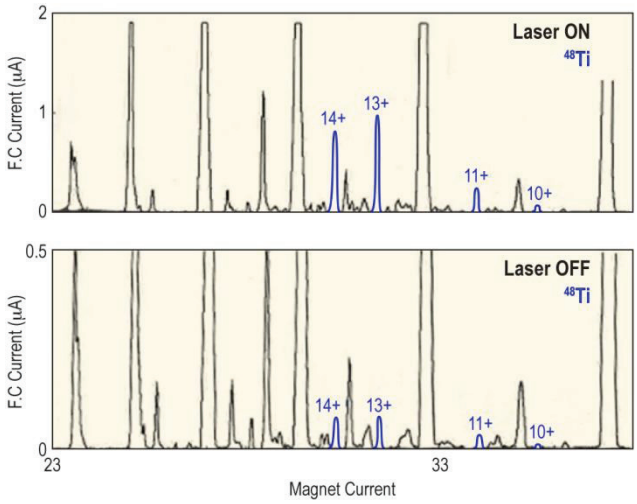

Figure 5: Charge state distribution of Ti beam. The Ti peaks are labeled with mass/charge state in the two figures. The charge–state distribution peaks at 13+. For sputter technique the charge–state distribution peaks at 10+-12+.

For long term stability (100minutes) we measured the $^{48}Ti^{13+}$ charge state. The laser energy that we used for those measurements was 1.5mj with 25Hz repetition rate. The laser beam diameter at the focal spot was 0.5mm. Fig 6 shows the faraday cup current trend with the corresponding laser energy. The generated beam is around 4 μA and stable for the first 10 minutes and then it drops by 80% for the next 20 minutes while on the same time the laser energy is stable. After that the beam stays stable at a lower level of 0.6 μA for more than an hour.

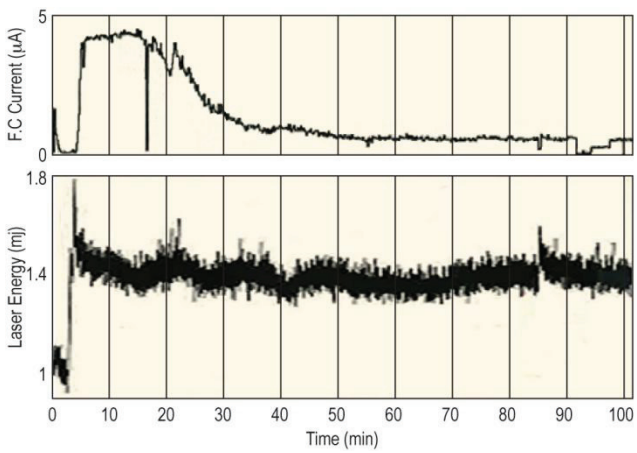

Figure 6: Long term of Ti beam and the corresponding laser energy for 0.5mm diameter in the focal spot.

One of the reasons for this beam current instability is the drilling rate of the laser in the sample.

Terbium Oxide Sample at the ECR Ion Source

In order to lower the drilling rate and to gain more stability we used a laser beam manipulator and moved the laser beam on the sample at a constant rate. The beam manipulator consists of two controlled motors that are connected to the aligning knobs of the last mirror that sends the beam into the vacuum chamber (see figure 1). The minimal step size on the target using the beam manipulator is 110μm.

In this test we used a terbium oxide powder as a sample. The powder was packed into one of the multisample changer holder. The laser parameters in this test were100Hz repetition rate and energy of 2.3mj per pulse. The overall consumption rate was 0.32mg per hour. Figure 7 shows the time dependence of the $^{145}Tb^{24+}$ charge state. From the term it is evident that there is a periodic pattern in the beam production. This periodicity is attributed to the pattern of the laser beam raster. The beam was moving over a region of 0.36mm^2.

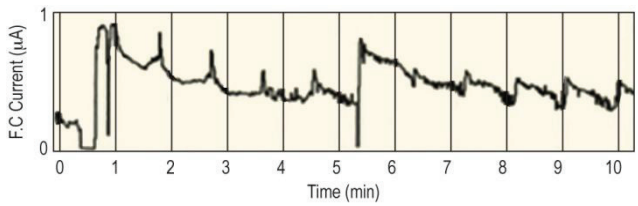

Figure 7: Tb beam time dependence with a constant rate moving of the laser beam on the sample.

Figure 8 shows the charge state distribution of the Tb beam produced by means of laser ablation.

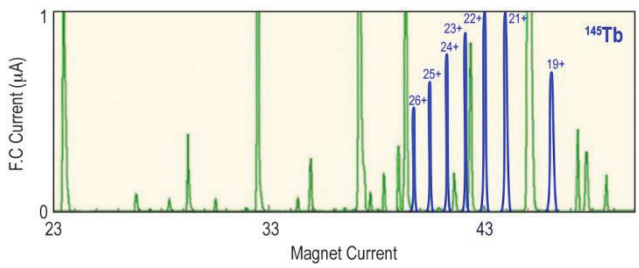

Figure 8: Charge state distribution of Tb beam. The Tb peaks are labeled with charge state. The charge–state distribution peaks at 22+.

Aluminum Sample

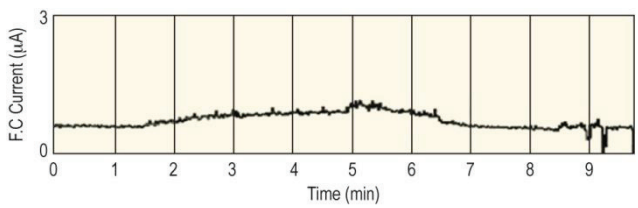

Figure 9: Term of Al beam with a constant sweep rate of the laser beam on the sample.

After some adjustment with the raster pattern of the laser beam (we reduced the moving region to be 0.2mm^2) we were able to stabilize the beam production. Figure 9 shows the beam production of $^{27}Al^{8+}$ where the periodic pastern is gone but the overall production is low. The

ISBN 978-3-95450-123-6

Copyright © 2012 CC-BY-3.0 and by the respective authors

laser parameters in this test were100Hz repetition rate and energy of 2.2mj per pulse. The overall consumption rate was 0.45mg per hour.

Uranium Oxide Sample

The uranium oxide powder was packed also to one of the multisample holders. In this test the laser parameter were 200-400Hz repetition rate and energy of 5mj per pulse. Figure 10 shows the charge distribution of the uranium ion beam. The overall consumption rate was 0.7mg per hour. We were not able to measure the beam long term because the production of the beam was neither high enough nor stable.

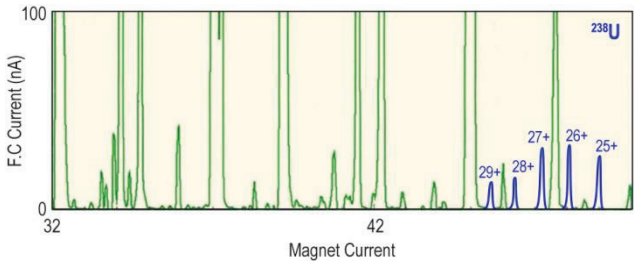

Figure 10: Charge state distribution of Uranium.

NEW DESGIN FOR THE SAMPLE LOCATION

During the tests we noticed that the source performance even without the laser ablation were low and unstable. The production of $^{16}O^{6+}$ beam (oxygen is the supporting gas) was 35μA compared to 160 μA under similar conditions. After some investigation we came to the conclusion that the missing bias disc at the center axis of the plasma chamber has a significant effect on the ECR ion source performance. The production of $^{16}O^{6+}$ beam was restored to normal levels with the disc filled with Al at the center. Therefore we are redesigning the injection system in order to move the location of the sample target to be 0.3 inches off the center. This way the bias disc center is solid aluminum where most of the plasma hits. The hole in the disc is not interfering with the performance of the source. Also this may further reduce the beam from the sample when the laser is turned off. We tested the source with the new location for the hole in the bias disc and got the same results as with the complete bias disc.

CONCLUSIONS

We have demonstrated high charge state beams generated at the ECR source from laser ablated material. To improve the production of the generated ion beam we plan to move the sample location to be off axis. In addition we plan to investigate the influence of the spatial beam profile, especially a flat top profile, on the production of the ion beam.

REFERENCES

[1] M.Salvatores, "Nuclear Data for Advanced Fuel Cycles", Proc. Int. Conf. IEMPT-10, Mito, Japan, 6-10 October 2008.
[2] G.Youinou, et al., INL/EXT-09-16091, 2009; http://www.inl.gov/technicalpublications/Documents/4282336.pdf.
[3] G.Youinou, et al., “An Integral Reactor Physics Experiment to Infer Actinide Capture Cross-Sections From Thorium To Californium With Accelerator Mass Spectrometry”, Eleventh International Conference on Nuclear Data for Science and Technology, Jeju Island, Korea, 2010.
[4] M. Schlapp, et al.,"A new 14GHz electron-cyclotron-resonance ion source for the heavy ion accelerator facility ATLAS” Rev. Sci. Instrum. 69 (1998) 631.
[5] C.N. Davids, et al., “Startup of the Fragment Mass Analyzer at ATLAS”, Nucl. Instrum. and Meth. B 70, 358(1992).
[6] S. Mao et al., “Initiation of an early-stage plasma during picosecond laser ablation of solids” Appl. Phys. Lett. 77, 2464 (2000).
[7] M. Gaelens, et al., Rev. Sci. Instrum. 75, 1916 (2004).
[8] R. Harkewicz, et al., Rev. Sci. Inst. **65**(4), 1104(1994).
[9] R C Pardo, et al., Rev. Sci. Inst. **75** (5), 1427(2004).
[10] S. Gammino, et al., J. App. Phy. **96** (5), 2961 (2004).
[11] E.G.Gamaly, “The physics of ultra-short laser interaction with solids at non-relativistic intensities” Phy. Reports. **508** 91 (2011).
[12] S. Nolte et al., “Ablation of metals by ultrashort laser pulse” J. Opt.Soc. Am. B **14** (10)2716(1997).
[13] P.T. Mannion, et al., “Langmuir probe investigation of plasma expansion in femto-and picoseconds laser ablation of selected metals” J. of Phy :Conference series **59** 753 (2007). Conference on Laser ablation (COLA'05) Banff, Canada 2005.
[14] W. Marine, et al.,”Laser induced plasma formation by picoseconds pulse irradiation” Appl. Surf.Sci. **69** 290 (1992).
[15] T.Palchan, et al., HIAT2012, Chicago, Illinois (2012), TUC03, to be published.
[16] R.Vondrasek, et al. “A multi sample changer coupled to an ECR source for AMS experiments” these proceeding.

Copyright © 2012 CC-BY-3.0 and by the respective authors

ISBN 978-3-95450-123-6

ECRISs AT GANIL TODAY AND TOMORROW

P. Jardin*, O. Bajeat, C. Barué, C. Canet, P. Delahaye, M. Dubois, M. Dupuis, J.L. Flambard, R. Frigot, C. Leboucher, P. Lehérissier, F. Lemagnen, L. Maunoury, B. Osmond, J. Piot, E. Traykov, GANIL, Bvd H. Becquerel, BP 55027 14076 Caen cedex 5, France
C. Peaucelle, IPNL, 4, rue Enrico Fermi, 69622 Villeurbanne cedex, France
T. Thuillier, LPSC, 53, rue des Martyrs, 38026 Grenoble cedex, France
O. Tuske, IRFU, Bât. 141, Saclay, 91191 Gif sur Yvette cedex, France
B. Gall, J. Rubert, IPHC, 23 rue du Loess, 67037 Strasbourg cedex 2, France

Abstract

GANIL (Grand accélérateur National d'Ions Lourds) uses ECRISs for producing stable and radioactive ions for more than 20 years. Two ECR4 type ion source (IS) deliver intense multi-charged stable ion beams of gaseous and metallic elements feeding cyclotrons for post acceleration to energies up to 100 A.MeV. A full permanent magnet ECRIS is also employed for producing multi-charged radioactive ion beams in the frame of SPIRAL 1 (Système de Production d'Ions Radioactifs Accélérés en Ligne, part 1). For atomic and material physic experiments, a high performance ECRIS labeled GTS developed at CENG/ Grenoble (France) is currently used to deliver high intensity, high charge state and low energy ion beams. To extend the range of radioactive ion beams available at GANIL, two ISOL (Isotope Separator On Line) projects are underway (SPIRAL1 upgrade and SPIRAL 2). In the frame of these projects, radiation hard singly-charged ECRIS, Q/A=1/3, 1/6 ECRISs, 2.45 GHz deuteron ECRIS and permanent magnet target ion source system (TISS) using an ECRIS are under development in parallel. A review of the main uses, current developments and performances obtained or expected with ECRISs at GANIL are presented. Locations of all the setups mentioned below are indicated in Figure 1.

INTRODUCTION

In 1982, GANIL delivered its first stable ion beam at high energy, using Penning Ion Gauges (PIG) as injectors for cyclotrons. For reasons of short lifespan, the PIG Ion Sources (IS) were frequently replaced (every ~40 hours), reducing the available time for operation. In 1985, a 10 GHz ECRIS named MINIMAFIOS [1] and developed by R. Geller was installed as one of the two injectors. Its advantages were higher lifespan, intensities and stability. Three years later, it was replaced by a 10 GHz CAPRICE [2] ECRIS, allowing an enlargement of the beam range in term of charge states and elements, stretched to metallic elements. In 1991, PIGs are definitely abandoned. The second injector of GANIL is equipped with a 14 GHz ECR4 [3] type IS placed at 100 kV. Its commissioning in 1993 showed an important increase of beam intensities for gas and metallic elements compared to the ones obtained with CAPRICE. A gain of ionization efficiency was also observed using a micro-oven for several metallic elements. Finally, CAPRICE was replaced by an ECR4 IS in 1995.

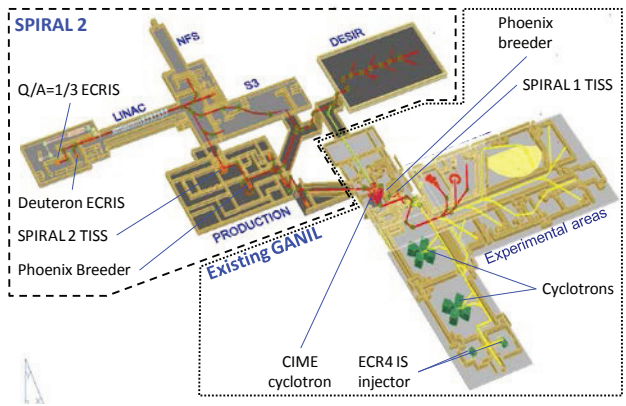

Figure 1: Schematic of the GANIL today and by 2020. Yellow lines: stable ion beams at GANIL. Red lines: SPIRAL 2 ion beam lines.

In 1994, GANIL decided to extend its range of ion beams to radioactive ones using the isotope separator on line (ISOL) method. The studies of SPIRAL 1 facility are undertaken and the first radioactive ion beam is delivered in 2001. Radioactive isotopes are produced in the target and ionized by an original permanent magnet ECRIS (NanoGan III [4]), designed to cope with the numerous constraints inherent to the generation of radioactivity. Ions emerging from the TISS are mass to charge separated and injected in the post-accelerator cyclotron CIME [5] to reach energies up to 25 A.MeV.

The increasing demand of radioactive ion beams encouraged GANIL to extend its range of available beams [6]. In 2006, the construction of a second radioactive ion beam facility (SPIRAL 2) was officially decided at GANIL. Beams of short lived heavy radioactive ions will be produced in flight by the S3 facility [7]. Longer lived isotopes will be produced by ISOL method in the production cave containing a TISS. Two production methods will be used:

- fission of uranium induced by neutrons, these latter being produced in a graphite converter on which a deuteron beam impinges,
- reaction of heavy ions on target material. Two ECRISs are chosen as injectors for the LINAC post-accelerator: an existing 2.45 GHz ECRIS delivering up to 5 mA of deuterons developed at

* jardin@ganil.fr

ISBN 978-3-95450-123-6

Copyright © 2012 CC-BY-3.0 and by the respective authors

IRFU/Saclay/France, and a multi-charged ECRIS being designed at LPSC/Grenoble which should deliver high intensities and heavy ion beams with masses higher than He.

In the target, a large variety of elements will be produced. Each of them will be ionized by a specific IS. For gaseous isotopes an ECRIS will be employed. Owing to the dose rate close to the production target, a specific radiation hard ECRIS (named MonoBob [8]) was designed. Technical difficulties have limited their performances to single ionization. Since ion beams must be multi-charged before being injected in the post accelerator CIME, a PHOENIX type charge breeder [9,10] will be inserted between the 1+ ECRIS and CIME. If not post-accelerated, the ions can be directly used by the DESIR [11] facility.

Since 2001, SPIRAL 1 is limited to the production of ions from gaseous elements. The chemical selection was obtained using a cold transfer region connecting the target to the ion source. To offer new radioactive ion beams to physicists while the SPIRAL 2 is being constructed, GANIL decided in 2011 to improve the SPIRAL 1 facility. After transformation, present TISS, surface IS [12] and FEBIAD as developed at ISOLDE [13] will be used in the production cave. As for SPIRAL 2, a PHOENIX type charge breeder will be installed between the singly-charged IS installed in the cave and CIME.

Since 2010, one last ECRIS development is underway to give an alternative solution to the additional stage of charge breeding in case of low charge state (Ar^{8+} for instance) [14]. The final version would consist in a compact, multi-charged and radiation hard ECRIS placed close to the target.

The previous overview shows that at GANIL, ECRISs are used for four different goals:

- highly charged stable ion beams
- high intensity ion beams,
- high ionization efficiency (for stable and radioactive ion beam production)
- high charge breeding efficiency

The range of ECRIS applications is indeed larger than the GANIL use, as the range of existing ECRIS technologies is larger than those employed at GANIL. Nevertheless, GANIL has the chance to be a laboratory where several ECRISs have been designed, constructed and used during years and thus benefits from an important operation feedback. Today, in most cases, due to their complexity, the future ECRISs can no longer be studied and developed in a unique laboratory. Collaborations are more than ever necessary, to go further in the future of ECRISs, as well illustrated by the actual instance of SPIRAL 2.

STABLE BEAM INJECTORS

The cyclotrons of GANIL are fed by stable heavy ion beams produced by two ECRIS: ECR4 type ion sources. The ion masses range from carbon to uranium and the post acceleration energy goes up to 95 A.MeV, depending on the ion mass to charge ratio. Current performances for some metallic beams can be found in reference [15] and on the GANIL web site [16]. More recent results related to I and Cs ion beam production are detailed in ref. [17].

New results for Ti have been obtained using the MIVOC method [18]. The compound (CH3)5C5Ti(CH3) synthesized by the IPHC/Strasbourg team [19] from natural Titanium (48Ti : 75%) has been used for tests. An intensity of 20 (±3) µA for 48Ti10+ was maintained for 4 days, while regulating the temperature of the MIVOC chamber. A consumption of 1.5 mg/h for the MIVOC compound has been deduced, i.e. 0.23 mg/h for 48Ti. The resulting ionization and transport efficiency of Ti for all charge states was of 10%. Corrected from the transport efficiency (33%), the ionization efficiency was close to 30%. The corresponding Ti spectrum is displayed in Figure 2.

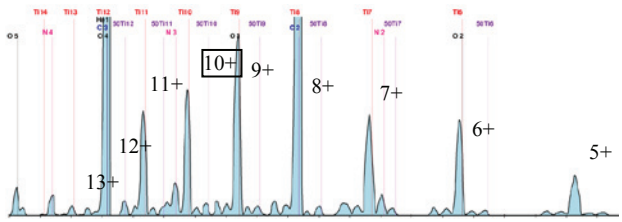

Figure 2. Charge state distribution of Ti. Optimized charge state: 10+ (20 µA). Mixing gaz He. RF power 170 W. Extraction voltage : 74 kV. Total extracted current from the source: 1.9 mA.

SPIRAL 1 ECRIS

Radioactive ion beams are produced by SPIRAL1 using TISSs. High energy ion beam, named “primary beam” coming from previous cyclotrons impinges on a thick carbon target. Helped by the target temperature, radioactive isotopes produced during the collision diffuse out of the carbon up to an ion source (see Figure 3).

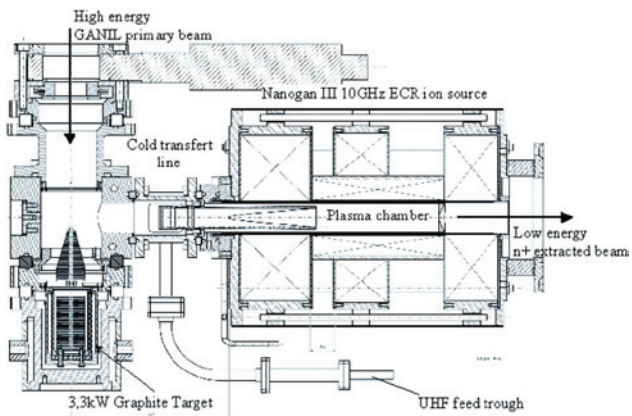

Figure 3: SPIRAL1 TISS

This source must cope with several requirements, *i.e.* mainly injection parameters of the post-accelerator cyclotron CIME and hostile neighborhood around the production target. That induces multi-charged ionization (typically $^{40}Ar^{8+}$), reliability, simplicity, radiation hardness and low cost. A simple permanent magnet ECR ion source was designed and is now used since 1998. According to the initial requirements of the SPIRAL1

Copyright © 2012 CC-BY-3.0 and by the respective authors

ISBN 978-3-95450-123-6

project, to the ECR principle and to the primary ion masses used, mainly radioactive ions from gases are produced, from He to Kr [20].

SPIRAL 2 PROJECT

The SPIRAL 2 project [21] is based on a multi-beam driver in order to allow both ISOL and low-energy in-flight techniques to produce Radioactive Ion beam (RIB). A superconducting light/heavy-ion LINAC with an acceleration potential of about 40 MV capable of accelerating 5 mA deuterons up to 40 MeV and 1 mA heavy ions up to 14.5 MeV/u is used to bombard both thick and thin targets. These beams could be used for the production of intense RIB by several reaction mechanisms (fusion, fission, transfer, etc.) and technical methods (ISOL, gas catchers, recoil spectrometers, etc.). The production of high intensity RIB of neutron-rich nuclei will be based on fission of uranium target induced by neutrons, obtained from a deuteron beam impinging on a graphite converter (up to 10^{14} fissions/s) or by a direct irradiation with a deuteron, ^{3}He or ^{4}He beam.

The atom-to-ion transformation will take place into the TISS. Owing to the large variety of radioactive atoms produced in the target, four different singly-charged ion source types are considered and are presently under development: Surface ion-source [22], FEBIAD IS, Laser IS [23] and ECRIS. Only this latter is presented in this paper.

Production of Primary Q/A=1/3 Ion Beam

As shown in the paper [24] of T. Thuillier, several beam intensities requested by the SPIRAL 2 project cannot be produced today by the most performing ECRISs, even if some of them already fit with the specifications (see Table 1).

Table 1: Non exhaustive list of ion intensities expected at the exit of the Q/A=1/3 ECRIS of SPIRAL 2.

Ion	SPIRAL 2 specifications	PHOENIX V2	Other ECRIS	Reference
$^{18}O^{6+}$	1000	1300	2850 ($^{16}O^{6+}$)	VENUS [25]
$^{40}Ar^{14+}$	420	50	514	VENUS [25]
$^{36}S^{12+}$	240	55	-	-
$^{48}Ca^{16+}$	160	16	70	SECRAL [26]
$^{58}Ni^{19+}$	57	19	50	SUSI [27]

Reaching the expected intensities needs to develop a new ECRIS. Regarding the requirement level, a large volume 28 GHz superconducting (SC) ECRIS seems to be the most adapted. Such a SC ECRIS has not been included in the SPIRAL 2 construction budget. Thus, the commissioning of the linear accelerator will be made by 2014 with the existing room temperature ECRIS PHOENIX V2 developed at LPSC/Grenoble/ France. It is presently under tests to produce Ar^{14+}, Ca^{16+} and Ni^{19+} beams. Its installation on SPIRAL 2 should take place by spring 2014. A new SC ECRIS would be developed if funding were granted.

Production of Primary Deuteron Beam

The 2.45 GHz ECRIS [28] developed at Saclay has already demonstrated its capability to respect the SPIRAL 2 specifications, *i.e.* to deliver more than 5 mA of deuteron at 40 kV of extraction voltage. The source and the low energy beam line with a part of their services will move at GANIL to be installed by the end of 2012.

Ion Beams Production from Gaseous Isotopes.

In order to ionize gaseous isotopes (of He, O, Kr or Xe…) coming from the target of SPIRAL 2, the design of a new radiation hard ECR source of singly-charged ions has started in 2002. The startup design is based on a previous ECRIS named MONO1000 [29] which presented several interesting features for ISOL use: simple mechanical arrangement, small, low cost, reduced weight and thus simplified retreatment process. Its ionization efficiency was high enough (~80% for Ar or for heavier noble gases) and the source presented a large aperture between the magnetic rings which allows connecting the target very close to the plasma chamber, which is important to succeed in producing short lived isotopes.

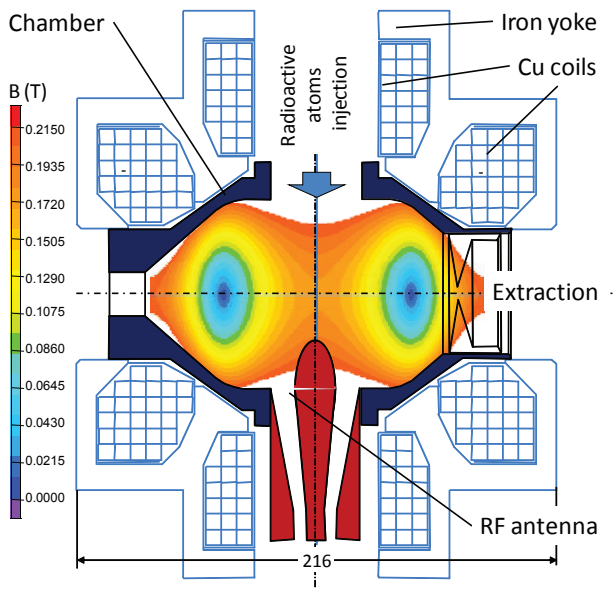

Figure 4: Schematic of the SPIRAL 2 singly-charged ECRIS.

To cope with the constraint of hostile environment around the target of SPIRAL 2, and of the installation of the TISS under vacuum, we attempted to reproduce the magnetic field and performances of Mono1000 by using only radiation hard components and low out-gassing materials. The final solution (MONOBOB) mainly consists in a magnetic structure where each permanent magnet ring was replaced by two coils insulated by glass fiber, and in a simple chamber free of O-rings. The

ISBN 978-3-95450-123-6

Copyright © 2012 CC-BY-3.0 and by the respective authors

2.45 GHz power is injected via an RF antenna which can deeply penetrate the chamber owing to the particular shape of the magnetic field. Cross section of the source is given Figure 4.

The current extracted from the source is generally lower than 1 mA and the ionization efficiency in the singly-charge state ranges from 40% to 100% for noble gases ranging from Ar to Xe. Extraction configuration must be improved, being for Xe close to 40% (at 14 kV).

SPIRAL1 UPGRADE

To reinforce the choice of ion beams to those made from condensable elements and with masses up to Xe, an upgrade of SPIRAL 1 has been undertaken [30]. Beams and technical options considered during the prospective phase [31] have been sorted out. A schematic of the ongoing upgrade is presented in Figure 5. Surface ionization, FEBIAD or new multi-charged ECR ion sources will be installed in the production cave after its modification. Out of the cave and after mass separation, an ECR Phoenix Booster type will be installed on the present low energy beam line to increase the charge of the radioactive ions from 1+ to N+ for post-acceleration.

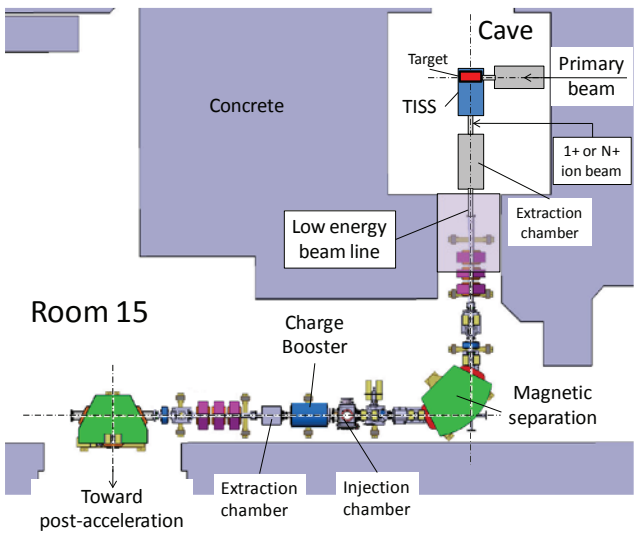

Figure 5: Schematic of the SPIRAL 1 upgrade.

Owing to the stringent regulation requirements the TISSs need to conform, the present TISS working in the cave will only be slightly transformed : The ECRIS will not be modified. Only the target and RF injection system will be improved to increase the global atom-to-ion transformation efficiency.

The booster that will be used on SPIRAL 1 is a commercial version of the Phoenix booster designed by LPSC Grenoble [32]. It has been first tested on-line at CERN [33] and is also under operation at TRIUMF [34]. Moreover, the breeding principle has been successfully tested at ANL [35]. Valuable feedback provides benefits to the design of our charge breeder [36] (see Figure 6): the vacuum system has been reinforced in the injection chamber to reach a very low pressure, important for getting a high 1+ to N+ transformation efficiency, narrowing the charge state distribution and to limit the presence of contaminants. The 1+ optical system has been studied to ensure an easy tuning of the beam injection with many degrees of freedom (vertical and horizontal steering, electrostatic lenses). A translational freedom of the coaxial injection tube along the booster axis has also been added to optimize the electric field shape near the plasma and thus the capture conditions. The possibility to make the 1+ and existing N+ beams going through the booster when it is off has been taken into account. This function is essential when the beam delivered by the TISS is directly used, *i.e.* without charge breeding, either for post-acceleration or in the experimental beam line LIRAT [37] (Ligne d'Ions Radioactifs A Très basse énergie). In this case, the coils of the booster are used to transport the singly-charged ion beam through the apertures of the booster electrodes. The beam can be adapted for injecting it inside the cyclotron by tuning of the beam line after the booster.

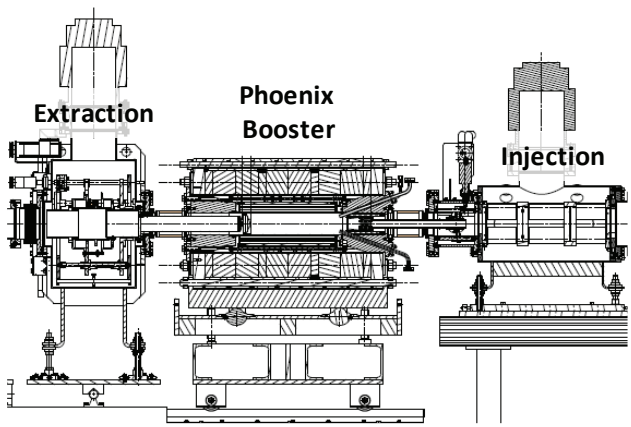

Figure 6: Injection, charge breeder and extraction for SPIRAL 1.

The singly charged ions coming from the cave will cover the range from He^+ to Xe^+, with post-accelerated energies ranging from ~25 A.MeV to ~7 A. MeV respectively, depending on the isotopes considered. The breeding efficiency is generally better for ion masses higher than ~30. Beyond mass higher than ~100, the transport between the TISS and the booster must be made at lower extraction voltage, due to the limit of the magnetic rigidity of the mass separator, which limits the transport efficiency. Thus the preferential mass range of SPIRAL 1 upgrade goes from ~30 to ~100.

The transformation had to be managed in a frame of very strict safety rules, leading to a stopping period of operation of 1.5 years from 2014 to beginning of 2015. The installation of the booster should be achieved by June 2014 and new beams should be available by spring 2015.

MULTIGAN

As previously demonstrated [38], the large and direct aperture performed between a two magnetic rings ECRIS permits a direct view between the target cavity and the plasma, making possible the production of radioactive ions from condensable elements. Years ago, this possibility incited us to transform a full permanent

Copyright © 2012 CC-BY-3.0 and by the respective authors

ISBN 978-3-95450-123-6

magnet singly-charged ECRIS [29] into a full coil singly-charged ECRIS to sustain the dose rate present around a TISS.

Producing multi-charged ions needs to restart the process: first, testing with permanent magnets if an arrangement as simple as for MONO1000 but with a reinforced magnetic field could cope with magnetic features requested for a multi-charged ionization. An ECRIS [14] has been built and is presently under test on a bench of the Pantechnik company. Preliminary results have showed the production of Ar^{4+} and Xe^{6+} but with a low intensity. Depending on the results, especially the ionization efficiencies, a version might be developed and adapted to be tested on SPIRAL1 for producing medium charge state condensable ions of short half-life (<100ms). In a second step, and if the results are encouraging, we will attempt to reproduce the magnetic structure with coils only.

REFERENCES

[1] R. Geller and B. Jacquot, Physica Scripta Vol. 3, (1983) 19-26

[2] B. Jacquot et al., « Source d'ions lourds CAPRICE 10GHz » Nuc. Instrum. and Meth. A 269 (1988) 1-6

[3] P. Sortais et al., Rev. Sci. Instrum. **61** (1990) 228

[4] L. Maunoury et al., Proceedings of the 13th International Worshop on ECR Ion sources, February 1997, College Station, Texas, USA

[5] CIME Working Diagram, 'http://pro.ganil-spiral2.eu/users-guide/accelerators/spiral-beams'

[6] P. Jardin et al., Rev. Sci. Instrum. **81**, 02A909 (2010)

[7] http://pro.ganil-spiral2.eu/spiral2/instrumentation/s3/s3-at-ganil

[8] M. Dubois et al, in *Proceedings of the 19th International Workshop on ECR Ion Sources, Grenoble, August 2010;* see http://www.jacow.org/ p. 64

[9] T. Lamy et al., Rev. Sci. Instrum. **77**, 03B101 (2006)

[10] T. Lamy et al., 'Charge breeding method results with the Phoenix booster ECR ion source', Proceedings of EPAC 2002, Paris, France

[11] See http://pro.ganil-spiral2.eu/spiral2/instrumentation/desir

[12] C. Eléon et al., Nuc. Instr. and Meth.. B **266** (2008) 4362-4367

[13] L. Penescu, R. Catherall, J. Lettry, T. Stora, Review of Scientific Instruments, 81 (2010), p. 02A906

[14] L. Maunoury, et al., in *Proceedings of the 19th International Workshop on ECR Ion Sources, Grenoble, August 2010;* see http://www.jacow.org/ p. 37

[15] P. Lehérissier et al., Rev. Sci. Instrum. **77**, 03A318 (2006)

[16] http://www.ganil-spiral2.eu/

[17] P. Lehérissier et al., Rev. Sci. Instrum. 77, 03A318 (2006)

[18] H. Koivisto, 13th Electron Cyclotron Resonance Ion Source workshop, College station, (1997) p.167

[19] J. Rubert, J. Piot et al., Nucl. Inst. Meth. B 276 (2012) 33

[20] G. Gaubert et al, Rev. Sci. Instrum., **79**, 02A309 (2008)

[21] M. Lewitowicz, 'The SPIRAL 2 Project', Nuclear Physics A, Volume 805, Issues 1-4, 2008

[22] A. Pichard et al., 'Development of a surface ionization source for the SPIRAL 2 project', Rev. Sci. Instrum. 81, 02A908 (2010)

[23] N.Lecesne et al., 'GISELE: A resonant ionization laser ion source for the production of radioactive ions at GANIL', Rev. Sci. Instrum. 81, 02A910 (2010)

[24] T. Thuillier et al., Rev. Sci. Instrum. **83**, 02A339 (2012)

[25] D. Leitner et al., in *Proceedings of the 17th International Workshop on ECR Ion Sources, Lanzhou, August 2006* [High Energy Phys. Nucl. Phys. 31 (suppl. I), 1 (2007)]

[26] H. W. Zhao and L.T. Sun, in *Proceedings of the 18th International Workshop on ECR Ion Sources, Chicago, September 2008;* see http://www.jacow.org/.

[27] L. T. Sun et al, in *Proceedings of the 19th International Workshop on ECR Ion Sources, Grenoble, August 2010;* see http://www.jacow.org/ P. 4

[28] O. Tuske et al., Rev. Scient. Instrum. **83**, 02A316 (2012)

[29] P. Jardin et al., Rev. Sci. Instrum. **73** (2002) 789-791

[30] P. Jardin et al., Rev. Sci. Instrum. **83**, 02A911 (2012)

[31] P. Jardin et al., Rev. Sci. Instrum. **81**, 02A909 (2010)

[32] T. Lamy et al., Rev. Sci. Instrum. **77**, 03B101 (2006)

[33] P. Delahaye and M. Marie-Jeanne, Nucl. Instrum. And Meth. B **266** (2008) 4429

[34] F. Ames et al., Rev. Sci. Instrum. **81**, 02A903 (2010)

[35] R. Vondrasek et al., Rev. Sci. Instrum. **81**, 02A907 (2010)

[36] P. Delahaye et al., Nucl. Instr. and Meth. in Phys. Res. A 693 (2012) 104-108

[37] See GANIL web page http://pro.ganil-spiral2.eu/laboratory/ experimental-areas/lirat/the-lirat-line

[38] P. Jardin et al., Rev. Sci. Instrum **75** (2004) 1617-1620

ISBN 978-3-95450-123-6

Copyright © 2012 CC-BY-3.0 and by the respective authors

STATUS OF ECR ION SOURCES FOR CARBON-ION RADIOTHERAPY IN JAPAN

A. Kitagawa, A.G. Drentje, T. Fujita, M. Muramatsu, NIRS, Inage, Chiba 263-8555, Japan
E. Takeshita, S. Yamada, Gunma Univ., Maebashi, Gunma 371-8511, Japan
M. Kanazawa, SAGA-HIMAT Foundation, Tosu, Saga 841-0033, Japan
N. Sasaki, W. Takasugi, Accelerator Engineering Corporation (AEC), Inage, Chiba 263-0043, Japan

Abstract

For the five Japanese carbon-ion treatment facilities the carbon beams are being produced with ECR ion sources of two types, both developed at NIRS. These sources satisfy all medical requirements. A study has been initiated for understanding the performance deterioration following long periods of carbon operation.

HISTORY AND GEOGRAPHY

Presently in Japan five carbon-ion radiotherapy (C-RT) facilities are situated. The Heavy Ion Medical Accelerator in Chiba (HIMAC), the Hyogo Ion Beam Medical Centre (HIBMC) and the Gunma University Heavy-ion Medical Centre (GHMC) are already under operation. Over 1100 patients have been treated by three facilities in 2011. The Saga Heavy Ion Medical Accelerator in Tosu (SAGA-HIMAT) and the Ion-beam Radiation Oncology Centre in Kanagawa (i-ROCK) are under construction.

The HIMAC project at the National Institute of Radiological Sciences (NIRS) was promoted by the Japanese government as a research project under the first "Comprehensive 10-year Strategy for Cancer Control [1984-1993]." HIMAC is the first medical dedicated carbon facility in the world[1], and has successfully treated close to 7000 patients with 140-400 MeV/u carbon beams since 1994. The clinical result at HIMAC clearly shows the effectiveness and safety of C-RT[2], therefore the newer Japanese facilities have chosen carbons as well for treatment, all being produced in ECR ion sources.

HIBMC is the first proton and carbon combined facility, and was mainly funded by a local government. In order to reduce the running cost and the risk of interruption due to troubles, two ECR ion sources with the same structure are utilized to produce proton and carbon ions. HIBMC is also the first commercial C-RT facility with the permission under the Japanese regulation law of medical instruments, and start the treatment since 2001.

Under the third 10-year Strategy [2004-2013], the government promotes development of downsizing technologies. NIRS designed a hospital-specified C-RT facility and developed prototypes of various components. The feature of the design is an exhaustive optimisation for treatment by carbon beams[3]. This realized a cost-effective and reliable facility's design. The ECR ion source was also renewed under this concept. GHMC was constructed as a demonstration facility by the government, and start the treatment since 2010[4].

Table 1 shows existing and planned ECR ion sources for C-RT in Japan. Type N, H, and K mean NIRS-ECR, NIRS-HEC and Kei-series described in the next section. Figure 1 shows their locations. SAGA-HIMAT is funded by a consortium of a local government and private companies[5]. i-ROCK belongs a local government.

Table 1: Chronology of ECR Ion Sources at Carbon-Ion Radiotherapy Facilities in Japan

Name	Type	Facility	Launch
NIRS-ECR	N	HIMAC	1993
NIRS-HEC	H	HIMAC	1997
ECR1	N	HIBMC	1999
ECR2	N	HIBMC	1999
KeiGM	K	GHMC	2009
Kei2	K	HIMAC	2010
KeiSA	K	SAGA-HIMAT	*2012(plan)*
?	K	iROCK	*2015(plan)*

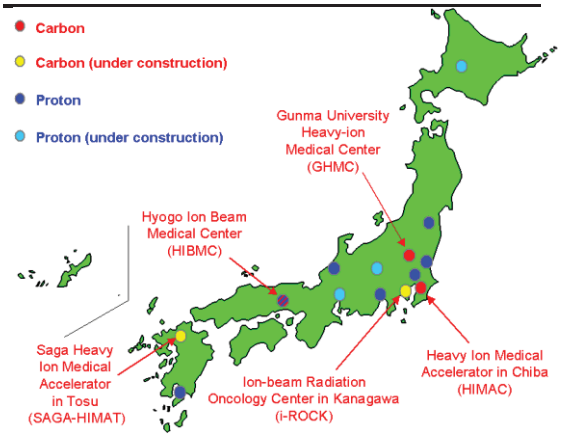

Figure 1: Geographical distribution of carbon-ion radiotherapy facilities in Japan.

DESCRIPTION OF SOURCES AND THE STATUS OF OPERATION

Four types of ion sources have experiences of C-RT; a 10GHz ECR ion source called 'NIRS-ECR', an 18GHz ECR ion source called 'NIRS-HEC', and 'Kei-series', and finally one PIG ion source called 'NIRS-PIG', which for the production of carbon ions, NIRS-PIG at HIMAC is being used temporally only[6]. The main purpose of NIRS-HEC is to produce heavier ions like Fe for

Copyright © 2012 CC-BY-3.0 and by the respective authors

ISBN 978-3-95450-123-6

fundamental researches[7]. Therefore we summarize here the most important types: NIRS-ECR and Kei-family

The NIRS-ECR Type

NIRS-ECR has a closed ECR zone with 10 GHz microwave shown in Figure 2[8]. The plasma chamber has an inner diameter of 70 mm and an inner length of 160 mm. Typical operational parameters for C^{4+} production are as follows. CH_4-gas is used to supply the carbon. The vacuum pressure in the plasma chamber was estimated to be around 3×10^{-4} Pa. The axial mirror fields at the injection side, the bottom of minimum B, and the extraction side are set to 0.8, 0.25 and 0.6 T, respectively. The radial sextupole field is 0.8 T on the chamber wall. The microwave is fed into the chamber through the open end of rectangular waveguide, which is simply connected with the end plate of chamber for the microwave shielding. Usually, the microwave power (typically 600 W) is operated in pulsed mode, but continuous wave mode is also available. The pulse width of 2 ms is enough for supplying beams, and the shorter duty cycle gives better reproducibility at the start up. The extraction voltage of 24 kV is applied to the plasma chamber matching injection into the NIRS RFQ linac. The distance between the plasma and the extraction electrodes is around 25 mm optimised to the beam transport.

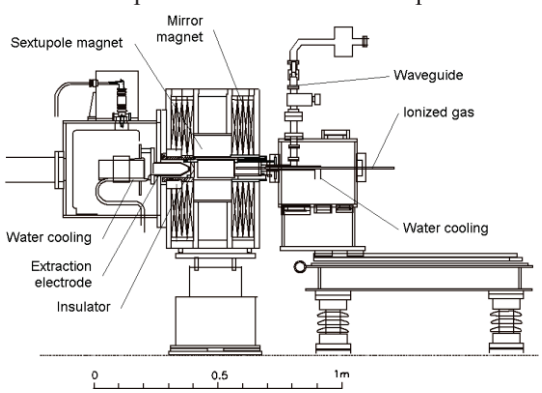

Figure 2: Schematic view of NIRS-ECR ion source.

NIRS-ECR does not need maintenance and beam tuning for the daily treatment, usually. The reproducible beam is realized with loading well-established parameters which were stored in the control system. The running time reached about 6000 hours in 2011. Since a few serious accidents occurred with the microwave amplifier, we replaced the klystron amplifier to a travelling wave tube amplifier. The present 10 GHz NEC amplifier did not give any trouble in the last 8 years. At present, small electronics circuits are routinely replaced every several years to prevent troubles. During last few years, we clean up the source including the plasma chamber once per year. However, we did not take care of the inside of source during a period of over 4 years; thus our experience is proving that such type of maintenance is strictly not necessary.

At HIBMC, the production of proton and carbon beams is required with the same ion sources and a common beam transport line and injector linacs. In order to improve the transmission efficiency, H_2^+ molecular ion beams with the higher energy of 35 keV/u are necessary to reduce the space charge effect between ion sources and the RFQ linac. Two copies of NIRS-ECR (with small modifications) were installed on the high voltage platform shown in Figure 3. The beams are extracted from the source with 25 kV from the plasma chamber and are accelerated from the high voltage platform with 45 kV and 80 kV for H_2^+ and C^{4+}, respectively[9].

ECR1 and ECR2 are usually assigned for each ion species. However, it is easy to exchange their roles for a scheduled maintenance and so on. The beam intensities at the front of RFQ for H_2^+ and C^{4+} are about 1300 and 400 eμA, respectively. These intensities are four times higher than required. The microwave amplifiers were also replaced from the old klystron to the same TWT as used for the NIRS-ECR.

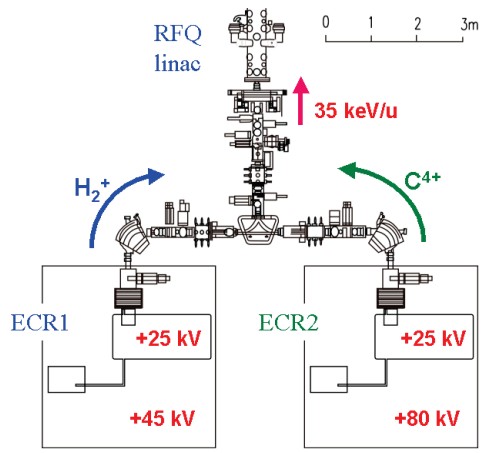

Figure 3: Layout of the high voltage platform at HIBMC.

The Kei Type ECR Ion Source

A compact ECR ion source called 'Kei' source was developed to reduce the size, initial construction cost, and electric power consumption. The design concept was how to reproduce well-established operational parameters of NIRS-ECR including the magnetic configuration by permanent magnets only[10]. Although the inner diameter and length of plasma chamber had to be shrunk to 50 mm and 60 mm, the result was promising. So the next prototype called 'Kei2' was developed to optimise the magnetic configuration and to improve the high voltage insulation[11]. The microwave amplifier was replaced by the same TWT amplifier as used for the NIRS-ECR. The maximum record of C^{4+} finally reached 1emA at extraction voltage of 40 kV. After successfully finishing the tests as a prototype, Kei2 has been installed in 2010 as an additional local injector of HIMAC for the backup of existing injector.

KeiGM was designed for GHMC and its general structure was copied from Kei2. The extraction electrode was simplified down to a fixed position shown in Figure 4. However, this modification also has given an increasing vacuum pressure in operation. Since the vacuum

Copyright © 2012 CC-BY-3.0 and by the respective authors

ISBN 978-3-95450-123-6

condition at the extraction region is more sensitive for a better stability, this effect has to be altered in order acquire an easier operation similar to Kei2.

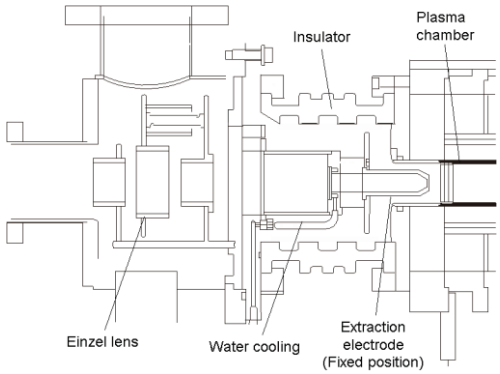

Figure 4: Schematic view of the extraction system of KeiGM.

Since KeiGM is the only ion source installed, it has to supply all beams. In about 4000 hours operation between 2010 and 2012. One of the most serious failures was due to breaking microwave amplifier after 14000 hours operation. The failure had been repaired by replacing. This amplifier was the same type as in the other facilities. There was rarely one accident at seven amplifiers.

KeiSA was manufactured for the installation into SAGA-HIMAT. This facility also adapts a single ion source like GHMC. The structure of KeiSA is completely same as KeiGM and the result of single preliminary test was also same. It will be launched to the linac in 2012.

Figure 5: ECR ion source has been installed in SAGA-HIMAT just before launch.

DIFFICULTY OF CARBON-ION PRODUCTION

Carbon ions are usually produced from gaseous compounds in an ion source. It means many carbon atoms are dissociated and are deposited on the wall. It is well-known from many experiences that such a deposition causes a deterioration of performance. Especially, decreasing of intensity and deterioration of electrical breakdown strength can give serious problems.

Decreasing of Intensity

In order to increase the intensity of highly charged carbon ions like C^{4+}, it's effective to feed hydro-carbonic C_xH_y gases. The other element in the gaseous compound plays the role of mixing gas[12]. On the other hand, carbon deposition is unavoidable with hydro-carbonic gases. Our experience shows that the C^{4+} intensity in several days decreases to about 70 % and further reduces a bit to a somewhat stable regime at say 60 % of the starting level. When the chamber wall is cleaned up, it is recovered to its earlier 100 % level. In order to check the possibility that electric conductive material deposited on the natural dielectric wall would form a Simon short circuit[13], we continuously collect samples for detailed analysis. However, from our preliminary measurements we are not able to draw any firm conclusion.

Electrical Breakdown Strength

We sometimes observed a corona discharge current increasing with increasing operation time. It is supposed that the carbon deposition also causes deterioration of electrical breakdown strength not only on the surface of insulators but also in vacuum between electrodes. However, the mechanism is still not clear. The phenomenon empirically depends on the vacuum pressure at the extraction region. In such a condition, we must find suitable parameters which can operate with better vacuum pressure. It constricts the margin of performance. We study the mechanism for improvement.

ACKNOWLEDGMENTS

The researches and developments at NIRS are based on many collaborations. The authors would like to thank Dr. S. Biri (ATOMKI), Prof. Y. Kato (Osaka Univ.), Prof. M. Sekiguchi, Prof. T. Hattori, Prof. Y. Yoshida (Toyo Univ.) and all of collaborators. The authors also thank Sumitomo Heavy Industry, Ltd. and Mitsubishi Electric Co. for supports of engineering manufacturing.

REFERENCES

[1] Y. Hirao *et al.*, Nucl. Phys. A 538, 541c (1992).
[2] D. Schulz-Ertner, H. Tsujii, Journal of Clinical Oncology, **2**, 953 (2007).
[3] K. Noda *et al.*, J. Radiat. Res. 48: Suppl. A43 (2007).
[4] S. Yamada *et al.*, J. Particle Accelerator Society of Japan, Vol.7, No.3, 192 (2010). (in Japanese)
[5] M. Kanazawa *et al.*, Proc. of the 8th Annual Meeting of Particle Accelerator Society of Japan, Tsukuba, 2011, p.161. (in Japanese)
[6] T. Miyata *et al.*, Rev. Sci. Instrum. **71**, 972 (2000).
[7] A. Kitagawa *et al.*, Rev. Sci. Instrum. **71**, 981 (2000).
[8] A. Kitagawa *et al.*, Rev.Sci.Instrum. **67**, 962 (1993).
[9] K. Sawada *et al.*, Rev.Sci.Instrum. **71**, 987 (2000).
[10] M. Muramatsu *et al.*, Rev.Sci.Instrum. **71**, 984 (2000).
[11] M. Muramatsu *et al.*, Rev. Sci. Instrum. **76**, 113304 (2005).
[12] A.G. Drentje, *et al.*, IEEE Trans. Plasma Sci., Vol.**36**, No.4, 1502 (2008).
[13] A. Kitagawa *et al.*, Proc. of ECRIS2010, Grenoble, 2010, p.20.

Copyright © 2012 CC-BY-3.0 and by the respective authors

ISBN 978-3-95450-123-6

ECRIS RELATED RESEARCH AND DEVELOPMENT WORK AT JYFL AND SOME FUTURE PROSPECTS*

H. Koivisto, O. Tarvainen, V. Toivanen, T. Kalvas, J. Komppula, J. Ärje, J. Laulainen and R. Kronholm, JYFL, Jyväskylä, Finland

Abstract

Since the last ECR workshop the JYFL ion source group has focused on 1) development of metal ion beams, 2) ion beam formation and transport, 3) plasma studies and 4) photoelectric effect in ion sources. The MIVOC method and sputtering technique were further studied in order to produce intensive titanium ion beams. As a result, an intensive $^{50}Ti^{11+}$ ion beam was successfully produced with the MIVOC method. An improvement in ion beam transport of the JYFL K130 cyclotron facility was achieved as a result of the work performed on ion beam formation. This work will be described in more detail elsewhere in these proceedings (see V. Toivanen et. al). The plasma research can be divided into plasma breakdown processes, plasma and ion beam instabilities, afterglow processes and plasma-wave coupling. The afterglow and instability experiments will be presented elsewhere in these proceedings (see. V. Skalyga et. al. and O. Tarvainen et. al.). In addition, studies involving in the photoelectric induced electron emission and charge exchange reactions will be briefly discussed.

METAL ION BEAM PRODUCTION

The metal ion beams and their production techniques can be considered as one of the key factors in nuclear physics laboratories using stable isotopes. Also at JYFL increasing requirements towards the availability of some refractory elements, like Ti, Zr and Mo has been expressed. In the following the development work for the sputter and the MIVOC technique will be presented.

Sputtering Technique

The sputter technique makes it possible to produce ion beams from the elements exceeding the capabilities of high temperature ovens. The efficiency of the method depends on the mass of projectile, its energy, angle of incident and naturally the sputter yield of the material to be sputtered. Unfortunately, the sputter yield tends to be low in the case of refractory elements, as is demonstrated in Table 1. However, the method still offers the intensities not available using the other methods. The method was first adopted at ANL, and since that it has been used in several laboratories on a day-to-day basis (see for example ref. [1,2]).

At JYFL the sputter technique has mainly been used for the production of Zr ion beams. Recently, strong effort has been made to produce ^{50}Ti ion beams by placing enriched ^{50}Ti powder into a small hole drilled in a metallic titanium rod [3]. This hole, including the enriched material, is placed to the spot where the sputtering mainly takes place. A test sample (with natural abundances) was exposed to plasma via radial port of the JYFL 14 GHz ECRIS. During the tests up to 20 µA of $^{48}Ti^{11+}$ beam was extracted from the ion source. Unexpectedly, the titanium ion beam remained even if the sputter voltage was set to zero. This indicated that the power was coupled directly to the sample causing vigorous heating and consequently the evaporation of titanium. The substantial evaporation of titanium requires the temperature of about 1800˚C. At this temperature a remarkable fraction of heat losses are caused via thermal radiation. This generated a strong heat load on the adjacent permanent magnets.

After the sputter experiment a clear degradation of source performance was noticed. The measurement of hexapole magnets confirmed that magnetic field was decreased approximately by 10 % close to the radial port used for the experiment. The destroyed hexapole was replaced and more efficient cooling scheme to minimize the heat load of the permanent magnets was designed. The sputter experiments will be continued with the new cooling scheme during the last quarter of 2012.

Table 1: Sputter yield Y for some elements. The yield is calculated for Oxygen or Argon projectiles at 1000 eV. Values calculated with Simple Sputter Yield Calculator (http://www.iap.tuwien.ac.at/www/surface/sputteryield)

Element	Y (with O)	Y (with Ar)
Ag	1.8	3.7
Ni	0.9	1.7
Mo	0.4	0.9
Pb	2.3	4.9
Ti	0.4	0.7
Zr	0.4	0.8

MIVOC Method

The MIVOC method [4] is very efficient in the case of some metal ion beams like Fe, Ni and Ti. As an example, in the case of $^{48}Ti^{11+}$ ion beam the intensity of 45 µA was produced using (trimethyl)pentamethylcyclopentadienyl-titanium)compound [5]. However, for the nuclear physics experiment at least 40 pnA of accelerated ^{50}Ti ion beam was needed. In order to meet this intensity requirement the afore-mentioned compound has to be synthesized using the enriched ^{50}Ti isotope. After an intensive development work the compound needed for the nuclear physics experiment was successfully synthesized by the Strasbourg group and subsequently tested using the JYFL 14 GHz ECRIS [6]. The $^{50}Ti^{11+}$ beam produced with the

ISBN 978-3-95450-123-6

Copyright © 2012 CC-BY-3.0 and by the respective authors

JYFL 14 GHz ECRIS was subsequently accelerated to the energy of 242 MeV in order to produce ^{256}Rf (Z = 104) evaporation residues. This enabled the first prompt spectroscopy of a superheavy element using the JUROGAM2/RITU/GREAT experimental set-up [7]. During the experiment the intensity of 15 - 20 µA was extracted from the ion source over the period of three weeks giving the required beam-on target intensity of 40 - 45 pnA. In order to meet the requirement for the next ^{50}Ti experiment the beam-on target intensity of higher than 200 pnA has to be produced. The requirement is 5 fold compared to the previous experiment in the fall 2011. In order to meet this requirement the intensity of Ti ions has to be increased and the transmission of the JYFL LEBT has to be improved.

BEAM FORMATION AND TRANSPORT

In the case of the JYFL K130 cyclotron facility the typical injection voltage is as low as about 10 kV, dictated by the cyclotron injection, making the low energy beam transport challenging. The emittance of the low energy beam is typically high and it tends to increase further during the beam transport due to the aberrations caused by different ion optical components and due to the space charge.

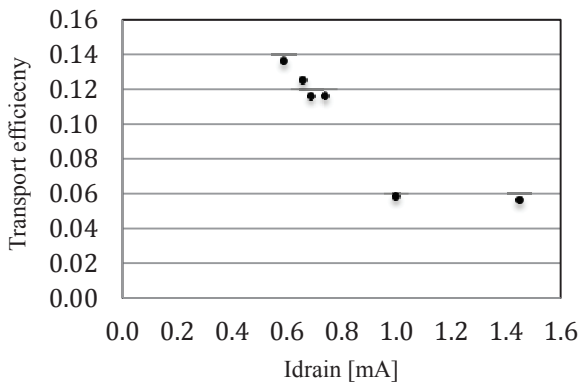

Figure 1: The Ar^{8+} transport efficiency from the first Faraday cup downstream the JYFL 14 GHz ECRIS mass separation to the first Faraday cup after the K130 cyclotron as a function of the drain current of the ion source high voltage power supply (U = 9.66 kV).

The typical behavior concerning the JYFL ion beam transport efficiency is presented in Fig. 1. The graph shows that the transport efficiency decreases when the total ion beam current from the JYFL 14 GHz ECRIS increases.

Comprehensive studies and development work have been performed in order to increase the ion beam intensity available after the K130 cyclotron (see for example [8, 9]). As a result of the studies it was realized, for example, that the beam emittance increases vigorously in the ion source extraction when the beam intensity exceeds the value of about 1 mA. A new extraction for the JYFL 14 GHz ECRIS was designed using a new ion beam simulation code IBsimu [10]. The first results have shown that the beam intensities after the K130 cyclotron have increased even by a factor of 2. This work and the results are presented elsewhere in these proceedings (see ref. 11).

PLASMA STUDIES

Intensive research of ion source plasmas has been performed at JYFL. This work can be divided into four different categories: 1) plasma breakdown, 2) plasma instabilities, 3) plasma afterglow and 4) plasma-wave coupling. This work will be presented in the following.

Plasma Breakdown

Plasma breakdown process has been studied extensively at JYFL with the aid of x-ray/gamma diagnostics (see for example [12, 13]). The most recent experiments were performed in collaboration with the LBNL, NSCL/MSU and IAP/RAS ion source groups using CdTe detector (1.5 – 400 keV) with 100 µs temporal resolution. The experimental setup and results are extensively presented in ref [14].

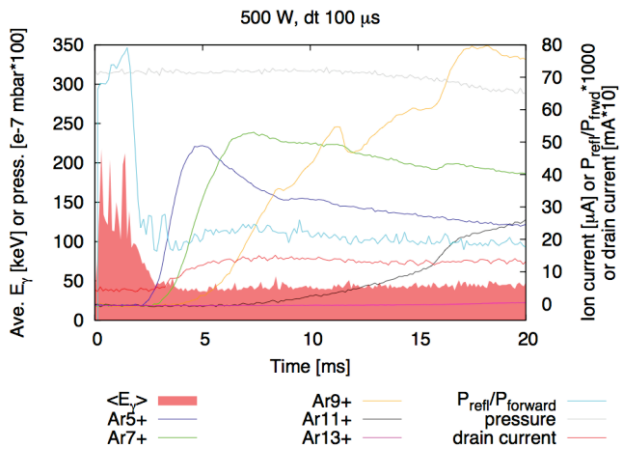

Figure 2: The time evolution of average bremsstrahlung energy during the plasma breakdown process. Pulse length of 500 ms with 1 Hz repetition rate was used.

Figure 2 shows the average bremsstrahlung energy during the plasma breakdown process. At the beginning of the microwave pulse the reflected power is high indicating the absorption of microwave power is low and consequently the plasma density is also low. At this moment, the electromagnetic field amplitude is high making a vigorous heating of electrons possible. As a result of this, the bremsstrahlung emission has relatively high average energy. The electron density increases exponentially and after some threshold density the microwave power is too low to maintain the high average energy of electrons. As a result of this also the average energy of measured photons decreases. During this transition also the reflected microwave power decreases vigorously (see Fig. 2) and the first ions are extracted from the plasma. In addition, at this point the preglow peak [15], normally attributed to low charges, can be observed.

Copyright © 2012 CC-BY-3.0 and by the respective authors

ISBN 978-3-95450-123-6

Plasma and Ion Beam Instabilities

The ion beam instabilities have been studied with VENUS [16] at LBNL and with JYFL 14 GHz ECRIS. The motivation of the studies was to define the fast scale beam instability behavior and the parameters affecting the amplitude and the frequency of the instabilities. The work was performed in collaboration with the LBNL ion source group and the experimental setup and the results are presented in ref. [17].

Afterglow

The afterglow behavior [18] is a well-known phenomenon in pulsed operation mode of ECR ion sources. The decay of afterglow peak with high temporal resolution was studied in collaboration with the IAP-RAS ion source group. The experimental setup and related results are presented in ref. [19].

Plasma-Wave Coupling

Frequency tuning effect has been found and studied by the INFN-LNS ion source team [20]. In this technique the microwave frequency is varied in order to select the efficient heating mode inside the plasma chamber of ECRIS. This plasma-wave coupling was studied also with the JYFL 14 GHz ECRIS by measuring the behavior of S_{11} parameter with the aid of a Rohde & Schwarz network analyzer using dual port technique. In this experiment the plasma was heated with TWTA (f = 11.56 GHz) and the other waveguide was used to define the behavior of S_{11} parameter by scanning the frequency of the low power probing signal of the network analyzer around 14 GHz. Waveguide effects were removed by calibrating the network analyzer with two different waveguide offset shorts and a load element in order to measure only the combined properties of the plasma and the cavity.

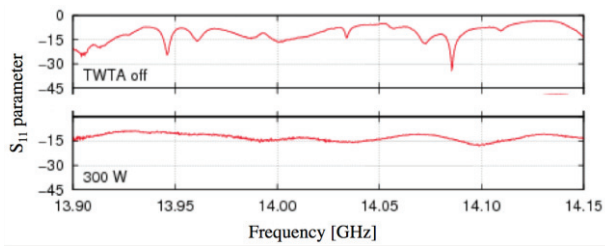

Figure 3: Plasma chamber S_{11} behavior with empty plasma chamber and with plasma maintained with the TWTA microwave power of 300 W at 11.56 GHz.

As a first step the properties of the empty plasma chamber (i.e. no plasma) was measured (see upper picture of Fig. 3). Next, the plasma was ignited and maintained with the TWTA at the microwave frequency of 11.56 GHz (lower picture of Fig. 3). As Fig. 3 shows, a fairly strong behavior of S_{11} parameter is present with the empty plasma chamber. This indicates that the quality factor Q of the empty plasma chamber is relatively high. In this case the quality factor was calculated to be of the order of 10^3. The Figure also shows that the plasma-loaded cavity strongly damps the mode behavior and consequently decreases the quality factor Q. This is due to the absorption of electromagnetic field. In this case the quality factor was estimated to be of the order of 10^2. A comprehensive report about the experimental setup and results are given in ref. [21].

PHOTOELECTRIC EFFECT AND ION SOURCES

The intensity of highly charged ions can be increased by increasing the product of $n_e\tau_i$, where n_e is the electron density of plasma and τ_i the confinement time of ion. The ion confinement is mostly governed by the ambipolar diffusion affected by the plasma potential. The confinement time can be increased by increasing the magnetic confinement, the size of the plasma and by decreasing the kinetic energy of ions. The electron density increases, for example, with the microwave power and microwave frequency used for electron heating (see for example ref. [22, 23, 24]). In addition, the secondary electron emission can increase the electron density and consequently the performance of ECR ion sources [25].

The JYFL ion source group has studied the VUV-light emission of different plasmas. The motivation towards the studies was to 1) define the power dissipation of different plasmas through the visible light and VUV- light emission and 2) find out if the light emission can yield a remarkable amount of photon induced electron emission from the plasma chamber walls. This would affect the performance of the ECR ion source. The third motivation was to find out if the light diagnostics can be used as a fault-finding tool. This subject is very complicated and will be studied later after more experience regarding the light spectroscopy has been gained.

A dedicated setup for studying the photon induced electron emission from different surfaces was designed and constructed (see Fig. 4). In this arrangement, a deuterium lamp is placed in front of a collimator structure. The cathode surface coated by the material of interest is exposed to photons emitted from the lamp. The photon-induced electrons are collected by the positively biased anode. The entire experimental setup is placed in vacuum in order to make the propagation of photons and induced electrons possible.

An Au cathode was chosen to be a target material in order to minimize different chemical surface reactions. The work function of the Au surface is 5.1 – 5.5 eV and the highest emission yield in VUV-region is reached at the photon energy of about 20 eV whilst the second maximum is reached at the x-ray energy of about 500 eV (see for example ref. [26] for quantum efficiency of Au). The optimization of the experimental setup, for the further studies with ion sources, was performed by using a deuterium lamp as a source of photons. The quartz structure of the lamp stops the photons exceeding the wavelength of about 160 nm. Consequently, the usable photon spectrum covers the range of 5.1 – 7.8 eV. As a next step, rotatable target system will be used in order to

ISBN 978-3-95450-123-6

Copyright © 2012 CC-BY-3.0 and by the respective authors

make the studies of different materials without breaking the vacuum possible.

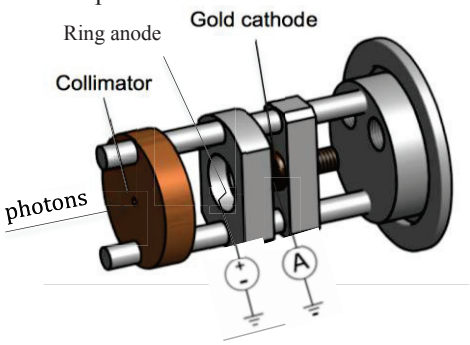

Figure 4: Setup for the studies of photoelectric effect.

The first results using deuterium lamp are presented in Fig. 5 showing the photon induced current as a function of anode voltage. During the experiment the photon emission current was measured to be of the order of 0.32 nA, whilst the VUV light power was measured to be 0.7 μW. This corresponds to the current to power ratio of about 0.5 mA/W. Here it should be noticed that the afore-mentioned efficiency is obtained with the narrow range of photon energies (5.1 – 7.8 eV), which does not correspond to the optimum spectrum for photon-induced emission. As can be estimated from ref. [27] this ratio can be remarkably higher (≈ 10 fold) if a more optimum spectrum of light is available. In this optimum case the photon-induced emission current can exceed the value of 5 mA/W.

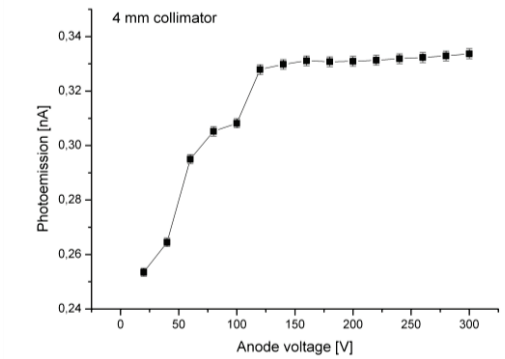

Figure 5: Photon induced electron emission measured from an Au cathode. Photons were produced by a deuterium lamp.

As a next step the experiments will be continue with the microwave ion source using a hydrogen plasma and later by using ECRIS plasma. The experiments at JYFL have indicated that the power dissipation of microwave ion source plasma via VUV light emission can be approximately up to 30 % of the microwave power fed into the plasma chamber [27]. Although the power of VUV light emission from the ECR ion source plasma is still unknown it probably is much lower than in the case of microwave ion source. This estimation is due to the operation pressure, which is 2 - 3 orders of magnitude lower in the case of ECR ion source. However, in the case of ECR ion sources the power dissipated via low energy x-ray emission (some hundreds of eV) can be at the level of W. This makes it possible that the photon induced electron emission can have an effect on the performance of ECR ion sources.

CHARGE EXCHANGE

The motivation towards the charge exchange studies was to estimate the effect of neutral pressure to the production rate of the highly charged ions. The maximum life-time of highly charged ion can be estimated if the cross section for the charge exchange reaction, the neutral pressure inside the volume of interest and energies of particles are known. This can be compared to the production times of highly charged ions for example in the pulsed operation mode of the ECRIS. The volume production rate of different charge states can be estimated with the aid of the balance equation (1). The production rate depends on the following parameters

$$\frac{dn_q}{dt} = n_e \langle \sigma_{q-1,q} v_e \rangle n_{q-1} + n_0 \langle \sigma_{q+1,q} v_i \rangle n_{q+1} - n_0 \langle \sigma_{q,q-1} v_i \rangle n_q - n_e \langle \sigma_{q,q+1} v_e \rangle n_q - \frac{n_q}{\tau} \qquad (1)$$

where the third parameter is linked to the charge exchange reaction. In the case of highly charged ions its cross section can be several orders of magnitudes higher than related ionization cross section. Consequently, the charge exchange can strongly limit the production of highly charged ion beams.

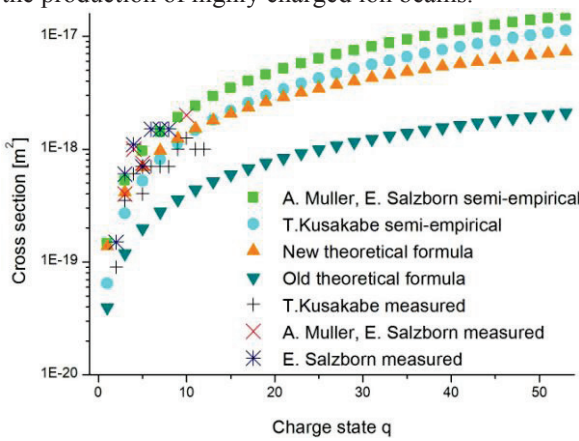

Figure 6: The charge exchange cross section σ for different xenon charge states.

During the literature study a fairly limited amount of experimental data regarding the charge exchange reactions for the highly charged ions, like Xe^{10+} or higher, was found. This is demonstrated in Fig. 6. In order to estimate the charge exchange cross section of high charge states, like Xe^{30+} or higher, semiempirical or fully theoretical equation has to be used. One generally used theoretical equation has been derived using the Bohr model of atom. The approach presented in [28] assumes that in the case of low energy ions the cross section of charge exchange reaction is independent on the ion velocity. As Fig. 6 shows there

Copyright © 2012 CC-BY-3.0 and by the respective authors

ISBN 978-3-95450-123-6

is a remarkable difference between the results obtained by the semiempirical models (based on the experimental data) and classical model. Very good agreement with the experimental data was achieved when we included the shielding of electrons in the old theoretical formula. The charge exchange cross section using a new theoretical formula is also shown in Fig. 6.

FUTURE PROSPECTS

The JYFL LEBT will be studied with the aid of simulations to further improve its performance. One option is to move the 14 GHz ECRIS closer to the dipole (to its object point). In addition, the first section of the LEBT, including the dipole, could be negatively biased making it possible to transport the beam through this section with higher beam energy. Both changes could decrease the space charge problems existing before the q/M separation. In addition, a new central area configuration for the cyclotron will be considered in order to make the use of higher injection voltages possible. This would also mitigate the space-charge problems in the JYFL LEBT.

Different radiation-hard ion source schemes, needed by RIB-ISOL facilities, will be studied by simulations. A so-called double helix structure is interesting option especially with the quadrupole multipole configuration. This configuration produces quadrupole-type plasma flux, which would have a perfect match between the beam properties and ion beam optics with quadrupole focusing. This structure can be considered as an intermediate step in the process of designing and constructing a more advanced ARC-ECRIS [29, 30]. This ion source can possibly be used as a radiation hard ion source and a beam merger. The project to design and construct a 18 GHz ECRIS for the future needs of the JYFL nuclear physics program will be also initiated. In addition to afore-mentioned projects the intensive program for plasma related experiments will be continued in strong international collaboration.

ACKNOWLEDGMENT

This work has been supported by the EU 7th framework programme “Integrating Activities - Transnational Access”, project number: 262010 (ENSAR) and by the Academy of Finland under Finnish Centre of Excellence Programme 2012-2017 (Nuclear and Accelerator Based Physics Research at JYFL).

REFERENCES

[1] R. Harkewicz, P.J. Billquist, J.P. Greene, J.A. Nolen, R.C. Pardo, Rev. Sci. Instrum. 66 (4), April (1995), p. 2883.
[2] R. Vondrasek, R. Scott and R. Pardo, High Energy Physics and Nuclear Physics, A Series Journal of the Chinese Physical Society (C), Vol. 31, Supp. I, Jul., (2007), p. 101.
[3] R. Vondrasek, private discussion
[4] H. Koivisto, J. Ärje and M. Nurmia, Nucl. Instr. and Meth. in Phys. Res., B94, (1994), p. 291.
[5] H. Koivisto, J. Ärje, R. Seppälä, M. Nurmia, Nucl. Instr. and Meth. in Phys. Res., B187, (2002), p. 111.
[6] J. Rubert et. al., Nucl. Instrum. and Meth. in Phys. Res. B 276 (2012), p. 33.
[7] P.T. Greenlees, et. al., Phys. Rev. Lett. 109, (2012), 012501.
[8] V. Toivanen, O. Steczkiewicz, O. Tarvainen, T. Ropponen, J. Ärje and H. Koivisto, Nucl. Instrum. and Meth. in Phys. Res. B 268 (2010), 1508.
[9] V. Toivanen, et. al., Rev. Sci. Instrum., 81, (2010), 02A319.
[10] T. Kalvas, O. Tarvainen, T. Ropponen, O. Steczkiewicz, J. Ärje, and H. Clark, *Rev. Sci.* Instrum. **81**, (2010), 02B703.
[11] V. Toivanen, et. al., elsewhere in these proceedings.
[12] O Tarvainen, T Ropponen, V Toivanen, J Ärje and H Koivisto, Plasma Sources Sci. Technol. 18, (2009), 035018.
[13] T. Ropponen, et. al., Rev. Sci. Instrum., 81, (2010), 02A302.
[14] T. Ropponen, et. al., Plasma Sources Sci. Technol. 20 (2011), 055007.
[15] I.V. Izotov, et. al., IEEE Trans. Plasma Sci. 36, (2008), p. 1494.
[16] C. M. Lyneis, D. Leitner, S. R. Abbott, R. D. Dwinell, M. Leitner, C. S. Silver, and C. Taylor, Rev. Sci. Instrum. 75, (2004), p. 1389.
[17] O. Tarvainen, H. Koivisto, J. Komppula, V. Toivanen, C. Lyneis, M. Strohmeier, elsewhere in thess proceedings.
[18] G. Melin, et. al., Rev.Sci.Instrum., 61, (1990), p. 236.
[19] I. Izotov, et. al., elsewhere in these proceedings.
[20] L. Celona, et. al., Catalano, Rev. Sci. Instrum. **79**, (2008), 023305.
[21] V. Toivanen, O. Tarvainen, J. Kauppinen, J. Komppula, and H. Koivisto, Rev. Sci. Instrum. 83, (2012), p. 02A306.
[22] D. Hitz, Advances in Imaging and Electr. Phys., Vol. 144, p. 1-164.
[23] A. Girard, D. Hitz, G. Melin and K. Serebrennikov, Rev. Sci. Instrum., 75, (2004), p. 1381.
[24] R. Geller, Electron Cyclotron Resonance Ion Sources and ECR Plasmas, Published by Institute of Physics Publishing, (1996), ISBN 0740301074.
[25] C.M. Lyneis, Proc. of 11th Cocnf. On Cyclotrons and theis Applications, Tokyo, (1987), p. 707.
[26] H. Henneken, F. Scholze, M. Krumrey and G. Ulm, Metrologia, Vol. 37, (2000), p. 485.
[27] J. Komppula, et. al., will be published.
[28] H. Knudsen, H.K. Haugen and P. Hvelplund, Phys. Rev. A, Vol. 23, No. 2, (1981), p. 23.
[29] P. Suominen, T. Ropponen and H. Koivisto, Nucl. Instrum. and Meth. in Phys. Res., A578, Issue 2, (2007), p. 370.
[30] H. Koivisto, P. Suominen, O. Tarvainen and P. Spädtke, Rev of Sci. Instrum. **83**, (2012), 02A312.

ISBN 978-3-95450-123-6

Copyright © 2012 CC-BY-3.0 and by the respective authors

List of Authors

Bold papercodes indicate primary authors

— A —

Adachi, T. WEYO01
Adroit, G. FRXA01
Aihara, T. THXO03
Ames, F. **THYO01**
Andò, L. TUPP08
Angot, J. WEZO01, WEZO03, **THYO02**
Ärje, J.E. TUPP05, FRYA03

— B —

Baartman, R.A. THYO01
Bajeat, O. FRYA01
Balint, P. WEZO01
Barue, C. WEZO03, FRYA01
Baskaran, R. WEXO05
Bauder, W. FRXA03
Beijers, J.P.M. TUZO02, WEXO03
Bekhterev, V. TUPP18
Bellodi, G. TUPP10
Benitez, J.Y. TUXO01, **THXO02**, THYO03
Berg, J.F. FRXA03
Biri, S. TUXO03, **WEXO02**
Bogard, D. FRXA01
Bogomolov, S.L. TUPP18
Boswell, R.W. TUYO04
Bowden, M.D. TUYO04
Brandenburg, S. TUZO02
Bricault, P.G. THYO01
Büchel, A.B. TUPP03
Bultman, N.K. THYO03
Button, D.T. **TUPP02**

— C —

Canet, C. WEZO03, FRYA01
Cao, Y. FRXA02
Cee, R. TUPP03
Celona, L. TUPP08
Chang, D.S. TUZO01
Charles, C. TUYO04, **WEXO01**
Chauvin, N. FRXA01
Chen, J. WEPP14
Chen, J.E. WEPP14
Ciavola, G. **TUPP08**
Cole, D.G. TUZO04
Collon, P. TUPP01, FRXA03
Conradie, J.L. TUPP14
Cortázar, O.D. **TUYO01**

— D —

Daversin, C. WEZO01
Debray, F. WEZO01
Deibel, C. TUPP01
Delahaye, P. THYO04, FRYA01
Delferrière, O. WEPP16, FRXA01
DiGiovine, B. TUPP01
Dobrescu, S. TUYO03
Drentje, A.G. TUPP04, FRYA02
Dubois, M. FRYA01
Dupuis, M. WEZO03, FRYA01

— E —

Efremov, A.A. **TUPP18**

— F —

Flambard, J.L. FRYA01
Fourel, C. WEZO01
Fourie, D.T. TUPP14
Franzen, K.Y. THXO02
Frigot, R. FRYA01
Fujimaki, M. THXO03
Fujita, T.F. TUXO03, TUPP04, FRYA02
Furukawa, K. TUPP12

— G —

Gaffron, A. TUPP03
Gall, B.J.P. FRYA01
Gammino, S. TUPP08
Gauthier, Y. WEPP16, FRXA01
Girardot, P. FRXA01
Giraud, J. WEZO01
Gobin, R. WEPP16, **FRXA01**
Grahn, T. WEPP03
Greene, J.P. TUPP01
Greenlees, B. TUPP02
Greig, A.D. **TUYO04**
Guo, Z.Y. WEPP14

— H —

Haba, H. THXO03
Haberer, Th. TUPP03
Harrault, F. WEPP16, FRXA01
Hattori, T. **WEPP02**
Hawkins, R.P. TUYO04
Hayashizaki, N. WEPP02
Henderson, D. TUPP01
Higurashi, Y. TUPP12, TUPP17, WEZO02, WEPP08, **THXO03**
Hojo, S. TUPP04
Hotchkis, M.A.C. TUPP02
Hwang, C.K. TUZO01

ISBN 978-3-95450-123-6

— I —

Imel, G. FRXA03
In, S.R. TUZO01
Iwata, Y. TUPP04
Izotov, I. TUYO02, WEXO04, WEZO01, **WEPP03**

— J —

Jacob, J. WEZO01
Jang, S.O. **WEPP12**
Jannin, J.L. WEPP16, FRXA01
Jardin, P. **FRYA01**
Jayamanna, K. THYO01
Jeong, S.H. TUZO01
Jiang, C.L. TUPP01
Jin, J.-T. TUZO01
Jung, Y.-H. WEPP12

— K —

Kalvas, T. TUXO02, TUZO03, WEXO04, WEPP03, FRYA03
Kamigaito, O. THXO03
Kanazawa, M. FRYA02
Kanjilal, D. WEXO05
Kashiv, Y. TUPP01
Katagiri, K. TUPP04
Kato, Y. TUXO03
Kidera, M. THXO03
Kim, E.-S. TUZO01
Kim, T.S. TUZO01
Kinoshita, N. **TUPP01**
Kitagawa, A. **TUXO03**, TUPP04, WEPP02, **FRYA02**
Koivisto, H. A. TUXO02, TUZO03, WEXO04, WEPP03, **FRYA03**
Komiyama, M. TUPP12, THXO03
Komppula, J.P.O. TUXO02, TUZO03, WEPP03, FRYA03
Kondev, F.G. FRXA03
Kondrashev, S.A. FRXA03
Kostyukhov, Yu.K. TUPP18
Kremers, H.R. **TUZO02**
Kronholm, R.J. FRYA03
Küchler, D. **TUPP10**, TUPP14
Kutsaev, S.V. THYO04

— L —

Lakshmy, P.S. WEXO05
Lamy, T. WEZO01, WEZO03, THYO02
Lang, R. WEYO03, WEPP15
Latrasse, L. WEZO01
Laulainen, J.P. FRYA03
Lebedev, N. TUPP18
Leboucher, C. FRYA01
Lee, C.H. TUZO01
Lee, K.W. TUZO01
Lehérissier, P. WEZO03, FRYA01
Leitner, D. TUZO04
Lemagnen, F. WEZO03, FRYA01
Leo, K.W. WEYO01
Lho, T.H. WEPP12
Li, J.Q. FRXA02
Li, J.Y. FRXA02
Liu, Z.W. TUPP13
Loginov, V.N. TUPP18
Loiseau, D. FRXA01
Lombardi, A.M. TUPP10
Lu, P.N. WEPP14
Lu, W. **WEPP13**, THXO01, THXO04
Lyneis, C.M. **TUXO01**, TUXO02, THXO02, THYO03

— M —

Ma, B.H. WEPP13, FRXA02
Ma, H.Y. TUPP13
Ma, L.Z. THXO01
Machicoane, G. THXO02, **THYO03**, TUZO04
Maddock, T. FRXA03
Mäder, J. WEYO03, WEPP15
Magee, C. TUPP02
Maimone, F. WEYO03, WEPP15
Mandal, A. WEXO05
Mansfeld, A. WEPP03
Marie-Jeanne, M. **WEZO01**, WEZO03, THYO02
Marley, S.T. TUPP01
Marti, F. TUZO04
Mascali, D. TUPP08
Mathur, Y. WEXO05
Mattei, P. FRXA01
Maunoury, L. WEZO03, THYO04, FRYA01
May, D.P. **TUPP05**
Megía-Macías, A. TUYO01
Mironov, V. TUZO02, TUPP18, **WEXO03**
Mjøs, A. THYO01
Morgan, G. THYO03
Mosthaf, J.M. TUPP03
Muramatsu, M. TUXO03, **TUPP04**, WEPP02, FRYA02

— N —

Naas, B. TUPP03
Nair, C. FRXA03
Nakagawa, T. TUPP12, TUPP17, WEZO02, WEPP08
Nakanishi, T. TUPP01
Nyckees, S. WEPP16

— O —

O'Neil, M. TUPP10
Oh, B.H. **TUZO01**

ISBN 978-3-95450-123-6

Ohnishi, J. **TUPP17**, WEZO02, WEPP08, THXO03
Osmond, O. WEZO03, FRYA01
Ozeki, K. TUPP12, **WEZO02**, **WEPP08**, THXO03

— P —

Palchan, T. WEPP17, **FRXA03**
Pálinkás, J. WEXO02
Palmotti, G. FRXA03
Panitzsch, L. **WEYO02**
Pardo, R.C. TUPP01, WEPP17, THYO04, FRXA03
Paul, M. TUPP01, FRXA03
Peaucelle, C. WEZO03, FRYA01
Peleikis, T. WEYO02
Peng, S.X. **WEPP14**
Peters, A. TUPP03
Peters, C.E. WEPP17
Peura, P. WEPP03
Phair, L. THXO02
Piot, J. FRYA01
Power, M.A. WEPP17
Pozdeyev, E. THYO03

— R —

Rácz, R. TUXO03, WEXO02
Rao, X. THYO03
Razin, S. TUYO02, WEXO04
Rehm, E. TUPP01
Ren, H.T. WEPP14
Roberts, E. TUPP02
Robertson, D. TUPP01
Rodrigues, G.O. **WEXO05**
Roger, A. FRXA01
Roßbach, J. WEYO03, WEPP15
Roy, A. WEXO05
Ruan, L. WEPP13
Rubert, J. FRYA01

— S —

Sakamoto, Y. TUPP04
Salvatores, M. FRXA03
Saminathan, S. TUZO02
Sasaki, N. TUXO03, FRYA02
Sato, S. TUPP04
Schächter, L. TUYO03
Schmitt, C.J. TUPP01
Schreiner, J. TUPP03
Scott, R.H. TUPP01, WEPP17, THYO04, FRXA03
Scrivens, R. TUPP10
Senée, F. FRXA01
Seo, C.S. TUZO01
Sidorov, V. **TUYO02**, WEXO04
Skalyga, V. TUYO02, **WEXO04**, WEZO01, WEPP03
Sortais, P. WEZO01, THYO02
Spädtke, P. **WEYO03**, WEZO03
Stafford-Haworth, J.T. TUPP10
Stalder, M. WEYO02
Stiebing, K.E. **TUYO03**
Strohmeier, M.M. TUXO01, TUXO02, THXO02
Sun, L.T. TUPP13, WEPP13, THXO01, THXO02, THXO04, THYO03, **FRXA02**
Sutton, Y.C. TUYO04

— T —

Tabacaru, G. TUPP05
Takasugi, W. TUXO03, FRYA02
Takayama, K. **WEYO01**
Takeshita, E. FRYA02
Tamura, M. THXO03
Tang, X.D. TUPP01
Tarvainen, O.A. **TUXO02**, TUZO03, WEXO04, WEPP03, FRYA03
Thomae, R.W. TUPP10, **TUPP14**
Thuillier, T. WEZO01, **WEZO03**, THYO02, FRYA01
Tinschert, K. WEYO03, **WEPP15**
Tobos, L. TUZO04
Todd, D.S. TUXO01
Toivanen, V. TUXO02, **TUZO03**, WEPP03, FRYA03
Traykov, E.K. FRYA01
Trophime, C. WEZO01
Tuske, O. **WEPP16**, FRXA01, FRYA01

— U —

Uchiyama, A. THXO03, **TUPP12**

— V —

Veys, S. WEZO01
Vizcaíno-de-Julián, A. TUYO01
Vondrasek, R.C. TUPP01, **WEPP17**, **THYO04**, FRXA03

— W —

Wang, H. WEPP13, FRXA02
Wimmer-Schweingruber, R. WEYO02
Winkelmann, T.W. **TUPP03**
Winklehner, D. **TUZO04**
Wu, Q. TUPP13

— X —

Xia, J.W. FRXA02
Xie, D. WEPP13, **THXO01**, THXO04, FRXA02

ISBN 978-3-95450-123-6

Xiong, B. WEPP13
Xu, Y. WEPP14

— Y —

Yamada, S. FRYA02
Yang, Y. TUPP13
Yazvitsky, Yu. TUPP18
Yokoyama, A. TUPP01
Yoo, S.J. WEPP12
You, H.J. WEPP12
Youinou, G. FRXA03

— Z —

Zhang, W.H. TUPP13, FRXA02
Zhang, X.Z. TUPP13, WEPP13, THXO01, THXO04, FRXA02
Zhang, Z.M. **TUPP13**
Zhao, H.W. TUPP13, WEPP13, THXO01, **THXO04**, FRXA02
Zhao, J. WEPP14
Zhu, L. THXO01
Zorin, V. TUYO02, WEXO04, WEZO01, WEPP03

ISBN 978-3-95450-123-6

Institutes List

AEC
Chiba, Japan
- Sasaki, N.
- Takasugi, W.

ANL
Argonne, USA
- Deibel, C.
- DiGiovine, B.
- Greene, J.P.
- Henderson, D.
- Jiang, C.L.
- Kondev, F.G.
- Kondrashev, S.A.
- Kutsaev, S.V.
- Marley, S.T.
- Nair, C.
- Palchan, T.
- Pardo, R.C.
- Peters, C.E.
- Power, M.A.
- Rehm, E.
- Scott, R.H.
- Vondrasek, R.C.

ANSTO
Menai, Australia
- Button, D.T.
- Greenlees, B.
- Hotchkis, M.A.C.

ASI
Fyshwick, Australia
- Magee, C.
- Roberts, E.

ATOMKI
Debrecen, Hungary
- Biri, S.
- Rácz, R.

CEA Cadarache
Saint Paul Lez Durance, France
- Salvatores, M.

CEA/DSM/IRFU
France
- Adroit, G.
- Bogard, D.
- Chauvin, N.
- Delferrière, O.
- Gauthier, Y.
- Girardot, P.
- Gobin, R.
- Harrault, F.
- Jannin, J.L.
- Loiseau, D.
- Mattei, P.
- Roger, A.
- Senée, F.
- Tuske, O.

CEA/IRFU
Gif-sur-Yvette, France
- Nyckees, S.

CERN
Geneva, Switzerland
- Bellodi, G.
- Küchler, D.
- Lombardi, A.M.
- O'Neil, M.
- Scrivens, R.
- Stafford-Haworth, J.T.

CNAO Foundation
Milan, Italy
- Ciavola, G.

CSFNSM
Catania, Italy
- Mascali, D.

ESS Bilbao
LEIOA, Spain
- Cortázar, O.D.
- Megía-Macías, A.
- Vizcaíno-de-Julián, A.

FRIB
East Lansing, Michigan, USA
- Bultman, N.K.
- Machicoane, G.
- Morgan, G.
- Pozdeyev, E.
- Rao, X.

GANIL
Caen, France
- Bajeat, O.
- Barue, C.
- Canet, C.
- Delahaye, P.
- Dubois, M.
- Dupuis, M.
- Flambard, J.L.
- Frigot, R.
- Jardin, P.
- Leboucher, C.

ISBN 978-3-95450-123-6

- Lehérissier, P.
- Lemagnen, F.
- Maunoury, L.
- Osmond, O.
- Piot, J.
- Traykov, E.K.

GHMFL
Grenoble, France
- Daversin, C.
- Debray, F.
- Trophime, C.
- Veys, S.

GSI
Darmstadt, Germany
- Lang, R.
- Mäder, J.
- Maimone, F.
- Roßbach, J.
- Spädtke, P.
- Tinschert, K.

Gunma University, Heavy-Ion Medical Research Center
Maebashi-Gunma, Japan
- Takeshita, E.
- Yamada, S.

HIT
Heidelberg, Germany
- Büchel, A.B.
- Cee, R.
- Gaffron, A.
- Haberer, Th.
- Mosthaf, J.M.
- Naas, B.
- Peters, A.
- Schreiner, J.
- Winkelmann, T.W.

IAP/RAS
Nizhny Novgorod, Russia
- Izotov, I.
- Mansfeld, A.
- Razin, S.
- Sidorov, V.
- Skalyga, V.
- Zorin, V.

IBS
Daejeon, Republic of Korea
- Kim, E.-S.
- Seo, C.S.

IEAP
Kiel, Germany
- Panitzsch, L.
- Peleikis, T.
- Stalder, M.
- Wimmer-Schweingruber, R.F.

IEE
Beijing, People's Republic of China
- Ruan, L.
- Xiong, B.

IFIN
Magurele- Bucuresti, Romania
- Dobrescu, S.
- Schächter, L.

IGCAR
Channai, India
- Baskaran, R.

IKF
Frankfurt-am-Main, Germany
- Stiebing, K.E.

IMP
Lanzhou, People's Republic of China
- Cao, Y.
- Li, J.Q.
- Li, J.Y.
- Liu, Z.W.
- Lu, W.
- Ma, B.H.
- Ma, H.Y.
- Ma, L.Z.
- Sun, L.T.
- Wang, H.
- Wu, Q.
- Xia, J.W.
- Xie, D.
- Yang, Y.
- Zhang, W.H.
- Zhang, X.Z.
- Zhang, Z.M.
- Zhao, H.W.
- Zhu, L.

IN2P3 IPNL
Villeurbanne, France
- Peaucelle, C.

INFN/LNS
Catania, Italy
- Andò, L.
- Celona, L.
- Ciavola, G.
- Gammino, S.
- Mascali, D.

ISBN 978-3-95450-123-6

INL
Idaho Falls, Idaho, USA
- Berg, J.F.
- Maddock, T.
- Palmotti, G.
- Salvatores, M.
- Youinou, G.

IPHC
Strasbourg Cedex 2, France
- Gall, B.J.P.

ISU
Pocatello, Idaho, USA
- Imel, G.

iThemba LABS
Somerset West, South Africa
- Conradie, J.L.
- Fourie, D.T.
- Thomae, R.W.

IUAC
New Delhi, India
- Kanjilal, D.
- Lakshmy, P.S.
- Mandal, A.
- Mathur, Y.
- Rodrigues, G.O.
- Roy, A.

JINR
Dubna, Moscow Region, Russia
- Bekhterev, V.
- Bogomolov, S.L.
- Efremov, A.A.
- Kostyukhov, Yu.K.
- Lebedev, N.
- Loginov, V.N.
- Yazvitsky, Yu.

JYFL
Jyväskylä, Finland
- Ärje, J.E.
- Grahn, T.
- Kalvas, T.
- Koivisto, H. A.
- Komppula, J.P.O.
- Kronholm, R.J.
- Laulainen, J.P.
- Peura, P.
- Tarvainen, O.A.
- Toivanen, V.

KAERI
Daejon, Republic of Korea
- Chang, D.S.
- Hwang, C.K.
- In, S.R.
- Jeong, S.H.
- Jin, J.-T.
- Kim, T.S.
- Lee, C.H.
- Lee, K.W.
- Oh, B.H.

Kanazawa University
Kanazawa, Japan
- Nakanishi, T.
- Yokoyama, A.

KEK
Ibaraki, Japan
- Adachi, T.
- Furukawa, K.
- Takayama, K.

KVI
Groningen, The Netherlands
- Beijers, J.P.M.
- Brandenburg, S.
- Drentje, A.G.
- Kremers, H.R.
- Mironov, V.
- Saminathan, S.

LBNL
Berkeley, California, USA
- Benitez, J.Y.
- Franzen, K.Y.
- Lyneis, C.M.
- Phair, L.
- Strohmeier, M.M.
- Todd, D.S.
- Winklehner, D.

LPSC
Grenoble Cedex, France
- Angot, J.
- Balint, P.
- Fourel, C.
- Giraud, J.
- Jacob, J.
- Lamy, T.
- Latrasse, L.
- Marie-Jeanne, M.
- Rubert, J.
- Sortais, P.
- Thuillier, T.

MSU
East Lansing, Michigan, USA
- Deibel, C.

ISBN 978-3-95450-123-6

National Institute of Radiological Sciences
Chiba, Japan
- Fujita, T.F.

NFRI
Daejon, Republic of Korea
- Jang, S.O.
- Jung, Y.-H.
- Lho, T.H.
- Yoo, S.J.
- You, H.J.

NIRS
Chiba-shi, Japan
- Hattori, T.
- Hojo, S.
- Iwata, Y.
- Katagiri, K.
- Kitagawa, A.
- Muramatsu, M.
- Sakamoto, Y.
- Sato, S.

NSCL
East Lansing, Michigan, USA
- Cole, D.G.
- Leitner, D.
- Machicoane, G.
- Marti, F.
- Tobos, L.

Osaka University, Graduate School of Engineering
Osaka, Japan
- Kato, Y.

PKU
Beijing, People's Republic of China
- Chen, J.E.
- Chen, J.
- Guo, Z.Y.
- Lu, P.N.
- Peng, S.X.
- Ren, H.T.
- Xu, Y.
- Zhao, J.

RIKEN Nishina Center
Wako, Japan
- Fujimaki, M.
- Haba, H.
- Higurashi, Y.
- Kamigaito, O.
- Kidera, M.
- Komiyama, M.
- Nakagawa, T.
- Ohnishi, J.
- Ozeki, K.

RLNR
Tokyo, Japan
- Hayashizaki, N.

SAGA HIMAT
Saga, Japan
- Kanazawa, M.

SHI Accelerator Service Ltd.
Tokyo, Japan
- Aihara, T.
- Tamura, M.
- Uchiyama, A.

Sokendai
Ibaraki, Japan
- Adachi, T.
- Leo, K.W.
- Uchiyama, A.

SP3
Canberra, Australia
- Boswell, R.W.
- Charles, C.
- Greig, A.D.
- Hawkins, R.P.

Texas A&M University Cyclotron Institute
College Station, Texas, USA
- May, D.P.

Texas A&M University, Cyclotron Institute
College Station, USA
- Tabacaru, G.

The Hebrew University of Jerusalem, The Racah Institute of Physics
Jerusalem, Israel
- Paul, M.

The Open University
Milton Keynes, United Kingdom
- Bowden, M.D.
- Sutton, Y.C.

TRIUMF, Canada's National Laboratory for Particle and Nuclear Physics
Vancouver, Canada
- Ames, F.
- Baartman, R.A.
- Bricault, P.G.
- Jayamanna, K.
- Mjøs, A.

ISBN 978-3-95450-123-6

University Debrecen
Debrecen, Hungary
- Pálinkás, J.

University of Notre Dame
Indiana, USA
- Bauder, W.
- Collon, P.
- Kashiv, Y.
- Robertson, D.
- Schmitt, C.J.
- Tang, X.D.

UTTAC
Tsukuba, Ibaraki, Japan
- Kinoshita, N.

ISBN 978-3-95450-123-6